Characterising low-cost sensor performance for the design and development of a low-cost, high-precision, multi-parameter clustered sensor instrument for outdoor air quality monitoring.

Katie Rose Smith

PhD

University of York

Chemistry

January 2019

Abstract

Low-cost sensors (LCS) for the detection of atmospheric composition are being increasingly used for monitoring air quality. Increasing the number of measurements locations in an air quality network can be useful for the validation of atmospheric models and provide improved estimates of personal pollution exposure. Performance of LCS, relative to existing reference instruments, has been seen to be highly variable, but there are currently no formalised standards or certified calibration procedures for their use. Within this project, laboratory studies and field-testing were undertaken to characterise the performance of several commercially available LCS. The sensors tested prioritised those atmospheric pollutants that are regulated under the UK and EU legislation, e.g. nitrogen dioxide. A range of sensor technologies, including electrochemical and metal oxide sensors has been evaluated. Clustering multiple identical sensors was an effective approach that improved data quality and reduced the required frequency of calibration with co-located reference instruments, also improving medium frequency noise and sensor reproducibility. New approaches to resolving sensor chemical cross-interferences were explored, from simple linear regression to machine learning algorithms. This improved the agreement between sensors and reference instruments in the laboratory and field. Clusters of sensors were built into a multi-pollutant instrument which was deployed in various locations to investigate sensor performance in different environments. Through the application of machine learning over all the sensor signals, it was possible to produce a signal that was close to the reference measurements, indicating that LCS can be used in a similar manner to an air quality monitoring station. One implication of this is that LCS can be used over the short term (weeks - months) to complement the existing networks by increasing the number of ground observations, which would facilitate the interpolation of pollutant concentration gradients between relatively sparse network stations to better estimate pollution maps.

Contents

Abstract **2**

List of Contents **3**

List of Tables **7**

List of Figures **30**

Acknowledgements **31**

Authors Declaration **32**

1 A review of low-cost sensors used in scientific research **33**

1.1 The importance of air quality monitoring 33

1.2 Ozone (O_3) 38

1.2.1 Tropospheric O_3 formation 39

1.2.2 Influence of stratospheric O_3 43

1.2.3 Reference ozone instrumentation 43

1.3 Nitrogen dioxide (NO_2) 44

1.3.1 Reference NO_2 instruments 47

1.4 Carbon monoxide (CO) 49

1.4.1 Reference CO instruments 51

1.5 Volatile Organic Compounds (VOCs) 53

1.5.1 Reference VOC instrumentation 57

1.6 Particulate Matter 59

1.6.1 Human health implications of PM 60

1.6.2 Reference PM instrumentation 62

1.7 Carbon dioxide (CO_2) 64

1.8 Performance criteria for instrumentation 65

1.8.1 Air Quality Monitoring 67

1.8.2 UK Air Quality Monitoring Networks 68

1.8.3 Monitoring with low cost sensors (LCS) 71

1.9 Sensor Technology 73

1.9.1 Metal Oxide Sensors (MOS) . . . 73
1.9.2 Electrochemical (EC) sensors . . . 77
1.9.3 Non-Dispersive Infra-Red (NDIR) sensors . . . 80
1.9.4 Low cost Optical Particle Counters (OPCs) . . . 81
1.10 Sensors in Atmospheric Research . . . 83
1.10.1 Aims of thesis . . . 84

2 Laboratory experiments to characterise the response and sensitivities of the Metal Oxide Sensors (MOS) 86
2.0.1 Introduction to low-cost MOS total VOC sensors . . . 86
2.1 Metal oxide sensors . . . 86
2.1.1 Analysis procedure . . . 89
2.2 MOS response towards VOCs . . . 90
2.2.1 Defining VOC gas cylinders used for calibration of sensors . . . 90
2.2.2 Concentrated VOC mix . . . 91
2.2.3 Diluted VOC mix . . . 93
2.3 MOS and the GC-MS . . . 98
2.3.1 Methods . . . 98
2.3.2 TGS2602 Total VOC sensors . . . 100
2.3.3 Ambient air sampling with co-located SIFT-MS . . . 104
2.3.4 The affect of flow rate upon the MOS sensors . . . 109
2.3.5 The affect of humidity and temperature upon the MOS sensors . . . 110
2.3.6 Manifold design . . . 114
2.3.7 Using a palladium catalyst to correct from cross interferences . . . 117
2.4 Characterising MOS cross interferences . . . 119
2.4.1 Carbon monoxide (CO) . . . 119
2.4.2 Nitric oxide (NO) . . . 121
2.4.3 Sulphur dioxide (SO_2) . . . 122
2.4.4 O_3 . . . 124
2.5 Different MOS sensors . . . 125
2.5.1 TGS2611: Methane sensors . . . 125
2.5.2 TGS2620: Alcohol sensors . . . 126
2.5.3 P-type MOS sensors . . . 129
2.5.4 Photo-ionisation Detectors (PID) . . . 131
2.6 Summary . . . 132

3 Using a clustering approach to optimise atmospheric sensor performance 135
3.0.1 Variability in individual sensors response to isoprene . . . 136
3.1 Characterising MOS response in zero air . . . 138
3.1.1 TGS2602 Total VOC MOS in zero air . . . 138

3.1.2 Power spectral density for MOS zero air response . . . 139
3.1.3 Autocorrelation plots for zero air MOS response . . . 141
3.2 Different types of MOS sensors in zero air . . . 143
3.2.1 Probability Density Function (pdf) for each MOS type in zero air . 145
3.3 Indoor ambient air sampling with MOS . . . 148
3.3.1 TGS2602 total VOC MOS indoor air experiment . . . 148
3.3.2 CO and OVOC MOS deployed in indoor air experiment . . . 154
3.3.3 Comparison of CO EC and CO MOS during indoor deployment . . 157
3.3.4 Clustering Total VOC MOS sensors . . . 159
3.4 Electrochemical sensor variability . . . 161
3.4.1 Electrochemical sensors and zero air . . . 161
3.4.2 Power spectra for EC sensors in zero air . . . 165
3.4.3 Autocorrelation plots for the EC in zero air . . . 167
3.4.4 CO EC variability . . . 169
3.4.5 Clustering EC and MOS . . . 172
3.5 Summary of Chapter 3 . . . 172

4 Initial field deployments of a clustered sensor device 176
4.0.1 Experimental . . . 176
4.0.2 Deployment of the sensor instrument at a static site in Beijing . . . 177
4.1 Warm-up time . . . 180
4.2 MOS sensor performance . . . 183
4.2.1 MOS temperature and humidity correction . . . 185
4.2.2 MOS versus GC-FID . . . 188
4.2.3 Field calibration of MOS using GC-FID . . . 193
4.2.4 MOS versus SIFT-MS . . . 195
4.2.5 MOS versus organic acids . . . 200
4.3 EC sensor performance . . . 202
4.3.1 Performance evaluation of individual EC sensors . . . 202
4.4 Simple linear regression . . . 203
4.5 Background to supervised machine learning (ML) . . . 208
4.5.1 Cross validation and Evaluation . . . 209
4.5.2 Boosted linear regression (BLR) and Boosted Regression trees (BRT) 211
4.5.3 Boosted linear regression (BLR) . . . 212
4.5.4 Boosted regression trees (BRT) . . . 214
4.5.5 Gaussian process (GP) ML . . . 219
4.6 Evaluating the different analytical techniques applied to EC sensors . . . 222
4.6.1 NO_2 . . . 222
4.6.2 O_X . . . 225
4.6.3 CO . . . 226

4.6.4 Overall . . . 227
4.6.5 MOS and machine learning . . . 227
4.6.6 NO - Concentration prediction without a sensor measurement . . . 233
4.7 Summary . . . 238

5 Robust quality comparison of a clustered sensor device against reference instruments 243
5.1 Introduction . . . 243
5.2 Static measurements using the sensor instrument . . . 244
5.2.1 Reference instruments during the NOAA deployment . . . 244
5.2.2 Static EC sensors . . . 245
5.2.3 CO_2 NDIR devices . . . 253
5.2.4 MOS sensors . . . 256
5.3 Machine learning using the static sensors . . . 262
5.3.1 Machine learning with the China BRT and BLR algorithms . . . 263
5.3.2 Retraining the ML algorithms using BRT . . . 267
5.4 Optical particle counters (OPCs) . . . 275
5.5 Mobile measurements of low-cost sensors . . . 279
5.5.1 Analysis of LCS installed on a mobile platform: mountain road . . . 281
5.5.2 Mobile measurements around the inner city and hydraulic fracturing region . . . 284
5.6 Deployment of a sensor instrument in a remote location . . . 292
5.7 Total VOC TGS2602 MOS in the rainforest . . . 294
5.7.1 TGS2620 OVOC MOS . . . 295
5.8 EC in the Rainforest . . . 302
5.9 Summary of Chapter 5 . . . 305
5.9.1 NOAA Summary . . . 305
5.9.2 Sensors in rainforest summary . . . 307

6 Recommendations regarding the use of sensors for scientific research 308
6.1 Comparison of different types of sensors used . . . 309
6.1.1 NO_2 EC . . . 309
6.1.2 CO EC . . . 313
6.1.3 O_X EC . . . 315
6.1.4 CO_2 NDIR . . . 318
6.1.5 MOS sensors . . . 319
6.1.6 Clustering . . . 323
6.1.7 Low-cost sensor instrument . . . 323
6.1.8 Calibration . . . 324
6.1.9 Machine Learning . . . 326

6.2 Applications of LCS 327
6.2.1 Future work 333
6.2.2 Overall summary 336

Abbreviations **338**

References **340**

List of Tables

1.1 Criteria pollutants and the thresholds for their concentrations in ambient air set by the WHO [193] and the EU [53] [52]. The countries that fall under these regulation are required to meet these objectives to ensure the regions have air of a sufficient quality. To assess air quality, ground observations of atmospheric pollutants made with standardised instrumentation are used. . 35

1.2 Examples of different groups of VOCs, example compounds, major emission sources and their impacts on human health and the environment [89]. . . . 55

1.3 A calculation of the area that each AURN site is represented of, assuming each monitoring site is equally spaced, with a total UK area of 242, 495 km^2. Number of sites for each pollutant was found using the DEFRA UK AIR website [41] 72

2.1 There are many different types of MOS sensors commercially available to monitor VOC compounds. Four Figaro MOS sensors, for monitoring Total VOC, methane, propane/butane and alcohol compounds were used as part of this research project. 89

2.2 A comparison between the performance of two MOS sensors after exposure to different VOC concentrations at different humidity ranges. The MOS sensitivity towards VOCs was calculated by producing a plot of VOC concentration (x-axis) against the MOS output voltage (y-axis). Linear regression was used to calculate a gradient (mV ppb^{-1}) which was defined as the sensitivity. A gas standard (VOC8) was used in conjunction with mass flow controllers to produce the different VOC concentrations. 92

3.1 The correlation coefficients calculated between the median OVOC, CO and VOC sensors whilst they were co-located during the indoor air experiment. 154

3.2 The magnitude of the random noise component of the variability between six of the CO, NO_2 and O_X EC after three and a half days of exposure to zero air. The random noise component for each sensor was calculated by subtracting the median response of the sensors in zero air from each sensor time series. The magnitude of the random noise component was determined by identifying the spread of the sensor signals. 165

4.1 Results from the linear regression of total alkanes, total alkenes and total aromatic compounds detected by the GC-FID after correlation with the corrected median MOS. 193
4.2 Each of the individual NO_2, O_X and CO EC were correlated with their respective reference observations to identify the spread in a cluster of 6 EC responses. 203
4.3 The NRMSE and RMSE (in brackets) between the NO_2 reference observations and the NO_2 observations made by the uncalibrated median EC and the NO_2 concentration estimate after SLR, BLR, BRT and GP were all applied separately. The different concentration ranges were investigated as the NRMSE and RMSE were computed for data that fell between 0 - 25 %, 25 - 50 %, 50 - 75 % and 75 - 100 % of the maximum NO_2 reference concentration. The NRMSE was calculated by dividing the RMSE between the reference observations and the sensor values by the mean reference concentration for the respective bin. 224

5.1 The people at NOAA who were responsible for each of the different reference instruments used to to evaluate the performance of the sensors. 245
5.2 Linear regression parameters to describe the linear relationship between the temperature of the air flow and the median MOS signal for the VOC, PrBu and OVOC MOS clusters. 262

6.1 The linear regression parameters obtained when 6 NO_2 EC and the instantaneous median NO_2 EC were correlated with the reference NO_2 instrument during the Beijing deployment (24 days). The linear parameters obtained for the same deployment when different methods (SLR, BLR, BRT and GP) were applied to improve the quality of sensor data. The predicted NO_2 concentration was then evaluated against the reference NO_2 observations using linear regression. 311
6.2 The linear regression parameters obtained when 6 CO EC and the instantaneous median CO EC were correlated with the reference NO_2 instrument during the Beijing deployment (24 days). The linear parameters obtained for the same deployment when different methods (SLR, BLR, BRT and GP) were applied to improve the quality of sensor data. The predicted CO concentration was then evaluated against the reference CO observations using linear regression. 314

6.3 The linear regression parameters obtained when 6 O_X EC and the instantaneous median O_X EC were correlated with the reference O_X instrument during the Beijing deployment (24 days). The linear parameters obtained for the same deployment when different methods (SLR, BLR, BRT and GP) were applied to improve the quality of sensor data. The predicted O_X concentration was then evaluated against the reference O_X observations using linear regression. 317
6.4 The Total VOC median, OVOC median, CH_4 median and PrBu median MOS signals were correlated with the humidity of the air reaching the sensors and the temperature to identify if the MOS signals were detecting changes to these environmental conditions. 322
6.5 Improvements to the LCS instrument, to optimise the performance of the instrument and to make it simple to use and robust in the field. 333

List of Figures

1.1 The longer a species exists in the atmosphere, the further it can be transported, with some pollutants, e.g. CO_2, which has an atmospheric lifetime of up to 200 years, being defined as well-mixed because they are transported over large, hemispherical distances. Figure adapted from Seinfield and Pandis 1998, [161]. 37

1.2 A brief summary of the sources and impacts of tropospheric O_3. 38

1.3 Photochemical production of tropospheric ozone via the primary emissions of VOCs and NO_X. 41

1.4 A brief summary of the sources and impacts of nitrogen dioxide (NO_2). . . 45

1.5 The ambient UK NO_X concentrations were due to decrease with the introduction of each successive Euro standard that applied increasingly stringent restrictions upon the pollutants emitted from vehicles in Europe. However, the ground observations of NO_X were different to how they should appear if the Euro standards were successful. 46

1.6 A brief summary of the sources and reactions of carbon monoxide in the troposphere. 49

1.7 Schematic to show the gas filter half filled with CO, for the reference CO measurement, and N_2, to allow for a measurement of CO in the sample of air. 51

1.8 Schematic to show the operation of a VUV fluorimeter, used to detect CO with a very fast time response and lower detectable limits. 52

1.9 A brief summary of the sources and impacts of volatile organic compounds. 54

1.10 Oxidation of propene, via OH addition over the double bond. The peroxy radical (RO_2) formed will go on to react with other species such as NO or HO_2 in the atmosphere. 56

1.11 A brief summary of the sources and impacts of particulate matter (PM). . 60

1.12 Performance criteria for NO_X, O_3 and CO instruments to monitor ambient concentrations of these pollutants. There are experiments conducted in the laboratory (blue), under controlled conditions and in the field (brown) to ensure the performance of the instrument is reliable when it has been deployed. 66

1.13 Performance criteria for instruments to continuously monitor benzene in the ambient troposphere. 66
1.14 A map of the UK, with the locations of the seven CO AURN sites shown as green pins and a breakdown of the different site classifications. 69
1.15 The locations of the 158 NO_2 AURN sites that are currently reporting data. The coloured boxes show the classification of the sites. 70
1.16 The locations of the AURN sites that currently monitor hourly ozone concentrations. The coloured boxes show the classification of the sites. 70
1.17 A schematic to show the resting state of a tin dioxide surface, with the adsorbed oxygen molecules and electrons being drawn out of the conductance band, causing an increase in the energy of the conductance band near the surface. This band bending leads to a reduced conductance. 74
1.18 Schematic to show a reducing compound reacting on the MOS active surface. By engaging the oxygen ions in a reaction, more electrons remain free to move in the conductance layer, inducing an increase in conductivity. . . 75
1.19 Diagram to show the internal layout of a typical amperometric electrochemical gas sensor. 79
1.20 A schematic of a CO_2 NDIR device. 80
1.21 The Beer-Lambert Law, rearranged to calculate concentration of the target gas (CO_2) in the NDIR sample tube. 81
1.22 Schematic to show the operation of a low-cost OPC device. 82
1.23 The price that each of the sensors was purchased at for use in this study. . 83

2.1 A Figaro TGS2602 Total VOC MOS sensor. The diameter of the sensor is 9.2 mm, with a total height of 10 mm. 87
2.2 Photo of a cluster of 8 MOS TGS2602 total VOC sensors, inserted into their Teflon housings which allowed electrical contact between the sensors and custom built circuit board. The white Teflon housings had a gold casing coating the holes where the MOS pins were inserted. 88
2.3 A schematic of a laboratory experiment. This experimental set-up was used to calibrate two MOS sensors with changing concentrations of a VOC mixture gas standard. For this schematic the VOC gas standard was located at the Gas Cylinder location and the flow was introduced to the zero air flow to allow for maximum mixing of the VOC standard with the zero air. The humidity and temperature were controlled and kept constant during calibrations. The sensors were housed in a metal box to act as a Faraday cage and reduce electrical noise. MFC = Mass Flow Controller. 90
2.4 Calibration curves to show the performance of a) MOS1 and b) a second sensor, MOS2 during exposure to changing concentrations of the VOC mixture, at 50 - 60 %, which is typical of the UK humidity. 91

2.5 Calibration curves to show the performance of a) MOS1 and b) MOS2 during exposure to a larger range (0 - 500 ppb) of VOC concentrations. . . 93
2.6 a) The MOS (MOS1: green, MOS2 : red) displayed different sensitivities towards changing total VOC concentration at different humidity ranges. b) As the calibrations were run at higher humidity's, the Normalised Root Mean Squared Error (NRMSE) of the calibrations decreased. The three calibrations with the concentrated (VOC8, total [VOC] = 40 ppm) mixture are shown as stars and the more dilute calibrations (total [VOC] = 1040 ppb) are shown as circles. 94
2.7 The eight MOS housed inside the custom-built Teflon manifold, with the sensors in series. Air was pushed through the system from the Pure Air Generator (PAG) and flowed around the Teflon block in accordance with the red arrows. 95
2.8 The sensitivities of 24 TGS2602 MOS sensors after exposure to a) VOC8 and b) OVOC gas standard calibrations at different humidity's. The box edges represent the interquartile range, the whiskers show the 5^{th} and 95^{th} percentiles and the line in the middle is the median. The black dots signify each sensors slope for the calibration. The light blue dashed line is at 0, to show some sensors displayed a negative correlation. 96
2.9 A flow diagram to show how a sample from a gas cylinder goes through the GC-MS system, with detection by either the mass spectrometer or MOS sensor. 99
2.10 Time series to show a GC-MS chromatogram (black) and corresponding MOS signal (blue), for the detection of peaks using the NPL30 standard. The table to the right of the plot displays the compounds, the peak numbers that were identified as being that compound and the mixing ratio of the compound in the cylinder. 100
2.11 Peakutils determined a baseline (blue) and the peaks (coloured sections of the black line) of the compounds were determined by comparing the GC-MS trace with the MOS signal over the same duration of time. 101
2.12 The peaks were integrated using the same methods for both the MOS sensor and the GC-MS spectra. The mean peak area over five injections of 700 mL of NPL30 gas standard, for each numbered peak was plotted to compare how well the GC-MS and MOS detect certain compounds. The standard deviation of the five spectra are plotted as black lines. 102
2.13 A comparison of the traces for the TGS2602 MOS signal (red) and GC-QTOF-MS (green) using the OVOC gas standard. 103

2.14 The peak areas were averaged over each of the OVOC gas standard injections for both the MOS trace (red) and the mass spectrum (green). The vertical black lines depict the standard deviation each of the averaged peak areas. 104
2.15 Experimental set up for the comparison of the SIFT-MS and two clusters of MOS. The instruments were co-located in the laboratory and used the same sample line, and the inlet was fed through the wall and sampled outdoor air. A diaphragm pump pulled air through the lines at a constant flow of 2500 sccm. 105
2.16 a) Time series of the NO+ compounds (black) with the median of MOS cluster 1 (green) and MOS cluster 2 (red). b) The correlation plot for the two median signals versus the SIFT measured concentration of the total NO+ ion count. 106
2.17 a) Each variable was plotted up with the median signal from each cluster, and a slope determined from the correlation plot. The slopes are colour-coded, with red being the highest slope, and blue the lowest. b) From each correlation plot for every variable, the R^2 value was determined and is also colour-coded to show the strength of the correlation between each variable. 107
2.18 The linear regression between the MOS and SIFT-MS was calculated three more times, with a scaling factor of 5 applied to a) the aromatic compounds, benzene, toluene and TMB, b) ketone compounds, acetone, 3-buten-2-one and butanone and c) alkenes, isoprene and 1,3-butadiene. 108
2.19 Analysing the affect of the flow rate upon 16 TGS2602 MOS sensors. The black dots show the MOS sensitivity towards the OVOC calibrations at the different flow rates and the colours indicate the NRMSE of each calibration. 109
2.20 Two TGS2602 MOS sensors were exposed to different humidity's of air for at least 6 hours. For each humidity, the mean (orange and pink dots) and standard deviation (black lines) of the MOS signal for each 10 % RH bin was calculated. 111
2.21 The calibration curve for the median from each sensor cluster as the humidity of the air flow to the sensors was changed. The dots are the mean MOS signal for each 10 % humidity bin, and the black lines are the standard deviation for each data point. The calibration curves for a) the total VOC MOS sensors (TGS2602), b) propane/butane (TGS2610) MOS sensors, c) methane (TGS2611) MOS and d) OVOC (TGS2620) MOS sensors. 112

2.22 The four clusters of TGS2602, TGS2611, TGS20 and TGS2610 sensors were housed in an instrument box and therefore the box could be heated. The temperature in the plots refers to the temperature of the air flowing to the sensors, and the calibration plots for all four different types of sensor are as follows, a) the total VOC MOS sensors (TGS2602), b) propane/butane (TGS2610) MOS sensors, c) methane (TGS2611) MOS and d) OVOC (TGS2620) MOS sensors. 113
2.23 Manifolds 1, 2 and 3 and the sensor response to two OVOC calibrations were run through the set up. The slope for each sensor against OVOC concentration was colour-coded according to the colour bar. The arrows on the sensor diagrams show the flow of air around the manifolds. 116
2.24 Experimental set up for monitoring the affect of scrubbing VOCs with a palladium catalyst. During the experiment with no catalyst, the palladium catalyst was removed and extra tubing added in place to ensure the air travelled the same distance before reaching the MOS sensors. 117
2.25 Three VOC8 calibrations were conducted at 85 % RH with 8 TGS2602 MOS sensors. a) The first experimental set-up was done with no catalyst, b) the second included the palladium catalyst cold (at r.t.p.) and c) the third plot shows how the sensors responded when the palladium catalyst was switched on and was heated to 375 °C. 118
2.26 Calibration curves for a) MOS1 and b) MOS2 when exposed to changing concentrations of CO. 120
2.27 The MOS sensitivity towards CO (MOS1 : pink, MOS2: purple) was small compared to the MOS sensitivity towards a dilute mixture of VOCs (MOS1: green, and MOS2 : red) at a humidity range of 0 - 10 % RH, which typically shows the highest MOS sensitivity. A dashed line, depicting 0 mV ppb^{-1} is also shown for reference. 121
2.28 The MOS sensitivities for two sensors towards NO (MOS1 : blue, MOS2 : navy) and VOCs (MOS1: green, and MOS2 : red), for calibrations run at different humidity's. A dashed line, depicting 0 mV ppb^{-1} is also shown for reference. 122
2.30 Boxplots to show the distribution of the SO_2 sensitivities from each of the ten individual MOS sensors. The boxes display the 25^{th} and 75^{th} quartiles, the whiskers show the 5^{th} and 95^{th} percentiles of the data and the line through the box is the median sensitivity (mV ppb^{-1}). The calibrations were run at two different humidity's to determine if the performance of the sensors changed in more humid air. 123

2.29 Experimental set up for ten MOS sensors being tested to investigate their response towards cross interferences. The eight MOS that were added to the set up were housed in a custom-built Teflon manifold to flow air over each sensor in series. 123
2.31 Box plots to show the variation in the MOS sensitivities towards changing ozone concentrations as the humidity of the air the sensors are exposed to increases. The box edges are the 75^{th} and 25^{th} quartiles, the line in the middle of the box is the median slope and the whiskers are representative of the 5^{th} and 95^{th} percentile slopes for the calibrations conducted at five different humidity's. 125
2.32 The TGS2611 methane MOS signal (blue) during five injections of VOC8 into the GC-MS. The corresponding GC-MS spectra are shown in black. . 126
2.33 An example of a 10 mL VOC8 injection into the GC-MS with TGS2620 MOS in the olefactometer port. All 8 compounds were identified using the NIST library and the mass spectrum. The MOS peaks were assigned accordingly. 127
2.34 Comparing the peak areas for the GC-MS and the TGS2620 OVOC MOS sensor when the VOC8 gas standard was injected into the GC five times, with 10 mL sample volume. 127
2.35 Using the GC-QTOF MS experiments described in Chapter 2, the relative responses of the VOC and OVOC sensors have been summarised with a simplified plot to show how different locations (with different VOC compositions) would affect the VOC and OVOC sensors differently. By comparing the responses of both sensors, it would be possible to obtain an estimate of the VOC composition. 128
2.36 The slopes of the a) p-type and b) n-type MOS sensors when an OVOC calibration was run, at 3 % RH humidity in the laboratory. Both plots share a y-axis for ease of comparison. Each MOS sensor position within the manifold was given a different colour to identify individual n-type or p-type sensors. 129
2.37 P-type sensors responding to changing VOC concentrations with the temperature pulsing mode operational. The table shows the individual p-type sensors sensitivity and RMSE for the OVOC calibrations. 131
2.38 The five subplots show five different PIDs responding to typical amounts of isoprene (concentrations shown in black) in a laboratory experiment. . . . 132
2.39 A comparison of the peak area response for the TGS2602 and TGS2620 MOS sensors. Only compounds that eluted as single peaks are shown, and the compounds are colour-coded to identify VOC groups. 133

3.1 The TGS2602 total VOC MOS display different sensitivities towards changing concentrations of isoprene at different humidity's. In dry air (0 - 10 % RH) the MOS sensitivity is high, but is very variable which would make it difficult to quantify the isoprene concentration. Figure taken from Smith et al. 2017. [165] 137
3.2 The seven total VOC MOS sensors sampled zero air over the weekend, with a constant humidity of 0 % RH and temperature of 25 °C. A typical MOS sensitivity of 12.5 mV ppb^{-1} has been applied to convert the signals from voltages to equivalent $ppb_{[VOC]}$. a) The individual sensor signals are shown as coloured traces, and the median of the seven working sensors in the black trace. b) Each sensor with the median TGS2602 sensor subtracted to leave the residual noise of the seven normalised sensor signals. 139
3.3 The power spectra for the one of the MOS TGS2602 sensors to investigate the different frequencies that make up the sensor signal (black) and the normalised sensor signal (red, with the median trace subtracted from the sensors time series). The power spectra are plotted with logarithmic x and y axes and resemble red/pink noise for both signals. 140
3.4 Autocorrelation plots for the TGS2602 MOS sensors signals and their normalised signals (with the median MOS sensor trace subtracted). The coloured lines represent the autocorrelation for seven MOS sensors and the shaded areas display the regions of 95 % confidence intervals. The sensor signals begin with a high amount of autocorrelation and this decreases linearly before the sensors become uncorrelated and enter the 95 % confidence interval at around 30 minutes. 142
3.5 The other types of MOS sensor, the propane/butane MOS (teal), the OVOC MOS (orange) and the methane MOS (pink) all displayed signs of an upwards temporal drift over the two days during the zero air experiment. . . 144
3.6 Probability density function (pdf) plots for the zero air experiment, for each different type of MOS sensor. The top row of plots are the pdfs for each sensor in zero air: a) seven TGS2602 total VOC MOS, b) eight TGS2610 propane/butane MOS, c) eight TGS2611 methane MOS and d) eight TGS2620 OVOC MOS. For each type of MOS sensor, the individual sensors within the cluster all have very similar shaped pdfs, and hence show similar variability about the average signal. The bottom row (e to h) are the pdfs for the normalised sensors after the median signal for each respective cluster has been subtracted, and are in the same order. The pdfs for the sensors in zero air are typically wider, showing a larger range than the pdfs for the normalised MOS. 146

3.7 Time series for 21 MOS sensors sampling the indoor ambient air in an office environment. The sensors were all offset to 0V at the beginning of the experiment and left to run over the next five weeks. Every Friday, at midnight is marked on the time series with a red dashed line, to indicate where the weekends begin and sampling weeks. Times where there were no people in the office, are marked as shaded yellow blocks, to better show times where less variability in the MOS signals was expected. 149
3.8 The median MOS signal (black) was compared against the temperature (a, red) and humidity (b, blue) during the deployment of the desk sensors after the 20th December. 150
3.9 Each of the 21 total VOC MOS sensors was correlated with all the other total VOC MOS sensors and the R^2 value for these 210 correlations is shown in the box plot. The middle line is the median, the outer edges of the box plot are the interquartile range and the whiskers are the 5th and 95th percentiles of the R^2 values. The diamonds show outlying points, which were all R^2 values from correlating 20 MOS sensors with the poorest performing sensor (blue line in Fig. 3.7.) 151
3.10 Rank order plot to show how the sensors were ordered by sensor output voltage over the five weeks. The data was binned into 1-hour bins, with the average value of each bin determined. The MOS ranked from 1 - 21 depending on the magnitude of the average, and this ranking has been colour coded from purple (low ranking sensors) to green (a sensor reporting a high value). 153
3.11 Time series for the a) OVOC MOS and b) CO MOS in the indoor air experiment, with the difference between the maximum and minimum reporting sensor after each week. The yellow shaded area represents time during the experiment when the office was vacant. 155
3.12 Rank plots for a) The eight CO MOS sensors and b) the eight alcohol MOS sensors, with all MOS sensors displaying a large degree of variability and lots of random changes to the sensors ranked position. The y-axis for (a) ad (b) is a number from 1 to 8 to indicate the magnitude of the sensor response relative to the other sensors in the cluster. The sensor with the highest reporting signal is assigned number 8 and the sensor with the lowest reporting value assigned number 1. 156
3.13 Comparing the response between the seven CO MOS sensors against the CO electrochemical sensor during the indoor air low-cost sensor experiment. Each of the different CO MOS sensors were assigned a different coloured set of data points and linear regression line. 157

3.14 The kernel density function to compare the median CO MOS response with the CO EC response during the indoor air experiment. 158
3.15 Figure taken from Smith et. al. 2017 manuscript [165]. Box plots to show how, as the number of sensors within a cluster increases, the median signal in a subset of sensors (containing one, two, three, ... to 11) gets closer to the median sensor signal for 21 sensors. The red diamonds within the box plots show the mean slope, the grey solid lines show ±3 standard deviations from the mean. The blue and red dashed lines are for the ±3 standard deviations on the mean with a 1/N decrease and a $1/\sqrt{N}$ decrease respectively. 160
3.16 Zero air analysis for the CO EC sensors a) The CO sensors, each with their unique factory calibration applied, offset to 0 ppm at the beginning of the zero air experiment. The black line is the instantaneous median for the CO EC cluster and the coloured lines are the individual sensor traces. b) The trace for each CO EC after the median sensor signal has been subtracted from it, leaving the random noise signal. 162
3.17 The temperature of the air flow to the sensors becomes much more variable after 45 hours since the experiment began. The time scales in the temperature variability are matched by the increased variability in all 6 CO EC sensors responding to the same air. 163
3.18 a)Time series to compare the median of the six CO EC sensors (black) and the CO EC outlying sensor (blue). The two signals exhibit high covariance until mid-way through the zero air exposure. b) The correlation plot between the outlying CO EC sensor (blue in plot a) with the median CO EC to identify if the two data sets were still correlated even after the outlying CO EC began to show drift. The data points are colour coded by time, dark colours representing the start of the experiment, lighter colours towards the end. 164
3.19 Each of the 18 electrochemical sensors was analysed by determining the power spectrum for that sensor. The power spectra all looked very similar for each sensor in it's respective CO, NO_2 and O_X sensor clusters, and so just one sensor from each clusters Fast Fourier transform is shown. The dark red, dark green and dark blue colours are the power spectra for one of each of the a) CO, b) NO_2 and c) O_X sensors and the lighter colours are the power spectra for the same sensors after normalisation. 166
3.20 The autocorrelation plots for the 6 CO sensors in zero air (a) and the 6 normalised CO EC (b), after the median CO signal was subtracted from each sensor signal. 167

3.21 Plots a), b) show the autocorrelation plots for the O_X and NO_2 EC sensors during the zero air experiment. Plots c) and d) are the resulting autocorrelation plots when the median O_X and NO_2 EC sensor signal were subtracted from the respective signals to investigate the randomness in the EC noise signals. The shaded areas represent the regions of 95 % confidence levels. . 168
3.22 a) The time series of CO EC sensors (coloured lines) co-located with a CO Aerolaser reference instrument (black line). b) The rank order plot for 6 CO EC sensors sampling in Beijing, November and December 2016. 170
3.23 The slopes for the CO Aerolaser plotted against the average of different amounts of CO EC sensors. The red diamond is the mean slope, the edges of the box and whisker plots show the interquartile ranges and the whiskers show the 5^{th} and 95^{th} percentiles. The solid grey line is the ± 3 standard deviation of the mean. Plot taken from Smith et al. 2017 [165]. 171
3.24 A comparison of the cost and power usage of a single EC sensor, a cluster of six EC and the respective O_3 reference instrument. 172

4.1 Electronic schematic to show how half of the sensors will be laid out in the sensor instrument. Two MOS sensors were permitted for each ADC channel, and the number of the sensors, relating to their position on the circuit board is shown in the schematic. The EC sensors required data collection from both the working and auxiliary electrode therefore there could only be one sensor per address. The humidity and temperature probes are recorded via this Arduino too. This set up was then duplicated for the other 25 gas sensors. A mini-computer (LattePanda 4G/64GB, Latte Panda) formatted and stored the sensor data after receiving it from the Arduinos. 178
4.2 Photographs of the two layers of components within the sensor instrument deployed in Beijing, China. Components of interest are labelled with blue arrows. 179
4.3 The blue pin shows the location of the measurement campaign site where the sensor instrument was located (IAP site) with respect to the surrounding region of Beijing, China. The inset map shows the central and northern location of the IAP site amongst Beijing's road network. 179
4.4 The a) NO_2, b) O_X and c) CO EC during the warm-up period between 1700 H on 30^{th} May 2017 until 00:00 on the 2^{nd} June 2017. 181
4.5 Each of the EC sensors experienced a step change that occurred within two hours of the power to the sensor instrument being switched on. This was attributed to the sensors warming up after being packed in a shipping box for a month. 182

4.6 The interaction between the median total VOC MOS signal (black) and the individual MOS sensor signals (purple) was consistent throughout the warm-up period. The variations in the median MOS signal were more influenced by the temperature of the air (b, red trace) flow than displaying any discrepancies due to MOS requiring a warm up period. 182
4.7 The instantaneous median (red) of all 31 TGS2602 total VOC working MOS sensors (grey) represents the general trends of all the MOS sensors well. . . 184
4.8 A correlation matrix, using the Pearson's coefficient to compare the correlations between every MOS with all the other MOS sensors. The colour bar shows that a high correlation is denoted by a red colouring and no correlation is dark blue. The majority of MOS sensors are highly correlated, displaying a Pearson's coefficient of greater than 0.8. 184
4.9 Timeseries of the median MOS signal (dark red) and the temperature of the air flowing to the sensors (yellow). 185
4.10 The correlation between temperature and the median MOS signal during the deployment of the sensor instrument in Beijing. b) The kernel density function for the temperature and median MOS data to display the relative distributions of data. 186
4.11 The original median MOS sensor (dark red) had the temperature correction (red) subtracted away from it to leave the temperature corrected MOS signal (green). The temperature correction was determined by calculated the expected MOS signal, from fluctuations in temperature, using the linear equation in Fig. 4.9. 187
4.12 There was a negative correlation between the median MOS signal and the relative humidity as measured by two RH probes (a). b) The kernel density plot for the relative humidity and median MOS signal. 188
4.13 The MOS sensors are easily affected by changing RH and temperature in their environment and so both a temperature and humidity correction, calculated using the China MOS signals, has been subtracted from the median MOS signal (purple). The temperature and humidity corrected MOS signal is shown in dark red. 189
4.14 a) The temperature and humidity corrected median MOS signal (purple) plotted alongside the sum of all the VOC measured by the GC (black). b) The difference between the corrected median MOS and the total VOC concentration from the GC. If the GC time series is greater than the MOS the colour is green, and if the MOS is greater than the GC, the shading is red. 190

4.15 a) Correlation plot between the total VOC from the GC and the corrected median MOS. b) A comparison between the distributions of the corrected median MOS data and the total VOC concentration reported by the GC FID. 192
4.16 The median MOS signal (mV, light purple) is shown for the entire campaign. The first week of deployment was used as a calibration week and a linear equation to compare the median MOS signal (V) and the total VOC concentration as detected by GC (grey) was determined. This equation was then rearranged so that the median MOS could better predict the total VOC concentration (green). 194
4.17 The correlation between the GC compounds and the MOS calibrated with sum of the a) alkane, b) alkene, c) aromatic and d) total VOC compounds from the GC. The aromatic compounds provided the strongest match to the reference measurements. 195
4.18 A stacked plot to show the relative concentrations of the different class of VOC compounds measured by the SIFT-MS. The number of compounds that make up each compounds groups are displayed in the parenthesis, next to the class name. The median MOS signal ($ppb_{[VOC]}$) is shown as a light green line and this generally follows the same pattern as the total VOC concentration (black line) from the SIFT. 197
4.19 The median MOS voltage signal was compared with the SIFT-MS Total VOC concentration using a correlation plot (a) and a kernel density function (b). 197
4.20 Four covariance-variance matrices of the normalised SIFT-MS and MOS data to show how well the total VOCs measured by the SIFT-MS and the median MOS signal co-vary after different time averages were applied. The yellow outlined boxes represent the covariance between the two variables, with the red outlined box highlighting the time averaging that produced the highest covariance. The top left box, is the variance within the SIFT-MS total VOC signal and the bottom right is shows the variance in the median MOS sensor. 198
4.21 The comparison between the temperature and humidity corrected MOS signal and the different compound classes from the SIFT-MS measurements using a) R^2 and b) NRMSE parameters. 199
4.22 The MOS sensors were weakly and negatively correlated with four organic acids measured by a Chemical Ionisation Mass Spectrometer (CIMS) operated by the University of Manchester. Each plot represents the median MOS signal compared to a different organic acid measured by the CIMS: a) $C_3H_4O_3$-$C_4H_8O_2$, b) $C_5H_{10}O$, c) $C_3H_6O_2$ and d) $C_2H_4O_3$. 201

4.23 Timeseries of 6 NO_2 EC sensors deployed in Beijing (coloured lines), plotted on the same axis as the median NO_2 EC to display that the instantaneous median of the EC cluster detected the variance in NO_2 concentrations detected by each NO_2 EC. 204
4.24 a) Time series of the instantaneous median NO_2 EC sensor (grey). The median sensor appeared to over compensate for fluctuations in the NO_2 concentration, when compared to the reference NO_2 measurements. b) The correlation plot used to determine the linear parameters for *in situ* calibration of the NO_2 EC sensors, and c) two over-laid correlation plots to compare the difference between the un-calibrated and SLR calibrated NO_2 sensors in the testing period. 205
4.25 The correlation between the O_X (a) and CO (b) EC sensors with their respective reference measurements. The grey scatter plot shows the correlation between these when the sensor median has not been calibrated using simple linear regression, whereas the a) O_X blue and b) CO red scatter plots show the impact of *in situ* calibration with co-located reference instruments, upon the EC sensors. 206
4.26 The spread of the uncalibrated (red) and calibrated a) O_X EC (blue) when the (O_3+NO_2) measurements were 39.9 - 40.1 ppb, and b) NO_2 (green) EC when the NO_2 reference reported 39.9 - 40.1 ppb. The EC sensors both show a large amount of variability that means that it would be impossible to rely on these measurements to observe if the concentration is violating any regulations. The application of SLR narrows the spread of sensor data points, improving the accuracy of the sensor data a bit. 207
4.27 Schematic to explain how ML techniques can help to correct from cross interferences, by identifying all the relationships between the sensor box measurements and the reference data. 209
4.28 Predicted O_X median sensor (blue) using boosted linear regression. The reference O_X measurements were used as the training label (red) in the training period, but used to compare with the predicted O_X in the testing data set (black). The grey line is the median O_X sensor with no calibrations apart from the Alphasense conversion factors applied. Inset: The correlation plot between the predicted O_X sensor and the reference measurements in the testing set. 213

4.29 Using BLR to predict the a) NO_2 median sensor concentration estimate (green) and b) CO median concentration estimate. For both types of EC, the training period included 8490 data points, although the CO started a little later due to an offset in the CO Aerolaser on the 2nd June 2017. The reference measurements for the training period are in red, and the NO_2 and CO median sensor with no calibration is shown in grey for the respective plots, over both the training and testing periods. Where the reference data was used purely to compare the performance of the BLR predictions it is plotted as a black line. The green shaded area in the NO_2 plot (a), marks where the NO_2 concentration exceeds the maximum value in the training period. 215
4.30 a) The time series of the BRT predicted NO_2 sensor signal (green) compared to the uncalibrated NO_2 EC sensors (grey) and the NO_2 CAPS reference measurements (black). The purple circles in both a) and b) show where the BRT prediction failed to extrapolate the learnt trends to capture the NO_2 concentrations, when they exceed 193 ppb (shown as the shaded light green area). 217
4.31 For each BRT analysis conducted upon the a) O_X, b) NO_2 and c) CO EC sensors the relative contributions of each variable to the overall BRT algorithm used to make the the prediction was determined. 219
4.32 The correlation between the a) GP predicted NO_2, b) GP predicted O_X and c) GP predicted CO concentrations and their respective reference instrument measurements. 220
4.33 a) The GP predicted NO_2 concentration (green) with the 3x standard deviation from the GP estimate (yellow) plotted too. The NO_2 reference observations are shown in black. The GP prediction and NO_2 CAPS observations are plotted on a logarithmic axis to emphasise the differences between the two time series and to highlight where the greatest uncertainty in the GP prediction occurred. The temperature and humidity time series, b) are plotted to indicate that the uncertainty for the GP prediction was highest when the temperature was greater than 30 °C, or when the RH was greater than 85 %. GP was therefore a technique to identify interfering conditions that impact the EC sensors performance as these periods of uncertainty occur when the relationships between the sensors are different. compared to the relationships in the training data. 221

4.34 Comparison of the different approaches to optimise the NO_2 sensor data so that it provides a more robust and accurate measurement of the environment. The GP prediction of NO_2 displayed the lowest RMSE when compared to the reference measurements. There were two NO_2 CAPS instruments on site to enable a reference versus reference comparison to be made. 223
4.35 Comparison of the different approaches to optimise the a) O_X and b) CO EC sensor data so that it provides a more robust and accurate measurement of the two pollutants in Beijing. 226
4.36 a) The training and testing time series using the total SIFT ion count as a training label during the training phase (red) and using this with BRT and all the sensor data from the sensor instrument to make a total SIFT prediction (teal) in the testing phase. The grey line shows the median MOS signal (V), corrected by temperature and humidity which was used for the prediction. b) The correlation plot for the reference Total SIFT and the BRT prediction, showing a moderate, positive correlation (R^2: 0.4 and slope: +0.5) and c) the gain feature from the decision trees used to train the BRT algorithm to predict the total SIFT concentration levels using all available sensors in the sensor instrument. The NO_2 and CO EC made the largest contributions towards the total VOC prediction. 228
4.37 The timeseries for the BRT-predicted a) aldehyde (brown) and b) aromatic (olive green) concentration estimates. The median MOS signal is shown in grey, and the reference SIFT-MS total aldehyde (a) and total aromatic (b) concentrations are in red for the training data set and black for the testing set. 230
4.38 Correlation plots comparing the BRT predictions of a) the sum of the aldehyde compounds and b) the concentration of the sum of all the aromatic compounds, to the reference measurements of these classes of compound as measured by the SIFT-MS. 230
4.39 BRT analysis performed upon the sensor instrument data, using benzene from the SIFT-MS measurements as a training label (red). The first 30% of the data was used for training and the remainder is the testing set and the benzene BRT prediction (brown). The grey line depicts the original median MOS signal. 231
4.40 A kernel density distribution plot was produced to further examine the relationship between the SIFT-MS benzene observations and the BRT-predicted benzene concentration. 232

4.41 The result from using the sensor data to predict the NO concentration, without there being a NO sensor measurement. The black line is the NO reference instrument and the pink is the NO prediction based upon the median NO_2, O_X, CO, VOC, RH and temperature sensors. 234
4.42 The bivariate kernel density function for a) the full range of NO concentrations and b) NO concentrations observed by both the reference and the prediction between 0. and 10 ppb 234
4.43 Using the NO_2, O_3, O_X (O_3 + NO_2, CO reference instrument data in place of the median NO_2, O_X, O_3 (O_X - NO_2, CO EC data to predict the NO concentration with BRT. 236
4.44 The gain contributions for the reference NO BRT concentration estimate made using the NO_2, O_X (O_3+NO_2), CO reference instruments, the median VOC MOS, RH and temperature as training variables (black bars). The gain contribution for the sensor predicted BRT concentration estimate is shown with the coloured bars. The sensor predicted BRT NO concentration estimate used the median NO_2, O_X, O_3 (O_X - NO_2), CO EC sensor signals as well as the median VOC MOS sensor, RH and temperature sensors as training variables. 237

5.1 The median (green) and the individual (grey) NO_2 EC sensor signals. There are only five NO_2 EC as one failed, therefore there are only five grey lines. 246
5.2 a) A comparison of the median NO_2 EC sensor (green) against the reference NO_2 chemiluminescence measurements (black). b) The correlation plot between the two instruments showing how well they correlated. 247
5.3 Timeseries to compare the variance displayed in the a) O_X reference and median EC sensor signals and in the b) CO reference and median EC signal. 248
5.4 The correlation and kernel density distribution plots for the O_X (a and b respectively) and CO (c and d respectively) median EC signals compared against their relevant reference observations for the duration of the static deployment of the sensor instrument. 249
5.5 The green, blue and red box plots show the slopes of the individual NO_2, O_X and CO EC sensors respectively, when plotted against their corresponding reference instruments. The grey coloured box plots indicate how well correlated the six sensors were to the reference observations as they show the spread of the R^2 values for the linear regression. For all box plots the middle line is the median, the edges of the box represent the interquartile range of the data and the whiskers are for the 5^{th} and 95^{th} percentiles. Any points that lie outside the box are marked as diamonds and indicate anomalous data. 251

5.6 The degradation of the O_X EC sensor performance as the relative humidity of the air reaching the EC sensors becomes very low. The probe measured negative values for RH, and this indicated that the air was very dry, around 0 % which is the limit of detection for the RH probe. 253
5.7 The time series, a) of the median of the three CO_2 NDIR (purple) and the CO_2 reference observations (black). The general profile of the reference measurements was detected by the NDIR devices, but the low-cost sensors did not mange to identify the correct absolute CO_2 concentrations. The correlation plot b) of the median NDIR and the reference instrument showed a high degree of linearity in the results, but a lower sensitivity for the NDIRs compared to the reference CO observations. 254
5.8 A covariance-variance matrix for the three NDIR sensors and the CO_2 reference measurement. 255
5.9 The seven methane MOS sensors were constantly offset to all begin at 1 V at the beginning of the deployment to investigate the degree to which they spread apart from each other. The pink lines indicated the individual methane MOS signals, and the black lines represent the highest and lowest reporting sensor. 257
5.10 The median methane MOS was correlated with a) the relative humidity and b) the temperature of the air flow to allow linear correction factors to be determined in order to correct for changing environmental conditions. . . . 257
5.11 The median methane MOS signal before (grey) and after (pink) RH and temperature corrections were applied to the data. The black line is the methane reference measurement. 258
5.12 a) The ambient methane concentration as measured by the reference instrument (black) and the temperature and humidity corrected median methane MOS (pink), plotted on the secondary y-axis. b) Correlation plot between the two methane measurements. 259
5.13 The interquartile ranges for the a) total VOC MOS, b) propane/butane and c) OVOC MOS sensors are shown as shaded regions. The grey lines in each plot represent the 5^{th} and 95^{th} percentiles and the black lines are the median of the cluster of MOS sensors. 260

5.14 a) Each of the median OVOC, PrBu and VOC MOS sensors were correlated separately against the relative humidity of the air flow reaching the sensors. The linear parameters describing their relationships were determined and the slope, R^2 and NRMSE for this regression are in the table. All had strong, positive correlations with the humidity of the air, $R^2 > 0.91$. b) The RH corrected data for the OVOC (orange), VOC (dark red) and PrBu (teal) MOS sensors. A MOS prediction based purely on the RH was determined using the slope and intercept from the linear correlation plots and then this was subtracted away from the median MOS signal to leave the RH corrected signal. After RH correction, the MOS signals all covaried, with each displaying a similar time series. 261
5.15 The hyper-parameters were unchanged from the China BRT analysis to identify how well the NO_2 BRT algorithm performed when the Boulder static measurements were used as a testing set. The China-trained BRT model predicted the NO_2 concentration (green). The NO_2 reference observations are plotted in black, and the median NO_2 sensor with no calibration model applied is shown in grey. 264
5.16 Summarising the performance of the uncalibrated median EC, the China-trained BRT and China-trained BLR algorithms when they were used to predict the concentration estimate of NO_2 (green), O_X (blue) and CO (red). 265
5.17 The correlation plots between the uncalibrated median sensors (grey) and BRT concentration estimates after the algorithm was trained using only data it had observed in Boulder. a) NO_2 prediction (green), b) O_X prediction (blue), c) CO prediction (red) and d) the CO_2 prediction (purple). The trendlines and parameters calculated via linear regression are also shown for the uncalibrated sensors (grey lines and boxes) and the BRT-predicted concentration estimates (coloured lines and boxes). 269
5.18 The relative contributions of each variable to the CO_2 BRT concentration estimate. CO and CO_2 contributed the most, to very similar degrees. . . . 271
5.19 The distribution of the training (purple) and testing (green) data for the Boulder data, for a) CO, b), NO_2, c) CO_2 and d) O_X. The more similar the distributions of training and testing data sets, the better the ML prediction. This is because the relationships learnt by the algorithm in the training data will be true of the relationships in the testing data set. 272
5.20 The timeseries to investigate the training and testing data for the NO_2 median EC and to compare the NO_2 median EC with the BRT predicted NO_2 concentration estimate. 273

5.21 The median O_X EC sensor (grey) exhibited a large amount of noise towards the end of the static deployment in Boulder (26^{th} Feb. This influenced the BRT O_X prediction (blue) and other predictions that the median O_X EC was involved with. Reference O_X observations are shown in red and black for the training and testing periods, respectively. 274
5.22 Photos of the OPC instrument, containing 4 OPC devices. a) The OPC instrument was located on the roof of a shipping container in the NOAA car park, with the inlets proud of the edge of the container. The inlets had rain shields on the end to minimise water entering the OPC device and to minimise the impact of turbulent air altering the flow of air to the sensor. The black wires which go out the bottom of the photo connect to the front of the main sensor instrument for data storage. The sensor instrument was located inside the shipping container to protect it from the elements. b) A view of the OPC box, which had a transparent lid with labelled parts. Through the lid, the Raspberry Pi's used for data collection and storage, and the OPCs themselves are visible. 276
5.23 Each OPC device recorded the a) PM_1, b) $PM_{2.5}$ and c) PM_{10} levels in the ambient air outside in the NOAA car park. The OPCs PM_1 signal displayed the most variability during the deployment, but the PM_{10} concentrations were much higher than PM_1 or $PM_{2.5}$. 277
5.24 The three covariance-variance matrices for the four OPC devices for a) the PM_1 data, b) the $PM_{2.5}$ data and c) the PM_{10} data. These were colour-coded by the value of covariance and variance, with lighter colours depicting higher values. The same colour scale was used between all three matrices so they can be compared easily. 278
5.25 Photos of NOAA's mobile laboratory. a) A side profile, upon which the sample inlets can clearly be seen on the roof of the laboratory, well away from the vans exhaust. b) A photo from the back, with the door open to reveal the GC-MS WAS system loaded into the rack at the back of the van and c) photo of the sensor instrument strapped down to the racks that contain some suspension. 280
5.26 The NOAA mobile laboratory moved around Boulder County and the different regions are marked out on the map in the different coloured boxes, with photos showing the region. The blue square depicts the location of the NOAA Laboratories, where each van drive began and ended, and where the sensor instruments were located during the static deployment. Green boxes depict the mountainous region, purple is the urban region of Boulder City and red shows an image of one of the fracking facilities. 280

5.27 The first drive took the mobile laboratory up Flagstaff mountain, where it was expected the emissions of a) CO_2, b) CO and c) CH_4 to be relatively low. The reference observations are shown as black lines, and the instantaneous median of CO_2, CO and CH_4 are pink, red and orange, respectively. 282
5.28 The magnitude of the normalised CO concentration at each point of the drive around Boulder for, a) the reference CO instrument and b) the median CO EC sensor. The data points are colour coded so that normalised data points with a value that is close to 0 are purple, and normalised data points close in value to 1 are yellow. 283
5.29 The magnitude of the normalised CO_2 concentration at each point of the thirty minute Mountains drive for, a) the reference CO_2 instrument and b) the median CO_2 NDIR sensor. The colour of the data point indicates it's value; normalised data points with a value close to 0 are red, normalised data points with a value close to 1 are blue. 284
5.30 Two more drives were completed whilst the sensor instrument and reference instruments for CO, CO_2 and CH_4 were installed inside the van. On the first drive, which occurred at 1930 on the 1_{st} March 2018 and lasted two hours, the van went to a region with a high density of fracking well pads (shaded red). During the second drive the van was driven through the city of Boulder. This drive began on 2^{nd} March (0710H) and lasted for four hours. In between drives the van was stationary and returned to the NOAA car park whereupon the reference and sensor instruments received power via the mains. The reference observations (black) and sensor data (coloured traces) for a) CO (red) , c) CO_2 (purple) and e) CH_4 (pink) are plotted as a timeseries to evaluate the sensor performance. Linear regression, between the reference observation and the sensor measurements was also conducted (see corresponding correlation plots) to provide parameters to describe the linear relationship between the two data sets. 286
5.31 The normalised CO reference and sensors data, at the different locations. a) and b) show the reference and sensor measurements at the fracking site. C) and d) are the projections of the measurements when the van was driving through the city centre. For the city drives, the data is on a logarithmic scale to show the changes in variation more. 289
5.32 The normalised CO_2 reference and median NDIR sensor data, at the different locations. a) and b) show the reference and sensor measurements at the O&NG area. C) and d) are the logarithmic projections of the measurements when the van was driving through the city centre. 290
5.33 Photos to show a) the rainforest surrounding the GAW site where the sensor box was deployed and b) the building that the instruments were housed in. 292

5.34 The sensor instrument, running at Danum Valley, Borneo. The instrument was located inside a building, with the sampling inlet for all instruments located outside, and a pump to draw in ambient air. The screen displayed the live incoming data going to the Latte Panda for storage and collection. 293
5.35 The median MOS (a) displayed lots of daily variation during deployment at Danum Valley, and the standard deviation of the 12 working MOS sensors appeared relatively consistent during the 68 days of sampling. The range of the 12 MOS sensors (b) shows that the lowest reporting sensor records much less variation in total VOC than the maximum sensor. 295
5.36 The range between the instantaneous highest and lowest reporting OVOC sensors is shown as the pink shaded area, with the largest range between the TGS2620 sensors as 285 mV, on the 8th Aug. The median and mean are also shown here, as green and purple traces respectively. 296
5.37 The total VOC TGS2602 MOS sensors had a strong negative correlation with humidity and a strong positive correlation with temperature. The OVOC were less sensitive per mV to either condition. 297
5.38 Determining the uncertainty in the sensitivity of the median OVOC MOS towards a) temperature and b) RH. 298
5.39 The a) temperature and median VOC MOS were binned into 1 °C bins and the mean (red) and standard deviation (1 σ were determined for each bin (grey shaded region). The b) humidity and median VOC MOS were binned into 5 % RH bins and the mean (blue) and standard deviation (1 σ were determined for each bin (grey shaded region). The trendlines between a) temperature and b) RH with the median VOC MOS, the median VOC + 1 σ and the median VOC - 1 σ were calculated to investigate the significance bands of the relationship between the median MOS and environmental conditions. 299
5.40 Diurnal profiles for a) the median OVOC (TGS2620) MOS sensor and b) the VOC (TGS2602) MOS sensors after temperature and humidity corrections. 300
5.41 Diurnal profiles for a) the total VOC, b) the sum of the aromatic compounds, c) the sum of the alkenes an d) the sum of the alkanes from a reference GC-FID measurement made in 2015. 301
5.42 Diurnal profile for isoprene concentrations with $\pm$ 1 σ, between August and September, measured as part of the OP3 campaign. 302
5.43 The working a) NO_2, b) O_X and c) CO EC sensors monitoring their respective pollutants over the duration of the deployment of the sensor instrument at Danum Valley. The instantaneous median of the cluster is shown in black, and there were two large gaps in the data due to power cuts at the GAW site.303

5.44 Diurnal profiles for a) O_3 and b) NO_2 EC show that, during the deployment of the sensors there was very little NO_2, yet more O_3 observed by the EC - between 10 and 40 ppb- that have a more distinctive daily pattern. 304

6.1 Comparing the EC performance over the experiments and field work conducted in the project. The normalised root mean squared error (NRMSE) was used in order to compare between the EC sensor response as the value of NRMSE is not affected by the concentration range over which the evaluation metric was computed (as RMSE is). 312

6.2 Photo showing a version of the sensor instrument which contains different sensors to detect multiple pollutants. 324

6.3 Flow chart to show the process by which the real-time spikes in total VOC levels detected by the MOS sensors could be useful for automatically sampling the air for GC-MS analysis. This would decrease the chances of missing peaks in the VOC mixing ratio and help atmospheric research. 332

6.4 Photos to show some of the changes being made to the next iteration of the sensor instrument. These alterations are occurring to enable the sensor instrument to be easy to use and be able to be assessed remotely. 333

Acknowledgements

I'd like to acknowledge the support and guidance of my supervisor, Alastair Lewis during my PhD. The contribution that Pete Edwards made; helping me in the laboratory and giving great ideas for analysis was also invaluable. There were multiple colleagues at the Wolfson Atmospheric Chemistry Laboratories who let me borrow their instruments or helped me collect data to evaluate the sensors performance, so I'd like to thank them all too. I really enjoyed working with everyone involved with the APHH programme in Beijing, China and the Tropospheric Chemistry group at NOAAs Chemical Science Division were helpful, welcoming and friendly too. Thanks to the people at the Danum Valley GAW site for looking after us in the rainforest.

I'd like to thank my family, in particular my Mum, for their unwavering support and excellent motivational tips!

Authors Declaration

I declare that this thesis is a presentation of original work and that I am the sole author. This work has not previously been presented for an award at this, or any other University. All sources are acknowledged as References.

I confirm that the work submitted is my own, except where work which has formed part of jointly-authored publications has been included. My contribution and those of the other authors to this work have been explicitly indicated below. I confirm that appropriate credit has been given within this thesis where reference has been made to the work of others.

The work relating to using a clustered approach to improve sensor performance, presented in Chapter 2 was previously published in Faraday Discussions as 'Clustering approaches that improve the reproducibility of low-cost air pollution sensors', 2017, by K. Smith (thesis author), P. Edwards, M. Evans, J. Lee, M. Shaw, F. Squires, S. Wilde and A. Lewis (thesis authors supervisor). DOI: 10.1039/C7FD00020K. I carried out the laboratory experiments and contributed to a large fraction of the data analysis.

The work relating to different analysis approaches upon NO_2 and O_X electrochemical sensors e.g. machine learning, presented in Chapter 4 is currently under review for submission to Atmospheric Measurement Techniques (AMT). The manuscript is entitled 'An improved low power measurement of ambient NO_2 and O_3 combining electrochemical sensor clusters and machine learning' with authors: K. Smith (thesis author), P. Edwards, P. Ivatt, J. Lee, F. Squires, C. Dai, R. Peltier, M. Evans and A. Lewis (thesis authors supervisor). I was responsible for the building of the sensor instrument, carried out the field work and conducted the simple linear regression, boosted linear regression and boosted regression trees analysis upon the sensor data.

Chapter 1

A review of low-cost sensors used in scientific research

1.1 The importance of air quality monitoring

The quality of the air we breathe has an impact upon human health [195] [40]. Air quality is determined by the presence and the amounts of various compounds in the atmosphere. Some of these chemical species, which lead to detrimental effects upon the environment and human health are pollutants. Emissions of pollutants can arise from a variety of sources, both natural [96] [65] and anthropogenic [101] [204] [75]. The composition of the pollution is dependent upon the emission sources, which can vary hugely and lead to very different environmental impacts. For example the major particulate matter (PM) emission sources for the US are due to power generation and traffic [101], whereas in India and China residential energy use dominates PM emissions [204] and in Europe, East Asia and Russia agricultural emissions make huge contributions to the PM budgets [101]. Exposure of humans to harmful atmospheric pollutants is a major factor for premature death and may lead to an increased risk of cardio-respiratory diseases [195].

Air pollution has been declared a public health emergency by the World Health Organisation (WHO) because poor air quality affects all age groups and lifestyles, greatly increasing the global burden of disease. Outdoor air pollution alone is attributed to 3 million deaths annually [195] and indoor household pollution is believed to have contributed to approximately 4 million premature deaths per year [194]. Since approximately one in nine deaths are linked to poor air quality it has been identified as the largest environmental risk regarding human health and is recognised in the sustainable development agenda as a global health priority [195].

Air quality monitoring is essential for recognising areas with poor air quality and determining the major emission sources. This can lead to bespoke mitigation strategies to improve the air quality of a particular region and reduce the amount of people suffering from diseases that are linked to exposure to pollution such as stroke, heart disease and lung

cancer and asthma [24]. Across the globe, there are regions that experience acute pollution events that lead to a large number of people exposed to levels of atmospheric contaminants that exceed the guidelines for human health [195]. There was a haze episode that spread over Northern, Eastern and Central China in January 2013 and this pro-longed pollution event lead to nearly 800 million people exposed to dangerously high concentrations of $PM_{2.5}$ [202]. Pollution events can also occur on smaller spatial scales; it is common for cities, such as Los Angeles [133], London [16] and Delhi [68], to experience pollution episodes as there are a large variety of pollutants simultaneously emitted from a number of sources. Globally, nine out of ten people who reside in urban areas are located in cities that do not comply with the World Health Organisation (WHO) guidelines for air pollution [195].

Pollution control strategies, often implemented by national governments [202] [40] or local authorities [50], are one method for improving air quality and by doing so, protecting the public from harmful exposure to pollution. Short-term mitigation programmes include the reduction of pollution emissions in Beijing, China during November in 2014, to improve air quality for the Asia-Pacific Economic Co-operation (APEC) [107]. Longer term mitigation strategies aimed at reducing pollution concentrations on a national scale are more common for meeting air quality requirements set by the WHO and, for European member states, the EU [52] [53]. In the UK, local authorities are responsible for monitoring criteria pollutants and producing an Air Quality Plan which is implemented if the ground observations of pollution in the local region exceed certain thresholds [36]. This Plan will detail measures, such as control of traffic flow, to implement and methods to monitor and evaluate the effectiveness of the scheme [36].

Pollutants are often emitted from a variety of sources, with pollutants from anthropogenic activities greatly contributing to the quality of the air in the troposphere [196]. There are regulations in place to control the amount of anthropogenic emissions and to monitor the ambient concentrations of various criteria pollutants to identify areas where people are at risk of exposure to harmful levels of contaminants. One example of a regulation to control pollution is the Commission Regulation (EC) number 715/2007 which states that all cars in Europe must be fitted with a catalytic converter to reduce road traffic emissions and this is also a requirement of UK Law [56]. The EU Directives instruct member states to monitor air pollution. To comply with these Directives the monitoring networks must met the minimum requirements which direct the state regarding which species to monitor, where the monitoring stations must be and give target or limit values for pollutants to categorise the quality of air within the member state [53] [52].

The criteria compounds, for which either the EU or the WHO have set limit values for, include carbon monoxide (CO), nitrogen dioxide (NO_2), tropospheric ozone (O_3) and particulate matter (PM), see Table 1.1. Ground observations using instrumentation to monitor the concentrations of these criteria pollutants are used to investigate whether a

Table 1.1: Criteria pollutants and the thresholds for their concentrations in ambient air set by the WHO [193] and the EU [53] [52]. The countries that fall under these regulation are required to meet these objectives to ensure the regions have air of a sufficient quality. To assess air quality, ground observations of atmospheric pollutants made with standardised instrumentation are used.

Atmospheric pollutant	World Health Organisation (WHO) guideline	European Union (EU) guideline
Particulate matter ($PM_{2.5}$)	10 μg m^{-3} annual mean 25 μg m^{-3} 24 hour mean	25 μg m^{-3} annual mean
Particulate matter (PM_{10})	20 μg m^{-3} annual mean 50 μg m^{-3} 24 hour mean	40 μg m^{-3} annual mean 50 μg m^{-3} 24 hour mean
Ozone (O_3)	100 μg m^{-3} 8 hour daily maximum	120 μg m^{-3} max. 8 hour mean
Nitrogen dioxide (NO_2)	40 μg m^{-3} annual mean 200 μg m^{-3} 1 hour mean	40 μg m^{-3} annual mean 200 μg m^{-3} 1 hour mean
Sulphur dioxide (SO_2)	20 μg m^{-3} 24 hour mean 500 μg m^{-3} 10 minute mean	125 μg m^{-3} 24 hour mean 350 μg m^{-3} 1 hour mean
Carbon monoxide (CO)	No values set	10 mg m^{-3} max. daily 8 hour mean
Benzene	No values set	5 μg m^{-3} annual mean
Polycyclic aromatic hydrocarbons (PAHs)	No values set	1 ng m^{-3} annual mean (of benzo(a)pyrene)

region complies with these limit values. Elevated levels of pollutants in the atmosphere also impact ecosystems. For example, tropospheric ozone damages plants and has been found to reduce crop yield [124], and emissions of ammonia (NH_3) and nitrogen oxides (NO_X) in the atmosphere contribute to nitrogen deposition which can affect the soil acidity and alter the way species interact [15] [182]. Both short-term pollution events (i.e. acute NO_2 roadside emissions impacting the human cardio-respiratory system [115]) and chronic exposure (i.e. elevated O_3 concentrations affecting crop yields [17]) to elevated concentrations of contaminants may have detrimental impacts to human health and the ecosystems [2] [141].

Atmospheric pollution monitoring is important for ensuring that major emission sources are identified, pollutants that are a concern for human health are regulated, any pollution mitigation programmes are efficient, areas with a high risk of exceedances are identified and control strategies are implemented and ensuring regions comply with air pollution regulations [195]. The results from the UKs national networks provide scientifically robust measurements for the further development of policy. Source apportionment is crucial for estimating the areas located downwind of the source, which might be exposed to high levels of atmospheric contaminants. Determining the air quality of a particular region includes identifying pollutants of concern, locating pollutant emissions sources and determining the quantity of pollutant species in the atmosphere. Epidemiological studies use the results from air quality monitoring to investigate the pollutants impact on human

health and the environment [101] [84].

In order to understand the behaviour of air pollution after it is emitted to the air, it is important to understand the structure of the Earths atmosphere. The Earth's atmosphere is structured into layers, based on temperature. From the ground to increasing altitudes, these are the troposphere (from ground 0 km to approximately 10 km up [27]), stratosphere (10 - 30 km), mesosphere (30 - 50 km), thermosphere (50 -400 km) and exosphere (500+ km). The distances of the boundaries between the layers are not constant and can fluctuate [162]. The troposphere is the layer closest to the ground and hence where the vast majority of global emissions occurs. The planetary boundary layer (PBL) is a sub-division of the troposphere; it lies closest to the Earths surface and is defined with a distinct boundary based upon air movement. The thickness of the PBL is highly variable (from 100 m to several km high) and the characteristics of this layer are defined by air turbulence and the thermal and dynamic properties of air within the PBL as well as other factors such as synoptic divergence [134]. The air within the PBL is considered well-mixed in convective conditions [134] and, in this regime pollutants undergo atmospheric dispersion, although the concentration of these pollutants is largely influenced by PBL height [134]. The air above the PBL is called the free troposphere. The PBL has different air movements, which are mainly influenced by the Earth's surface, to the rest of the troposphere, and moisture, heat and pollution are all redistributed throughout the PBL due to turbulence [77]. The world's population reside in the troposphere and are affected by the distribution of pollution in the PBL as this is where the majority of people spend most of their time.

The atmospheric lifetime of a species is dependent upon the rate at which it is deposited to surfaces and its reactivity with other atmospheric species. Some compounds, such as carbon dioxide have long atmospheric lifetimes, and hence they have evenly distributed concentrations across the globe and are well mixed in the atmosphere. Compounds with moderate atmospheric lifetimes, between a few days to months can be transported in the air over large spatial scales see Fig. 1.1 and by crossing international boundaries, pollution mitigation becomes a global issue [163] [161] [182].

Many multi-national organisations are already concerned with addressing the issues with trans-boundary pollution and there are Protocols and Conventions already in place to attempt to control both national pollution and emissions from neighbouring countries. An example protocol is the Gothenburg Protocol, which has been in existence since 1999 and has been amended several times with regards to the Convention on Long-range Trans-boundary Air Pollution [182]. One such amendment focuses on the reduction of VOC emissions from the use of solvents and instructs the Parties how to monitor the emissions, suitable instrumentation for monitoring, and presents various solvent management plans [200].

Atmospheric components are monitored to ensure that a specified region is meeting the requirements for air quality and that concentrations of contaminants are below certain

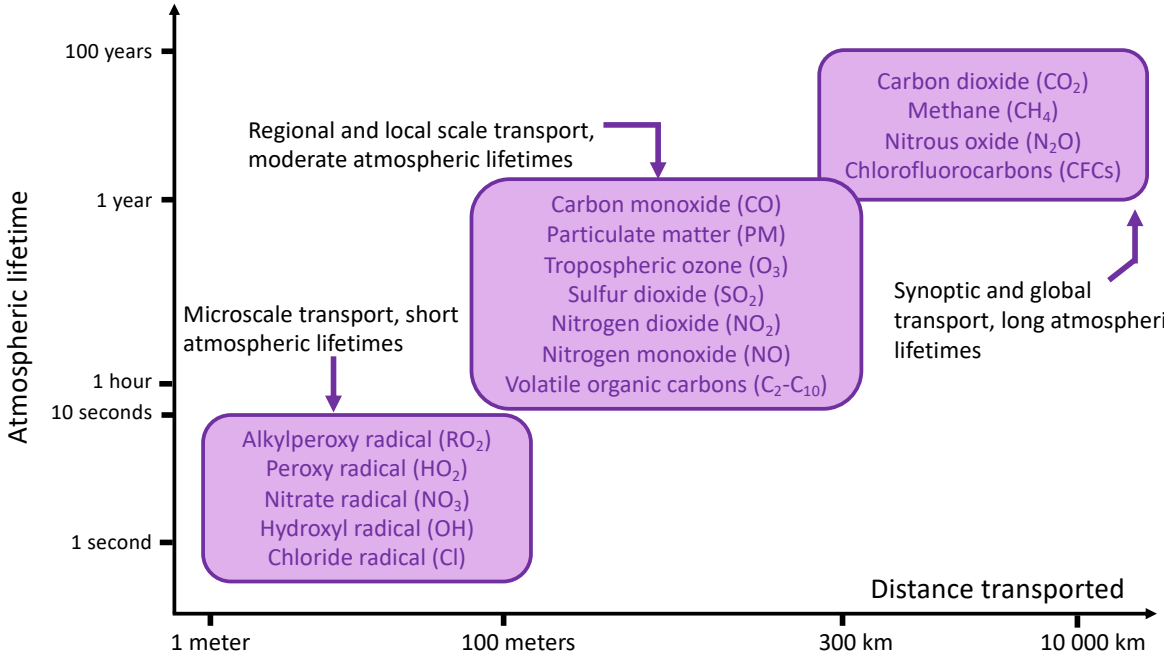

Figure 1.1: The longer a species exists in the atmosphere, the further it can be transported, with some pollutants, e.g. CO_2, which has an atmospheric lifetime of up to 200 years, being defined as well-mixed because they are transported over large, hemispherical distances. Figure adapted from Seinfield and Pandis 1998, [161].

thresholds, for example limit values in the EU Directives, statutory thresholds and upper limits for atmospheric concentration targets. The EU for example, published a series of Directives with limit and target values for certain pollutants for Member States to adhere to [53] [52]. Personal exposure to air contaminants is increasingly becoming a concern for the public and monitoring networks allow the general population access to reliable information about their local areas. Informing the public about the impact of their actions can help to reduce emissions, i.e. making people aware that idling causes poor air quality outside schools. Action can be taken on a more local scale to improve air quality for that region. It is not just human health that is detrimentally impacted by poor air quality, as livestock and vegetation can suffer from over exposure to certain atmospheric pollutants. Monitoring ambient concentrations of pollutants is useful for estimating the impact to the ecosystems [118], [40]. There are multiple studies to estimate the impact of ambient O_3 upon crop yields and vegetation, for example [17], [124]. Booker et al. found that exposure of the tomato plant to 75 ppb of ozone led to a decrease in the chlorophyll content in the plants leaves, in some plants chlorophyll was decreased by a factor of two [17].

The atmosphere is a complex mixture of many different compounds, each with their own reactivity and impact on human health. A list of the criteria air pollutants follows, each with a description of their common emission sources and their impact on human health and the environment.

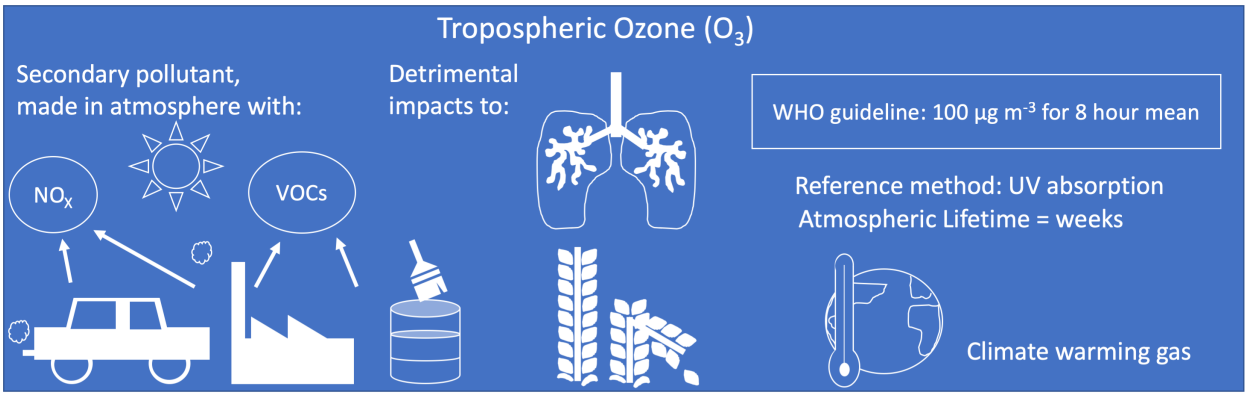

Figure 1.2: A brief summary of the sources and impacts of tropospheric O_3.

1.2 Ozone (O_3)

O_3 is ubiquitous in the troposphere and it's atmospheric lifetime is long enough (approximately several weeks) for it to be transported across continents [126] [182]. Raised concentrations of O_3 at ground-level has detrimental impacts upon human health and the surrounding environment [126], [91]. It is estimated that O_3 alone causes 5 – 20 % of all air-quality related deaths due to its reactive nature [126]. Exposure to elevated concentrations of gaseous O_3 causes decreased lung function [111], aggravation of asthma, respiratory disease and difficulties with breathing [137]. From a regulatory point of view, O_3 is monitored as an 8 hour average($[O_3]$8hr-mean). The WHO guidelines in 2006 stated that the maximum $[O_3]$8 hour-mean should not exceed 50 ppb.

The highly oxidising nature of O_3 causes detrimental affects to vegetation [124] and damages crop yields [189]. Tropospheric O_3 is also a potent greenhouse gas (GHG) [189], [126], and the presence of O_3 in the troposphere contributes a positive radiative forcing; the tropospheric concentrations of O_3 and it's GHG potency put it in the top three anthropogenic GHG compounds [189]. It is therefore important to monitor O_3 to asses the effects it has upon climate change [126] [189].

Haze events may occur in regions with poor air quality. O_3 is a major component of this photochemical smog [204], although the loss of visibility is due to the presence of PM. Photochemical smog is generated in the troposphere via a series of reactions that are initiated in the presence of sunlight [204] [126]. O_3 is often a key reactant in these photochemical reactions as O_3 reacts readily with compounds such as NO_X and VOCs [189] [126].

The concentrations of O_3 at any particular location are governed by the amount transported [182] as well as local sources of O_3 precursor compounds, weather conditions and the geographic location. There is also a positive correlation between the background ambient O_3 mixing ratio and altitude [91] for the lower troposphere. Nearer to Earth's surface there are more loss mechanisms for ambient O_3, such as dry deposition or titration by reacting rapidly with surface emissions [91], so the ambient concentrations generally in-

crease with distance from the ground [27]. O_3 concentrations within the PBL are also more variable than the O_3 in the free troposphere as O_3 concentrations are more influenced by weather and O_3 undergoes transportation at a synoptic scale within the PBL [27]. At the boundary to the PBL, there is a distinct change in the O_3 concentration relationship with altitude. In the free troposphere the gradient for increasing O_3 with altitude can become up to ten time less steep than for O_3 within the PBL [27].

1.2.1 Tropospheric O_3 formation

In the troposphere, in combination with the presence of NO_X, O_3 concentrations may exist in a photostationary state that can be described by the Leighton Relationship, 1.4 [100]. This photostationary state is comprised of Equations 1.1, 1.2 and 1.3, which form a null cycle because O_3 is produced and destroyed at rapid reaction rates, leading to no overall change in O_3 concentration [181]. In Equation 1.1 NO_2 is photolysed to NO and an oxygen atom in an excited state ($O(^1D)$. The photodissociation constant for this reaction is given by J_{NO2} [181]. The excited O atom has enough energy to react with an oxygen molecule (O_2 to produce O_3, Equation 1.2. O_3 is then destroyed by reaction with NO to reform NO_2 and O_2, Equation 1.3. Reaction 3 is the slowest reaction in the Leighton Relationship, with a rate constant, k_3. M is a molecule, commonly N_2, that is not involved in the reaction in any way except to stabilise the reaction through collisions.

$$NO_2 + hv \longrightarrow NO + O(^1D) \tag{1.1}$$

$$O(^1D) + O_2 + M \longrightarrow O_3 + M \tag{1.2}$$

$$O_3 + NO \xrightarrow{k3} NO_2 + O_2 \tag{1.3}$$

The concentration of tropospheric O_3 under these conditions is dependent upon the ratio of NO and NO_2 and the intensity of sunlight (hv), see Fig.1.4.

$$\frac{[NO_2]}{[NO]} = \frac{k_3[O_3]}{J_{NO2}} \tag{1.4}$$

For O_3 production in the troposphere there must be another route by which NO_2 is produced, without the destruction of O_3. O_3 is a secondary pollutant and as such, is not emitted directly into the atmosphere but is instead made by chemical reactions of atmospheric O_3 precursor compounds, Fig. 1.3 [4]. The reactions of these precursor compounds in the troposphere contribute 5000 Tg yr^{-1} of O_3 to the global ground-level budget [126]. Since their relationship with ozone concentration is non-linear [111], see Fig 1.3, O_3 mitigation programs are bespoke for each region. CO, methane (CH_4), non-methane hydrocarbons (NMHC) and NO_x are major O_3 precursor compounds and these

react via a series of reactions, some of which require sunlight. There is an increase in tropospheric O_3 concentrations when NO_2 formation occurs without the loss of O_3. Increasing O_3 concentrations occur in the presence of NO_X and VOCs as, VOC oxidation forms an organic peroxy alkyl radical (RO_2) which can react with NO (in place of O_3) to form NO_2, without the loss of O_3 [181]. Therefore both NO_X and VOCs are required for net O_3 formation.

The hydroxyl radical (OH) is an important oxidising molecule that initiates the removal of pollutants from the atmosphere. OH is fairly ubiquitous in the atmosphere during the daytime, yet because it is very reactive it typically has an atmospheric lifetime of less than 1 second and an typical ambient concentration of 1 ppt [161]. The reaction of molecules such as VOCs with OH forms more oxidised products, that are more water soluble, and hence it facilitates the removal of pollutants from the atmosphere by wet deposition [188]. In the reaction 1.5 a VOC (RH), for example an alkane molecule, is oxidised by the OH to produce an alkyl radical (R) and water. The alkyl radical undergoes a rapid reaction with oxygen to form an organic peroxy radical (RO_2), Equation 1.6 [181].

$$RH + {}^{\cdot}OH \longrightarrow R^{\cdot} + H_2O \tag{1.5}$$

$$R^{\cdot} + O_2 + M \longrightarrow RO_2{}^{\cdot} + M \tag{1.6}$$

$$RO_2{}^{\cdot} + NO \longrightarrow NO_2 + RO^{\cdot} \tag{1.7}$$

Reaction of RO_2 with NO forms NO_2 without the destruction of an O_3 molecule, Equation 1.7, to form an alkoxy radical (RO).

$$RO^{\cdot} + O_2 \longrightarrow RCHO + HO_2{}^{\cdot} \tag{1.8}$$

The RO radical subsequently reacts with an oxygen molecule forming an aldehyde (RCHO) and the peroxy radical (HO_2), Equation 1.8. In Equation 1.9 the peroxy radical reacts with NO to produce a second NO_2 molecule, without the destruction of O_3.

$$HO_2{}^{\cdot} + NO \longrightarrow NO_2 + {}^{\cdot}OH \tag{1.9}$$

Both the NO_2 molecules formed by VOC oxidation photodissociate, forming two excited $O(^1D)$ atoms, which react with oxygen molecules to produce two O_3 molecules, Equations 1.10 and 1.11 [181].

$$2(NO_2 + hv \longrightarrow NO + O(^1D)) \tag{1.10}$$

$$2(O_2 + O(^1D) \longrightarrow O_3) \tag{1.11}$$

When cities are considering ozone mitigation programmes it is important to understand the concentrations and behaviour of ozone precursor compounds. The relative proportions of NO_X and VOC concentrations in the region influence the O_3 concentration. Often O_3 isopleths are drawn for a region to determine the most effective O_3 reducing action plans [48]. These isopleths consist of a plot of VOC concentration versus NO_X and will identify the maximum possible O_3 that could potentially arise from an initial ratio of NO_X to VOCs [48] [150] [14]. Where the NO_X concentrations are high relative to the VOC concentrations, due to large amounts of NO_X emissions, the O_3 production is described as being VOC limited [14]. For this region, lowering the NO_X emissions will have little to no effect upon the overall O_3 concentration. The O_3 mitigation programmes required to reduce O_3 would identify a strategy to reduce the VOC emissions or change the VOC composition to be composed of fewer molecules with a high O_3 formation potential. Subsequently, regions with high atmospheric VOC concentrations compared to the NO_X concentrations are classified as NO_X limited [14]. O_3 mitigation programmes would therefore identify methods to reduce the NO_X concentrations for that local area. For effective and efficient O_3 pollution control, it is therefore important to monitor the precursor compounds as well as O_3 to investigate the effectiveness of O_3 reduction strategies [150].

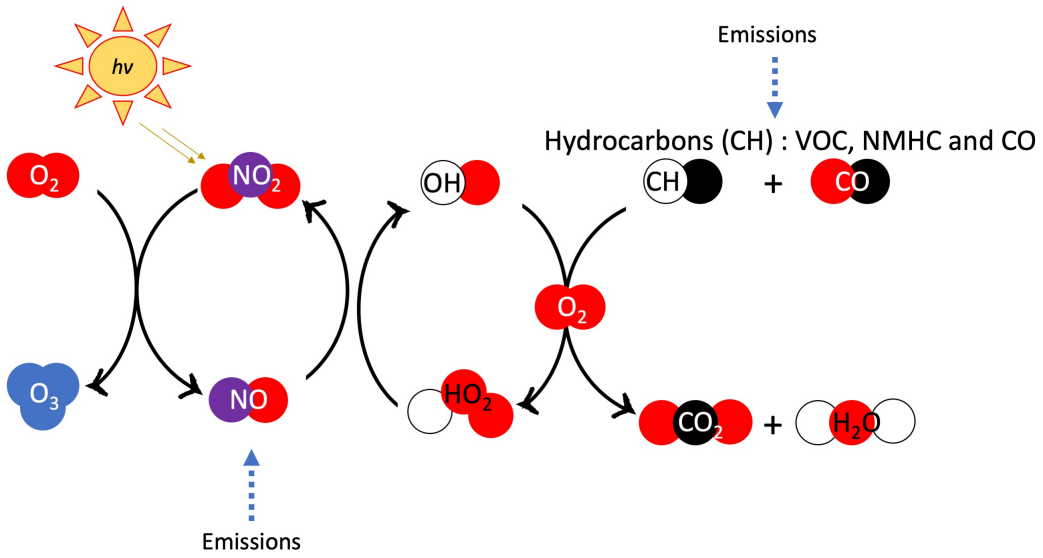

Figure 1.3: Photochemical production of tropospheric ozone via the primary emissions of VOCs and NO_X.

A large proportion of the precursor emissions come from vehicles and industrial processes with urban and industrial regions around the world reporting high ozone concentrations [111], usually on hot, still sunny days [103] and especially during and after a heatwave where these conditions may lead to a build-up of O_3 [152]. O_3 production is driven by photochemical reactions and therefore a diurnal pattern of O_3 concentrations

exists, with peak O_3 concentrations typically occurring just after midday [14] [48]. There is also a seasonal variation of O_3 concentration, which is driven by the strength of the sun, i.e. less O_3 produced by photochemical reactions during Winter months [201]. Therefore, more people are exposed to elevated O_3 in Summertime, when the O_3 are higher and people spend more time outdoors [201]. Concentrations of O_3 vary on a number of temporal and spatial scales and when monitoring this criteria pollutant, it is important to consider both the vertical and horizontal gradients of O_3 over time. The short-term (hour-to-hour variability) peaks in O_3 concentration and the longer-term background O_3 trends (seasonal and annual variability) must be considered separately since these can often show disparity. The long-term background O_3 levels are increasing due to increased global emissions of methane and other precursor compounds. Increased background O_3, due to elevated methane concentrations has been observed in Europe and North America [91] [126]. However, the maximum concentrations of O_3 have decreased on a day to day basis. Studies have shown that the maximum peak concentrations of O_3 are generally decreasing over time in Europe [168] and the United States due to a series of strategies such as the NO_X State Implementation Plan which halved the NO_X emissions in the Eastern US [152]. The health impacts associated with tropospheric O_3 occur from both chronic [176] and acute [13] exposure and it is therefore important to continue monitoring in such a way so that both the short term and long term O_3 events are detected.

O_3 is lost from the troposphere via reactions, deposition to surfaces and transportation to other regions in the atmosphere. Tropospheric O_3 undergoes photolysis in the troposphere (wavelength of light required for O_3 photolysis, hv = 340 nm [181]) and the excited $O(^1D)$ atom produced by O_3 photolysis subsequently reacts with water vapour to form the hydroxyl (OH) radical (see Equations 1.12 and 1.13). This is the major route for OH radical formation [149]. A significant proportion of the oxidisation reactions in the troposphere use OH as an oxidant. It is extremely reactive, plays a key role in the removal rate of many chemical species and is known at the atmospheric detergent of the troposphere [149]. Therefore O_3 concentrations indirectly contribute to the oxidative nature of the local environment [4] as well as O_3 being a direct atmospheric oxidant itself.

$$O_3 + \mathrm{hv} \longrightarrow O_2 + O(^1D)) \tag{1.12}$$

$$O(^1D) + H_2O \longrightarrow 2{\cdot}OH \tag{1.13}$$

O_3 is itself an oxidant and hence will oxidise unsaturated VOC compounds such as alkenes, by addition of $O_a$cross the double bond. In a high NO_X environment, O_3 may also react with NO, to produce NO_2, or will react with NO_2 to produce the nitrate radical (NO_3). Deposition of O_3 to surfaces is also a major O_3 loss function [139] [126].

Climate change may cause an increasing frequency of weather events such as anti-

cyclonic conditions in Europe. This is generally predicted to lead to an increase in the ambient O_3 concentrations in urban regions as the balance of O_3 deposition and rate at which O_3 is vertically transported will be affected by changing meteorological conditions [91] [44]. On a regional and local scale, surface layer O_3 behaviour is governed by a number of variables and there is much to consider when determining how best to monitor O_3 for different locations. Whilst it would be expected that urban areas present elevated concentrations of O_3 compared to their rural counterparts, this is not always the case. The titration of O_3 by nitrogen monoxide (NO), leads to smaller than expected O_3 concentrations in regions with a high proportion of traffic emissions and in this instance, the surrounding rural regions may exhibit higher concentrations of O_3 than the urban environment [91]. The fraction of urban pollution transported into the rural areas will not undergo the same amount of titration with NO, leading to increased O_3 concentration in downwind rural areas.

1.2.2 Influence of stratospheric O_3

There are also a number of mechanisms for O_3 transportation from the stratosphere to the troposphere leading to increased tropospheric O_3 concentration [145]. The boundary between the troposphere and the stratosphere is called the tropopause. This is a dynamic boundary, and folds in this boundary occur when stratospheric air intrudes down into the troposphere [34]. Intrusion events can lead to large quantities of O_3 transported from the stratosphere into the troposphere [145] [39]. The stratospheric concentration of O_is much higher (1 - 10 ppm) than the tropospheric O_3 concentration (10 – 100 ppb) [39]. The formation of O_3 is driven through via ultra-violet (UV) radiation from the sun promoting the photolysis of oxygen molecules to atoms. These atoms then have sufficient energy to react to form stratospheric O_3. Eddy diffusion of O_3 in stratospheric folds results in a net transport of O_3 from the stratosphere to the troposphere [4], however this is a weak mechanism for stratospheric to tropospheric exchange [162]. O_3 can be transported both up and down through large cumulonimbus clouds which breech the tropopause. Height changes in the tropopause also lead to O_3 exchange [39]. These different processes contribute to the tropospheric O_3 budget, and occasionally influences O_3 within the boundary layer. The vast majority of O_3 variability in the PBL does however, occur via photochemical transformations with pollution in the PBL [4].

1.2.3 Reference ozone instrumentation

For regulatory monitoring of ambient tropospheric O_3, dual-cell UV absorption photometry is used [168], [40]. The instruments alternate between measuring a reference gas in one cell and the sample of air in the other and has been used as a method for determining the O_3 concentration since 1979 [179]. It is well documented that O_3 absorbs UV light at ap-

proximately 254 nm [179], [168], and since very few other atmospheric compounds absorb light at this wavelength, the technique experiences no cross sensitivities when monitoring ambient air. Monochromatic light at 254 nm is shone into a chamber filled with air. The amount of light absorbed by O_3 molecules is directly proportional to the concentration of O_3 in the air in the chamber, via the Beer-Lambert Law [168], see Equation 1.14.

$$C = \frac{ln\frac{I_{lamp}}{I_{detector}}}{\alpha L} \tag{1.14}$$

C is the concentration of the absorbing species in the sample (ppb)), I_{lamp} is the intensity of radiation at the source (W cm^{-1}), $I_{detector}$ is the intensity of light at the detector after it has passed through the sample cell (W cm^{-1}), α is the absorption coefficient of the absorbing species (cm^{-1}) and L is the path length (cm). Modern day instruments have improved upon the original instrumental designs by improving the critical parameters for the Beer-Lambert Law, for example determining the absorption cross section of O_3 and maximising the length of the cell [168]. This method is the standard technique and is detailed in EN 14625:2012 for monitoring outdoor O_3 concentrations, up to 250 ppb, for background, rural and urban locations [127], [40] [53].

1.3 Nitrogen dioxide (NO_2)

Nitrogen dioxide (NO_2) is considered a criteria pollutant due to its direct detrimental effects upon human health and its role in the formation of secondary contaminants. Exposure to elevated concentrations of NO_2 cause decrease in lung capacity, inflammation of the respiratory system, a greater risk of respiratory illnesses and a heightened response to allergens [97], [40]. Acute exposure to high concentrations of NO_2 initiates inflammation of the lungs and both daily fluctuations in NO_2 mixing ratios and elevated levels lasting for much longer time scales effects mortality [40]. Due to the short-term detrimental impacts of NO_2 upon human health, the WHO state that the 1-hour mean of NO_2 should not exceed 200 μg m^{-3} [193].

The presence of NO_2 in the troposphere also causes significant impacts to the environment as it influences the N-cycle and is a precursor for nitric acid. The main sink for ambient NO_2 is via it's reaction with the hydroxyl radical (OH) to form nitric acid (HNO_3) [47]. The nitric acid is removed from the atmosphere via wet deposition, which increases the acidification of precipitation. In regions with elevated emissions of ammonia, the nitric acid will combine with ammonium to form ammonium nitrate [10] and this forms a significant fraction of $PM_{2.5}$, which has it's own health impacts. Changes to the nitrogen cycle [15] lead to eutrophication of aquatic domains and NO_2 reaction to form nitric acid causes acidification within terrestrial ecosystems [76], [40]. The effects of NO_2 have led to it becoming a hazardous air contaminant for which there is legislation in place

to ensure that the general public are only exposed to safe levels [90]. The World Health Organisation state that the NO_2 concentrations should not exceed a 40 μg m^{-3} for the annual mean and the 1-hour mean should not exceed 200 μg m^{-3}.

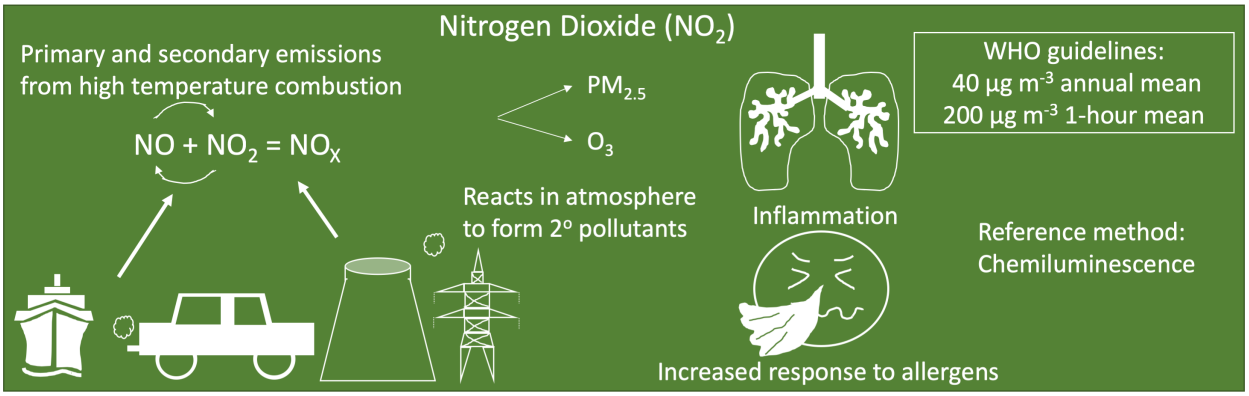

Figure 1.4: A brief summary of the sources and impacts of nitrogen dioxide (NO_2).

There are direct sources of NO_2, but the greatest proportion of NO_2 is formed from the primary pollutant NO reacting with O_3 in the atmosphere [97]. The day time chemistry of NO and NO_2 is very closed linked and therefore these two compounds are collectively called NO_X. Since the majority of NO_X emissions result from the generation of electricity via fossil fuel combustion [76] [97] and vehicle emissions [159] the greatest change in the levels of ambient NO_2 came about during industrialisation and the development of agriculture [90]. Rapid urbanisation and large vehicular fleets mean that mega-cities often experience elevated ambient levels of NO_2 [76]. There are natural sources of NO_2; soil emissions from microbial activity [4], biomass burning [76], and the high temperature conditions induced by lightening initiate the reaction of N_2 and O_2 to form NO which is rapidly oxidised to NO_2. Diesel engines also directly emit NO_2 to the troposphere. Due to it's relatively short lifetime in the atmosphere, exposure to NO_X depends on how close the source is [159]. The UK is currently trying to reduce peoples exposure to road side NO_X which is emitted from fossil fuel-based vehicles. The UK laid out plans in July 2017 to specifically target NO_2 concentrations –'The UK Plan for Tackling Roadside NO_2 concentrations' [38] in places which frequently exceeded the NO_2 safety thresholds. These regions are designated Air Quality Management Areas (AQMAs) for NO_2, and within these areas emissions from vehicles and other road was identified as being the main source of NO_2 in 96 % of these NO_2 AQMAs within the UK [38] [40]. European monitoring networks indicate that ambient NO_2 concentrations are not decreasing at the expected rate (Fig. 1.5), and that many locations regularly exceed the NO_2 limit values [36]. Due to the introduction of increasingly stringent regulations on vehicle emissions [55] across Europe the NO_2 and NO_X trends decreased for a decade, beginning in the mid-1990's, yet this trend has plateaued across the continent more recently [23], see Fig. 1.5.

This plateau, and a general increase in the number of reported NO_2 hourly exceedances

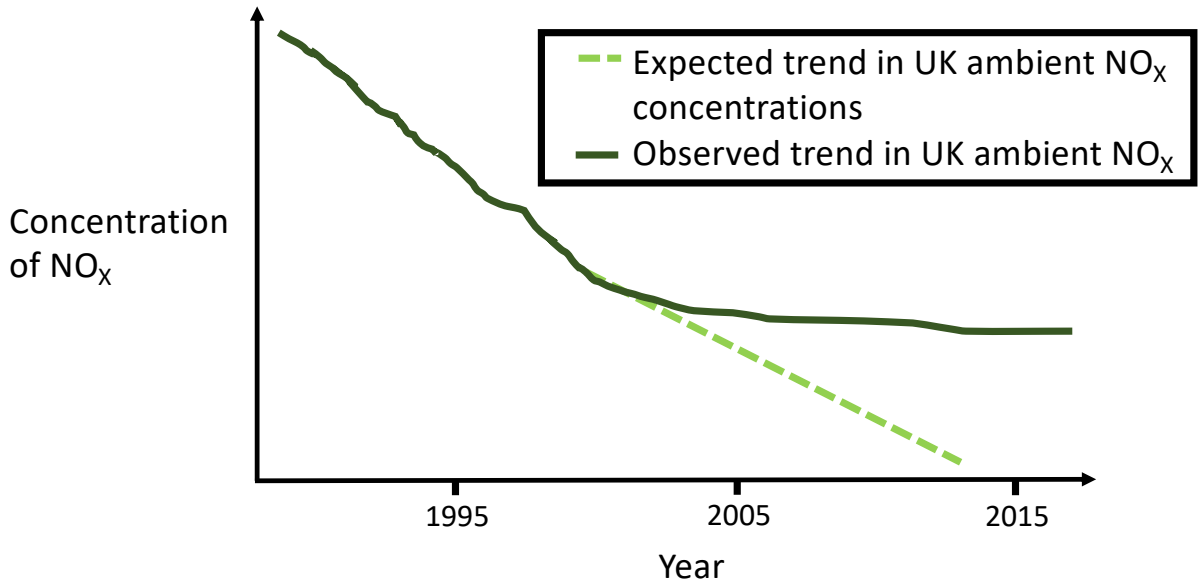

Figure 1.5: The ambient UK NO_X concentrations were due to decrease with the introduction of each successive Euro standard that applied increasingly stringent restrictions upon the pollutants emitted from vehicles in Europe. However, the ground observations of NO_X were different to how they should appear if the Euro standards were successful.

in urban, suburban and rural areas is potentially due to diesel cars fitted with emission control technologies that emit NO_2 [97] [23]. However, reducing the ambient NO_2 mixing ratio is not as simple as decreasing the ambient NO_X concentrations, as reactions with NO_X and O_3 are complex and non-linear, increasing the difficulty of regulating NO_2 [42].

Due to the relatively short atmospheric lifetime of NO_2 it does not experience intercontinental transport rather, NO_2 is a regional issue [76]. Consequently the highest concentrations of NO_2 are found close to the emission sources within the PBL [76]. The lifetime of NO_X was estimated to be on the order of a few hours near power plants and mega-cities with a large vehicular fleet. The atmospheric lifetime of NO_2 is OH-dependent, as reaction with the hydroxyl radical is the main sink for NO_2, and this leads to HNO_3 formation [154]. The concentration of NO_2 in the surface layer is also dependant upon dilution and the local meteorological conditions, for example, wind velocity, are important variables [112] with regard to ambient NO_2 concentrations. The ability of NO_2 to photolyse, yielding NO and an excited $O(^1D)$ molecule means that it is an important precursor compound for O_3 production. Photochemical reactions involving NO_X and VOCs lead to O_3 formation and due to this monitoring and mitigating NO_2 pollution is often a key strategy to reduce ambient O_3 levels [90]. There is added complexity with O_3 mitigation protocols, as reducing the NO_2 levels will only result in lower O_3 when the region is NO_X-limited. Both NO and NO_2 can be oxidised by O_3, see Equations 1.15 and 1.16. The reaction of NO_2 with O_3 forms the nitrate (NO_3) radical, which is an important oxidant during the absence of sunlight [98].

$$NO + O_3 \longrightarrow NO_2 + O_2 \tag{1.15}$$

$$NO_2 + O_3 \longrightarrow NO_3 + O_2 \tag{1.16}$$

During the day, nitrate radicals are still formed in this manner, but it is quickly destroyed as it undergoes rapid photolysis, Equation 1.17. However, at night, with no light source to promote the photolysis, NO_3 concentrations increase and the nitrate radical is the dominant oxidising species for VOCs such as alkenes and aromatic compounds [98].

$$NO_3 + hv \longrightarrow NO_2 + O(^3P) \tag{1.17}$$

The nitrate radical can subsequently react in a reversible reaction with NO_2, producing dinitrogen pentoxide (N_2O_5) [98], Equation 1.18. The N_2O_5 either reforms NO_3 and NO_2 or can react with water molecules to produce nitric acid [4], contributing to the acidification of the environment.

$$NO_3 + NO_2 \rightleftharpoons N_2O_5 + O(^3P) \tag{1.18}$$

The nitrate radical also contributes to the ambient concentrations of particulate matter ($PM_{2.5}$ and PM_{10}) as these radicals can react with ammonium to form inorganic aerosols [40] [154]. PM has it's own health and environmental impacts [90].

1.3.1 Reference NO_2 instruments

Chemiluminescence (CL) is the standard method for monitoring NO and NO_2 in the ambient air (EN 14211:2012) [40], [159] [53]. It is used globally to determine the concentrations of NO_2 and is in use by both the UK's Automatic Urban and Rural Network (AURN) monitoring network [40] and is recognised as a Federal Reference method by the Environment Protection Agency in the US [47]. The technique works via a two-step process. Ambient air is sampled into the instrument, whereupon the NO is measured directly by reacting it with an excess of O_3, to produce NO_2 in an excited state (NO_2^*) [61]. The excited NO_2^* fluoresces as it relaxes to return to the ground state. The NO_2 fluoresces and emits specific wavelengths of light, therefore selectivity is achieved by selecting the correct light filter. The intensity of this emitted light is measured with a photo-multiplier tube [61] and is proportional to the amount of NO in the sample [151]. In the second state, the air is passed over a catalyst to convert all NO_X to NO first, then the total NO_X concentration in determined by the same chemiluminescent reaction. The NO_2 concentration is the result of the subtraction of NO from the total NO_X concentration [47]. The calibration procedure involves introducing known concentrations of NO_X, from a gas standard (typically NO in N_2), into the CL instrument and monitoring the photon count [61], [47].

The instrument is relatively simple and inexpensive, requiring a lamp to generate O_3 and a photomultiplier that needs to be cooled to -4°C [47]. Although there are known interferences – due to the instrument not detecting NO_2 directly e.g. conversion efficiency, and other nitrogen-containing compounds besides NO_2 being converted to NO in the second state [47] – the technique is relatively reliable.

In research, and recently for more routine monitoring, a second type of instrumentation is also used for the measurement of real-time NO_2 concentrations in ambient air, which can offer detection limits of less than 0.06 ppb and drift over a few months of 0.5 ppb [93]. The NO_2 Cavity Attenuated Phase Shift (CAPS) detects NO_2 using a cavity lined with two highly reflective mirrors, facing each other. The reflectivity of the mirrors is a known constant, R. Blue light of a specific wavelength (430 nm), emitted by a light emitting diode, is introduced to the mirror-lined cavity and is reflected back and forth between the two mirrors. Each time a photon makes the journey between the two mirrors is defined as a trip, and the number of trips (n) the photon is likely to make is defined in Equation 1.19. The photons slowly leak out of the cavity at a defined rate, which is defined as photon decay.

$$n = \frac{R^2}{(1 - R^2)} \tag{1.19}$$

The light introduced to the cavity is a continuous light source in the form of a sine or square wave - as light reflects it will be superimposed on light already being reflected between the mirrors in the cavity. This causes a phase shift of the resulting waveform that is detected, with high accuracy, by a Lockin detector [92]. When a gaseous sample is introduced to the cavity the NO_2 molecules in the sample selectively absorb photons of light with a wavelength of 430 nm. The amount of absorbed photons is proportional to the amount of NO_2 in the chamber. The absorption of photons is a loss mechanism that causes there to be less photons making trips within the cavity and therefore a faster decay of energy stored in the cavity is detected. The rate of decay of the photons, and hence measured phase shift is proportional to the amount of NO_2 in the reflectivity chamber [92]. The CAPS monitor provides a direct measurement of NO_2, without the need to convert NO_2 to NO prior to analysis. The use of the molybdenum catalyst in the CLD measurement converts the NO_2 in the air sample to NO to allow a measurement of NO_2 to be made. However, the major limitation of the CLD technique is that other compounds, such as peroxy acyl nitrates (PAN) are also converted to NO_2, leading to an inaccurate NO_2 estimate of the atmosphere. The direct NO_2 CAPS measurement eliminates the risk of other N-containing species interfering with the measurement and minimises the need for frequent maintenance. The CAPS device is highly selective as it uses absorption to directly measure NO_2 and the wavelength of light to be absorbed can be carefully selected. This type of measurement requires less frequent calibration as the technique relies upon absorption and the Beer Lambert Law.

1.4 Carbon monoxide (CO)

The main emission of CO is from incomplete combustion of fuels that contain carbon [57]. CO is a colourless, odourless gas that is a useful pollutant to monitor in air quality networks because it can be used as a tracer for combustion emissions [57] and can therefore be used to provide information about other combustion pollutants. Typical concentrations of atmospheric CO vary greatly throughout the year, depending on the quantity of biomass burning but can be expected to fall between 60 – 300 ppb in background air. Atmospheric concentrations of CO are much higher in urban regions; the maximum hourly concentration of CO in Beijing has been observed as being greater than 5 ppm [85].

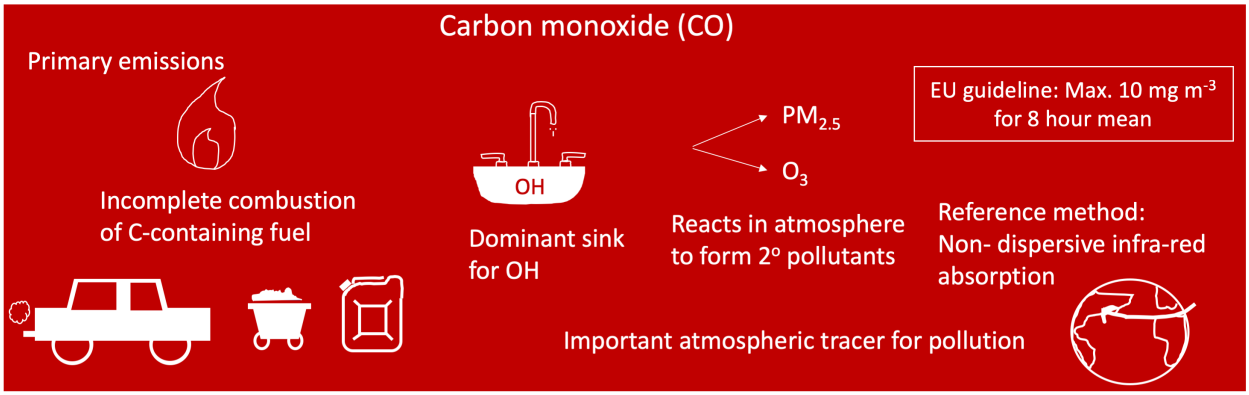

Figure 1.6: A brief summary of the sources and reactions of carbon monoxide in the troposphere.

Exposure to elevated CO levels is harmful to human health. Depending on the person, exposure time and concentration it can cause damage to the cardiovascular system, central nervous system and haemoglobin in blood. The main human health impacts are caused because in the presence of CO, haemoglobin preferentially combines with CO to make a stable molecule called carboxyhaemoglobin (COHb) [29], rather than forming oxyhaemoglobin (HbO2) which is the product of the reaction of haemoglobin with O_2. HbO2 is required to oxygenate vital tissues around the human body. CO therefore removes some of the haemoglobin available for binding with oxygen, and decreases the quantity of oxygen carried by the blood resulting in a reduction in the oxygen received by the human bodies organs and tissues [57] [29]. However, ambient CO concentrations in the UK fall well below the thresholds set to protect human health, but this is not always the case for mega-cities in countries such as India and China [85]. The largest ambient CO emissions are from vehicular transport and industrial process in urban areas so CO is a good tracer for anthropogenic activities [159]. The Euro Standards for regulating vehicular emissions also limit the CO emissions from passenger vehicles [54] but CO emissions from road transport are still a large source of tropospheric CO. In urban areas where traffic emissions dominate, VOC concentrations are often well correlated with ambient CO concentrations, which is indicative of their similar sources [186]. Calculating the ratio between CO and various

VOCs is useful for allowing comparisons to be made between cities and to help identify if pollution control strategies are working [186]. CO pollution events within cities have been shown to correlate with PM episodes and since forecasting CO is much simpler than predicting future levels of PM, CO has been used to determine PM estimates [157].

CO plays a large role in determining the oxidative nature of the atmosphere; as it is the main sink for the hydroxyl (OH) radical, via the reaction in Equation 1.20. The hydrogen (H) radical produced by this reaction is very reactive and reacts with oxygen in the atmosphere to form the peroxy radical (HO_2), which ultimately leads to O_3 production.

$$CO + {}^{\cdot}OH \longrightarrow CO_2 + H^{\cdot} \tag{1.20}$$

The yearly variation in CO is mainly driven by the concentration of OH; during the summer when the atmosphere contains maximal OH levels, the CO concentrations are typically at their lowest for the year [159]. Local CO emission sources and transport of CO will also influence the regional CO variability. CO has an indirect positive radiative forcing effect upon the atmosphere which stems from the main reaction route of CO, with OH. Due to the fast reaction of OH and CO (Equation 1.20) this often dominates how the OH radical reacts as CO is present at relatively high concentrations in the troposphere too. Therefore, a further increase in ambient CO concentrations leads to a decrease in OH concentrations as more OH reacts with the additional CO. A decrease in OH impacts the oxidising capacity of the atmosphere as there is less OH available to oxidise various other carbon-containing compounds, for example methane [33]. Methane has a very significant climate warming affect, hence an increase in CO indirectly leads to more climate warming as less OH is available to oxidise methane into a molecule with a smaller greenhouse gas potential [33]. Since the concentration of CO impacts the concentration of OH, this has a subsequent impact upon the oxidising capacity of the atmosphere and the rate at which pollutants are converted to more soluble species. The oxidation of pollutants by OH it vitally important for the removal of pollutants from the atmosphere because this oxidation procedure makes pollutants more soluble and therefore more likely to wash out of the troposphere in wet deposition. Equation 1.20 also produces CO_2, which is well known for having a positive climate affect.

The atmospheric CO levels are related to geographic location – the Northern Hemisphere displays higher ambient CO concentrations and on a more local scale the surrounding environment and time of the year can cause the lifetime of CO to be between 10 days to 1 year [159]. CO can therefore be transported over long distances and is sometimes used as a tracer for atmospheric transport [159]. It is important to monitor the ambient concentrations of CO as it is an O_3 precursor compound and it influences the concentrations of OH in the troposphere. Ground observations of CO have been used to better understand the behaviour of O_3 precursor compounds and therefore aid policy-makers to develop efficient O_3 mitigation programmes [186].

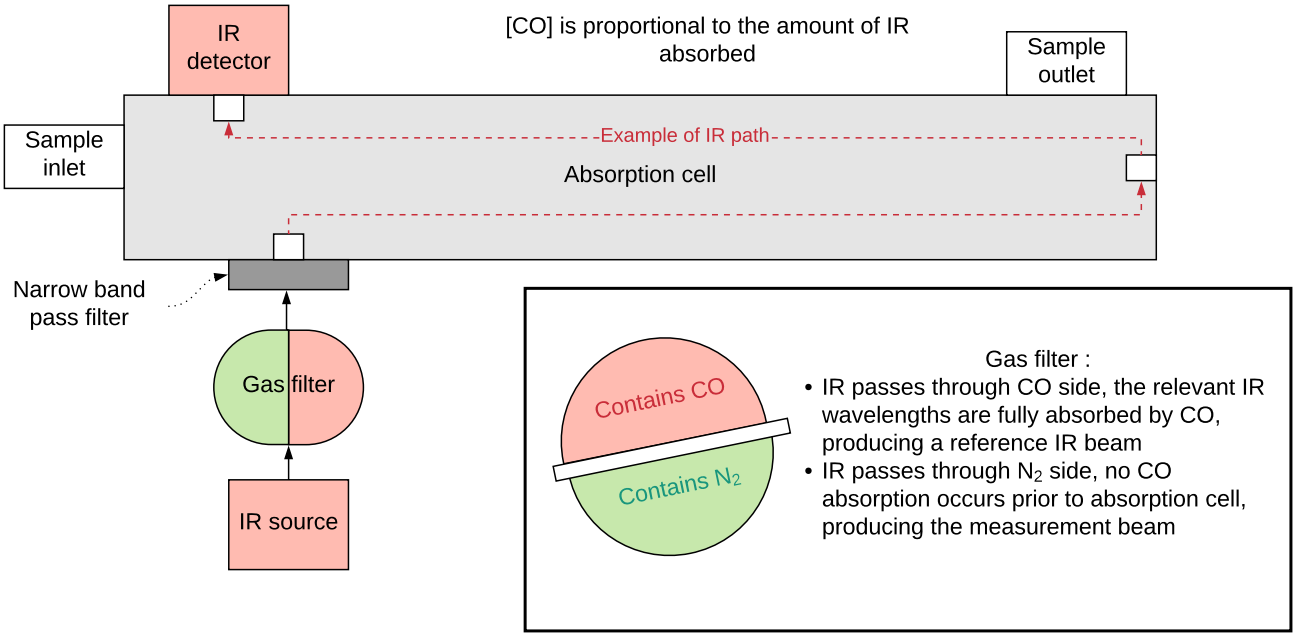

Figure 1.7: Schematic to show the gas filter half filled with CO, for the reference CO measurement, and N_2, to allow for a measurement of CO in the sample of air.

1.4.1 Reference CO instruments

Atmospheric levels of CO are measured within the UK's AURN network using Non Dispersive Infra-Red (NDIR) spectroscopy [40], detailed in EN 14626:2012 [53]. NDIR uses the principle of CO molecules absorbing IR radiation to quantify the amount of CO in an air sample. This device was developed to provide an automatic, continuous measurement of ambient CO concentrations [132]. A gas filter is used to provide both a reference measurement and a measurement of CO in the sample. The device switches between making these reference and sample measurements, using the gas filter, shown in Fig. **??**. This filter is typically cylindrical in shape, with one half containing CO gas (reference filter) and the other half filled with nitrogen (N_2) gas (measurement filter). During the reference measurement, the gas filter is positioned so that the IR radiation passes through the side containing CO. IR radiation that is able to be absorbed by CO molecules is fully absorbed by the CO in the filter. Any IR radiation that is not absorbed by the CO in the reference filter cannot be absorbed by CO molecule and therefore the fingerprint of IR radiation is saturated at the CO-absorbing wavelengths after passing through the reference filter. Hence, there is no change in the radiation at the CO-absorption wavelengths, even after passing through the sample cell which may contain CO molecules.

When making a measurement of the amount of CO in the sample, the gas filter is positioned so that the IR radiation passes through the N_2 filled section of the filter. All IR radiation passes through the filter and none is absorbed by the N_2 molecules. The IR passes into the absorption tube where the CO molecules may be present in the air

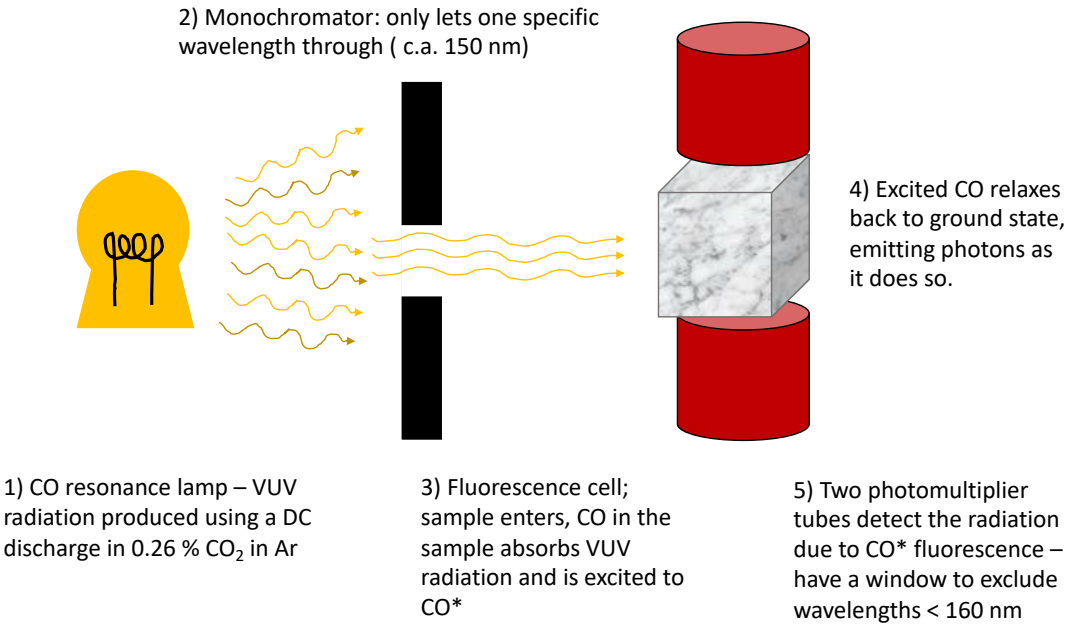

Figure 1.8: Schematic to show the operation of a VUV fluorimeter, used to detect CO with a very fast time response and lower detectable limits.

sample, and any CO molecules in the sample will undergo IR absorption. The amount of light absorbed by the CO in the sample is proportional to the concentration of CO in the sample [132], [159], [129] and hence the CO concentration can be determined. CO molecules in the air sample absorb certain wavelengths of IR radiation and therefore, the difference between the reference measurement and the sample measurement will indicate the quantity of CO in the sample [132]. CO NDIR can be affected by water vapour in the air and although the research NDIR instruments have a detection limit of around 50 ppb [129], the limits of detection for the instruments in the AURN in more like 1 ppm; close to the daily limit. It is one of the most common methods of the measurement of ambient CO concentrations due to the stability of the measurements over long time scales, although to achieve high repeatability there needs to be long averaging time (1 hour) [159]. There are other methods for monitoring CO concentrations, and the CO Aerolaser is one that is commonly used in research applications. The Aerolaser has a fast time response (less than 0.01 seconds), low limits of detection (3 ppb) and high precision (1.5 ppb at 100 ppb of CO) [63]. A CO_2 resonance lamp is used to produce Vacuum Ultra-violet (VUV) radiation, of approximately 150 nm. The resonance lamp produces VUV radiation using a D.C. discharge in the presence of a 0.26 % carbon dioxide CO_2 in argon (Ar) atmosphere [178]. The radiation is filtered, to select just one wavelength (150 nm) with the aid of an optical filter. This monochromatic light enters the fluorescence chamber and is energetic enough to be absorbed by the CO molecules in the sample and excite the fourth positive band of CO molecules1.8. The excited CO relax back to their lower energy states and emit photons of a characteristic wavelength; they fluoresce at 160 – 190 nm (still in the VUV spectrum). The photons from the fluorescence are detected by two photomultiplier

tubes and a counter to allow a concentration of CO to be determined [63]. A window on the PMT prevents wavelengths of less than 160 nm from entering the PMTs, as these are due to elastic scattering of light, not CO fluorescence [178]. The fast time response and real-time measurements of VUV-fluorimetry means that it is suitable for continuous, real-time measurements of CO for ground-based observations but is also suitable for use on aircraft. The automated calibration procedure only takes a few minutes and requires a small amount of CO gas standard.

1.5 Volatile Organic Compounds (VOCs)

The term volatile organic compounds (VOCs) refers to a group of C-containing compounds that have a high vapour pressure and low boiling point. They therefore exist as gases in the atmosphere and can be emitted from surfaces as a result of these highly volatile compounds evaporating or sublimating from a solid or liquid phase [108] [4]. Hydrocarbons with approximately 2 to 10 carbon molecules are often classified as VOCs, this includes alkanes, alkenes and these are typically C-containing species with little functionality. Examples of VOCs are ethane, propane, formaldehyde, toluene and isoprene. Low-volatility organic compounds (LVOCs) are similar compounds with a larger molecular weight, for example more carbon atoms or increased functionality, which causes their boiling points to increase and vapour pressures to be smaller than the VOCs. Polycyclic Aromatic Hydrocarbons are an example of LVOCs. LVOCs can be subdivided into two further categories; intermediate volatility organic compounds (IVOCs) and semi-volatile organic compounds (SVOCs). IVOCs are defined as having a saturation vapour concentration between 10^3 and 10^6 μg m^{-3} [31]. The saturation vapour concentrations for VOCs are higher than this range. IVOCs typically have more functionality than an equivalent VOC with the same number of carbon atoms, which makes the compounds more polar and increases the boiling point. Or the IVOC will have a larger number of carbon atoms (e.g. greater than 12). However, they are emitted from similar sources to VOCs, are observed to be entirely in the gas phase and may potentially contribute more effectively to SOA [108] [31]. SVOCs have a saturation vapour concentration of between 10^{-1} and 10^2 μg m^{-3} [31], and therefore once they are emitted into the atmosphere they partition between the gas and solid phase [31].

VOCs are abundant and reactive in the troposphere [46] [140]. In the presence of sunlight and NO_X, VOCs are precursors to ground level O_3 [66], or can form secondary organic aerosol (SOA) [46] via oxidation. Different reactivities of VOC compounds causes them to each have unique O_3 producing potentials, for example, carbonyl compounds have a higher ozone producing potential than alkanes [46]. The reactivity of VOCs causes them to exhibit a range of lifetimes in the atmosphere [79], from a few minutes (monoterpenes) to months (ethane and acetone) [159]. The atmosphere contains a mixture of VOCs, which can be present in clean areas at relatively low concentrations, as low as parts per trillion

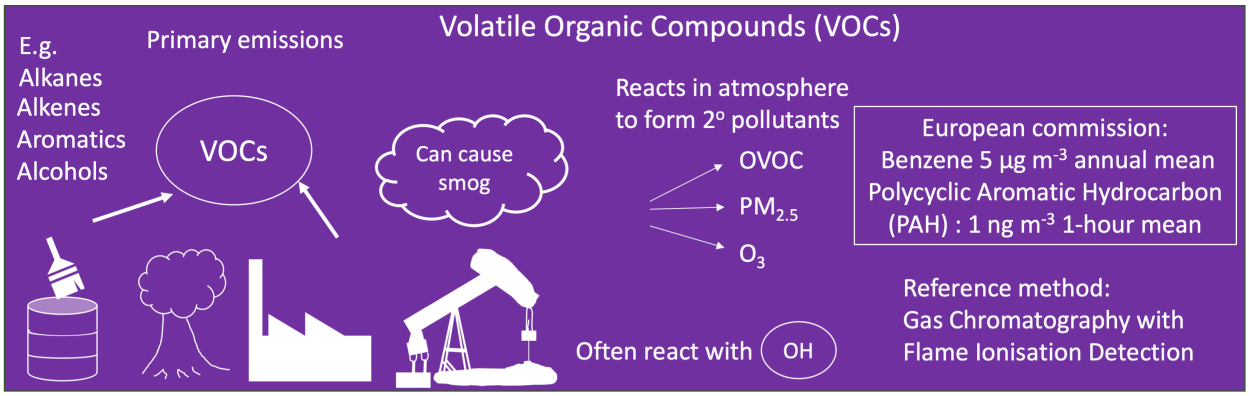

Figure 1.9: A brief summary of the sources and impacts of volatile organic compounds.

(ppt) concentrations in remote locations [140]. The global background concentrations varies by hemisphere, the Northern Hemisphere includes greater emissions of VOCs and therefore VOC concentrations are higher than in the Southern Hemisphere [159]. Individual compound concentrations vary depending on the lifetime of the species but the highest concentrations do not typically exceed a ppm [159].

Some VOC compounds, such as 1,3-butadiene, are also directly harmful to human, animal and plant health [140] [204], and others, such as benzene are known carcinogenic compounds [153] [42]. Whilst some VOC compounds are relatively non-hazardous the World Health Organisation has set no "safe" level for these. The European Commission set standards for two VOCs; benzene should not exceed 5 μg m^{-3} on a yearly average [53] and the maximum annual mean of 1,3-butadiene should not exceed 2.25 μg m^{-3}. The effect that VOCs have upon the environment and human health is dependant upon their emission sources, the VOC species emitted and the quantity of emissions [89], Table 1.2.

Across the globe, the majority of VOC emissions by mass are from the biosphere, produced from vegetation [159]. Approximately half of all the global biogenic VOC emissions (1000 Tg yr^{-1} [12]) are due to isoprene (C_5H_8) [12]. However, local regions can be dominated by anthropogenic VOC emissions, which includes emissions from solvents, combustion [89] and the extraction of Oil and Natural Gas (O&NG) [66] among other sources. The majority of anthropogenic VOC emissions have been attributed to vehicular transport and the Oil and Natural Gas (O&NG) industry [66]. In recent years, however, the contribution of emissions from domestic solvents has become more important [185].

There are a number of reactions involving VOCs that influence the tropospheric oxidative capacity as VOCs react with oxidants such as the hydroxyl (OH) radical and O_3 [140] during the daytime. For a general hydrocarbon reaction with OH, see Equations 1.5 - 1.11. During the nighttime, NO_3 concentrations increase and this becomes the main route by which VOCs are oxidised [79], rather than via the OH radical which is not formed in

Table 1.2: Examples of different groups of VOCs, example compounds, major emission sources and their impacts on human health and the environment [89].

VOC group	Major emission source	Example	Impact
Alkanes and alkenes	Unburnt fuel Fugitive emissions from oil and gas industry [137] Alkenes also from biogenic emissions	Ethane Propene	Precursors to aldehydes Some are respiratory irritants
Alcohols and ketones	Evaporation from cosmetic products Also products such as varnishes and paint thinners	Ethyl alcohol Acetone	Irritatant to eyes, nose, and throat
Aromatics	Incomplete vehicular combustion	Benzene Toluene	Toxic and carcinogenic Smog
Aldehydes	Products of a series of VOC oxidation reactions Biogenic emissions	Formaldehyde Acetaldehyde	Human health - toxic after chronic exposure respiratory irritation
Halogenated VOCs	Waste water after industrial processes	Chloroform Dichloromethane	Bioaccumulate in environment Toxic Do not degrade easily

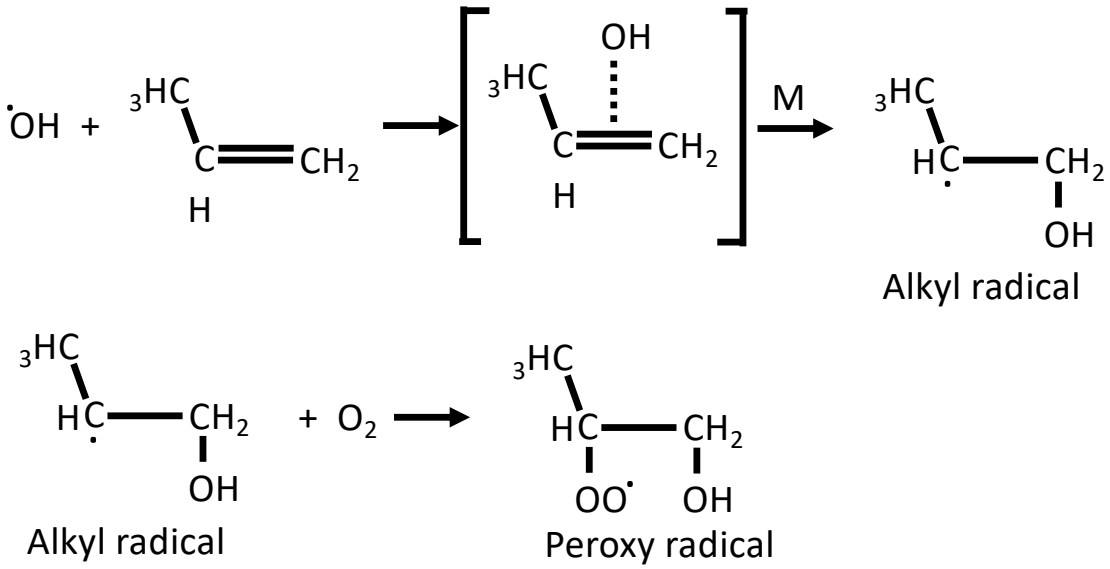

Figure 1.10: Oxidation of propene, via OH addition over the double bond. The peroxy radical (RO_2) formed will go on to react with other species such as NO or HO_2 in the atmosphere.

the absence of sunlight. In general, saturated compounds, such as alkanes, aldehydes, and alcohols will undergo H abstraction upon a reaction with an oxidant [190], see Equation 1.21. Generally, the greater the number of C-H bonds in a molecule, the greater the reactivity of the VOC with the oxidant, since the radical ($R^{\cdot}$ formed is more stable. Equation 1.21 shows how the NO_3 radical abstracts a hydrogen atom from the alkane (RH) to form nitric acid (HNO_3) and an alky radical (R).

$$RH + {}^{\cdot}NO_3 \longrightarrow R^{\cdot} + HNO_3 \tag{1.21}$$

Unsaturated species, such as alkenes, will undergo oxidant addition across the double bond, see Fig. 1.10. The more unsaturated a compound, the higher the reactivity with an oxidising species as the resulting radical is more stable [103] [4].

The oxidation of VOCs transforms them to oxygenated VOCs (OVOCs) which are less volatile [123]. These oxygenated compounds, for example, aldehydes and carboxylic acids are more water soluble than their reduced counterparts and can be more effectively removed from the atmosphere via wet deposition. However, since these oxidation products are less volatile they are typically more susceptible to partitioning to the solid phase and forming SOA [31]. SOA forms a large fraction of PM and is the main cause for photochemical smog which occurs in urban regions as a product of the tropospheric reactions occurring between VOCs, NO_X to form SOA and O_3 [107]. Smog impacts the health of residents and the presence of SOA causes a haze in the air which reduces visibility [103].

OVOCs will continue to react with other species in the atmosphere, often continuing to be oxidised, ultimately resulting in carbon dioxide (CO_2 and water (H_2O) or uptake

to form SOA. OVOCs, such as peroxyacyl nitrate (PAN) are harmful to humans [140]. Direct emission of OVOCs, from biological sources, evaporating solvents and incomplete combustion also contribute to the global OVOC concentrations. These oxygenated compounds, which include aldehydes, ketones, esters and alcohols are generally more reactive than their reduced precursors. The most abundant OVOC is methanol; biogenic emissions of methanol in 2012 exceeded 100 Tg yr^{-1}, and anthropogenic sources added 65 Tg yr^{-1} to the global annual emissions [123].

Polycyclic Aromatic Hydrocarbons (PAHs) are another class of organic compounds that are regulated by the EU Directives [52] due to them being carcinogens. Whilst a few of the lighter PAHs (e.g. naphthalene, acenophthylene) are volatile enough to be considered VOCs, the majority of them are known as Persistent Organic Pollutants (POPs) and are IVOCs. PAHs are a sub-group of VOCs that contain 2 or more benzene rings within a fused structure. They exist in the troposphere as gaseous, liquid and solid molecules, depending on their vapour pressures, which are relatively low for lower weight PAHs. All PAHs are suspected as being carcinogenic, and their toxicity increases with their molecular weight too [148]. The main source of PAHs is attributed to the pyrolysis and incomplete combustion of coal, oil and gas [148]. The annual average for Polycyclic Aromatic Hydrocarbon (PAHs) should not be greater than 1 ng m^{-3} at any time, and typically monitoring the ambient concentration of benzo[a]pyrene is used as a proxy for all PAHs to assess their atmospheric behaviour and deposition rates of PAHs in the troposphere [52].

1.5.1 Reference VOC instrumentation

As the typical concentration of VOCs in the troposphere can be low (pptv) the instrumentation used to detect the compounds must be sensitive. The most common method of VOC detection is to use Gas Chromatography with Flame Ionisation Detection (GC-FID).

The sample of ambient air is often pre-concentrated to increase the sensitivity of the technique and allow precise and accurate qualitative and quantitative measurements to be made. Pre-concentration of a sample of air for VOC analysis is conducted using an adsorbent trap [159].

The next stage of VOC analysis involves separating the mixture of VOC compounds out in order to detect individual VOC compounds. The VOC compounds in the sample are separated out into individual species using GC. The GC consists of a long, thin column inside an oven. The air sample flows down the column via a carrier gas (mobile phase, often helium or hydrogen) and VOCs in the sample interact with the coating (stationary phase) on the inside of the column. A dynamic equilibrium, between VOCs in the mobile phase and VOCs adsorbed to the stationary phase is established. Different VOCs will exhibit different equilibrium's with some compounds being in the mobile phase much more than others. These will pass through the column quicker than VOCs that spend more time

adsorbed to the GC column stationary phase, hence separation of the compounds can occur. The choice of column will depend on the specific compounds to be detected and the resolution and separation of VOC peaks in the chromatogram. After eluting off the GC column the individual VOC species must be identified and quantified. For use in long-term, ambient VOC monitoring networks the most common method of detection is by Flame Ionisation Detection (FID) [159], [140] [79] as it is a very stable detection technique. The UK's Automatic Hydrocarbon Network uses GC-FID to produce hourly VOC concentration data [37]. As each compound passes through the FID system, it is ionised and the increased current due to the extra ions is detected [73]. The increase in current is proportional to the amount of carbon atoms in the sample. The performance of GC-FIDs in the monitoring networks is monitored with formal inter-comparisons [37] [140], synthetic gas standards containing VOCs in N_2 and Whole Air Standards [159]. The limit of detection (LoD) for GC-FID depends on the GC technique, chosen column and the individual VOC compound. Dual channel GC-FID has been shown to detect and quantify up to 64 individual VOCs, all with varying LoDs [79]. Alkene and alkane compounds display similar LoDs from 1 ppt for n-hexane and 1-butene to 7 and 9 ppt for ethene and ethane respectively [79]. Hexane and butene have lower LoDs due to them containing more carbon atoms per molecule, since FID detects the carbon atoms within the molecule, molecules with more C atoms are easier to detect. The pre-concentration, drying and separation of compounds all takes time, so typically a GC will yield one chromatogram every 40 minutes. This sample will be an average of the compounds present during the sampling time (often ten minutes). Therefore, although the chromatograms provide detailed information about the composition of a mixture of air, they provide a snapshot of the VOC concentrations during the sampling time and cannot necessarily detect the short term VOC concentration peaks that people are exposed to. VOCs may exist only in very low concentrations in the ambient environment and even with pre-concentration, their peaks in the chromatograms are sometimes too small to be above the noise. 2D gas chromatography is one alternative method around this problem [201].

Other detection techniques are available and compatible for use with a GC e.g. time of flight or quadrupole mass spectrometry (MS). A Selected Ion Flow Tube Mass Spectrometer (SIFT-MS) is an alternative method to sampling VOC compounds in the atmosphere with a higher time resolution than an automatically operated GC. The SIFT uses an ion source to generate a mixture of reagent ions which can have either positive or negative charges [164]. Examples of positive reagent ions: NO+, H_3O+, O_2+. Examples of negative reagent ions: O–, O_2–, OH–, NO_2–. One types of these reagent ions is selected from the mixture using a quadrupole mass filter which only allows one type of ion with a particular charge and mass to pass through [164]. The selected reagent ions pass through a Venturi-type orifice (1 -2 mm diameter) [164] and enter a fast flowing inert carrier gas (typically helium) which carries the reagent ions to the air sample. Soft chemical ionisation

occurs, whereupon the reagent ions ionise the compounds and species within the ambient air sample [164]. The reagent ion collides with the VOC and forms an adducts with the VOC compounds. These VOC ion-adducts then pass through a second quadrupole where they are sequentially detected. The VOC-ion adducts produce a signal by impacting onto a surface which generates a current. The current is multiplied using an electro-multipler to allow the signal to be large enough for detection [11]. The SIFT-MS technique allows for real-time measurements of VOC compounds and has sufficient sensitivity to detect trace compounds in amibent air.

1.6 Particulate Matter

Particulate matter (PM) refers to solid or liquid particles suspended in the air. Both as a solid or as liquid droplets, PM can be composed of a variety of chemicals from metals to organic matter and acids [2]. Particulate matter can be emitted directly to the atmosphere (primary) or is formed from the reactions of other atmospheric species (secondary PM). Primary emissions, from electricity-generation in power plants, combustion and industrial activities, transportation and biomass burning contribute to regional PM levels [203]. Depending on location, the total suspended particles (TSP) can be dominated by primary natural emissions with sources from deserts, sea salt, volcanoes and emissions from plants and fungi [5]. In the dry season mineral dust emissions, estimated to be between 400 - 2200 Tg $year^{-1}$, from the Sahara desert make the largest contributions to the PM concentrations in North and West Africa [88].

Secondary PM is formed via a series of chemical reactions in the atmosphere. SOA, is comprised of lower volatility compounds such as LVOC, and can be produced after the oxidation of VOCs in the atmosphere [18]. There is also secondary inorganic aerosol, which typically forms from the reaction of gaseous ammonia with sulphur dioxide or nitrates from NO_X. Gaseous ammonia dissolves into aerosols and this increases the rate at which dissolved SO_2 reacts to form sulphate ions (SO_4^{2-}). The ammonium species preferentially combines with SO_4^{2-} to become ammonium bisulphate $(NH_4)SO_4)^-$. If the SO_4^{2-} concentration is high enough ammonium sulphate ($(NH_4)_2SO_4$) will form. If there are relatively high nitrate ions, and low sulphate concentrations in the aerosol then ammonium nitrate ($(NH_4)NO_3$))aerosol is produced [10].

Although made up of a variety of compounds, the characteristics of PM and its impacts to the environment and human health are determined by the size and composition of the particles. $PM_{0.1}$, PM_1, $PM_{2.5}$ and PM_{10} are the typical classifications for PM and these have an Aerodynamic Equivalent Diameter (AED) of 0.1, 1, 2.5 and 10 $\mu g\ m^{-3}$ respectively. The emissions, impacts, transportation and concentrations of PM_1, $PM_{2.5}$ and PM_{10} are often independent of each other [2].

The boundary layer (BL) height will influence the observed PM concentrations; at

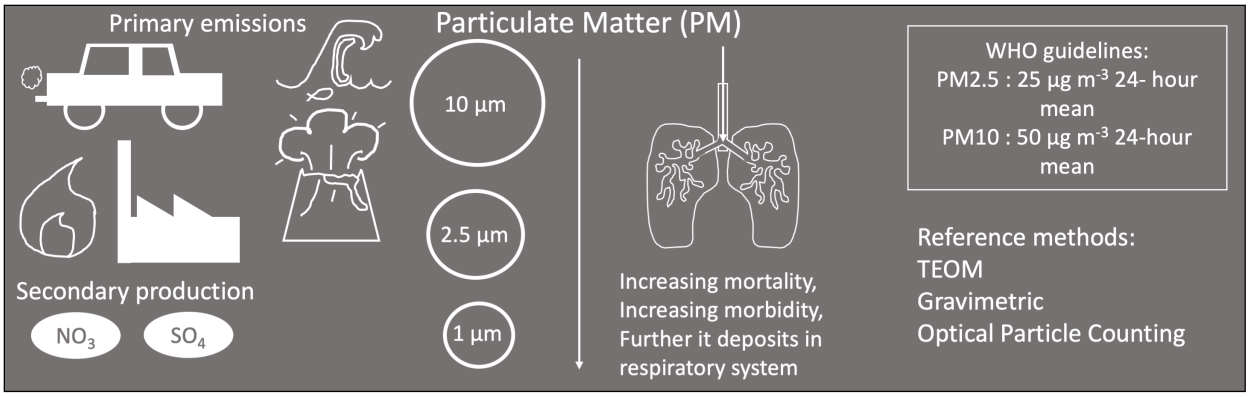

Figure 1.11: A brief summary of the sources and impacts of particulate matter (PM).

night when the BL is typically lower the concentrations of PM are often higher as there is less PM dispersion. During the daytime, the PM concentrations are often higher as the BL is higher and there is more dispersion of PM through vertical mixing and turbulent air [3]. Meteorological conditions hugely influence the levels of PM and wet deposition is the leading cause of PM loss from the atmosphere. PM can become incorporated into rain droplets and it rained out of the atmosphere or is entrained into the droplets as the precipitation falls to the ground (washed out). Either route leads to the removal of suspended particles and hence lower PM concentrations. Regions which experience a wet and dry season will have seasonal trends that are mainly driven by the amount of precipitation occurring [88]. Wind-speed impacts the regional levels of PM in a slightly more complex manner and the effect of wind-speed is dependent upon the surrounding environment. At coastal regions an increase in wind-speed leads to an increase in sea salt PM. However, on still days in continental locations, a slight increase in the wind leads to PM becoming more diluted and hence lower observed PM concentrations. High wind-speeds in continental locations may also cause re-suspension of particles and so increase PM concentrations [5]. Strong winds over desert regions causes the emission of dust PM [88]. Seasonal trends vary depending on location too and in remote areas where biogenic sources dominate, PM will be increased in Summer when the higher temperature and more intense sunlight stimulate photosynthesis leading to greater plant activity and emissions. In urban areas, where anthropogenic activities dominate PM emissions the reverse is often true, as there is greater combustion for heating and electricity during the Winter months, leading to increased PM during the Winter [5].

1.6.1 Human health implications of PM

There are multiple health effects associated with exposure to elevated concentrations of PM, and the WHO has set thresholds for fine ($PM_{2.5}$) and coarse (PM_{10}) particulate matter. There are positive correlations between the levels of $PM_{2.5}$ and PM_1 in the atmosphere and increased mortality [195] [101]. The chemical composition of PM varies and

therefore so does the toxicity of the particles, with carbonaceous material considered more toxic that inorganic aerosol or PM derived from crustal sources [101]. The majority of the detrimental health impacts caused by PM is due to the chemical species that are coated onto or contained within the PM [109]. Heavy metals, PAHs and other harmful species are bound to, adsorbed onto or absorbed into PM and these are causing the adverse health impacts [109].

Since there are health affects associated with both acute and chronic exposures to PM [18] [45], the WHO has set guidelines for the annual mean: $PM_{2.5}$ <10 μg m^{-3}, PM_{10} <20 μg m^{-3}, and also limits for short-term exposure, a 24-hour mean: $PM_{2.5}$ <25 μg m^{-3}, PM_{10} <50 μg m^{-3}. The limit values set out in Annex XI in the EU Directive 2008/50/EC [53] also consider both short term and long term exposure to PM. The daily average of PM_{10} should not exceed 50 μg m^{-3}, or 40 μg m^{-3} over a calendar year. The annual average of $PM_{2.5}$ should not exceed 25 μg m^{-3}. The presence of PM in the atmosphere greatly reduces the air quality, and is a huge expense to the world health care budget due to detrimental impacts upon human health [2].

$PM_{2.5}$ is often used as an indicator to estimate the effect of overall air pollution on the global burden of disease [18] and is the cause for thousands of deaths globally every year – the WHO estimated 800,00 in 2010 [2] [195] [101]. There is an increased number of people suffering from cerebrovascular disease and ischaemic heart disease, both of which contribute to premature mortality due to exposure of elevated PM concentrations [101]. Increases in $PM_{2.5}$ concentration will result in an increased number of hospital admissions related to cardiovascular and respiratory illness [45]. People with existing respiratory illness are also likely to experience exacerbated symtons from chronic exposure to elevated PM levels [2]. PM_{10} and $PM_{2.5}$ are attributed to increased mortality [128], $PM_{2.5}$ can cause lung cancer [180] and all three fractions: PM_1, $PM_{2.5}$ and PM_{10} increase the risk of cardio-pulmonary morbidity [170]. The lower WHO guideline values for $PM_{2.5}$ reflect the expected concentrations of PM in the atmosphere and also the impact upon the respiratory system. The different size fractions of PM lead to different health impacts upon exposure to them, as they infiltrate to different amounts into the human respiratory system [170]. The smaller sized particles penetrate further into the human respiratory tract and $PM_{2.5}$ is known to reach the delicate alveoli in the lungs, increasing respiratory morbidity [45] [180]. Once inhaled PM causes inflammation of the airways and oxidative stress [2] which results in pulmonary infections and diseases.

It is understood that airborne ultra-fine PM is more toxic per particle than the larger fractions of PM due to faster uptake into the respiratory tract [21] and its ability to cross the lung-blood barrier. Particles that have an AED of less than 0.1 um are considered ultrafine and due to their small size these particles are not filtered out by the nose or deposited in the upper respiratory tracts so reach, and can subsequently damage, delicate lung tissue [45] [21] [2].

Existing health conditions are exacerbated for people living in areas with pro-longed exposure to elevated PM leading to premature death [2]. There are more hospitalisations during short-term PM events [45] [2]. There are studies showing positive correlations between lung cancer and the exposure to $PM_{2.5}$ [180], increased risk of cardio-pulmonary disease, inflammation of the airways with the effects of PM associated with oxidative stress [2]. The WHO estimated that 5% of cancers found on the trachea, bronchus and lung were due to exposure to elevated levels of $PM_{2.5}$ [180] [195]. Indoor biomass burning for residential heating or cooking in low to middle income countries [194] leads to extremely raised concentrations of PM, with measurements displaying concentrations over 200 μg m^{-3} [2]. This increases the risk of lung infection and reduced lung function [2]. PM derived from combustion sources, both indoor and outdoor are more likely to cause adverse health effects [128].

Recent analysis of $PM_{2.5}$ has shown that concentrations are increasing in areas which are developing quickly, related to the rapidly increasing population [18]. For example, over the past few decades Beijing has experienced increasingly poor air quality and increasing $PM_{2.5}$ concentrations linked to the increase of coal combustion due to it's expanding population requiring electricity and heating for their homes [202].

Suspended particles in the atmosphere can initiate cloud formation by acting as cloud condensation nuclei (CCN). In general, for an air parcel with a certain supersaturation, the more CCN there are, the more water droplets there will be and the smaller the size of these droplets. Clouds with smaller droplets are more reflective, hence the presence of more CCN leads to greater radiative back scattering of incoming solar radiation, leading to an overall cooling effect on Earths climate, deemed the Twomey effect [20]. Clouds with smaller droplet sizes are less likely to undergo precipitation and so the presence of PM and hence CCN, will prolong the lifetime of the cloud, causing an additional indirect climate cooling effect [20].

1.6.2 Reference PM instrumentation

Ambient concentrations of particulate matter are measured as part of the UK's AURN network using four techniques which have undergone extensive testing to prove they are equivalent to the European Reference method for PM monitoring [40] [53]. The EU Reference method for PM analysis is gravimetric analysis, and the procedure is laid out in the European Standard EN 12341:2014. The four techniques that are considered equivalent to the EU Reference method are:

- Tapered Element Oscillating Microbalance (TEOM)
- Offline gravimetric PM analysis using a Partisol high volume sampler to sample ambient air onto a filter for in-laboratory analysis
- Beta-attenuation Monitor (BAM)

- Optical Particle Counter (OPC)

These techniques used for reference PM measurements are described in more detail.

Tapered Element Oscillating Microbalance (TEOM)

A Tapered Element Oscillating Microbalance (TEOM) measures PM in real-time and provides precise PM measurements every ten seconds. The instrument contains a glass tube which is tapered and a filter that can be exchanged. Both are oscillating at resonant frequency. Air is drawn in and PM begins to build up on the filter, causing a slight increase in weight, which in turn changes the resonant frequency of the devices [192]. The change in frequency is detected and the mass of the PM on the filter is calculated [94]. Having two filters and separating out the $PM_{2.5}$ and PM_{COARSE} particulates (PM_{COARSE} refers to the sum of PM_{10} and $PM_{2.5}$), then weighing the filters continuously and simultaneously allows for the determination of the concentration of $PM_{2.5}$ and PM_{10} [94]. A Filter Dynamic Measurement System (FDMS) is sometimes used with the TEOM to capture the more volatile species on PM, whilst still allowing for the removal of water from the sample.

Beta- Attenuation Monitor (BAMS)

Used as a reference method by the EPA in the USA, BAMS measure PM_{10} and $PM_{2.5}$ over a range of 0 – 1000 μg m^{-3}, with a resolution of ± 0.1 μg m^{-3}. The BAMS provide hourly measurements of the two different PM fractions and the results are often averaged over 24 hours [160]. PM in the sample is separated into coarse and fine particles, and the two different streams of PM are then directed to and deposited onto two glass fibre filters. Beta decay of ^{14}C provides a source of β- particles, which are then directed towards the PM on the filters. The amount of β- absorbed is exponentially related to the thickness of the PM, and therefore the attenuation of the β- particles is used to calculate the mass of PM on the filter. The remaining β- particles that pass through the filter are detected using a silicon surface barrier [116] positioned on the other side of the filter.

Optical Particle Spectrometer (OPCs)

PM can also be detected using light scattering. Particles pass thorough a beam of characterised light, and the amount of light elastically scattered by the particle yields information about the particle number and morphology. The scattering intensity is dependant on the size of the particle, and the technique produces reliable results for particles larger than 100 nm in diameter [177]. The OPC uses radiation from a laser, and the light will have a characteristic wavelength that will be smaller than the diameter of the particles1.22. This results in Mie Scattering which is advantageous over Rayleigh Scattering as the scattering effect is much more pronounced and hence the technique is more sensitive. This technique is widely used for characterising particulate matter in the troposphere [177] and the technology and relatively simple components allows for the miniaturisation of the device, making it more portable. One example of a minaturized OPC device is the Printed Optical Particle Spectrometer (POPS). The POPs counts particles using a portion of the light scattered when a particle passes through a 405 nm laser beam. The scattered light

is detected by a photomultiplier, which converts the intensity of light to an electrical current [62]. 3D printing technology is used to produce some of the structure for the POPS instrument, hence the word 'Printed' in the name. Using a 3D printer means that the parts can be built in-house at a reduced cost and time for production [62]. The POPS monitors particles with a diameter of 140 – 3000 nm and has shown evidence of producing stable results for 7 months [62].

Off line PM analysis

A high volume sampler, such as the Partisol 2025 can be used to actively sample ambient air onto glass fibre filters. A large sample volume is collected to ensure that there is a sufficient amount of PM collected on the filter for an accurate determination of the PM amount and composition. A typical flow rate for air through the Partisol would be approximately 16.7 LPM. The air is drawn in through an inlet head, to ensure that particles larger than 10 microns in diameter do not enter the device [37]. Some high volume samplers are configured to automatically change the filters to minimise the frequency for which the filters need to be collected. The sampled filters are sent to the laboratory to undergo analysis by weighing the amount of PM on the filter, a gravimetric technique [37].

1.7 Carbon dioxide (CO_2)

Anthropogenic activities involving the combustion of fossil fuels are the greatest contributor to CO_2 emissions to the atmosphere [82] [158]. CO_2 is well-documented as a potent greenhouse gas (GHG) and it is important to monitor the global concentrations and trends in atmospheric CO_2. The average global CO_2 concentration increased from 280 ppm to greater than 400 ppm, since the pre-industrial era [119]. CO_2 from fossil fuel combustion and industrial activities during 1970 to 2010 made up 78 % of the total GHG [82]. An increase in the global levels of GHG leads to climate warming which has many impacts upon the Earth's ecosystem, for example ocean acidification, changing weather systems and failing crop yields [82]. A large portion of these anthropogenic CO_2 emissions arise from urban areas and there is concern that CO_2 anthropogenic emissions will rise further with anticipated urban populations in the coming years [82] [158]. There are multiple cities, such as Boston and Paris that use a top-down observational approach to determine their contribution to CO_2 emissions [158]. Multiple (often between 3 – 12) CO_2 reference monitors on towers in metropolitan areas are used to support inverse modelling of the CO_2 flux for that region [158], [119]. An increase in the spatial measurements for the calculation of the CO_2 flux would mean that the inversion estimates are better and more constrained [119]. Fossil fuel CO_2 emissions vary on localised scales as they are emitted from a plethora of sources from single power-generating facilities to road segments [70]. There is a drive to understand the carbon flux of the atmosphere at a local level to identify effective policies and strategies out in place to reduce fossil fuel CO_2 emissions [70].

The levels of CO_2 fluctuate annually, with an increase in atmospheric CO_2 concentrations occurring in the Northern Hemisphere in autumn and winter associated with a decrease in the plant life. As plants die off over winter less CO_2 is taken in by them during photosynthesis, and this is more evident in the Northern hemisphere as the majority of vegetation is in that hemisphere [144].

CO_2 is considered safe at concentrations inhaled in outdoor air [131]. Chronic exposure to CO_2 concentrations that exceed 5 % may cause health affects in extreme cases with symptoms such as muscle tremors, loss of vision or consciousness, headaches, sweating becoming more pronounced, and even death in a few circumstances [198]. The levels of outdoor CO_2 do not usually reach levels that are close to this threshold however, it is important for small sub-groups of people, for example people working in underground subways [87]. CO_2 is also often associated with indoor air quality and hence real-time continuous CO_2 observations can be used for ventilation control [119] in the workplace. An increase in the ability to make building air-tight has led to a build-up of CO_2 in some workplaces, with detrimental health impacts, including sick-building syndrome [131].

1.8 Performance criteria for instrumentation

The Department for Environment, Food and Rural Affairs (DEFRA) and the Environment Agency (EA) have set performance criteria for instrumentation used in the field. The instrumentation must be tested to ensure that it meets these criteria in order to be used for ambient UK air monitoring and to allow spatial comparisons of the concentration of pollutants to be accurately assessed [49], see Fig. 1.12. These criteria include a range of laboratory experiments to identify the performance of the instrument in controlled conditions with typical gas calibration standards and zero air. There are also a series of field tests to ensure that the instruments continue to perform in real-world conditions.

Figure 1.12 shows the criteria that CO, NO_X and O_3 instrumentation must meet for the instruments to be used by as continuous ambient air quality monitoring systems in the UK's national air quality networks. There are also standard methods and procedures, detailed in the MCERTS Continuous Ambient Air Quality Monitoring Systems scheme [49], that state how the measurements, made by the instrumentation that meet the criteria, are to be carried out. The MCERTS scheme [49] details how the laboratory and field tests should be conducted, the different procedures and which gas calibration standards to use. The EA have produced similar criteria for instruments that measure the concentration of benzene in the atmosphere, Fig. 1.13. The regulation of instruments ensures that there is a high degree of reproducibility between instruments monitoring the same pollutants. Only then can there be confidence in the data that temporal and spatial variation within that compounds concentration is real and not due to the error within the measurements.

The instrumentation used for air quality monitoring, to detect atmospheric pollutants

Laboratory experiments / Field operation	Repeatability in zero air	Repeatability @ 1hr limit value	Short-term drift with zero air	Response time
NO_X and O_3 instruments	< 1 ppb	< 3 ppb	2 ppb over 12 hours	180 seconds
CO instruments	< 1 ppm	< 3 ppm	0.1 ppm over 12 hours	180 seconds

	Reproducibility	Long term drift in zero air	Unattended operation
NO_X and O_3 instruments	5 % of the average over 3 months	5 ppb	3 months (not less than 14 days)
CO instruments	5 % of the average over 3 months	5 ppm	3 months (not less than 14 days)

Figure 1.12: Performance criteria for NO_X, O_3 and CO instruments to monitor ambient concentrations of these pollutants. There are experiments conducted in the laboratory (blue), under controlled conditions and in the field (brown) to ensure the performance of the instrument is reliable when it has been deployed.

Laboratory experiments / Field operation	Repeatability at 0.5 µg m^{-3}	Repeatability @ limit value	Short-term drift at 70% limit
Benzene instruments	< ± 0.5 µg m^{-3}	< ± 5 %	< ± 5 %

	Reproducibility	Long term drift in zero air	Unattended operation
Benzene instruments	± 0.25 µg m^{-3}	± 10 %	Not less than 14 days

Figure 1.13: Performance criteria for instruments to continuously monitor benzene in the ambient troposphere.

and identify if locations are within regulatory concentrations must provide reliable results. The standards set in the EUs Directive 2008/50/EC [49] [53] emphasise the importance of using equipment that has high precision and accuracy, must be able to run continuously in the field unattended for a period of at least two weeks and have appropriate response times to effectively capture short-term pollution events. Instruments used must have minimal temporal drift and stable baselines to ensure that the observations remain accurate over time, with low limits of detection in order to detect the low concentrations of the contaminants that are likely to occur in the atmosphere. A low limit of detection often requires a small signal to noise ratio so random noise signals must be minimised. The instruments must be able to be installed in the field and therefore cope easily with only small dependencies on environmental conditions such as temperature and humidity. The troposphere is made up of a mixture of gases so the instrumentation will be selective to detecting its target compound and not be influenced by other atmospheric gases at the concentrations commonly found in the ambient air. The instruments must all meet the required standards of reproducibility and compare well with other instruments when they are co-located in a large inter-comparison. During an inter-comparison the instrument might be calibrated with a certified gas standard which contains a known amount of the target analyte, and is used for testing all the reference instruments. The response of these instruments must be very similar. For example, the absolute response should be within 5 % of the other instruments response to the same gas standard [37]. The linearity and span gas response, of the instruments is also compared by subjecting the instruments to a large range of target analyte concentrations. Instruments that make reproducible measurements and result in very similar responses to other instruments using the same scientific methods will then be considered appropriate. Then there will be high confidence in the observations and spatial variability of pollution can be assessed along with quantifying absolute compound concentrations and report data for long-term trend analysis [106]. Where the national networks are upgraded to new instrument techniques, to improve the quality of data collected, there needs to be a suitable co-location period to ensure that the data collected previously in not invalidated. The instruments might be replaced to ensure that the data has lower limits of detection, which is especially important for pollutants whose atmospheric concentration are declining [37]. The replacement equipment might be a newer version of the current technology or have a different principle behind the measurements. The calibration procedures must use traceable, certified reference materials in order to understand the different performance characteristics that might arise with replacing instrumentation in the national air quality networks [37].

1.8.1 Air Quality Monitoring

Monitoring the atmosphere is no easy task as the composition of the atmosphere is extremely complex and is constantly changing due to meteorological conditions such as

temperature, wind, humidity and incident sunlight [118]. In addition to these factors, the compounds of interest are may be present in very low concentrations [118] and have short atmospheric lifetimes due to complex reactions. Vertical mixing and horizontal movement further complicate the path of atmospheric components [28] and so collecting samples that reflect the movement of compounds can be challenging and require highly sensitive instrumentation, with the ability to provide good spatial and temporal resolution. Ideally, the instruments would be automated, have low installation and maintenance costs, require little or no personnel after deployment, be portable, have a rapid response time towards their target compound, and provide selective measurements for that compound [118].

It is difficult to measure the air quality of a region because contaminants arise from a variety of sources; some emission sources are mobile, e.g. vehicular emissions, others are stationary e.g. point sources such as industrial processes and factories. The quantity of emissions and pollutant dispersion varies greatly depending on factors such as wind speed and direction. Other pollution levels are determined by the amount of sunlight, their dispersion, their reactivity and the deposition onto the surfaces [125]. National monitoring networks, contain reference instruments to monitor key pollutants and are strategically installed at various locations around a country to ensure that the ground observations of pollutants are representative of pollution within the entire country. There must be sites with different characteristics, from remote rural to inner-city urban to build up a map of the pollution throughout the country and ensure that air quality meets national and EU standards [53] [52].

1.8.2 UK Air Quality Monitoring Networks

In the UK, there are several air quality monitoring networks, such as the Automatic Hydrocarbon Network, Particulate Concentration and Number (PCN) Network, Toxic Organic Micro Pollutant (TOMPs) Network, which are each installed to monitor the concentrations and trends of pollutants that are regulated by UK, EU and/or international legislation. The largest UK air quality monitoring network is maintained by the Department of Environment, Food, and Rural Affairs (DEFRA) and the Environment Agency (EA) and is called the Automatic Urban and Rural Network (AURN) [40]. There is a total of 170 sites across the UK used to quantify current concentrations of NO_X, particulate matter, ozone, sulphur dioxide and carbon monoxide pollution and evaluate the long term trends. Not all pollutants are monitored at each site. This long running network - the earliest measurements were made in 1973 - is continuously assessed and alters depending on the pollutants that are prioritised due to their impact on human health and whether or not the air quality within the UK is compliant with the standards set by the European Union and the World Health Organisation. Each pollutant has a number of sites located in strategic locations, often using guidelines laid out in the EU Directives [53] [52] to represent the behaviour of that pollutant across the entire UK. The sites have all been classified into

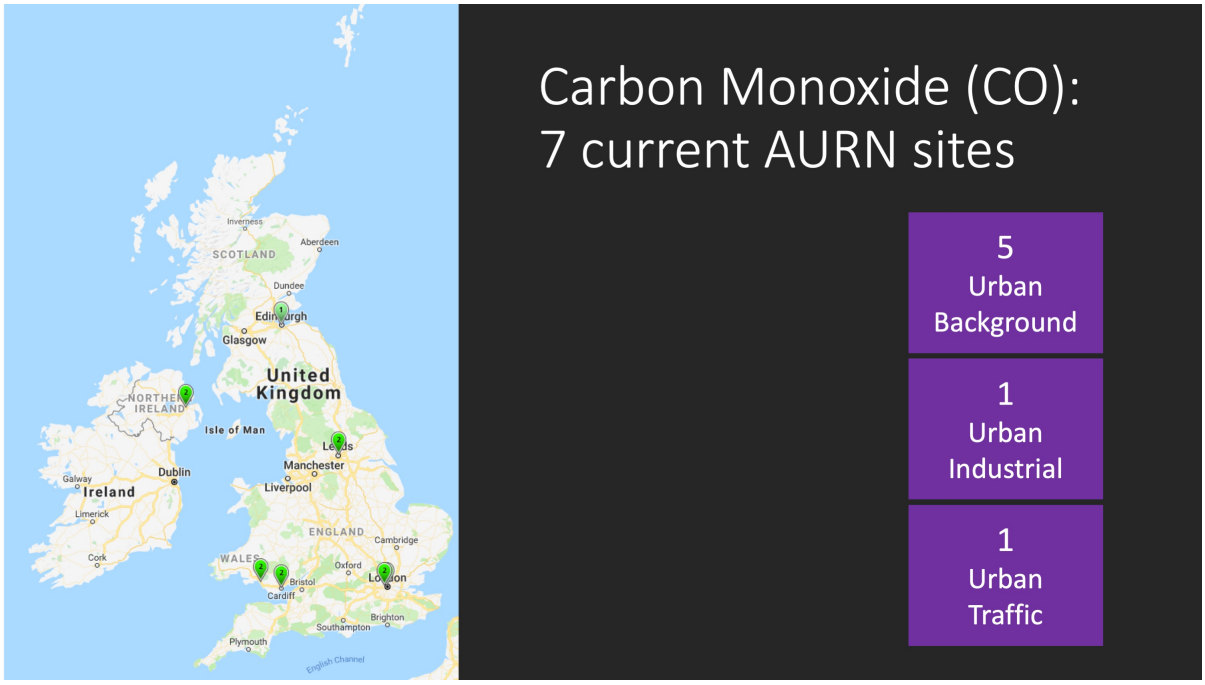

Figure 1.14: A map of the UK, with the locations of the seven CO AURN sites shown as green pins and a breakdown of the different site classifications.

12 types; there are industrial, traffic, background and unknown sub-groups for each of the three rural, suburban and urban classifiers.

The NO_X and CO measurement sites in Fig. 1.16 and Fig. 1.14 are colour coded to identify the locations classification according to the DEFRA definitions. The site locations are selected to ensure the air parcel the instruments will be sampling from is as representative of that local region as possible. For example, for the 7 CO sites, there are 5 that are classified as urban background, 1 urban industrial and 1 urban traffic location, Fig. 1.14. Due to ambient concentrations of CO falling below the regulatory thresholds, these sites are sparsely located, with only one in Scotland, one in Northern Ireland and only 5 to represent the ambient concentration of CO in England. Roadside levels of NO_X are an issue for the UK, with many sites exceeding the limit set by the EU. Therefore there are many more sites (158) within the network and these help identify NO_X hotspots that need to have mitigation programmes, Fig. 1.16.

Ozone is monitored at 76 sites within the AURN, with the majority of sites located to represent the background concentration of O_3; 43 sites are classified as urban background and 22 located in regions classified as rural background.

29 VOC compounds, chosen because they are ozone precursors, are monitored hourly as part of the Automatic Hydrocarbon Network consisting of 4 sites. In accordance with the EU 2008/50/EC Directive, fortnightly benzene observations are additionally collected with sample tubes containing Carbopack X as an absorbent, at 34 sites, making up the Non-Automatic Hydrocarbon Network (34 sites) [53]. The information regarding the location, sampling periods and classification of AURN sites was collected from the Department

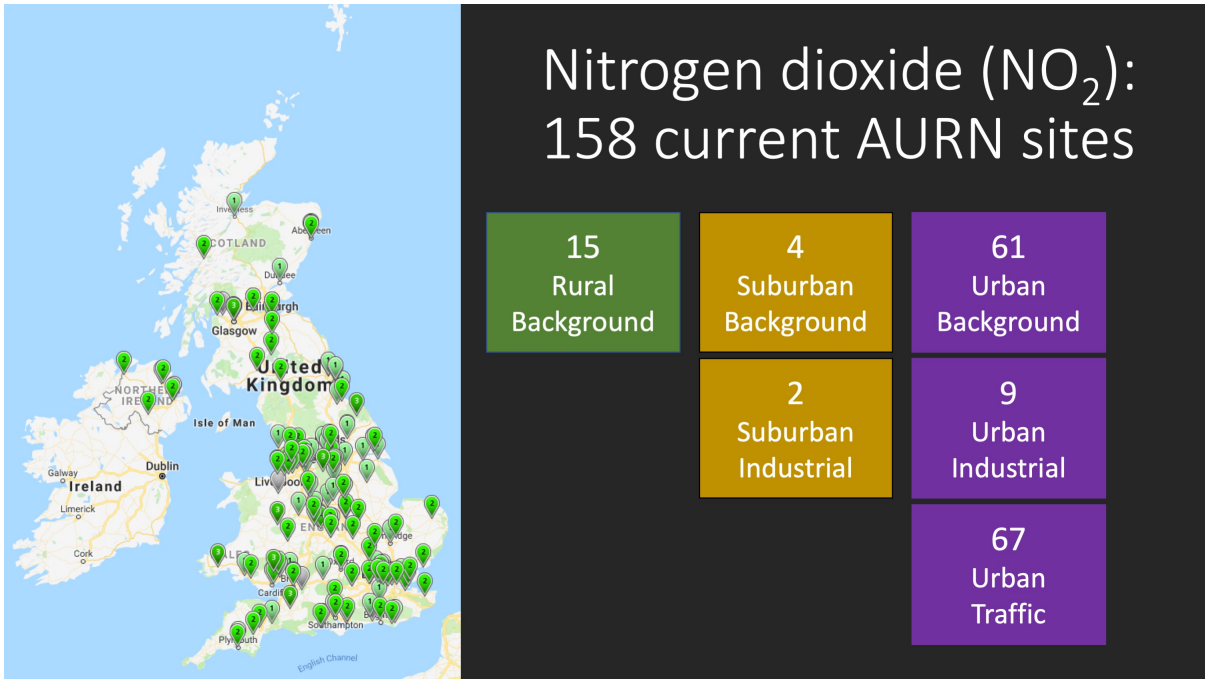

Figure 1.15: The locations of the 158 NO_2 AURN sites that are currently reporting data. The coloured boxes show the classification of the sites.

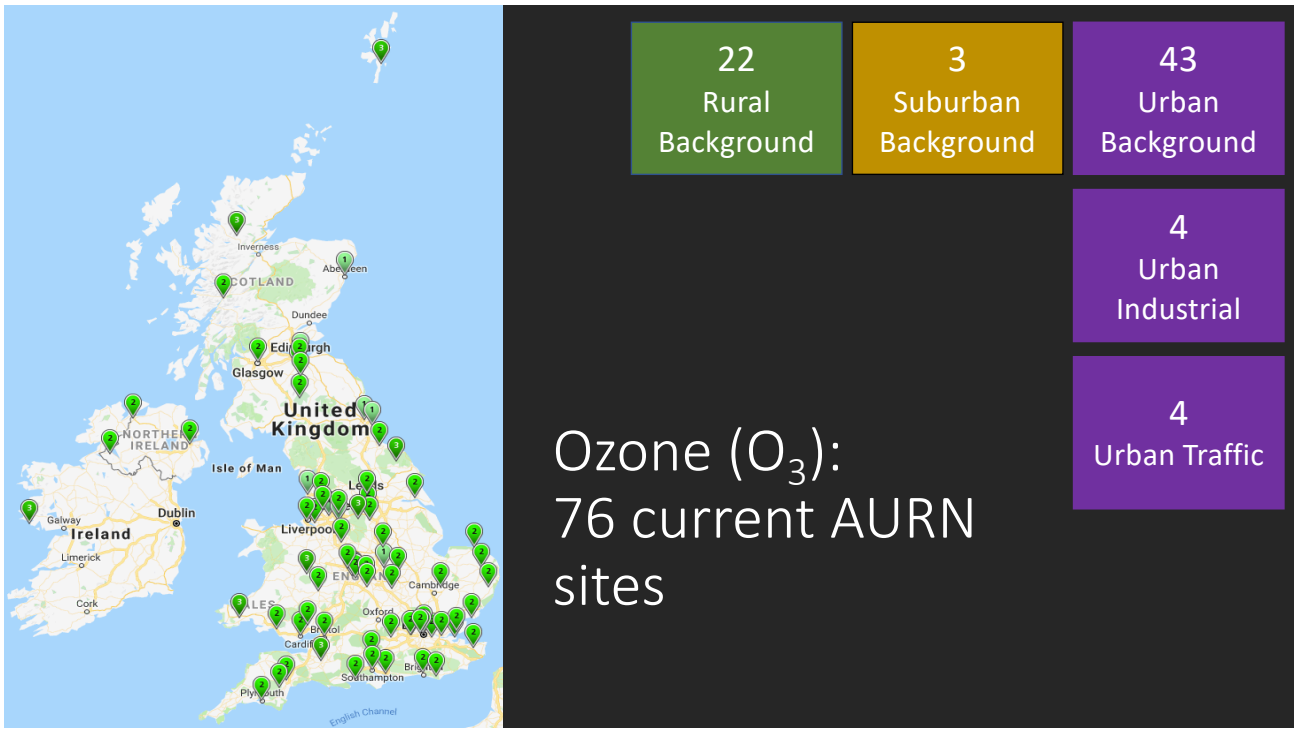

Figure 1.16: The locations of the AURN sites that currently monitor hourly ozone concentrations. The coloured boxes show the classification of the sites.

for Environment, Food and Rural Affairs (DEFRA) UK AIR Air Information Resource website [41].

Atmospheric chemistry models can interpolate between the reference monitors to estimate the concentrations of the pollutants in regions where there are no monitoring stations, but the further apart the sites are, the greater the uncertainty in these pollution estimates. Currently the AURN network, although the largest in the UK, is still relatively sparse, especially for some pollutants, e.g. CO for which the UK regularly complies with the limits set by the EU and WHO. Therefore, even when using all the sites for analysis, it is difficult to determine a highly resolved observational pollution map. Short, intense, field campaigns have been used to gain more insight into atmospheric composition over a few weeks or even months, but these also tend to be located in one spot and are only maintained for short periods of time [125]. In order to fully map the pollution that a region experiences, more measurements are required on a highly resolved spatial scale, which is comparable to the spatial scales over which pollution occurs. Monitoring stations within air quality monitoring networks are spread over a large area with typically one station representing an area of 1 - 10 km^2 [121]. However, the concentration gradients for pollutants are often steep [19], and there can be pollution hotspots that only effect a much smaller area, with pollutant concentrations being highly variable over 1 - 100 m [167]. A good example of this is NO_2 because of it's short atmospheric lifetime, elevated NO_2 concentrations are only observed within a few meters downwind of the emission source [167]. Increasing the number of ground observations would improve the validation of atmospheric models, allow for better calculation of concentration gradients between monitoring stations and better identify pollution hotspots [122].

1.8.3 Monitoring with low cost sensors (LCS)

Increasing the density of atmospheric observations would have huge benefits for the scientific community; it would be easier to identify sources of emissions, atmospheric models could be better validated and improved estimates of personal pollution exposure [106] [165]. Sensor networks, using multiple deployed sensors around a specific location have been used to gain further insight into pollution patterns over a local region and distinguish between local emissions and pollutants background concentrations [142]. These sensor observations can than provide additional data for atmospheric models and emission inventories to better characterise the pollution for that region [142]. The monitoring networks that exist in the UK and other countries are relatively sparse. Within the UK, the largest air quality monitoring network for gaseous pollutants and PM_{10} and $PM_{2.5}$ is the Automatic Urban and Rural Network (AURN). The area of the UK is 242, 495 km^2 [67], therefore it was calculated that each monitoring site within the AURN was representative of 1000s of km^2, see Table 1.3.

The AQM stations are located further apart than the distances over which most pol-

Table 1.3: A calculation of the area that each AURN site is represented of, assuming each monitoring site is equally spaced, with a total UK area of 242, 495 km^2. Number of sites for each pollutant was found using the DEFRA UK AIR website [41]

Pollutant	Number of UK AURN sites	Area represented by 1 AURN site (km^2)
CO	7	34, 642
NO_2	158	1, 535
O_3	76	3, 191
SO_2	28	8, 661
PM_{10}	78	3, 109
$PM_{2.5}$	81	2, 294

.

lutant exhibit concentration gradients [121] [19], therefore localised pollution events are likely to be missed [122]. Due to the high cost of the individual reference instruments (£5000, to £100,000) the expense of maintenance and regular calibration, and other resources required to install an Air Quality Monitoring station [122] it is impractical to install and maintain more AQMs with research-grade instrumentation. In some countries the networks are even more limited with very few or no routine monitoring occurring. Even within countries with the densest monitoring networks, the sites are typically located around 1 - 10 km^2 apart [121]. The concentration gradients associated with some atmospheric pollutants can be steep and vary over much smaller distances [19], leading to pollution behaviour that is not well characterised.

Some of the attributes associated with LCS, for example, inexpensive and continuous measurements, mean that they have the potential to be used to complement the existing monitoring network by increasing the spatial resolution of observations [35] [122] and generate a more detailed map of pollution on shorted spatio-temporal timescales. In some cases, such as the routine measurements of VOCs, the temporal resolution could also be improved. LCS are defined here as costing less than a tenth of the price of the equivalent reference method. LCS are an economically viable method to increase the number of measurements, and there are increasing numbers of studies where gas sensors have been deployed for both indoor [201] [22] [99] and outdoor use [122] [86] [138].

However, due to a lack of understanding about sensor characteristics and performance in real-world applications, such as the stability of the measurements and the reproducibility and reliability of sensor data [165], sensors are not widely used to produce absolute values for pollutant concentrations or for air quality monitoring. There are not currently standard methods available to direct how sensors should be used, deployed and calibrated making sensor inter-comparisons challenging as different sensor set-ups will lead to different sensor responses. Gas-sensors cannot be calibrated using the same gas standards (known concentration of target analyte in a dry matrix of zero air or N_2) as their equivalent reference instruments and therefore it is difficult to trace the sensors response to a

certified standard over time. Inner cities in particular experience hugely complex pollution patterns because there are lots of emission sources and urban architecture can lead to a build-up of pollution, called the canyon effect [183]. Not all streets experience this and therefore there are examples where the AQM stations do not detect these high-risk areas and therefore the exposure estimate of the urban population is not well represented [183]. LCS could be used in this instance to monitor different road segments to identify streets which experience the canyon effect.

1.9 Sensor Technology

There are a variety of different sensor technologies commercially available for the monitoring atmospheric concentrations of gaseous pollutants.

1.9.1 Metal Oxide Sensors (MOS)

Metal oxide sensors (MOS) are commercially available, small (approx. 1 cm diameter) and are inexpensive (£10 each). They can be used to monitor ambient concentrations of various gaseous compounds; total VOCs [155], H_2S [74], NO_2 [74], O_3 [172] to name but a few. The manufacturing method is relatively simple, can be automated [172] and allows large scale production of lightweight, durable sensors that have a relatively high sensitivity (a few ppb) towards atmospheric constituents [59]. Typically, the response rate is on the order of a few minutes and allow for relatively high temporal resolution of measurements [59].

A metal oxide sensor comprises of a sensing surface, internal heater and electronic infrastructure for the detection. The sensing surface is a semi-conductor material that, printed onto a substrate, which is typically aluminium oxide (Al_2O_3) [9]. The electronic structure of the sensing surface determines its suitability for use detecting a target measurand. The sensor relies on changing the conductance of the surface upon reaction with the target measurand [9] and therefore semi-conductor materials are chosen for the sensing surface. The optimal electronic structure for the detection of gases in the atmosphere is found in or near the transition metals with a d^0 or d^{10} configuration. Often, the semi-conductor materials used in metal oxides are tin dioxide (SnO_2, d^{10}, post-transition metal) or titanium dioxide (TiO_2, d^0, pre-transition metal) [187]. SnO_2 is used as an active surface for the detection of VOCs by MOS [197], [7]. The SnO_2 acts as an n-type semi-conductor, with a relatively large band gap between the valence and conductance bands [6], and more electrons in the conductance band, than there are positive "holes" in the valence band, leading to electrons being the predominant charge carriers [59].

SnO_2 resting state:

The internal heater increases the temperature of the sensing surface to between 150 – 400 °C, at these temperatures oxygen molecules in the air will chemisorb to the metal oxide

surface [9]. The oxygen will dissociate to form an oxyanion layer upon the surface of the SnO_2 material. The oxyanions are formed due to oxygen species having a high affinity for electrons, and hence the adsorbed oxygen molecules attract the electrons towards them. This 'pulls' the electrons partially out of the conductance band to form oxyanions and trap the electrons near the surface [187]. The trapping of electrons near the surface of SnO_2 causes an increase in the energy of the conductance band at the surface of SnO2. This effect is called band bending and leads to a reduced conductivity of SnO_2 surface compared to when the SnO_2 has no O^{-2} chemisorbed [187]. The reduced number of electrons in the conductance band, and the increased amount of ionised species causes bending of the band [187] resulting in the tin dioxide active surface being less conductive than when there was no oxygen present, i.e. it has a reduced resting conductance [7], see Fig. 1.17.

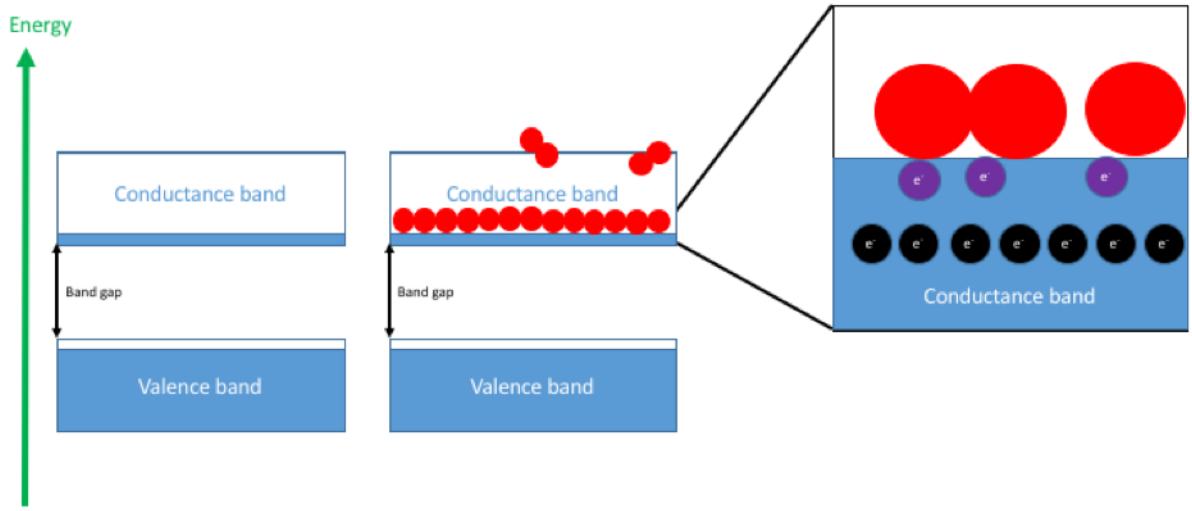

Figure 1.17: A schematic to show the resting state of a tin dioxide surface, with the adsorbed oxygen molecules and electrons being drawn out of the conductance band, causing an increase in the energy of the conductance band near the surface. This band bending leads to a reduced conductance.

SnO_2 in the presence of a reducing gas: The oxyanions on the active surface remain there until a compound interacts with them. If a reducing compound, such as VOCs or H_2S comes into proximity with the active surface, then the reaction between the oxyanions and the reducing compound leads to less electrons being trapped near the surface in the conductance band. The band bending is reduced as the electrons are less drawn to the oxyanions and so more are available to freely move around in the conductance band, resulting in an increase in the conductivity of the SnO_2 surface [7]. Reducing gases such as VOCs cause an increase in the conductivity of the surface [59], [197], [7] because there are now less oxyanions on the surface to attract the electrons, and this change in the conductivity is detectable by electrical circuitry [59], see Fig. 1.18. The greater the concentration of the reducing gases, the greater the change in the resistance on the MO surface, and this is observed as a larger MOS signal [59] [7]. Oxidising gases can also

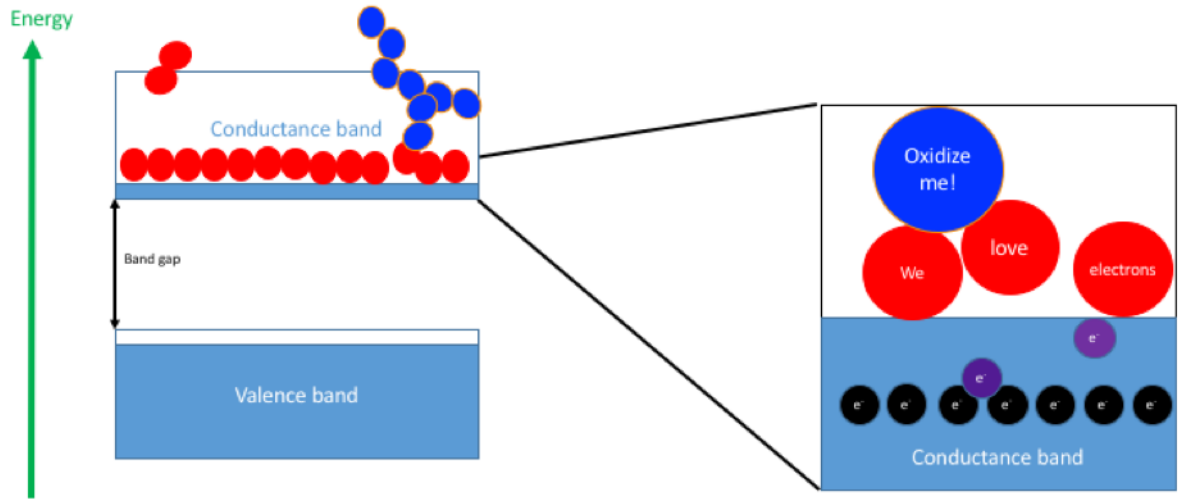

Figure 1.18: Schematic to show a reducing compound reacting on the MOS active surface. By engaging the oxygen ions in a reaction, more electrons remain free to move in the conductance layer, inducing an increase in conductivity.

reverse the band bending as they can compete with oxygen for sites on the MOS surface, and hence lead to a change in the conductance of the MO active surface [187]. The sensing technique is considered non-destructive, because although the reducing compounds react with the oxyanions to produce a new species and diffuse away, the oxyanions are replaced by more chemisorption of oxygen molecules. The amount of reducing gases constitutes a tiny fraction of the air sampled and therefore the change in the composition of the air sample is considered negligible [7].

Metal oxide sensors for the detection of bulk VOCs in the atmosphere were used in this study. There are no other LCS available to monitor changing VOC concentrations which cost on the order of £10 and since data capture occurs on the order of seconds the MOS might potentially be able to return near real-time information. The low-power consumption [187] associated with MOS and their small size means that they are suitable to be deployed as an array of sensors [9]. There are some known issues with MOS sensors, the detection technique is not selective towards any particular VOC and therefore they cannot speciate between compounds [104]. Due to the non-selective nature of detection, they are particularly prone to responding to compounds that are not their target measurand, know as cross interferences [19]. It can be difficult to calibrate MOS in the ambient air because their signals have a lack of linearity and they are susceptible to interferences from other compounds and meteorological conditions [172] [104]. They also exhibit a large response with changing humidity and hence calibration with dry gas standards is not appropriate as it is not representative of real-world conditions where the MOS response will be very different.

The MOS sensors show huge potential for total VOC measurements because of their fast response towards changing VOC concentrations and almost continuous measurements.

These are both hugely advantageous properties when comparing the MOS sensor measurements to a Gas Chromatograph (GC); currently used for VOC reference measurements. Used under laboratory conditions, some studies showed that MOS were capable of partially differentiating and quantifying some VOC compounds, but these were used in conjunction with calibration models and multi-regression methods [86] [201] [78]. Using MOS to selectively monitor VOC compounds is not achievable as the technique does not speciate between compounds, but it may be possible to review the total VOC concentration in a local area. Whilst this is promising, the complexity of both indoor and outdoor environments would require the calibration models and regression algorithms to be altered for ambient use to make the MOS useful for complementing AQMs and able to quantify total VOC [99] [171] [199]. The under-lying scientific principles behind the MOS sensors are different to the GC reference method which means that comparing the two techniques leads to discrepancies. For example, the MOS sensors are non selective and measure bulk VOC, the GC speciates and quantifies individual compounds. However, MOS can still be used to complement the reference VOC instruments, if it is assumed that the composition of VOCs is unlikely to change for a particular region, and the MOS are calibrated by the reference instrument at a nearby location. Due to the impracticality of deploying a reference monitor into the field, MOS would be most useful for mapping VOC distributions in a local region and benefiting from the higher temporal resolution of measurements that the sensors provide. In order to use MOS to map pollution, the sensors must be highly reproducible, otherwise it would be impossible to make comparative statements about the spatial distribution of the VOC concentration, e.g. to know for certain if location A was measuring more total VOC than location B. LCS have the potential to reduce the uncertainty in the current reference VOC measurements. Gas Chromatography (GC) is a reliable and accurate method to sample the VOC compounds for a snapshot of time and samples are typically measured every 40 minutes. GC is a powerful tool for the separation, identification and quantification of individual VOC compounds from the ambient air. However, GC has several limitations. The quantity of VOC that is measured by the GC is an averaged amount over the sampling time, making it difficult for the GC to fully capture pollution patterns, for example maximum quantities of VOC. The whole process takes around 40 minutes to an hour, limiting the temporal resolution of GC measurements. It would be very useful to have a more continuous real-time measurement of VOCs and MOS sensors have the ability to take readings of total VOC concentrations every two seconds. If the sensors and the GC agree, then the sensors can provide VOC measurements at a higher time resolution and therefore reduce the uncertainty between each GC measurement and allow for a better understanding of VOC emissions. Total VOC MOS have the potential to improve observations of VOC concentration fluctuations and personal exposure estimates to VOC compounds, compared to the reference monitoring method. The MOS sensors have a higher temporal resolution than the GC methodology

and therefore, with proper calibration to a co-located GC reference method the MOS could allow for better estimations of peak VOC mixing ratios. In this way, the GC system and the MOS sensors would complement each other; the speciation and relative ratios of VOCs can be determined by the GC method, and the sensors provide more frequent bulk VOC measurements, assuming that the ratio of VOCs stays constant, which is typically the case.

The low-cost and low-power requirements of MOS sensors have meant that there have been lots of investigation for their use as environmental monitors [99], [60], [99], [172]. Typically, researchers have used an array of different MOS sensors and have required post-processing analysis (such as partial least squares regression [199]) to extract useful information from the MOS response. Laboratory experiments with MOS have proven that they exhibit an increased response to increasing VOC concentrations, [95] [59] although humidity [169] and temperature [81] may cause large interference on the MOS signal. Laboratory experiments with MOS sensors have proven that they are capable of detecting and distinguishing between three VOC compounds (formaldehyde, benzene and naphthalene) with the use of pattern recognition software [99]. The MOS sensor displayed different sensitivities towards the different compounds, exhibiting the lowest sensitivity towards benzene [99]. Fonollosa et al. [60], used an array of different MOS sensors to detect VOCs in laboratory experiments and identify MOS sensors drift. The MOS sensors are susceptible to temporal drift over time [184], although there is a study that shows that although MOS displayed a sensor conductance drift of 0.04 kS over 21 months, univariate regression is a good technique for accounting for the drift [155]. MOS used to detect O_3 were shown to have a range of response times, from 8 minutes to 52 minutes, depending on the manufacturer of MOS [172]. A high temperature and humidity dependence of the MOS was noted, as well as interferences from other gaseous compounds [172]. There are a few issues to overcome regarding the use of MOS sensors for atmospheric research, however the initial laboratory experiments have been somewhat promising and the near-real time data, low-cost and portability advantages make MOS measurements for VOC concentrations attractive.

1.9.2 Electrochemical (EC) sensors

Electrochemical (EC) sensors are commercially available from a number of companies to monitor atmospheric trace gases. There are EC which are sensitive to detecting NO, NO_2, O_3, CO or SO_2 and there are examples in the literature where laboratory studies have been undertaken to characterise their performance [104]. Outdoor deployments in city centres are a popular application for EC sensors [110] and they have been used in networks to monitor outdoor urban pollution [122]. Indoor air studies have also used an array of different EC sensors because, among other properties, they are smaller, quieter and less expensive than their reference counterparts [22]. Sensor devices containing multiple EC to

detect a range of pollutants are also commercially available, e.g the AQMesh device used by Jiao et al. 2016 [86] [24], AIRSense used by Cross et al., 2017 [32], RAMP used by Zimmerman et al., 2017 [206]. Calibration of EC sensors is often conducted with co-located reference instruments in the field to be representative of the environment the sensors are to be deployed in [206] [32] [71]. The EC performance is typically evaluated by comparing the measurements from the reference instruments in the field to the EC measurements [114] and EC have proven to have exhibited high correlations (R^2 >0.8) with the reference observations after simple correction procedures [142], [143] [110] [19] [205]. Typically gaseous pollutants such as CO, NO_2 [122], SO_2 [205] and O_3 [86] are monitored with EC sensors.

The electrochemical sensors used in this study operate using a three-electrode system to maintain stability within their linear response to gaseous atmospheric compounds over a large range of concentrations. The electrodes are as follows; the working electrode (WE), the counter electrode (CE) and the reference electrode (RE) [1]. The target gases diffuse onto the surface of the WE and undergo a redox reaction, aided by the presence of a high surface area catalyst. This generates a current at the WE. Redox reactions occur in pairs and the WE reaction is balanced by a corresponding reaction on the CE, causing the potential of the CE to change [142]. This balances current produced at the WE [120]. Since the WE potential is fixed – by the presence of a potentiostat connected to both WE and RE – a potential difference between the CE and the WE occurs in the presence of the target gas [1]. The output of the sensor is therefore the electrical current induced by the potential difference. To allow for the flow of charge throughout the electrochemical cell, wetting filters are employed between each electrode [122] [1]. To ensure the sensor output is proportional to the concentration of the target measurand, the rate limiting step for the procedure is the diffusion of the gas to the WE [122] [142]. The measurand must diffuse across the gas space, through the membrane and onto the electrolyte film on the WE electrode before it undergoes the redox reaction [142]. To calculate the overall current the each of the currents produced at each of the three sections that the analyte must diffuse through are summed. This total current, and hence sensor output is given by Equation 1.22, [142] where I is the current generated across the electrolyte and electrode.

$$I = -\frac{nFADC}{a} \tag{1.22}$$

n is the number of electrons required for the relevant redox reaction, F is Faraday's constant (charge carried per mole of electrons: 9.6485×10^4) and A is the surface area of the metal oxide sensing surface. D is the Diffusion coefficient of the gas analyte across each interface and this constant relates the total current generated to the diffusion rate of the target gas analyte [142], C is the change in concentration of gas analyte between the electrolyte and electrode, and a is the distance that the gas analyte must diffuse across to undergo a redox reaction. Equation 1.22 relates the output current of the sensor to the

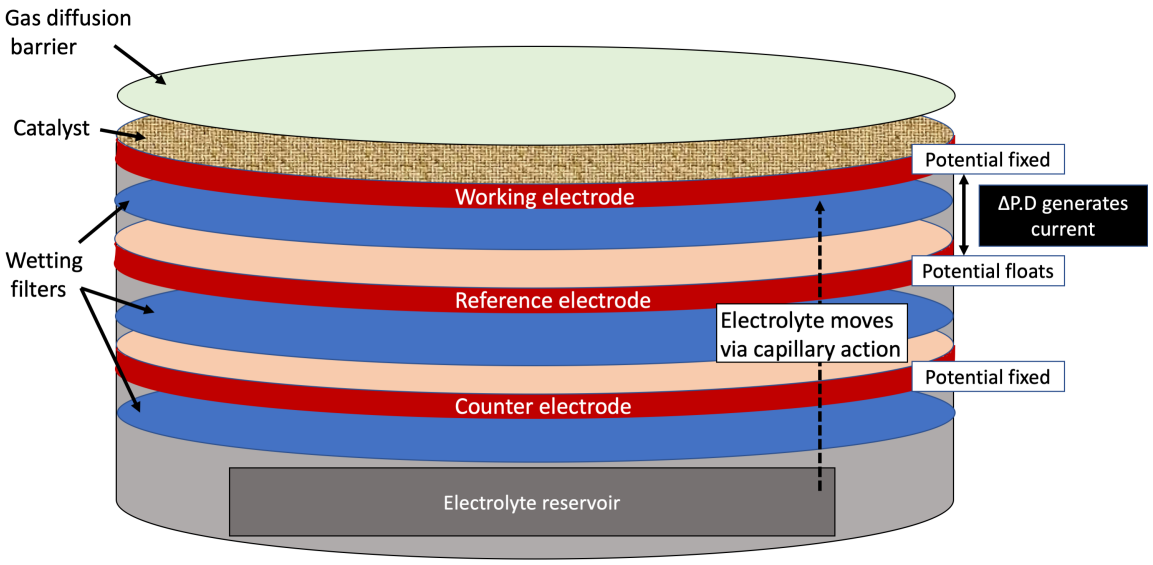

Figure 1.19: Diagram to show the internal layout of a typical amperometric electrochemical gas sensor.

rate of diffusion of the gas analyte to the location where the redox reaction occurs [142]. To ensure that the sensor is responding to changes in the concentrations of target analytes with small recovery times the rate of diffusion is the slowest step in the sensing process. There can be issues with the conversion of the raw signal to a pollutant concentration as the size of the current generated is small, and the fluctuations in the current can change by as little as 1 μA. The electronics are required to be of a high enough resolution to detect these fluctuations and therefore make quantitative measurements [32].

There are some published issues regarding the use of EC sensors to quantify pollutants concentrations. At the typical concentrations of atmospheric gases, the EC have shown some cross sensitivity towards gases other than their target measurand [104] or environmental conditions [122]. These cross interferences occur because the EC do not selectively undergo redox reactions with just one species and hence other chemical gas species can induce a sensor response by reacting on the EC electrode surface and inducing a current in the CE. This is of particular concern when the relative ambient concentrations of the target species is near or smaller than the ambient concentrations of the interfering species [105]. Where the sensor responds to a cross interfering compound that is expected to have a high ambient concentration the EC sensor response to the target gas might potentially be overwhelmed by the response to the interfering species [105]. The EC rely upon the diffusion of the target gas to the working electrode but there are no filters to prevent other gases diffusing too, therefore sometimes the EC WE has been poisoned by other components reacting irreversibly with the sensing surface [130]. Environmental interference also occurs too and the EC have been shown to exhibit a response to changing humidity and temperature [32] conditions, and increasing the humidity also changes the sensitivity of the EC to detect the target gas species [105] [165].

1.9.3 Non-Dispersive Infra-Red (NDIR) sensors

Non-dispersive Infra-Red (NDIR) sensors contain an IR lamp to provide IR radiation at one end of a sample tube, and an optical pass filter in front of an IR detector at the opposite end, see Fig. 1.20. The optical pass filter is set to remove all wavelengths of light, barring the specific wavelength that the target measurand absorbs at. For CO_2, this is 4.28 μm. CO_2 molecules in the sample cell absorb this particular wavelength of light and the amount absorbed is proportional to the concentration of CO_2 in the tube. This is calculated using an IR detector and the amount of radiation detected is subtracted from the original amount transmitted by the IR lamp. The scientific technique means that NDIRs can highly selective towards their target measurand if no other molecules absorb at the same wavelength. Ideally, for the technique to be selective, the wavelength is chosen so that only the particular compound of interest absorbs at this wavelength. However, other compounds such as CO, SO_2, NO_X, N_2O, NH_3, HCl and methane [43] can be measured using NDIR sensors that utilise different wavelengths of IR radiation so these species may be a source of cross interferences for CO_2 NDIRs. The choice of filter will limit the interference of water and other molecules and most NDIR techniques require correction factors to be applied to further minimise the cross interferences response [43]. These devices are more expensive than the MOS or EC sensors (c.a £ 200) but are still considered low-cost as they are less than a tenth of the price of a CO_2 research-grade instrument.

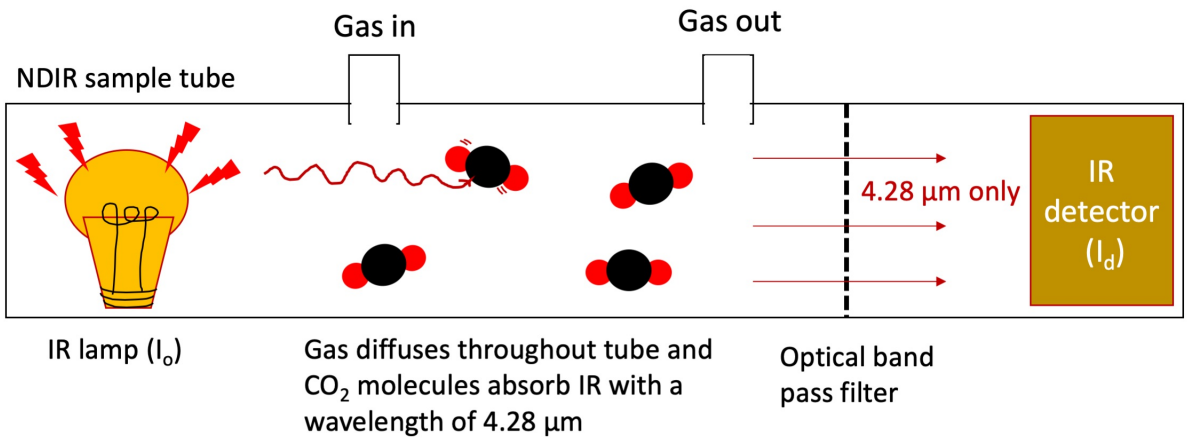

Figure 1.20: A schematic of a CO_2 NDIR device.

NDIR technology is one of the most common methods of real-time detection of CO_2 in the ambient air with low-cost sensors [87]. The Beer Lambert Law re-arranged to yield the concentration of CO_2 using NDIR sensing is shown in Fig. 1.21.

$$Concentration(ppm) = \frac{\ln(\frac{I_o}{I_d})}{\alpha L}$$

I_o : Intensity of 4.28 µm at the IR lamp (W cm^{-2})
I_d : Intensity of 4.28 µm at the IR detector (W cm^{-2})
α : Target measurand (e.g. CO_2) absorption coefficient (cm^{-1})
L : Optical path length (cm)

Figure 1.21: The Beer-Lambert Law, rearranged to calculate concentration of the target gas (CO_2) in the NDIR sample tube.

The Beer-Lambert Law is used to quantify the CO_2 in the sample tube and therefore the sensitivity of the CO_2 NDIR sensors can be made more sensitive by employing highly reflective mirrors to extend the optical path length (L) [87]. The IR lamp intensity and the type of IR detector also influence the limits of detection of the device and the sensitivity towards CO_2 [43]. CO_2 NDIR sensors have been found to have an accuracy of ± 30 ppm and a response time of between 30 – 120 seconds in an indoor air study [87].

Chemical methods of detecting CO_2 in the air are available but NDIR sensors are more stable over long term deployments and make more accurate CO_2 measurements [135]. Commercially available CO_2 NDIR sensors cost between USD 100 – 200 (Martin et al., 2017), and this is more affordable than the equivalent reference instruments, which can be of the order of USD 50 000 [119]. The low power consumption of an IR lamp emitting wavelengths of light between 1- 15 um [43] means that operating costs are also reduced since it requires no personnel to collect samples for in-laboratory analysis like the flask system for monitoring CO_2 [119]. However, the IR detectors used in NDIR sensors can be influenced by air temperature resulting in misleading results when the environmental temperature fluctuates [135]. Correcting for cross sensitivity's such as temperature and pressure can improve the error in CO_2 concentration estimates to 1 % of the observed values [119].

1.9.4 Low cost Optical Particle Counters (OPCs)

There are low-cost versions of Optical Particle Counters (OPCs) that detect the scattering of light when particles are introduced to the device. Each device is designed so that the light is focused, usually using a laser (Alphasense OPC-N2 uses a laser with a maximum power consumption of 26 mW, wavelength of light 658 nm), onto an individual particle. This particle scatters light depending on its size and composition, therefore, after calibration with particle standards, these two parameters can be estimated [170], see Fig. 1.22. The wavelength of light is chosen to be smaller than the size of the particle to ensure Mie Scattering occur [177]. Mie Scattering is a much stronger affect than Rayleigh Scattering which occurs if the wavelength of light is larger than the particle scattering the light. The scattering can identify particle concentration, particle mass and size distribution, although is limited to particles larger than 0.1 μm and more often 0.4 μm, as, if the particles are

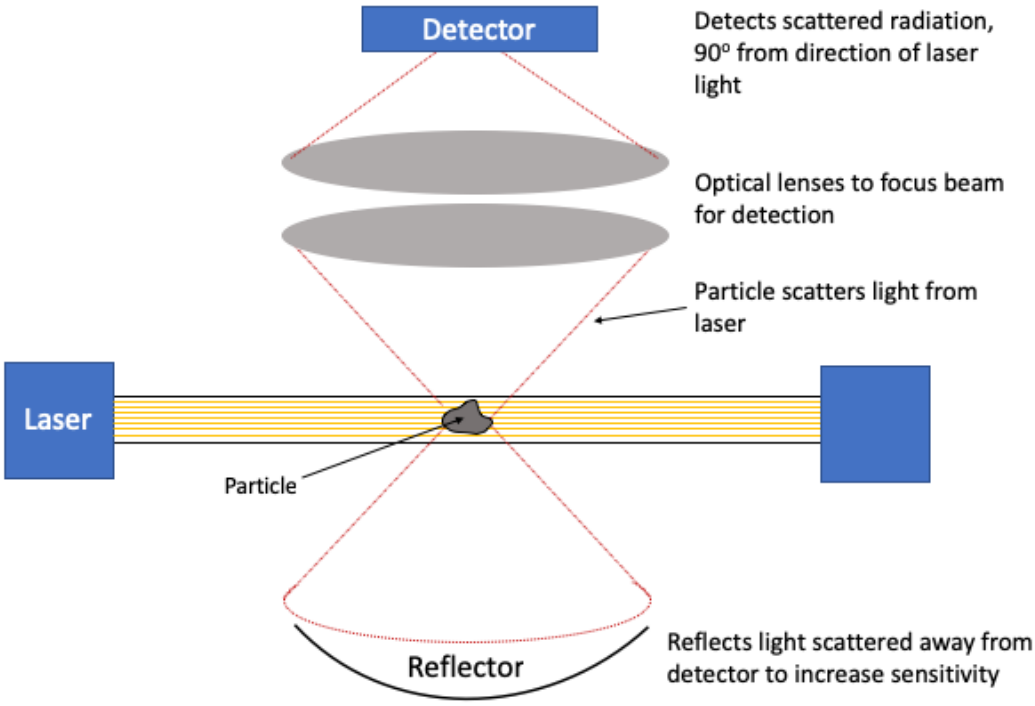

Figure 1.22: Schematic to show the operation of a low-cost OPC device.

smaller than this the incident scattered light is undetectable [170] [177] due to Rayleigh Scattering occurring.

These devices have shown to have a reasonable comparison with equivalent reference instruments and have been found to be suitable for use in outdoor studies to assess the spatial concentration gradients of particles in the ambient air [30]. However, to achieve the precision and accuracy required to quantify airborne particulate matter, calibration and humidity corrections are required [30]. Monitoring particulate matter (PM) is becoming increasingly important as the understanding about the relationship between the levels of PM and human health are better understood. There are multiple manufacturers producing OPCs for commercial purchase (Alphasense, Airsensor, Dlyos) and their relative affordability (£250) compared to the reference instrumentation for monitoring PM means that they are becoming increasingly popular for PM spatial distribution analysis [30]. The OPCs portability (size : 75 mm x 60 mm x 65 mm, weight : 105 g) is also advantage when considering them for use as personal air quality monitors [30]. The limit and guideline values set by the EU and the WHO are in μg m^{-3}. However, due to the sampling technique used by the OPCs, the units for the PM concentrations are particles cm^{-3} and it is challenging to convert the OPC measurements into the units used in regulation. The size of the hygroscopic particle is dependant upon relative humidity, as is the OPC response. For use in the field, OPCs must be calibrated for both high and low humidity's as it has been shown that they exhibit different behaviour when sampling air with a relative humidity greater than 85 % [30].

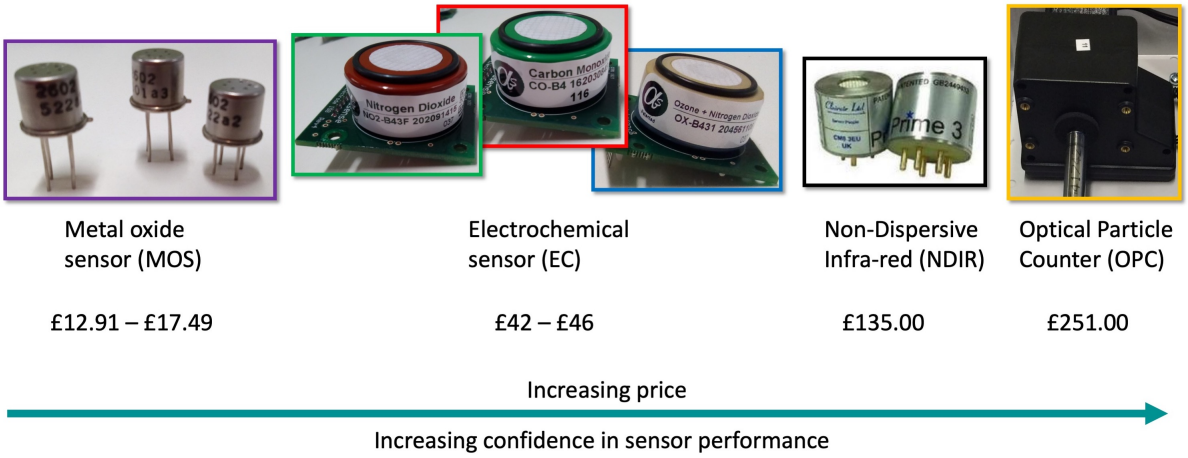

Figure 1.23: The price that each of the sensors was purchased at for use in this study.

1.10 Sensors in Atmospheric Research

The popularity of using LCS to monitor ambient pollution, from gaseous pollutants with MOS and EC, climate gases with NDIR and PM with OPCs, is increasing due to their availability and cost. There are a range of low-cost sensor devices commercially available, from single sensors to multi-sensor arrays containing one of each pollutants sensor in a bid to monitor multiple pollutants of interest [205], similar to a reference air quality monitoring (AQM) station. These AQM stations usually house a variety of research grade instruments to provide highly accurate and precise data about their immediate surroundings. The expense to install and maintain these stations is one of the major reasons for an increase in demand for a low-cost sensor platform. A variety of sensor technologies means that there are low-cost sensors available for monitoring most criteria pollutants, and in an ideal world, where low-cost sensors have minimal inter-sensor variability, no temporal drift and they can produce reliable data, they would be used to complement the current AQM network [106]. There currently exists a somewhat sparse spread of atmospheric measurements across the UK, which cannot capture all the different patterns of pollution and an increase in the spatial density of the network would be helpful when determining compound behaviour, for validating atmospheric models and identifying pollution hotspot areas [122]. Sensors can be used to provide short-term temporal variability of one location, but as of yet, their performance in real-world conditions means that they are not always suitable for other research questions, such as spatial variability of pollutants and long-term trend analysis [106]. Sensor performance must be better characterised before they can be used to provide data that the users can have confidence in. For example, issues such as the low reproducibility of identical sensors must be addressed before spatial variability in pollution estimates can be made [105]. The effects of cross interferences must be fully understood, especially for pollutants that interfere with the sensors signal at typical ambient concentrations [104] and the rate of temporal drift must be better understood. In general,

the more expensive the low-cost device, the better the output of the sensor was expected to be. For example, the MOS sensors are the least expensive LCS sensor used here, and their inexpensive price was related to the quality of data that they produce. Using a metal oxide sensing surface is a non-selective technique and can only provide the user with a bulk overview of the temporal variability of the total VOC signal. The electrochemical sensors, are slightly more expensive and are more selective towards their target compounds. They also contain a third auxiliary electrode to attempt to minimise the effects of cross sensitivities. The CO_2 NDIR sensors were more expensive again, and the method of detection - using IR wavelengths specific to the CO_2 molecule - is more selective too. Figure 1.23 shows the different sensors used in this study and the target compounds that they detect. As the general public are becoming increasing aware of the impacts of pollution upon human health and the environment, low-cost sensors are an attractive prospect for them to investigate personal exposure towards harmful contaminants. There is a concern that use of LCS by the general public may lead to inaccurate conclusions about pollution levels due to unpredictable drift in LCS and low reproducibility of signals leading to users having a false confidence in the numbers output by the sensors due to a lack of understanding about the requirement for calibration and post-processing methods. It is important to understand how the LCS behave in the laboratory and during deployment in the field in order to advise how best to use LCS and suggest techniques to standardise their use.

1.10.1 Aims of thesis

Users of sensor technology must be aware of the limitations of current sensor performance to avoid misinterpreting the data. This project aims to characterise sensor performance by conducting laboratory investigations with MOS (for the detection of total VOCs) and EC (for the detection of CO, NO_2 and O_X) sensors to understand the sensors responses to the target measurand and cross interfering species. The noise of the sensors in zero air was also investigated for the MOS and EC to characterise the behaviour of the sensors in the absence of their target compounds. The laboratory experiments also identified a clustering technique for increasing the reproducibility of the sensor response over the short to medium (hours to week) timescales. The MOS sensors have the potential to improve the temporal resolution of VOC measurements as well as increasing the spatial density. The MOS were evaluated to identify if they have the potential to complement the GC-FID technique and provide new insights into VOC pollution patterns. The MOS, EC and environmental sensors were collated together to produce a multi-pollutant sensor instrument for deployment in the field, to characterise low-cost sensor behaviour when co-located with reference instruments in real-world conditions. The potential for the sensor instrument to be used in an analogous manner to a reference monitoring station was assessed and techniques to improve the quality of sensor data were investigated to resolve issues with cross interferences and changing environmental conditions. The use of the

sensor instrument data as a whole, in combination with three different machine learning algorithms were used for the correction of cross interferences. This study identifies a suitable method for the calibration of the sensors inside the instrument, by co-location with a reference instrument in the environment where the sensors are to be deployed. By characterising the performance of a multi-pollutant sensor instrument the thesis aims to identify several applications where LCS would be beneficial for use in scientific research.

Chapter 2

Laboratory experiments to characterise the response and sensitivities of the Metal Oxide Sensors (MOS)

2.0.1 Introduction to low-cost MOS total VOC sensors

Low cost sensors are increasingly attractive to both the public and scientific researchers because they can provide continuous, low-cost, low-power measurements to indicate the quality of ambient air. A working low-cost total VOC sensor would be useful for complementing current techniques and increasing our understanding of VOC emissions and sources. The Total VOC MOS sensors can capture data every few seconds, and this would greatly improve the temporal resolution of the GC-FID technique which is currently used in the national monitoring networks for an automatic measurement of VOC in the UK. Assuming the VOC composition remains relatively constant the total VOC measurement would be able to identify when the VOC concentrations in the ambient air are high and locate pollution hot spots or predict VOC pollution patterns near a point source.

2.1 Metal oxide sensors

Metal oxide sensors (MOS) are commercially available and for this study were purchased from Figaro, one of the largest global MOS manufacturers [9]. These MOS sensors are therefore widely used and were inexpensive, costing approximately £10 per sensor. The power consumption for a Figaro MOS sensor is low, 280 mW for internal heater and running of sensor. The Figaro TGS2602 MOS was advertised as a Total VOC sensor (Fig. 2.1), and so this model was investigated for use as a low-cost VOC sensor in the laboratory and for deployment in the real-world. There are other MOS VOC sensors, see Table 2.1,

Figure 2.1: A Figaro TGS2602 Total VOC MOS sensor. The diameter of the sensor is 9.2 mm, with a total height of 10 mm.

and these all have a common tin dioxide active surface, with different surface properties governing the selectivity of the sensors. Surface properties such as the grain size and hence surface area of the sensing material, the temperature the sensing surface is held constant at and doping the semi-conductor sensing material are altered to change which compound the MOS sensor is more selective towards [187].

Each sensor contains four pins; two are an integrated heater, to maintain the active surface at the optimum temperature for the adsorption of oxygen to form oxyanions [9], and to optimise the reaction kinetics for the adsorption and reaction of reducing compounds such as VOCs (270 °C) with the oxyanions on the sensor surface. The other two pins are the aluminium oxide substrate with the printed tin dioxide sensing surfaces. The four pin ends are housed inside a small (10 mm diameter) aluminium can and this comprises of the MOS sensor in Fig. 2.1. Electrical circuitry is required to obtain a signal from the MOS. The MOS sensor pins extrude out of the metal can (Fig. 2.1 and all four pins are inserted into holes with a Teflon manifold. These pin holes were coated with gold to allow electrical contact between the circuit board and the MOS sensor via a gold casing. An example of these white Teflon MOS manifolds can be seen in Fig. 2.2; there are eight MOS sensors and Teflon manifolds mounted in a circle upon a green electrical circuit board. The circuit boards were purchased from Eurocircuits who manufactured them based upon a design developed by the University of York's Chemistry Electronics Department, who designed them especially for use with MOS sensors. The circuit board (Fig. 2.2) met the electrical requirements for the MOS sensors (5 volts d.c. is required for the sensing pins and 7 V d.c. for correct heater operation) and where possible, minimised electrical noise.

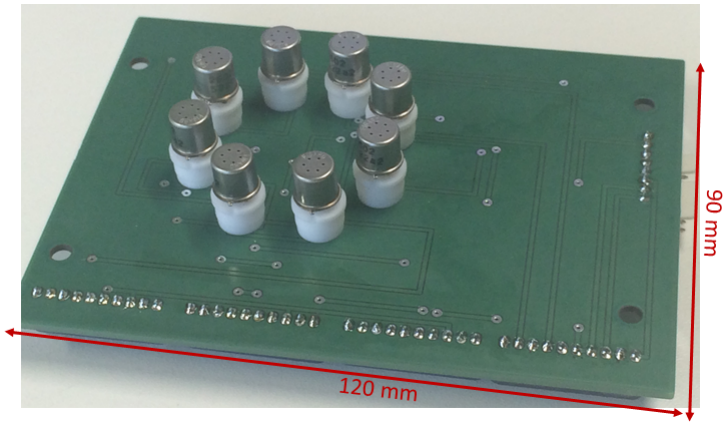

Figure 2.2: Photo of a cluster of 8 MOS TGS2602 total VOC sensors, inserted into their Teflon housings which allowed electrical contact between the sensors and custom built circuit board. The white Teflon housings had a gold casing coating the holes where the MOS pins were inserted.

Figure 2.2 shows eight MOS sensors mounted onto the green circuit board which ensured that each sensor received the correct (and equal) amounts of supply voltage to it, and it's internal heater. Adafruit ADS1115 16-Bit Analog-to-Digital Converter (ADC) boards were mounted to the opposite side to the circuit boards to address the sensors and further minimise electrical noise. For all eight MOS, the sensor output voltage (sensor data) was collected from this board via an Arduino micro-controller and saved onto a laptop. The sensors are designed for the diffusion of ambient air over the active surface therefore, for laboratory experiments they required a method of directing a controlled flow of air, that was isolated from the laboratory air. A Teflon manifold was designed for this purpose in order to carry out sensor calibrations and characterise the sensors response to different conditions. The target compounds for the Figaro TGS2602 sensors are total VOCs, and so the response of the MOS was investigated for a variety of different VOCs, including oxygenated compounds, alkanes and aromatics. These sensors work by detecting reducing compounds via the diffusion of molecules onto the sensor active surface. There is no filter or barrier to deter other compounds in the atmosphere to the sensing surface and so it is likely that other reducing and/or reactive compounds can adsorb and react on the surface, causing a misleading signal. These compounds, which are not the target compounds but which induce a sensor response are referred to as cross interferences and the MOS response to these was characterised, as well as the MOS response to environmental conditions. The sensors require some oxygen to replenish the oxyanions on the active surface and therefore the VOC gas standards, which are in N_2 were mixed with air from a Pure Air Generator (PAG) during calibrations. The air flow was controlled by mass flow controllers. Where possible, the experimental set ups were enclosed within a Faraday cage to further minimise electrical noise in the sensor signals.

An example experimental set-up using two MOS sensors is shown in Fig. 2.3. Mass flow controllers were used to provide a precise flow of air so that is was possible to calculate

Table 2.1: There are many different types of MOS sensors commercially available to monitor VOC compounds. Four Figaro MOS sensors, for monitoring Total VOC, methane, propane/butane and alcohol compounds were used as part of this research project.

Metal oxide sensor	Target species	Limits of detection
TGS2602	Total VOC	1 - 30 ppm of ethanol (EtOH)
TGS2611	Methane	500 - 10,000 ppm of methane
TGS2610	LP gas, propane and butane	500 - 10,000 ppm
TGS2620	Solvent vapours and alcohols	50 - 5,000 ppm

the exact concentrations of the target compound or cross interferences from synthetic gas standards (shown in Fig. 2.3 as the dilute VOC mixture cylinder). Other gas standard cylinders containing other compounds of interest at different concentrations could be easily swapped in and out. During the laboratory experiments, the flow of air was kept constant, unless otherwise stated, and the humidity was controlled and routinely changed using a bubbler installed in the air flow after the mass flow controllers. The humidity was changed to incorporate expected humidity ranges for locations where the sensors were likely to be deployed, as it was known that MOS sensors exhibit a non-linear response to humidity [105]. The copper tubing was used to keep the temperature of the air flowing to the sensors as constant as possible to minimise the risk of temperature affecting the sensor signal during calibrations.

The sample lines were 1/4" Perfluoroalkoxy (PFA) tubing to reduce losses of compounds to the tubing walls, with stainless steel Swagelok fittings to maintain air tightness throughout the system. Compressed air was pushed from the PAG, through the set up to prevent any contamination from leaks in the set up or MOS manifold, although both were tested to be air tight prior to the experiments. Temperature and humidity probes were installed to monitor the conditions of the air reaching the sensor surface.

2.1.1 Analysis procedure

During calibrations, a compound or compound mix, e.g. a gas cylinder containing known quantities of VOCs in N_2 was introduced to the set up. The concentration of the compound or mixture was changed by programming the MFCs to allow different flows of either compressed air or gas standard into the experimental set up. The concentrations were stepped up and down and during each step change, the concentrations were held constant for a minimum of 30 minutes to allow for a full MOS sensor response. All calibrations were run in the laboratory at room temperature and pressure. During analysis, the differential of the compound concentration was calculated and data points removed during the time it

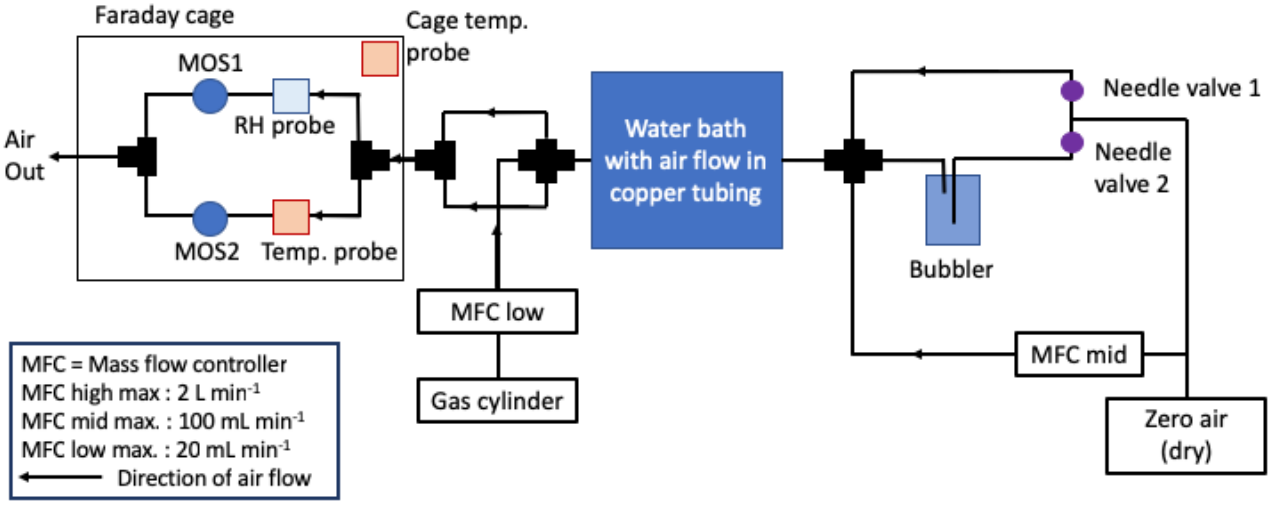

Figure 2.3: A schematic of a laboratory experiment. This experimental set-up was used to calibrate two MOS sensors with changing concentrations of a VOC mixture gas standard. For this schematic the VOC gas standard was located at the Gas Cylinder location and the flow was introduced to the zero air flow to allow for maximum mixing of the VOC standard with the zero air. The humidity and temperature were controlled and kept constant during calibrations. The sensors were housed in a metal box to act as a Faraday cage and reduce electrical noise. MFC = Mass Flow Controller.

took for the concentration to change (where the differential was greater than +0.02 or less than −0.02). This was because during the concentration change, the MFC required time to adjust to the new air flow and would typically open fully for a short amount of time. This was enough for a sharp increase in air flow from the dry gas standard and hence, for a second the MOS were exposed to a high concentration of the gas standard and drier air, affecting the MOS signal. The MOS signal is output as a voltage and this was binned for each concentration step. The mean and standard deviation for each bin was calculated and the calibration plots show the mean MOS signal (V) on the y-axis versus the binned compound concentration (x-axis), with the standard deviation plotted as a black line.

2.2 MOS response towards VOCs

2.2.1 Defining VOC gas cylinders used for calibration of sensors

To characterise the MOS responses to VOCs and potential cross interferences, several different gas standards were used in succession. A list of the cylinder name, number and composition of the standard is defined below:

- NPL30 NPL30 cylinder contains 30 VOCs in N_2, cylinder number: D836639. The compounds are as follows, with the concentrations in the cylinder shown in brackets, in parts per billion (ppb): ethane (4.03), ethene (3.88), propane (4.07), propene (3.99), 2-methylpropane (4.18), butane (3.96), ethyne (4.11), *trans*-but-2-ene (3.95),

but-1-ene (3.96), *cis*-but-2-ene (4.00), 2-methylbutane (4.02), n-pentane (4.02), 1,3-butadiene (3.94), *trans*-pent-2-ene (3.95), pent-1-ene (3.96), 2-methylpentane (4.04), n-hexane (3.97), isoprene (4.00), n-heptane (4.00), benzene (3.98), 2,2,4-trimethylpentane (3.97), n-octane (4.01), toluene (3.98), ethylbenzene (3.98), *m+p*-xylene (8.00), *o*-xylene (3.98), 1,3,5-trimethylbenzene (3.99), 1,2,4-trimethylbenzene (4.01) and 1,2,3-trimethylbenzene (4.02).

- OVOC The OVOC cylinder was made up in the laboratory at the Wolfson Atmospheric Chemistry Laboratories (WACL). It contains six compounds: acetone, ethanal, methanol, propane, n-hexane and benzene at 5 ppm each, in N_2. Cylinder: D953613

- VOC8 The VOC8 cylinder was also made up in the laboratory at WACL and contains n-pentane, n-heptane, n-octane, n-nonane, toluene, ethyl benzene, *m*-xylene and *p*-xylene all at 5 ppm in N_2. Cylinder: D838940

2.2.2 Concentrated VOC mix

The VOC8 cylinder was used to determine the responses of two TGS2602 MOS sensors to ozone precursor VOCs, in a set up similar to Fig. 2.3. The total VOC concentration in the cylinder was 40 ppm, and this was diluted with PAG air to lower the concentrations to those more typical of ambient air and to maintain a good supply of oxygen to the MOS sensor surfaces. The total VOC concentration ranged between 0 - 150 ppb in the calibration. These concentrations would be considered very high for ambient concentrations of any individual VOC, however almost 200 ppb of bulk VOC concentrations have been observed in mega-cities [191].

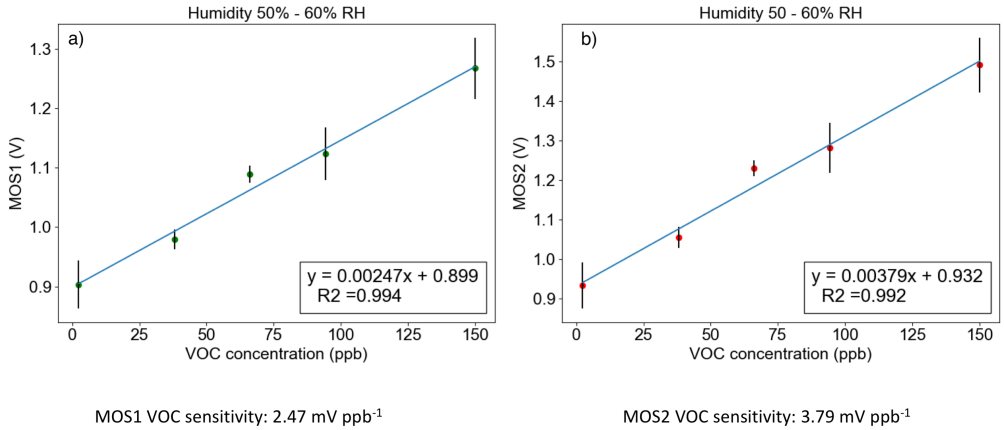

Figure 2.4: Calibration curves to show the performance of a) MOS1 and b) a second sensor, MOS2 during exposure to changing concentrations of the VOC mixture, at 50 - 60 %, which is typical of the UK humidity.

The calibrations using the VOC8 cylinder were repeated at a range of humidity's to identify how this affected the MOS sensitivity towards the VOC mixture (Table 2.2).

Table 2.2: A comparison between the performance of two MOS sensors after exposure to different VOC concentrations at different humidity ranges. The MOS sensitivity towards VOCs was calculated by producing a plot of VOC concentration (x-axis) against the MOS output voltage (y-axis). Linear regression was used to calculate a gradient (mV ppb^{-1}) which was defined as the sensitivity. A gas standard (VOC8) was used in conjunction with mass flow controllers to produce the different VOC concentrations.

Relative humidity (%)	MOS1 sensitivity (mV ppb^{-1})	MOS2 sensitivity (mV ppb^{-1})
10 - 20	2.48	2.63
40 - 50	2.61	3.75
50 - 60	2.47	3.79

Figure 2.4 shows the two sensors calibration curves at 50 - 60 % relative humidity, after the analysis described above in 2.1.1 Analysis Procedure was applied. Linear regression was performed and the gradient of the line was taken as the MOS sensitivity. For the two sensors in Fig. 2.4, the MOS1 and MOS2 have sensitivities of +2.47 and +3.79 mV ppb^{-1} respectively. The calibration curves for MOS1 and MOS2 at both the 40 - 50 % and 50 - 60% RH ranges were similar; with the MOS's displaying a linear response and a strong positive correlation to VOC concentration. The calculated sensitivities of the same two MOSs from the calibrations conducted at other humidity's are shown in Table 2.2.

From Fig. 2.4 and Table 2.2, MOS2 was much more sensitive than MOS1 to changing VOC concentrations as the slopes were always greater than the respective MOS1 slopes. This reinforces the requirement that all low-cost MOS sensors must be individually calibrated before deployment, as using one calibration for all sensors would lead to misleading results. Both sensors exhibit very linear relationships with VOC concentration, and were highly correlated with R^2 >0.99 for the calibrations that occurred at humidity's greater than 40 %. Although the two sensors had different sensitivities towards VOCs, their individual sensitivity towards changing VOC concentration was relatively consistent in more humid air (>40 %). Increasing the humidity, changed the VOC sensitivity differently for the two MOS sensors. As humidity increased from 10 - 20 % to 40 - 50 % and then 50 - 60% for MOS 2, the VOC sensitivity increased. For MOS1 however, the MOS sensitivity towards VOCs increased when the RH was increased to 40 - 50 %, but decreased at the higher (50 - 60 %) relative humidity conditions.

Further VOC8 calibrations were conducted using the same MOS sensors, this time using dry air (RH range 0 - 10 %). A larger VOC concentration range was used, between 0 to 450 ppb of total VOCs exposed to the MOS sensors, Fig. 2.5. The resulting calibration curves, seen in Fig. 2.5, were less linear and had lower correlations (R^2 for MOS1: 0.86, R^2 for MOS2: 0.84). MOS2 displayed a lower VOC sensitivity, compared to the calibrations conducted with more humid air. The non-linearity was due to a decreasing sensitivity of the MOS sensors at higher VOC concentrations. At the lower VOC concentrations (0 -

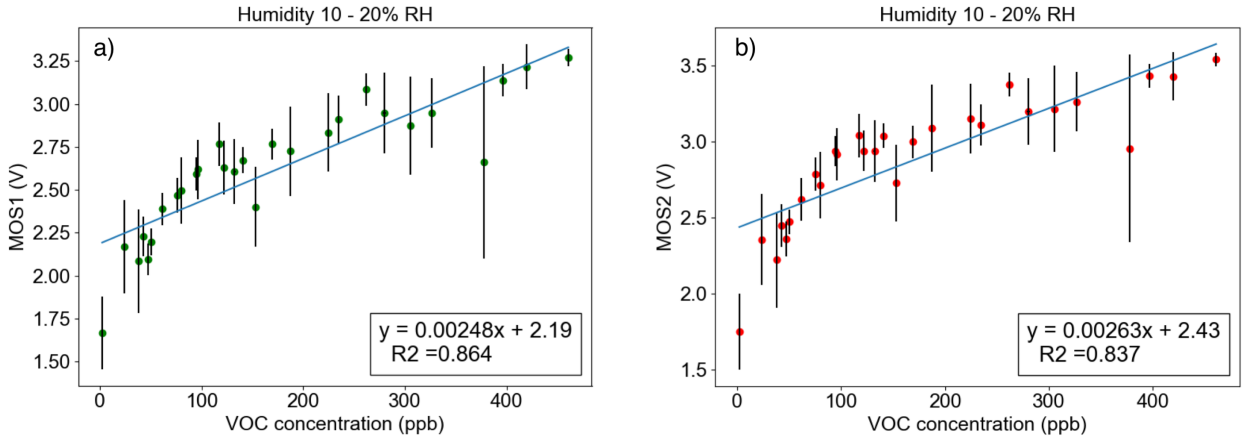

MOS1 VOC sensitivity: 2.48 mV ppb^{-1}
RMSE : 216.2
NRMSE (RMSE / [VOC range])= 0.472

MOS2 VOC sensitivity: 2.63 mV ppb^{-1}
RMSE : 215.9
NRMSE (RMSE / [VOC range])= 0.471

Figure 2.5: Calibration curves to show the performance of a) MOS1 and b) MOS2 during exposure to a larger range (0 - 500 ppb) of VOC concentrations.

100 ppb) the curves for both MOS sensors were steep and relatively linear. MOS1 (green) had a gradient of 10.08 mV ppb^{-1} and MOS2 (red) a gradient of 12.59 mV ppb^{-1}. However, at concentrations exceeding 100 ppb the MOS slopes plateaued: MOS1 and MOS2 have slopes of 1.89 and 1.83 mV ppb^{-1} respectively. Therefore the sensors became less sensitive towards the VOCs at higher concentrations of VOC8. It is thought that at the higher concentrations of VOC (>200 ppb) there were more VOC molecules available to adsorb to the MOS sensing surface and more molecules occupying sites on the surface at any given time. When more reducing compounds approach the active surface, their adsorption was potentially blocked due to the MOS sensing surface becoming saturated and therefore the MOS sensitivity decreases. Over the concentration ranges expected in ambient air however, (0 - 120 ppb) both MOS responses were considered linear.

2.2.3 Diluted VOC mix

The VOC8 standard was very concentrated (total VOC concentration = 40 ppm) and the calibrations were non-linear at the high concentrations of VOCs (150 - 500 ppb). However, ambient concentrations of VOCs are more typically between 0 - 150 ppb and therefore the calibrations were repeated using a different, more dilute standard of VOC8. This 'dilute-VOC8' contained the same compounds and the same ratio of these compounds to each other but compressed air was added in order that the total VOC concentration was 1040 ppb. Within the dilute-VOC8, each compound was present at 130 ppb.

The same experimental set-up as before was used, with PAG air introduced to the set up via the MFC to further dilute the VOC concentration. Linear regression was used to

determine MOS sensitivity at different humidity's and the results are summarised in Fig. 2.6.

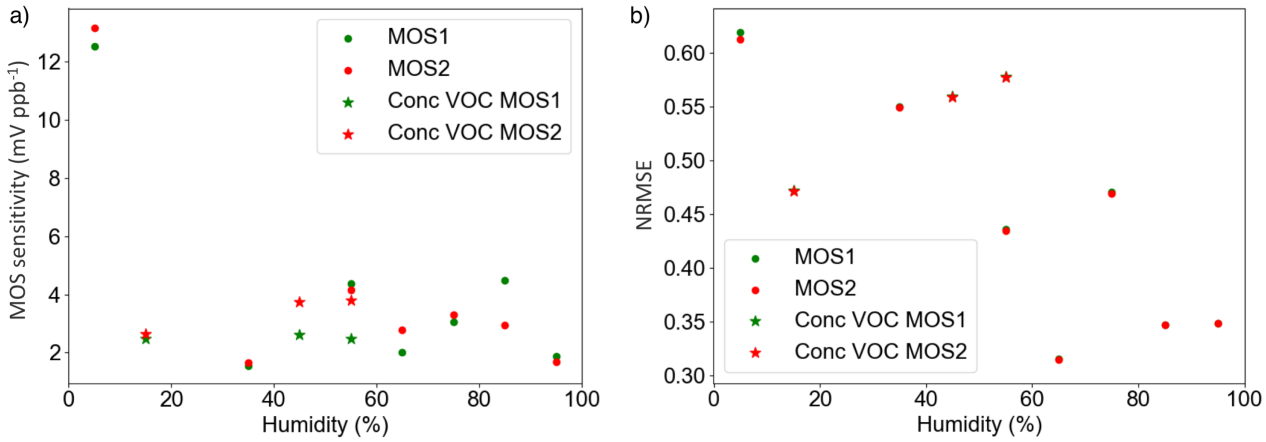

Figure 2.6: a) The MOS (MOS1: green, MOS2 : red) displayed different sensitivities towards changing total VOC concentration at different humidity ranges. b) As the calibrations were run at higher humidity's, the Normalised Root Mean Squared Error (NRMSE) of the calibrations decreased. The three calibrations with the concentrated (VOC8, total [VOC] = 40 ppm) mixture are shown as stars and the more dilute calibrations (total [VOC] = 1040 ppb) are shown as circles.

In dry air (0 - 10 % RH), with the diluted gas standard, the sensors were very responsive to the changing VOC concentrations (MOS1 sensitivity: 13.1 mV ppb^{-1}, MOS2 sensitivity 12.4 mV ppb^{-1}) and exhibited higher VOC sensitivities. As the humidity of the air increased to greater than 10 % RH, these values for the VOC sensitivity decreased by a factor of four, from c.a. +12 mV ppb^{-1} to approximately +3 mV ppb^{-1} for both MOS, Fig. 2.6a. However, between 10 and 100 % RH the VOC sensitivity remained relatively consistent. The calibrations with the concentrated mix of VOCs are also included in Fig. 2.6a (as circle data points, rather than stars) to show that the responses when using dilute or concentrated gas standards were relatively reproducible.

The Root Mean Squared Error (RMSE) for the calibration curves ([VOC] versus MOS voltage) was calculated and then divided by the range of VOC concentrations for that particular calibration to determine the normalised root mean square error (NRMSE). NRMSE is used because the RMSE scales with the magnitude of the data values. Normalising the RMSE, by dividing the RMSE obtained for each calibration curve by the range in sensor observations (maximum MOS value subtracted by minimum MOS value in the data set used for the calibration), allows the RMSE and uncertainty in the MOS responses to be compared. The NRMSE provided information about the uncertainty in the observations and was used to identify if there was more or less uncertainty associated with changing humidity conditions, Fig. 2.6b. In dry air, although the MOS sensitivities were high, the sensors displayed the greatest NRMSE, so there was more error associated with these calibration curves. The greater uncertainty results in complicated calibration procedures

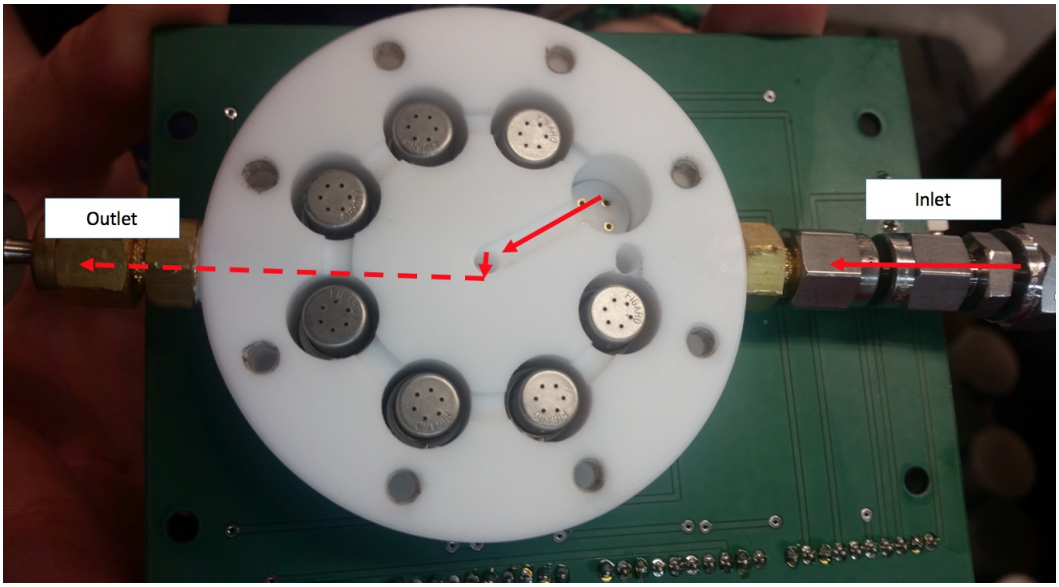

Figure 2.7: The eight MOS housed inside the custom-built Teflon manifold, with the sensors in series. Air was pushed through the system from the Pure Air Generator (PAG) and flowed around the Teflon block in accordance with the red arrows.

and they were likely to exhibit a greater deviation from the linear trend-line, Fig. 2.6b. In general, as the humidity of the air for the calibration increased, the NRMSE in the calibration decreased and there was less uncertainty in the sensor calibrations. The lowest NRMSE was observed for both sensors at 60 - 70 % RH, which is advantageous because the sensors will be used for deployment to monitor outdoor air and the UK typically experiences between 50 - 90 % relative humidity. A consistently lower NRMSE, with a more predictable VOC sensitivity is advantageous, even at the cost of the maximum sensitivity. The two MOS sensors (red and green data points) often displayed very similar values for VOC sensitivity, however, there were instances where they exhibited large differences in sensitivity for the same calibration. More TGS2602 MOS sensors were added to the set-up to identify the spread of the sensitivities and determine which of the observed MOS sensitivities was more typical of other MOS sensors. Three clusters of eight TGS2602 MOS sensors, purchased from the same manufacturing batch were used in the subsequent laboratory experiments. Each cluster of eight sensors were housed in a custom-built Teflon housing on a larger circuit board, Fig. 2.7.

Within the Teflon manifold the set of eight sensors were were arranged in series (see Fig. 2.7). The air flowed through the inlet and emerged at the first sensor housing, then travelled around the manifold and exited the manifold through the centre. The sensitivities of the sensors installed within this manifold towards different gas standards and different humidity's was investigated. As compounds adsorb to the sensor surface, they become oxidised and the compounds react to different molecules, changing their physical and electronic properties. Due to this, MOS sensing is a destructive process. However, only minute amounts of the air are detected by one sensor, and so it was hoped that the air

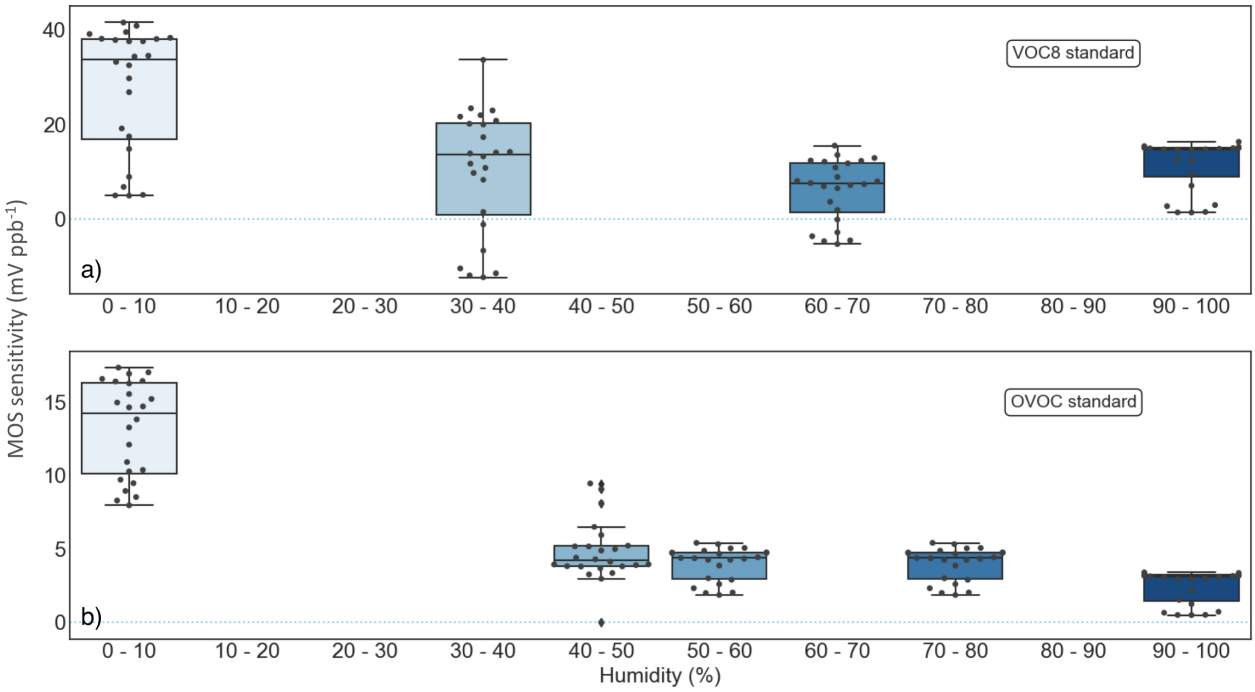

Figure 2.8: The sensitivities of 24 TGS2602 MOS sensors after exposure to a) VOC8 and b) OVOC gas standard calibrations at different humidity's. The box edges represent the interquartile range, the whiskers show the 5^{th} and 95^{th} percentiles and the line in the middle is the median. The black dots signify each sensors slope for the calibration. The light blue dashed line is at 0, to show some sensors displayed a negative correlation.

flow was large enough (at least 1000 sccm) to compensate for the sensors to be in series. PAG air was mixed with either the VOC8 or OVOC gas standards to dilute the VOC concentrations to be more representative of ambient concentrations, and calibrations were again conducted at room temperature but with different humidity ranges.

Figure 2.8a shows the 24 MOS VOC sensitivities to the VOC8 gas standard. The calibrations were conducted at a range of humidity's and the results are depicted as a box and whisker plot for each 10 % humidity range.

The 24 MOS sensors exhibited different VOC sensitivities when the calibrations were repeated with a different gas standard (OVOC), Fig. 2.8b. The magnitude of the MOS response was found to be dependant on the composition of the gas mix. This is due to the different compounds having different properties such as; size of the molecule, the diffusion rate and the reactivity of the molecule, which impacts the ability of the MOS active surface to detect a change in the surface conductivity. The MOS sensors were generally more sensitive towards the VOC8 standard (Fig. 2.8a), with a maximum sensitivity of 41.6 mV ppb^{-1} recorded by MOS10 compared to a maximum of 17.4 mV ppb^{-1} for the OVOC standard (Fig. 2.8b), recorded by MOS18. Both of these maximum sensitivities were recorded when the sensors were in dry air (0 - 10 % RH). The MOS sensors are potentially more sensitive towards the VOC than OVOC compounds because they OVOC may not adsorb to the oxyanion surface as readily as the VOC compounds. In more humid

air (90 - 100 % RH) the maximum sensitivity was 13.3 compared to 3.4 mV ppb^{-1} for the VOC8 and OVOC standards respectively. The sensors that reported the highest VOC sensitivities in dry air were found to be the the most sensitive at the higher humidity's as well (MOS10 for the VOC8 experiment, MOS18 for the OVOC experiment).

At all humidity's there was a range of MOS sensitivities towards changing VOC concentrations, even though the MOS sensors are all the same model and from the same manufacturer. This variability in the MOS responses, after experiments in the laboratory, under controlled conditions is a concern for their use as it makes comparing sensors deployed in different locations very challenging. It emphasises the requirement for bespoke calibrations for individual MOS sensors and further investigations are required to identify if these VOC sensitivities remain constant over time for each MOS sensor. The range of sensitivities towards VOC8 decreased as the humidity increased: from 36.7 mV ppb^{-1} at 0 -10 % RH to 14.96 mV ppb^{-1} at 90 - 100 % RH. There was more variability in the sensors slopes for the VOC8 gas standard, than was observed for the slopes calculated from the OVOC calibrations. This was evident because the ranges for the OVOC sensitivities were much lower, often below 5 mV ppb^{-1}, and the decrease in the variability of the sensitivities was still observed as the humidity increased (9.4 mV ppb^{-1} at 0 - 10 % RH to 2.92 mV ppb^{-1} at 90 - 100 % RH). The spread of sensitivities within the MOS sensors was concerning and re-iterates the requirement for frequent, individual calibrations for MOS sensors. The total VOC ambient mixing ratios are expected to be between 0 - 150 ppb and this appears to vary on the same magnitude as the spread in the MOS sensitivity measurements.

In Fig. 2.8a, one of the MOS sensor clusters was reporting lower sensitivities towards VOC8 than the other two clusters as the 8 sensors in this cluster are 5 - 10 mV ppb^{1} lower. This cluster was potentially not receiving the same amount of power as the other two clusters, due to a technical fault, as it would be unlikely for all 8 sensors to begin failing by exhibiting a low response, simultaneously.

There was a similar trend between Fig 2.6a and b, with both sets of calibrations displaying higher and more variable sensitivities in dry conditions. The findings here suggest the MOS sensitivity was dependant on the VOC composition of the air, therefore during deployment the sensors need to be calibrated with a standard that is representative of the air that the sensors will be used to monitor. This also broadly shows that the MOS sensors were more sensitive towards alkanes and aromatics (in VOC8)than they are towards oxygenated compounds such as acetone and methanol (found in OVOC gas standard).

The trend in the changing sensitivity of the MOS sensors was consistent with the findings from the experiments with other VOC mixes and MOS sensors. It has also been noted in the literature [105]. This non-linear relationship with humidity and MOS sensitivity must be better understood in order to recognise the optimum conditions for MOS sensing and to correct for humidity when sensors are deployed. It underpins the

importance of monitoring environmental conditions alongside the sensors when they are used in deployment. To correct for temperature and humidity effects upon the MOS sensor response, the temperature and humidity of the air flow reaching the MOS sensors needs to be monitored. When the environmental conditions enter a range for which the MOS sensitivities are likely to be very high or very low then further analysis of the data would be required.

2.3 MOS and the GC-MS

2.3.1 Methods

The MOS technology revolves around a compounds ability to adsorb to the active surface of the MOS. Therefore different compounds are going to have different adsorption rates to the surface and thus the MOS sensors may have different limits of detection for individual compounds. One way to test the MOS response to individual compounds was to use a GC with a split outlet. A MOS sensor received half of the outlet flow, and the other half was speciated and quantified by mass spectrometry (MS).

Gas standards containing a variety of Non-Methane Hydrocarbons, which are typically found in the troposphere were used to inject known quantities of VOCs into the instrumentation.

VOCs from the gas cylinder first passed through a cold finger, held at -37 °C to remove any water from the gas mixture. The dry gas mix then entered the Markes Unity Series 2 Thermal Desorption Unit, whereupon the VOCs in the mixture were flowed over the trap which contained a Tenax adsorbent. During adsorption, the trap was held at a low temperature (- 30 °) to ensure that all VOC compounds, even the most volatile, are captured on the trap. Helium passed over the trap at a flow rate of 100 mL min^{-1}, for one minute to ensure that permanent gases are removed and will not interfere with the chromatography or mass spectrometer. Using a trap ensures that a specific amount of sample is injected simultaneously into the GC system (Agilent Technologies 7890B Gas Chromatogram, see Fig. 2.9). To desorb the VOCs and inject them into the GC column (with a flow rate of approximately 2 mL min^{-1} the trap was rapidly heated to 300 °C and this temperature is held for 3 minutes. The GC column used here was the BPX5 (5 % Phenyl Polysilphenylene-siloxane) column which has a length of 50 m, an internal diameter of 0.32 mm and a film thickness of 1.5 μm. The BPX5 column is a general purpose column with a non-polar stationary phase so suitable for the separation of VOC compounds. The GC oven follows a set temperature regime to ensure the VOCs in the gas mixture elute off in a suitable time period. The column begins at 40 °C then after three minutes, the GC oven temperature is ramped at a rate of 15 °C min^{-1} until the temperature reaches 125 °C. When it reaches 125 °C, the temperature is ramped at a faster rate (20 °C

min^{-1}) until 250 °C is achieved. This final temperature is held for a further two minutes. Upon exiting the columns, the flow was split 50:50 and one half of the sample went to the Agilent Technologies 7200 Accurate Mass Time-of-Flight Mass Spectrometer (QTOF-MS) for identification and the other half flowed to the sensor in the olefactometer port. For detection with the QTOF-MS the VOCs are ionised and each given the same potential energy, which is converted to kinetic energy. The positive ions are attracted to a negative charge and hence travel down the time-of-flight tube. The velocity of the ions is related to their molecular mass and hence they reach the detector in mass order.

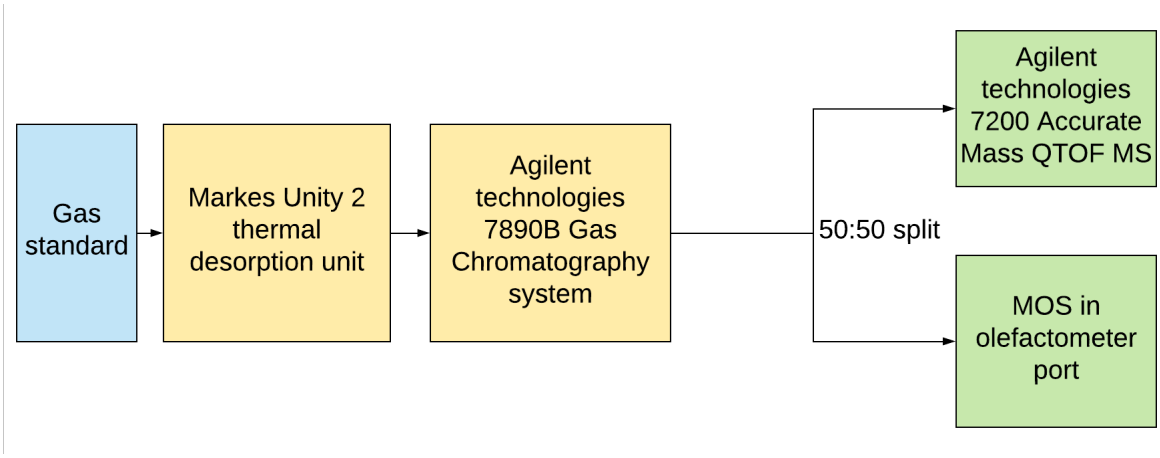

Figure 2.9: A flow diagram to show how a sample from a gas cylinder goes through the GC-MS system, with detection by either the mass spectrometer or MOS sensor.

The MOS are non-selective towards different reducing compounds and therefore can detect many carbon containing compounds. This investigation was conducted to characterise the sensitivity of the MOS towards different compounds, and determine which homogeneous groups induce the strongest response from the MOS sensors. From the previous work in Chapter 2.23, it was hypothesised that compounds such as alkanes and aromatics are likely to show a larger response than oxygenated compounds.

One MOS sensor was placed in a custom built Teflon casing, designed to have an airtight fit into the GC-MS olefactometer port. Different synthetic standards (NPL30 and OVOC), containing a variety of common atmospheric VOC pollutants were introduced to the system. The standard was pre-concentrated onto the adsorbent trap and separated using gas chromatography, with a helium carrier gas flow of 2 mL min^{-1}. Peaks were identified using their retention times and MS accompanied with use of the National Institute of Standards and Technology (NIST) library for the identification of compounds. A python script, using the open-sourced package Peakutils was used to fit a baseline to the traces and subsequently integrate the GC chromatograms as well as the MOS trace where the spectra were well resolved.

Sensors require oxygen for proper function however, the gas standards contained the VOC compounds in N_2 and the carrier gas used for GC analysis was helium, leading

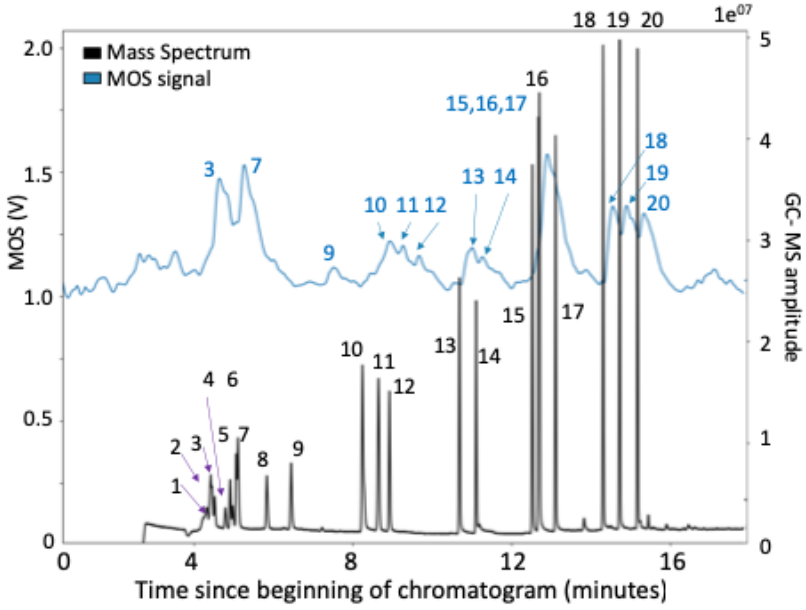

Peak	Compound	NPL30 Conc. (ppb)
3	Light compounds	
7	Isoprene and n-pentane	~8.02
8	2-methylpentane	4.04
9	n-Hexane	3.97
10	Benzene	3.98
11	2,2,4-trimethylpentane	3.97
12	n-Heptane	4.00
13	Toluene	3.98
14	n-Octane	4.01
15	Ethylbenzene	3.98
16	(m+p)-Xylene	8.00
17	o-Xylene	4.00
18	1,3,5-trimethylbenzene	3.99
19	1,2,4-trimethylbenzene	4.01
20	1,2,3-trimethylbenzene	4.02

Figure 2.10: Time series to show a GC-MS chromatogram (black) and corresponding MOS signal (blue), for the detection of peaks using the NPL30 standard. The table to the right of the plot displays the compounds, the peak numbers that were identified as being that compound and the mixing ratio of the compound in the cylinder.

to a potential degradation of the sensor surface after repeated use. As each run takes approximately thirty minutes the number of injections was limited to a maximum of five injections in a row for each MOS sensor.

2.3.2 TGS2602 Total VOC sensors

The GC separated out the compounds in the NPL30 synthetic gas standard. The chromatogram shows that it took 15 minutes between elution of the first compounds (a mixture of lighter <C5 compounds) and the last compounds which were the three trimethylbenznenes. Due to the time required for pre-concentration, trapping and separation of the compounds, an entire run took approximately 30 minutes. The sample volume was 700 mL and the resultant chromatogram displayed 13 resolved peaks, allowing the identification of 13 individual compounds with mass spectrometry (black line in Fig. 2.10). A dual peak of isoprene and n-pentane was also detected by mass spectrometry (peak 7) and was included in the analysis because it appeared as a large peak in the MOS trace. The lighter compounds with 2 to 5 carbons, for example ethane, ethene, to butane and pentenes, did not appear well resolved well in either the mass spectrum or the MOS traces.

An initial glance at Fig. 2.10 shows that the MOS was able to detect individual compounds as they elute off the column, albeit with poorly resolved peaks compared to the GC-MS chromatogram. Although compounds often eluted with less than 2 minutes between each the MOS' time response was quick enough to show a small peak for each

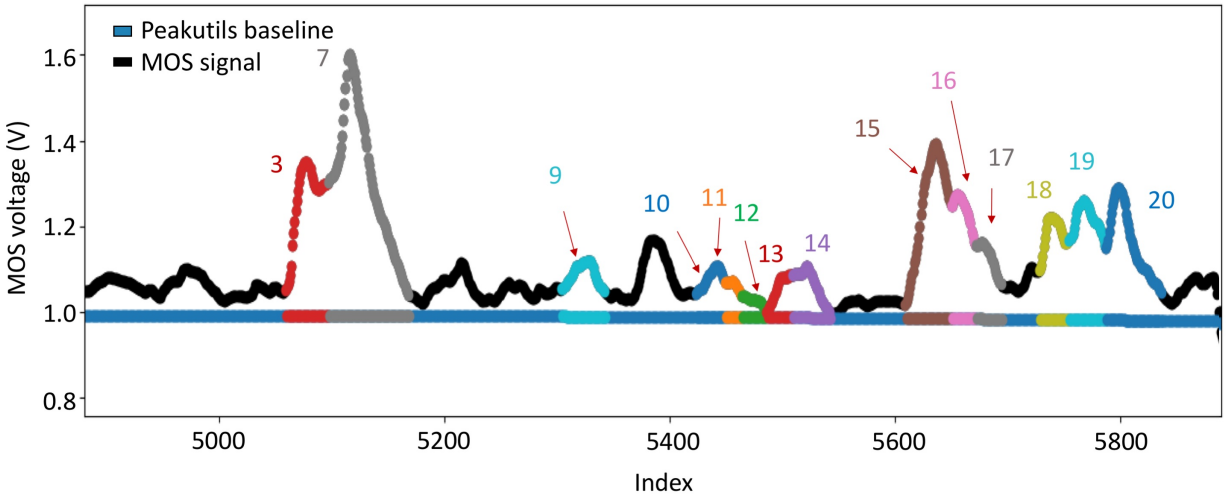

Figure 2.11: Peakutils determined a baseline (blue) and the peaks (coloured sections of the black line) of the compounds were determined by comparing the GC-MS trace with the MOS signal over the same duration of time.

compound, even if the resolution was not good enough for complete separation. The noise in the MOS baseline was low enough to observe very similar MOS responses for each injection of the NPL30 sample. The peaks in the MOS trace were identified by time aligning the MOS and mass spectra, and the subsequent peaks are labelled in Fig. 2.11. For all five injections of NPL30, both the MOS (see Fig. 2.11) and MS spectra were integrated using the Peakutils python package. As part of the integration process a baseline was required, and this was determined by the Peakutils package; an example baseline can be seen in Fig. 2.11, under the MOS time series.

Figure 2.11 shows each assigned peak as a different colour. The easiest compounds to identify were the three trimethylbenzenes as they presented with a large three pronged peak. Compounds 10 to 14 were harder to identify as the peaks were smaller and did not stand out as much from the baseline. The mass spectrum in Fig. 2.10 was much more resolved over the same elution time, but this was expected and the investigation was only designed to get a general idea of which compounds the sensors exhibit the largest response to, and not to propose a new, fully resolved detection system for speciating VOCs. The MOS sensor did show larger peak areas for some compounds e.g. trimethylbenzenes, compared to others e.g. n-Hexane (Fig. 2.12). The GC-MS peak areas were also calculated using the Peakutils package to check that the integration algorithm was working properly. Figure 2.12 compares the mean peak area for each compound over the five injections. Heavier compounds, such as toluene, ethylbenzene and the trimethylbenzenes displayed larger peak areas in the mass spectrum and in the MOS signal. Branched compounds, 2-methylpentane and 2,2,4-trimethylpentane displayed the smallest peak areas for the MOS. This is potentially because the branching means that these compounds have a large amount of steric hindrance and so do not diffuse as easily onto the MOS active surface.

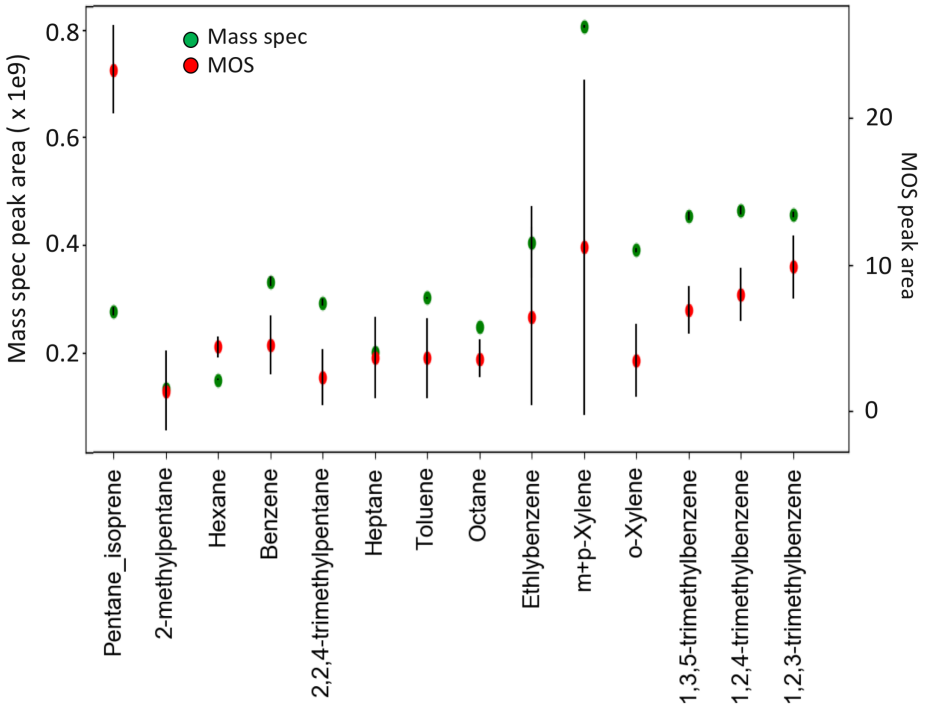

Figure 2.12: The peaks were integrated using the same methods for both the MOS sensor and the GC-MS spectra. The mean peak area over five injections of 700 mL of NPL30 gas standard, for each numbered peak was plotted to compare how well the GC-MS and MOS detect certain compounds. The standard deviation of the five spectra are plotted as black lines.

The mass spectrum had the smallest peak for hexane. The largest standard deviation for the 5 integrals were found for compounds such as ethylbenzene and *m+p*-xylene and this is potentially due to these compounds presenting as a dual peak in the MOS trace, making it difficult to identify the beginning/end of a peak. As expected, the MOS signal displayed a larger standard deviation than the mass spectrum.

m+p-Xylene displayed the largest peak for both the GC-MS and MOS methods; which was unsurprising as these isotopes elute together, effectively doubling the quantify of eluted VOC and therefore an increased size of the peak compared to the other individual compounds was expected. Both the MOS and the GC-MS displayed high peak areas and lower standard deviation values for the C8 and C9 aromatic compounds, e.g. ethylbenzene, the xylenes and the trimethylbenzenes.

The same process was repeated with three 10 mL injections of the OVOC standard, see Fig. 2.13. Due to the GC column and methodology the lighter compounds, methanol, propane and ethanal did not separate out in the GC column and eluted as one peak in both the GC-QTOF mass spectrum and the MOS trace. The GC QTOF mass spectrum and MOS traces had very similar profiles for each of the three injections of the OVOC standard, with each of the four peaks (in order of elution: propane/ethanal/methanol, acetone, hexane, benzene) well separated from the others. The propane/ethanal/methanol peak appeared in the MOS signal as the second largest peak, but since they could not be

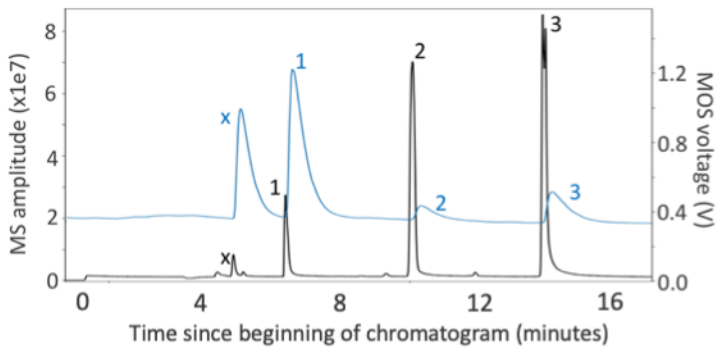

Peak	Compound	Cylinder conc. (ppm)
X	Unknown – maybe propane/ethanal or methanol	Each compound present at 5 ppm
1	Acetone	5
2	Hexane	5
3	Benzene	5

Figure 2.13: A comparison of the traces for the TGS2602 MOS signal (red) and GC-QTOF-MS (green) using the OVOC gas standard.

distinguished in the MS, it was unknown whether the MOS was responding to all three equally or if the MOS sensor was just more sensitive to one of these compounds.

There was more time between each of the peaks for the OVOC compounds as they eluted off the columns, and this meant that the MOS had more time to respond to the changing VOC concentrations. This allowed for for better resolved peaks in the MOS spectrum and it was easier to identify and integrate the three injections of OVOC standard using the time-aligned MS, than it was for the NPL30 standard. Acetone was the only oxygenated peak to be individually identified and this OVOC compound presented as the largest peak in the MOS spectrum, Fig. 2.14. For deployment of the MOS sensors outdoors, it is important to know that they exhibit a large response towards acetone as it can be present at significant concentrations in the troposphere (0.2 to 3 ppb) [83]. The second largest peak in the MOS trace was the combined peak for propane/methanol and ethanal; this was expected to be a larger peak since it consists of three compounds. The TGS2602 MOS sensors displayed two resolved peaks for hexane and benzene, but these were much smaller than the acetone and combined peak. The GC mass spectrum however displayed peak areas that were larger for benzene and hexane than they were for the lighter compounds, see Fig. 2.14, green data points. The MOS response towards benzene was greater than the response towards hexane, more evidence that the sensors are more sensitive towards large, aromatic compounds, rather than their aliphatic counterparts. The smaller MOS response to hexane is consistent with the findings from the previous GC-MS result with the NPL30 standard. The standard deviation between the three injections was relatively consistent for the MOS sensors: ranging from 0.465 for the combined peak to 1.156 for the benzene peak. Benzene was the least well-resolved peak as it was shallower and wider than the others (Fig. 2.13) and this explains why the standard deviation between the benzene peak for the three injections was increased compared to the other peaks (Fig. 2.14). The last injections of both the VOC and OVOC gas standards displayed similar peak areas for each compound compared to the first injection. Therefore it was assumed that there were no noticeable impacts on MOS sensitivity during the GC-MS run time

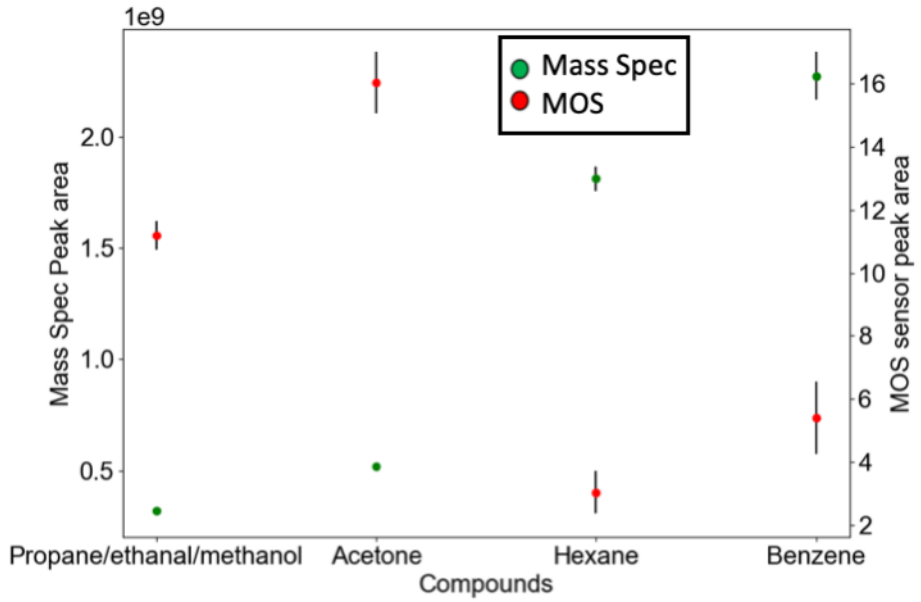

Figure 2.14: The peak areas were averaged over each of the OVOC gas standard injections for both the MOS trace (red) and the mass spectrum (green). The vertical black lines depict the standard deviation each of the averaged peak areas.

due to them sensing gases in the absence of oxygen.

2.3.3 Ambient air sampling with co-located SIFT-MS

The MOS sensors had been tested in the laboratory against synthetic standards, and yet they were destined for outdoor use to monitor ambient air. Therefore, two clusters of eight MOS were co-located in the laboratory with a Selected Ion Flow Tube - Mass Spectrometer (SIFT-MS), Fig. 2.15 to sample air from outdoors. The SIFT-MS and sensor instrument had a joint sample line, with the inlet running through the wall to outside the building. Air was pulled through to the SIFT-MS and then flowed to the MOS clusters using a diaphragm pump. The air temperature and humidity was monitored to ensure that the environmental conditions were kept relatively constant during the sampling duration. The experiment took place between the 9th February 2017 and the 13th March 2017, and the sensors and SIFT-MS ran continuously during this time. Dr. Marvin Shaw was responsible for operating the SIFT-MS and supplying the SIFT data. Several compound concentrations, for the H_2O+ and NO+ reagent ions, were supplied in the SIFT-MS data and these were compared with the MOS.

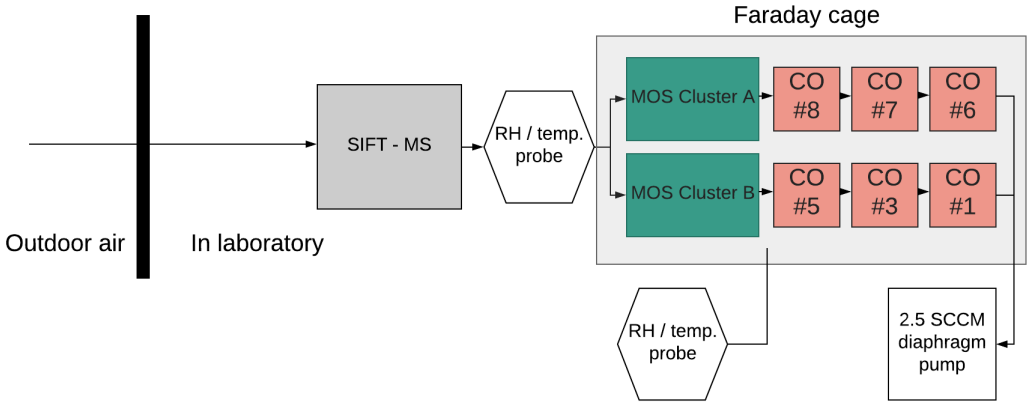

Figure 2.15: Experimental set up for the comparison of the SIFT-MS and two clusters of MOS. The instruments were co-located in the laboratory and used the same sample line, and the inlet was fed through the wall and sampled outdoor air. A diaphragm pump pulled air through the lines at a constant flow of 2500 sccm.

The SIFT-MS detects compounds by counting the amount of NO+ or H_3O+ adduct ions that reach the detector. The H_3O+ adducts produced very noisy signals and so just the NO+ adduct ions were used for analysis, as recommended by Dr. Marvin Shaw. There were eight VOCs detected with the NO+ reagent ion: acetone, isoprene, 3-buten-2-one, butanone, benzene, toluene, 1,2,4- trimethylbenzene and (1,3)-butadiene. Each individual compound detected via the SIFT-MS required a correction factor, derived from the drift tube pressure, to compensate for temporal drift in the SIFT detection method. A total VOC NO+ was calculated by summing all the eight VOCs compounds together at a given time. To reduce the noise in the SIFT signal, a 15 minute resample was used, with the mean value over the 15 minutes calculated and used for analysis. This process was also used on the MOS data to allow for a time based merge of the two data sets. Three out of 16 MOS sensors failed and the median signal for the MOS cluster1 and cluster2 was determined and was used for analysis. There were six co-located CO electrochemical sensors also sampling downstream of the MOS sensors in the same experimental set up.

The MOS sensors detect the bulk VOC concentration and therefore the summation of the eight VOC compounds detected by the NO+ ion (the total NO+ ion adduct signal) was looked at initially Fig. 2.16. The time series for the MOS did not show many peaks for the MOS or the SIFT during the first three weeks of sampling, Fig. 2.16a. The total NO+ ion adduct signal showed some variability, with peaks at c.a. 60 ppb between the 17th and 24th of February 2017. The total NO+ adduct signal detected a lot more variability in the VOC concentration on 9th March 2017 and yet the MOS sensors did not display much of a response until the following day, where the MOS output voltage increased from c.a. 1 V to c.a. 1.5 V. Figure 2.16b shows the correlation plot for the total NO+ ion VOCs and the median of MOS cluster1 and cluster2 in green and red, respectively. The slope for the median MOS sensitivity towards the total NO+ ions was very low (2 to 5 x10^{-2} mV ppb^{-1})

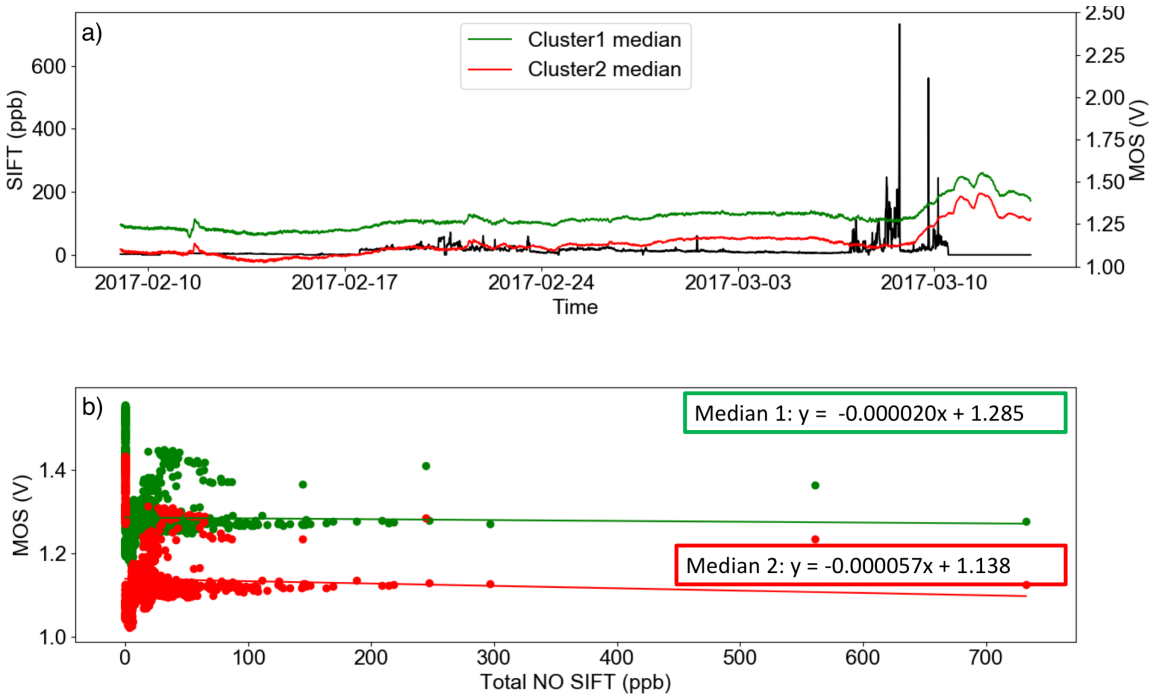

Figure 2.16: a) Time series of the NO+ compounds (black) with the median of MOS cluster 1 (green) and MOS cluster 2 (red). b) The correlation plot for the two median signals versus the SIFT measured concentration of the total NO+ ion count.

and was negative. The R^2 values for these plots were also very small and unmeaningful (R^2 <0.02), leading to the conclusion that the total NO+ ion VOCs do not correlate with the MOS signal.

The eight compounds detected by the SIFT-MS were analysed individually with the median MOS signal to assess if the MOS sensors had a better correlation with the compounds when investigated on their own. The slope of median MOS and each individual compound was positive and larger in magnitude than the bulk total NO+ trace, Fig.2.17a.

Using linear regression, the slopes were calculated between the median of MOS cluster1 and each of the 8 SIFT-MS compounds, the total NO+ ions and also the slope between MOS cluster1 and humidity and temperature. The same linear regression was re-calculated for MOS cluster2. The plots in Fig. 2.17 showed that out of the compounds detected by the SIFT-MS, the MOS were most sensitive to butanone and responded the least to trimethylbenzene (TMB). However, correlation between the MOS response and the butanone signal was still low, R^2 = 0.21 for both clusters of MOS. The slopes are shown as mV ppb^{-1}, and were similar to what would be expected for VOCs at 30 - 60 % relative humidity. The strongest sensitivity by far was the median of cluster 2 with laboratory temperature, with 7.2 mV °C. The temperature fluctuated between 20 and 21.5 °C, and was somewhat controlled as both the sensors and SIFT were in the laboratory for the duration of the experiment. Since the two devices were located indoors the fluctuations in the humidity of the air that reached the SIFT or MOS were reduced. This led to a small correlation with relative humidity. Figure 2.17b shows the R^2 values for each of the

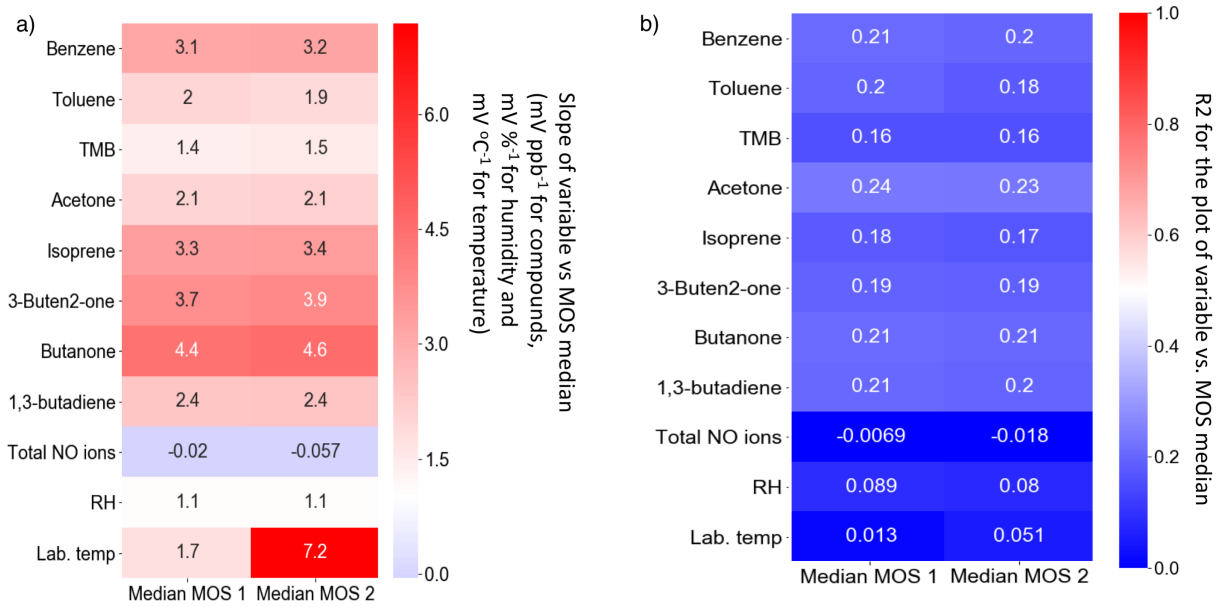

Figure 2.17: a) Each variable was plotted up with the median signal from each cluster, and a slope determined from the correlation plot. The slopes are colour-coded, with red being the highest slope, and blue the lowest. b) From each correlation plot for every variable, the R^2 value was determined and is also colour-coded to show the strength of the correlation between each variable.

variables correlation plots with the median MOS for each cluster. Although the comparison between the MOS and the SIFT-MS was improved when analysing each compound individually, the correlations were all relatively weak, with only benzene, acetone, butanone and 1,3-butadiene displaying R^2 that were greater than 0.2. The weak correlations might be due to the individual compounds that the SIFT can detect being different to the compounds that are more detectable by MOS sensors. In this experiment, the SIFT was only able to detect eight VOC compounds and yet from previous experiments the MOS sensors are known to respond to much more than that.

From the GC-MS experiment, it was known that the MOS sensors are more sensitive to particular compound groups over others, and the results from that experiment suggested that the MOS sensors display a larger response towards aromatic compounds. This was investigated using the SIFT-MS data. A scaling factor of 5 was applied to the aromatic compounds (benzene, toluene and trimethylbenzene (TMB)) to emulate a higher MOS sensitivity towards these three compounds, Fig. 2.18a. Five was chosen as an arbitrary number so that the individual VOC compound concentrations would be increased, relative to the other compounds in order for an investigation to determine whether the MOS sensors were more sensitive to the VOC composition changing.

However, the slopes for the scaled up aromatic compounds with the median MOS sensors were found to be lower than when the aromatic compounds were not scaled up. The total NO+ ion slopes remained very similar to before the aromatic compound scaling. It was expected that the slope for total NO+ VOC ions against the median MOS would

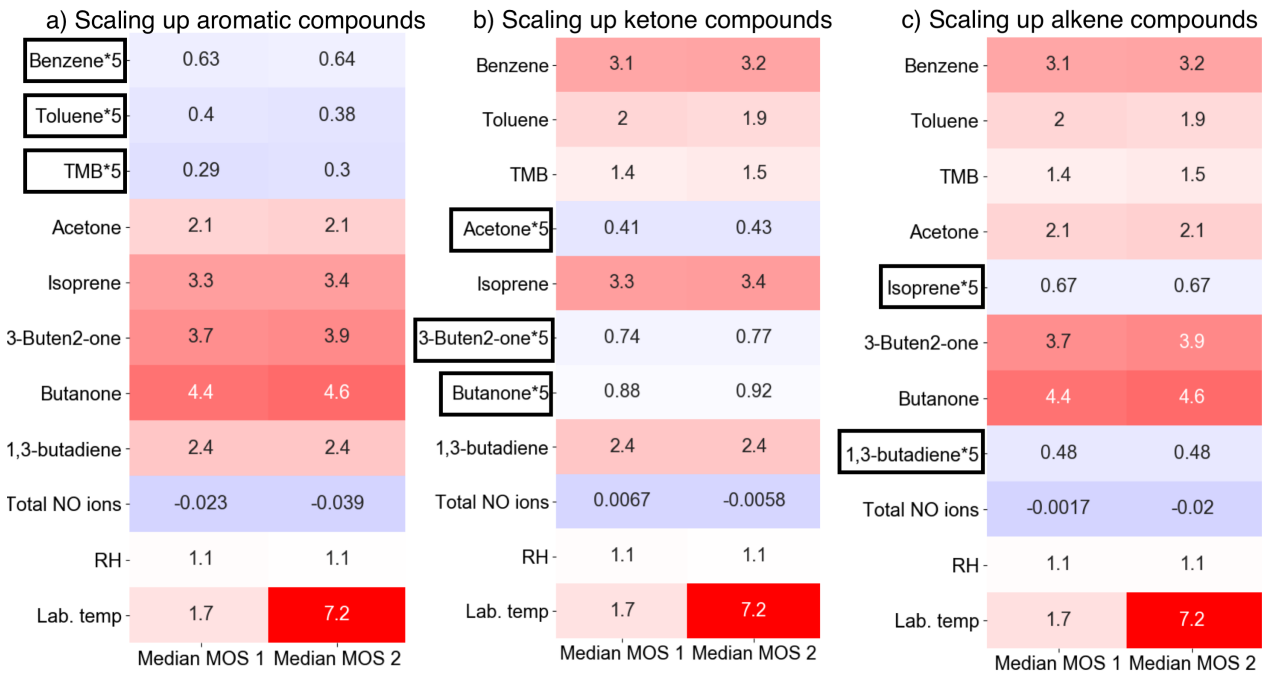

Figure 2.18: The linear regression between the MOS and SIFT-MS was calculated three more times, with a scaling factor of 5 applied to a) the aromatic compounds, benzene, toluene and TMB, b) ketone compounds, acetone, 3-buten-2-one and butanone and c) alkenes, isoprene and 1,3-butadiene.

be increased if the MOS were more sensitive towards VOCs, so this was a bit surprising.

When the ketones, acetone, 3-buten-2-one and butanone were all scaled up by five, their slopes against the median MOS signals also decreased, but the total NO+ VOC ions changed, Fig. 2.18b. For the median of cluster 1, the total NO+ vs. MOS slope became slightly positive, and yet the slope for the total NO+ ions with scaled up ketones median of cluster 2 became more negative. This was surprising because with no scaling factors applied, butanone and 3-butan-2-one exhibited the largest magnitude of slope for the correlation plots.

Scaling the alkenes, isoprene and 1,3-butadiene, traces by five changed the total NO+ VOC ions to have slopes of -0.02 and -0.057 mV ppb^{-1} for cluster 1 and cluster 2 respectively to -0.0017 and -0.02 mV ppb^{-1}. This is getting closer to 0, which would indicate that the total VOC sensors did not detect SIFT-MS ions at all.

The MOS sensors did not present any simultaneous noticeable peaks with the total VOC SIFT-MS NO+ ion adduct signal. This was very concerning as it was thought that the MOS would compare better to the SIFT-MS than to a GC-MS or FID instrumentation due to the scientific principles. The SIFT-MS provides a more real-time measurement of VOCs and is likely to capture a greater range of VOC compounds as it can detect any VOC that can be ionised with the reagent ions. Therefore it was thought that summing the SIFT VOC compounds would be a more similar measurement to the bulk VOC measurement made by the MOS. This experiment would suggest that the MOS are not currently suitable

for the detection of ambient concentrations of VOCs, under real-world environmental conditions as all correlations with the SIFT-MS data were poor (R_2 <0.3) indicating that the MOS signals were not detecting any of the compounds detected by the SIFT-MS. The SIFT-MS would typically provide a wider range of VOCs measured and, in the mode that is was operated in it did not detect VOCs that might potentially have a greater concentration in ambient air, which would be detected by the MOS. There were no high correlations with any individual compound detected by the SIFT-MS and the MOS signals either.

2.3.4 The affect of flow rate upon the MOS sensors

All the laboratory experiments so far were run with a constant flow rate of air controlled by mass flow controllers from either the PAG, compressed air or, for the SIFT experiment, a diaphragm pump. The flow of air will affect the rate of oxyanion replenishment upon the sensing surface and the speed of the VOCs passing the sensors, so the sensor sensitivity might be dependant upon the rate of air flow. Calibrations run using the OVOC gas standard were conducted using four different flow rates for the PAG air. The humidity was held at below 5 % RH, across all the calibrations and there were two clusters of eight TGS2602 MOS sensors.

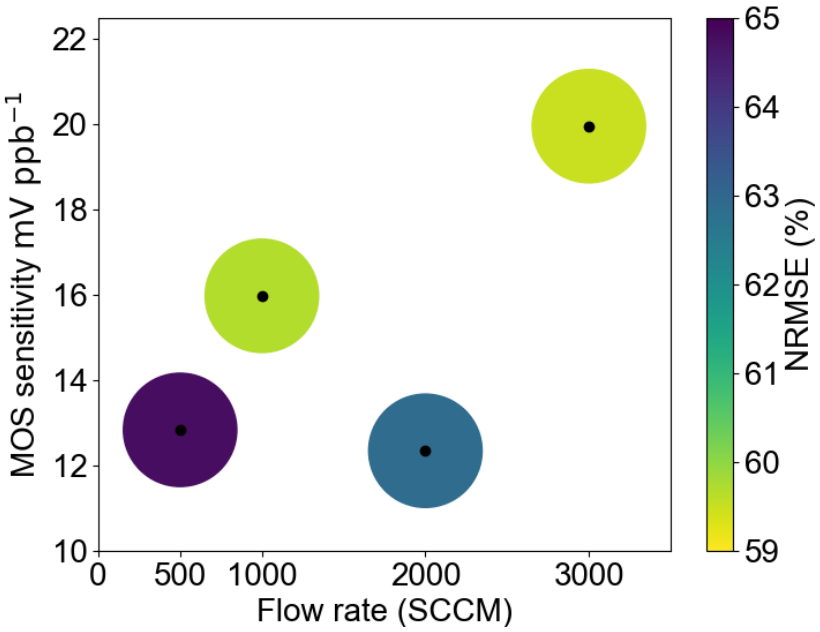

Figure 2.19: Analysing the affect of the flow rate upon 16 TGS2602 MOS sensors. The black dots show the MOS sensitivity towards the OVOC calibrations at the different flow rates and the colours indicate the NRMSE of each calibration.

The Normalised Root Mean Squared Error (NRMSE) was calculated by dividing the RMSE by the OVOC concentration range over which the calibration was run. The colour

bar covers a narrow range in NRMSE (from 59 % to 65 %) because the OVOC calibrations with different flow rates all returned calibration plots with a similar amount of error in the liner regression analysis. The colour bar set to just highlight the small changes in error observed. The MOS sensitivity towards OVOCs almost doubled as the flow rate was increased from 500 sccm (13 mV ppb^{-1}) to 3000 sccm (20 mV ppb^{-1}. From Fig. 2.19 it can be seen that the highest MOS sensitivity was observed with 3000 sccm flowing over the sensors and this also displayed the lowest error for the OVOC calibrations. 1000 sccm appeared to be another optimum flow rate as the MOS sensitivity was high, c.a. 16 mV ppb^{-1}, with a relatively low magnitude of error. For practical reasons, a lower flow rate will consume less power and therefore 1000 sccm would be optimum for deployment of a low cost sensor system. It is advisable to keep the flow rate consistent during deployment of the sensors and use the sensors in a manifold with the air flow controlled by a pump or mass flow controller to avoid wind speed and direction affecting the sensor signal.

2.3.5 The affect of humidity and temperature upon the MOS sensors

In dry air, the MOS rely on oxyanions chemisorbed to their active surface for operation, so require a steady flow of oxygen. Reducing compounds such as VOCs, react with these anions upon adsorption to the MOS active surface ultimately leading to change in the conductivity of the MOS surface and the reducing compound being detected. The presence of water near the surface of the sensors greatly affects the sensors because hydroxide anions (-OH) from the water adsorb to the surface occupy the site normally taken up with oxyanions. The adsorption of -OH ion causes a change in MOS signal (see Fig. 2.20) and the subsequent interaction of VOCs and hydroxide ions is different to the reaction of VOCs and the oxyanions and therefore the detection of VOCs by MOS is impacted.

Figure 2.20 shows that as the relative humidity of the air reaching the sensing surface increased, the MOS output voltage decreased in a non linear fashion. At very low humidity's (0 - 10 % RH) the MOS sensors displayed the highest conductance, outputting a signal voltage of c.a. 1.7 V. As the air flow to the sensors contained more water vapour, (from 20 to 80 % RH) the conductance of the sensor surface decreased with a flatter gradient. The decrease in conductance at the MOS sensor surface with increasing humidity is thought to be due to the HO- ions adsorbing to the surface and replacing some of the oxyanions. The OH- ions are less able to attract electrons towards the surface of the semi-conductor sensing material. This results is less band bending of the conductance bend and hence a lower decrease in conductance than if oxyanions were chemisorbed [187]. Linear regression was performed to get a general idea of the sensitivity of the MOS towards changing humidity levels. MOS1 and MOS2 were found to have slopes of -8.2 and -8.3 mV $\%^{-1}$ respectively.

This was further investigated with four clusters of MOS sensors, with each cluster

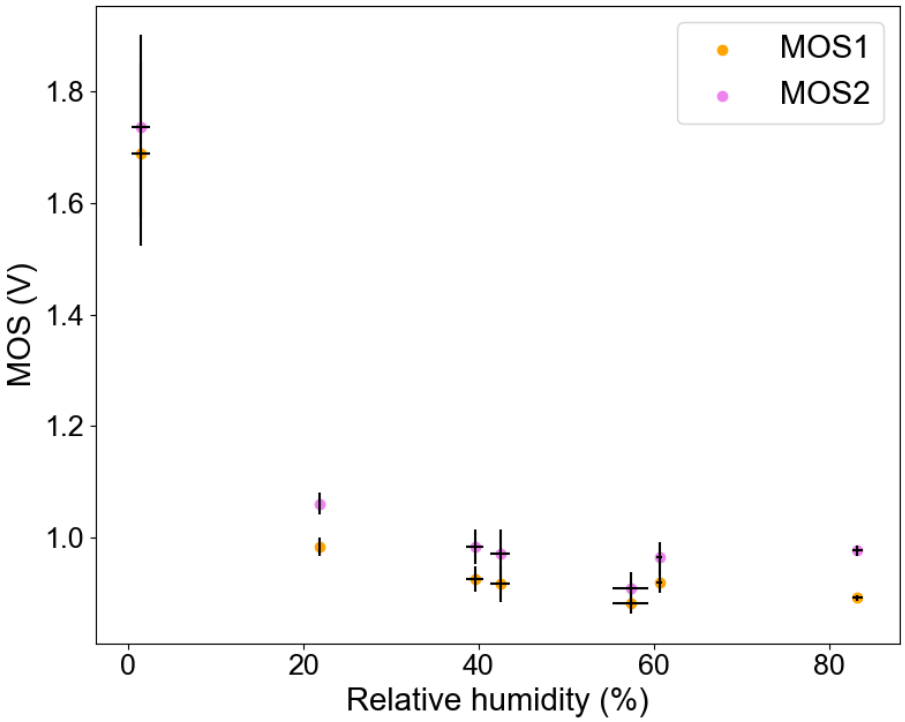

Figure 2.20: Two TGS2602 MOS sensors were exposed to different humidity's of air for at least 6 hours. For each humidity, the mean (orange and pink dots) and standard deviation (black lines) of the MOS signal for each 10 % RH bin was calculated.

containing a different type of MOS sensor. The set of tested sensors comprised of four clusters of eight total VOC (TGS2602), methane (TGS2611), propane/butane (TGS2610) and OVOC (TGS2620) metal oxide sensors. They were all simultaneously exposed to different amounts of humidity to observe if they all exhibited similar behaviour to the TGS2602 in Fig. 2.20. For the analysis, the median sensor from each cluster was calculated and the humidity binned into 10 % RH bins, with the mean and standard deviation determined for each bin.

The total VOC sensors (TGS2602) displayed similar behaviour to previous experiments; a negative correlation with increasing humidity, albeit with a slightly lower sensitivity of around -2.6 mV $\%^{-1}$, Fig. 2.21a compared to Fig. 2.20. When compared to the 2 MOS sensors responding to increasing humidity in Fig. 2.20 the sensitivity of the MOS sensors towards RH appeared to be decreased. The lower RH sensitivity was likely due to only using air with a humidity of >15 % RH as the really dry air (0- 10 % RH) in Fig. 2.20 indicated a much larger conductance which influenced the magnitude of the overall slope.

The other three types of MOS sensor performed very differently as the median signal for the sensors all increased with increasing humidity. They all exhibited much larger sensitivities to humidity, with the slopes all being positive: +7.19, +9.92 and +11 mV $\%^{-1}$ for the propane/butane, methane and OVOC MOS respectively. The correlations were all very linear and strong with R^2 values all >0.98. It is important to have fully characterised

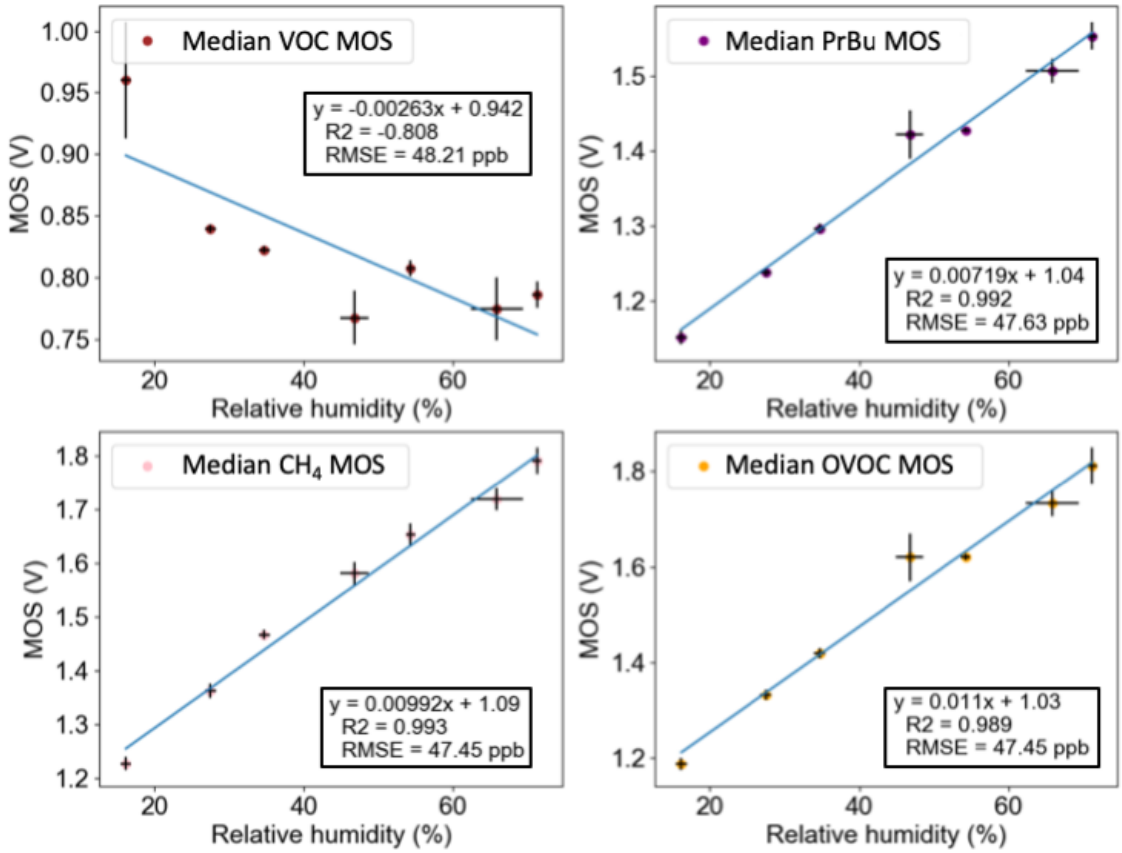

Figure 2.21: The calibration curve for the median from each sensor cluster as the humidity of the air flow to the sensors was changed. The dots are the mean MOS signal for each 10 % humidity bin, and the black lines are the standard deviation for each data point. The calibration curves for a) the total VOC MOS sensors (TGS2602), b) propane/butane (TGS2610) MOS sensors, c) methane (TGS2611) MOS and d) OVOC (TGS2620) MOS sensors.

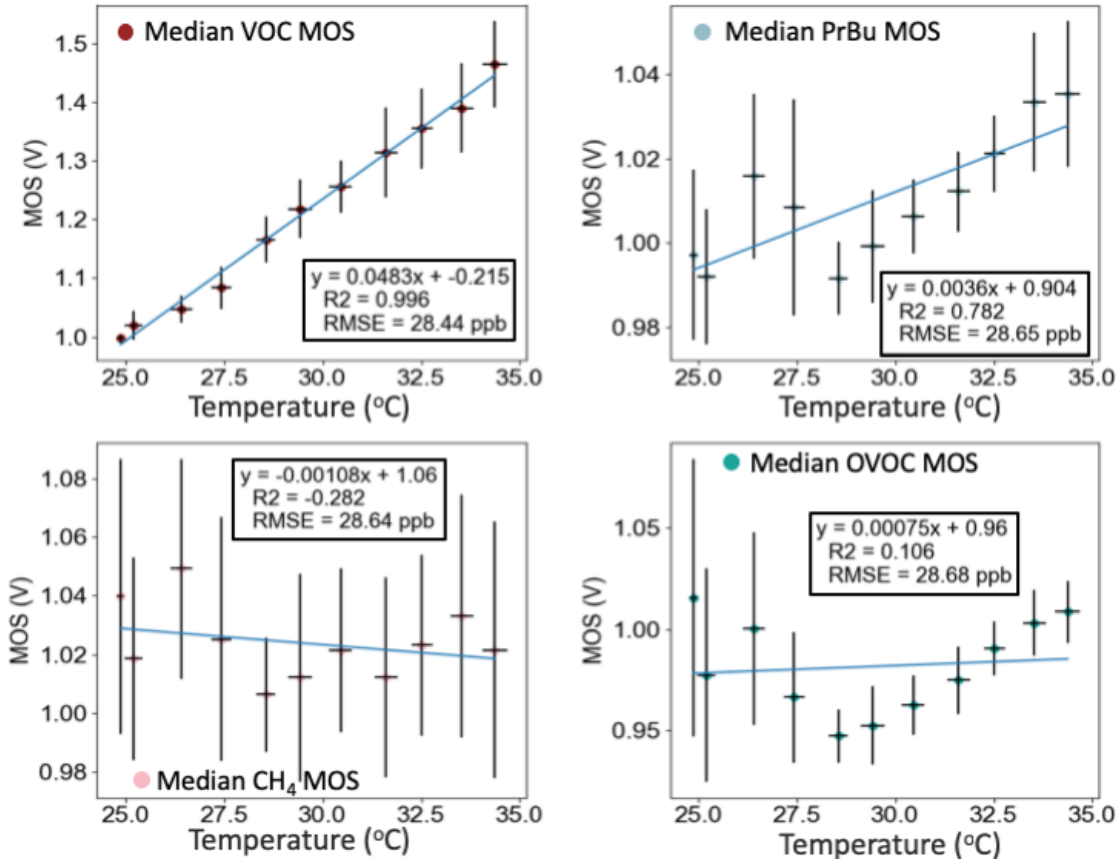

Figure 2.22: The four clusters of TGS2602, TGS2611, TGS20 and TGS2610 sensors were housed in an instrument box and therefore the box could be heated. The temperature in the plots refers to the temperature of the air flowing to the sensors, and the calibration plots for all four different types of sensor are as follows, a) the total VOC MOS sensors (TGS2602), b) propane/butane (TGS2610) MOS sensors, c) methane (TGS2611) MOS and d) OVOC (TGS2620) MOS sensors.

the behaviour of the different types of MOS sensor as this might influence which sensors are chosen for deployment. All MOS displayed a RH dependency and exhibiting a linear response to RH is advantageous because this is easier to correct for during post-analysis.

Temperature

The four sensor clusters were housed inside a box that was heated from underneath to increase the temperature surrounding the sensor manifolds and the air flowing to the sensors. The temperature of the air to the sensors was monitored and the four calibration plots for each MOS type are shown in Fig. 2.22. The data was binned into 1 °C bins over the temperature range (24 to 35 °C), and the data points represent the mean of the bin, whilst the black lines are the standard deviation.

The total VOC MOS displayed the most positive sensitivity to the air temperature, with a slope of +48.3 mV $°C^{-1}$ and a strong correlation ($R^2 = 0.99$), Fig. 2.22a.

The propane/butane (TGS2610) and OVOC (TGS2620) displayed weakly positive sensitivities towards increasing temperature (3.6 and 0.8 mV $°C^{-1}$), although these plots appeared less linear than the plot for total VOC MOS, Figs. 2.22b and d. The calibration

curves for both increased between 24 and 26.5 °C, then both dipped around 28.5 °C and then rose again at higher temperatures.

The profile for the methane MOS sensors (TGS2611), Fig. 2.22c, was similar in shape between 24 to 30 °C but overall led to a negative slope for temperature and MOS signal (-1.1 mV °C^{-1}).

Temperature is also expected to impact the sensitivity of the MOS sensors towards VOCs. This is expected to be a non-linear response because increasing the external temperature at lower temperatures leads to faster reaction kinetic and therefore an increase in the sensitivity of the MOS. However at higher temperatures, increasing the temperature may lead to faster desorption rates, decreasing the sensitivity of the MOS sensor [187]. This reiterates the requirement for calibrating different types of sensors, with the expectation that models of sensors experience different temperature and humidity dependencies. It is advised to calibrate the MOS sensors for the temperature range that the MOS are expected to experience during deployment. The plots in Fig. 2.22 depict the median MOS sensor of each cluster and the standard deviation of each data point is noticeable. This emphasises that each individual MOS within the cluster also has a unique temperature response. There are two ways of minimising the impact that changing environmental conditions have upon the MOS sensor response. The MOS sensitivity towards each environmental condition, temperature, humidity etc. could be characterised and individual correction factors determined for each sensor, but this is a time intensive form of sensor correction. Another method would be to control the temperature and humidity of the air flow reaching the MOS sensors. This would cost more, to install equipment to maintain constant sampling conditions during a deployment but could potentially be more cost and time effective overall as the correction and analysis of the sensors would be easier. There are disadvantages to using extra equipment to obtain constant air flow conditions; the units could be costly, consume lots more power to run or require frequent maintenance, which do not match the low-power, low-cost advantages gained using LCS unattended in the field. For example, using a cold finger to remove humidity from the air flow consumes power as the cold finger needs to be constantly cooled to - 30 ° and the water in the cold finger would need to be removed at regular intervals for locations such as the UK with moderate to high humidity's.

2.3.6 Manifold design

When deploying the sensors in the field, more than one sensor was used and diaphragm pumps were required to ensure a consistent flow of air over the sensor surfaces. Three custom built manifolds were designed to investigate the best way to encase multiple MOS sensors in an air-tight manifold, see Fig. 2.23. Manifold 1 was built using a Teflon block to minimise VOCs reacting on the manifold surface and changing the concentration of VOCs in the sampled air. The air flowed around the block, in a circular pattern, with the 8 MOS

sensors arranged in series in manifold one. This was the manifold that has been used in the prior analysis of MOS in the laboratory, see Fig. 2.7 for a photo of this manifold. Manifold 2 was designed from a solid piece of acetal and had the inlet in the centre of all the sensors. Each sensor had an equal path length to it to ensure every sensor saw the air sample simultaneously. The air flow exited the manifold by flowing out to an exit channel that went around the circumference of the sensors. Like manifold 2, manifold 3 was also designed from acetal, to minimise the materials cost for the building of the manifolds, whilst still minimising reactions to the surface of the blocks. Manifold 3 was based upon a chamber-type design; the inlet input the air into the centre of a hollowed out block which all the sensors sat in. This design will potentially allow all the MOS to respond to the same air simultaneously, but the chamber allows for a large volume surrounding the sensors. One at a time, the same sensors were put into the same positions within each manifold. Then an OVOC calibration was run and each sensors slope was determined for the OVOC concentration and the MOS signal.

Figure 2.23 depicts the different designs of the manifolds and additionally each sensor position is colour-coded based upon the sensitivity displayed by the sensor that was in that particular position. Sensors which displayed a higher sensitivity towards VOCs are shown with a more yellow colouring and sensor positions that displayed a lower VOC sensitivity are coloured more purple. Manifold 3, where the sensors were surrounded by a chamber performed the worst, with all sensors displaying the lowest sensitivities towards changing OVOC concentration. This is potentially due to the large dead volume around the sensors leading to slower response times and lower sensitivities. Manifold 1 had displayed a reasonable consistency in the MOS VOC sensitivities, but it was noted that there was a gradual decline in the MOS VOC sensitivities as the air flowed around the manifold. This indicates that having the sensors in series was not the optimum method for future VOC detection. Manifold 2, the acetal enclosure with each sensor having an equidistant inlet, performed the best displaying the most consistent and highest sensitivities. For deployment of the sensors out in the field, a design based upon manifold 2 will be used.

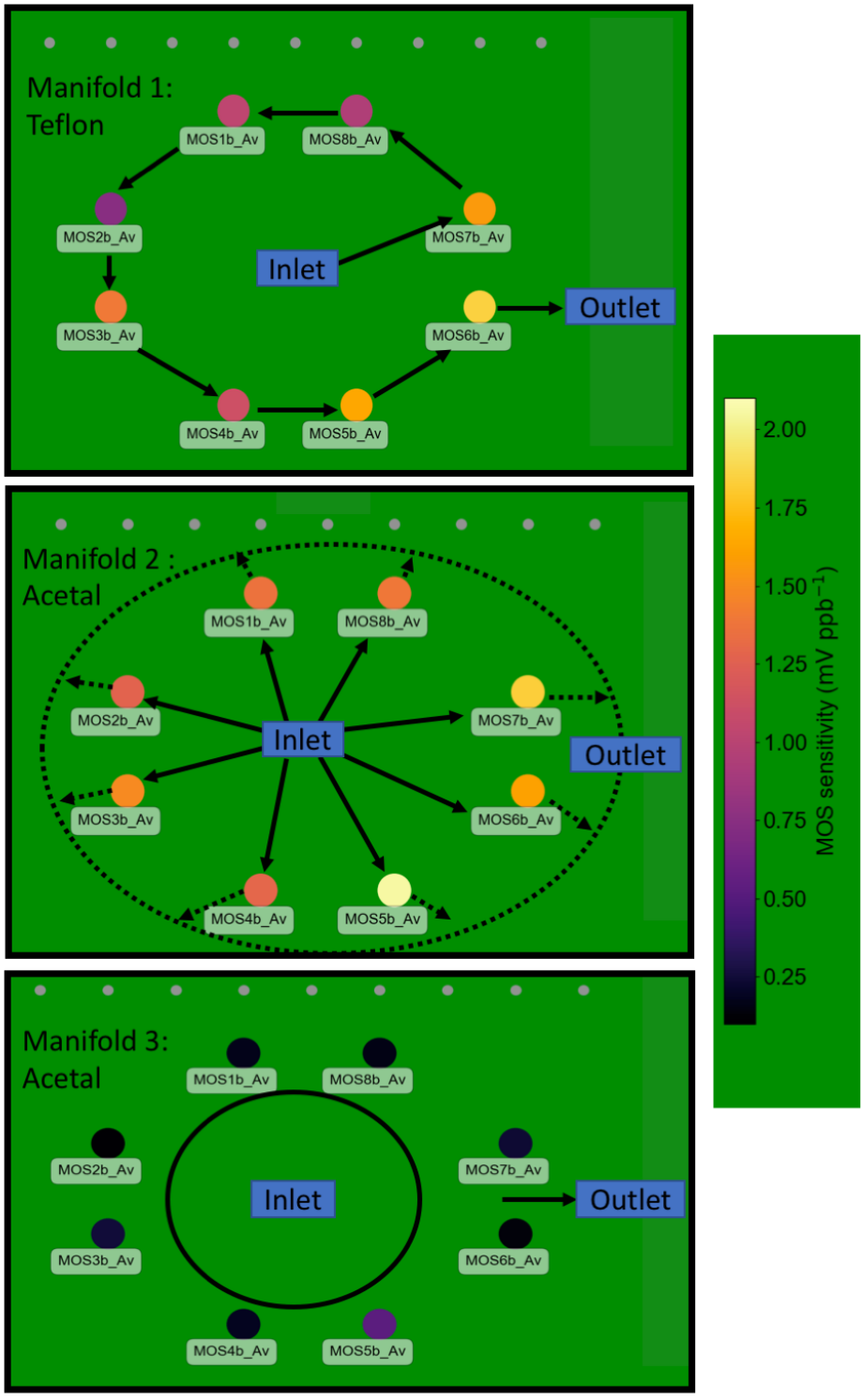

Figure 2.23: Manifolds 1, 2 and 3 and the sensor response to two OVOC calibrations were run through the set up. The slope for each sensor against OVOC concentration was colour-coded according to the colour bar. The arrows on the sensor diagrams show the flow of air around the manifolds.

2.3.7 Using a palladium catalyst to correct from cross interferences

The laboratory experiments have provided evidence that the MOS sensors are prone to responding to environmental conditions that are not the target compounds, for example the MOS signal is dependant on humidity, flow rate and other cross interferences. One method to remove the affect of interferences from the MOS signal would potentially be to have two sensor clusters set-up in parallel. One cluster would sample the air as normal, exposed to VOCs and other ambient components in air, and the other has a palladium catalyst placed in front of it, to scrub VOCs from the sample line. This second cluster would respond to the environmental conditions and the cross interferences (compounds not scrubbed by the palladium catalyst) and effectively acts as a 'control' cluster. The control MOS signal can then be subtracted away from the MOS detecting VOCs to remove the affects of the environmental conditions and minimise the affect of cross interferences. To investigate the practicalities of using a Pd catalyst the set up in Fig. 2.24 was used to test the performance of the sensors with: i) no Pd catalyst, ii) a cold catalyst and iii) the catalyst at optimum temperature. For a fair comparison, due to the differences in the MOS response during VOC calibrations, the same sensors and manifold were used and the set-up was changed, rather than placing the sensors in parallel initially.

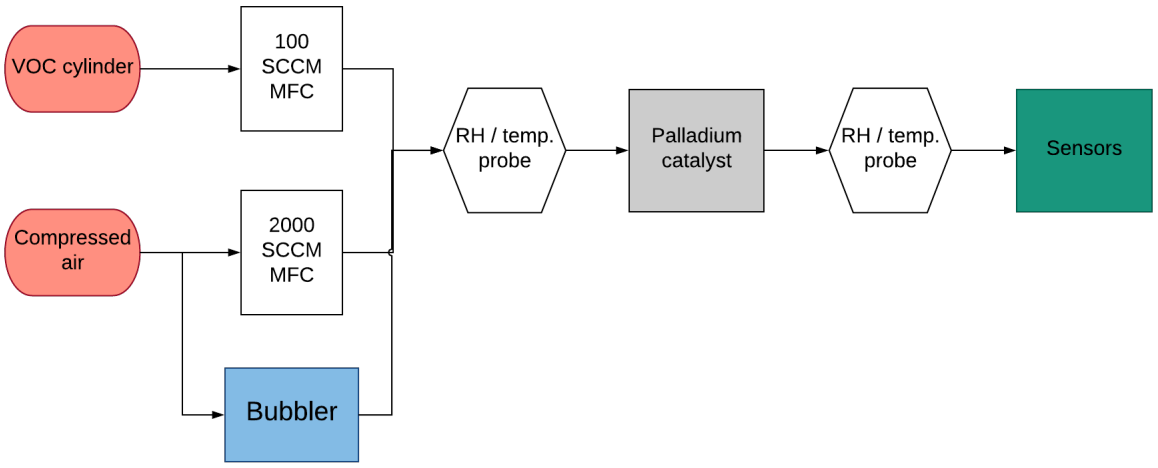

Figure 2.24: Experimental set up for monitoring the affect of scrubbing VOCs with a palladium catalyst. During the experiment with no catalyst, the palladium catalyst was removed and extra tubing added in place to ensure the air travelled the same distance before reaching the MOS sensors.

The catalyst was heated to its optimum temperature (375 °C) to scrub all of the VOCs from the air flow, and a diluted version of the VOC8 standard was used for the source of VOCs. The palladium catalyst scrubs out the VOCs by catalysing combustion and oxidising the VOC compounds to CO_2.

Figure 2.25a shows how the sensors behave at 90 % RH, in typical laboratory conditions, with no palladium catalyst in the experimental set up. The sensor output voltage

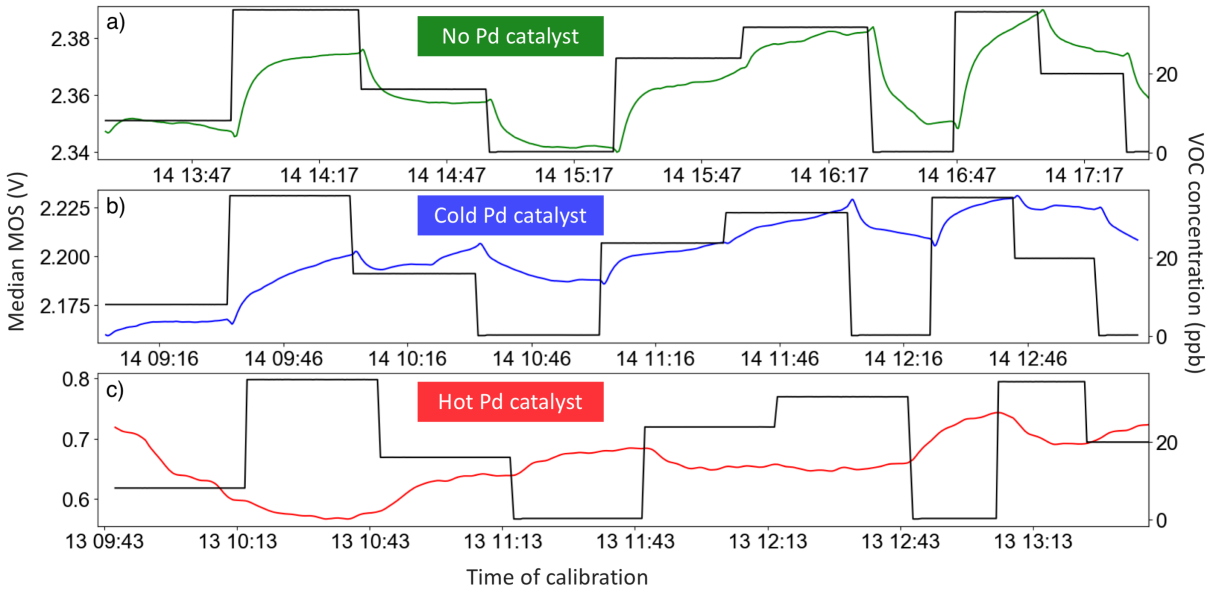

Figure 2.25: Three VOC8 calibrations were conducted at 85 % RH with 8 TGS2602 MOS sensors. a) The first experimental set-up was done with no catalyst, b) the second included the palladium catalyst cold (at r.t.p.) and c) the third plot shows how the sensors responded when the palladium catalyst was switched on and was heated to 375 °C.

was positively and highly correlated with the VOC concentration and the median sensor displayed a sensitivity of +0.7 mV ppb^{-1}, with an R^2 of 0.79 and a NRMSE of 60 % for the linear regression. The palladium catalyst was then inserted into the set up, as in Fig. 2.24b and the VOC calibration at 90 % RH was repeated. The air was flowing through the catalyst, but it was operating at room temperature. The median MOS sensitivity decreased to +0.6 mV ppb^{-1} (NRMSE of 65 %), but it still displayed a linearly positive correlation with the VOC concentration (R^2 = 0.40). The trend line for the VOC calibration was less linear as the R^2 value was not as high as it was for the set up with no palladium catalyst. In Fig. 2.25c, the palladium catalyst was switched to heat to 375 °C, the optimum temperature for scrubbing VOCs. The median MOS signal then displayed a negative and lower correlation with VOC concentration with an R^2 of -0.39. This was due to the MOS signals decreasing with increasing CO_2 concentration as the VOC compounds were combusted by the catalyst. The magnitude of the MOS sensitivity to the CO_2 produced by the palladium catalyst was lower than when the MOS was responding to VOCs (-0.18 mV pp^{-1}, NRMSE : 62 %), and this indicates a CO_2 cross interference.

As stated before, there was a possibility that a palladium catalyst could be used as a control for one MOS cluster, and then be used to correct the others, sampling ambient air, to be corrected for all other cross interferences. Since the air flow was also heated as it passed through the palladium catalyst it was hoped that this method might be useful to minimise temperature and humidity variability of the air flow as an additional advantage. However, the addition of the Pd-catalyst caused more complexity to the system because there was a the negative correlation with increasing CO_2 concentration (due to increased

VOC concentrations being combusted). When the sampling cluster of MOS was corrected by the signal from the cluster exposed to Pd-catalysed air - by subtraction of the signal - the resulting corrected VOC signal would be overestimated. When designing the sensor instrument, it was decided to not include the Pd-catalyst as the advantages it afforded do not surpass the disadvantages: extra complexity of signal correction, expense, large power consumption and weight. Therefore this technique was not used in further MOS deployments.

2.4 Characterising MOS cross interferences

The MOS sensors are useful if they can be deployed in ambient air, without the need for air purification, temperature control or humidity extraction prior to detection as these are costly and require more power and maintenance. Therefore the MOS response to changing humidity's and other common atmospheric compounds must be characterised to gain insight into how the MOS will perform outdoors. Using the experimental set up outlined in Fig.2.3 the MOS were exposed to different amounts of atmospheric gases such as CO, O_3, SO_2 and NO in the laboratory.

2.4.1 Carbon monoxide (CO)

Carbon monoxide (CO) is present in the atmosphere at relatively high levels (30 - 300 ppb in background regions [159]) and has the potential to have a significant effect upon the MOS sensors as a cross interference due CO being present at higher ambient concentrations than total VOC compounds (likely to be between 1-100 ppb) and it's ability to undergo either a reduction or oxidation reaction at an electrode [80]. Different concentrations of CO, obtained from a gas cylinder where CO was present in N_2, were introduced to two the MOS sensors, in an analogous set up to Fig. 2.3, used previously.

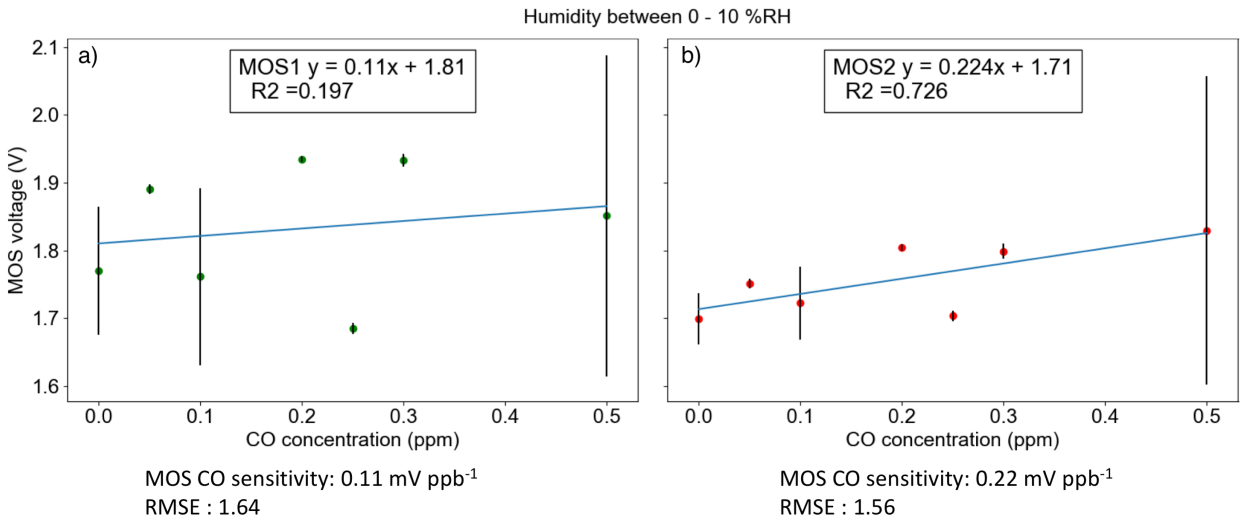

Figure 2.26: Calibration curves for a) MOS1 and b) MOS2 when exposed to changing concentrations of CO.

The CO calibrations were run at 0 - 10 % humidity, and the CO sensitivity was calculated at being +0.11 and +0.22 mV ppb^{-1} for MOS1 and MOS2 respectively. The CO concentration range was between 0 and 500 ppb to emulate real-world ambient concentrations. Both sensors exhibited a positive correlation with CO concentration therefore CO acted as a reducing compound upon the MOS active surface. MOS2 exhibited a more linear response to increasing CO concentration, with the data points for Fig. 2.26b located much closer to the trend line than in Fig. 2.26a. The two CO sensitivities calculated in the experiment were smaller than the MOS sensitivity towards total VOCs (c.a. 10 mV ppb^{-1} at the same humidity range), approximately ten percent of the sensitivities for total VOC, see Fig. 2.27.

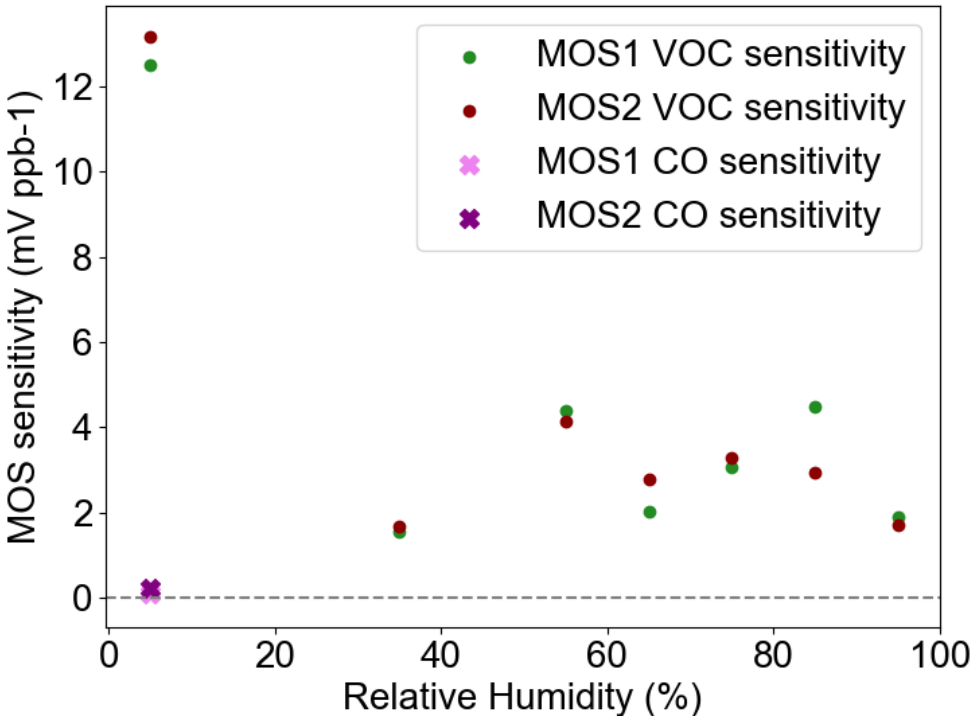

Figure 2.27: The MOS sensitivity towards CO (MOS1 : pink, MOS2: purple) was small compared to the MOS sensitivity towards a dilute mixture of VOCs (MOS1: green, and MOS2 : red) at a humidity range of 0 - 10 % RH, which typically shows the highest MOS sensitivity. A dashed line, depicting 0 mV ppb^{-1} is also shown for reference.

CO therefore did act as an interfering gas, and so it is worth monitoring CO within the sensor instrument when deploying MOS sensors out in the field as ambient CO concentrations may span a wider range than VOC concentrations, in order to correct for a CO cross interference. However it would be expected that the CO interference signal would be relatively small.

2.4.2 Nitric oxide (NO)

Nitric oxide (NO) is a primary pollutant which is emitted during combustion and a major emission source is traffic [97], therefore it is important to understand the MOS response to NO as the sensors were likely to be deployed near a roadside. As in Fig. 2.3, two MOS sensors were subjected to changing concentrations of NO, with calibrations conducted at different humidity's to characterise their response to this potential cross interference.

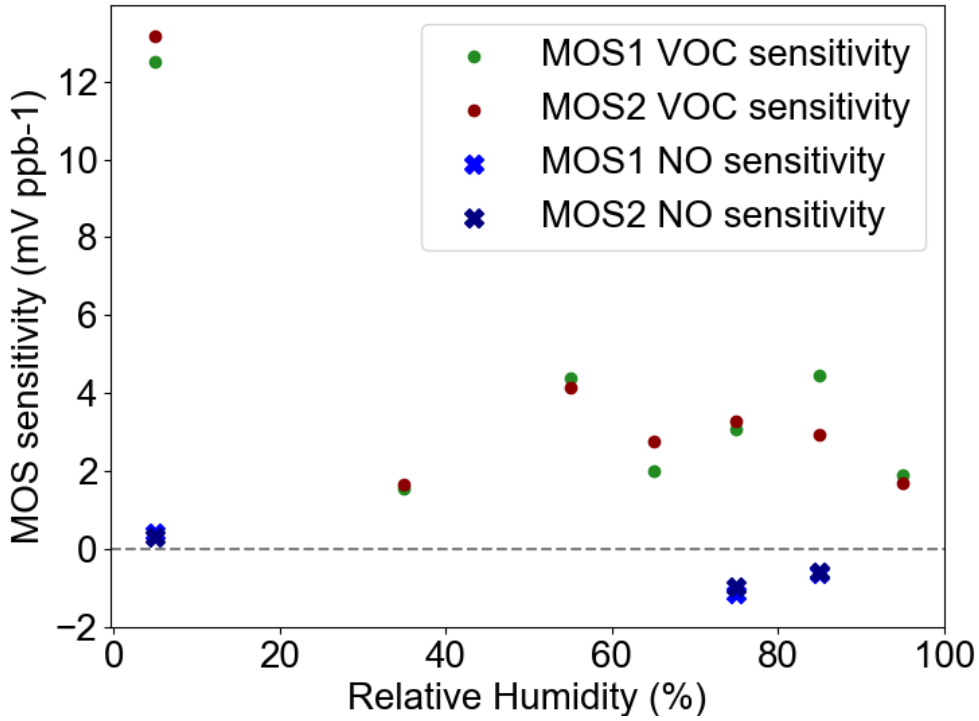

Figure 2.28: The MOS sensitivities for two sensors towards NO (MOS1 : blue, MOS2 : navy) and VOCs (MOS1: green, and MOS2 : red), for calibrations run at different humidity's. A dashed line, depicting 0 mV ppb^{-1} is also shown for reference.

There were three NO calibrations run for the two MOS, at 0 - 10 % RH, 70 - 80 % RH and 80 - 90% RH, with the concentration range of 0 - 100 ppb for NO. The NO MOS sensitivities were positive when the air was drier (0.29 and 0.42 mV ppb^{-1}), but in more humid conditions the NO MOS sensitivities were found to be negative (range:-0.54 - -1.23 mV ppb^{-1}). The TGS2602 MOS sensitivities towards NO were plotted on the same axis as the TGS2602 MOS sensitivities towards VOCs, see Fig. 2.28, to allow the cross interference response to be compared to the MOS response to the target analyte.

Potentially the MOS sensors behave differently in the drier conditions because there were less -OH ions around to coat the MOS active surface with the oxyanions. NO molecules might take up these sites on the active surface instead leading to different chemical reactions on the sensing surface. Whilst operating in more humid conditions the -OH ions greatly outnumber the NO molecules and so the method of sensing with the MOS is unchanged, leading to a change in sensitivity of the MOS. NO undergoes rapid oxidation to NO_2 in the atmosphere and therefore, for MOS deployment in the field it is recommended to monitor either NO or NO_2 as a cross interference.

2.4.3 Sulphur dioxide (SO_2)

SO_2 is present in the atmosphere from emissions such as coal combustion and shipping pollution, and sensors are likely to be exposed to SO_2 if located near ports or power plants. Ten MOS were exposed to a range of SO_2 concentrations (0 and 80 ppb) of SO_2

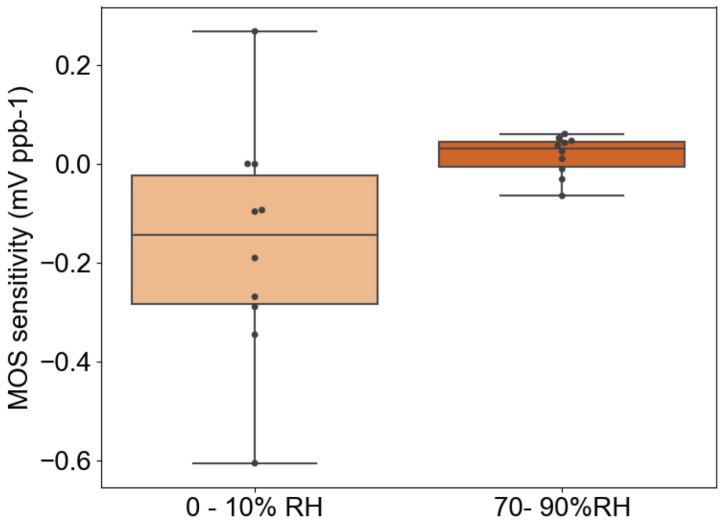

Figure 2.30: Boxplots to show the distribution of the SO_2 sensitivities from each of the ten individual MOS sensors. The boxes display the 25th and 75th quartiles, the whiskers show the 5th and 95th percentiles of the data and the line through the box is the median sensitivity (mV ppb^{-1}). The calibrations were run at two different humidity's to determine if the performance of the sensors changed in more humid air.

to determine the sensitivity of the MOS towards SO_2. The extra 8 MOS sensors were added to the experimental set up and these were all housed in a custom-built 8 sensor manifold, see Fig. 2.29. All sensors were housed in the Faraday cage to minimise electrical interference.

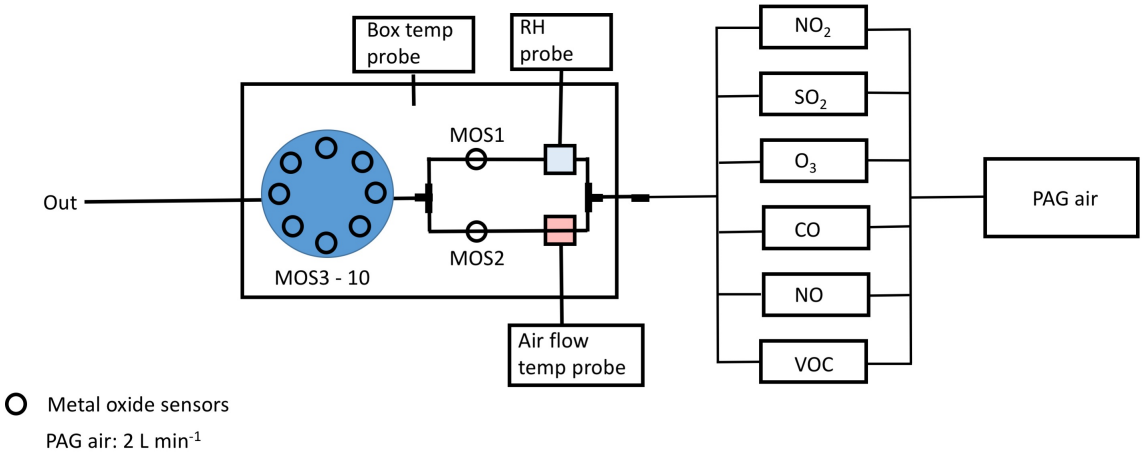

Figure 2.29: Experimental set up for ten MOS sensors being tested to investigate their response towards cross interferences. The eight MOS that were added to the set up were housed in a custom-built Teflon manifold to flow air over each sensor in series.

SO_2 was added to the set up from a cylinder of SO_2 in N_2 at two different humidity ranges (0 - 10 % and 70 - 90 % RH).

The MOS sensitivities from the calibration run at 70 - 90 % RH were clustered around 0, with the maximum and minimum calibration slopes +0.060 to - 0.065 mV ppb^{-1} respec-

tively. At these higher humidity's the sensitivities were considered low enough in typical ambient conditions for SO_2 to be considered not a cross interference for the MOS.

In typical fashion, the MOS sensitivities for the ten sensors were a lot more varied when the calibrations are run in dry air (-0.60 mV ppb^{-1} to +0.26 mV ppb^{-1} at 0 - 10 % RH) and nine out of the ten sensors displayed a negative sensitivity towards SO_2.

For deployment of the sensors to monitor outdoor air the ambient humidity is likely to be greater than 50 % RH, and unless the sensors are located near an SO_2 point source, the impact of SO_2 on the MOS sensors will be negligible over the concentration range of 0 - 80 ppb. However, monitoring SO_2 concentrations with another LCS would be useful if deploying the sensors in a location with unknown emissions or in a location where there are SO_2 emissions that might influence the signal. By monitoring SO_2 concentrations in the same location as the VOC MOS sensors, the MOS signal can be corrected for SO_2 interferences.

2.4.4 O_3

Since the formation of O_3 relies upon photochemical reactions the ambient O_3 concentration often follows a diurnal pattern, which may be observed in the MOS signal if O_3 is a significant cross interference. Since VOC emissions may also follow diurnal patterns, e.g. isoprene emissions from plants peak twice during the day [139], VOC emissions from road traffic peak at rush hour [65], it is important to establish that any periodic variability in the MOS sensors is due to VOC variability. Since the MOS sensors were likely to be deployed for weeks at a time it was beneficial to know if the MOS sensors respond to the daily fluctuations in O_3 concentration. Due to it's oxidising ability, the O_3 concentration and the MOS voltage output were predicted to have a negative correlation. Ten MOS sensors were used to determine the relationships between O_3 and MOS voltage, using the same set up as the SO_2 experiment, Fig. 2.29.

The MOS sensitivities towards ozone were positive and more variable in the 0 - 10 % RH air, with the median MOS sensitivity being 1.1 mV ppb^{-1}. For comparison, an average MOS total VOC sensitivity was c.a. 12 mV ppb^{1} for the same humidity range. This would imply a potential MOS O_3 cross interference which is approximately 10 % of the magnitude of the MOS response to VOCs. However, for more humid conditions the MOS ozone sensitivity decreases and the majority of the sensors show sensitivities that are close to zero, indicating that in conditions typical of the outdoors the MOS sensors will not, on average, respond to ozone. Whilst the box and whiskers depicted relatively reproducible sensitivities for the ten MOS sensors at the higher humidity's, there was a lot of variability in the ten MOS sensitivities for the 50 - 60 % RH range. This is concerning because, for outdoor deployments the humidity would be expected to be within this range and at yet this RH range half the MOS displayed a positive sensitivity to O_3 and half would produce a negative response. This would make calibration of individual MOS sensors challenging and

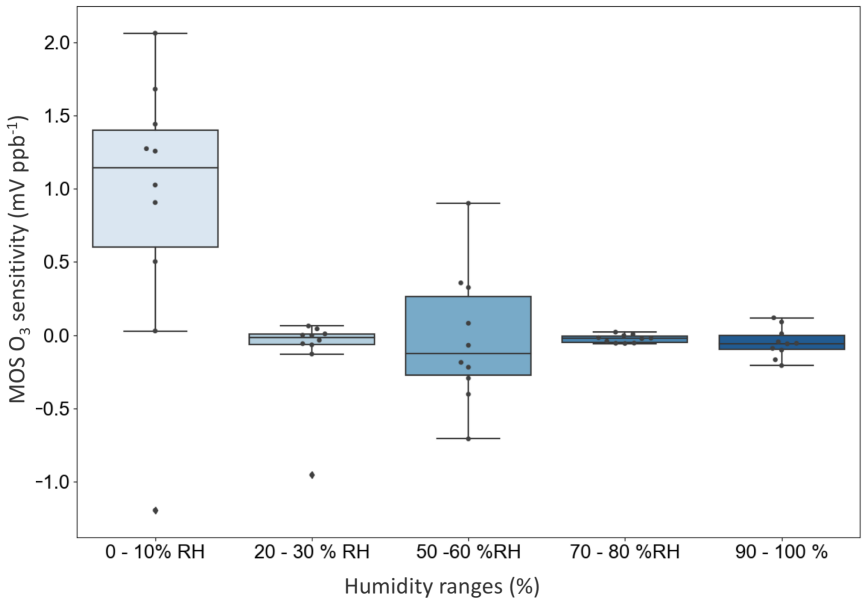

Figure 2.31: Box plots to show the variation in the MOS sensitivities towards changing ozone concentrations as the humidity of the air the sensors are exposed to increases. The box edges are the 75^{th} and 25^{th} quartiles, the line in the middle of the box is the median slope and the whiskers are representative of the 5^{th} and 95^{th} percentile slopes for the calibrations conducted at five different humidity's.

each would require an individual calibration model to correct for an O_3 cross interference. MOS response to in The MOS responses are unique towards cross sensitivities and this result highlights the sensor variability towards interfering compounds and hence the need for a technique to improve sensor performance.

2.5 Different MOS sensors

A selection of other types of MOS sensors were used to investigate their ability to detect VOC compounds in the olefactometer port of the GC-MS to investigate if they have similar detection sensitivities as the TGS2602 MOS. All MOS sensors were manufactured by Figaro.

2.5.1 TGS2611: Methane sensors

The TGS2611 is designed to detect methane, and this was an investigation to identify if the sensor was likely to respond to other VOCs as cross interferences. VOC8 was used as the testing gas standard, with a sample volume of 5 and 10 mL.

There were no discernible peaks observed in the MOS signal during the three 5 mL sample volume injections, Fig. 2.32. The sample volume was increased to 10 mL for two injections and yet there were still no peaks in the MOS signal that were identifiable as a response to the VOCs, since there was no consistent patterns in the TGS2611 MOS trace

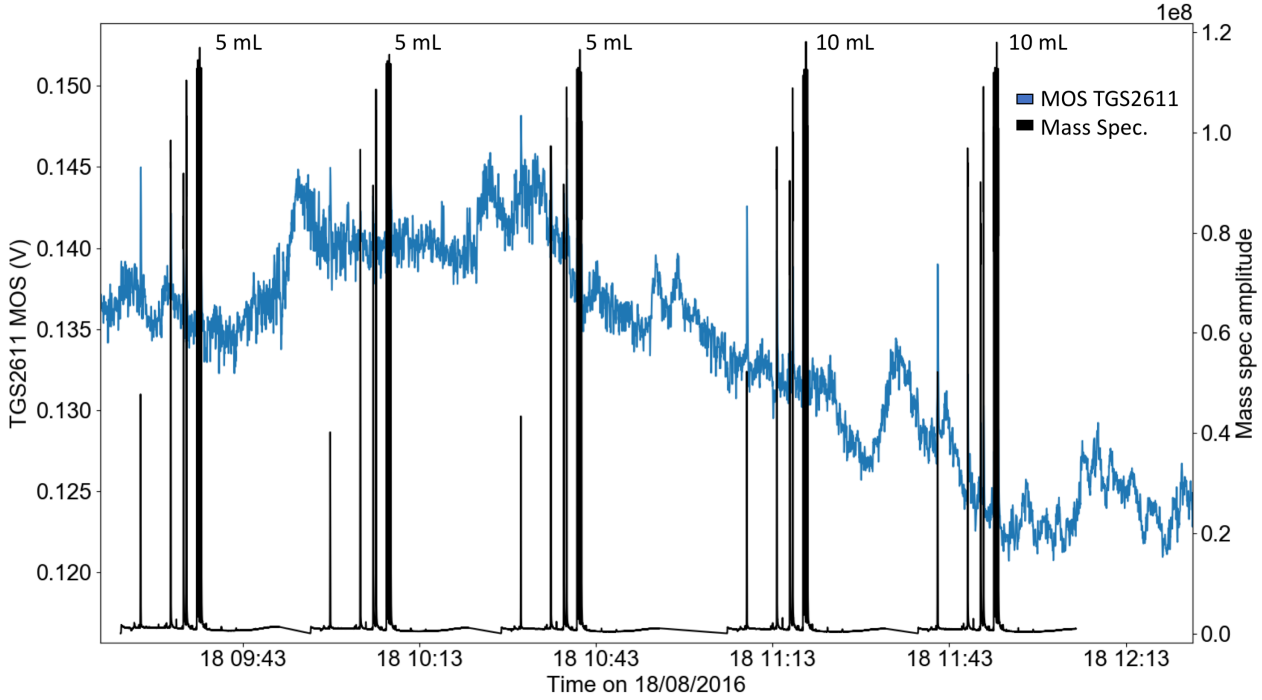

Figure 2.32: The TGS2611 methane MOS signal (blue) during five injections of VOC8 into the GC-MS. The corresponding GC-MS spectra are shown in black.

after each injection of VOC gas standard to suggest the methane MOS responded to the eluting compounds. To conclude, the TGS2611 displayed no sign of detecting the 8 VOC compounds during this experiment, Fig. 2.32. Since the methane sensors are designed to detect methane, it is advantageous that they do not display a response to these VOCs as they would be a cross interference on the methane signal. The TGS2611 baseline was rather noisy, displaying random fluctuations that were not associated with VOC peaks or due to methane, which is disadvantageous. The TGS2611 methane MOS had a noiser signal than the TGS2602 total VOC MOS sensors.

2.5.2 TGS2620: Alcohol sensors

The TGS2620 MOS sensors are said to be sensitive towards oxygenated VOCs and alcohols such as ethanol, in particular. The TGS2620 MOS sensor was placed in the olefactometer port and 10 mL of the VOC8 standard were injected five times into the GC-MS system. It was interesting to investigate the response of the OVOC MOS when alkane and aromatic VOCs were sampled, rather than oxygenated compounds. The TGS2620 MOS detected all 8 compounds present in the cylinder and the identification of the peaks is shown in Fig. 2.33.

The peaks were well resolved from the baseline and were assigned by aligning the MOS trace with the mass spectra and identifying the peaks in the mass spectra using the elution order determined by the NIST library. All peaks were integrated for the five mass

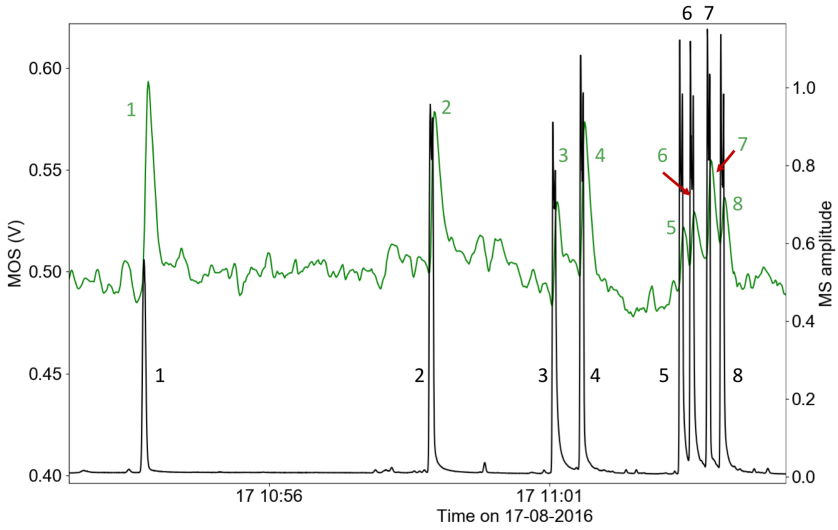

Peak	Compound	Conc. In cylinder (ppm)
1	n-Pentane	5
2	n-Heptane	5
3	Toluene	5
4	n-Octane	5
5	Ethyl benzene	5
6	m- Xylene	5
7	Nonane	5
8	o- Xylene	5

Figure 2.33: An example of a 10 mL VOC8 injection into the GC-MS with TGS2620 MOS in the olefactometer port. All 8 compounds were identified using the NIST library and the mass spectrum. The MOS peaks were assigned accordingly.

spectra and MOS files. The mean peak area and standard deviation for each compound was computed. The compounds in VOC8 have enough time between eluting to allow for good identification of peaks in the MOS signal. Indeed, it was clear there are at least four stand alone peaks in the MOS trace. This is advantageous as it was easier to determine the MOS peak area accurately.

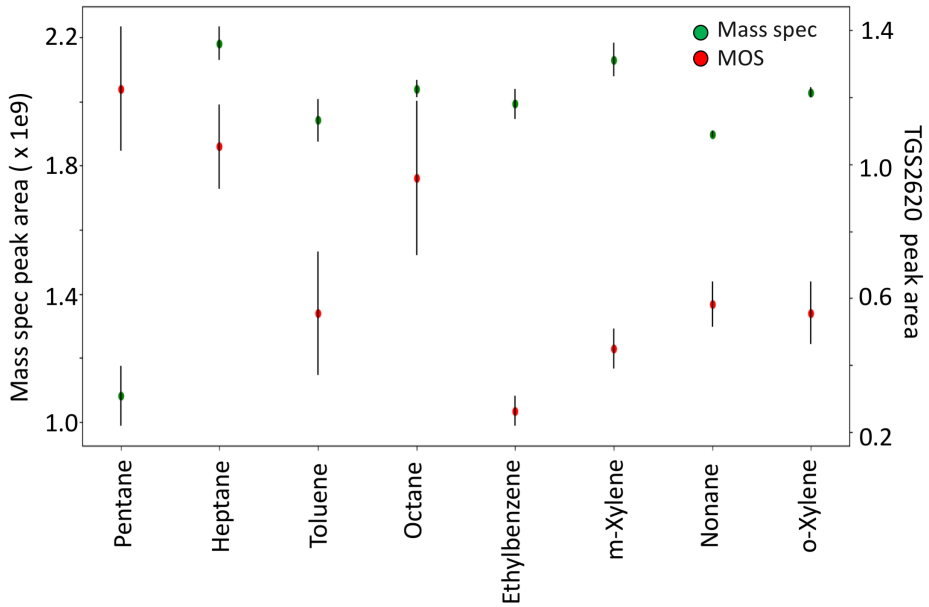

Figure 2.34: Comparing the peak areas for the GC-MS and the TGS2620 OVOC MOS sensor when the VOC8 gas standard was injected into the GC five times, with 10 mL sample volume.

Figure 2.34 plots the mean peak area for each compound with the standard deviation shown as a black line for the TGS2620 OVOC MOS sensor. Alkane compounds; n-pentane,

n-heptane, n-octane and n-nonane, displayed the largest peak areas for the TGS2620 sensor. As the number of carbons in the alkane increased, the peak area of the OVOC sensor decreased, see Fig. 2.14. The aromatic compounds: toluene, ethylbenzene and the two xylenes, produced smaller peak areas, with the largest aromatic response being towards toluene. This is different to the TGS2602 total VOC MOS in Fig. 2.12, which detected larger peak areas for aromatic compounds compared to alkanes. The differences between the sensing surfaces of the two types of MOS sensors do cause a different response to the same compounds. Therefore, using the two types in combination might prove useful

Relative response of VOC and OVOC sensor towards different groups of VOC compounds

Compound	VOC sensor response (unit area of peak produced upon exposure to 1 ppb of VOC)	OVOC sensor (unit area of peak produced upon exposure to 1 ppb of VOC)
Alkanes	1	10
Alkenes	10	10
Alcohols	1	20
Aromatics	10	1

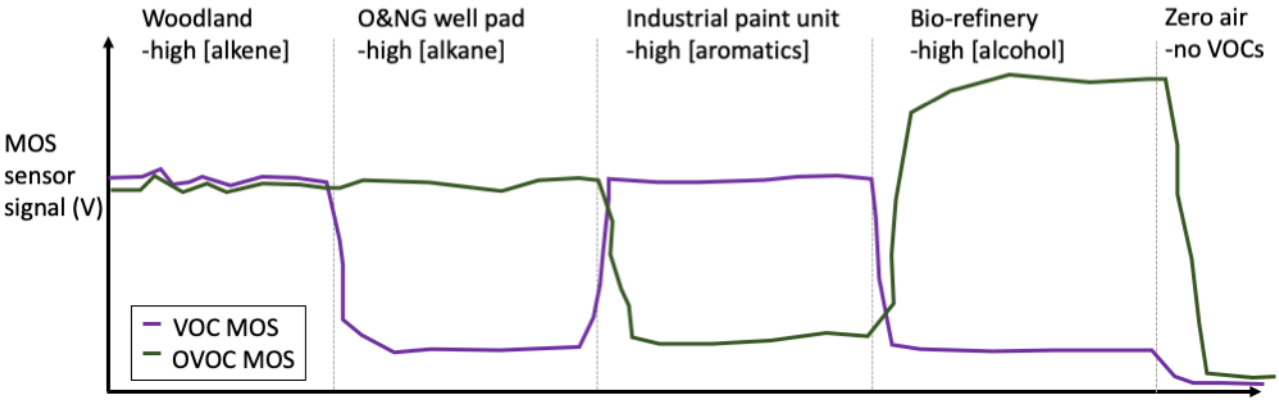

Figure 2.35: Using the GC-QTOF MS experiments described in Chapter 2, the relative responses of the VOC and OVOC sensors have been summarised with a simplified plot to show how different locations (with different VOC compositions) would affect the VOC and OVOC sensors differently. By comparing the responses of both sensors, it would be possible to obtain an estimate of the VOC composition.

as different information can be extracted about the ambient VOC composition, see Fig. 2.35 for a simplified example as to how this could be achieved.

2.5.3 P-type MOS sensors

P-type MOS sensors use a different technology to detect VOCs in the atmosphere. An internal heater which heated to 450 °C was added to the sensor to increase the desorption of compounds off the active surface and essentially clean it for the next round of compounds, as well as using a sensing surface with different physical properties. This technology might be able to increase the response times of the MOS sensors and reduce the effects of changing environmental conditions. The OVOC gas standard was used to conduct p-type VOC MOS calibrations, under laboratory conditions at 3 % RH. A cluster of p-type and n-type MOS sampled in parallel.

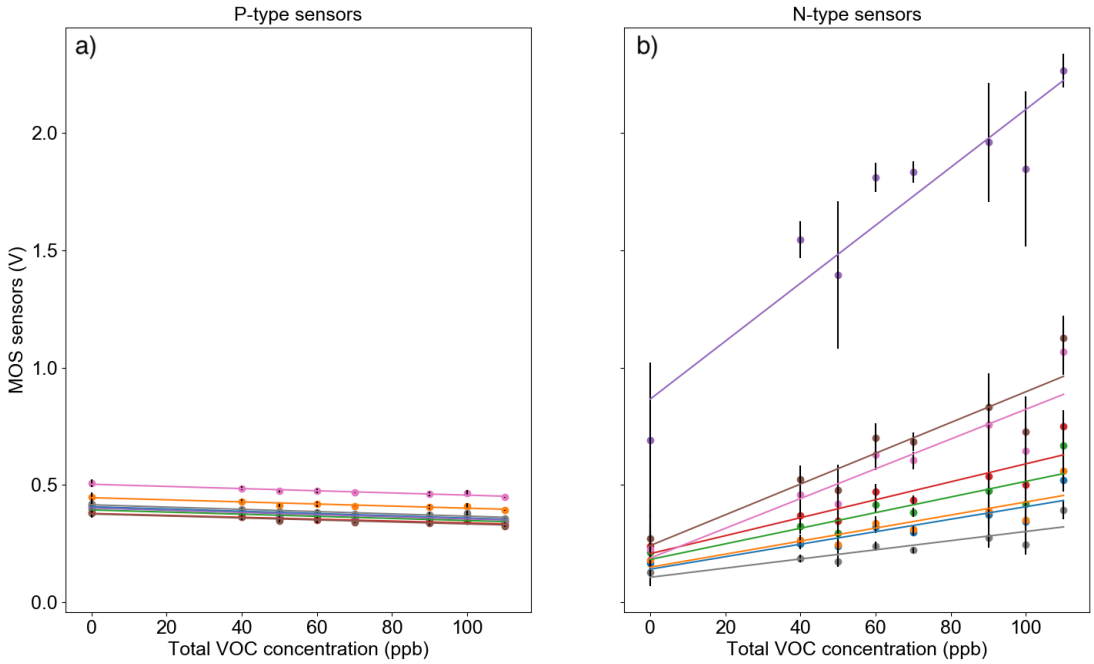

Figure 2.36: The slopes of the a) p-type and b) n-type MOS sensors when an OVOC calibration was run, at 3 % RH humidity in the laboratory. Both plots share a y-axis for ease of comparison. Each MOS sensor position within the manifold was given a different colour to identify individual n-type or p-type sensors.

There were found to be three major differences between the n- and p-type behaviour. Both the n-type and p-type MOS displayed a linear correlation with increasing VOC concentration, however, the n-type sensors showed an increase in MOS output voltage as the VOC concentration increased but the p-type sensors displayed the opposite behaviour, with a decrease in MOS voltage.

The n-type sensors (Fig. 2.36a) all displayed greater magnitudes of slopes than the p-type sensors (Fig. 2.36b) implying that the n-type sensors were more sensitive to changing VOC concentrations. The mean n-type slope was +4.98 mV ppb^{-1}, whereas the mean p-type slope was calculated to be −0.45 mV ppb^{-1}, a magnitude lower than the n-type sensor. There might be a few possible reasons for the lower sensitivity of the p-type sensors. The internal heater inside the sensors was heated to a consistent 450 °C, rather than working

in the temperature cycling mode which regularly fluctuates the heater temperature. The calibrations were also only run at 3 % RH, and it is known that the MOS sensors display higher, and more variable sensitivities towards VOCs at low humidity's. The advantage of the p-type sensor was supposed to have been a reduction in the cross interference effect of compounds including water. Potentially, the slope calculated in the calibration at 3 % RH would remain the same across the entire range of humidity's, while the n-type sensor sensitivity decreases to approximately 1 mV ppb^{-1}. However, the average VOC sensitivity of the total MOS sensors at higher humidity's were previously found to be 1 mV ppb^{-1}, and this was still twice as sensitive as the p-type sensors in dry air. The mean value for the p-type sensor slope was lower than was expected. The sensor slopes for the n-type MOS sensors displayed more variability than the p-type sensors. The range of the n-type sensors was 10.41 mV ppb^{-1}, whereas the spread between the maximum and minimum p-type slopes was only 0.082 mV ppb^{-1}. One of the n-type MOS sensors (purple n-type in Fig. 2.36) recorded a slope that was much higher than the other 7 sensors (12.4 mV ppb^{-1}), suggesting this might be an anomalously high sensitivity for the n-type sensors. It is advantageous to have low inter-sensor variability as evidence that all sensors are responding to the same environmental changes in a similar manner, and this gives more reproducible sensor responses.

The manufacturer of the p-type sensors (Alphasense) recommended to turn on temperature pulsing, where the routinely temperature fluctuated between 400 ° and 525 ° to 'reset' the sensor surface by encouraging desorption of the compounds that have already been detected. The optimum temperatures for the temperature pulsing were supplied by the manufacturers and it was assumed that these were sufficient for the total desorption of the adsorbed compounds. A high temperature of greater than 400 ° is sufficient to remove adsorbed surface OH- anions that form after exposure of the sensing surface to humid air [187] so this temperature pulsing may potentially minimise humidity effects upon MOS sensors. The impacts of accelerated ageing of the sensor surface due to high temperatures was not investigated in this study although frequently heating the MOS sensing surface to high temperatures is likely to cause faster aging of the MOS sensor surface. Aging leads to a degradation in the MOS sensor response and the sensitivity of the MOS towards VOCs would irreversibly decrease. Therfore, using high temperature pulsing may require more frequent replacement of the sensors in the field. An OVOC calibration was run with temperature pulsing switched on, see Fig. 2.37, whereupon the temperature was held at 525°C for 2 minutes, in between 4 minute intervals of the internal heater being at 400°C.

The p-type sensitivity of the p-type MOS decreased when the temperature pulsing was switched on. Without temperature pulsing the average sensitivity of each sensor was -0.45 mV ppb^{-1}, with temperature pulsing the average sensitivity of the sensors was: -2.3 x 10^{-5} mV ppb^{-1}. Out of the eight p-type sensors tested, two of them (sensors 2 and 4)

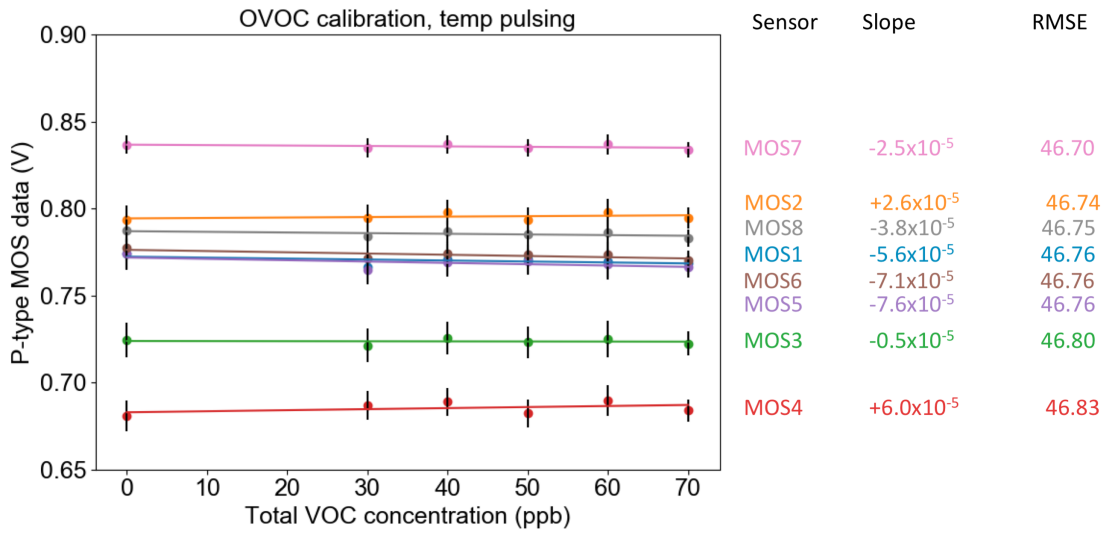

Figure 2.37: P-type sensors responding to changing VOC concentrations with the temperature pulsing mode operational. The table shows the individual p-type sensors sensitivity and RMSE for the OVOC calibrations.

displayed displayed a positive correlation with increasing OVOC concentrations, whereas the other 6 had negative sensitivities. There was a high degree of linearity for all eight sensors in the calibrations, and all displayed similar values for RMSE (46.70 - 46.83) over the 0 - 70 ppb VOC concentration range. The data sheet for temperature pulsing claims that it helps with baseline stability and faster response times too, both of which were not investigated here. A few files were ran overnight, with just zero air from the PAG and no other compounds or humidity going through the lines. It was noticeable by eye that these zero air files consisted of more noise in the p-type MOS sensor signals compared to the n-type sensors. A quick signal-to-noise (StN) calculation, where the mean was divided by the standard deviation revealed that, on average the p-type sensors have an StN ratio (162.20) that is thirteen times higher than the n-type MOS (average StN: 12.17). The p-type sensors were not used in any further work due to their low sensitivity towards VOCs and high noise signals.

2.5.4 Photo-ionisation Detectors (PID)

PIDs (manufacturer: Alphasense, model: PID-AH) were investigated as a low cost method for measuring VOCs. They afford a certain degree of selectivity as only molecules that absorb photons of a certain wavelength can be ionised and hence detected. The are more costly; each unit costs about £200, and they are commercially available. However, their performance at low concentrations of isoprene showed that the devices cannot observe isoprene at typical ambient concentrations or meteorological conditions.

The five PIDs in Fig. 2.38 all produced noisy signals with the isoprene calibrations and were unable to distinguish between the differing concentrations of isoprene when the mixing ratios were changed. The PIDs were calibrated multiple times and the result was

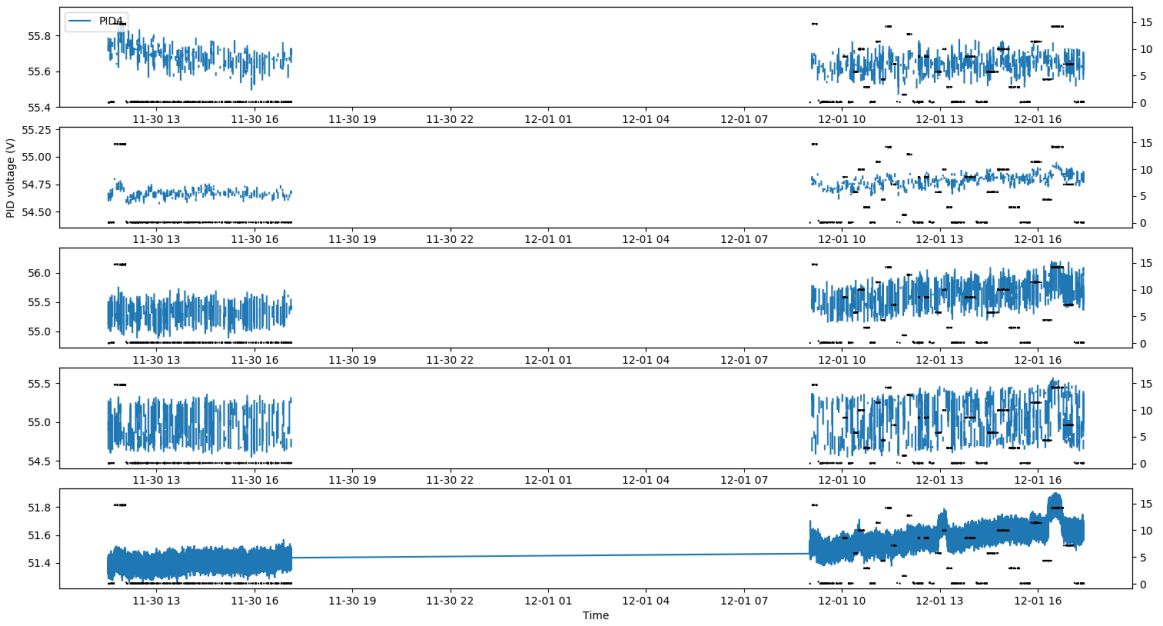

Figure 2.38: The five subplots show five different PIDs responding to typical amounts of isoprene (concentrations shown in black) in a laboratory experiment.

always similar to Fig. 2.38. Due to the PID response towards isoprene being indistinguishable from the noise of the PID these devices were not used in future sensor development work or for deployments.

2.6 Summary

The laboratory experiments with the TGS2602 total VOC MOS sensors show a variety of results.

- Laboratory calibrations using the total VOC MOS sensors indicated that the total VOC MOS sensors had a linear, positive correlation with increasing VOC concentrations up to 150 ppb. This means that for typical ambient levels of VOCs the MOS response will be largely linear.

- Sensor sensitivity is governed by the sites available on the active surface and how well the molecule adsorbs. Therefore, other meteorological conditions can affect the adsorption process and hence these relationships must be characterised in order to correctly calibrate the MOS.

- Humidity, temperature and rate of air flow to the surface all affected the MOS signals. MOS response towards environmental conditions must be characterised for the full range of expected conditions before deployment. If different MOS are to be used, these need to be individually characterised as they have shown to have very different responses.

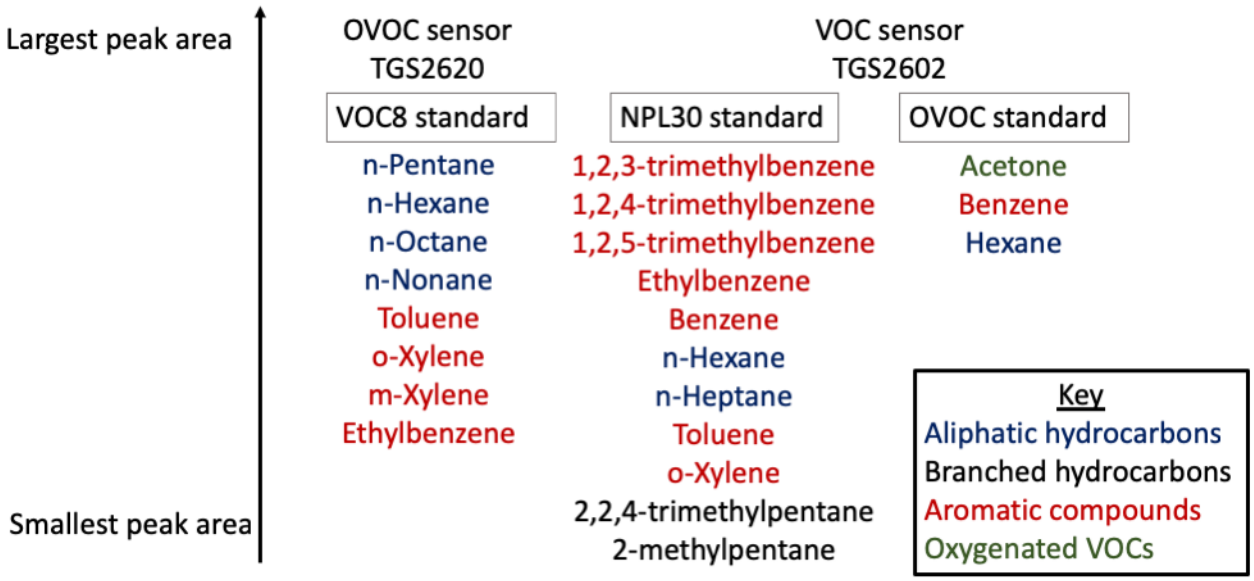

Figure 2.39: A comparison of the peak area response for the TGS2602 and TGS2620 MOS sensors. Only compounds that eluted as single peaks are shown, and the compounds are colour-coded to identify VOC groups.

- The total VOC sensors all responded in a similar manner (e.g. all sensors display similar trends) towards VOCs, environmental conditions and cross interferences however there are differences in each individual sensors sensitivity to these variables.
- During VOC calibrations using gas standards with a mixture of VOC compounds, the total VOC MOS exhibited a different magnitude of response towards each different compound. The experiments indicated that the larger and more aromatic compounds tend to show the largest response.
- The MOS sensors did not display any strong correlations with the compounds detected by the SIFT-MS when ambient air was sampled by the co-located instruments. The conclusion of the SIFT-MS experiment was that MOS are not currently suitable to use in the field under real-world conditions.
- In general, the effect of cross interferences was smaller than the expected effect from changing environmental conditions, especially for outdoor deployment where the humidity is greater than 10 % RH. The response of the total VOC sensors towards NO, O_3 and SO_2 were negligible when the air flow had a humidity of 20 % RH or more, and their concentrations were at typical ambient levels. CO was the only compound tested that had a cross interferences effect at in these conditions.
- Since different MOS types, TGS2602 Total VOC and TGS2620 OVOC sensors, displayed different responses towards the same VOC compounds they could be co-located to obtain further information about VOC composition, Fig. 2.39.

It was found that the TGS2602 total VOC sensors displayed the highest responses towards aromatic compounds, whereas the TGS2620 MOS sensors had higher peak areas for alkanes. By comparing their relative responses towards the same air mass, it would be possible to estimate which type of VOCs were currently dominating the bulk VOC signal.

- MOS sensor behaviour is complex and there are potentially other non-linear relationships that must be understood in order to robustly calibrate sensors in-field. One method to eliminate the possibility of changing sensitivities in the field would be to control the RH and temperature of the air flow to the sensors. However, these techniques are costly and require more maintenance so negate the advantages of low-cost, low-power sensors. The cost of using RH/temp etc. controls for deployment of sensors as a network or as a sensor device would need to be evaluated against the cost and time expense of correcting for these environmental conditions post-analysis. Either way, it is important to use sensors to monitor the environmental conditions of the sample air flow to the sensors, to identify if there are large changes to the air flow and to allow corrections to be made.

- A palladium catalyst was used to provide a zero-VOC response from the MOS sensors, as a potential method of correcting for all cross interferences at once. However, there was a complex response from the MOS sensors towards CO_2, a product of the VOC scrubbing from the air flow. This affect, and the expense of installing and operating a palladium catalyst (maintaining a constant high temperature) in the field meant that it was unsuitable for use with the deploying MOS sensors, especially if the sensors were required to be deployed as a network.

- The p-type MOS and PIDs did not perform well in the laboratory experiments and so it was decided to not continue to use them for future sensor investigations.

Chapter 3

Using a clustering approach to optimise atmospheric sensor performance

This chapter aims to characterise the performance of EC and MOS sensors for the detection and monitoring of gaseous pollutants in ambient air. Laboratory experiments, to characterise the noise and reproducibility of electrochemical (EC) and MOS sensor signals were conducted to optimise the solutions to some of the challenges involved when deciding how best to operate low-cost sensors. The multiple drawbacks associated with low cost sensor performance and reproducibility is the reason that they are not more widely used. Low-cost sensors are not suitable to deploy in the field straight 'out-of-the-box'. Like regular scientific instruments, they must be regularly calibrated to ensure they are producing consistent results that can be interpreted to produce a measure of the pollution concentration. The previous laboratory experiments showed that for the same type of sensor, e.g. the TGS2602 total VOC MOS, individual sensors display unique sensitivities to the target compound, as well as cross interferences to other compounds and signal interference with changing environmental conditions [104]. The differences in the, supposedly identical, sensors lead to a group of sensors displaying a high degree of inter-sensor variability in both the sensor signals and variability in the sensitivities of the devices, Fig. 3.1. It is considerably more challenging to deploy low-cost sensors outside of the laboratory, and collect data that can be used for quantifying the absolute concentrations of pollutants. Calibrating the EC and MOS under laboratory conditions for deployment outdoors, for example, would not be appropriate as the conditions they experience under calibration conditions would be vastly different to that of the ambient air [105]. Laboratory calibrations - e.g. using synthetic gas standards with controlled humidity and temperature - can give scientists a general idea of how the sensors will respond to various factors, but these are not representative of outdoor conditions and so cannot be used to quantify outdoor pollutants. Thus, in-field calibrations, where low-cost sensors are co-located with respec-

tive research grade instruments is mandatory if the sensors are to provide any information that can be used comparatively between sensors. The in-field calibration must occur in a similar environment to which the sensors will be deployed in. Calibrating sensors next to an AQM located in the middle of London, will only be representative for a central London deployment of sensors and would not be appropriate for deployment of these sensors on a rural village green where the sensors would be likely to experience a different composition of pollutants. The required frequency of LCS calibrations is yet to be determined, as the sensors are likely to experience temporal drift over short (hour) to long (week+) timescales [165]. Often, LCS have fast response times and are capable of detecting short term pollution events. However, the previous laboratory experiments in Chapter 2 showed that these responses can be slightly different for each sensor, and this, in combination with unique sensor sensitivities, means that each sensor might require its own unique calibration model for deployment alone. Since the sensors are known to be sensitive to a range of other measurable environmental factors (cross interferences, humidity and wind speed) it is recommended to measure all these variables to allow for post-processing corrections.

3.0.1 Variability in individual sensors response to isoprene

It is known from previous experiments that the MOS sensitivity towards VOCs changes significantly and non linearly as different environmental conditions change, see Fig. 3.1 adapted from our published work in [165]. An example of this, where the MOS was calibrated with single VOC compound (isoprene) at different humidity's is shown. This is a more simple example of the changing sensitivity of the MOS towards VOCs that was observed in the laboratory experiments in Chapter 2. Figure 3.1 shows the slopes from the isoprene calibrations of eight MOS sensors as box and whisker plots. There is a box and whisker plot at each humidity to observe the typical, non-linear trend of MOS sensitivity variability towards VOCs with relative humidity.

The highest isoprene sensitivities (approximately 5 mV ppb^{-1}) were found when the MOS were detecting isoprene in dry air (0 - 10 % RH), however there was a lot of variation in the MOS isoprene sensitivities for the eight sensors (range of slopes: 1.7 mV ppb^{-1}) in the cluster (Fig. 3.1). In more humid air (40 - 60 % RH) the MOS isoprene sensitivity decreases to approximately 1 mV ppb^{-1} but the range of sensitivities is much smaller (at 40 - 60 % RH the range was 0.7 mV ppb^{-1}), as seen by the narrower box and whisker plots in Fig. 3.1 showing that the sensors exhibit more similar behaviour with some humidity present. Interestingly, the isoprene sensitivity increases again to 2 mV ppb^{-1} at 90 % RH, and the range of the sensor sensitivities remains small (0.4 mV ppb^{-1}). In relative terms however, the variability appears better under dry air conditions. For 0 - 10 % RH the MOS VOC sensitivity was calculated to be 5 mV ppb^{-1} $\pm$ 17 %. At higher humidity's, 40 - 60 % RH the relative variability in the MOS sensitivity was 1 mV ppb^{-1} $\pm$ 35 % for 8 total VOC MOS sensors. However, this appears to be due to one MOS sensor out of

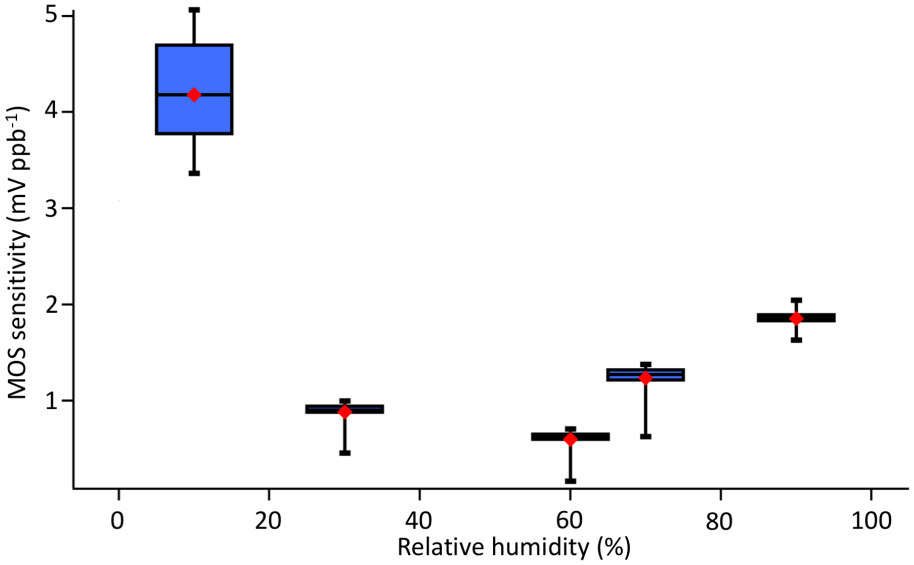

Figure 3.1: The TGS2602 total VOC MOS display different sensitivities towards changing concentrations of isoprene at different humidity's. In dry air (0 - 10 % RH) the MOS sensitivity is high, but is very variable which would make it difficult to quantify the isoprene concentration. Figure taken from Smith et al. 2017. [165]

the cluster exhibiting an unusually low VOC sensitivity compared to the others as the 5th to 95 th box is much narrower than the whiskers. Repetition of the calibrations with the same MOS sensors several days later, using the same humidity ranges, revealed that individual sensor sensitivities can vary by a factor of two. It is therefore very difficult to correct for conditions such as humidity for any individual sensor over week+ timescales. This was potentially due to chronic exposure to high humidity levels resulting in a layer of hydroxyl anions covering the MOS sensing surface over time, and blocking the adsorption of oxygen to form oxyanions. To ensure complete removal of the OH- ions the sensing surface requires heating to greater than 400 °C [187], which the internal MOS heaters cannot achieve. The sensing surface would be susceptible to these environmental conditions in the field. For MOS sensors to be successfully deployed outdoors their responses to changing environmental conditions and mixing ratios of measurand and interferences must be fully characterised. However, because each individual sensor exhibits a unique magnitude of response to each variables, individual calibration models are required for the sensors to be deployed singularly. There would need to be frequent re-calibrations for the sensors to ensure the sensors produced reproducible data that could be used for making assumptions about the spatial distribution of pollution. This Chapter aims to investigate the reproducibility of sensor data, the frequency of required calibrations and how best to improve the robustness of sensor measurements to minimise this.

3.1 Characterising MOS response in zero air

The laboratory calibrations and Fig. 3.1 have shown that the MOS often display non-linear relationships with humidity and temperature and these more complex relationships are therefore harder to characterise and account for during calibration and data analysis. The MOS and EC sensors were exposed to zero air to extract out signals that were due to the changing environmental conditions of the MOS sensors and the fraction of the MOS signal that is due to noise. The MOS noise in zero air was characterised and a variety of MOS sensors were deployed in an indoor environment to investigate the temporal drift of MOS sensors.

3.1.1 TGS2602 Total VOC MOS in zero air

To investigate the degree of inter-sensor variability, eight TGS2602 total VOC MOS, eight TGS2620 OVOC, eight TGS2610 propane/butane MOS and eight TGS2611 methane MOS sensors sampled zero air from the PAG, at a constant humidity of 0 % RH and temperature of 25 °C in the laboratory over the weekend. One total VOC MOS failed immediately and hence has been removed from the subsequent analysis. Each of the individual MOS sensors had their signals normalised to 0 V at the beginning of the experiment, with the initial offset value applied to the entire data set. The sensors continuously sampled zero air for two and a half days. In previous laboratory experiments the TGS2602 MOS sensors have expressed a sensitivity towards the total VOC concentration of approximately 12.5 mV ppb^{-1} in these temperature and humidity conditions. Hence, this sensitivity has been used to convert the TGS2602 MOS output voltages to an equivalent mixing ratio of total VOC ($ppb_{[VOC]}$) for Fig. 3.2, to better understand the affect these changes in MOS signal have on the data.

Figure 3.2a shows that during the zero air experiment, each MOS sensor displayed a substantial amount of variability as each sensor experienced a range approximately equivalent to 13 $ppb_{[VOC]}$. Towards the end of the zero air experiment (from 2000H on 15^{th} April 2018), all the MOS sensors displayed much more variability in their signals, which appeared to have a periodic frequency of approximately 30 minutes. This would be indicative of some environmental condition, for example the activation of an air conditioning unit, changing on a similar timescale which influenced the MOS sensors response. Each MOS sensor produced very similar looking time series indicating that the variability in the zero air must be due to the sensors responding to common factors and is not just random. This is likely to be small changes in the environmental conditions, such as temperature and humidity as the concentration of total VOC in the zero air is known to be zero ppb. The zero air generated by the PAG is routinely checked to ensure the scrubbers and filters employed to minimise the concentrations of compounds other than O_2 and N_2. Since all the Total VOC MOS sensors were responding to the zero air in a similar manner is is a non-

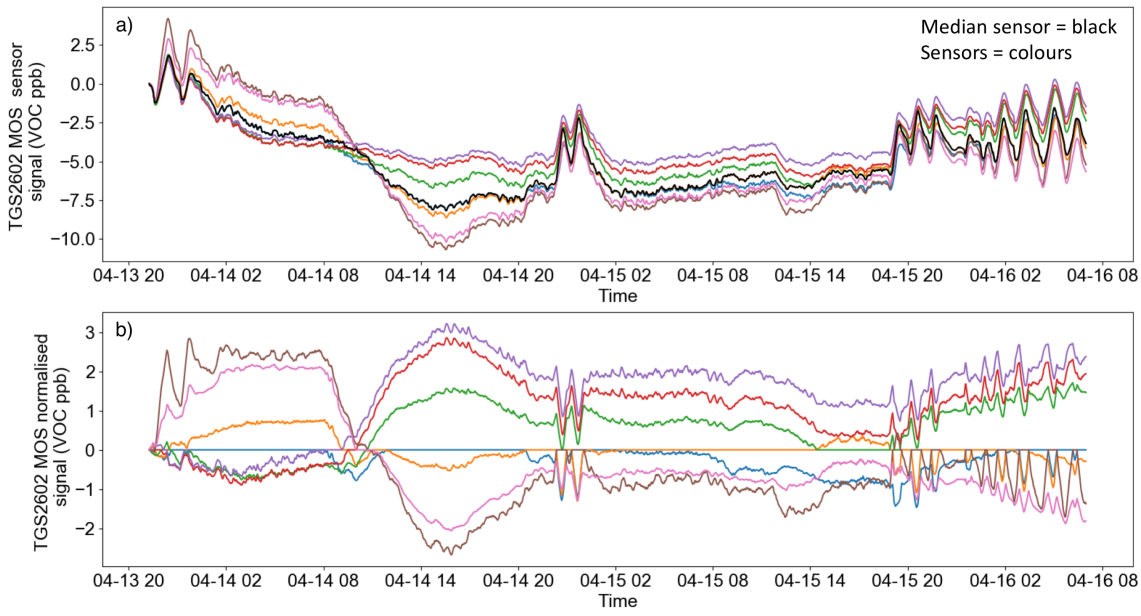

Figure 3.2: The seven total VOC MOS sensors sampled zero air over the weekend, with a constant humidity of 0 % RH and temperature of 25 °C. A typical MOS sensitivity of 12.5 mV ppb^{-1} has been applied to convert the signals from voltages to equivalent $ppb_{[VOC]}$. a) The individual sensor signals are shown as coloured traces, and the median of the seven working sensors in the black trace. b) Each sensor with the median TGS2602 sensor subtracted to leave the residual noise of the seven normalised sensor signals.

random component of the sensor zero air response. To remove the non-random component from each of the individual sensor responses, the instantaneous median was calculated for the cluster of MOS. The median (black line in Fig. 3.2a) was then subtracted from each of the individual sensor traces (coloured lines in Fig. 3.2a) in turn, to leave the amount of random noise variability, Fig. 3.2b. After the subtraction of the median, the variability in each of the sensor timeseries was reduced from 13 $ppb_{[VOC]}$ to ± 3 $ppb_{[VOC]}$ over 2.5 days. The majority of the effect of the environmental interferences upon the MOS sensors was therefore removed and the remaining variability is due to both random sensor noise and the small differences in the individual sensor response towards environmental conditions. During the 2,5 days of the zero air experiment, there was a small amount of downwards drift in the MOS responses, with the majority of the sensor signals beginning to report negative values after the initial 12 hours. The signals remained negative for the remainder of the experiment.

3.1.2 Power spectral density for MOS zero air response

Power spectra were computed for each of the seven TGS2602 total VOC MOS sensors in the zero air experiment. To calculate this, a Fast Fourier Transform (FFT) was plotted against the different frequencies in the MOS signal on logarithmic axes. The power spectra display the different amount of power at each frequency and therefore allow some information

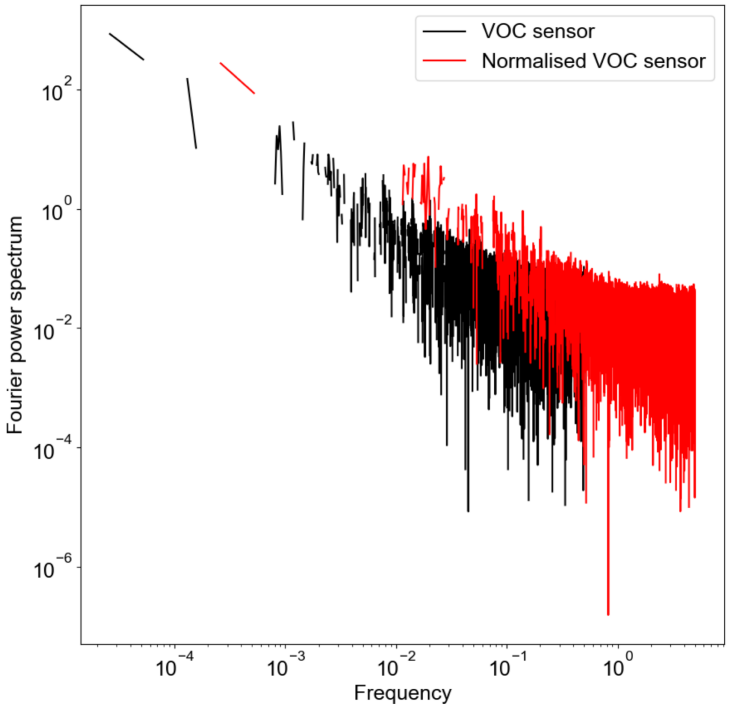

Figure 3.3: The power spectra for the one of the MOS TGS2602 sensors to investigate the different frequencies that make up the sensor signal (black) and the normalised sensor signal (red, with the median trace subtracted from the sensors time series). The power spectra are plotted with logarithmic x and y axes and resemble red/pink noise for both signals.

about the noise to be obtained. All seven sensors produced very similar looking power spectrum plots so just one spectrum is shown in Fig. 3.3. Both the MOS sensor traces and the normalised sensors (where the median had been subtracted from the trace) were examined. A power spectrum for one of the MOS sensors (Fig. 3.3, black) is shown on the same axis as the power spectra for the same sensors normalised signal (Fig. 3.3, red), where the median MOS sensor had been subtracted from the individual sensor trace.

The power spectral density plots were useful for characterising the noise of the MOS sensors in zero air. The power spectrum of the MOS sensors in zero air (Fig. 3.3, black lines) displayed higher power in the lower frequencies. The power in the frequencies increases as the frequency decreases from 10^{-1} to 10^{-4} Hz. Figure 3.3 is a logarithmic plot, and the decrease in power as the frequency of the signal increases is linear on the logarithmic axis. This shape of the power spectral density is typical of pink noise [146] and is indicative that the MOS response in zero air is not random at 10 – 1000 seconds. The power spectral density plot would appear flat upon the same logarithmic axis if the MOS signal in zero air was representative of white noise. For white noise there would be equal power across the range of frequencies in the signal [146]. For frequencies greater than 10^{0} Hz (less than 0.1 seconds), the power spectral density exhibits white noise and therefore the MOS zero air response is random at these frequencies and on these timescales. A zero response exhibiting pink noise is more challenging to correct for compared to a zero sensor

response that exhibited white noise. This is because techniques that are more complex than time-averaging the data need to be required in order to smooth the data and average out noise in the sensor response. Typically, smoothing techniques can be applied to minimise noise, but whilst these work well for data with white noise characteristics, these are not as effective for pink/red noise and different approaches are required to reduce the noise component. However, there was high covariance between the 8 MOS sensors in zero air, indicating that the pink noise characteristic observed in Fig. 3.3 is potentially due to the sensor response affected by environmental factors that change on these timescales (10 to 1000 seconds), rather than the MOS response being characteristic of pink noise.

The normalised zero air MOS response was plotted as a power spectral density on the same axis (Fig. 3.3 red lines). The normalised zero air MOS response had some of the variability due to changing environmental factors removed by subtracting the median trace from the sensor trace. The power spectrum for the normalised MOS response to zero air (Fig. 3.3 red lines) is of a similar shape to the MOS sensor power spectrum (Fig. 3.3 black lines), with the higher frequencies (10_0 Hz) of noise still exhibiting white noise characteristics. The power spectral density for the normalised signal is shifted to the right indicating that the non-random component of noise that is characteristic of pink noise has shifted from the seconds-minutes timescale to the second-subsecond timescale. The slope at which the power decreases as the frequency decreases is lessened for the normalised MOS sensor and is therefore more characteristic of white noise. The residual noise, after accounting for some of the environmental factors, is therefore more random. This is evidence that by accounting for the environmental conditions experienced by the MOS sensor, the sensor noise can be treated and smoothed as if it was white noise.

3.1.3 Autocorrelation plots for zero air MOS response

Autocorrelation plots are used to investigate the amount the time series is correlated with itself at different time lags and can indicate periodicity in the data over time or randomness. To calculate an autocorrelation plot, a timeseries is correlated with itself and given a Pearson's coefficient. This process is repeated after the timeseries is shifted by a certain time period (time lag). The Pearson's coefficient for each of the time lags is plotted on the y-axis and the time lags for the MOS data are found along the x-axis. The time lags from 0 to 5000 seconds are shown here, to allow comparisons to be made between the MOS and the normalised MOS time series. The pink shaded areas represent the 95 % confidence intervals, so data outside of this region is considered highly correlated and significant, statistically. Where the MOS time series enter the 95 % confidence intervals the time series becomes uncorrelated with itself and this can indicate randomness in the data set. For the zero air experiment with the sensors not responding to anything other than VOCs, the residual noise would be expected to be random and therefore the autocorrelation plots for the MOS sensors would display insignificant correlation coefficients of 0 for all

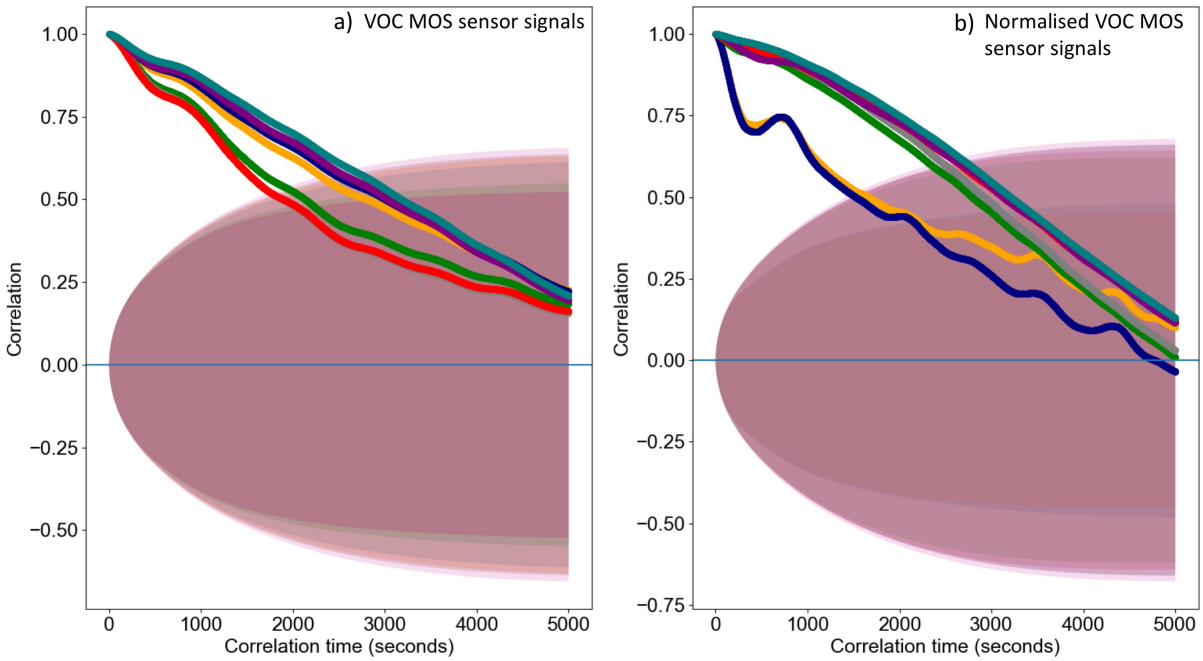

Figure 3.4: Autocorrelation plots for the TGS2602 MOS sensors signals and their normalised signals (with the median MOS sensor trace subtracted). The coloured lines represent the autocorrelation for seven MOS sensors and the shaded areas display the regions of 95 % confidence intervals. The sensor signals begin with a high amount of autocorrelation and this decreases linearly before the sensors become uncorrelated and enter the 95 % confidence interval at around 30 minutes.

time lags. Where the data is non-randon the Pearsons Coefficient will be non-zero and outside of the 95 % uncertainty zone.

The autocorrelation plots for the MOS sensors (Fig. 3.4a) in zero air provided more evidence that the MOS sensors are not exhibiting a random noise signal as the MOS signal was correlated with itself at time lags between 0 – 1500 seconds. The Pearson's Coefficient was greater than 0.75, so the data set was statistically significant and highly correlated for time lags up to 1000 seconds. The fact that the autocorrelation plot is indicative of a non-random signal is additional evidence that during the zero air experiment the MOS sensors were responding to external factors, such as slight differences in the environmental conditions. As the times lags increase the autocorrelation decreases linearly and at time lags of approximately 2800 seconds (45 minutes) the MOS signals became uncorrelated as the sensors enter the 95 % confidence intervals. Therefore, the MOS response in zero air becomes uncorrelated with itself at time lags that are greater than 45 minutes. The correlation between the time series and a time-lagged copy of itself is no longer statistically significant and this can indicate random fluctuations in the time series'. The autocorrelation for each MOS sensor continues to decline in the linear manner and reaches 0.25 at a time lag of 5000 seconds. Two of the MOS sensors (Fig. 3.4a, red and green traces) became uncorrelated earlier than the others (1800 seconds), although the decrease in correlation as the time lags increase remained relatively linear. The autocorrelation plots for these

two sensors indicated they respond slightly differently towards the changing environmental conditions compared to the other MOS.

Figure 3.4b displays the autocorrelation plot for the normalised MOS sensor during the zero air experiment. The shape of the autocorrelations was similar between the MOS signal and the normalised MOS zero air signal however, there were some differences of note. The normalised MOS sensors did not exhibit completely random as there were some time lags for which the autocorrelations were statistically significant. This is evidence that subtracting the median response does not entirely remove the sensor variability due to external conditions. Five of the normalised MOS sensor autocorrelations in Fig 3.4b began highly correlated with a Pearson's value of greater than 0.75 until time lags of 2000 seconds, compared to 1000 seconds for the MOS sensors. This indicates that there was less variability in the normalised MOS sensor signals for up to a 30 minute time lag. However, as the time lags increased from 2500 seconds to 5000 seconds there was a steeper decrease in the Pearson's Coefficient, and the correlations reached 0 at 5000 time lags. This indicated that over longer time scales the normalised MOS sensor response was more random than the MOS sensors without the median subtracted. This result was expected as subtraction of the median signal removes some of the general sensor trends. Two of the normalised sensors (yellow and purple) have a much lower autocorrelation and with more variability in their autocorrelations that are more indicative of a sinusoidal pattern. They reach the 95 % confidence interval at 2000 seconds but the different pattern suggests that they would require a different model for prediction.

The normalised MOS signals in zero air became uncorrelated faster than the MOS signals but all had high levels of autocorrelation over thirty minutes, suggesting that over minutes to hours, the TGS2602 MOS sensor zero air response to cross interferences and environmental conditions can be assumed to be moderately stable. Neither the MOS or normalised MOS signals were random in zero air so both still exhibited signals influenced by external conditions.

3.2 Different types of MOS sensors in zero air

Three other types of MOS sensor, TGS2610 propane/butane, TGS2620 OVOC and TGS2611 methane MOS, were exposed to PAG air for the same period of time to investigate their response to zero air, see Fig. 3.5. The eight TGS2610 propane/butane (PrBu) MOS sensors were the least spread out of all the MOS sensors, with all the signals staying very close together - the range in the PrBu sensors at the end of the experiment was 6.27 mV. The PrBu, methane and OVOC MOS were not calibrated in the laboratory with gas standards, but applying the typical Total VOC MOS sensitivity of 12.5 mV $ppb_{\text{-}1}$ this is equivalent to 0.5 $ppb_{[VOC]}$. The eight OVOC MOS displayed a much larger spread, especially at times were the OVOC sensors displayed the highest voltage outputs, e.g. the range of the

OVOC sensors between the OVOC sensors was 28.8 mV (2.3 $ppb_{[VOC]}$) between 1400H and 2000H on the 15th of April when the signal was high (c.a. 0.15V). The range between the maximum and minimum reporting OVOC sensors was a lot lower (5.3 mV, 0.42 $ppb_{[VOC]}$) when the signal was lower (c.a. -0.01 V between 0200H and 0800 H on the 15th April).

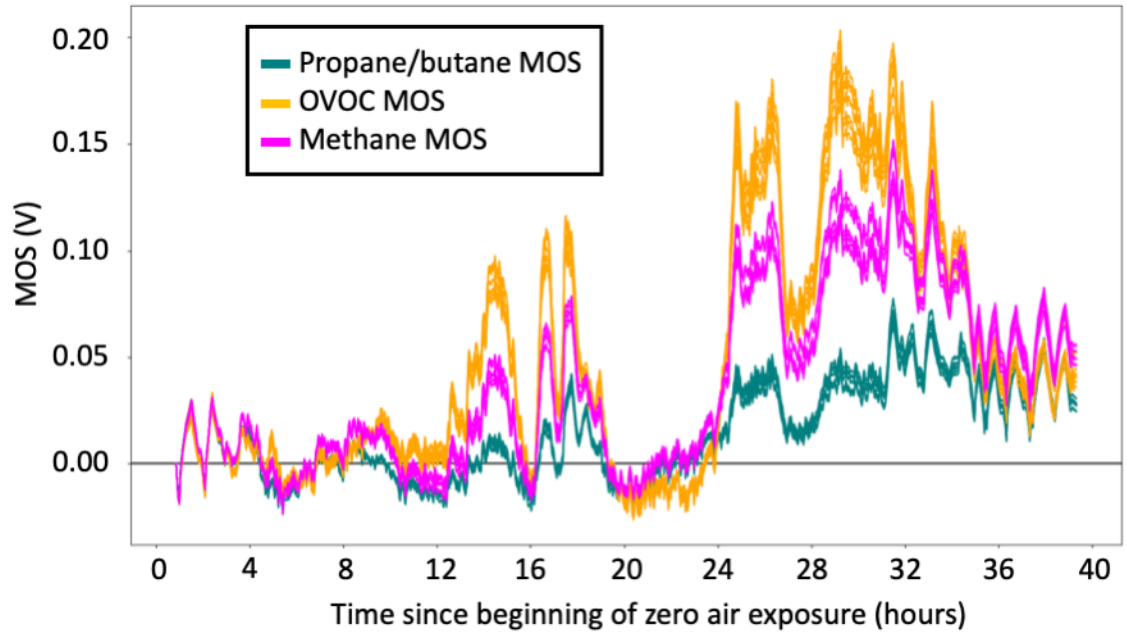

Figure 3.5: The other types of MOS sensor, the propane/butane MOS (teal), the OVOC MOS (orange) and the methane MOS (pink) all displayed signs of an upwards temporal drift over the two days during the zero air experiment.

On the 15th April 2018 at 08:00 all the MOS sensors in Fig. 3.5 show a sudden increase in their signals by 0.05 to 0.15 V which then continues for the remainder of the experiment. This upward shift of the signals is pronounced in all signals and therefore is likely to be due to an external condition changing at this point. This would also explain the increased spreading out of the signals as the sensors after the step change as each sensor has a unique responses to the different variables. The increased variability observed in the Total VOC MOS signals after 200H on 15th April (see Fig. 3.2 was also noticeable in the PrBu, OVOC and methane MOS after 34 hours exposed to zero air, although the increased variability that occurred prior to this time is of a larger magnitude. The correlation between each individual sensor with the other individual sensors of the same type was very high. The range of R^2 values were: 0.9946 - 0.9998 for the PrBu MOS, 0.9968 - 0.9998 for the methane MOS and 0.9938 - 0.9995 for the OVOC sensors. These values are reflected in the MOS time series for the zero air experiment - all sensors are responding to common factors and the patterns reported by the sensors are very alike (Fig. 3.5). This suggests that, like the total VOC MOS sensors, the PrBu, OVOC and CH4 MOS all respond to common variables leading to the similar time series, and each individual sensor has a unique sensitivity towards each variable leading to the gradual spreading out of sensors.

3.2.1 Probability Density Function (pdf) for each MOS type in zero air

Figure 3.6 shows the pdf for each different type of MOS sensor during the zero air exposure. The top row in Fig. 3.2 (a - d) depicts the pdfs for the sensors after they were offset to 0 initially then left to respond to the zero air. All seven total VOC MOS (Fig. 3.6a) have a very similar shaped pdf implying that the variability in the sensor signals are a result of all the sensors responding to the same variables. The pdf is centred at -0.15 V, suggesting a slight downward drift over the course of the zero air experiment. The Total VOC MOS each displayed one major peak, centred around -0.15 V, and a minor shoulder peak centred closer to zero. This suggests that there was a small offset that influenced the Total VOC signals, potentially this occurred on the morning of the 15th April 2018, or towards the end of the experiment 2000H on 15th April 2018 when all MOS sensors exhibited more variable signals.

The other types of MOS sensors (propane/butane, OVOC and methane) have a different shape compared to the total VOC MOS pdfs, with all sensors displaying more distinct multiple peaks. These second and third peaks arise when the MOS sensors signal suddenly increases and becomes more positive. The eight methane and eight OVOC (Fig. 3.6c and d) pdfs exhibit three peaks in the signal at 0.0, 0.05 and 0.1 V and this is due to the the sensor's baseline stepping up on 15th April 2018 at 08:00, and then displaying a large amount of variability after the change. However, all of the peaks observed in the pdfs for these three types of sensors were centred around a value that is more positive than 0 (e.g. +0.1 V for the methane sensors in plot (c)) suggesting a slight upwards drift for the other MOS as they responded to external conditions. All the sensors of the same type also displayed very similar profiles for their respective pdfs and therefore they have common drivers for variability. The OVOC and VOC sensors displayed the most variability during the course of the zero air experiment, with ranges of 230 mV and 186 mV, respectively.

Figure 3.5 e,f,g and h) show the pdfs for the normalised Total VOC, PrBu, OVOC and methane MOS sensors after the median signal of the respective cluster was subtracted from each of the MOS within that corresponding sensor cluster. As discussed previously with the Total VOC MOS sensors, this removed the major trends due to sensors responding to changing external conditions. These normalised sensor signals are a combination of the each sensors unique sensitivity towards the environmental conditions and random noise. From these lower plots in Fig. 3.6, it can be seen that the propane/butane MOS exhibited the narrowest pdf (±7 mV), meaning that the noise characteristic variability for these normalised sensors was lower than for the other sensor types. The sensors which display the highest degree of inter-sensor variability in the noise were the VOC MOS, as their random noise signal spans 73 mV, equivalent to 5.8 $ppb_{[VOC]}$. Since these sensors displayed the strongest temperature sensitivity in previous laboratory experiments, and the temperature of the air fluctuated more than the humidity during the zero air experiment it makes sense

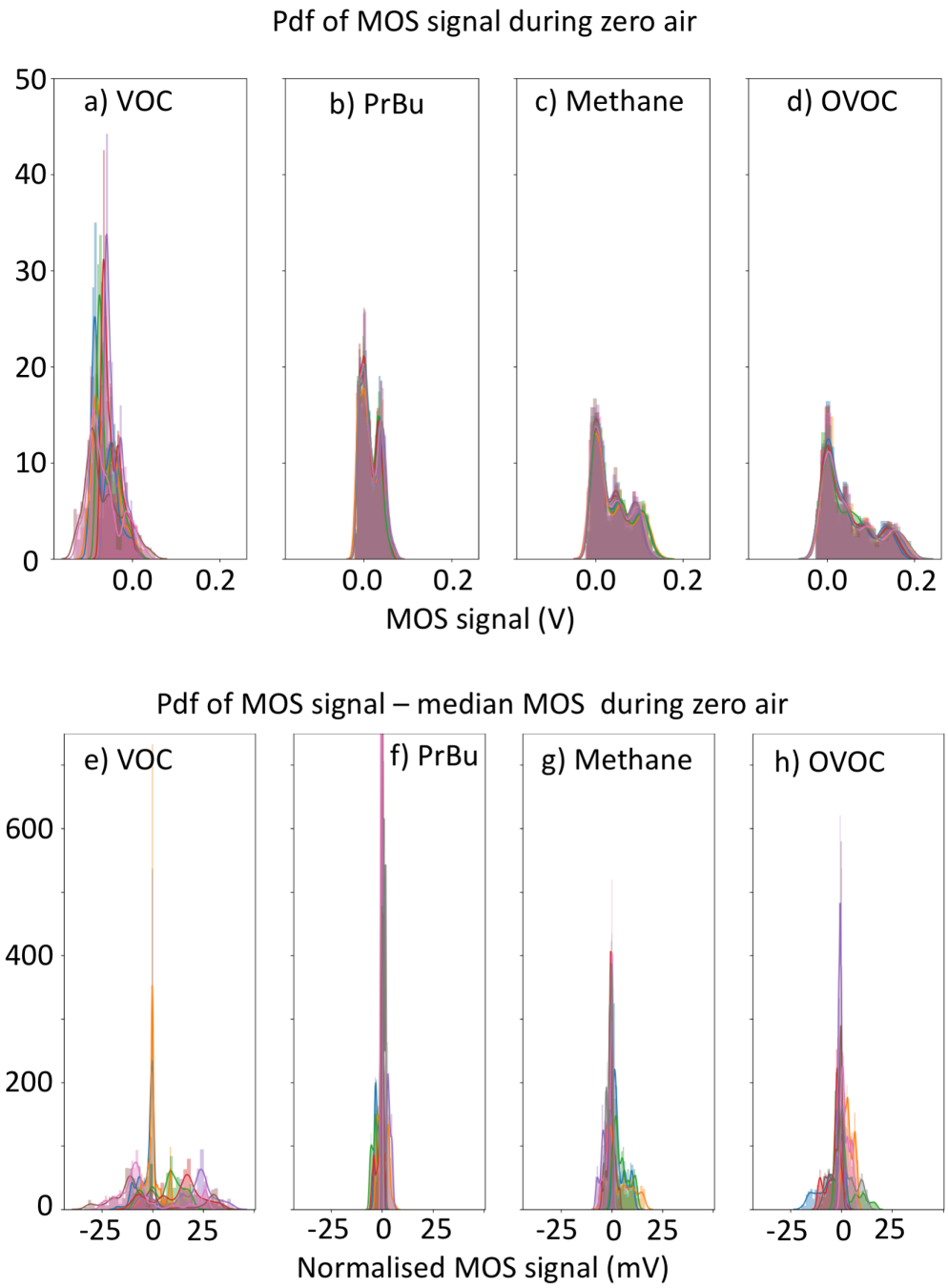

Figure 3.6: Probability density function (pdf) plots for the zero air experiment, for each different type of MOS sensor. The top row of plots are the pdfs for each sensor in zero air: a) seven TGS2602 total VOC MOS, b) eight TGS2610 propane/butane MOS, c) eight TGS2611 methane MOS and d) eight TGS2620 OVOC MOS. For each type of MOS sensor, the individual sensors within the cluster all have very similar shaped pdfs, and hence show similar variability about the average signal. The bottom row (e to h) are the pdfs for the normalised sensors after the median signal for each respective cluster has been subtracted, and are in the same order. The pdfs for the sensors in zero air are typically wider, showing a larger range than the pdfs for the normalised MOS.

that these sensors have greater differences between their response to temperature. The random noise pdfs ranges for the other sensor types were as follows; 13.6 mV for the propane/butane (TGS2610) MOS, 24.15 mv for the methane (TGS2611) MOS and 37.7 mV for the TGS2620 OVOC MOS. All of the normalised sensors pdfs were centred around 0 V, indicating that subtracting the median sensor removes the effect of drift and large changes to external conditions. The individual profiles of the pdfs for the sensors were not always similar which demonstrates the differences in the composition of noise even for sensors of the same type.

3.3 Indoor ambient air sampling with MOS

A selection of LCS were deployed inside an office environment (Fig. 2.2), with passive sampling of ambient indoor air to the sensing surface for the investigation of the variability of the sensors over longer time scales. The deployment was over five weeks, rather than three days to determine the degree to which they drift over this time. The office environment was chosen because the mixing ratios of compounds fluctuated throughout the day, exposing the sensors to changing concentrations of their target gases. Also the environmental conditions, whilst not specifically controlled, had reduced ranges compared to outdoor deployments. Therefore the impact of environmental conditions upon the MOS sensors would not overwhelm the VOC signal as much. During the experiment the humidity ranged between 30 and 50 % RH, and the temperature fluctuated between 18 and 26.5 °C. MOS sensors were mounted in clusters of eight onto circuit boards as described in Chapter 2 (Fig. 2.2). There was no Teflon manifold placed over the MOS sensors as they were sampling the indoor air via diffusion of VOCs over the MOS sensing surface. The sensors were left to sample indoor air on a table located under an empty desk to minimise turbulence of the air from people walking around the office. The sensors monitored continuously for over a month. There were 24 TGS2602 total VOC, 8 TGS2620 OVOC and 8 TGS2600 CO MOS deployed. All of MOS sensors were offset to 0 V to bring all of the MOS sensor voltages together at the beginning of the experiment to identify how much the inter-sensor variability there was during the deployment. Figure 3.7 shows the time series for 21 of the 24 total VOC MOS, with 0 V marked as a horizontal black dashed line.

3.3.1 TGS2602 total VOC MOS indoor air experiment

The sensors recorded for 34 days and during that time they measured a lot of variation in their environment. After the initial offset to 0 V, the majority of the sensors reported negative readings, indicating a slight downwards drift over time, or that the sensors began recording data time when the common factors that sensors respond to led to a high instance of MOS output voltage. Three of the TGS2602 MOS sensors failed immediately and were removed from the subsequent analysis. The Total VOC MOS sensor signals began diverging from each other immediately after they were offset to 0 V, and the increase in inter-sensor variability continued throughout the remainder of the deployment.

During the weekends (see time after the red dashed lines in Fig. 3.7) and over the Christmas period (23rd December 2016 to 3rd January 2017) there was a lot less activity in the office environment (denoted by yellow shaded areas) and this was reflected in the lower values (Total VOC MOS sensors reported values between -0.4 and -0.6 V) reported by the MOS sensors. The MOS sensor signals were also much less variable during these periods of low activity within the office environment. The lower and less variable MOS

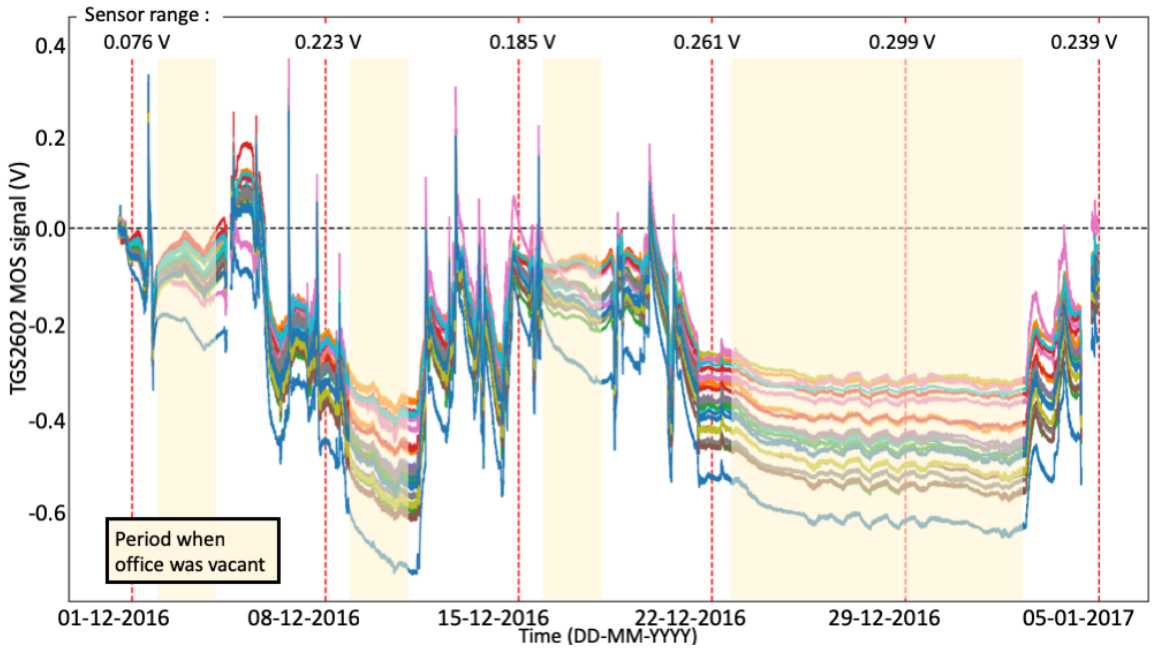

Figure 3.7: Time series for 21 MOS sensors sampling the indoor ambient air in an office environment. The sensors were all offset to 0V at the beginning of the experiment and left to run over the next five weeks. Every Friday, at midnight is marked on the time series with a red dashed line, to indicate where the weekends begin and sampling weeks. Times where there were no people in the office, are marked as shaded yellow blocks, to better show times where less variability in the MOS signals was expected.

output voltages during times when the office was vacant correlated with what would be expected of the temporal VOC concentration patterns. Less people in the room would lead to lower and less variable indoor VOC concentrations. It was however, difficult to distinguish which variables the MOS were responding to as this was probably due to a combination of lower mixing ratios of total VOC in the room and less changes in the temperature and humidity of the environment during times when the office was vacant. At times when the office was vacant the MOS sensors also generally displayed a downwards drift in signal indicating that temporal drift over the experiment was generally down wards. The impact of changing temperature and humidity upon the MOS sensor response was investigated. The were temperature and humidity sensors co-located with the MOS sensors, however they only began recording on the 20th December 2016 so the time series comparing the temperature and humidity with the MOS response begins on this date, Fig. 3.8.

The median TGS2602 MOS sensor co-varied with temperature in Fig. 3.8a. Peaks in temperature were matched by peaks in the median MOS signal and temperature fluctuations had a large impact upon the MOS sensor signals. There was less evidence of co-variance between the median MOS signal and the humidity of the air as, during a period of time when the humidity was varied (23rd Dec to 2nd Jan) the MOS signal did not display a correlated signal, rather was low and less variable Fig. 3.8b. However, there

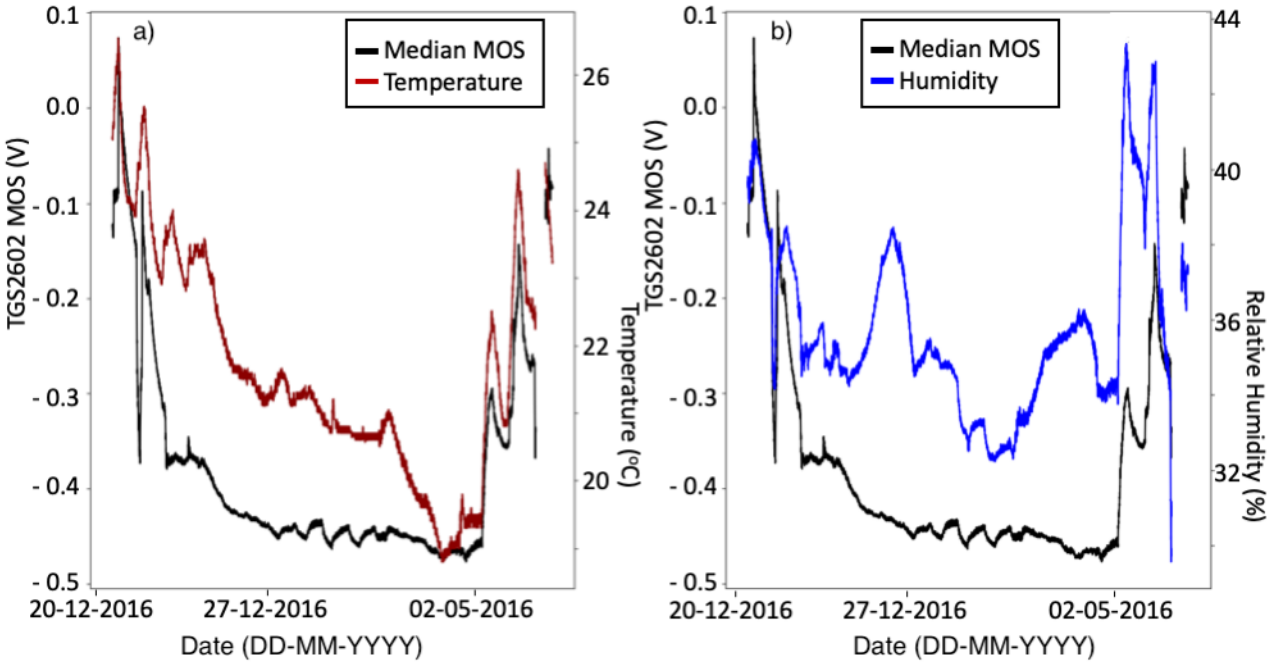

Figure 3.8: The median MOS signal (black) was compared against the temperature (a, red) and humidity (b, blue) during the deployment of the desk sensors after the 20th December.

were times where the RH and MOS signal was correlated and therefore it was assumed that environmental conditions such as temperature and RH interfered with the MOS sensor signal. The variability in the MOS signal was potentially overwhelmed by changing environmental conditions and the response with respect to VOCs was smaller than the response towards these interfering factors.

As expected, the sensor signals spread out over the duration of the experiment and the range of the 21 total MOS sensors after 7 days of sampling is marked on Fig. 3.7 at the top of the plot. Throughout the six week experiment, the range between the maximum total VOC sensor and the minimum reporting sensor increased from 0 V to 0.24 V, which, using the laboratory determined total VOC MOS sensitivity of 5 mV ppb^{-1} (for 40 - 50 % and 24 °C), is equivalent to a spread of 48 ppb$_{[VOC]}$. One sensor in particular shows a significant decrease over the experiment: the blue sensor in Fig. 3.7 is consistently reporting a lower signal than the other 20 sensors. The experiment shows that for 24 MOS sensors in the indoor air experiment, three failed immediately and one sensor records anomalously low readings after the first six hours. Yet if these sensors were calibrated in the laboratory and then deployed in a network of individually located Total VOC MOS to spatially observe VOC mixing ratios this would be an issue. For the first six hours of deployment, the blue sensor performs exactly like the other sensors and then suddenly the signal drops to be approximately 150 mV lower - equivalent to 30 ppb$_{[VOC]}$ in 30 % RH - than the lowest of the other 20 sensors. If this set of sensors was to be deployed as individual sensors to spatially monitor the VOCs, then it would be impossible to determine that this sensor

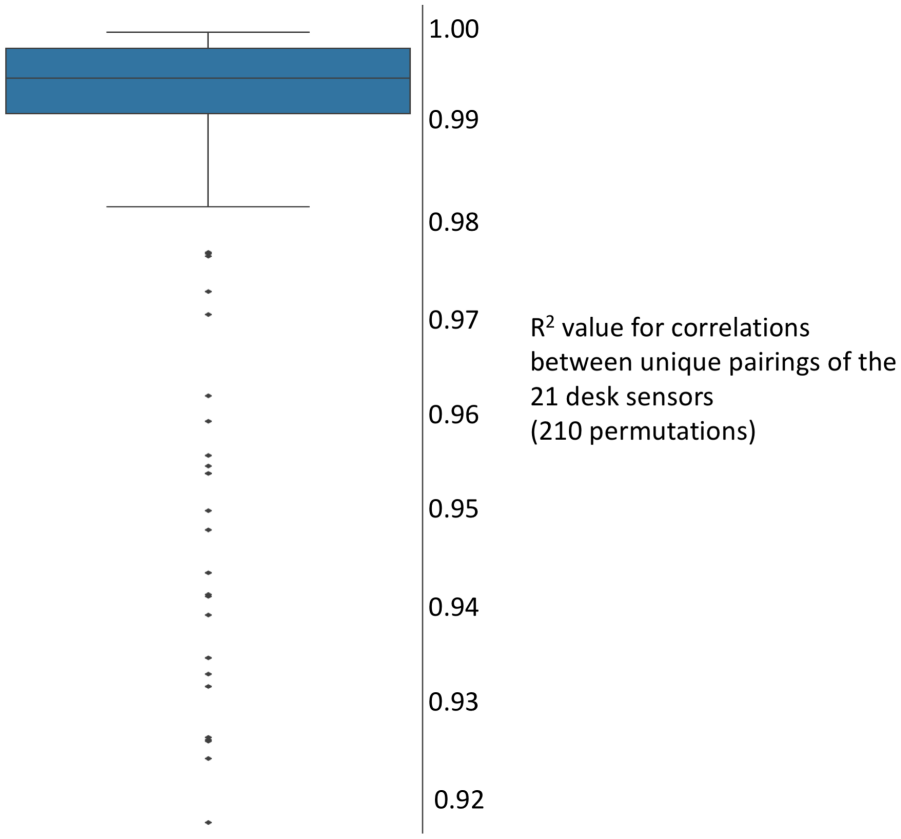

Figure 3.9: Each of the 21 total VOC MOS sensors was correlated with all the other total VOC MOS sensors and the R^2 value for these 210 correlations is shown in the box plot. The middle line is the median, the outer edges of the box plot are the interquartile range and the whiskers are the 5^{th} and 95^{th} percentiles of the R^2 values. The diamonds show outlying points, which were all R^2 values from correlating 20 MOS sensors with the poorest performing sensor (blue line in Fig. 3.7.)

reports unusually low values and it would be assumed instead, that the region where this particular MOS sensor was located had lower concentrations of VOCs. Using a group of identical sensors co-located in one region means that it is possible to determine if one sensor begins to behave peculiarly and experience large amounts of drift compared to the rest. For identification of outlying sensors at least three sensors are required to identify which sensor is behaving anomalously, and it can be difficult to distinguish between drift and a signal as the temporal drift of the MOS may be upwards or downwards.

The total VOC sensors all followed a similar pattern over the five weeks, Fig. 3.7, with all of the individual sensors responding to similar variables leading to the same fluctuations in signal (R^2 between all 21 ranged from 0.918 to 0.999, see Fig. 3.9, and Pearson's coefficient of >0.9 for all). Even the poorest performing sensor (blue line in the Fig. 3.7) with the lowest reporting values still responded to the MOS common factors, and this resulted in slightly lower R^2 values (observed in Fig. 3.9 as the 20 outlying R^2 values ranging between 0.92 and 0.98), but these were all greater than > 0.92, so the inter-sensor correlation remained high. This sensor experienced an unusually large amount of

drift but still identifies the major common drivers for MOS variations in it's environment. Highly correlating sensors is advantageous for MOS deployment as it makes correcting the sensors for interferences much simpler and allows for more reproducible results. However, the sensing signals still spread out over the duration of the experiment, reiterating that the sensitivity of the MOS sensors to these common factors is not identical, making a single-sensor calibration model difficult.

The slow separation of sensor signals is due to the sensors all having unique sensitivities towards humidity, temperature and other environmental conditions. The sensor with the highest signal over the first few hours, does not necessarily remain the highest sensor over the next hours and Fig. 3.10 shows this more clearly. After each hour the sensor signals were ordered according to the magnitude of the sensor voltage, and given a number between 1 and 21 relating to their order. For example, in hour 1, the lowest reporting sensor outputs the lowest voltage and therefore is given a rank of 1. This is colour coded in Fig. 3.10 as a dark purple colour. The next hour is averaged and the sensors are all given ranks according to the order of the magnitude of their output signals. Higher ranked sensors are shown with a dark green colouring. Every sensor contains both green and purple colouring over the five weeks therefore every sensor changes from being one of the highest reporting sensors to one of the lowest at some point over the course of the experiment. The sensors swap rank order rapidly and randomly in the first few weeks, e.g. sensor 4 begins as one of the lowest ranked sensors, then is the highest reporting sensor and so forth. The swapping of sensor rank shows how the different sensor sensitivities are unpredictable and causes variability in the rank order plot over 6 hours to a day time scale. Positions are changed rapidly and randomly depending on the individual sensors sensitivity towards external conditions.

The time series (Fig. 3.7) and rank order plot (Fig. 3.10) shows that the MOS sensors display multiple levels of temporal drift and therefore correcting the individual sensor signals is more complicated than assuming a linear interpolation between two calibration points. The sensor variability over a few hours causes short term noise in the data and the temporal drift over a week or so is significant enough that from the 22nd of December 2016 the order of the sensors becomes more stable (the horizontal lines in Fig. 3.10 have more consistent colouring). This is due to the sensors all drifting far enough apart that small random changes to the sensor signals are not large enough to change rank order with more than two sensors. Sensor 11 is an anomaly to the others as, although it is a high ranked sensor for the first hour, it quickly becomes the lowest and remains so for the rest of the sampling time (blue sensor from Fig. 3.7).

The rank plot (Fig. 3.10) contains a series of vertical lines where a lot of sensors changed rank simultaneously. During these times the temperature and humidity of the room changed significantly, over a short time scale, exaggerating the impact of the individual sensor responses to these variables. This short and mid-term random noise signal that

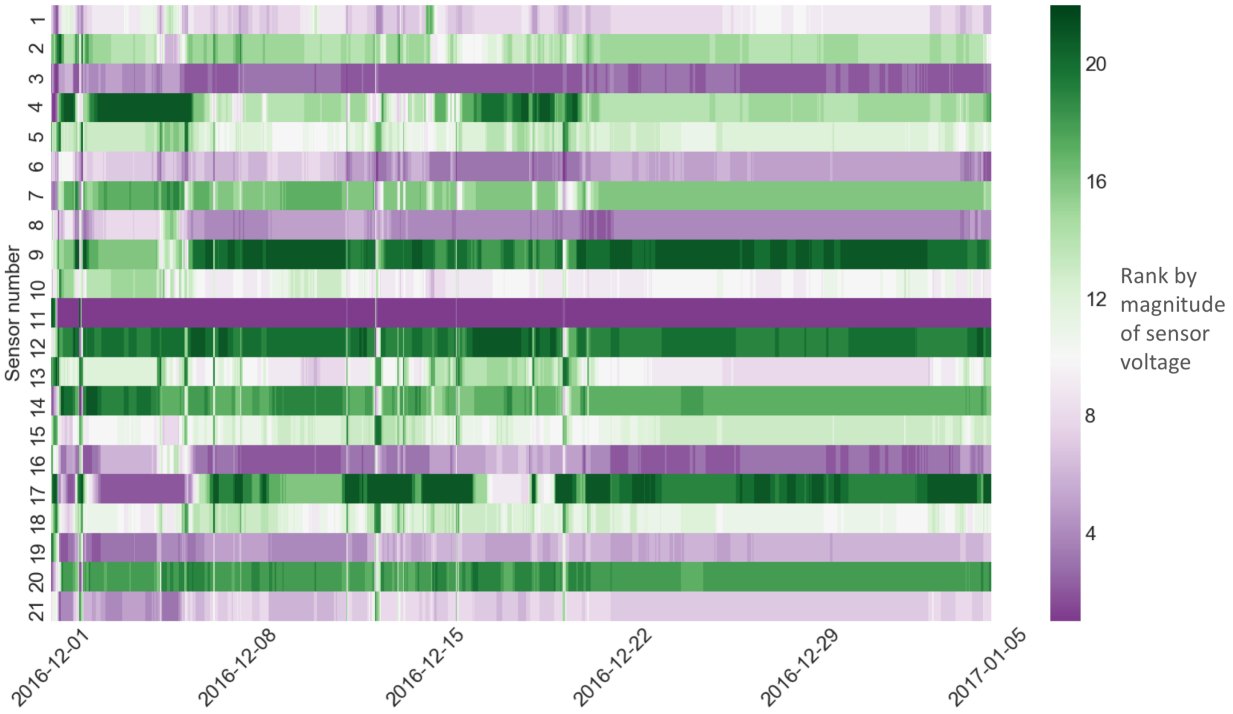

Figure 3.10: Rank order plot to show how the sensors were ordered by sensor output voltage over the five weeks. The data was binned into 1-hour bins, with the average value of each bin determined. The MOS ranked from 1 - 21 depending on the magnitude of the average, and this ranking has been colour coded from purple (low ranking sensors) to green (a sensor reporting a high value).

is evident in the rank plot (Fig. 3.10) for the MOS sensors means that the purchase of one sensor and deploying it can lead to misleading results without frequent in-field calibration. The sensitivity of the sensor towards its target compound must be characterised, as well as its response towards other environmental factors, such as other atmospheric compounds, temperature and humidity. The combination of two or more of these factors changing may also effect the response of the sensor, for example, with a large fluctuation in humidity the sensitivity of MOS to total VOC may change by a factor of five. The drift of the total VOC MOS sensors over the full experiment was approximately 1V, equivalent to 200 ppb of VOC (for a sensitivity of 5 mV ppb^{-1} at 30 - 40 % RH, 24 °C) which is larger than the VOC mixing ratio expected for an actual VOC measurement. The MOS sensors deployed without a reference instrument cannot be used to quantify total VOC emissions but if the impact of temperature and humidity can be corrected for, the overall trends in the MOS data might be of use for helping to identify patterns of VOC pollution. The superposition of the drift at the different time scales further complicates the quantitative comparison between sensors - especially because individual sensor have slightly different amounts of drift, accounting for the large degree of inter-sensor variability. Between 0 - 6 hours, the MOS sensors have stable responses to their environment and so quantitative comparisons between the sensors could be comprehensible, with proper calibration initially. There are different time scales over which the temporal drift changes and this results in the temporal

drift being non-linear and variable over time, which complicates the corrections required to account for temporal drift. Corrections for temporal drift of the MOS will be complex, may be unique for each sensor and calibration would need to be frequent and on the same time scale as the shortest drift observed (6 hourly). Exhibiting variable drift in the MOS response is disadvantageous as calibrations over time will not be reproducible and there will be little confidence in the data obtained from deployed MOS in between calibrations.

3.3.2 CO and OVOC MOS deployed in indoor air experiment

There were eight OVOC (TGS2620), eight VOC (TGS2602) and eight CO MOS (TGS2600) sensors recording data in the same indoor air experiment as described in the previous section. These MOS sensors are the same size, have the same pins and power requirements so were mounted onto identical versions of the Eurocircuit boards as the TGS2602 MOS. The OVOC and CO MOS were also located on a table under an empty desk, away from the centre of the room to minimise the impact of turbulence of the air due to people walking past the sensors. After 3 days of sampling one of the OVOC sensors failed so was removed from the data used in the analysis. The eight CO MOS sensors were highly correlated with each other during the experiment, as were the eight OVOC MOS sensors. Each of the OVOC sensors were correlated against the other six OVOC MOS and the Pearson's Standard correlation coefficients ranged between 0.993 to 1.000 to three decimal points. The Pearson's Standard correlation coefficient for the correlation between each of the 8 CO MOS sensors was greater than 0.999 for all correlations, excluding the sensors correlated with themselves.

The three different types of MOS sensor (VOC, OVOC and CO) displayed very similar time series, Fig. 3.11. The median sensor for each MOS sensor was calculated and the R^2 between the three different types of sensor are displayed in Table 3.1.

Table 3.1: The correlation coefficients calculated between the median OVOC, CO and VOC sensors whilst they were co-located during the indoor air experiment.

Sensor signals correlated	R^2 value
Median OVOC and median CO	0.998
Median OVOC and median VOC	0.950
Median VOC and median CO	0.963

The high correlation between the three different types of MOS sensor may indicate:

- All types of MOS sensor responded to each others target measurand, i.e. the OVOC sensors respond to changing CO concentrations as well as the CO MOS.

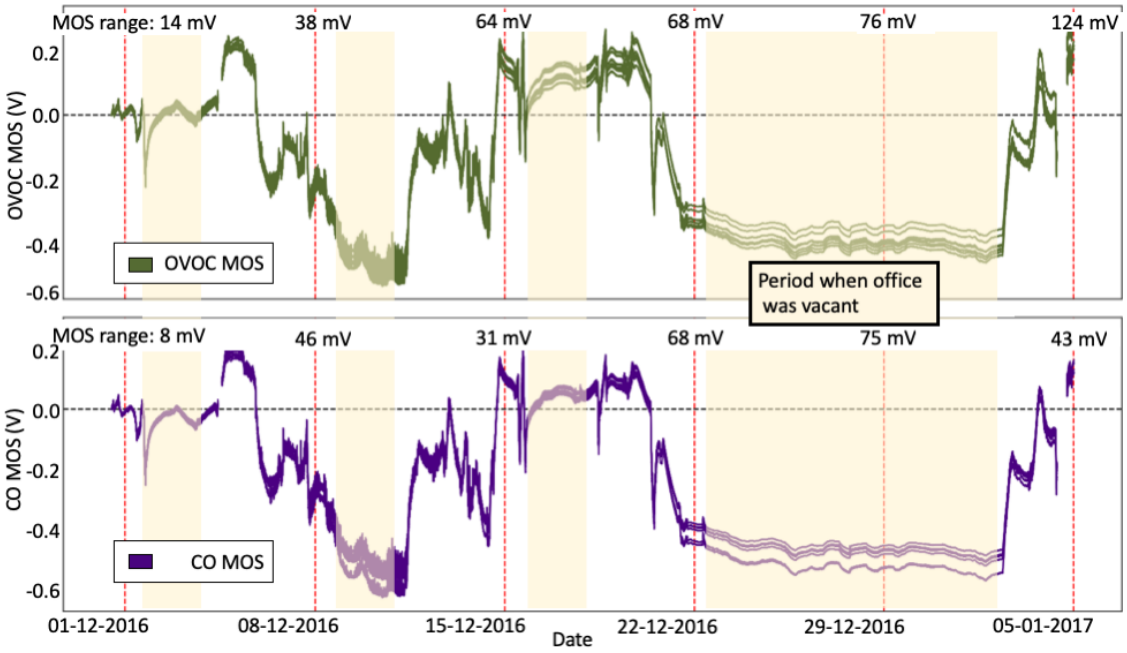

Figure 3.11: Time series for the a) OVOC MOS and b) CO MOS in the indoor air experiment, with the difference between the maximum and minimum reporting sensor after each week. The yellow shaded area represents time during the experiment when the office was vacant.

- Both the OVOC MOS , VOC MOS and CO MOS sensors are impacted by the changing environmental conditions within the office environment. The TGS2602 Total VOC MOS sensor signals were hugely impacted by the temperature of the office environment and potentially these MOS exhibit a similar sensitivity towards temperature.

- The VOC, OVOC and CO concentrations in the office environment are correlated

The temperature co-varied with the variability observed in the OVOC and CO sensors indicating that this had a similar impact upon the CO and OVOC MOS, as it did for the VOC MOS. This would indicate that all three different types of MOS sensors are influenced by the changing temperature of the surroundings, more so than they are impacted by the changing VOC composition and concentration of the indoor environment.

All sensors were offset to 0V at the beginning of the analysis to identify drift and to investigate the spreading out of the co-located sensor signals. Both sets of CO and OVOC sensor clusters displayed some inter-sensor variability during the deployment as there was some spreading out of their signals, see Fig. 3.11.

The OVOC sensors show ever-spreading MOS signals of the seven sensors, with the difference between the maximum and minimum OVOC sensor being around 125 mV over five weeks of continuous measurements. The 8 CO TGS2600 MOS sensors displayed the least spreading out of signals during the indoor experiment, reporting a maximum range of 75 mV. This was not observed at the end of the deployment, but during the time when

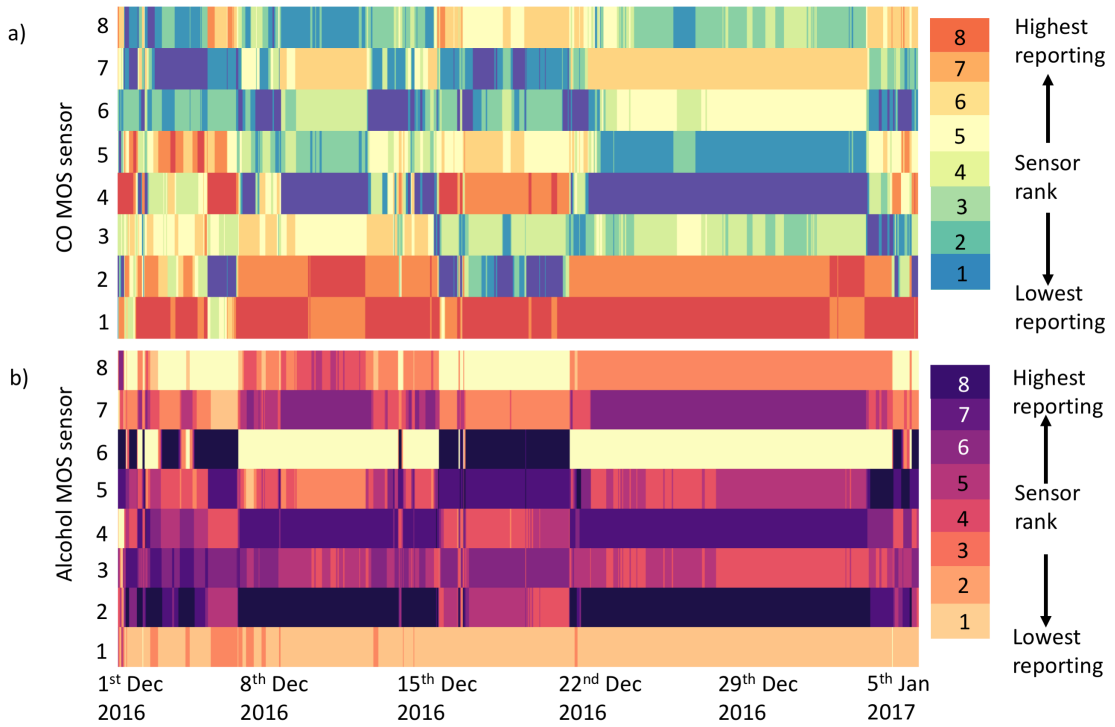

Figure 3.12: Rank plots for a) The eight CO MOS sensors and b) the eight alcohol MOS sensors, with all MOS sensors displaying a large degree of variability and lots of random changes to the sensors ranked position. The y-axis for (a) ad (b) is a number from 1 to 8 to indicate the magnitude of the sensor response relative to the other sensors in the cluster. The sensor with the highest reporting signal is assigned number 8 and the sensor with the lowest reporting value assigned number 1.

the office was vacant over the holidays.

Rank order plots were calculated for the CO and OVOC MOS sensors used in the indoor air experiment; eight TGS2600 MOS for the detection of CO and hydrogen as well as eight TGS2620 OVOC MOS sensors, Fig. 3.12.

The OVOC and CO MOS clusters yielded a similar degree of inter-sensor variability throughout the indoor air sampling (Fig. 3.12) as the Total VOC TGS2602 MOS clusters. Towards the beginning of the sampling period the sensors are ranked randomly, and there is less switching of rank positions as the experiment gets into the third week, whereupon the sensors are too spread out to cross over each other. For all the MOS sensors in Fig.3.10 and Fig. 3.12 there is evidence of drift over the medium time scales - 6 hours to a few days - as there is a considerable amount of variability and changing rank during these time periods. In all the MOS rank figures, there was a distinction where drift over longer time spans - greater than a week - led to the sensor signals no longer swapping positions due to them being too far apart for the shorter term variability to allow signals to cross over.

3.3.3 Comparison of CO EC and CO MOS during indoor deployment

There was an electrochemical (EC) sensor detecting CO during the indoor air experiment with low-cost sensors. Although this is not a reference instrument, it was useful to compare the CO MOS sensors with a different sensing technology. A correlation plot between the CO EC and each of the seven CO MOS (after the offset to 0 V at the beginning of the experiment was applied) was established, Fig. 3.13. The impact of changing environmental conditions and cross interferences is limited with the CO EC as it contains an auxiliary electrode to subtract some of the cross sensitivities from the EC signal, so this was plotted on the x-axis.

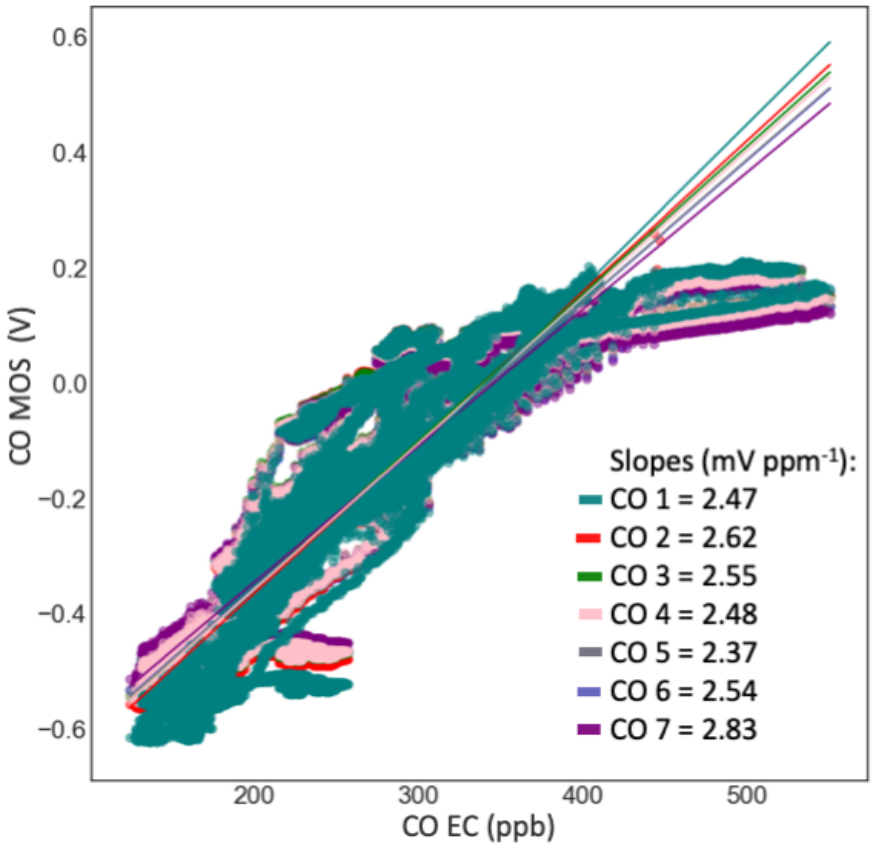

Figure 3.13: Comparing the response between the seven CO MOS sensors against the CO electrochemical sensor during the indoor air low-cost sensor experiment. Each of the different CO MOS sensors were assigned a different coloured set of data points and linear regression line.

The CO EC and CO MOS sensors had good agreement during the duration of the indoor air experiment when the CO EC was detecting less than 400 ppb of CO. For CO EC observations greater than CO the relationship between the CO MOS and CO EC was still linear but the gradient had become less steep, Fig. 3.13. Linear regression between each of the CO MOS and the CO EC was performed to determine the slope and hence relative sensitivity of the devices. The seven slopes (noted in Fig. 3.13) had a range of

0.46 mV ppm^{-1} (18 % of 2.55 mV ppb^{-1}, the mean sensitivity), and there was only a small amount of inter-MOS-sensor variability. The correlation plots for each CO MOS against the CO EC in Fig. 3.13 were approximately linear over the observed range of 0 - 400 ppm for the CO EC sensor, and then the CO MOS signal plateaued to produce a curved MOS response at higher observed CO EC concentrations (400 - 600 ppb). This was similar to the calibration curve of VOC MOS sensors exposed to total VOC concentrations over 150 ppb. As before, with the non linear calibration of the Total VOC sensors with VOC concentrations over 150 ppb, this was potentially due to saturation of the MOS sensing surface at higher concentrations. The kernel density function between the median CO

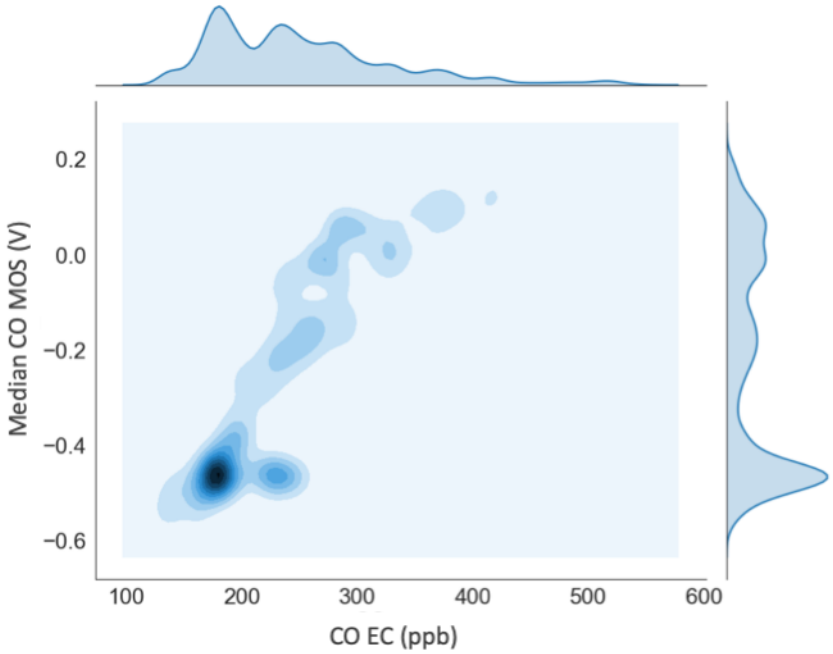

Figure 3.14: The kernel density function to compare the median CO MOS response with the CO EC response during the indoor air experiment.

MOS signal (which is representative of the behaviour of all 7 CO MOS sensors) and the CO EC response during the indoor air experiment showed the distribution of data within the correlation plot in Fig. 3.13. There were multiple modes occurring in the calibration plot, see Fig. 3.14, as the kernel distribution data for both the median CO and CO EC signals had multiple peaks. The majority of the data points occurred at 200 ppb for the CO EC, and this was matched by a dense set of MOS data points around -0.5 V. The CO EC data displayed two large peaks where data was concentrated, at 200 ppb and 250 ppb then in general, as the concentration of CO increased there were less data points. However, the median CO MOS signal displayed a different shaped kernel distribution plot indicating that the MOS sensors did perform differently to the CO EC. There was one major peak (at -0.5 V), very few data points at -0.4 V and then a relatively even amount of data points between -0.2 and 0.1 V, Fig. 3.14. This reflects the curved section of the calibration plot (Fig. 3.13 where, at CO EC concentrations of greater than 400 ppb, the

CO MOS sensor response plateaued off in comparison with the CO ES.

3.3.4 Clustering Total VOC MOS sensors

Short term random noise is relatively simple to account for; the sensor signals can be time averaged to minimise the random noise over minutes to an hour. The MOS sensors and their sensitivities (towards their target compounds as well as to other cross interferences) suffer from semi-random drift over the medium time scales which is more difficult to correct for. A time intensive and costly approach would be to subject the MOS sensors in the field to regular *in situ* calibrations with reference instruments, but this is impractical and in conflict with the idea of low-cost sensors. Using the indoor air experiment as a guide, these multivariate extensive field calibrations would have to be conducted daily for the MOS sensors to be able to be used for the quantification of total VOCs. The indoor experiment was used because the changes to the environmental conditions would be reduced, compared to outdoor deployment and therefore the calibration would potentially be required more frequently for the MOS sensors to be used in this manner outside. Clustering identical sensors and using the median signal from the ensemble is a method for minimising the variability and drift for any one MOS sensors, over the medium time scales. Certainly, for total VOC MOS sensors, it is still low-cost to use ten MOS sensors than to install and maintain a reference VOC instrument (GC-FID installation costs are typically >£100,000).

There were 21 total VOC MOS sensors used in the indoor air experiment, and the median of all 21 sensors was calculated over the duration of the experiment. This represents the general trends of the sensors well, and therefore allows certain conclusions about the total VOC mixing ratios in the indoor environment to be made. This was plotted against the average of a subset of unique permutations of the same MOS sensors. The correlation slope between these was calculated and the range of slopes determined for each unique set of permutations for each amount of sensors is depicted as box and whisker plots in Fig. 3.15. For example, for three as a number of unique sensors there are 1330 different combinations of three sensors using the twenty one sensors, with no sensor used twice in one grouping, and no groups repeated. For each of the 1330 combinations of three sensors, the instantaneous median was calculated for the duration of the indoor air experiment. The slope for the median of the combination of three sensors and the median of 21 MOS sensors over the same time was determined and is shown in the third box and whisker plot from the left in Fig. 3.15. The standard deviation in Fig. 3.15 decreases as the number of sensors in each average increases, similar to 1/N and therefore, despite the fact that the MOS sensors display a large amount of inter-sensor variability, the medium term drift can be minimised by using multiple identical sensors in a cluster. The median signal of the ensemble of identical sensors is then likely to be less effected by the randomised drift than the individual sensors themselves. This has implications in the field for calibrating the sensors; the time required between each MOS sensor cluster calibration will be increased

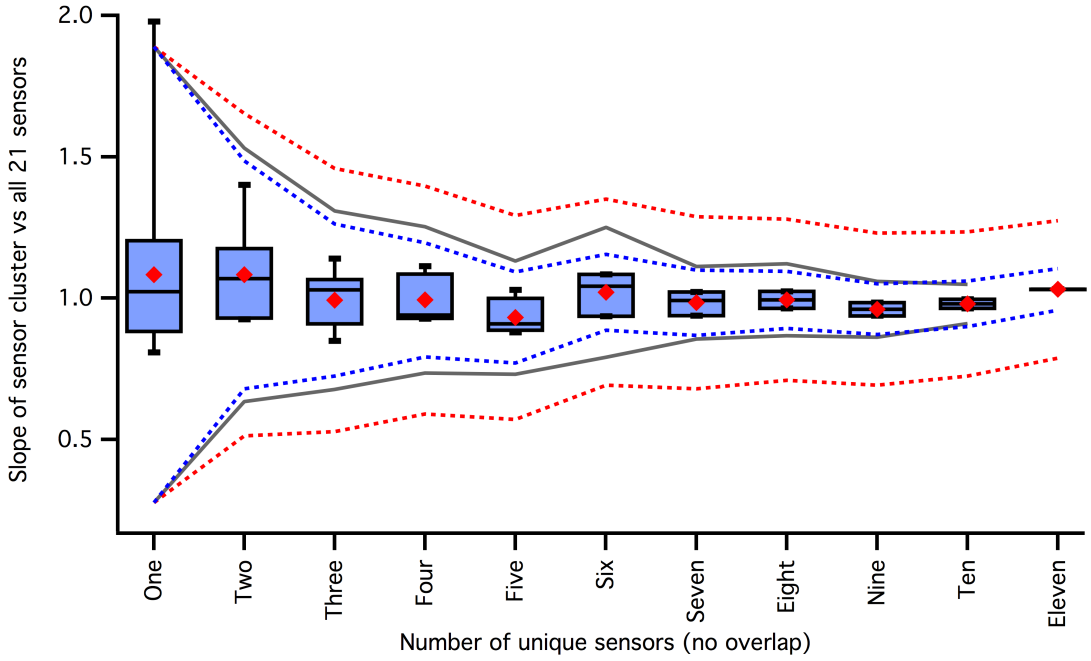

Figure 3.15: Figure taken from Smith et. al. 2017 manuscript [165]. Box plots to show how, as the number of sensors within a cluster increases, the median signal in a subset of sensors (containing one, two, three, ... to 11) gets closer to the median sensor signal for 21 sensors. The red diamonds within the box plots show the mean slope, the grey solid lines show ± 3 standard deviations from the mean. The blue and red dashed lines are for the ± 3 standard deviations on the mean with a 1/N decrease and a $1/\sqrt{N}$ decrease respectively.

compared to calibrating individual sensors. Since the clustering technique selects and uses the instantaneous median signal of the sensors within it, outlying sensors - which exhibit erroneously reporting signals - are excluded from the analysis, and therefore the calibration process doesn't need to account for these. Using a cluster causes the calibrations to be more robust.

The VOC sensors used here are the same Figaro TGS2602 total VOC MOS sensors used in the laboratory calibrations in Chapter 2. When increasing the number of simultaneous VOC concentration observations in the field, it would be more practical, cost-effective and require less power to operate multiple MOS sensors, rather than deploying multiple GC equipment or taking multiple, simultaneous WAS samples. One MOS sensor costs £10 and requires 295 mW power consumption and a cluster of 8 MOS on a custom circuit board can be made for approximately £100 and uses 2.5 W. It would require a large sum of money and consume lots of power if multiple GC-FIDs were used to increase the number of automatic VOC measurements as the entire GC-FID system costs more than >£100,000, the operational power required is approximately 250 Wh and skilled personnel is also required for operation and analysis. Deploying multiple WAS sample canisters in the field within a VOC network, for analysis upon a GC-FID system in the laboratory, would be more practical than deploying more automatic GC-FID systems however, this would be more impractical than installing MOS sensors as operators are required to deploy and collect samples and the technique is limited due to the sample taken being an average VOC concentration over the sampling duration.

Sensor variability on an hourly time scale can be corrected using the time averaging method and the medium sensor variability can be removed using the clustering technique. Sensors that fail during the deployment will not affect the sensor median, and the cost and ease of sensor sampling would mean that they can be replaced whilst still allowing continuous sampling from the other sensors within the cluster. After a few weeks of continuous deployment, as with most scientific instruments, the sensors performance will begin to decline and show a decrease in sensor sensitivity towards the VOCs decreases. Since using an ensemble of identical sensors cause the daily variations to be minimal the performance decline is systematic and therefore linear interpolation between the calibrations is more likely to be sufficient.

3.4 Electrochemical sensor variability

3.4.1 Electrochemical sensors and zero air

The electrochemical (EC) sensors use a different technology for the detection of their target compounds, and contain an internal auxiliary electrode to minimise the affect of environmental conditions and cross interferences. The EC sensors are expected to perform

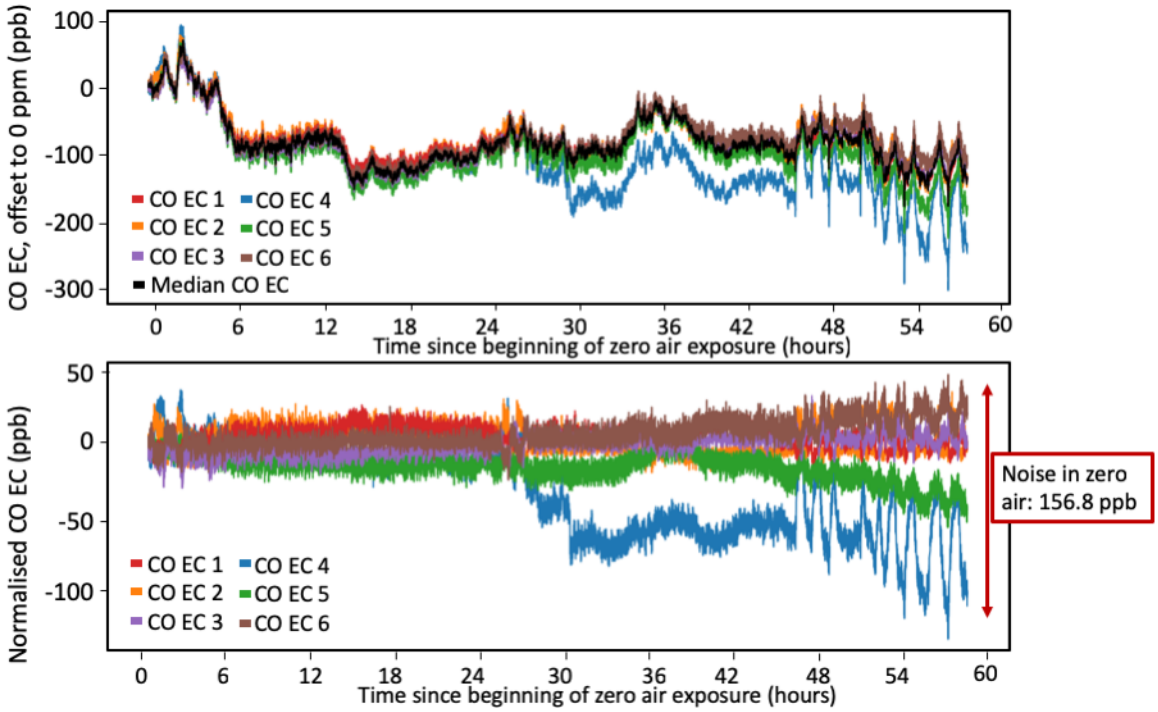

Figure 3.16: Zero air analysis for the CO EC sensors a) The CO sensors, each with their unique factory calibration applied, offset to 0 ppm at the beginning of the zero air experiment. The black line is the instantaneous median for the CO EC cluster and the coloured lines are the individual sensor traces. b) The trace for each CO EC after the median sensor signal has been subtracted from it, leaving the random noise signal.

differently to the MOS sensors in zero air and will have different amounts of random noise signal, which must be investigated. There were eighteen EC sensors sampling zero air; six CO, six NO_2 and six O_X (O_3+NO_2) EC. Every EC sensor comes with it's own unique factory conversion factor that is applied to convert the EC voltage output to a parts per million mixing ratio. After applying the specific conversion factors to the respective sensors, the sensors were offset to 0 ppm and an instantaneous median for each cluster of EC sensors was calculated (for an example see the black line in Fig. 3.16) to identify the drift of the sensors over the 2.5 day sampling period.

During the first day, the CO EC sensors show minimal amounts of inter-sensor variability and all are closely following the same trends. Zero air is scrubbed and cleaned in before entering the system and so we expect a limited amount of CO to reach the sensors. The CO EC do not produce a signal that is flat from 0 ppm however, and since all show the same pattern all sensors are responding slightly differently towards a common factor, that is likely to be changing environmental conditions. Towards the end of the zero air exposure the 6 CO EC sensors all show increased variability in their signals (45 hours since experiment began), which is due to the temperature of the air flow to the sensors also becoming more variable at this time, see Fig. 3.17. The variability of the temperature occurred on the same timescales as the variability observed in the CO EC timeseries. One day after the sensors began sampling the zero air (at 24 hours) however, they all begin to

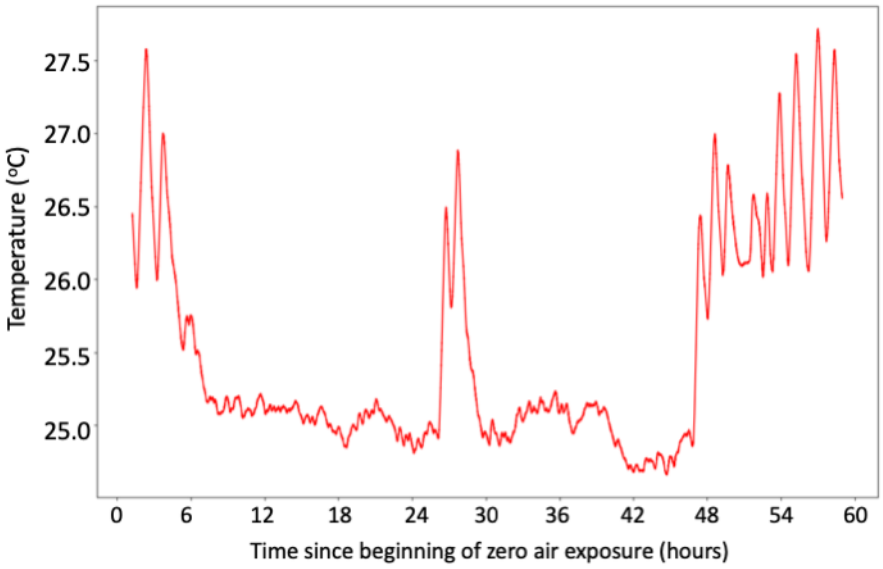

Figure 3.17: The temperature of the air flow to the sensors becomes much more variable after 45 hours since the experiment began. The time scales in the temperature variability are matched by the increased variability in all 6 CO EC sensors responding to the same air.

spread out more and one sensor (CO EC 4, blue in Fig. 3.16) shows significant drift and becomes consistently lower than the other five EC sensors after this point. Since these sensors all show signs of responding to the surrounding environmental conditions - they all follow the same trend and therefore all sensors are responding to a common factor - the median was subtracted to identify the random noise component of the variability of six CO EC in zero air. This was 157 ppb for the CO EC sensors, and Fig. 3.16b) shows that a large proportion of this is due to the sensor that began to display a low offset, compared to the others. Removing this CO EC from the cluster and repeating the analysis, the residual noise was reduced to 100 ppb. However, in a real-world deployment where individual CO EC sensors were used in a network to map CO pollution in a localised area there would be no indication that this sensor has begun to exhibit an outlying signal. For the first 24 hours of deployment the CO EC signal is very close to the median CO for the cluster and the signal is not considered outlying at this point, see Fig. 3.18a. However, after 24 hours this particular CO EC sensor deviates away from the median CO signal, as becomes an outlier. Due to the outlying CO EC not failing completely as it still continues to detect the same peaks and variance as the median CO it would not be identified as failing if deployed alone as part of a CO sensor network. Rather, it would be assumed that at that particular location the CO concentration was decreased relative to the other CO EC sensor locations. The median CO and outlying CO EC signals were correlated and multiple phases of correlation were observed during the 60 hours of exposure to zero air Fig. 3.18b. The data points were coloured according to the time since the beginning of the experiment and the 1:1 line is plotted as a grey dashed line in Fig. 3.18b. There

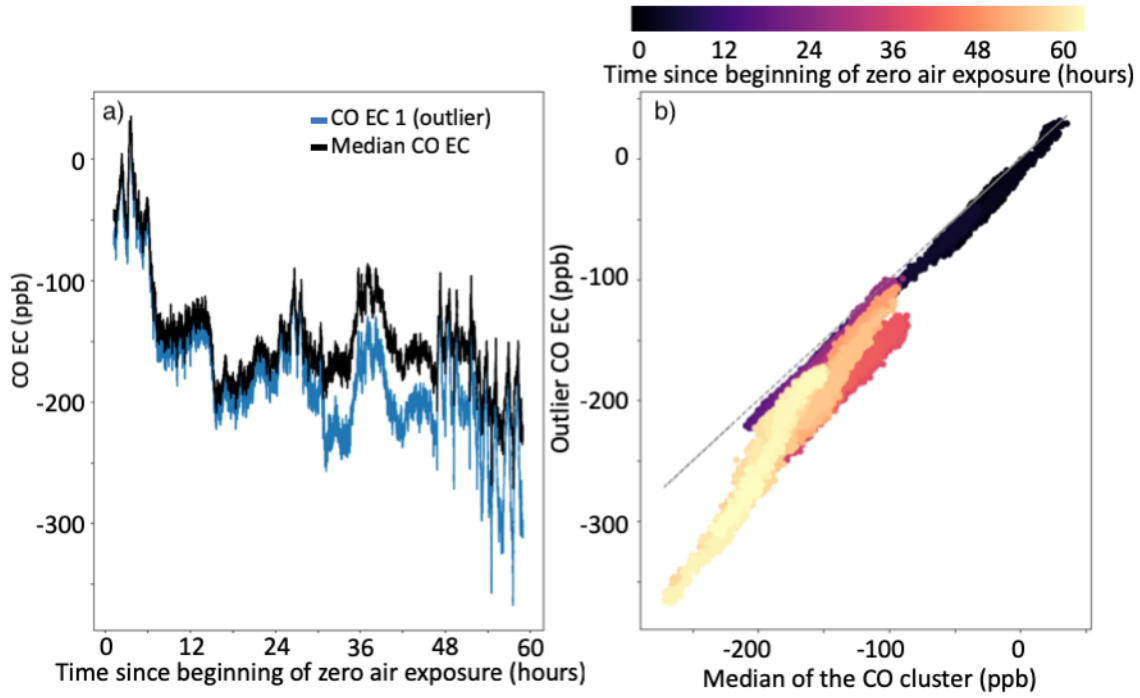

Figure 3.18: a)Time series to compare the median of the six CO EC sensors (black) and the CO EC outlying sensor (blue). The two signals exhibit high covariance until mid-way through the zero air exposure. b) The correlation plot between the outlying CO EC sensor (blue in plot a) with the median CO EC to identify if the two data sets were still correlated even after the outlying CO EC began to show drift. The data points are colour coded by time, dark colours representing the start of the experiment, lighter colours towards the end.

Table 3.2: The magnitude of the random noise component of the variability between six of the CO, NO_2 and O_X EC after three and a half days of exposure to zero air. The random noise component for each sensor was calculated by subtracting the median response of the sensors in zero air from each sensor time series. The magnitude of the random noise component was determined by identifying the spread of the sensor signals.

EC sensor	Component of random noise (ppb)
CO	156.8
NO_2	3.82
O_X	9.17

was a close to 1:1 relationship between the median CO and outlying CO EC at the start of the experiment (dark purple), and as the time since the beginning of the experiment increased (data points become more yellow in Fig. 3.18b) the relationship deviated further and further from this 1:1 ratio. However, when the data points are colour coded yellow in Fig. 3.18b, between hours 48 - 60 of the zero air experiment, the relationship between the median CO and the outlying CO sensors is still linear, which suggested that there was a gradual change in the outlying EC's sensitivity to environmental conditions and indicated that this would continue to occur over time.

The NO_2 and O_X were subject to the same analysis as the CO EC sensors and the variability due to random noise after 2.5 days between the EC sensors was calculated and is summarised in Table 3.2. One of the O_X sensors failed immediately and therefore was removed from the cluster, so the zero air O_X analysis is for five EC sensors.

The NO_2 and the O_X sensors displayed a relatively small amount of variability with the sensors generally staying in the order that they were originally, Table 3.2. For example, the sensor displaying the highest signal shortly after the beginning of the zero air experiment remained the highest reporting sensor throughout the zero air sampling period.

3.4.2 Power spectra for EC sensors in zero air

The EC zero air experiment was analysed by applying a Fast Fourier Transform over the signal frequencies to determine a power spectrum and characterise the noise in each of the EC sensor signals. All the same type of EC sensor showed very similar Fast Fourier Transforms (FFT) so just one example sensor power spectra from the cluster is pictured in Fig. 3.19. The darker shade of colour is used to depict the power spectrum for the EC sensor time series and the lighter shade shows the resultant spectra for the normalised EC sensor - with the median sensor signal subtracted.

With the exception of a small number of small frequencies, the power spectra for the EC sensors displayed more equal power across the frequency range than the MOS sensors in zero air exhibited (see Fig. 3.3a-c). These flatter power spectral densities for the EC

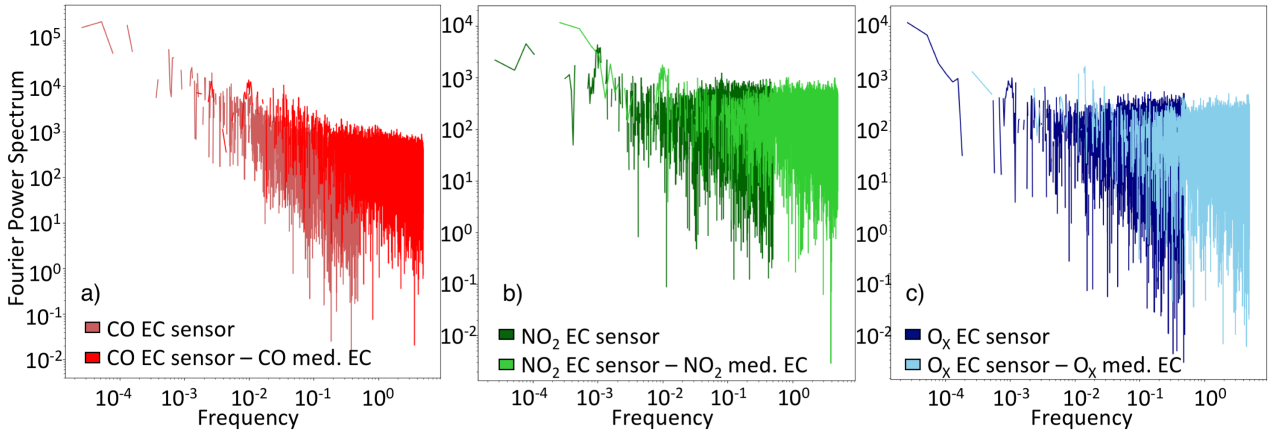

Figure 3.19: Each of the 18 electrochemical sensors was analysed by determining the power spectrum for that sensor. The power spectra all looked very similar for each sensor in it's respective CO, NO_2 and O_X sensor clusters, and so just one sensor from each clusters Fast Fourier transform is shown. The dark red, dark green and dark blue colours are the power spectra for one of each of the a) CO, b) NO_2 and c) O_X sensors and the lighter colours are the power spectra for the same sensors after normalisation.

sensors exposed to zero air are more characteristic of white noise, than they are of pink or red. It is advantageous to have residual noise being characteristic of white noise because it means that the residual noise was random and the noise was less due to impact from interfering factors. Environmental conditions, such as humidity and temperature, have less of an impact upon the EC sensor signals than they did upon the MOS signal. Smoothing and low-pass filtering techniques are more applicable for the reduction of noise in the EC sensors due to the residual noise being more representative of white noise. All three types of EC sensor did exhibit a small amount of higher power in the lower frequencies; for CO frequencies smaller than 10^{-1} Hz there was a slight increase in the power, for NO_2 and O_X EC there was an increase in power for frequencies smaller than 10^{-2} Hz. This is equivalent to the sensor signals displaying a non-random component of their signal in zero air over timescales for 10 seconds for CO and 100 seconds for NO_2 and O_X. These non-random variations over seconds to minutes the EC signals occur on similar timescales for which external factors vary. Using the normalised EC signals, by subtracting the median signal from the EC, caused the small increases in power to shift to higher frequencies; 10_0 Hz for CO, 10_{-1} Hz for NO_2 and O_X. This therefore, removed some of the influence of the environmental conditions upon the sensors as the non-random component of the residual noise then occurred over 10 seconds for NO_2 and O_X and 1 second for CO. The CO power spectrum (Fig. 3.19a) displayed the largest slope for the relationship between the frequency decreasing and the power increasing in both the EC and normalised EC power spectral density. This indicates that the CO EC are more influenced by the environmental factors compared to the NO_2 and O_X EC sensors (Fig. 3.19b and c).

3.4.3 Autocorrelation plots for the EC in zero air

Autocorrelation plots for the 6 CO, 6 NO_2 and 5 O_X sensors in zero air were determined to further assess the non-random component of the sensor noise.

The 6 CO sensors in zero air displayed autocorrelation plots that all began at 1, then as the time lags increased the autocorrelation between the original timeseries and time-lagged timeseries decreased relatively linearly (Fig. 3.20). At a time lag of 2000 seconds (approximately 30 minutes), all of the CO autocorrelation traces reached the 95 % confidence region. This means that the 6 CO EC sensors data was significantly correlated and non-random over timescales of less than 30 minutes. At time lags of greater than 3000 seconds (50 minutes) the correlation between the original timeseries and time lagged series has an autocorrelation coefficient of zero. At this point the variability of the 6 CO EC sensors in zero air is uncorrelated and potentially random. Variability in the sensors zero-air signal with a periodicity of greater than 50 minutes is not due to the sensors responding to changing environmental conditions or external factors, rather it is random.

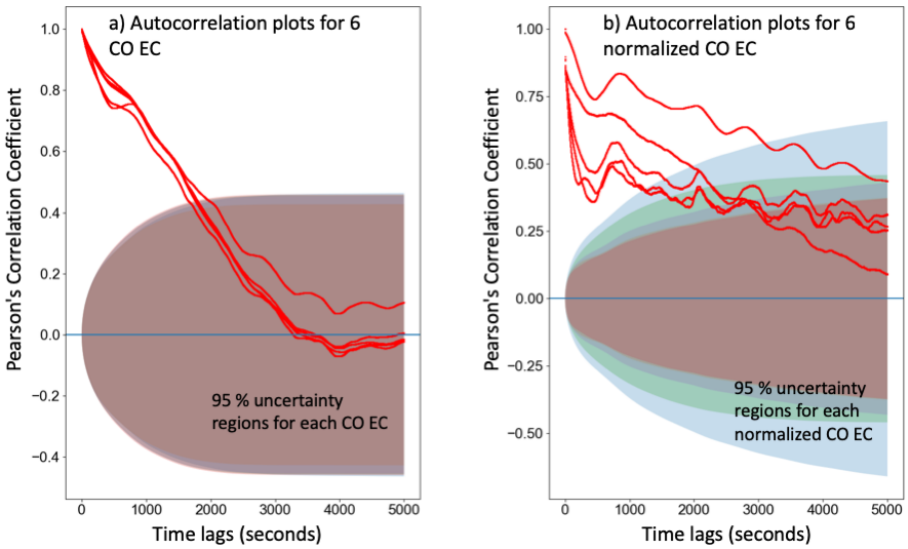

Figure 3.20: The autocorrelation plots for the 6 CO sensors in zero air (a) and the 6 normalised CO EC (b), after the median CO signal was subtracted from each sensor signal.

The six CO EC were normalised and the subsequent autocorrelation plots for the normalised sensors is displayed in Fig. 3.20b. Subtracting the instantaneous CO cluster median from each CO EC signal altered the autocorrelation plot but did not reduce the non-randomness in the CO signal. There was still statistically significant correlation for time lags up to 2000 seconds as before. The steepness of the slope by which the normalised EC became uncorrelated as the time lags increased was reduced compared to the CO EC and the correlation coefficient did not reach 0 at 4000 seconds (or even 5000 seconds) time lags. Therefore the normalised CO EC sensors displayed residual noise that appeared equally or even less random than the unnormalised sensors. The CO EC response was

influenced by factors other than changing CO concentrations and these interfering factors need to be accounted for before smoothing and averaging techniques are applied. For this experiment, subtracting the CO EC cluster median was not sufficient to remove the majority of variability in the CO EC responses that was due to the EC responding to interfering factors such as fluctuating temperature.

Figure 3.21 (a and b) shows the autocorrelation plots, with shaded 95 % confidence level, for the O_X and NO_2 EC, respectively. The O_X and NO_2 EC exhibited different performances compared to the CO EC in the zero air experiment.

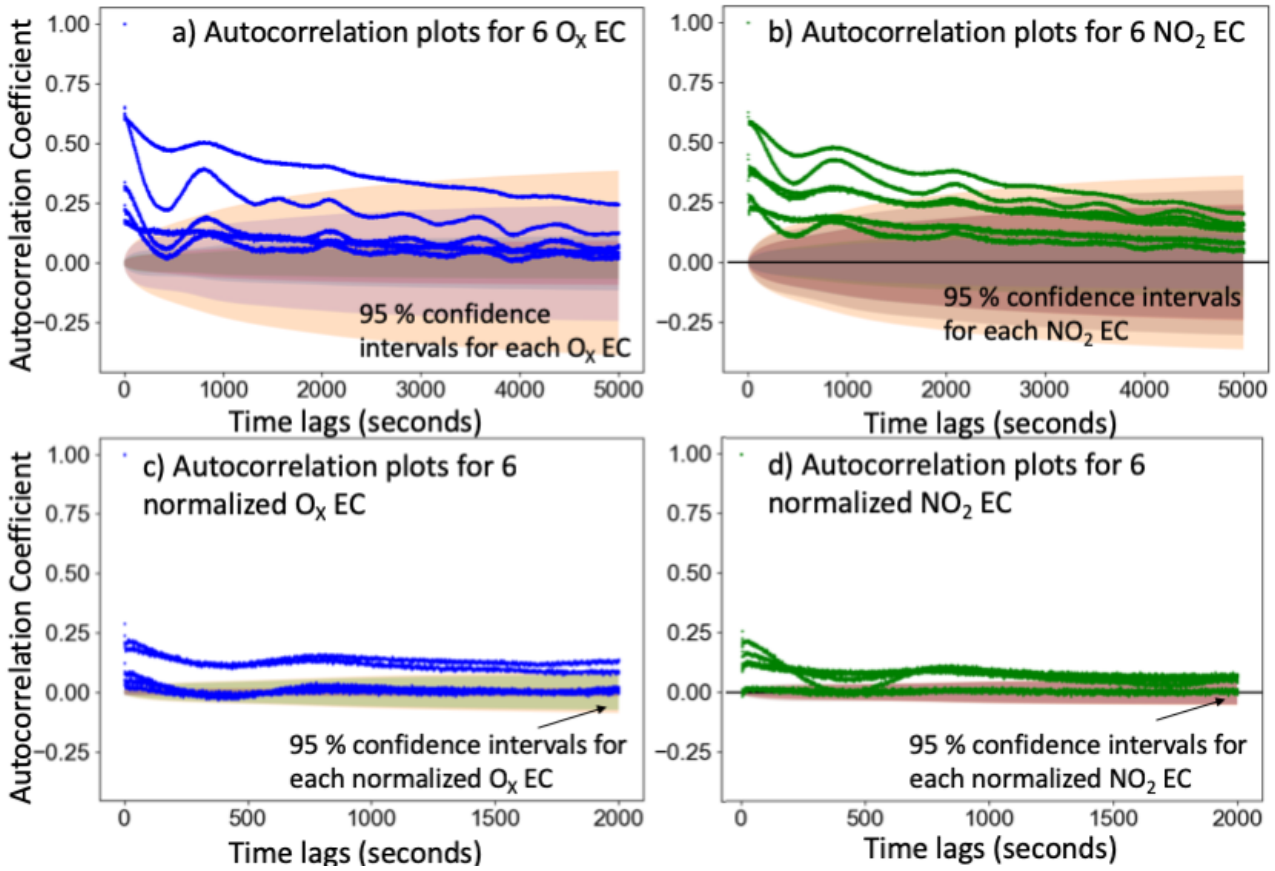

Figure 3.21: Plots a), b) show the autocorrelation plots for the O_X and NO_2 EC sensors during the zero air experiment. Plots c) and d) are the resulting autocorrelation plots when the median O_X and NO_2 EC sensor signal were subtracted from the respective signals to investigate the randomness in the EC noise signals. The shaded areas represent the regions of 95 % confidence levels.

The NO_2 and O_X EC signals began with a moderate amount of autocorrelation, c.a. 0.5 Pearson's coefficient for time lags between 1 and 200 seconds. At a time lag of 200 seconds, three of the four O_X responses in zero air entered the 95 % confidence interval. Although the zero air response for the OX sensors was non-random, the correlation between increasing time lags became statistically insignificant over a shorter timescale than the CO EC. The NO_2 performance in zero air was similar to the O_X EC, with the data considered statistically uncorrelated over the majority of the time lags.

Subtracting the median of the O_X and NO_2 clusters from each of the sensors in the respective clusters removed the majority of the influence of external factors. The autocorrelation plots for the normalised O_X and NO_2 EC in zero air were much more representative of randomness in the data set. There was low correlation over any of the time lags as the autocorrelation coefficient was close to zero and entered and remained inside the 95 % confidence intervals at very small time lags up to greater than 2000 seconds. Autocorrelation plots such as Fig. 3.21 c and d are what is expected for the residual noise in the EC signal to be considered random, not influenced by external factors and able to be treated as white noise.

3.4.4 CO EC variability

Six CO EC were deployed in Beijing, China for one month over the winter to investigate the performance of low cost sensors in a location where a large dynamic range of pollutant concentrations was expected. The CO EC sensors and CO reference instrument (CO Aerolaser) were co-located at the Institute of Atmospheric Physics (IAP), to the north of central Beijing (latitude 39.978, longitude 116.387). The sensors were housed inside a mobile laboratory (shipping container) which minimised the large fluctuations in environmental conditions. A KNF vacuum pump supplied a constant air flow rate of 1.5 sccm, and the CO EC were co-located and sampling from the same sampling line as a CO Aerolaser - the reference instrument for CO measurements. Every nine hours, using a BOC standard gas cylinder containing 1 ppm of CO in air, the Aerolaser AL5002 vacuum UV instrument was calibrated and zeroed. The CO EC sensors were all purchased from Alphasense and for the duration of this experiment were housed in a single machined flow cell, in rows of three. With each sensor purchased, Alphasense provides a unique factory calibration which was applied to the respective CO EC. The EC sensors were allowed 12 hours to acclimatise and warm up after initially receiving power, then they were all offset to each other, by 324 ppb - the difference between the CO EC and the Aerolaser in zero air.

Figure 3.22a shows the period of time where the Aerolaser and the sensors were running together. Each CO EC correlated really well with the Aerolaser (R^2 all greater than 0.95), depicting the same trends in the CO concentration and reporting the peaks and troughs to a similar degree. Nevertheless, in Fig. 3.22a it becomes apparent that already the sensors begin to spread out after a few days, with the response of the blue CO EC beginning to drop in particular. After this four-day period, the range between the six EC sensors was approximately 370 ppb. This is of concern if the sensors were to be spread out individually in a sensor network, as an ambient change of 370 ppb of CO is significant. For the campaign the spread in the CO EC sensors equated to 7 % of the total range of CO concentrations observed by the CO EC sensors.

In order to not report misleading results, the EC sensors would require daily calibration

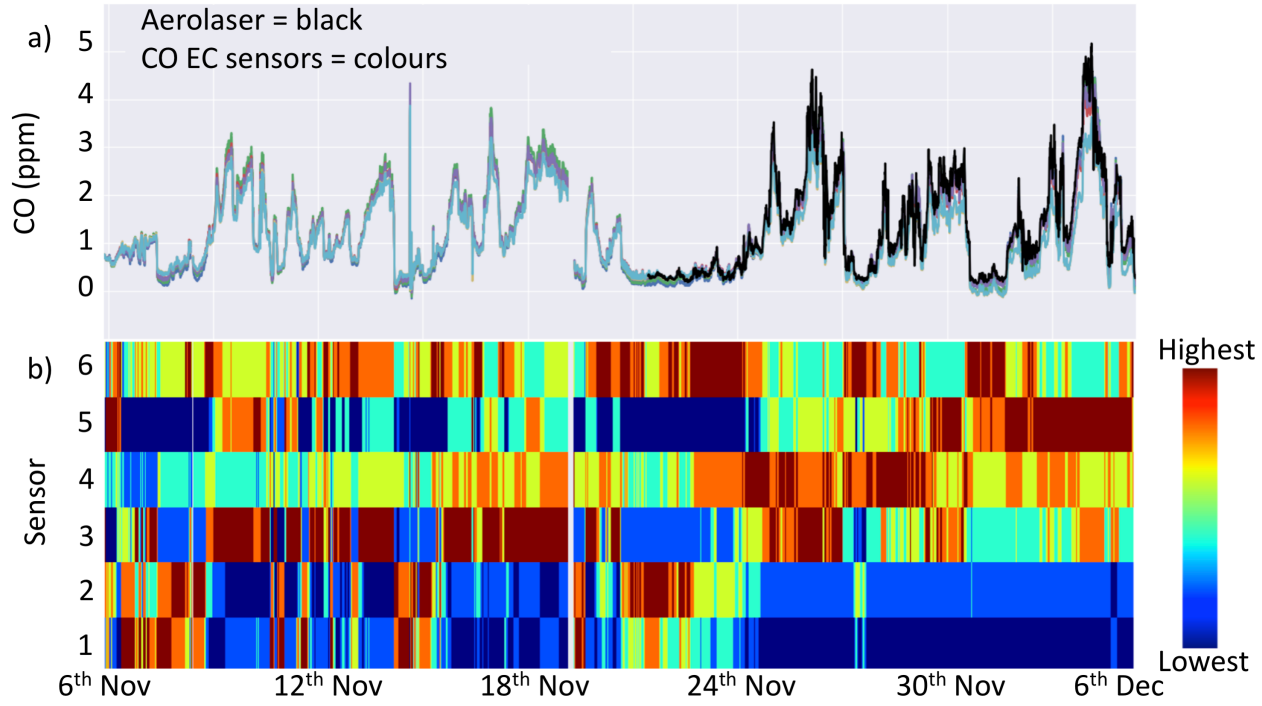

Figure 3.22: a) The time series of CO EC sensors (coloured lines) co-located with a CO Aerolaser reference instrument (black line). b) The rank order plot for 6 CO EC sensors sampling in Beijing, November and December 2016.

to be able to draw some information about the difference in CO in different locations with individually deployed devices. A clustering approach, as was introduced for the MOS sensors, where identical EC sensors are co-located and the median of the sensor ensemble is used as the CO signal for that area, was also investigated for use with the CO EC. The drift in the sensor response is very similar to that of the MOS sensors, with multiple time scales over which the sensors are affected by temporal drift. A rank order plot of the six CO EC sensors used here, is shown in Fig. 3.22b and the short term variability is evident by the constant changing of sensor ranked positions over the first few days. The amount that the six sensors change positions decreases after the 24$^{\text{th}}$ November, after 18 days of sampling indicating that the EC are still subject to medium term drift yet the signals have drifted too far apart to change the EC rank order after this time. For deployment, a calibration procedure must be developed. The random noise component of the EC noise on the short scales can be minimised by time averaging to a time scale less than the expected CO variability e.g. 15 minutes. The systematic decrease in sensor performance leading to medium term drift could be characterised more robustly using the ensemble technique. Clustering the EC would again provide the ability to apply a more appropriate linear interpolation between calibrations and any effects from outlying sensors would also be removed.

The CO Aerolaser provided a reference CO measurement for comparison with the individual and an increasing number of CO used in a cluster of CO EC sensors. The

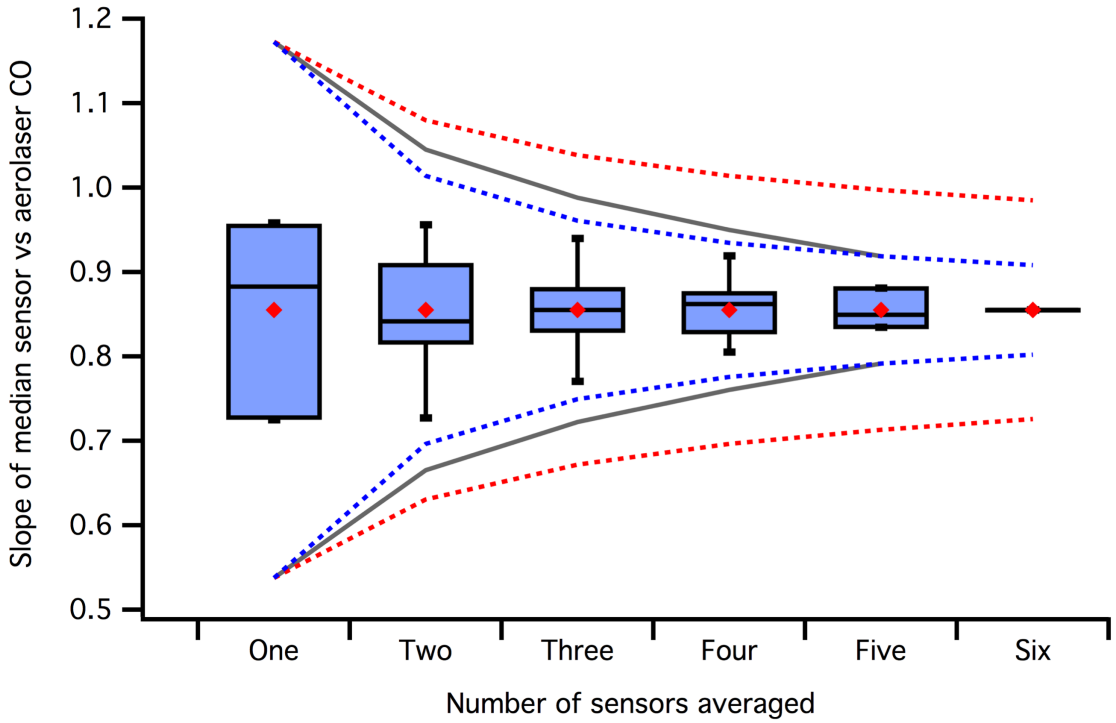

Figure 3.23: The slopes for the CO Aerolaser plotted against the average of different amounts of CO EC sensors. The red diamond is the mean slope, the edges of the box and whisker plots show the interquartile ranges and the whiskers show the 5^{th} and 95^{th} percentiles. The solid grey line is the ± 3 standard deviation of the mean. Plot taken from Smith et al. 2017 [165].

number of sensors included in a EC sensor cluster increase from one to six, with different combination of the sensors for each subset. E.g. For 'Two' in Fig. 3.23 there are 15 unique combinations of the six sensors when they are put into pairs. The average of these pairs was correlated with the CO Aerolaser and the slopes plotted as a box and whisker plot. The range of slopes decreases by 1/N as the sensor number increase from one sensor to six sensors in a cluster. The slopes approached 0.9, as more sensors were added showing that the sensors are not quite as sensitive to CO as the reference instrument was. The standard deviation of the slopes decreases as more sensors are used within a cluster and allows for better characterisation of the sensor drift, allowing for improved calibration. The EC reported a median slope of 0.997 during the first two days of the co-located sampling with the Aerolaser (21^{st} and 22^{nd} of November) and this decreases linearly to 0.917 for a two day period, ten days later. As the number of CO EC in the cluster increased the range of CO EC sensor sensitivities towards CO computed by averaging the sensors decreased. Figure 3.23 therefore indicated that for a cluster of EC the optimum number of EC sensors required is 6 sensors to obtain the maximum benefits from using a cluster of EC over individually located EC sensors.

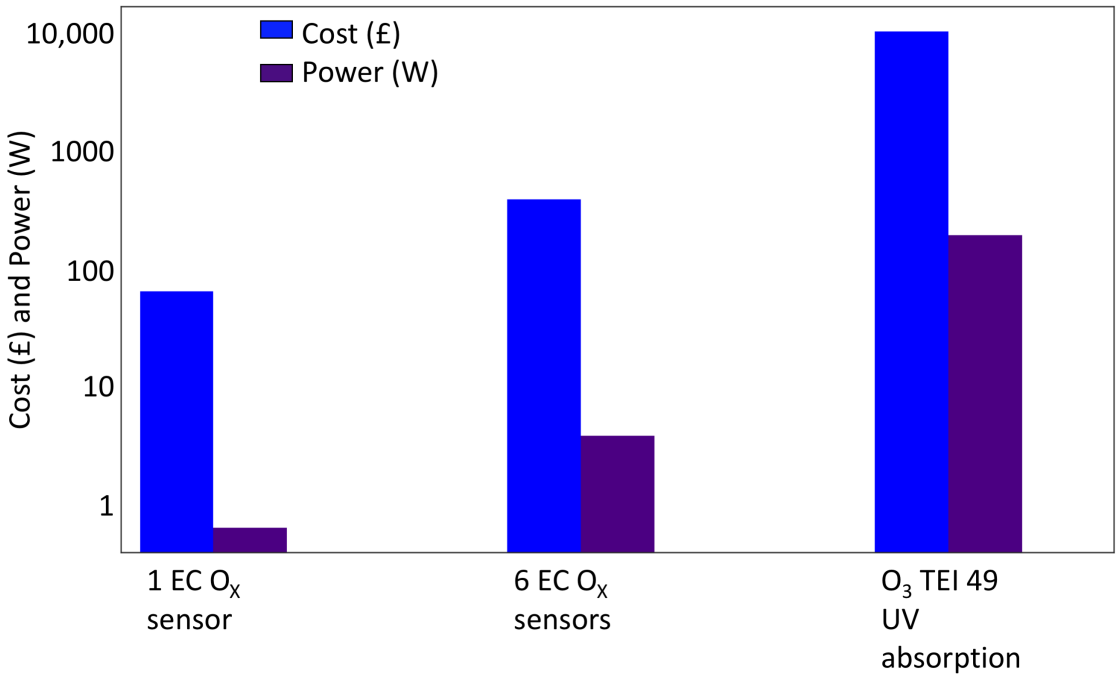

Figure 3.24: A comparison of the cost and power usage of a single EC sensor, a cluster of six EC and the respective O_3 reference instrument.

3.4.5 Clustering EC and MOS

As mentioned previously, clustering identical MOS or EC sensors increases the confidence in the VOC measurements made by MOS and can make the EC sensor measurements more robust. Calibrations can be less frequent (weekly, rather than daily) and linear interpolation between calibrations is sufficient for low-cost sensors. For subsequent low-cost sensor deployments as part of this project, clusters will be used and the instantaneous median for further analysis. This means that multiple sensors will be purchased and installed, but the overall cost of a cluster of these devices is still within the definition of 'low-cost'; less than a tenth of the cost of an equivalent reference instrument. The power consumption for a cluster of EC (same for O_X, NO_2 and CO) is 6 W, which is much smaller than the power requirements for the UV O_3 absorption instrument (150 W), see Fig. 3.24. This power saving is really important for deployments of low-cost sensors for remote locations or regions where there is a limited supply of electricity. MOS sensors are less expensive than EC so requiring eight sensors in a cluster, rather than six for the EC is still beneficial cost wise.

3.5 Summary of Chapter 3

The main findings from Chapter 3 are as follows:

- Individual MOS sensors exhibit different responses to VOCs when calibrations at the same humidity's were run a few days later. The sensitivity of the sensors was

shown to change by a factor of two over a week+ timescale.

- MOS sensors exposed to zero air for 2.5 days showed that they all responded to common factors in a similar manner, leading to a large variance in any single MOS sensor output. The variance was very similar between sensors and therefore subtracting the median MOS response from each of the individual zero air MOS traces lead to the variability due to environmental conditions being largely removed. This left a random noise signal that was more indicative of white noise and which was equivalent to ± 3 $ppb_{[VOC]}$.

- The indoor air experiment, which was conducted in relatively controlled conditions explored the differences between minute/hourly variability - which is correctable using linear interpolation - and changes to individual MOS sensor responses over week+ timescales. All 21 sensors, exhibited a high degree of correlation over the extent of the experiment, but the rank plot shows that there was evidence of long term drift as sensor signals spread out significantly.

- The MOS sensor output from the indoor air experiment was a combination of short term (6 hrs - 2 days) variability in the MOS sensitivities, mid-term (week+) drift due to the broadening of the sensor signals over this time and longer term drifts. The magnitudes and factors contributing to the drifts for the MOS sensors were non linear and complex leading to linear interpolation between MOS insufficient for deployment. For a working sensor network with individual MOS distributed to identify spatial trends quantitatively, calibrations would have to be on a daily basis. This is not viable as it would be impractical, for cost and time reasons.

- The MOS sensors deployed in the indoor air environment did exhibit timeseries' with a variability that would be expected of changing VOC concentration fluctuations. When there were fewer people in the office, the MOS signals were all low with less variability.

- There were no VOC reference measurements made during the indoor air experiment, but a co-located temperature measurement indicated that a large proportion of the variability observed in the MOS sensors signal was either due to the MOS response towards temperature fluctuations in the office, or temperature and VOC concentrations co-varying.

- The rank plot (Fig. 3.10) indicated that although the MOS sensors all generally displayed a high degree of covariance, individual MOS sensors within the group were all exhibiting small differences in their sensitivity to all eternal factors. This led to the MOS sensors randomly changing their ranked positions over short timescales, until the individual sensor signals were too spread out to cross over.

- As the Fig. 3.15 showed, the variability in the MOS slopes decreased as the average number of sensors was used in each group identical co-located sensors was used. The larger the group (up to c.a. 10 MOS sensors) the smaller the range of the slopes of the median sensor in the group compared to the median sensor over 21 sensors. This plot indicated that the optimum number of MOS sensors in a cluster was approximately 8 to 10 and the Fig. 3.23 suggested that 6 EC sensors was suitable for a sensor cluster.

- The EC sensors were exposed to zero air for 2.5 days and the autocorrelation plots and power spectrum indicated that these sensors also responded to changing environmental conditions. However the impact of these changing environmental conditions was less than for the MOS sensors. The normalised EC signals were more representative of white noise and therefore the residual noise was classified as random, so subtracting the median from each EC sensor was sufficient to largely remove the impact of the EC responding to interfering factors.

- The CO EC displayed a higher temperature dependency than the O_X or NO_2 EC.

- There was one MOS during the indoor air experiment that began to display large amounts of drift relative to the other MOS sensors. One CO EC sensor out of six in the zero air experiment also began reporting large amounts of drift relative to the other co-located CO EC. These sensors did not fail completely and still displayed similar variance in their signals compared to the other sensors in their clusters. This was a concern as it would not be suitable to deploy either EC or MOS sensors singly for use in a sensor network because it would not be apparent that these sensor had begun to drift if they was deployed on their own.

- Using a clustered approach, co-locating identical sensors and finding the instantaneous median of the cluster is a technique used here to improve sensor data quality, whilst maintaining the advantages of sensor technology. Clusters will increase the reproducibility of sensor data and make them more applicable for identifying target measurand distributions.

- Clustering approaches with MOS and EC is advantageous for improving the quality of low-cost sensor data, and a cluster of sensors still only costs a fraction of the price, and requires a small amount of power, compared to a research grade instrument.

- Using the clustering approach for MOS measurements will increase the robustness of the MOS data, however, currently the MOS sensors are not suitable to be deployed to make absolute VOC concentration measurements. The MOS response, with proper calibration for environmental conditions may still be suitable to investigate temporal patterns in total VOC pollution.

- The clustered approach was used for all future work with EC and MOS sensors to improve the quality of senor data. The instantaneous median of a sensor cluster was used to minimising the mid-term drift in the sensors, facilitate the identification of outlying sensors and remove the effects of sensors experiencing large amounts of drift, whilst still being representative of the cluster.

- The next part of the sensor development process was to develop a multi-pollutant sensor device, containing clusters of LCS to monitor ambient pollution with co-located reference instruments.

Chapter 4

Initial field deployments of a clustered sensor device

A multi-sensor instrument, incorporating clusters of low-cost sensors was designed and built to monitor several common gaseous pollutants.

4.0.1 Experimental

There were four clusters of eight TGS2602 total VOC sensors, and one cluster each of six CO EC, six NO_2 EC and six O_X EC, contained inside one instrument manifold. The number of 6 sensors per EC cluster and 8 sensors per MOS cluster was derived from the experiments from the previous section, see Fig. 3.23 and Fig. 3.15. The previous laboratory experiments have shown that the sensors are all sensitive to large changes to the humidity and temperature of the air, and that they produce a more consistent performance with a steady flow of air. To that note, two KNF pumps were installed inside the box to pull 2500 sccm over the sensors and two humidity and temperature probes monitored the flow of air to the sensing surface. Each MOS contains an internal heater so to minimise the affect this may have on the temperature/humidity or composition of the air the MOS were placed to receive air after the EC. There were four custom circuit boards with identical circuitry to the boards used in previous experiments to mount the 32 MOS. A custom-designed Teflon manifold isolated the air flow to the sensors from the air inside the instrument. The EC were purchased with their own Individual Sensor Boards (ISB) and a second, custom designed circuit board was connected to this to control the supply voltage and set an address for each sensor. To maintain an airtight manifold throughout the sensor instrument, the EC sensors were mounted upon an Alphasense housing connected by Swagelok.

In total, there were 50 gas sensors detecting air contaminants and two temperature and humidity probes. There were two micro-controllers (Arduino Uno) which collected 3 Hz data from each set of 25 sensors, (Fig. 4.1), to allow data to be transmitted every two

seconds, with minimal data loss due to the time required for the micro-controller to dispatch each data point. The schematic in Fig. 4.1 was then exactly duplicated for the second Arduino. Figure 4.1 also shows the addresses given to each sensing device. The multiplexer allowed multiple 12C channels - labelled in Fig. 4.1 as the white boxes - and therefore the four different 12C addresses were allowed per channel.

A 19" 4U aluminium box was used to house the sensors and all the electronics, see Fig. 4.2. The two sets of sensors sat on shelves within the sensor instrument. Fans were built into the sides of the box to maintain a good flow of air around both of the shelves of the box to prevent the MOS heaters, the pumps and the power supply causing overheating of the EC and MOS sensors. Noisy electronic devices, such as the power supplies and pumps were kept apart from the sensors, on the other side of a metal partition which acted as a Faraday cage.

The entire sensor instrument had a total expense of £5k, yet since this was to be used to monitor multiple pollutants (O_3, NO_2, CO and VOCs) it is still considered low-cost because the combined cost of all these species reference instruments is approximately £200k. The combined power usage of the sensor instrument was approximately 52 W, maintaining the power benefits of low-cost sensor technology. The sensor instrument was built and tested in the laboratory in York, then deployed as part of a large air quality campaign occurring in Beijing, China.

4.0.2 Deployment of the sensor instrument at a static site in Beijing

The sensor instrument (Fig. 4.2) was located at the Institute of Atmospheric Physics (IAP), to the north of central Beijing (latitude 39.978, longitude 116.387). The instrument was co-located with other research-grade instruments as part of a large summer air pollution campaign, between 29th May and 26th June 2017. Beijing is a mega city; with a large population, extensive vehicular fleet and lots of industrial factories [69]. Therefore the gas contaminant levels were expected to have both a large dynamic range and be elevated, giving the low-cost sensors the best possible chance of detecting pollution patterns. The sensor instrument was installed inside a mobile laboratory (customised shipping container), which semi-controlled the meteorological conditions experienced by the sensors. The air humidity ranged between 3.82 and 17.83 g m^{-3} (17 to 90 % RH) over the course of the campaign, and the air temperature varied between 15.6 °C and 41.2 °C. There were several reference instruments located at the same site and the measurements from these were used for evaluating sensor performance. The references for VOCs, NO_2 and O_3 were connected to the same 3 m high sampling line as the sensor instrument and therefore the sensor instrument and reference instruments were all sampling the same air and could be used evaluate the sensor performance. The sample line had a diaphragm pump to provide

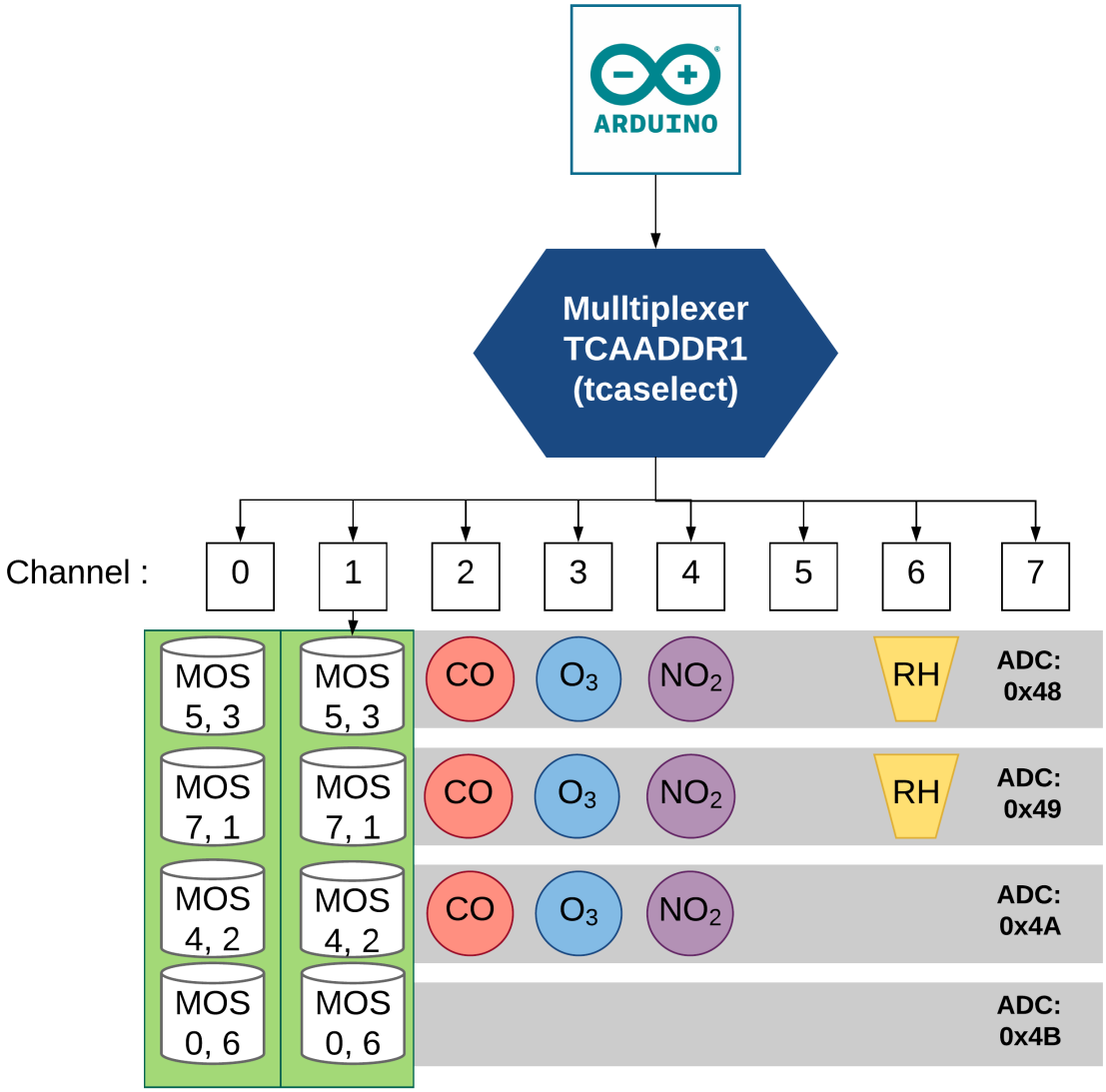

Figure 4.1: Electronic schematic to show how half of the sensors will be laid out in the sensor instrument. Two MOS sensors were permitted for each ADC channel, and the number of the sensors, relating to their position on the circuit board is shown in the schematic. The EC sensors required data collection from both the working and auxiliary electrode therefore there could only be one sensor per address. The humidity and temperature probes are recorded via this Arduino too. This set up was then duplicated for the other 25 gas sensors. A mini-computer (LattePanda 4G/64GB, Latte Panda) formatted and stored the sensor data after receiving it from the Arduinos.

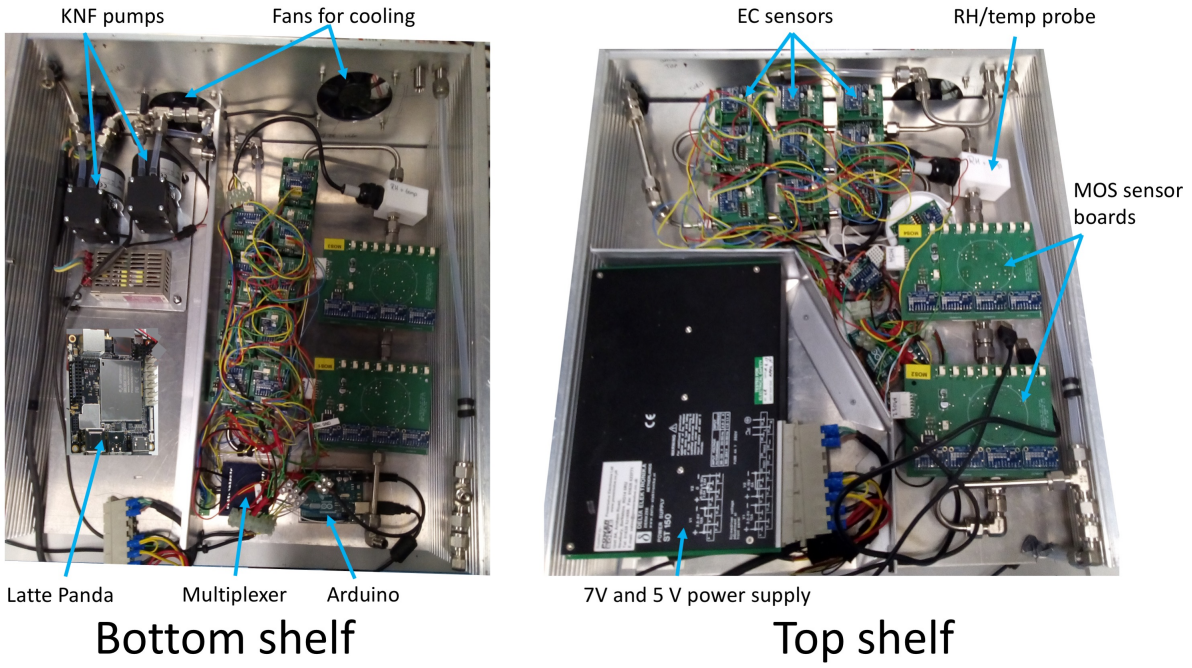

Figure 4.2: Photographs of the two layers of components within the sensor instrument deployed in Beijing, China. Components of interest are labelled with blue arrows.

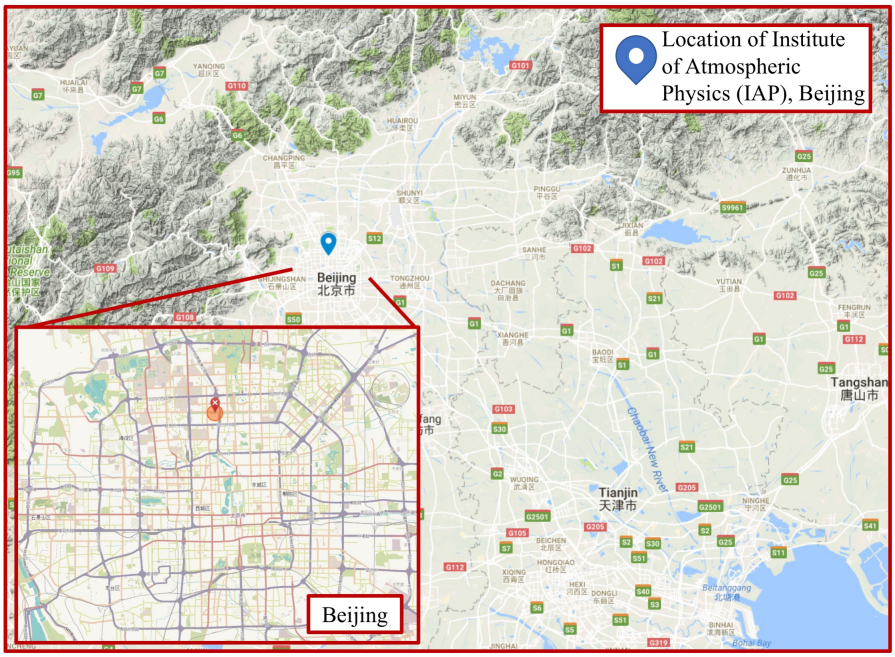

Figure 4.3: The blue pin shows the location of the measurement campaign site where the sensor instrument was located (IAP site) with respect to the surrounding region of Beijing, China. The inset map shows the central and northern location of the IAP site amongst Beijing's road network.

a flow through to all instruments connected to it.

The reference instruments were as follows:

- Cavity Attenuated Phase Shift (CAPS) for the measurement of NO_2 (Teledyne T500U, Teledyne California), which was calibrated regularly using a certified 100 ppb NO_2 in N_2 cylinder. NO_2 can be measured with this instrument with a precision of 0.1 ppbv and 5 % uncertainty. Operated by Professor James Lee and Freya Squires during the campaign.

- A Thermo Environmental UV absorption photometer (TEI49i) monitored O_3 with a precision of 1 ppb and an uncertainty of 2 %. A reading was taken every 1 minute and the instrument is calibrated with a National Physics Laboratory O_3 gas standard. Operated by Professor James Lee and Freya Squires during the campaign.

- GC-FID was used as a reference instrument for VOCs. This is a very precise and accurate method and can quantify C2 to C10 carbon containing compounds. Operated by Dr. James Hopkins and Dr. Rachel Dunmore during the campaign.

- A CO Aerolaser VUV fluorescence analyser model AL5002 measured CO at 5 Hz, with 3 ppb precision and 2 % uncertainty. This however, was not located in the same shipping container, but sampled CO 100 m above ground. Operated by Professor James Lee and Freya Squires during the campaign.

4.1 Warm-up time

The entire deployment of the sensor instrument at the IAP site in Beijing, China lasted from 1700H on the 30th May 2017 until the 26th June 2017. However, the data analysis begins at 00:00 on the 2nd June 2017 to give the sensors enough time to warm up; time to reach chemical equilibrium with the atmosphere after receiving power [136]. The sensor instrument had been packed up for a month before receiving power and the time required for the sensors to acclimatise can be up to several hours. During the warm-up period, any volatile compounds that may have adsorbed to the cold sensing surfaces will evaporate [136] and the sensing surfaces will reach their optimum temperature for operation. Allowing for a warm-up period ensures that the sensors are responding to changes in their surroundings and the sensor response is not due to the sensor signal impacted by acclimatisation, e.g. as the MOS sensing surface heats to its optimum temperature, the sensor signal will be impacted as the rate of reactions and interactions of the surface are increased. Alphasense supplied the EC sensors and there are sensor model specific warm up periods recommended on the Alphasense website. These were 2 hours for the NO_2, O_X and CO EC. Therefore it was thought that a warm-up period of two days would be

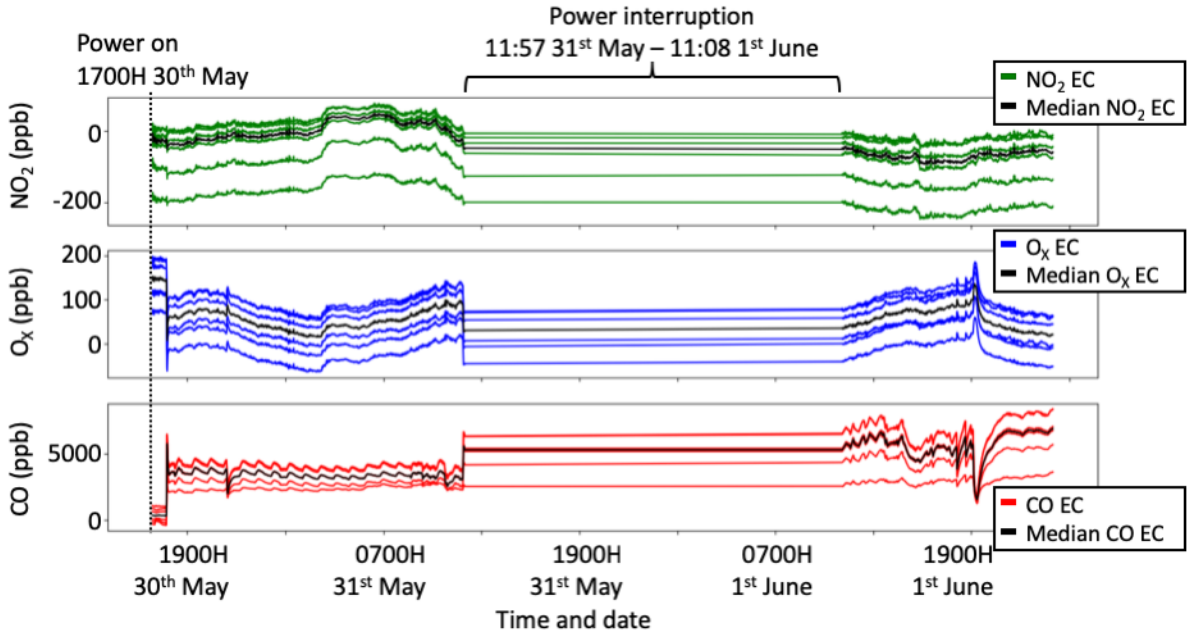

Figure 4.4: The a) NO_2, b) O_X and c) CO EC during the warm-up period between 1700 H on 30th May 2017 until 00:00 on the 2nd June 2017.

sufficient for the sensor instrument. The time series for the NO_2, O_X and CO EC during the warm up period are displayed in Fig. 4.4.

All EC sensors exhibited a step change in their signals after an hour of deployment (Fig. 4.5) that was attributed to the sensors acclimatising to their environment after the power was supplied to the sensors. The environmental conditions, RH and temperature remained constant during this time so were not responsible for causing this change. This step change of -23.3 ppb for NO_2, -135 ppb for O_X and +5414 ppb for the CO EC was therefore assumed to be the sensors responding within their warm-up period and not due to changes in the atmospheric composition. All of the median EC signals experienced a large step change that began at 17:44 and peaked 2 minutes later (17:46). The signals then partly recovered so that the NO_2 stabilised at -52 ppb, the O_X median stabilised at 61 ppb and the CO stabilised at 3371 ppb, 8 minutes after the step change began.

The power was interrupted after the sensors had run for 19 hours (Fig. 4.4). It was thought that the power supply was not disrupted for long enough to require a second warm up period, but the EC signals were monitored in case one was needed. There was no evidence of another step change within two hours of the power being restored. However, the overall warm-up period was extended to 00:00H on the 2^2 June as a precaution.

There was less evidence of the MOS signals requiring a warm-up period, as the MOS sensor signal appeared to perform in the same manner consistently throughout the warm-up week. The MOS sensing surfaces are required to reach an optimum temperature of 270 °C, and it was thought that the MOS sensor baseline would increase steadily whilst the sensing elements were increasing in temperature [136]. However, the median MOS signal

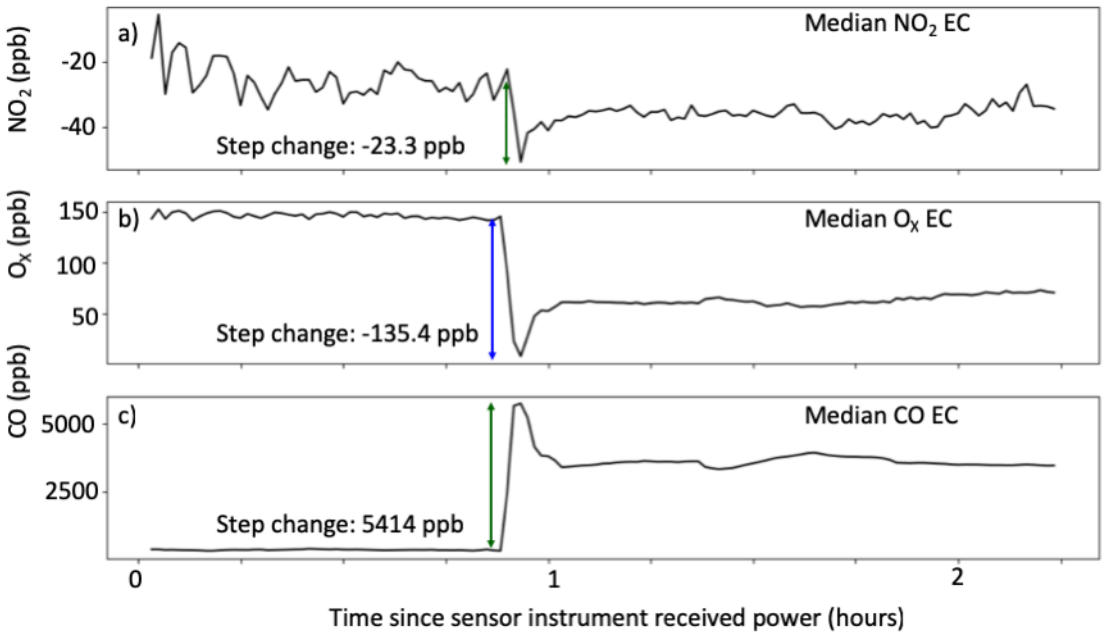

Figure 4.5: Each of the EC sensors experienced a step change that occurred within two hours of the power to the sensor instrument being switched on. This was attributed to the sensors warming up after being packed in a shipping box for a month.

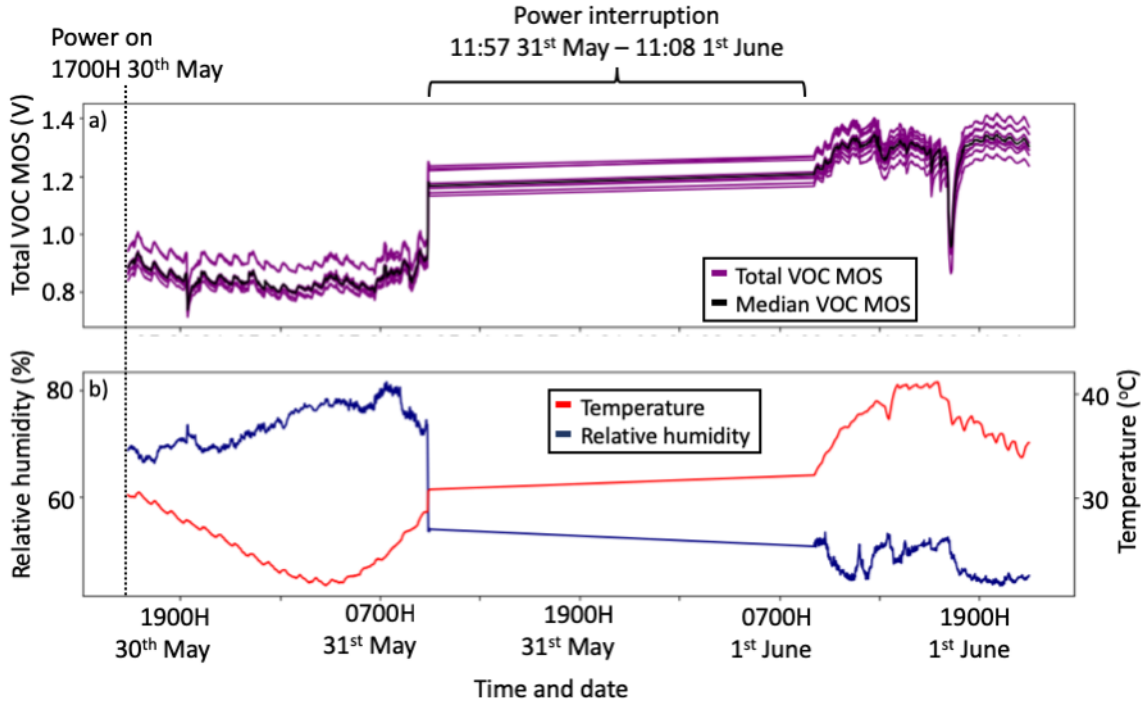

Figure 4.6: The interaction between the median total VOC MOS signal (black) and the individual MOS sensor signals (purple) was consistent throughout the warm-up period. The variations in the median MOS signal were more influenced by the temperature of the air (b, red trace) flow than displaying any discrepancies due to MOS requiring a warm up period.

decreased from 0.8 to 0.9 V over nine hours (until 0400H 31st May, before beginning to increase again. There were regular high-frequency fluctuations (approximately every 30 minutes) in each MOS signal; this feature, and the steadily decline in the MOS signal over 9 hours were attributed to the changing temperature of the air flow as this varied on the same timescales. The CO EC sensors also exhibited high frequency fluctuations in their signals which occurred every 30 minutes, Fig. 4.4c. The changing temperature of the air flow to the sensors caused this feature and the effect was therefore minimised when the sensor instrument was insulated from the temperature source (GC oven) so the effect disappeared after 1300H on the 1st June and was not observed again. The RH ranged between 43 - 82 % (mean (62 %) during the warm-up week, however there were no sudden changes and although the RH would have influenced the MOS signal baseline, the effect was minimal. Overall, the EC exhibited behaviour within an hour of receiving power that was not attributable to the temperature or RH and was believed to be due to the EC sensors requiring a warm-up period. This agrees with Alphasense, that the EC sensors required a two hour warm up period. After the disruption of power mid way through the warm-up week however, there was no evidence in the EC data that they required a second warm-up period. The MOS sensors did not exhibit behaviour that was attributed to them not responding to the changing conditions of their surroundings. The temperature of the air flow to the MOS had the greatest impact upon the MOS signals.

4.2 MOS sensor performance

One MOS sensor failed upon arrival and was subsequently removed from all analysis. The first three days (30th May to 2nd June 2017) of analysis were also disregarded as the MOS sensors require a warm-up period after being packed up and turned off for travelling. The 31 working MOS sensors were all offset to 0 V at the beginning of the time series (2nd June) and left to run continuously for 24 days (Fig. 5.35). The sensors behaved as expected, with all 31 sensors show a lot of variation during their deployment.

As observed previously with MOS, all 31 sensors respond to common factors leading to high amount of inter-sensor correlation (Fig. 4.8) and a general trend that is well represented by the median sensor signal. Two of the MOS report noticeably higher values compared to the other 29 MOS sensors, and the use of the median, rather than the mean MOS, ensures that this effect is removed from the average MOS signal.

The correlation matrix clearly identifies the two anomalously highly reporting MOS sensors as sensors 8 and 15 in Fig. 4.8. This was a good method for detecting which MOS sensors are potential outliers and could be used in the future to pre-select the MOS senors before deployment in the sensor instrument. The Pearson's coefficient between all other sensors are greater than 0.8, indicating a high degree of correlation. MOS sensors 2 and 14 in Fig. 4.8 also show a lower Pearson's coefficient than the other 27 sensors, suggesting

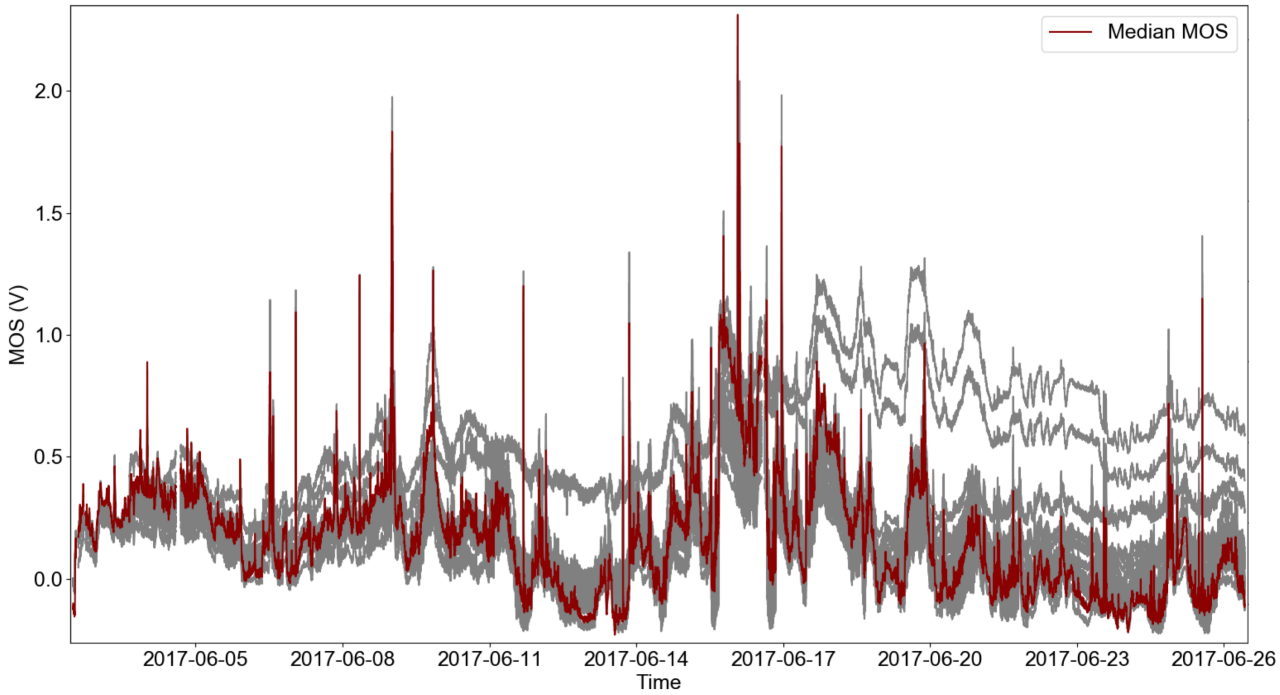

Figure 4.7: The instantaneous median (red) of all 31 TGS2602 total VOC working MOS sensors (grey) represents the general trends of all the MOS sensors well.

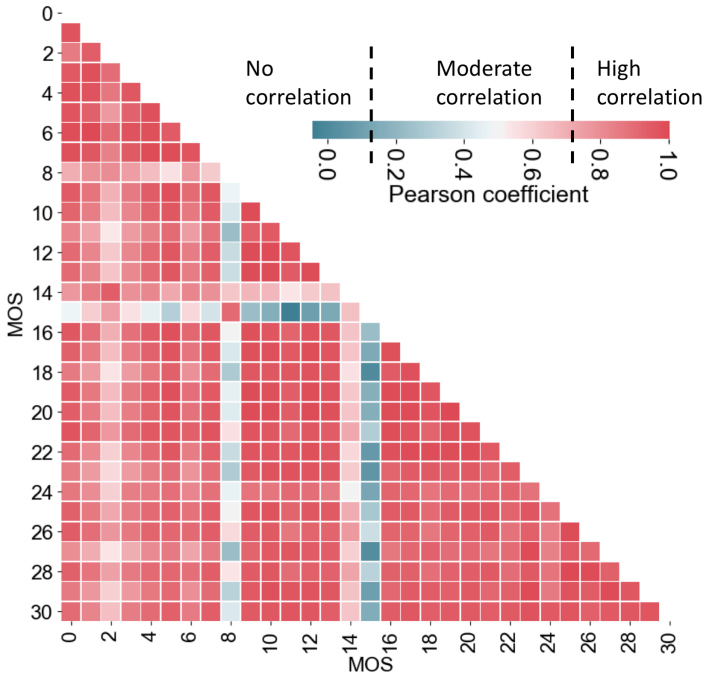

Figure 4.8: A correlation matrix, using the Pearson's coefficient to compare the correlations between every MOS with all the other MOS sensors. The colour bar shows that a high correlation is denoted by a red colouring and no correlation is dark blue. The majority of MOS sensors are highly correlated, displaying a Pearson's coefficient of greater than 0.8.

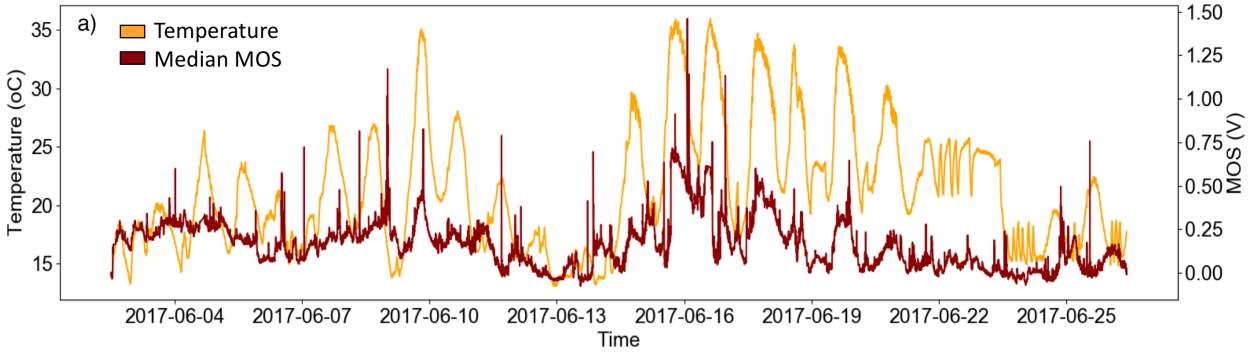

Figure 4.9: Timeseries of the median MOS signal (dark red) and the temperature of the air flowing to the sensors (yellow).

that these might be subject to a large amount of drift and could potentially join sensors 8 and 15 as failing sensors in the near future. Flagging up sensors in this manner is useful as sensors can be swapped out for working sensors easily. Each time multiple identical MOS sensors have been used for an experiment some have failed immediately and require removal from the data or swapping out straightaway or after a few days of deployment. This emphasises the need for clusters of MOS sensors, as, experience has shown that typically 10 % of sensors exhibit large amounts of drift (e.g. sensors 2 and 14 in Fig. 4.8) or fail, either upon deployment or a short time later. Using large numbers of these sensors improves the reproducibility of the sensor measurements and using the median removes the effects of sensors experiencing anomalous amounts of drift.

4.2.1 MOS temperature and humidity correction

The temperature and humidity probes monitoring the conditions of the air reaching the sensors were compared to the median MOS signal to gauge the effect of these two variables upon the MOS baseline.

There was a lot of variation in the temperature of the air flow reaching the sensors, Fig. 4.9 and may have impacted the median MOS sensor signal. However, the median MOS trace does not entirely correlate with the temperature variations and there are some MOS peaks that occur on a shorter timescale than the fluctuations in temperature.

There is some structure within the median MOS timeseries that does not appear in the temperature timeseries (Fig. 4.9) indicating that the median MOS signal is a superposition of a signal due to the total VOC concentration and the sum of the signals due to environmental conditions such as temperature and humidity. Generally, there was a positive correlation between the median MOS and temperature timeseries; as the temperature increased, the median MOS sensor signal increased, see Fig. 4.10a.

The gradient between the two parameters was +0.0136 V $^{\circ}C^{-1}$, and this was comparable to the laboratory experiments which had a slope of +0.0483 V $^{\circ}C^{-1}$ (these were conducted under different conditions e.g. at 0 % RH so were expected to be slightly different but

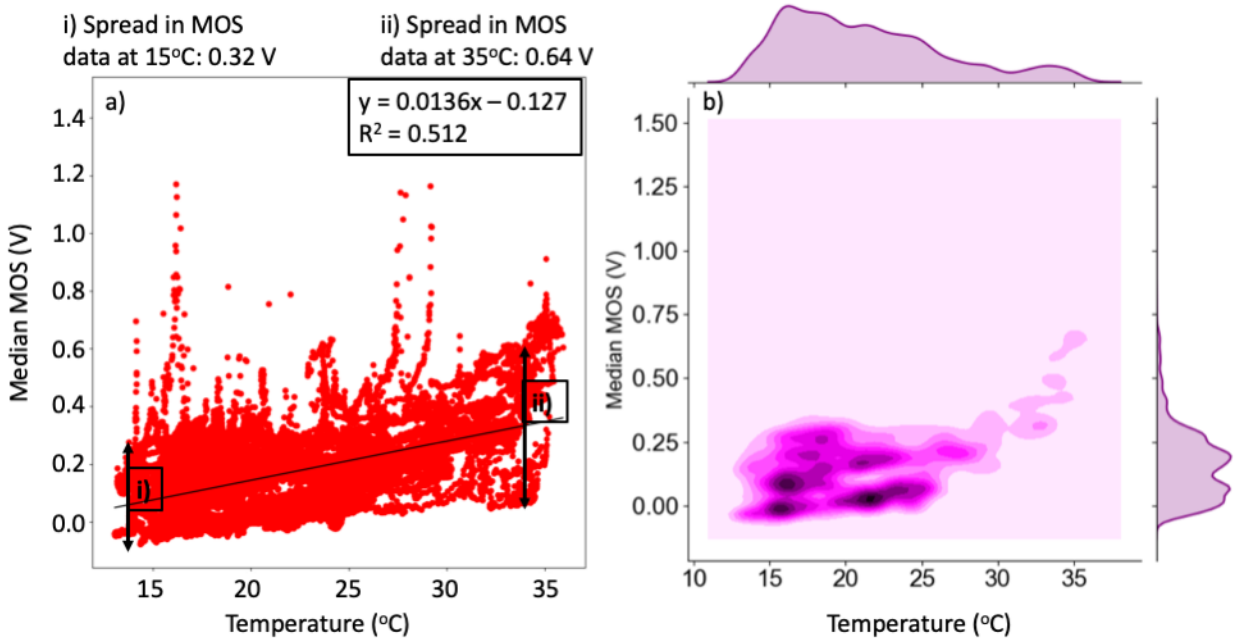

Figure 4.10: The correlation between temperature and the median MOS signal during the deployment of the sensor instrument in Beijing. b) The kernel density function for the temperature and median MOS data to display the relative distributions of data.

within the same magnitude) and an R^2 of 0.5. However, the median MOS sensor data was spread over a large range around the trend line, with the uncertainty around the gradient approximately ±0.16 V at 15 °C and this increased to ±0.32 V at higher temperatures (35 °C). The kernel density distribution, Fig. 4.10b shows the distributions of the median MOS and temperature timeseries. The majority of temperatures observed were between 15 and 25 °C, with fewer higher temperatures recorded. The kernel density plot shows that there are two distinct subsets of data for these temperatures, each with a linear gradient. The two gradients appeared to be very similar, with an offset between the two trend lines, Fig. 4.10b, rathe than a chagne in the magnitude of slope. The two subsets of data led to two distinguishable peaks within the MOS distribution between -0.05 and 0.25 V. This indicates that the MOS sensitivity towards temperature may have changed over the course of the sensor deployment in Beijing.

A temperature correction was determined by using the linear equation derived from the correlation plot in Fig. 4.10a to calculate the expected MOS signal at the temperature of the air flow.

$$y(MOS(V)) = 0.0136x(Temperature(^{\circ}C)) - 0.127 \tag{4.1}$$

This temperature correction (Fig. 4.11, red trace) was then subtracted from the original median MOS to leave the temperature corrected median MOS signal, see Fig. 4.11, green trace.

After the temperature correction was subtracted, the remaining MOS signal had a

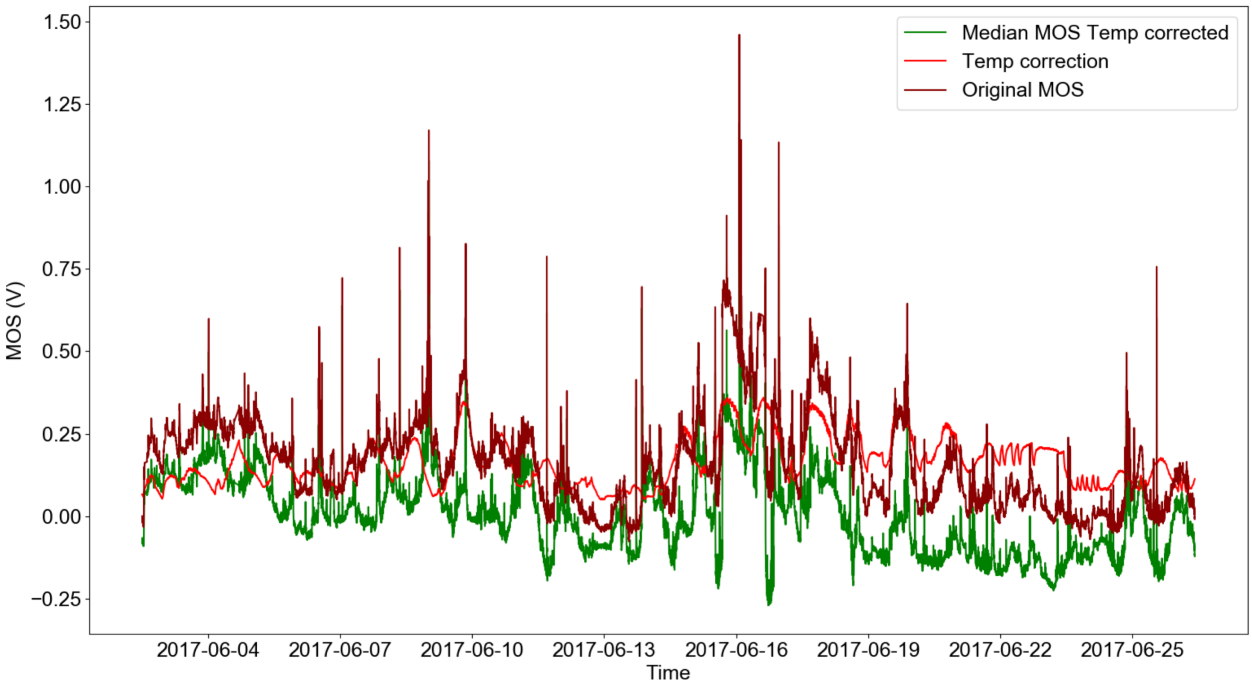

Figure 4.11: The original median MOS sensor (dark red) had the temperature correction (red) subtracted away from it to leave the temperature corrected MOS signal (green). The temperature correction was determined by calculated the expected MOS signal, from fluctuations in temperature, using the linear equation in Fig. 4.9.

flatter baseline, with less evidence of drift and some of the large fluctuations in baseline reduced, leaving the spikes in the MOS signal more prominent. This was advantageous because the MOS signal is a superposition of the MOS responses to VOCs, RH, temperature and other cross interferences, but can be corrected for temperature. The partial removal of the impact that fluctuating temperature has on the MOS emphasises the peaks in the MOS signal that are due to other variables, namely changing VOC concentration.

A similar process was used upon the original MOS signal to determine a RH correction. There were two RH probes monitoring the relative humidity of the air reaching the sensors. These reported relative humidity values which were then used to identify how the humidity of the air affected the MOS sensors. The RH probes did however, report RH values that were greater than 100 %, so it was assumed that they had an offset. The data was not removed because the RH probes did not show any indication of failing as there was still structure in the data and the variance within the RH was more important than the absolute values for assessing the RH impact upon the MOS.

The kernel density distribution in Fig. 4.12b, shows that there was a lot of variation in the RH of the air to the sensors although the RH was approximately 90 % for the majority of the deployment. There was no evidence of two RH gradients within the kernel density distribution for the median MOS and RH, but the overall negative correlation between these variables was observed in Fig. 4.12b. The correlation plot of RH and MOS (Fig.

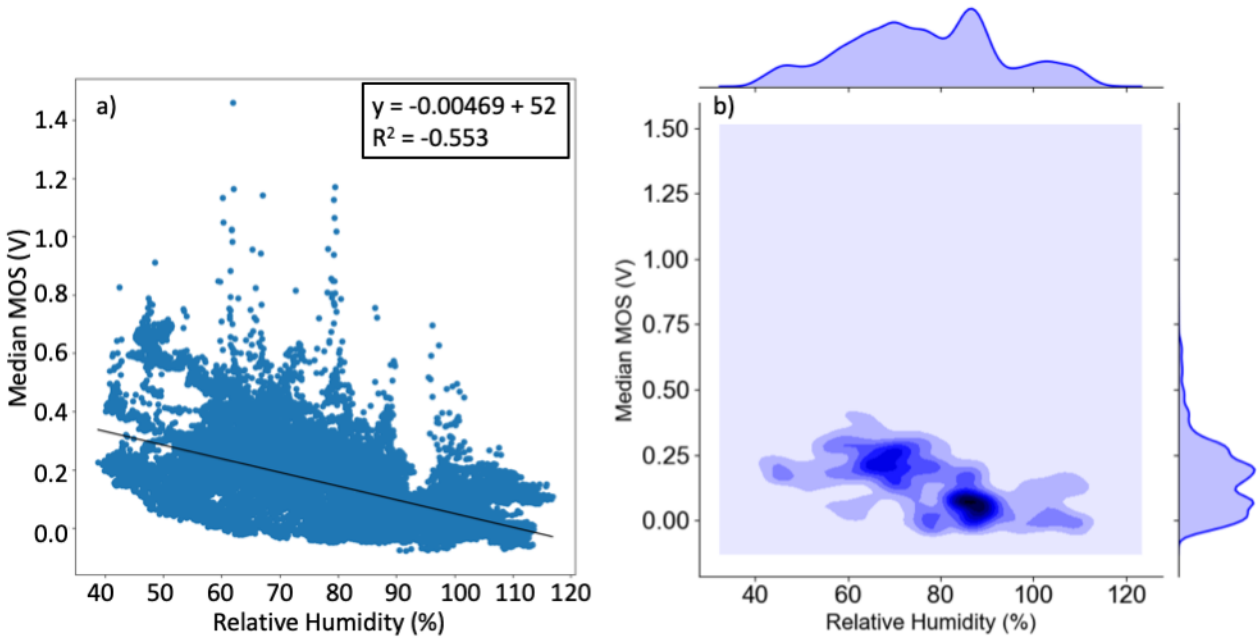

Figure 4.12: There was a negative correlation between the median MOS signal and the relative humidity as measured by two RH probes (a). b) The kernel density plot for the relative humidity and median MOS signal.

4.12a) yielded the linear equation: y(MOS) = -0.00469 x(RH) + 0.52, and this produced an RH correction (MOS signal calculated entirely from the fluctuations of RH). The R^2 for the RH and median MOS correlation was moderate and negative (-0.55). To correct for both temperature and humidity, both the temperature correction and RH corrections were subtracted from the median MOS signal, leaving the dark red line in Fig. 4.13.

The corrected median MOS displayed a flatter baseline compared to the uncorrected median MOS signal. There was still a lot of variance within the corrected median MOS signal and this was potentially due to changed to the VOC concentration in the sampled air flow. The remaining spikes and variance within the median MOS signal were examined to see if they were related to the MOS responding to fluctuating VOC concentrations, by comparing with the VOC reference instruments, such as GC-FID.

4.2.2 MOS versus GC-FID

There were a few challenges when comparing GC-FID observations to the MOS performance because of the differences in sampling techniques.

Each data point from the GC represents an average of ten minutes sampling to the trap. The time resolution is limited to the time required for the compounds in the sample to elute through the column, in this case 40 minutes, leading to a 10-minute averaged data point every 43 minutes. Data from the median MOS timeseries was selected where it temporally overlapped with the GC-FID ten-minute sample time. An average, the mean, of the instantaneous median MOS signal was calculated for this ten-minute period and

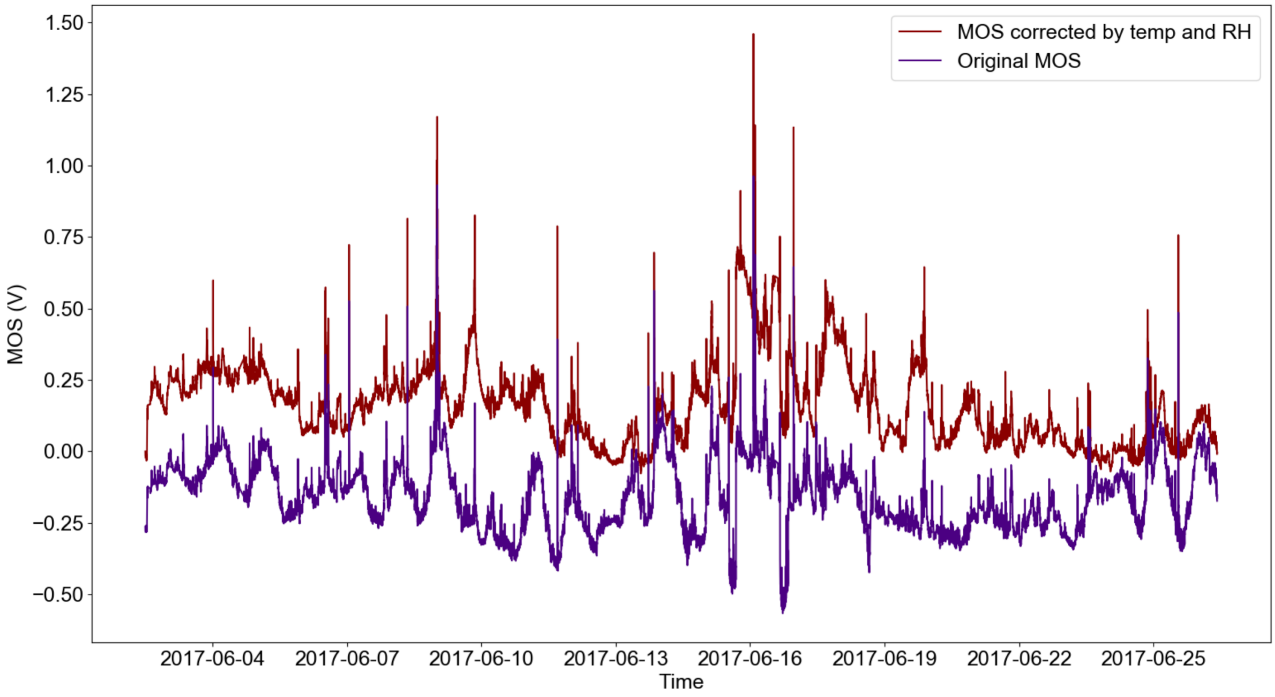

Figure 4.13: The MOS sensors are easily affected by changing RH and temperature in their environment and so both a temperature and humidity correction, calculated using the China MOS signals, has been subtracted from the median MOS signal (purple). The temperature and humidity corrected MOS signal is shown in dark red.

this was compared to the GC-FID to evaluate the performance of the MOS relative to the *in situ* GC-FID. The MOS and GC data sets were merged and where there was no time overlap between data points these were removed, so that they both contain the same amount of data points that occur at the same time. The MOS signal is a measure of the bulk VOC concentration in the air sample and therefore the GC-equivalent of Total VOC was computed by summing up the concentration of each of the 29 VOC compounds that the GC-FID detected during that sampling time. The temperature and humidity corrected median MOS signal was used to compare against the GC. The median MOS was offset to 0 V at the beginning of the analysis and a sensitivity of 5 mV ppb^{-1} was used to convert the voltage signal to $ppb_{[voc]}$. The absolute values of the median MOS are meaningless and the purpose of the investigation was to identify covariance between the GC-FID data and the median MOS, so 0 V was chosen as an initial MOS voltage and concentration to help identify any drift in the MOS signal too.

Referring to the general shape of the total VOC concentration from the GC versus the corrected median MOS in Fig. 4.14a, there was a reasonable comparison between the two instruments. The median MOS signal identifies a lot of the same main peaks, resulting in the same approximate pattern in VOC concentration as the GC time series. Between the 9^{th} and the 15^{th} June, both the GC-FID and the MOS signals show lots of variability in the total VOC concentration, with the peaks in both signals occurring at the same time.

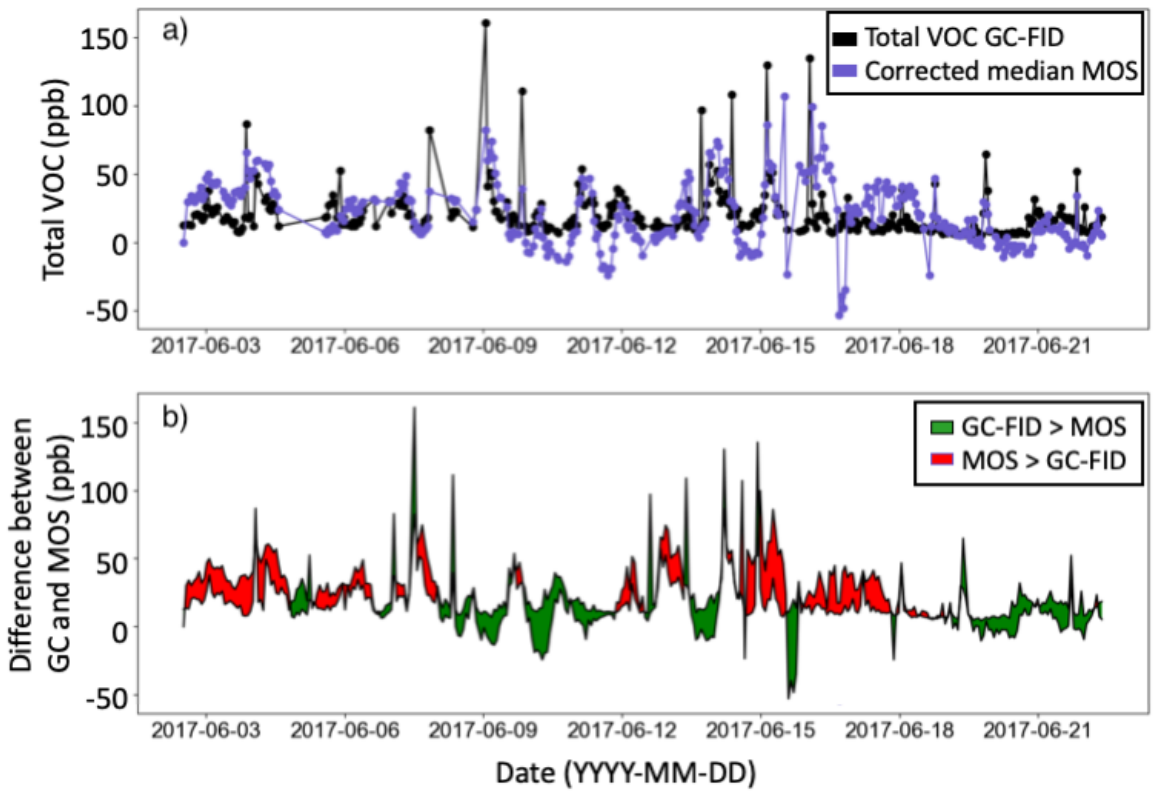

Figure 4.14: a) The temperature and humidity corrected median MOS signal (purple) plotted alongside the sum of all the VOC measured by the GC (black). b) The difference between the corrected median MOS and the total VOC concentration from the GC. If the GC time series is greater than the MOS the colour is green, and if the MOS is greater than the GC, the shading is red.

The signals become less variable after the 15th June for both the MOS and GC which was encouraging as this was evidence that the MOS respond to VOCs and it was not just a co-incidence that the MOS signal varied on the same time scale as the GC-FID. There were some differences between the two instruments, the most notable occurring when the MOS median signal decreased rapidly to -50 $ppb_{[VOC]}$ on the 16th June, with no decrease in the GC-FID trace. This was similar to what would be expected of the MOS sensors with a sudden change in their environmental surroundings, which was not accompanied by a change in the VOC concentrations.

Figure 4.14b is a plot of the two time series, colour coded to show the overlap between them. Where the total VOC GC signal was greater than the MOS, e.g. between the 9th - 11th June 2017, the shading is green, and it is red where the MOS signal was larger. Where this band is narrow, there was a small difference between the two sets of observations. There was no constant offset between the two instruments, and the difference between the two techniques was variable. Typically, where the signal peaks, there is more red shading indicating the MOS signal over-predicts the total VOC concentration and the troughs are generally green, so the median MOS under-predicted the total VOC concentration. However, this bi-directional variance was not consistent throughout the entire deployment some on other occasions the GC-FID reported higher values for peaks in VOC concentrations than the MOS.

The GC detected 29 VOC compounds and there will be more VOC compounds in ambient air that are not detected by the GC-FID. However, the MOS sensors may be sensitive towards these missing VOC species and will show a response towards important VOCs or IVOCs that are present, some of which may have relatively high concentrations in the troposphere. The over-predicted VOC peaks in the MOS signal is evidence that the GC-FID did not detect the full suite of VOC compounds that the MOS were responding to during the deployment. There were periods where the MOS under-predicted the total VOC concentration leading to the conclusion that the MOS sensors are potentially more sensitive to a different VOC composition than the suite of 29 compounds detected by the GC FID. This would account for the MOS not consistently displaying a higher sensitivity than the GC-FID towards the total VOC concentration. The two signals co-vary as the total VOC concentrations fluctuate, but where the VOC composition changes, the MOS potentially became more sensitive towards the different composition, and led to an over-prediction of VOC concentration as the sensors began to display higher sensitivity towards the total VOC.

There was a moderate strength (R^2: 0.21), positive (gradient between median MOS and GC-FID total VOC : +0.59) correlation between the GC-FID total VOC concentration and the corrected median MOS signal, see Fig. 4.15b. The correlation plot of total VOC concentration and median MOS, Fig. 4.15b, showed that overall the median MOS was less sensitive than the GC-FID, e.g. the slope between the two data sets was 0.6. There were

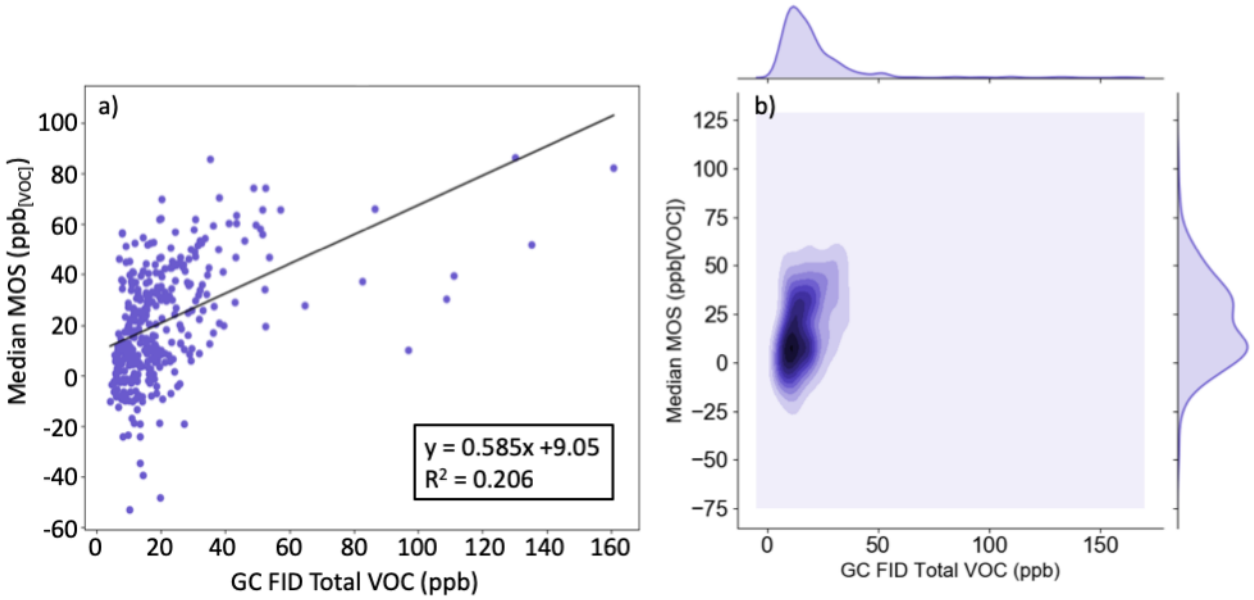

Figure 4.15: a) Correlation plot between the total VOC from the GC and the corrected median MOS. b) A comparison between the distributions of the corrected median MOS data and the total VOC concentration reported by the GC FID.

a few observations of higher concentrations of VOCs detected by the GC-FID (between 80 and 160 ppb), which were detected linearly by the median MOS sensors and these were instrumental in determining the slope. There was more variability in the median MOS sensor response for the lower VOC concentrations; when the GC -FID detected 0 - 50 ppb the corresponding median MOS response varied between -25 to 60 ppb, Fig. 4.15b. There was just one peak, at 20 ppb for the GC-FID distribution of data, but there was two for the median MOS signal, at 0 $ppb_{[VOC]}$ and 25 $ppb_{[VOC]}$ suggesting the median MOS sensitivity towards the total VOCs detected by the GC-FID may have changed during the deployment. The median MOS cannot be relied upon to quantify the total VOCs, but it was promising that there was a moderate correlation and that the two data sets exhibited similar variance during the deployment.

The MOS sensors detect more compounds than the 29 detected by the GC-FID and Figs. 4.14 and 4.15 indicated that the MOS sensitivity may have altered with changing VOC composition. Therefore the MOS response towards the different types of VOCs monitored by the GC-FID was investigated. The composition of VOCs was a mixture with 11 alkanes, 11 alkenes and 7 aromatic compounds. Each compound class was also analysed against the median MOS signal to identify if the MOS are reacting to one class more than the others. The 11 alkane, 11 alkene and 7 aromatic concentrations were summed to yield a total alkane, total alkene and total aromatic signal, respectively. Linear regression was used to compare the corrected median with the total alkane, total alkene and total aromatic concentrations during the deployment. The results of which can be found in Table 4.1.

Table 4.1: Results from the linear regression of total alkanes, total alkenes and total aromatic compounds detected by the GC-FID after correlation with the corrected median MOS.

VOC group	Gradient of VOC group concentration vs. median MOS	R^2 value	NRMSE
Total alkanes	0.64	0.172	0.16
Total alkenes	3.59	0.199	0.21
Total aromatics	9.06	0.269	0.14
Total VOC	0.59	0.206	0.17

The median MOS signal displayed the highest gradient (9.06) with the total aromatic compounds suggesting that the median MOS was more sensitive towards changing aromatic concentrations than it was to changing alkene (gradient: 3.59) or alkane (gradient: 0.64) concentrations. Alkanes has the lowest gradient between the GC-FID and median MOS comparison, and also the weakest correlation (R^2 : 0.17). The median MOS signal was therefore the least sensitive to changing alkane concentrations. The RMSE of the median MOS signal and the sum of the compounds in each class was calculated. The NRMSE was then determined by dividing the RMSE by the range of VOC concentrations in the class so that a direct comparison can be made between compound groups, see Table 4.1. The error within the correlations can be investigated by comparing the NRMSE. The compound class with the lowest error (14 % error) was the aromatics, with the MOS and alkenes (21 % error) displaying the highest error out of the different groups of compounds. The alkanes constituted a large proportion of compounds of the Total VOC measured by the GC-FID and therefore the error with the total VOC and the alkanes was very similar. The sum of all 7 aromatic compounds exhibited the lowest NRMSE when compared with the median MOS across the entire 20 days, Fig. 4.1. This was in agreement with the laboratory experiment with the MOS and GC-MS in Chapter 2, where it was shown that the MOS displayed a larger sensitivity towards the aromatic compounds than the other compound classes investigated. Potentially this is due to the compounds being more reactive and reducing, therefore reacting faster on the MOS active surface.

4.2.3 Field calibration of MOS using GC-FID

The median MOS signal was calibrated using the co-located GC instrument. They both ran for the first seven days (from 12:00 2nd June until 12:00 9th June 2017) and the equation from linear regression was computed (y(MOS in V) = 0.00229 x(Total VOC in ppb) - 0.166). These linear parameters were then applied to the MOS signal for the remainder of the campaign to determine the MOS values after calibration. The conditions experienced by the sensors during the calibration week were representative of the conditions experi-

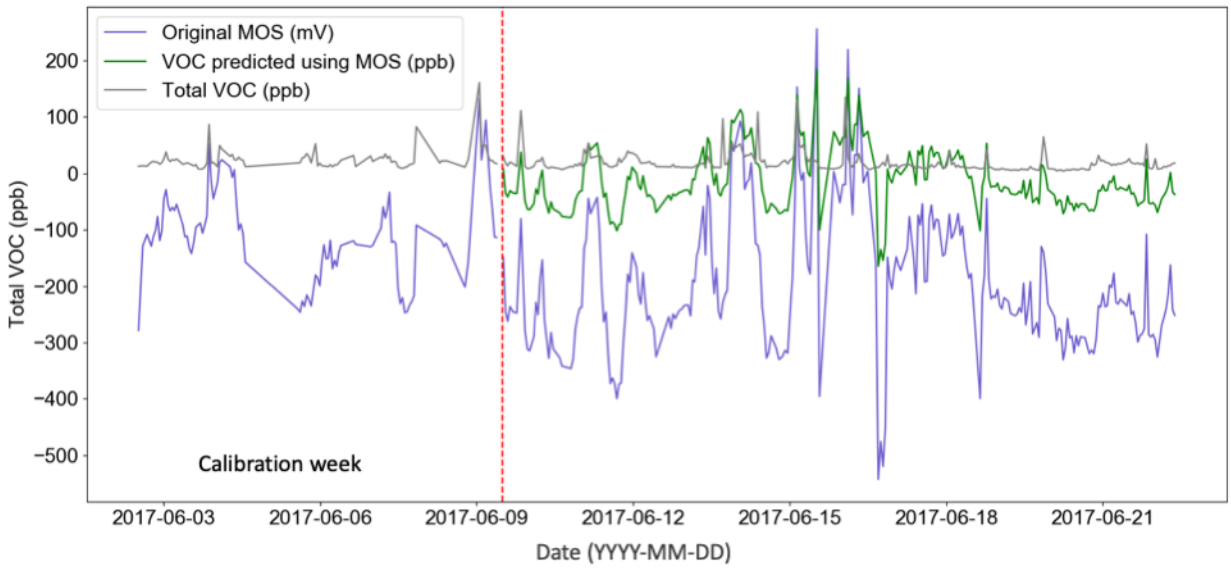

Figure 4.16: The median MOS signal (mV, light purple) is shown for the entire campaign. The first week of deployment was used as a calibration week and a linear equation to compare the median MOS signal (V) and the total VOC concentration as detected by GC (grey) was determined. This equation was then rearranged so that the median MOS could better predict the total VOC concentration (green).

enced by the MOS sensors during the subsequent deployment. The temperature range was 13.3 to 27.0 ° C and the humidity range was 51 to 95 % for the calibration week.

The green line in Fig.4.16 shows that the median MOS signal better represents the total VOC concentration after *in situ* calibration with the total VOC concentration from the GC. The predicted VOC concentration (green line) displays peaks where there are prominent peaks in the GC total VOC (grey) signal and they are much closer together. The NRMSE for the predicted VOC concentrations (16.4 %) were almost halved compared to the median MOS signal (30.5 %), so there was a large reduction in error when the *in situ* calibrations were used to determine the VOC concentrations compared to the just using the MOS. However, there was still a lot of variability in the predicted MOS signal, leading to only a minimal R^2 value increase when the predicted VOC concentration was correlated with the GC-FID total VOC concentration after the calibration week and the the original median MOS correlated with the GC-FID during the same period of time (rounded to 3 d.p the R^2 values for the predicted VOC vs. GC FID was 0.42 and for original MOS vs. GC-FID total VOC was 0.42).

The same process of applying simple linear regression (SLR) over the first week of deployment to calibrate the MOS sensors was repeated for the different compound classes of VOCs. The median MOS was calibrated with the sum of all the compounds in each group and linear parameters determined for the calibration. The initial calibration week was exactly the same length of time as for the total VOC concentration. These parameters were used to convert the rest of the MOS signal to ppb and compare against the GC reference concentration in Fig. 4.17. Calibrating the MOS with the aromatic compounds (Fig.

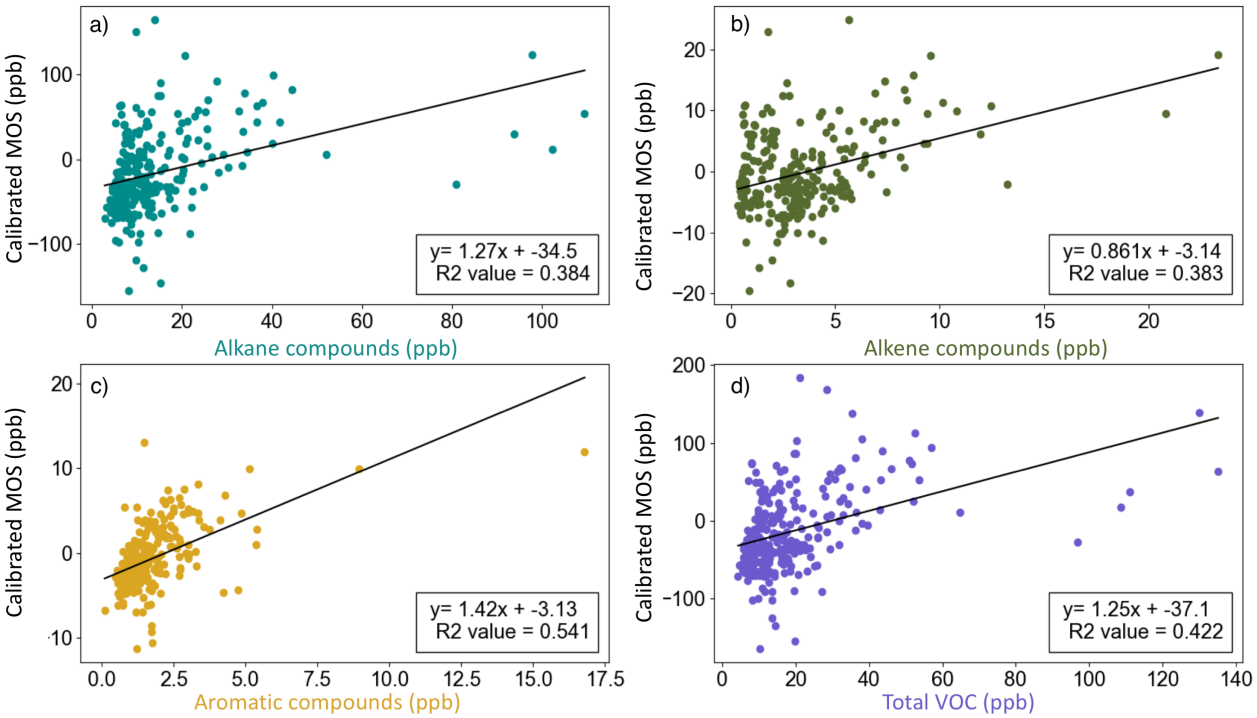

Figure 4.17: The correlation between the GC compounds and the MOS calibrated with sum of the a) alkane, b) alkene, c) aromatic and d) total VOC compounds from the GC. The aromatic compounds provided the strongest match to the reference measurements.

4.17c) produced the most positive correlation with the median MOS ($R^2 = 0.541$). The correlation plot of the predicted aromatic concentration with the aromatic concentration produced by summing aromatic GC-FID compounds also produced the largest gradient (1.42) and the smallest intercept indicating that the predicted aromatic concentration was bought closer to the GC-FID observed total aromatic concentration. Using the median MOS signal with an in-field calibration by GC-FID was therefore an effective method for improving the MOS data quality regarding aromatic compounds. This was expected as over the full data set the aromatics displayed the strongest correlation to the median MOS signal and the reactivity of the aromatics meant that in the GC-MS laboratory experiments in Chapter 2, large aromatic compounds presented with the largest response in MOS signals. All of the trend lines calculated in Fig. 4.17 were influenced by a few GC-FID observed high concentrations of VOC compounds. The MOS sensors did not predict these values to the same extent as the GC-FID, even after they were calibrated *in situ*.

4.2.4 MOS versus SIFT-MS

Selected ion flow tube mass spectrometry (SIFT-MS) uses ions to detect VOC compounds with a higher time resolution than the GC-FID. Where the GC-FID detects only a narrow range of VOC compounds, the SIFT-MS is capable of detecting any ionisable organic compound that makes it into the source and therefore is a more similar to the MOS detection technique than using a GC. There is some overlap with the compounds detected

by GC-FID, but the technique offers the detection of a wider range of VOC compounds, such as more oxygenated species, that were not detected by the GC-FID system deployed in Beijing. The SIFT-MS is less accurate than a GC-FID at determining the absolute concentrations of the organic compounds, however it is able to capture the VOC variability well and provided near more real-time measurment of VOC concentration. It was therefore expected that the total VOC from the SIFT-MS and the MOS sensors will compare better than when the GC-FID was used as a VOC reference. The 1-minute median MOS signal was converted to an equivalent mixing ratio of total VOC, using a sensitivity of 5 mV ppb^{-1}, which was typical for the humidity and temperatures of the deployment. A SIFT-MS instrument was operated in Beijing, by Dr. Marvin Shaw from the University of York, for the duration of the sensors deployment, therefore the SIFT-MS response was compared with the MOS response. In total the SIFT-MS detected 28 compounds, with a variety of reactivity covering five different classes of compounds (aromatic, aldehyde, ketone, biogenic and alcohol compounds), as well as a miscellaneous group containing butadiene, acetonitrile, methylisocyanate, methyltertbutylether and chloroform. During the air quality campaign the SIFT-MS was used to alternatively sample at ground level and at 100 m, since it was deployed to investigate VOC concentration fluxes. The sensor instrument was only located at the ground level and hence only ground-level SIFT-MS data was included in this comparison.

Figure 4.18 shows the fluctuation of the concentration of the different groups of compounds detected by the SIFT-MS. The alcohols (purple region), whilst only containing two compounds (methanol and ethanol) in their group, made up the largest portion of VOCs detected by SIFT-MS. However, it was noticeable that the ratio of all the different VOC classes did not change much throughout the duration of the campaign. This consistency between the ratios of VOCs is important for the MOS sensors, because it means that, even though the total VOC MOS sensors are inherently non-selective, some information can be gleaned about the different compounds if the total VOC composition is relatively constant. The SIFT-MS concentrations for each of the 28 compounds were summed to calculate a total SIFT VOC concentration, Fig. 4.18 black line. There was some agreement between the total SIFT VOC concentration (black line Fig. 4.18) and the median MOS signal (light green line) with the sensors identifying the majority of the peaks in the SIFT-MS traces. In general the variations of SIFT-MS signal were also observed in the MOS data. The inability of the sensors to quantify the total VOC concentration using a laboratory calculated sensitivity was evident as the sensors occasionally predicted negative concentration values, up to -120 ppb. Yet the higher concentrations observed by the SIFT-MS were 80 - 100 ppb and the median MOS was not too far off, observing 90 to 120 ppb for these VOC pollution events.

Rather promisingly, the SIFT-MS Total VOC concentration was positively correlated (R^2: 0.47) with the temperature and humidity corrected median MOS signal, Fig. 4.19a.

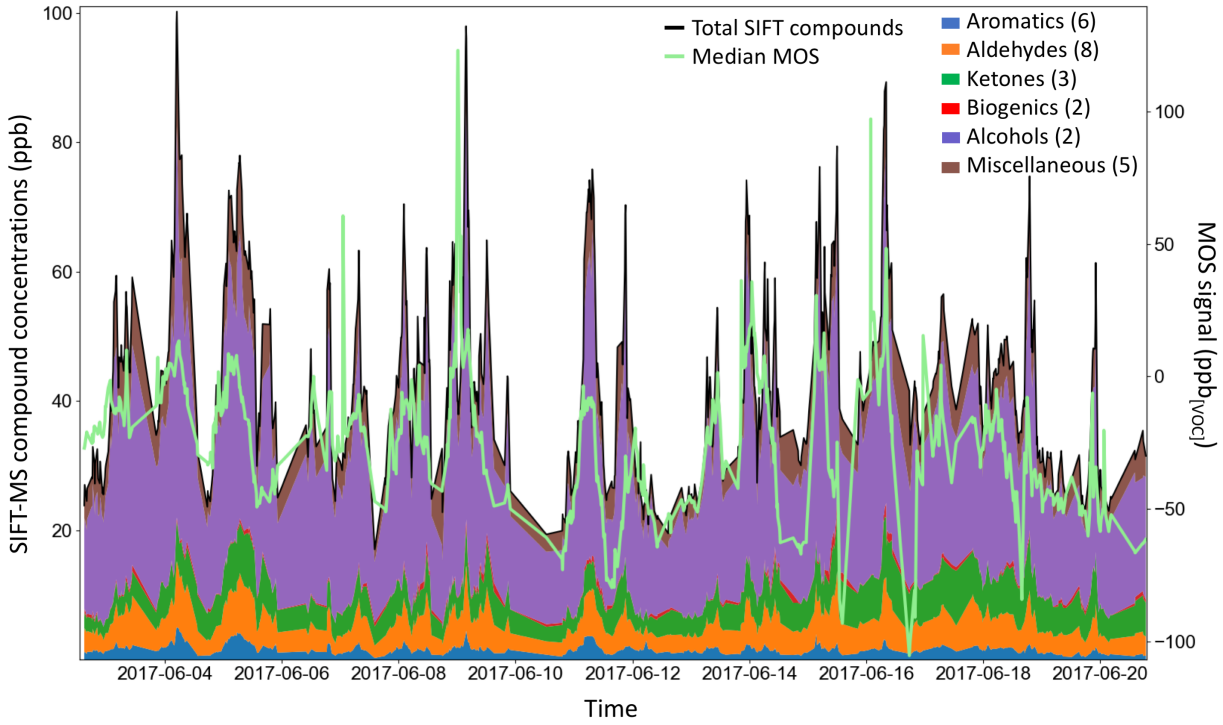

Figure 4.18: A stacked plot to show the relative concentrations of the different class of VOC compounds measured by the SIFT-MS. The number of compounds that make up each compounds groups are displayed in the parenthesis, next to the class name. The median MOS signal ($ppb_{[VOC]}$) is shown as a light green line and this generally follows the same pattern as the total VOC concentration (black line) from the SIFT.

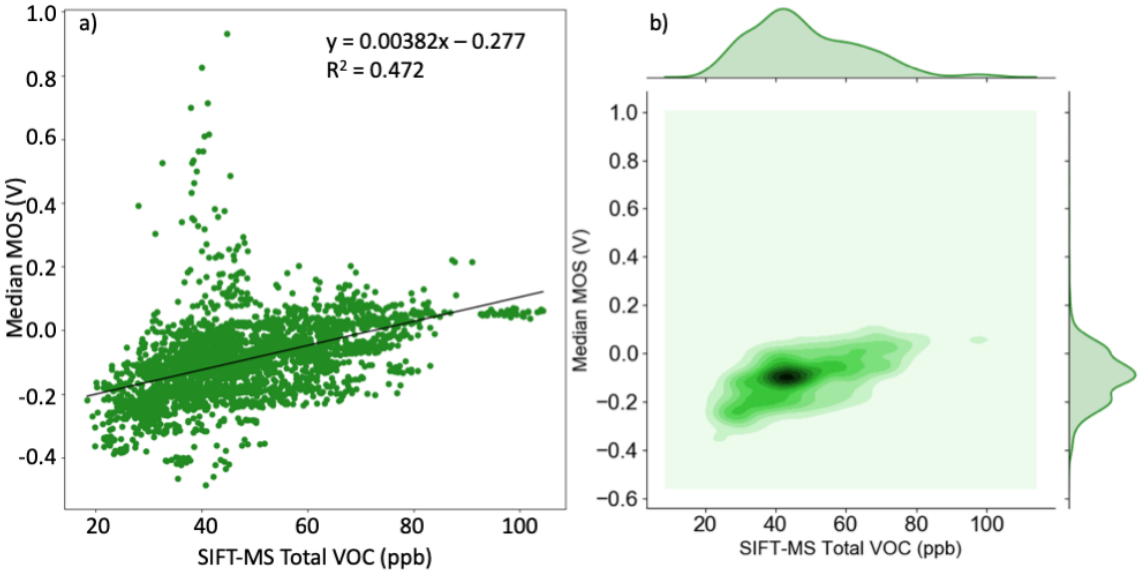

Figure 4.19: The median MOS voltage signal was compared with the SIFT-MS Total VOC concentration using a correlation plot (a) and a kernel density function (b).

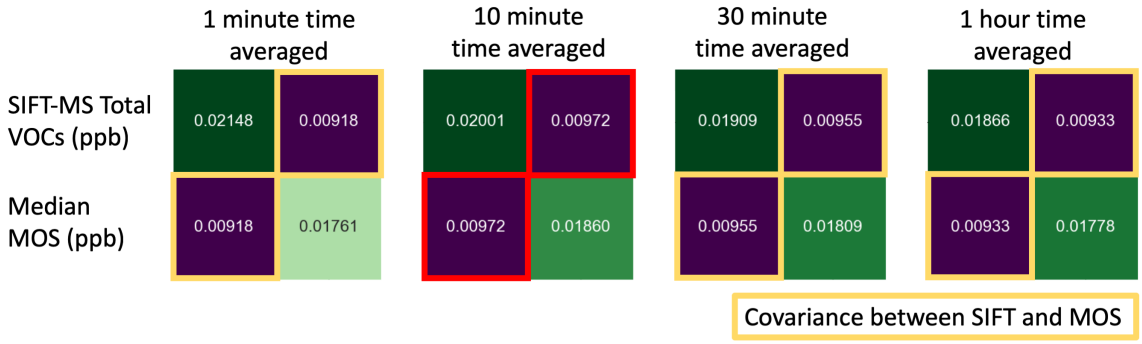

Figure 4.20: Four covariance-variance matrices of the normalised SIFT-MS and MOS data to show how well the total VOCs measured by the SIFT-MS and the median MOS signal co-vary after different time averages were applied. The yellow outlined boxes represent the covariance between the two variables, with the red outlined box highlighting the time averaging that produced the highest covariance. The top left box, is the variance within the SIFT-MS total VOC signal and the bottom right is shows the variance in the median MOS sensor.

This R_2 value was greater than that calculated for any of the comparisons made between the median MOS and the GC-FID concentrations. There was however, still a spread of MOS data points (approximately 0.3 V wide) around the linear regression calculated trend line. The distribution of SIFT-MS Total VOC data consisted of one main peak at 45 ppb, with shoulder peaks either side of this value, at 30 and 60 ppb, see Fig. 4.19. The median MOS data displayed a similarly shaped distribution, of a peak at -0.1 V, with two shoulder peaks at 0.0 and -0.2 V. This was advantageous as it indicated that the MOS sensitivity towards the compounds detected by the SIFT-MS did not change during the course of the experiment. The MOS and total VOC (SIFT-MS) displayed high co-variance during deployment, with the median MOS signal comparing better to the SIFT-MS at higher time resolutions than it did for the temporally limited GC-FID data points. Therefore, covariance-variance matrices were calculated for the normalised data for four different time averages of the data: 1 minute, 10 minutes, 30 minutes and 1 hour to investigate the covariance of the median MOS with the SIFT-MS at different time resolutions. As the time over which the averaging was applied increased (from 1- to 10- to 30-minutes to 1-hour) the variation in the data decreases as short term variations are averaged out. This analytical experiment was used to investigate at which of these time-averages do the sensors and the SIFT-MS experience the greatest level of covariance. This would help to identify the timescales of VOC concentration fluctuations that the MOS were able to detect. The greatest covariance between the SIFT-MS Total VOC concentration and the median MOS occurred when both data sets were smoothed using a ten-minute average, Fig. 4.20. This indicated that the median MOS detected changing total VOC concentrations on a ten minute timescale and this therefore identifies the MOS as being potentially suitable for improving the temporal VOC concentration gradient of VOC observations made using GC-FID. Consequently, the MOS sensors could be applied

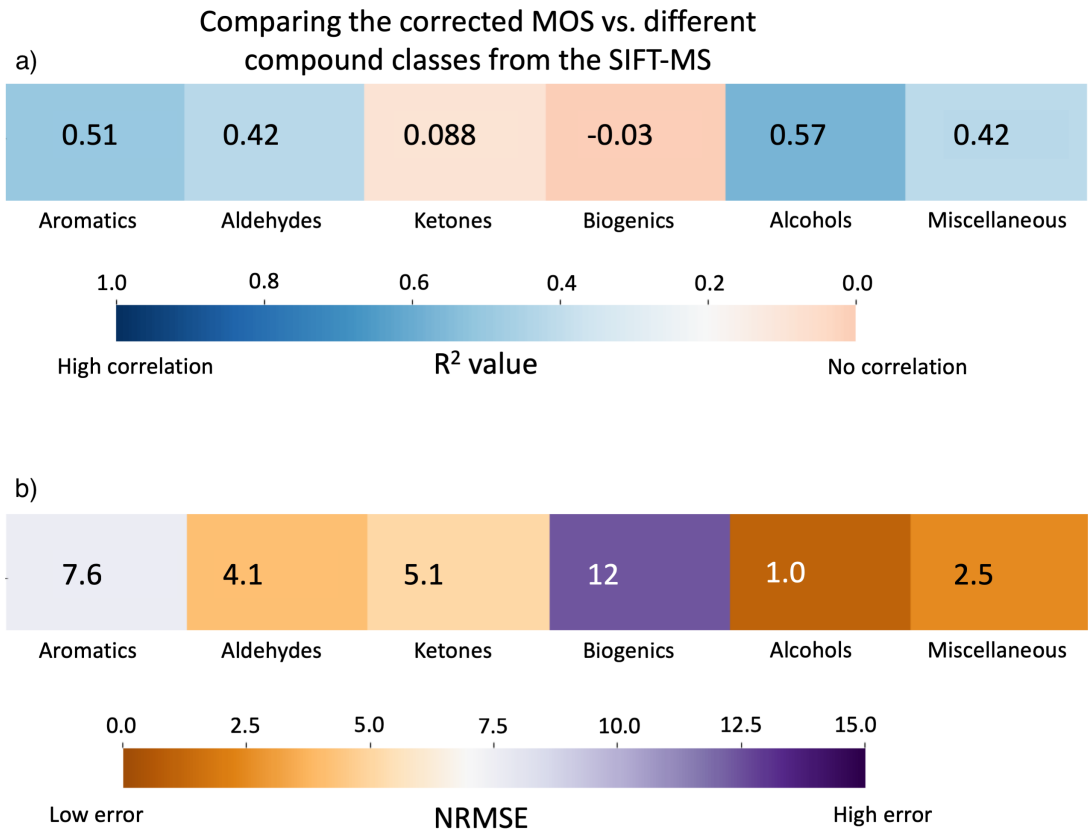

Figure 4.21: The comparison between the temperature and humidity corrected MOS signal and the different compound classes from the SIFT-MS measurements using a) R^2 and b) NRMSE parameters.

in to detect steep VOC concentration gradients that are occurring on short timescales of several minutes, making them useful for complementing GC-FID techniques. As the time averaging increases from 1 minute data to an hour, the variance within the total VOC SIFT-MS signal decreases, as the peaks occurring on shorter time scales are smoothed out. If the MOS responded to changing VOC concentrations with a response time of an hour or so, then averaging to an hour would mean that the covariance between the MOS and the SIFT would increase over the longer time scales - this is not the case and as the covariance is highest for the ten-minute averaged data, the MOS response must be of the order of a few minutes.

The alcohol and aromatic groups of compounds from the SIFT-MS displayed the highest R^2 values, see Fig. 4.21a, when compared against the temperature and humidity corrected MOS signal. The MOS signal has a moderate, positive correlation with the sum of the aromatics, alcohols and aldehydes (R^2 : 0.42 - 0.57). The ketones and biogenics essentially show no correlation at all with the MOS signal (R^2 : 0.09 for ketones and -0.03 for biogenic compounds). This poor correlation with ketones was unexpected considering that the median MOS was well correlated with the aldehydes and these compounds are chemically similar. However, this may relate to the aldehydes and ketones being emitted from different sources which would lead to one being more correlated than the other to

the median MOS. The NRMSE values were high - especially when compared to the GC NRMSE values which were 0.14 - 0.21, see Fig. **??**- due to a combination of high RMSE values (RMSE ranged between 36 - 54 ppb) and low compound concentrations. The compound classes displaying the least amount of error when compared to the median MOS signal was the alcohols (NRMSE : 1.0), the miscellaneous compounds and the aldehydes (NRMSE: 4.1). The aromatics, initially suspected of displaying a strong positive correlation with MOS exhibited a relatively high value for NRMSE, indicating that there was a large amount of uncertainty for the comparison between the SIFT-MS aromatic compounds and the median MOS. The biogenic compounds performance was more consistent, with no correlation and a high error value. The higher error values were thought to be due to the larger number of data points and higher temporal resolution of both techniques. For the GC-FID comparison the MOS data was a ten minute average whereas for the SIFT-MS NRMSE and R^2 value calculations the 1-minute data was used.

4.2.5 MOS versus organic acids

There were lots of reference instruments as part of the air quality campaign in Beijing, China and on site there was a Chemical Ionisation Mass Spectrometer (CIMS) to monitor organic acids in the air. This was maintained and run by the University of Manchester and they have provided data for four different organic acids. Although located at the IAP site, the CIMS instrument sampled from a different shipping container laboratory and was situated 50 m away from the sensor instrument. The GC-FID covers 29 VOCs, however, there are many more carbon containing compounds in the atmosphere that are likely to react with the MOS active surface and elicit a response. Organic acids are one group of compounds that are not detected by gas chromatography or the SIFT-MS, but the sensors may potentially respond to them as part of the 'total VOC' mixing ratio.

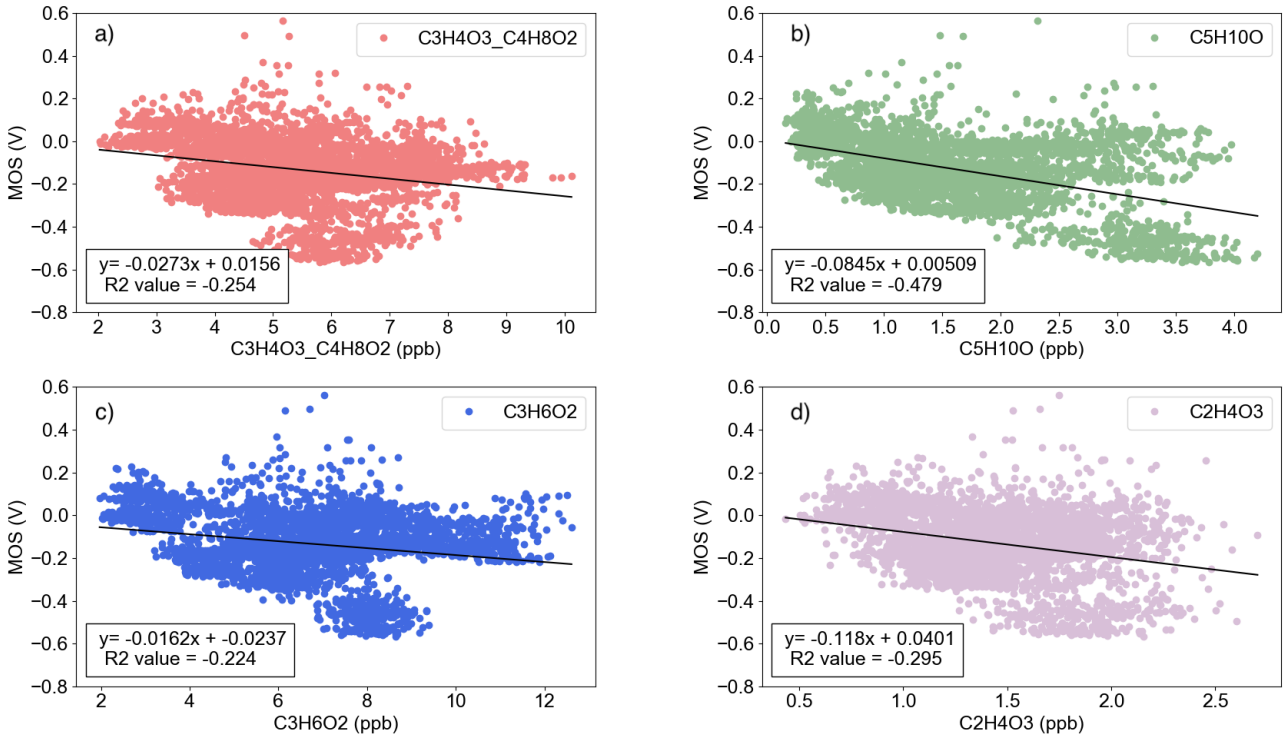

Figure 4.22: The MOS sensors were weakly and negatively correlated with four organic acids measured by a Chemical Ionisation Mass Spectrometer (CIMS) operated by the University of Manchester. Each plot represents the median MOS signal compared to a different organic acid measured by the CIMS: a) $C_3H_4O_3$-$C_4H_8O_2$, b) $C_5H_{10}O$, c) $C_3H_6O_2$ and d) $C_2H_4O_3$.

It was interesting to see that all the correlations between the organic acids with the median MOS were negative and moderate, Fig. 4.22. The negative correlation might be due to the more oxidising nature of organic acid, since increasing the concentration of reducing compounds typically leads to an increase in the conductivity of the MOS sensing surface. However, oxidising compounds, such as organic compounds will respond differently to the oxyanion adsorbed to the MOS sensing surface and will either not initiate a MOS response or lead to a decreased response if they affect the MOS' ability to detect other compounds. There was a large spread of MOS data over the different organic acid concentrations detected, e.g. for Fig. 4.22 d) when the CIMS detected 1.5 ppb of $C_2H_4O_3$ the MOS response varied by 867 mV. This spread in MOS response is relatively constant throughout all the mixing ratios of the different organic acids. The median MOS response was negatively correlated with organic acids during the deployment of the sensors. This potentially indicates that organic acids do influence the MOS signal and may lead to the MOS sensors under-predicting the total VOC concentration because increasing organic acid concentrations might offset the increase in conductance on the MOS sensor surface due to other VOC concentrations increasing.

4.3 EC sensor performance

EC were investigated for the detection of gaseous pollutants and all EC used in this study were purchased from Alphasense. The raw EC sensor output consists of two voltages; from the auxiliary electrode (AE) and the working electrode (WE) and both voltages are required for the conversion to concentration units. Equations 4.2, 4.3 and 4.4 show how each EC voltage output was converted to a ppm concentration.

$$CO(ppm) = \frac{(COWE(mV) - a) - (COAE(mV) - b)}{c(mVppm^{-1})} \tag{4.2}$$

$$O_X(ppm) = \frac{(O_XWE(mV) - a) - (O_XAE(mV) - b)}{c(mVppm^{-1})} \tag{4.3}$$

$$NO_2(ppm) = \frac{(NO_2WE(mV) - a) - (NO_2AE(mV) - b)}{c(mVppm^{-1})} \tag{4.4}$$

The EC sensors were all calibrated in the manufacturers factory before being purchased and each EC sensor arrives with individual factory conversion factors that are required for the conversion of voltages to a concentration (a, b, and c in Equations 4.2, 4.3 and 4.4). In all instances where EC were used the EC had their individual factory conversion factors applied.

4.3.1 Performance evaluation of individual EC sensors

Each of the six individual EC were correlated with their respective reference measurements for the entire campaign (00:00 2nd June - 26th June 2017 to examine the individual sensors performance. Each NO_2 EC exhibited a slightly different sensitivity towards ambient NO_2 concentrations, resulting in a range of gradients (2.01 to 2.45) for the linear regression, Table 4.2. This suggested that the NO_2 EC were sensitive to changing ambient NO_2 concentrations, but over-predicted high concentrations and under-predicted low NO_2 concentrations leading to gradients that were all greater than 1. All NO_2 EC exhibited a negative offset compared to the reference NO_2 observations, leading to negative intercepts (-3.15 to -207), but each NO_2 EC was strongly correlated to the reference measurements (R^2: 0.865 to 0.910). The instantaneous median NO_2 EC was strongly correlated with the NO_2 reference observations (R^2 : 0.87), and exhibited a gradient of 2.09, an intercept of -33.4 and an RMSE of 25.3 ppb.

The 6 O_X EC displayed a similar sensitivity towards the ambient O_X concentrations as the reference measurement as the gradient of the linear regression performed were all close to 1 (0.935 - 1.1). There was a high degree of linearity between the two measurements with both being strongly and positively correlated (R^2: 0.82 to 0.85). Two of the O_X had negative intercepts, whilst the others had four, indicating that there was no consistent

Table 4.2: Each of the individual NO_2, O_X and CO EC were correlated with their respective reference observations to identify the spread in a cluster of 6 EC responses.

Linear regression parameters	6 NO_2 EC	NO_2 median	6 O_X EC	O_X median	6 CO EC	CO median
Gradient	2.01 - 2.45	2.09	0.935 - 1.1	1.0	1.79 - 2.27	1.97
Intercept	-3.15 to -207	-33.4	-33.9 to +89.9	+41.9	123 to 647	424
R^2	0.865 to 0.910	0.87	0.818 to 0.854	0.835	0.554 to 0.833	0.64
RMSE	23.9 to 181.8	25.3	26.0 to 89.6	48.7	78 to 1370	1011

offset between the O_2 EC and reference observations. The median O_X EC performance over the entire campaign was also very linear (gradient: 1.0, R^2: 0.84) although did display a positive offset of 41.9 ppb.

The 6 CO sensors exhibited the largest range in performance, compared to the other clusters of EC deployed. There was a range of 1.79 to 2.27 for the gradients between each EC and the reference CO observations, with the relationship varying from only moderately correlated (lowest R^2: 0.56) to strongly correlated (highest R^2:0.83). This indicated that the linearity of the response for different CO EC sensors was not constant between 6 co-located CO EC. The median CO EC only exhibited a moderate correlation with the reference (R^2:0.64) with a gradient that of 1.97.

Whilst this analysis showed that some EC were likely to perform better than others and would closely match the reference, this was only up to two out of the six EC used in the cluster. The median EC represented the behaviour of all the EC in the cluster and gave a more robust EC measurement, which, as discussed in Chapter 3 would be more reproducible and minimise the mid-term drift of the EC response. The EC were deployed as clusters of six EC and the instantaneous median of each cluster was calculated and used for the subsequent analysis, where stated.

4.4 Simple linear regression

Using the unique conversion factors and Equations 4.2, 4.3 and 4.4, the EC signal was output as a concentration (ppm), yet also requires some form of calibration depending on the sensors environment. The factory conversion factors were calculated at the sensor factory, and the conditions under which these were determined will be different compared to the conditions of the outdoor deployment environment where the EC were to be located. An example of the NO_2 ensemble performance with just the factory conversion factors

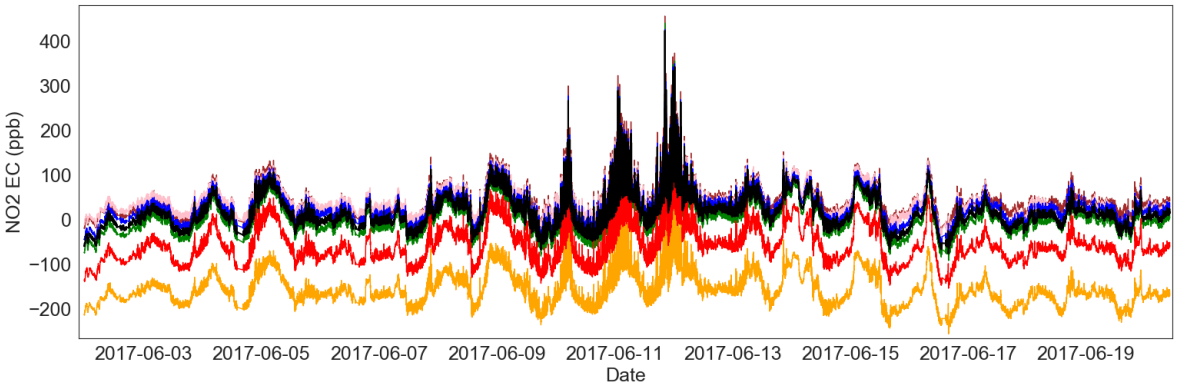

Figure 4.23: Timeseries of 6 NO_2 EC sensors deployed in Beijing (coloured lines), plotted on the same axis as the median NO_2 EC to display that the instantaneous median of the EC cluster detected the variance in NO_2 concentrations detected by each NO_2 EC.

applied is shown in Fig. 4.24, grey line. Each NO_2 sensor was individually converted to a concentration, then the median of the sensor ensemble was plotted alongside the reference NO_2 measurements. The instantaneous median NO_2 EC sensor represented the variance in NO_2 detected by all 6 NO_2 well, Fig. 4.23. However Fig. 4.24 showed that there were occasions during the deployment when there were large discrepancies between the absolute NO_2 concentration values detected by the median NO_2 EC sensor and the reference NO_2 CAPS observations (red trace for calibration week, black trace for subsequent deployment period.

The median sensor over predicted NO_2 when the reference NO_2 concentration was high, and under-predicted NO_2 during periods of low NO_2 concentrations. This led to gradients of 1.95 and 1.95 for the correlation plots of reference NO_2 concentrations versus the median NO_2 sensor observations, in the calibration week (Fig. 4.24b, grey) and during the comparison of the uncalibrated NO_2 median during the subsequent deployment (Fig. 4.24c, grey). At the lower concentrations (less than 50 ppb NO_2 in reference observations), the median NO_2 EC sensor exhibited a large spread in values making it difficult to use for ambient NO_2 concentrations, Fig. 4.24b and Fig. 4.24c, grey).

Since the reference instrument was co-located with the sensor cluster, it was possible to calibrate the sensors in the field using simple linear regression (SLR). The first six days (2^{nd} to 8^{th} June 2017) were used as a calibration week, and the sensors were correlated with the reference instrument for this initial week, Fig. 4.24b. Linear parameters were calculated, (Fig. 4.24b) and these were then used to correct the NO_2 sensor median over the remainder of the sampling period (8^{th} to 25^{th} June 2017). For the remainder of the deployment the SLR calibration factors were unchanged. The observations from the NO_2 reference instrument showed that the concentration of NO_2 exhibited a large dynamic range during the campaign, from less than 2.5 ppb to measurements in excess of 200 ppb. The SLR NO_2 data captured this concentration range well, detecting the higher concentrations and following a similar trend to the reference monitor. The upper

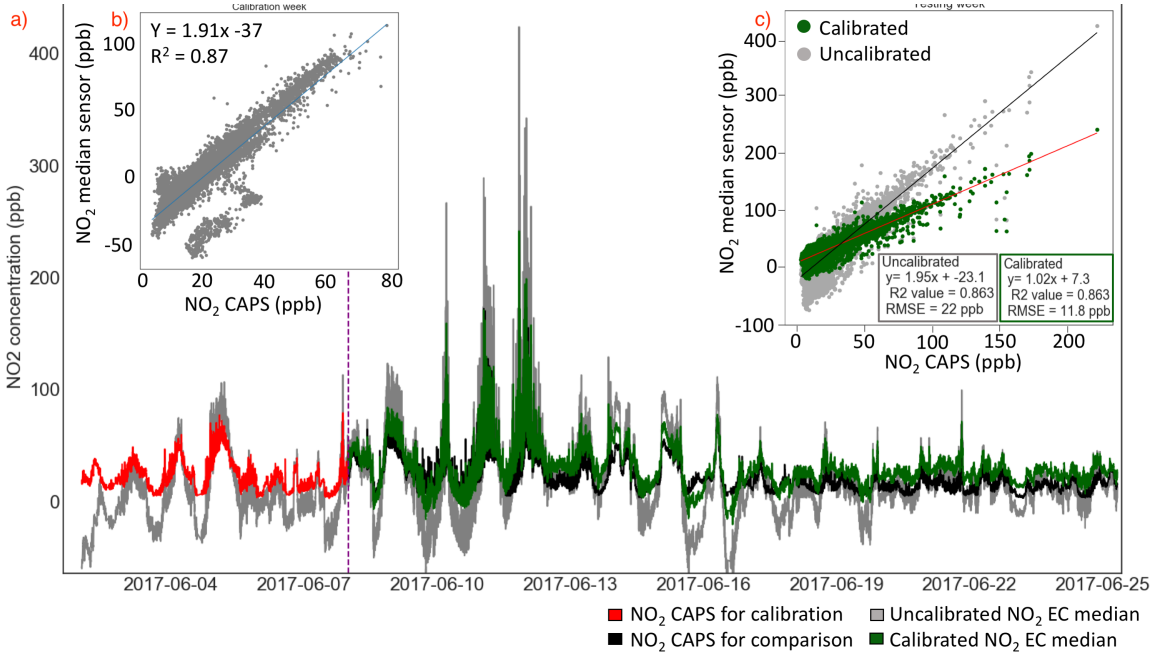

Figure 4.24: a) Time series of the instantaneous median NO_2 EC sensor (grey). The median sensor appeared to over compensate for fluctuations in the NO_2 concentration, when compared to the reference NO_2 measurements. b) The correlation plot used to determine the linear parameters for *in situ* calibration of the NO_2 EC sensors, and c) two over-laid correlation plots to compare the difference between the un-calibrated and SLR calibrated NO_2 sensors in the testing period.

right inset plot (Fig. 4.24c) shows the difference between the correlation plots for the un-calibrated (grey) and the calibrated sensor median (green). The spread of the data points around the trend line was reduced for the SLR-calibrated NO_2 EC signal (green) compared to the variability observed for the same values in the uncalibrated NO_2 EC median. For example, when the reference NO_2 mixing ratios were reported between 49.9 and 50.1 ppb the corresponding range of NO_2 concentrations as reported by the un-calibrated sensors was 4.04 - 121.34 ppb. This spread of NO_2 values was reduced for the SLR calibrated NO_2 EC as the range of NO_2 concentrations reported for the calibrated NO_2 median was 21.54 - 83.03 ppb when the reference observations reported 49.9 and 50.1 ppb. The gradient for the comparison between the reference NO_2 observations and SLR-calibrated NO_2 median was closer to 1 (un-calibrated: 1.98, calibrated: 1.02) and the RMSE was almost halved after *in situ* calibration (un-calibrated: 22 ppb, calibrated: 11.8 ppb). Field calibrations, with linear parameters was sufficient enough to improve the NO_2 data to ensure it was more comparable to observations from a research grade instrument. However, when the NO_2 concentration was reported by the reference instrument to be less than 10 ppb, there were still noticeable discrepancies between the reference and the SLR NO_2. This was in agreement with previous work by [104] where they stated that at low concentrations of the target measurand, the impact of cross interferences is greater.

SLR was applied to the CO and O_X EC sensor clusters to evaluate their sensor perfor-

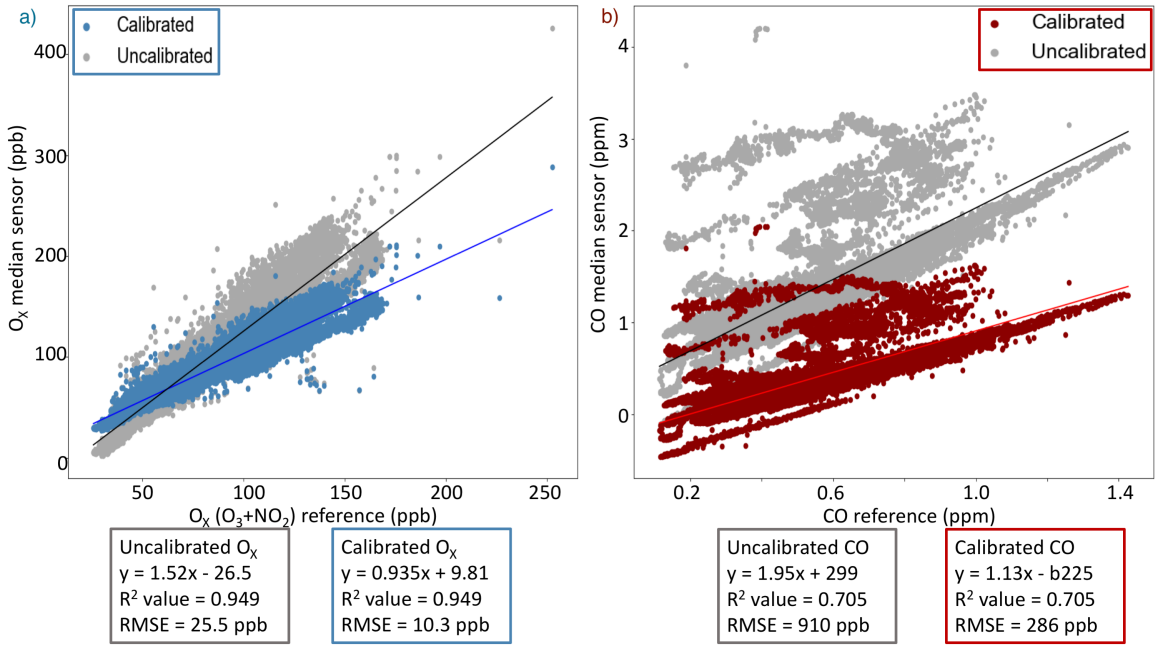

Figure 4.25: The correlation between the O_X (a) and CO (b) EC sensors with their respective reference measurements. The grey scatter plot shows the correlation between these when the sensor median has not been calibrated using simple linear regression, whereas the a) O_X blue and b) CO red scatter plots show the impact of *in situ* calibration with co-located reference instruments, upon the EC sensors.

mance against their respective reference instruments. The *in situ* calibration period was the same for the O_X sensors as it was for the NO_2 EC (00:00 2nd June - 00:00 8th June 2017), but the CO EC began 12 hours later because the CO Aerolaser had an instrumental offset that was corrected on the morning of the 2nd June. Therefore the calibration period for the CO EC was slightly shorter (12:00 2nd June to 00:00 8th June). Figure 4.25 shows the difference between the EC sensor performance after just the factory calibrations were applied (grey) and the improved performance after SLR analysis, after 00:00 8th of June 2017 until the end of the deployment.

For the assessment of the performance of the O_X EC sensors, the reference measurement was calculated by summing the NO_2 and O_3 reference observations together. The O_X are assumed to respond a proportional and independent response towards these two compounds. The O_X EC had very linear properties and displayed very good agreement with the sum of the NO_2 and O_3 reference measurements, even without in-field calibration (R^2 = 0.95). However, after the application of SLR there was still an improvement in the O_X EC sensor performance; reduced variability and an offset closer to 0 (intercept for un-calibrated: -26.5 ppb, calibrated: 9.81 ppb). The RMSE after in-field calibration decreased from 25.5 to 10.3 ppb as well, therefore there was reduced uncertainty in the SLR calibrated O_X data compared to the uncalibrated O_X median signal. After *in situ* calibration the O_X slope between the reference and the O_X median was closer to approaching 1:1 (slope for un-calibrated O_X: 1.52, calibrated O_X: 0.935).

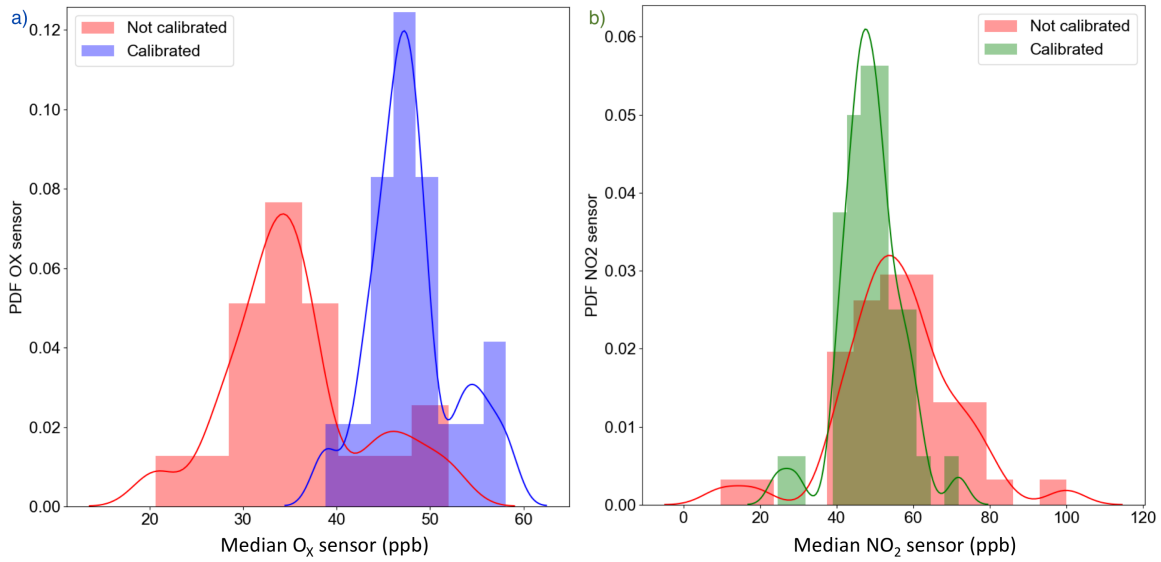

Figure 4.26: The spread of the uncalibrated (red) and calibrated a) O_X EC (blue) when the (O_3+NO_2) measurements were 39.9 - 40.1 ppb, and b) NO_2 (green) EC when the NO_2 reference reported 39.9 - 40.1 ppb. The EC sensors both show a large amount of variability that means that it would be impossible to rely on these measurements to observe if the concentration is violating any regulations. The application of SLR narrows the spread of sensor data points, improving the accuracy of the sensor data a bit.

The CO EC sensor appeared to perform poorer than the NO_2 and O_X EC sensors when compared against its respective reference measurements (CO Aerolaser). This was due to the CO Aerolaser sampling from 100 m above the ground and therefore it was hypothesised that during times of localised CO emissions, the sensors and Aerolaser detect CO in different packets of air, leading to a difference in their signals. Nevertheless, Fig. 4.25b did display a degree of linearity, with a positive correlation between the CO mixing ratio from the reference measurement and the CO as detected by the EC sensors. The spread in the data was reduced when in-field calibration of the CO EC was applied (uncalibrated CO RMSE: 910 ppb, calibrated CO RMSE : 286 ppb), but there was still evidence of the two different CO detection methods observing different air parcels.

To examine the variability in both the SLR calibrated and uncalibrated EC response, a probability density function (pdf) was plotted for the O_X sensors, when the reference measurements were between 39.9 and 40.1 ppb, see Fig. 4.26a. The uncalibrated O_X EC displayed a spread of 31.25 ppb, with measurements as low as 20.7 ppb and as high as 52.1 ppb. The pdf was centred around 34.3 ppb when the reference measurements were reporting 40 ppb. The range in the O_X EC measurements was reduced after *in-situ* calibration, (19.23 ppb) but the central point of the pdf was higher, at 47.3 ppb. There was a similar story with the NO_2 EC, the calibrated sensors had a narrower range of values that were centred around a value closer to the reference; uncalibrated range : 90.7 ppb and midpoint: 54 ppb, calibrated range: 47.2 ppb and midpoint: 48 ppb. There was an offset between the uncalibrated NO_2 and O_X distributions shown in Fig. 4.26a and b and

their SLR calibrated data sets. This was due to the SLR applying an offset (intercepts in linear regression) to bring the absolute concentrations of NO_2 and O_X closer to the values observed by their reference instruments. The spread of data points from both the NO_2 and O_X EC sensors suggest a large amount of variability in the EC response, compared to the reference measurements. The value of 40 ppb was chosen because it is a typical mixing ratio for NO_2 and O_X in outdoor environments and the EC sensors must provide reliable data at these concentrations and below if they are to be used to monitor common criteria pollutants. It is necessary to have a method to improve the EC sensor data if these measurements are to be used to check that regulations and mitigation programs are working and to have confidence in identifying if the level of contaminants has exceeded a certain threshold.

4.5 Background to supervised machine learning (ML)

The four main issues encountered when using LCS is that they are susceptible to cross interferences [173] [205], their sensitivities to their target measurand and other species can change over time [165] [125], there is high sensor variability [173] [104] and there is evidence that they drift [205], [24] and are noisy [165]. The noise can be minimised by careful selection of electronics and efficient data collection, and it has been shown previously, that clustering identical sensor and taking a median signal is a good method to minimise mid-term noise, and eliminates the effects of irreproducibility and individual sensors displaying large amounts of drift [165]. This also increases the time required between calibration. Machine learning algorithms and multivariate regression are used to identify relationships within data sets and were used as analytical techniques to improve the reliability of the EC sensor data by attempting to use the algorithms to better account for cross interferences [71] [35] [205]. In-field calibration with appropriate reference instruments at the site of deployment identifies potential cross sensitivities and can give an idea of how the sensors are going to behave, however it does not prevent or correct for cross interferences.

Machine Learning (ML) algorithms are used to detect trends within the sensor data by identifying the relationships between variables in a given training set. For the CO, O_X and NO_2 EC, the training period was exactly the same time as the calibration week used for SLR analysis, e.g. O_X and NO_2: 00:00 2nd June - 00:00 8th June 2017, CO: 12:00 2nd June - 00:00 8th June 2017. The ML algorithm is supervised and so uses a training label as a target for the overall ML prediction - in this case, the appropriate reference observation - and the relationships between all the available sensor data and the training label are identified in the training data set (Fig. 4.27). For example, the median NO_2, median O_X, median CO, temperature, humidity and median VOC signals were used in the training data set. The NO_2 CAPS reference data was the training label, with the notion that the ML technique identifies all the relationships between the median sensors and the

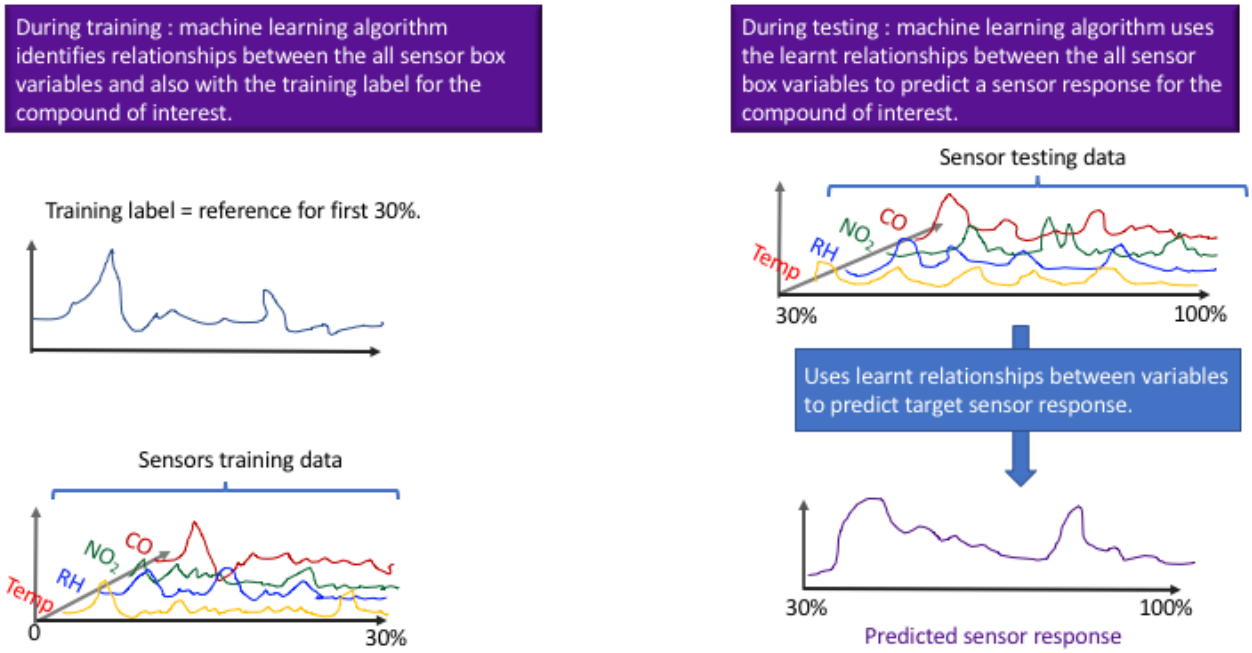

Figure 4.27: Schematic to explain how ML techniques can help to correct from cross interferences, by identifying all the relationships between the sensor box measurements and the reference data.

NO_2 CAPS, and determines a function that can be used to make a concentration estimate of NO_2 using sensor data in the testing set.

A section of the data, called the testing set, is kept completely separate from the training set. For the O_X, NO_2 and CO EC sensors the testing set was from 00:00 8th June 2017 until 26th June 2017, the last 70 % of the sensors deployment in Beijing. This second set contains all the same sensor variables as the training set, but no access to the training label as the algorithm calculates a concentration of the target compound using the model that was built during the training set. The reference measurement is purely used to evaluate the performance of the ML model by comparing the results. Continuing with the same example as before, during the testing period, the NO_2 CAPS reference measurements were removed and the algorithm predicts the NO_2 concentration estimate based purely upon the model it calculated from the training set. This predicted NO_2 signal can then be compared with the reference to identify how well the algorithm performed at determining the NO_2 concentration using the sensor data.

4.5.1 Cross validation and Evaluation

All ML algorithms use hyper-parameters to train the model, the tuning of which is conducted via cross validation (CV). CV allows the model to be optimised during the training period, and minimises the possibility of over-fitting to the data, which would result in misleading predictions [102]. When training the ML algorithm, only relationships that will

lead to the improvement of the sensor prediction are required; over-fitting occurs when the ML algorithm fits to all variations and trends within the data, including residual noise, which would lead to the ML prediction being of a poorer quality. Cross validation is a powerful approach to avoid over-fitting the ML algorithm within the training set. CV is a crucial process used to validate the ML algorithm and ensure it is detecting patterns due to the variables and not making predictions based upon the drift or noise in the EC data. During CV the ML algorithm is essentially tested upon small subsections of the training data, before the model is used to make the prediction upon the testing subset and compare against the reference observations. During CV, the testing data set is set aside completely, and the training data is split into smaller subsets of data called folds. All of the ML techniques used here utilised five-fold cross validation - splitting the training data into five equal sized segments - with a randomisation seed of 42 each time cross validation was performed. Introducing randomness when selecting a subset or fold for CV is another technique to minimise over-fitting and the seed ensures the randomisation process is consistent during CV to allow the hyper-parameters to be tuned. A minimal number of folds is selected to reduce the computational time required for CV, and each fold must be representative of the other folds within the training data [205]. Five folds was chosen here as it is a common number for a data set of this size. The algorithm trains upon and fits to four of the five folds. The fitting of the model is done using the Mean Absolute Error (MAE) as a loss function. The loss function changes when the different ML hyperparameters are changed and during CV multiple iterations of training are run with different values for hyperparameters. CV records the values of the hyperparameters required to minimise the loss function. Once the ML has determined a model to fit the four folds it has just trained with, it makes a prediction of the training label over the fifth fold, and CV estimates the error between the reference measurements and the sensor prediction. The process is repeated four more times, swapping the fold which had a prediction made over it to one of the other four folds, so that each individual fold has a prediction made over it. CV then averages the values of the hyper-parameters that made the least error from ML with each combination of four folds to produce a ML model that is ready to by used upon the testing data set. The hyper-parameters have now been tuned and are therefore these values are kept consistent throughout the model and the model was only then run on the testing data set.

The optimised ML model is applied to all the available sensor data in the testing set and the algorithm uses the trends and inter-variable relationships to predict a target compound concentration estimate, e.g. a NO_2 concentration. The prediction was then compared to the reference data over the testing period. The Root Mean Squared Error (RMSE) was the parameter chosen to determine how well the predicted sensor signal compared to the reference instrument in the testing period.

There were three different ML techniques- two parametric: boosted regression trees

(BRT) and boosted linear regression (BLR), and one non-parametric: Gaussian Process (GP)- applied separately to the same 1-minute averaged sensor data to make three different predictions of each compound. The same split to separate the training and testing data sets was used for each different type of ML, and all available sensor data from the sensor instrument was used in each technique. Five-fold cross validation, as described in this section was used to tune the different hyperparameters that each of the BLR, BRT and GP algorithms require to optimise the fitting of the different ML algorithms to the training label and training data, and to avoid over-fitting. The ML detects multiple patterns and correlations therefore it was hoped that it might prove useful for correcting some of the cross sensitivities that the sensors are prone to responding to, improving the target compound estimate overall. Three different ML algorithms were chosen to investigate which algorithms performed better at making a prediction of concentration using the sensor instruments data. Each of the ML algorithms was applied to the testing dataset to calculate a predicted concentrations based upon the relationships learnt by the models during training. The prediction was then compared against the reference observations (not given to the algorithm during testing) to evaluate the performance of the ML algorithm. RMSE was used as a comparative metric for evaluation.

4.5.2 Boosted linear regression (BLR) and Boosted Regression trees (BRT)

BLR and BRT were both applied to the sensors data set using the same open-sourced python package called Xgboost. The implementation uses extreme boosting to produce a strong learner from an ensemble of weak ones to efficiently build the ML model by optimising a loss function [26]. Essentially, this means that during boosting, an initial linear function or decision tree is calculated by the model. The subsequent tree or linear function then fits to the residuals - the data points that were not properly accounted for by the initial tree or linear function - as this will efficiently reduce the residual error and ensure the training is fast and streamlined. In this manner, it is computationally efficient and it provides good results from a variety of different research fields so is used on global platforms, such as Kaggle [26]. Five-fold CV was used to tune both the BRT and BLR parameters.

Gradient boosting works by optimising a given loss function:

1. A function was created by the algorithm to fit to the sensor data : $A_1(x)$.
2. A second function ($R_1(x)$) is created to fit to the residuals; the data points, not properly fit by the original function $A_1(x)$.
3. The two functions are combined $A_1(x)$ and $R_1(x)$ to produce the next model: $A_2(x) = A_1(x) + R_1(x)$.

4. The next step is to fit a function to $A_2(x)$ and it's residuals, $R_2(x)$ in a similar process: $A_3(x) = A_2(x) + R_2(x)$

5. These steps are repeated to create a model that is iteratively optimised by minimising the error - the error parameter was MAE for the sensors data - until the MAE is constant and cannot be reduced further, or if the number of iterations is reached.

The Mean Absolute Error (MAE) was chosen as a suitable loss function for the optimisation of both the BRT and BLR techniques.

4.5.3 Boosted linear regression (BLR)

To apply boosted linear regression (BLR) the booster is set to 'gblinear' and the specific BLR hyper-parameters were tuned with five-fold cross validation (see Section 4.4.1). The ML algorithm has an initial linear function (e.g. y in Equation 4.5) to describe the relationships between each of the sensors (e.g. NO_2 EC) within the training data set and the training label.

$$y = (a \times NO_2EC) + (b \times COEC) + (c \times O_xEC) + (d \times RH)... \tag{4.5}$$

Not all data points will be described by the initial function (these data points are the residuals) and therefore gradient boosting is applied to fit the next iterative function to these residuals. Available hyper-parameters tuned during cross validation of BLR:

- Alpha : L2 performs Ridge regression regularisation on weights.
- Lambda : L1 performs Lasso regression regularisation on weights - if a variable is below a certain level of importance the weight it is given is set to 0, ultimately removing the effect of the variable from the algorithm. This is an optimisation technique to improve the BLR model where there is a large amount of variables.
- ETA : Learning rate of the algorithm
- Number of boosting rounds: Number of iterations to perform each time CV was optimised on four folds.

During the training data, the algorithm identifies purely linear relationships between the variables and the training label. These linear trends are built into the ML model to predict the sensor instruments response to a target compound. Linear regression parameters allow for extrapolation of the results, so this technique is especially useful for when the concentration of the target measurand exceeds the maximum concentration of that compound observed in the training set.

BLR machine learning was applied to each of the three different types of EC sensor, in turn, with the same split for the training and testing data as explained previously. The

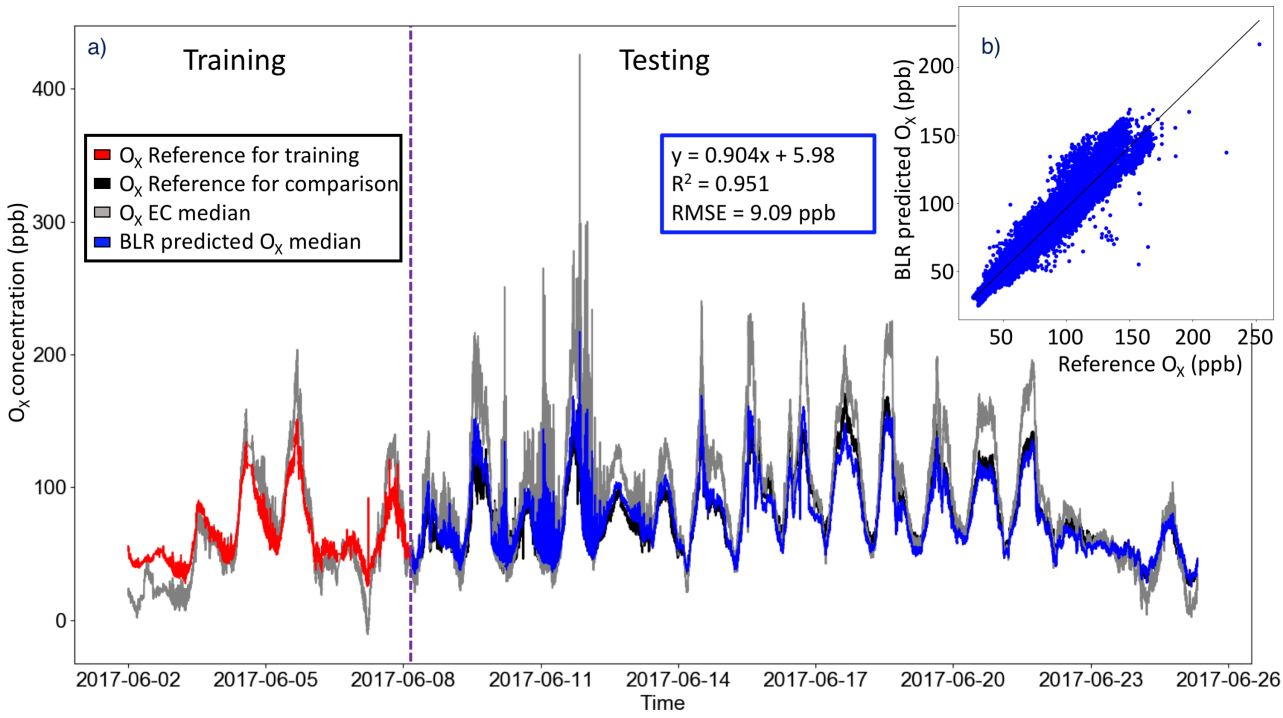

Figure 4.28: Predicted O_X median sensor (blue) using boosted linear regression. The reference O_X measurements were used as the training label (red) in the training period, but used to compare with the predicted O_X in the testing data set (black). The grey line is the median O_X sensor with no calibrations apart from the Alphasense conversion factors applied. Inset: The correlation plot between the predicted O_X sensor and the reference measurements in the testing set.

training labels were NO_2 CAPS measurement for the NO_2 EC, CO Aerolaser for the CO EC and the sum of the NO_2 and O_3 reference measurements as the training label for the O_X EC.

It was apparent from the in-field SLR calibration model in Fig. 4.25a, that the O_X sensors displayed a high degree of linearity in their responses towards O_3 and NO_2. Therefore it was no surprise when BLR, see Fig. 4.28 was able to predict a comparable O_X concentration with the reference measurements, Fig. 4.28a. The main driver for O_X EC response must have been due to the detection of O_X, as both the SLR calibration performed in the previous section and BLR results were similar. However BLR detected other smaller, linear relationships that were used to make an O_X concentration prediction that exhibited an even better agreement between the O_X EC and the reference as the RMSE was reduced from 10.3 ppb for SLR to 9.09 ppb, Fig. 4.28b. These other relationships might be a linear function fit to the NO_2 EC timeseries to describe the cross interferences of NO_2 upon the O_X EC sensor. The correlation of the BLR-predicted O_X concentration over the testing data set exhibited an R^2 value of 0.95 when compared with the reference O_X+NO_2 observations. The gradient of the linear regression between the BLR-predicted O_X and the reference measurements was 0.9, and the intercept was 6.0 ppb, (Fig. 4.28b) so the reference and BLR-predicted O_X measurements correlate with a relationship that is close

to 1:1.

BLR was also used to make concentration estimates for NO_2 and CO; identifying the linear trends between the sensor box variables (training data set 2^{nd} - 8^{th} June 2017) and both the NO_2 CAPS instrument and CO Aerolaser (used as training labels). To use the BLR algorithm to make the BLR-predicted NO_2 concentration the NO_2 CAPS was used as the training label. To produce the CO BLR-prediction the CO Aerolaser was used as a training label. The same procedures, five-fold cross validation, were used each time during the training of the algorithm.

The BLR algorithm worked really well when predicting the NO_2 concentrations over the testing set, Fig. 4.29a. There was a sudden increase in the reference observations of NO_2 between the 10^{th} and the 14^{th} June 2017 that was also detected by the NO_2 EC sensors. This was due to a known localised source of NO_2 and was not representative of the Beijing NO_2 daily mixing ratios. Figure 4.29a) indicates where the NO_2 concentrations reported by the NO_2 EC in the testing data set exceeded the maximum NO_2 EC observation in the training set. It is essential to train ML algorithms on data that experiences the same conditions as the testing set so it was interesting to see how the BLR algorithm would respond to this spike in NO_2 that greatly exceeds the maximum concentration of NO_2 observed in the training data. Since BLR detects linear functions between variables it was possible for the algorithm to extrapolate these trends to capture these NO_2 peaks. The BLR predicted NO_2 sensor showed a strong and positive correlation with the NO_2 CAPS, with a slope of 0.95, an R^2 equal to 0.94 and an RMSE of 6.52 ppb. The time between the 10^{th} - 14^{th} was removed, to see how well the BLR performed for the data more representative of the training data set and the RMSE was 6.3 ppb. The improvement in the BLR prediction was minimal evidence that the extrapolation to the higher NO_2 concentrations were good.

Considering there was a large amount of disparity between the CO EC sensors (Fig.4.29b, grey line) and the CO Aerolaser measurements due to the slightly different locations of the sampling inlet, the application of BLR analysis showed large improvements in the CO concentration estimate. BLR ML detected and corrected for the offset between the CO EC median (grey) and the reference (black) and the CO BLR-prediction was a lot more similar to the CO reference over the testing data set than the original CO EC response. The linear parameters describing the relationship between the CO reference measurements and the predicted CO concentration were; Slope : 1.03, R^2 : 0.83 and RMSE : 155 ppb respectively. This was a strong result and could lead to the improvement of CO EC data quality, increasing the confidence in observations made by EC sensors.

4.5.4 Boosted regression trees (BRT)

Xgboost was used to apply BRT to the sensor instrument data set during it's deployment in Beijing. The python package entitled 'xgtree' performs gradient boosting upon an

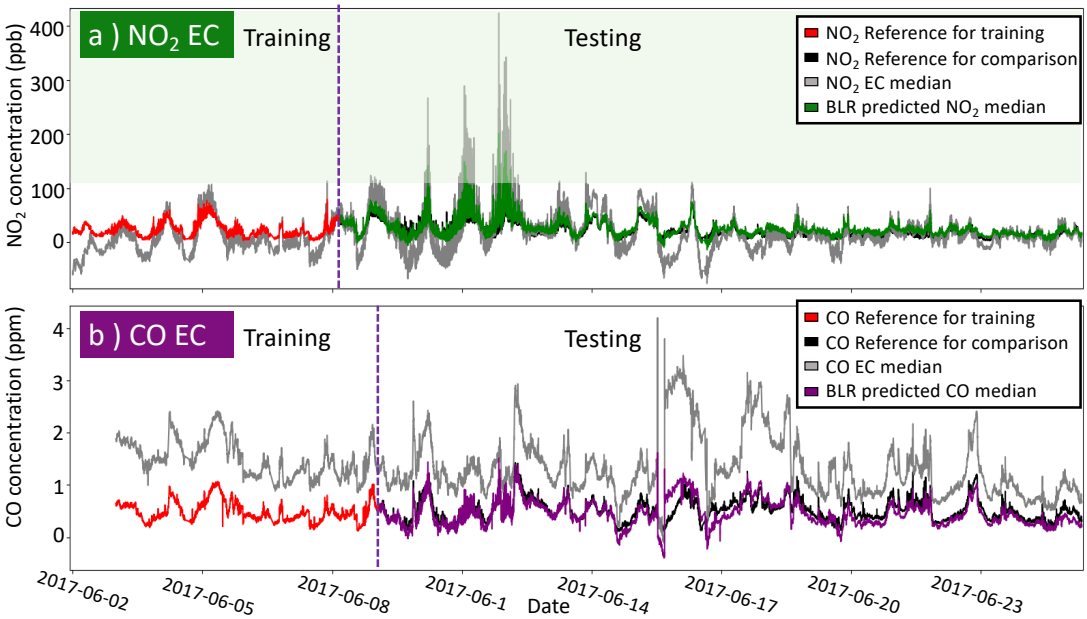

Figure 4.29: Using BLR to predict the a) NO_2 median sensor concentration estimate (green) and b) CO median concentration estimate. For both types of EC, the training period included 8490 data points, although the CO started a little later due to an offset in the CO Aerolaser on the 2nd June 2017. The reference measurements for the training period are in red, and the NO_2 and CO median sensor with no calibration is shown in grey for the respective plots, over both the training and testing periods. Where the reference data was used purely to compare the performance of the BLR predictions it is plotted as a black line. The green shaded area in the NO_2 plot (a), marks where the NO_2 concentration exceeds the maximum value in the training period.

ensemble of decision trees that are applied to the training data. The BRT algorithm discards poorly performing trees to optimise performance of an overall model. Generally, boosted regression trees are considered a more powerful technique than the boosted linear regression, and they have the added benefit that the package can provide information about the various weights given to certain decisions, which can be compared with laboratory experiments to justify why certain relationships are identified faster or more strongly than others. Five-fold CV was used to tune and optimise the hyperparameters available for the BRT algorithm, in order to fit the algorithm to the sensors data with minimal over-fitting. Hyper-parameters used in cross validation to tune to the BRT model:

- ETA : The learning step size
- Max depth: The maximum depth that the decision trees are allowed to reach - how many levels of decisions are allowed.
- Min child weight: The minimum number of data points that are allowed for a node to be split by a decision.
- Colsample : The trees were constructed and this value is the subsample ratio for the columns during the construction.
- Subsample : Value can be between 0 and 1 and refers to the subset of training data each tree is built of. If subsample was set to 0.8, each tree can be built from a random 80 % of the fold of data.
- Number of boosting rounds : This value corresponds to the quantity of trees built by the algorithm and is how many iterations are used in gradient boosting.

The iterative process identifies both linear and non-linear trends between all the variables of the sensor instrument using decision trees. This is useful for detecting smaller, less apparent relationships between variables and can therefore be very useful when predicting the non-linear lower measurements of the sensor. The objective was to investigate the optimisation of the concentration estimates, focusing on the lower, more typical concentrations of the common atmospheric pollutants as these concentrations are more typical of ambient air and are often near a threshold for regulatory purposes.

The BRT predicted NO_2 signal (green, Fig. 4.30a) was in much closer agreement with the NO_2 reference (black) than just the original median NO_2 EC sensor responses (grey). The really low dips in the NO_2 sensor data, for example, that occurred around the 16^{th} of June 2016 were corrected using BRT. These were most likely due to a cross interference that was measured by the sensor instrument and therefore simple to correct with machine learning techniques. The main peaks of the NO_2 fluctuations were matched by the predicted NO_2 signal, however the magnitude of the prediction did not always capture the highest NO_2 peaks. The overall RMSE for the NO_2 prediction (green) and

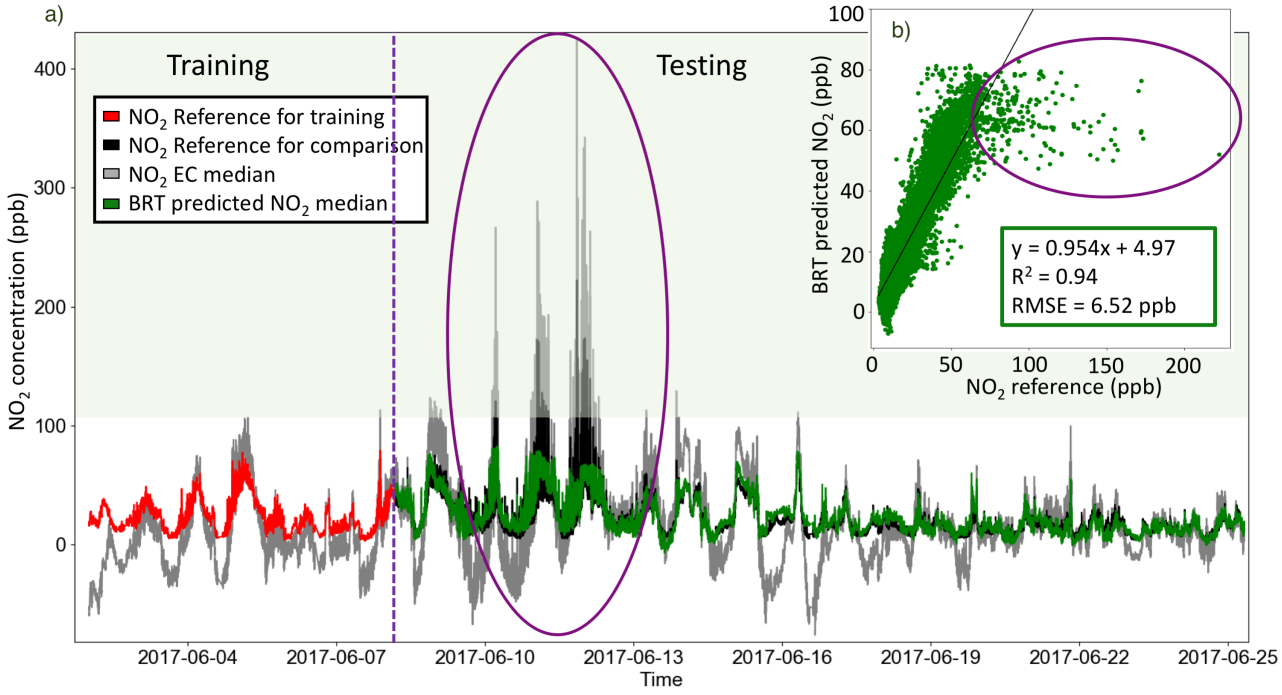

Figure 4.30: a) The time series of the BRT predicted NO_2 sensor signal (green) compared to the uncalibrated NO_2 EC sensors (grey) and the NO_2 CAPS reference measurements (black). The purple circles in both a) and b) show where the BRT prediction failed to extrapolate the learnt trends to capture the NO_2 concentrations, when they exceed 193 ppb (shown as the shaded light green area).

the reference (black) during the testing period was 6.52 ppb. The error in the prediction was therefore lower than the error calculated using SLR over the same time (SLR RMSE 11.8 ppb).

Figure 4.30 shows a major disadvantage of using BRT - since the BRT algorithm used decision trees to determine the sensor response, it was incapable of extrapolation. This was evident during the localised emission of NO_2 that occurred between the 10th and the 14th June; the BRT prediction failed to capture the NO_2 concentration when the EC sensors reported values in excess of 193 ppb (accentuated by the purple circles in Fig. 4.30). This value was the maximum concentration observed by the median NO_2 EC sensor in the training portion of the data, and the threshold for this is highlighted as green shading in Fig. 4.30a. This emphasises the importance of using a training data set that is representative of the testing set, where the sensors are exposed to the full range of expected environmental conditions. To use machine learning in the field there is a requirement to flag data that is collected at times when the conditions are not similar to the conditions that the algorithm trained in. For example, it is important to flag up the times where the NO_2 concentration observed by the sensors in the testing data is greater than the maximum NO_2 concentration in the training data, or when the environmental conditions experienced by the sensors in the testing set are outside the ranges of conditions experienced by the sensors in the training data set. After being flagged the data can be checked and re-

analysed to investigate how well the machine learning coped with predicting concentration estimates during these times. Laboratory experiments can be used to ensure that the sensors behaviour to unusually high concentrations of the target or cross interference compounds is captured in the training data so very little extrapolation is required in the testing set. Equally, iterative learning techniques, whereupon the training data set is expanded to include the time period over which the NO_2 concentrations increased (extend the training period until the 16^{th} June 2017) may be a powerful method of extending the ranges of conditions within the training period and hence may cause the ML to perform better. Iterative training was not used in this study but may be useful for sensors in the field.

To investigate the performance of the BRT prediction at the lower concentrations of NO_2, the RMSE was calculated when the days between the 10^{th} and 14^{th} June were removed. The RMSE decreased to 4.73 ppb; evidence that, when no extrapolation is required, BRT surpasses the BLR when there are more complex relationships between variables, by identifying smaller, more niche nuances in the NO_2 data, and correcting for non-linear cross sensitivities.

BRT analysis was applied to the available sensor data and trained to predict pollution estimates for O_X and CO. This was successful in improving the pollution estimates for both compounds as both models returned predictions that were closer to the reference observations (RMSE O_X : 9.18 ppb, and RMSE CO: 163 ppb) than the EC with the conversion factors applied.

An advantageous feature of BRT is that it is possible to extract information about how the decisions in the trees are made, and the weight each decision has on the overall tree. The contribution of each variable to the overall BRT algorithm (gain) is shown for the BRT analysis upon the three different EC sensors, see Fig. 4.31.

Promisingly, when using BRT to make the three separate predictions of O_X, NO_2, and CO concentrations, the overwhelming main contribution to the decisions made during the training of the BRT model were the median O_X, median NO_2 and median CO variables, respectively. This is strong evidence that the EC sensors were responding to and detecting their target compounds during the Beijing deployment, and that the BRT algorithm is detecting correlations and trends that are from the real sensor measurements. The gain feature can also be used to identify potential cross interferences; for example the second largest contributor to the NO_2 prediction was the median CO sensor, followed by humidity, see Fig. 4.31c. This can be corroborated with laboratory experiments, or be used to design experiments to test the EC sensors for responses to compounds that were not previously known to be interferents. Previous studies have shown that CO and humidity affect the NO_2 EC [104] and this information is evidence that the BRT can be useful for correcting cross interferences. The CO BRT prediction had the highest gain values from the median CO EC and the NO_2 which was also known to affect the CO response in other laboratory

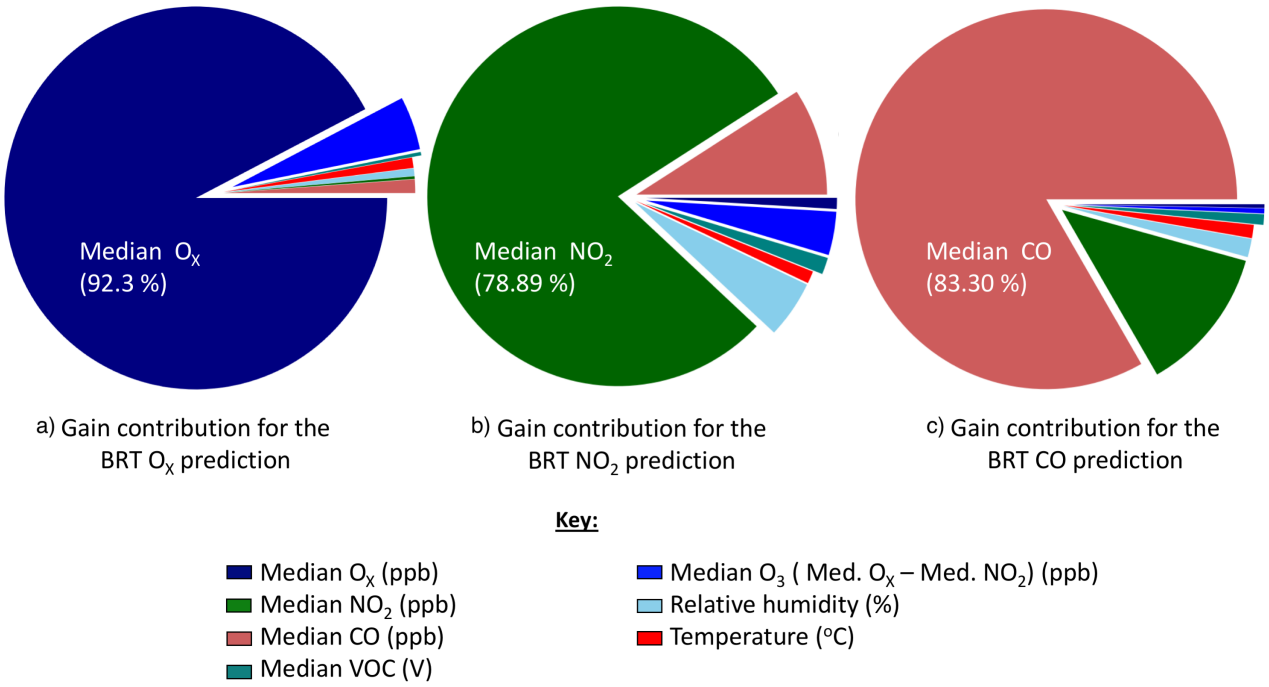

Figure 4.31: For each BRT analysis conducted upon the a) O_X, b) NO_2 and c) CO EC sensors the relative contributions of each variable to the overall BRT algorithm used to make the the prediction was determined.

studies [104]. Note, these gain results may prove useful for identifying new interferences, but the laboratory experiments are essential to characterise responses as it might just be a co-incidence that the two sensors are correlated. Correlation is not always causation.

4.5.5 Gaussian process (GP) ML

Gaussian process (GP) is a non-parametric ML process [147] which was implemented using a different python implementation, GPy, to the BRT and BLR algorithms. The supervised learning method trains, cross validates and tests the same set of sensor data as the parametric techniques. The training/testing split occurred in the same place to allow a fair comparison of the different ML algorithms. Multiple functions are identified by the GP algorithm and each one has a Gaussian distribution fitted; these are then generalised to form a model which is capable of regression and prediction. Specific kernels - covariance functions - must be chosen based on the data before the creation of the model [64]. Two kernels were chosen and used simultaneously for the use of a GP algorithm upon the sensor data, leading to an overall covariance function that was the summation of the Matern32 kernel and a linear kernel. This would be advantageous to allow GP to fit to non-linear trends in the sensor data and attempt to extrapolate in instances where the conditions in the testing set differs from the training set. It was known from the SLR that the relationships governing the sensor performance were often linear therefore the linear kernel was deemed a suitable choice. An important benefit from using GP is that, like the other

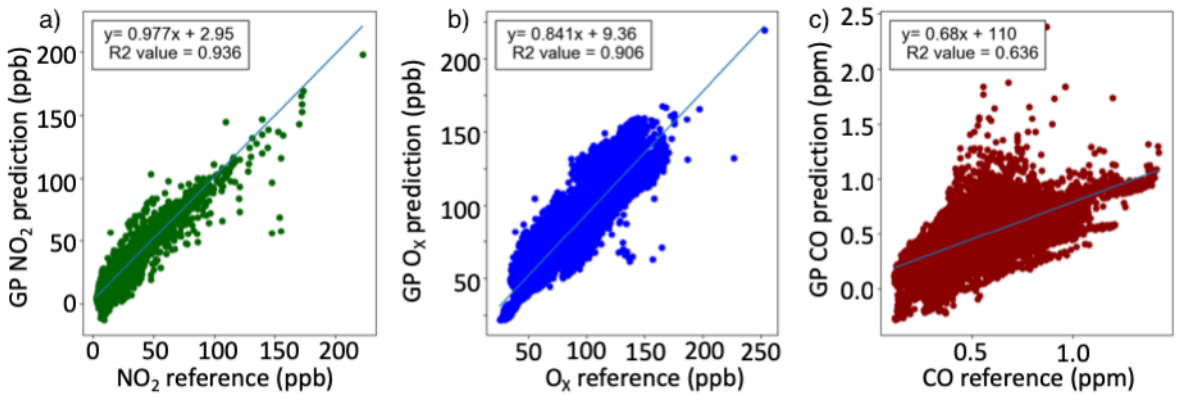

Figure 4.32: The correlation between the a) GP predicted NO_2, b) GP predicted O_X and c) GP predicted CO concentrations and their respective reference instrument measurements.

two ML techniques, it provides a prediction estimate, but additionally it also produces an uncertainty estimate for the prediction too. This is very useful when identifying times where the uncertainty is high and flagging up data that might be unusable if this portion of the data contains a high degree of error.

GPy was used with the sensor data and the respective reference observations to build three GP models for three predictions of CO, O_X and NO_2. These three pollution estimates displayed concentrations that were closer to the reference measurements than the EC alone. The GP predicted concentration estimates for NO_2 and O_X were highly correlated with their respective reference measurements, displaying R^2 values of 0.94 and 0.91 respectively, Fig. 4.32a and b. For NO_2 the GP predicted concentration estimate had a higher correlation than the uncalibrated median NO_2 sensor which had an R^2 of 0.88. However the uncalibrated O_X median EC sensor had a higher R_2 when correlated against the O_x reference instrument (0.95). The gradient between these GP predictions and the reference measurements were also close to 1 (GP-predicted NO_2 gradient: 0.98, uncalibrated NO_2 gradient : 1.98, GP-predicted O_X gradient: 0.84, uncalibrated O_X gradient: 1.52), indicating that the predictions made by GP enabled the EC predicted concentration estimates to be closer to the reference concentrations than the EC sensor data alone.

The GP predicted CO concentration was only moderately correlated with the CO reference data ($R^2 = 0.64$), and this was a weaker correlation than the correlation of the uncalibrated median CO EC sensor versus the CO reference displayed and R^2 of 0.71. The GP algorithm was therefore not very good at capturing the trends between sensors when the reference instrument was not co-located with the sensors.

The predictions for the GP NO_2, O_X and CO predictions detected the major trends in the data and the error was reduced to exhibit a NO_2 RMSE of 6.00 ppb, an O_X RMSE of 12.65 ppb and CO RMSE 193.5 ppb for each estimate versus the reference. GP can also be used as part of an *it situ* calibration procedure with co-located reference instruments to reduce the impact of cross interferences and hence led to higher quality EC sensors data. The advantage to using GP was that the uncertainty in the GP concentration

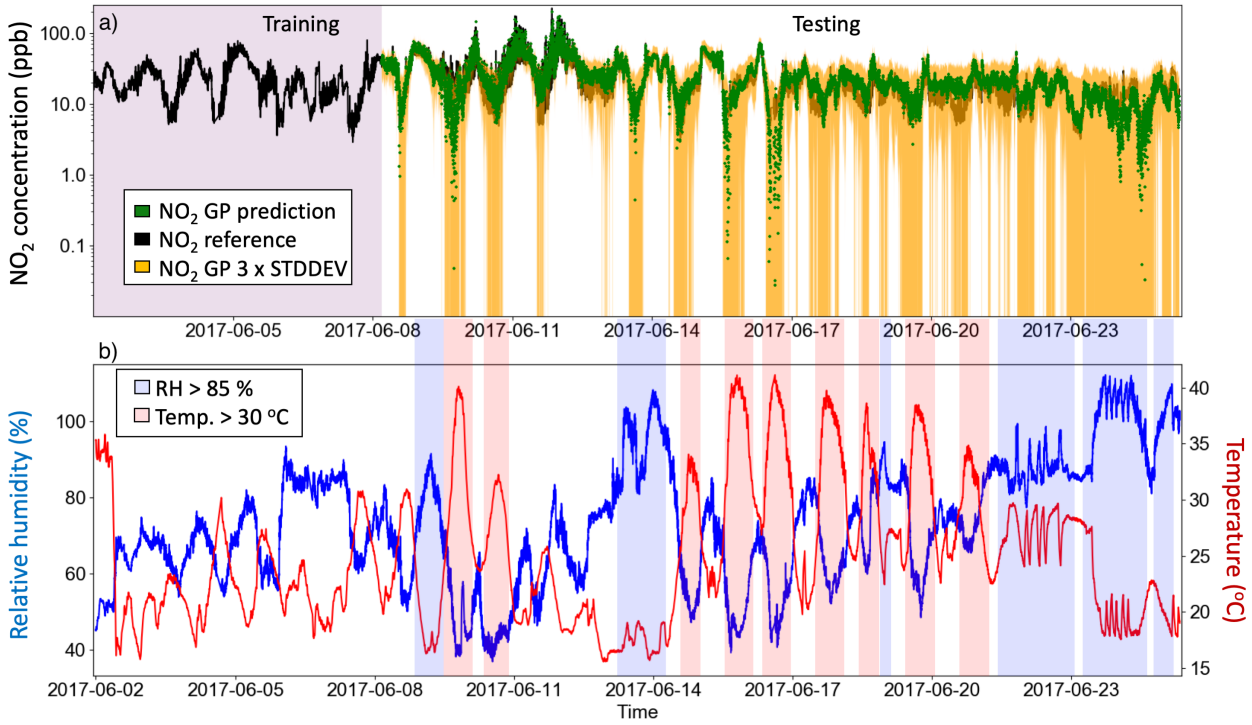

Figure 4.33: a) The GP predicted NO_2 concentration (green) with the 3x standard deviation from the GP estimate (yellow) plotted too. The NO_2 reference observations are shown in black. The GP prediction and NO_2 CAPS observations are plotted on a logarithmic axis to emphasise the differences between the two time series and to highlight where the greatest uncertainty in the GP prediction occurred. The temperature and humidity time series, b) are plotted to indicate that the uncertainty for the GP prediction was highest when the temperature was greater than 30 °C, or when the RH was greater than 85 %. GP was therefore a technique to identify interfering conditions that impact the EC sensors performance as these periods of uncertainty occur when the relationships between the sensors are different. compared to the relationships in the training data.

estimates can be extracted from the algorithm. Figure 4.33 shows the NO_2 GP prediction (green) with ±3 standard deviations (yellow) overlaid onto a logarithmic y-axis. The y-axis was logarithmic to highlight the differences between the NO_2 GP prediction and the NO_2 CAPS reference measurement, as well as emphasising the time periods when the uncertainty in the GP prediction was high. The uncertainty estimate was extracted from the GPy implementation and allows information about the reliability of the prediction to be examined. The NO_2 GP prediction was more uncertain during times when the temperature of the air reaching the sensors exceeded 30 °C or if the air flow contained greater than 85 % relative humidity, Fig. 4.33. Therefore, the uncertainty estimate was useful for identifying the environmental conditions that impact the sensors signal, as the changing RH and temperature caused the sensors relationships between each other to differ and led to high uncertainty. Previous experiments indicated that when the external conditions of the sensors surroundings changed the data was less reliable. The uncertainty estimate is a useful tool for identifying when the GP-prediction has high uncertainty, which means that the EC sensors will be behaving differently compared to when their performance during training. By identifying periods of uncertainty, and correlating this with other variables, for example temperature, humidity, the environmental conditions that impacted the prediction the most can be investigated. During training the sensor data did not observe these maximum temperatures or humidity's and therefore this uncertainty estimate suggested that for GP predictions to be more robust, the full range of conditions that the sensors will be subject to in the testing set should be met in the training data.

4.6 Evaluating the different analytical techniques applied to EC sensors

The EC sensors have been subject to several different methods to establish which method was optimum to improve the reliability and accuracy of low-cost sensor data.

4.6.1 NO_2

Figure 4.34 compares each of the analytical methods used to improve the quality of the NO_2 EC sensor data. Using the RMSE as an evaluation metric, Fig. 4.34 identified that GP ML produces a NO_2 concentration estimate that was closest to the reference observations as the RMSE comparison with the reference NO_2 observations was the smallest.

The inclusion of the Matern32 (non-linear) and linear kernels determined an algorithm that predicted the NO_2 concentration estimate RMSE (6.0 ppb) that was comparable to the RMSE calculated between the two NO_2 reference instruments (4.26 ppb). Using both kernels simultaneously allowed for a good estimate of the lower levels of NO_2, with the benefit of linear extrapolation to reach the NO_2 peaks when the sensors detected NO_2

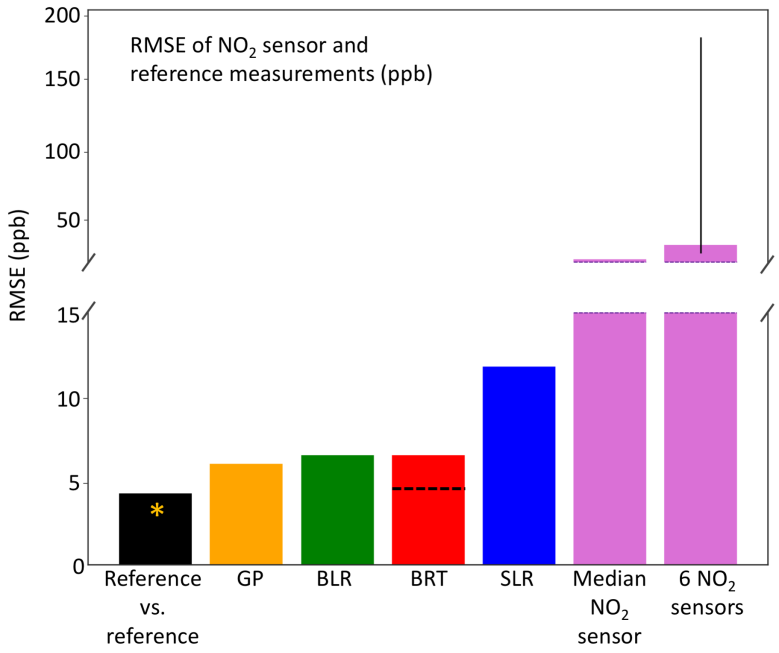

Figure 4.34: Comparison of the different approaches to optimise the NO_2 sensor data so that it provides a more robust and accurate measurement of the environment. The GP prediction of NO_2 displayed the lowest RMSE when compared to the reference measurements. There were two NO_2 CAPS instruments on site to enable a reference versus reference comparison to be made.

concentrations greater than 193 ppb in the testing set. The result was a NO_2 concentration estimate that was very similar to a reference measurement and that has a RMSE close in value to the RMSE when two NO_2 reference instruments were compared. There was a second NO_2 CAPS measurement at the IAP site (IAP CAPS) which also sampled at ground level around 50 m away from the York CAPS. The slight difference in location, however, did mean that the IAP CAPS instrument did not observe the high NO_2 levels between the 10^{th} and 14^{th} of June, because it was upwind of the localised NO_2 emission. Including all the data in the testing period, the RMSE between the two NO_2 CAPS instruments was 7.07 ppb; this was reduced to 4.26 ppb, if the high NO_2 concentrations were omitted.

All three of the ML techniques used to make an NO_2 concentration estimate displayed an improvement in the quality of the data (GP RMSE :6.0 ppb, BRT RMSE: 6.52 ppb and BLR RMSE :6.52 ppb), compared to the uncalibrated median NO_2 EC (RMSE: 22.0 ppb). There were small differences between the RMSE for all three ML concentration estimates and all the ML predictions performed well with each NO_2 concentration estimate displaying a similar amount of error in their measurements compared to the two reference instruments.

It was interesting to examine how well the ML algorithms performed for different concentration ranges in the data set. The maximum concentration (100 %) was used to split the data into four sections to evaluate (using the RMSE and NRMSE metrics) the

Table 4.3: The NRMSE and RMSE (in brackets) between the NO_2 reference observations and the NO_2 observations made by the uncalibrated median EC and the NO_2 concentration estimate after SLR, BLR, BRT and GP were all applied separately. The different concentration ranges were investigated as the NRMSE and RMSE were computed for data that fell between 0 - 25 %, 25 - 50 %, 50 - 75 % and 75 - 100 % of the maximum NO_2 reference concentration. The NRMSE was calculated by dividing the RMSE between the reference observations and the sensor values by the mean reference concentration for the respective bin.

Concentration range as a percentage of the max. conc. of NO_2	Uncalibrated median NO_2 EC	SLR	BLR	BRT	GP
0 - 25	1.04 (20.7)	0.59 (11.7)	0.32 (6.3)	0.28 (5.6)	0.29 (5.8)
25 - 50	0.69 (47.5)	0.19 (13.3)	0.12 (8.2)	0.22 (15.2)	0.11 (7.9)
50 - 75	0.72 (94.9)	0.23 (30.8)	0.26 (34.6)	0.55 (75.5)	0.26 (33.5)
75 - 100	0.85 (153.1)	0.10 (17.4)	0.10 (18.8)	0.67 (120.0)	0.10 (18.2)

performances of the ML at different concentration ranges; NO_2 concentrations that were a) 0 to 25 % , b) 25 to 50 %, c) 50 to 75 % and d) 75 to 100 % of the maximum NO_2 concentration, see Table 4.3. It was clear that the BRT algorithm did not perform well at extrapolating and capturing the higher concentrations of NO_2. Table 4.3 shows that the BRT algorithm was the most suitable ML algorithm for predicting the lower concentrations of NO_2 where the relationships between sensors may not always be linear.

Compared to the uncalibrated median NO_2 EC, there were improvements across all ranges of NO_2 concentration when the GP was used to predict NO_2 concentrations. SLR, BLR and GP were optimum for predicting higher concentrations of NO_2 and their ability to extrapolate is evident because at 75 - 100 % of the maximum observed NO_2 concentration they all exhibited very low uncertainties within their predictions (NRMSE of 0.1). However, these calibrations did not show the best improvements for the sensor concentration estimates at the lowest NO_2 concentrations, whereupon the BRT algorithm was optimum for minimising NRMSE. For the low concentrations of NO_2, 0 - 25 % of the maximum NO_2 observed, BRT displayed the smallest NRMSE (0.28) compared to all the other analytical techniques (for 0 - 25 %, SLR NRMSE: 0.59, BLR NRMSE:0.32 and GP NRMSE:29). This was evidence that there were non-linear trends that became important for making an NO_2 concentration estimate. As, for the latter half of the testing period during the BLR prediction, the NO_2 concentrations were much lower and there were slightly more deviations of the BLR-predicted NO_2 concentration from the reference (NRMSE:0.32). The BRT could not extrapolate and hence the NRMSE for BRT at 75 - 100 % was 0.67. However, there were fewer data points at the higher concentrations and

therefore BRT made a NO_2 concentration prediction that was comparable to BRT and GP. The GP performed well, with low NRMSE values at every concentration range; this was due to the non-linear Matern32 kernel capturing the smaller, non-linear relationships between sensors and the linear kernel capable of extrapolation. When the data containing the localised source of NO_2 (between the 10^{th} June and 12^{th} June) was removed from the BRT NO_2 prediction, the RMSE decreased to 4.73 ppb, dashed black line across the red bar). This was almost the same as the RMSE calculated for the two reference NO_2 instruments over the same time period (black bar with a yellow asterisk to mark the fact that this RMSE was determined without the data during the localised emission of NO_2 too.). This was encouraging when considering the EC for use as air pollution monitors in the ambient air as the spread of measurements at ambient levels is reduced and there is more confidence in the sensor measurements. When analysing the full training data set, the BRT and BLR predictions were similar, with the BLR able to extrapolate and capture the high NO_2 concentrations, whilst the BRT was better at predicting the lower levels of NO_2 on average. Both BLR and BRT are computationally inexpensive methods that can be applied during post-analysis to optimise sensor data and make it more useful for complementing Air Quality Monitoring stations in ambient deployment, as the NO_2 concentration estimates were more reliable and accurate using this technique.

The pink bars in Fig. 4.34 depict the RMSE for the comparison of the NO_2 EC with the reference observations after the factory calibrations were applied, just over the testing period to allow a fair comparison with the other techniques. There was a huge amount of variability in the six RMSEs for these comparisons; the sensor with the most error had a RMSE of 180.62 ppb, and the smallest RMSE was 26.22 ppb. Using just one sensor, out of the box, with no in-field calibration would result in little confidence for air quality measurements, as it would be difficult to identify how much error there is in the sensor data. However the NO_2 sensor data was improved and became much more reliable after clustering the sensors and using the median signal (RMSE decreases to 26 ppb). This was further optimised by utilising all the variables within the sensor instrument together with a ML algorithm (BLR and BRT RMSE were both 6.52 ppb for testing data).

4.6.2 O_X

There was a lot of variability between the six individual O_X sensor performances after the 8^{th} June leading to a large range of RMSE (26 to 82 ppb) when these were individually compared with the O_X reference measurement. In Fig. 4.28 the median O_X over-estimated the O_X concentration when the reference measurements were high and reported values that were lower than the reference when the O_X concentration was less than 50 ppb. This was reflected in the large RMSE (25.5 ppb) calculated when comparing the median O_X EC to the reference observations, Fig. 4.35a. The individual sensors therefore must exhibit more extreme behaviours than the average signal leading to the variability in

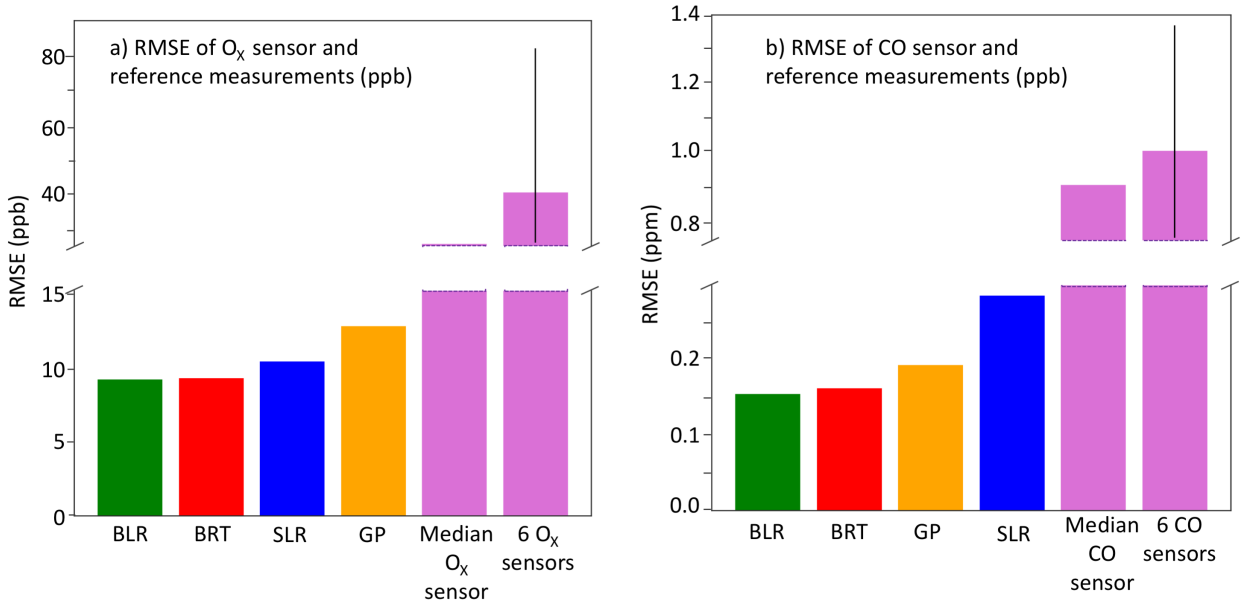

Figure 4.35: Comparison of the different approaches to optimise the a) O_X and b) CO EC sensor data so that it provides a more robust and accurate measurement of the two pollutants in Beijing.

the error parameter. All methods of regression were successful in reducing the error in the concentration to below 13 ppb. Out of the ML techniques used, the parametric ML techniques, BRT and BLR behaved very similarly and were optimum for producing an O_X measurement value that contained the smallest amount of error, with the RMSE being less than 9.2 ppb for both algorithms. BLR exhibited the lowest error therefore the relationships governing the sensor behaviour were mainly linear over the conditions experienced by the sensors during the campaign. More evidence for the high degree of linearity over the O_X sensor variable space was that even SLR was able to decrease the error in the O_X significantly (RMSE : 10.3 ppb) and this method even performed better at reducing the error in the median O_X EC signal than GP (RMSE: 12.65 ppb). It was surprising that GP did not perform better as the algorithm was still using a combination of the linear kernel and the Matern32 (non-linear) kernel. Potentially, there was a degree of over-fitting involved with the GP prediction. The algorithm may have identified trends within the data set that were more representative towards random noise in the data set which would impact the quality of the GP-prediction.

4.6.3 CO

The three ML algorithms made CO concentration predictions that contained the lowest amount of uncertainty, with BLR exhibiting a RMSE (155 ppb) that was almost half the value for SLR (RMSE: 286 ppb), Fig. 4.35b. Since the CO reference instrument was located and sampled at a different height to the CO sensors this was to be expected as the CO concentration determined by the sensors sampled different parcels of air occasionally.

During these times, the ML potentially utilised the relationship that CO has with the other sensor observations; for example CO and NO_2 levels are often highly correlated at the ground level because they are both emitted from traffic. The gain contribution for BRT identified NO_2 as being the second largest contributor to the CO-prediction, which supports this notion. Just applying the factory conversion values led to the individual CO EC sensors manifesting a large spread in the RMSE with the CO Aerolaser, and the bar chart in Fig. 4.35b supplied evidence that clustering sensors and using a median was a good way to increase the robustness of the CO sensor observations.

4.6.4 Overall

Applying ML techniques led to improved comparisons of the EC sensor data with the co-located reference instruments. By using a sensor instrument that monitored multiple pollutants the ML were able to correct for the majority of the impacts due to cross interferences and produce a concentration estimate that was closer to the reference observations. This made a cThere were seoncentration estimate that was ven the median EC sensor alone and will be useful for reducing the uncertainty within sensor measurements. Offsets due to inaccurate factory calibrations and electrical noise were reduced and there is more confidence in the absolute concentration values produced by the ML-concentration estimates. n variables avaimore robust thalable for the ML algorithms to learn from, the median NO_2, O_X, CO and O_3 (O_X EC - NO_2 EC) EC, median VOC MOS sensor, RH and temperature. ML techniques may be further improved if other variables that impact the sensor performance (for example, potentially other interfering gases, atmospheric pressure) are monitored within the sensor instrument. Expanding the range of conditions used in the EC sensors data will also improve the EC ML-concentration estimates.

4.6.5 MOS and machine learning

There were two reference methods available for evaluating the performance of the MOS sensors but the limited temporal resolution of the GC-FID meant that there was not a sufficient amount of data points for a machine learning algorithm to be able to train upon the GC reference data properly. The 1-minute SIFT-MS data was therefore used as the training label, however due to the SIFT-MS sampling technique (alternating at ground level to 100 m) there were fewer data points than for the O_X and NO_2 EC sensor and reference measurements. BRT was used to investigate the suitability of ML techniques applied to MOS. The MOS sensors are generally more prone to cross sensitivities than the EC sensors and therefore it was possible that ML algorithms might be a powerful method for determining a more accurate VOC concentration estimate. The BRT ML algorithm previously worked well using the EC sensors and had the added bonus of extracting information regarding the decisions from within the trees which is important for helping to

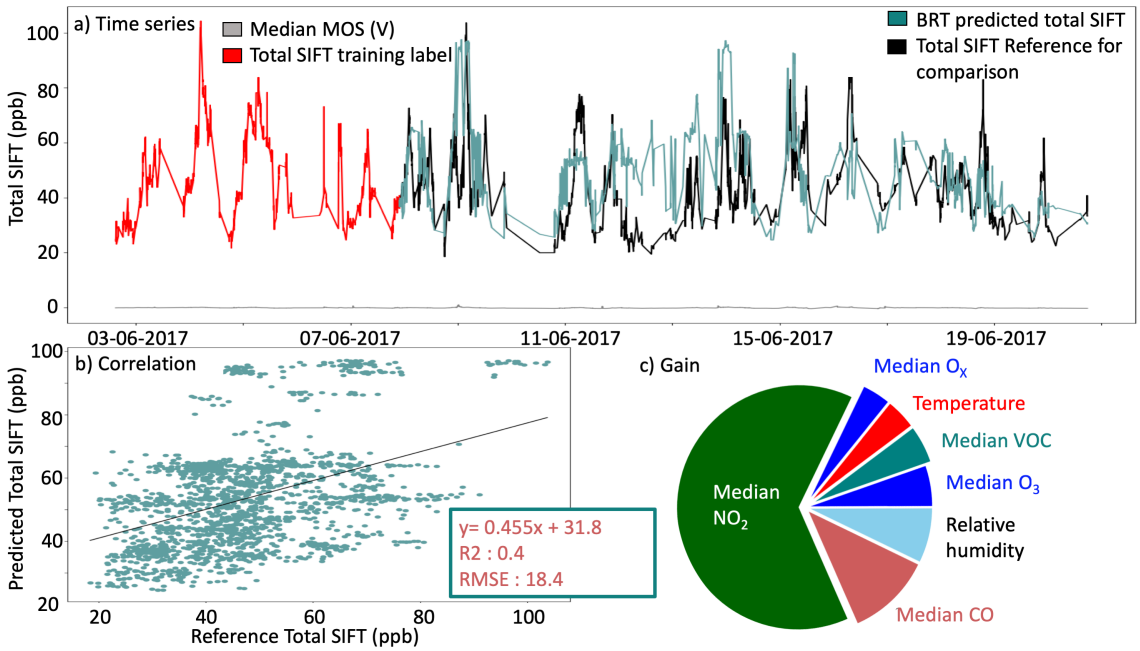

Figure 4.36: a) The training and testing time series using the total SIFT ion count as a training label during the training phase (red) and using this with BRT and all the sensor data from the sensor instrument to make a total SIFT prediction (teal) in the testing phase. The grey line shows the median MOS signal (V), corrected by temperature and humidity which was used for the prediction. b) The correlation plot for the reference Total SIFT and the BRT prediction, showing a moderate, positive correlation (R^2: 0.4 and slope: +0.5) and c) the gain feature from the decision trees used to train the BRT algorithm to predict the total SIFT concentration levels using all available sensors in the sensor instrument. The NO_2 and CO EC made the largest contributions towards the total VOC prediction.

identify the key drivers in the MOS response.

The BRT prediction of the summation of all 29 compounds measured by the SIFT-MS was conducted slightly differently to the other BRT predictions. The training data set comprised of 1000 data points and the testing set had 1921. The temperature and humidity corrected median MOS signal was used in the training data, and is shown in plot Fig. 4.36a as a light grey line, which appears around 0 as it is measured in Volts. BRT captured the general trends in the data and produced a moderate correlation of predicted total VOC with reference measurement (R^2 : 0.4). However, this was a weaker correlation than was observed for the median VOC MOS with no ML technique applied with the SIFT-MS Total VOC concentration, as this displayed an R_2 value of 0.47. There were clear sections of the time series where the SIFT-MS reference observations did not match up with the BRT predicted SIFT data: during the 12^{th}- 13^{th} June the BRT total VOC prediction was nearly 40 ppb higher than the SIFT-MS reference measurements. The NRMSE associated with the prediction was 0.25, indicating a reasonable uncertainty within the VOC prediction. The information from the gain function, supplied by the BRT ML package, was rather surprising, as the median MOS total VOC sensor was only

the fifth largest (out of the seven different types) low-cost sensor contributor towards the total VOC prediction. Since the MOS sensors were supposed to detect total VOC, and correlated reasonably well with the SIFT-MS Total VOC concentration in the previous section, it was expected that the MOS would make the largest contribution to the Total VOC concentration estimate. However, the largest contribution, by far, was from the median NO_2 EC sensor (64 %), followed by the median CO EC (11 %) sensor, see Fig 4.36c. There is potentially some logic behind these two EC sensors having the most contributions to a total VOC prediction; all three have common emission sources and the tropospheric reactions which govern their behaviour are linked, leading to their ambient concentrations being related. The BRT algorithm may have detected these relationships between the three compounds in the training period and then applied these trends to the sensor data in the testing period.

The total VOC signal is composed of multiple different compounds with varying reactivity that will elicit different responses on the MOS sensing surface. The SIFT-MS total compound signal might not be representative of the compounds that the MOS has a large response to and might be overwhelmed by certain compounds that the MOS sensors are not sensitive towards, leading to the poorer MOS performance. The preceding MOS analysis established that the MOS sensors had the best correlations with the aromatic and aldehyde compound classes, see Fig. 4.21. Consequently, the process of BRT analysis was repeated, using the same set of sensor data and the same training and testing data set splits, to provide a prediction of the total aldehyde component of the SIFT data, Fig. 4.38a, and then the total aromatic compounds, Fig. 4.38b. For the total aldehyde BRT prediction, the sum of all the aldehyde compounds monitored by the SIFT-MS was used as the training label and for total aromatic prediction the sum of the aromatics measured by the SIFT-MS was used for the training label.

The variation in the aldehyde concentration was largely detected by the aldehyde BRT-prediction, Fig. 4.37a, although there were occasions where there were aldehyde peaks predicted by BRT that were not observed in the reference aldehyde data. For example there was an aldehyde peak predicted on the 12^{th} of June that was wider and offset to the peak in the SIFT-MS aldehyde data, Fig. 4.37a. The concentration of the SIFT measured aromatic compounds varied between 0.1 and 6.2 ppb, and the aromatic BRT concentration estimate was able to reflect this and detect the majority of spikes in the aromatic concentration data, Fig 4.37b.

The correlation plots showing how the BRT predicted aldehyde (Fig. 4.38a) and the BRT predicted aromatic concentration estimate (Fig. 4.38b) compare to the reference counter-parts look relatively scattered. With the total aromatic signal as the training label, the BRT predicted aromatic measurement had an improved correlation ($R^2 = 0.5$) and a lower error value (RMSE: 0.79 ppb) than the BRT-predicted Total VOC SIFT concentration estimate. The median MOS responded with a greater sensitivity towards

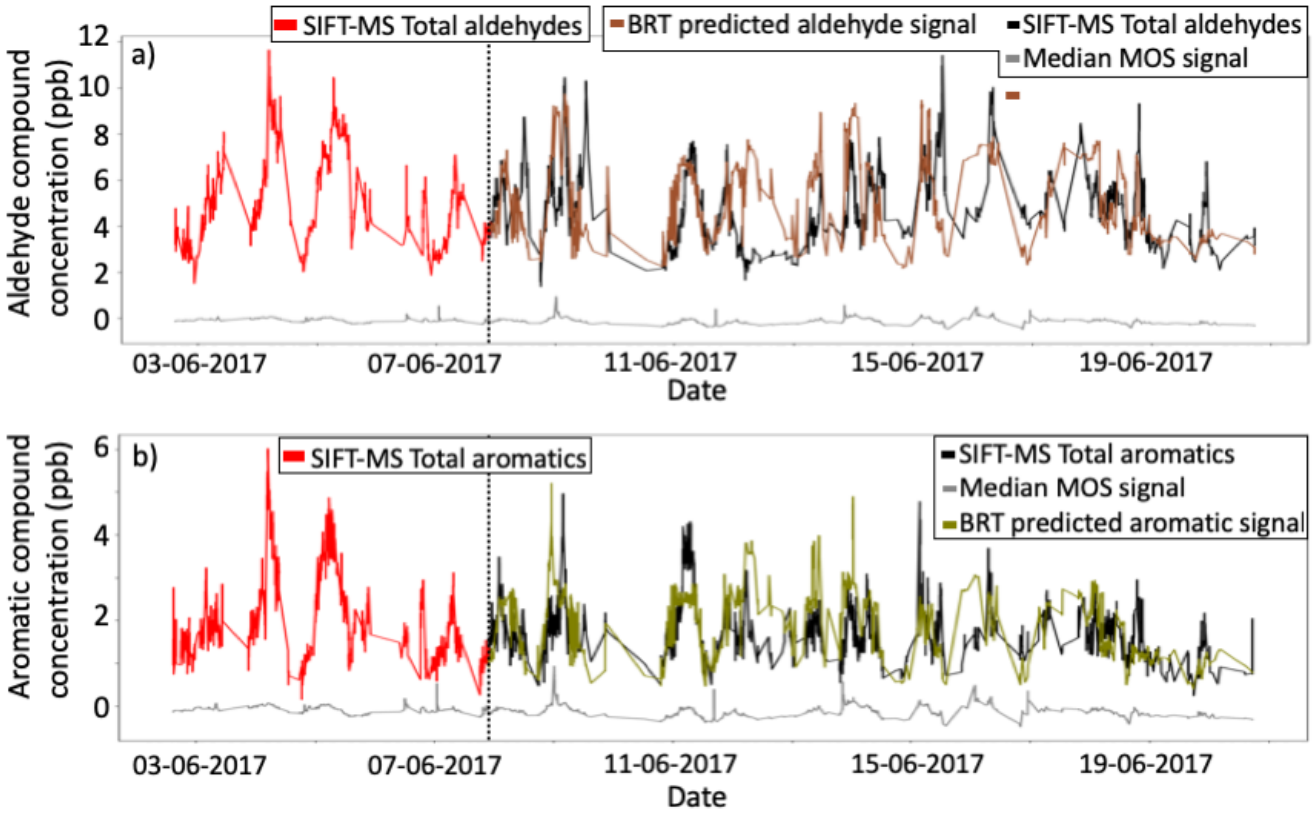

Figure 4.37: The timeseries for the BRT-predicted a) aldehyde (brown) and b) aromatic (olive green) concentration estimates. The median MOS signal is shown in grey, and the reference SIFT-MS total aldehyde (a) and total aromatic (b) concentrations are in red for the training data set and black for the testing set.

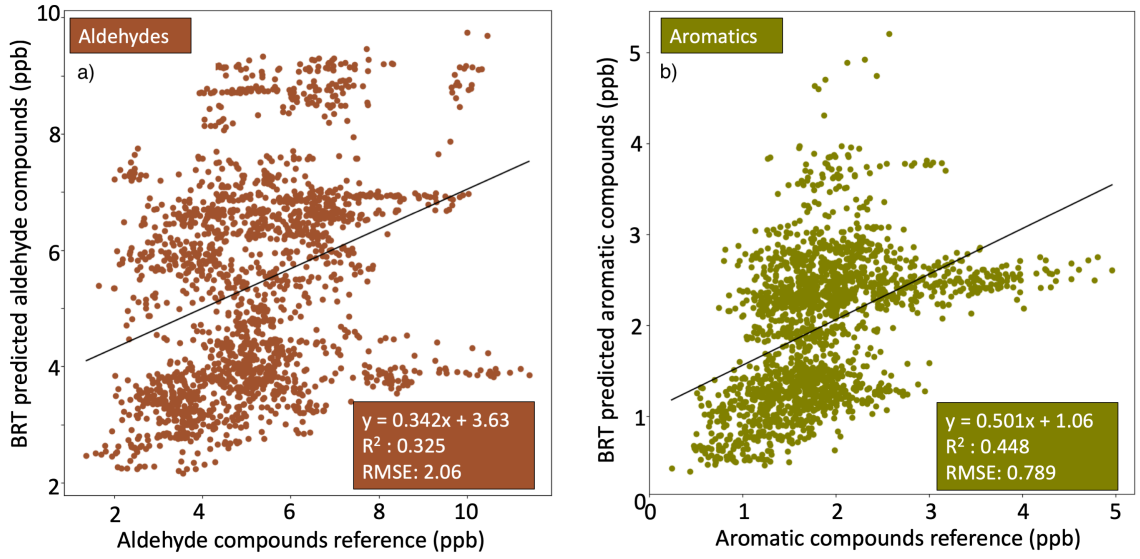

Figure 4.38: Correlation plots comparing the BRT predictions of a) the sum of the aldehyde compounds and b) the concentration of the sum of all the aromatic compounds, to the reference measurements of these classes of compound as measured by the SIFT-MS.

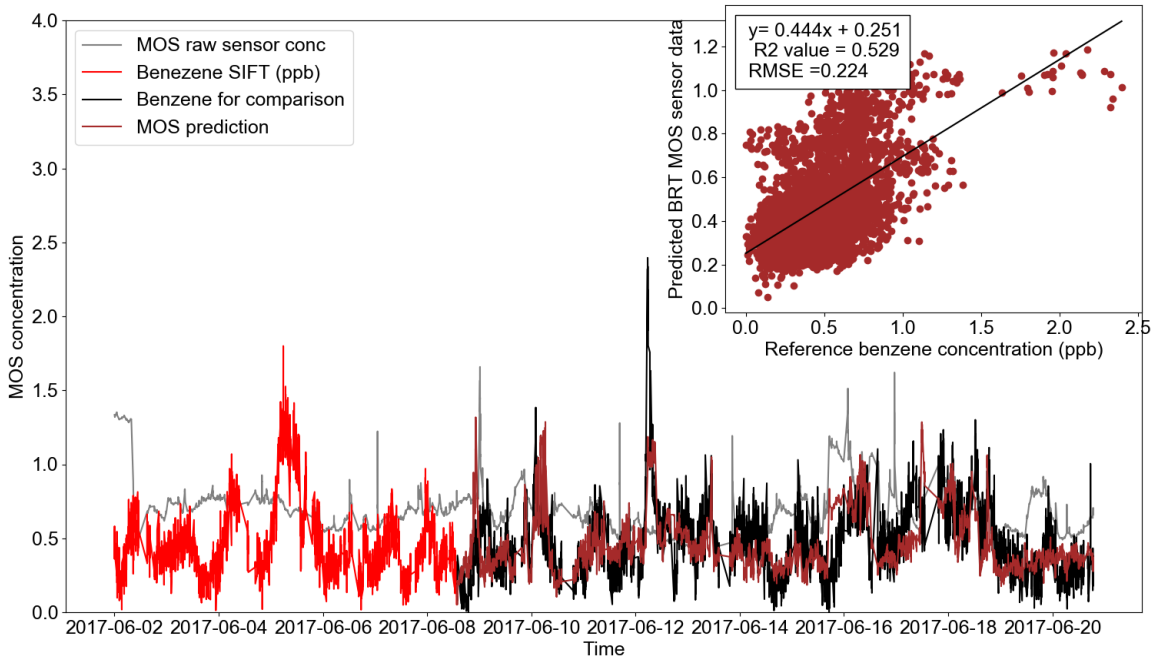

Figure 4.39: BRT analysis performed upon the sensor instrument data, using benzene from the SIFT-MS measurements as a training label (red). The first 30% of the data was used for training and the remainder is the testing set and the benzene BRT prediction (brown). The grey line depicts the original median MOS signal.

aromatic compounds previously and these results proved that still further as the total aromatic concentration estimate was closest in agreement to the reference observations. The total aldehyde BRT-prediction shows an improvement from the BRT-predicted Total VOC concentration estimate, but the correlation was not as strong (R^2: 0.33) as it was with the total aromatic portion of compounds. Interestingly, for all three BRT predictions using SIFT-MS as the training label, the algorithm used the relationships of the median NO_2 and median CO EC sensors the most when estimating the concentration of VOCs. The median MOS sensor was the fourth and fifth highest contributor out of the seven sensors for the BRT aromatic and aldehyde predictions respectively.

Individual compounds could also be predicted with the BRT and benzene was used as an example to predict the individual VOCs concentration estimate. Benzene was chosen because it is a relatively simple aromatic compound and previous laboratory experiments had showed that the MOS could detect benzene.

The two timeseries of the BRT predicted benzene concentration estimate and the benzene concentration recorded by the SIFT-MS look similar, Fig. 4.39a. They are both relatively noisy signals, although it appeared as if the prediction had correctly identified when the peaks in benzene mixing ratio occurred. The BRT benzene prediction was correlated with the SIFT-MS measured benzene concentration (Fig. 4.39b) to investigate how close the benzene prediction was to the reference observations. The gradient of the linear regression was 0.44, which indicated that the benzene prediction does not entirely

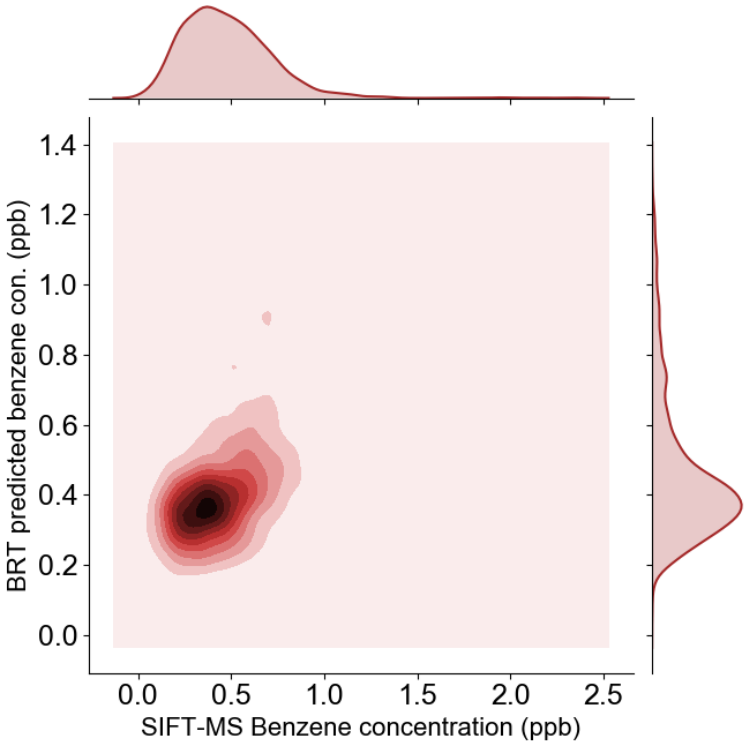

Figure 4.40: A kernel density distribution plot was produced to further examine the relationship between the SIFT-MS benzene observations and the BRT-predicted benzene concentration.

capture the peaks and troughs in the magnitude of the benzene concentration timeseries. The R^2 value (0.22) indicated a moderate correlation - suggesting that the MOS sensors contain useful information regarding VOC compounds that require a more in-depth analysis such as ML techniques to extract. The bivariate kernel density plot, Fig. 4.40, shows that the distribution of benzene observed by the SIFT-MS was centred around 0.37 ppb. The width of this peak is 0.86 ppb. The BRT predicted benzene concentration also only contained one major peak in the data distribution and this was centred around 0.36 ppb. This indicated that BRT was able to use the co-located SIFT-MS data to make a reasonable prediction of the absolute concentration of benzene over the testing data set, with one week used as the training data set. The BRT predicted benzene distribution was narrower (0.42 ppb), further evidence that the prediction did not fully capture the full magnitude of the fluctuations in benzene concentration. The median CO sensor was the variable that was used the most (36 %) to predict the benzene concentration, whereas the median MOS sensor the smallest contributor, only used 4 % of the time. Benzene emissions are associated with traffic and this also correlates with the CO concentration. The median MOS was again relatively insignificant when it came to producing the BRT benzene concentration estimate.

4.6.6 NO - Concentration prediction without a sensor measurement

ML algorithms are potent at detecting patterns within a data set and the work shown in this study was evidence that, used conjointly with an understanding for the data, ML techniques can improve the performance of LCS. Each of the sensor predictions made by the ML algorithms were justified by previous experience with working with the EC sensors in the laboratory and other studies. For example, the predicted NO_2 sensor response was formed based upon decisions trees that were primarily influenced by the median NO_2 sensor reading, then small adjustments were made to the prediction using the median CO EC and humidity data. These findings matched up with previous laboratory experiments showing NO_2 sensors responding to CO and changing humidity. When using the sensors to correct cross interferences and changing meteorological conditions, the prediction is an optimised version of the sensor response. However, ML algorithms can be used to make predictions of compounds, such as NO, that are correlated to the sensor variables, but that are not physically measured by a specific NO sensor. Since on site there was a nitrogen monoxide (NO) reference monitor, sampling from the same line as the sensor instrument this was used as a training label to make a NO-prediction using BRT. From previous laboratory studies, it is known that NO is a cross interference for the NO_2 and O_X EC sensors [105], and therefore we expected that the NO prediction would use these two variables for the prediction of NO. Equally, the ambient NO concentration is closely linked to the concentrations of NO_2 and O_3 via the Leighton steady state, and this underlying chemistry might be identified by the algorithm and used to predict NO. Since the ML algorithms are capable of detecting correlations and patterns within the data, it was likely that BRT would use either the cross interference or chemistry to predict NO. In this instance, where there was no NO sensor, the ML is working more as a modelling technique than correcting an existing sensor measurement for cross interferences. The training set comprised of all the 1-minute averaged sensor instrument data and the BRT model was trained using the same CV process as the other EC sensor models and the training/testing data split was the same.

BRT did a reasonable job at predicting variance in the NO response, as the algorithm correctly identified when the major NO peaks occurred, see Fig. 4.41. However, the correlation plot in Fig. 4.41 and the bivariate distribution plot, Fig. 4.42a showed that the BRT predicted NO concentration did not make an accurate prediction of NO at low NO concentrations as there was a large spread in the predicted NO compared to the reference observations. At times when the reference instrument was reporting NO concentrations between 0 and 2 ppb, the BRT NO prediction reported a range of 0 - 7 ppb, Fig. 4.42b.

The BRT NO prediction distribution had two peaks (Fig. 4.42b), at 1 and 5 ppb, whereas the NO reference only exhibited one distribution peak at 1 ppb. The NO prediction did seem to display a 5 ppb offset in the lowest NO concentrations reported in the

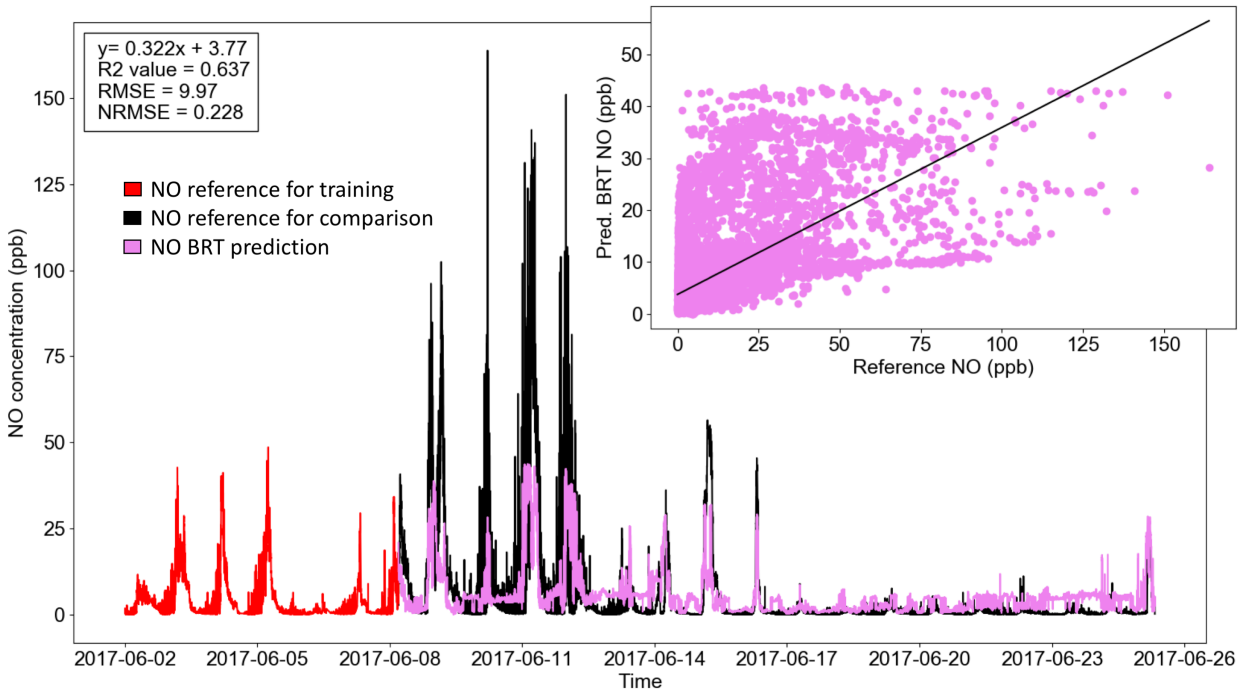

Figure 4.41: The result from using the sensor data to predict the NO concentration, without there being a NO sensor measurement. The black line is the NO reference instrument and the pink is the NO prediction based upon the median NO_2, O_X, CO, VOC, RH and temperature sensors.

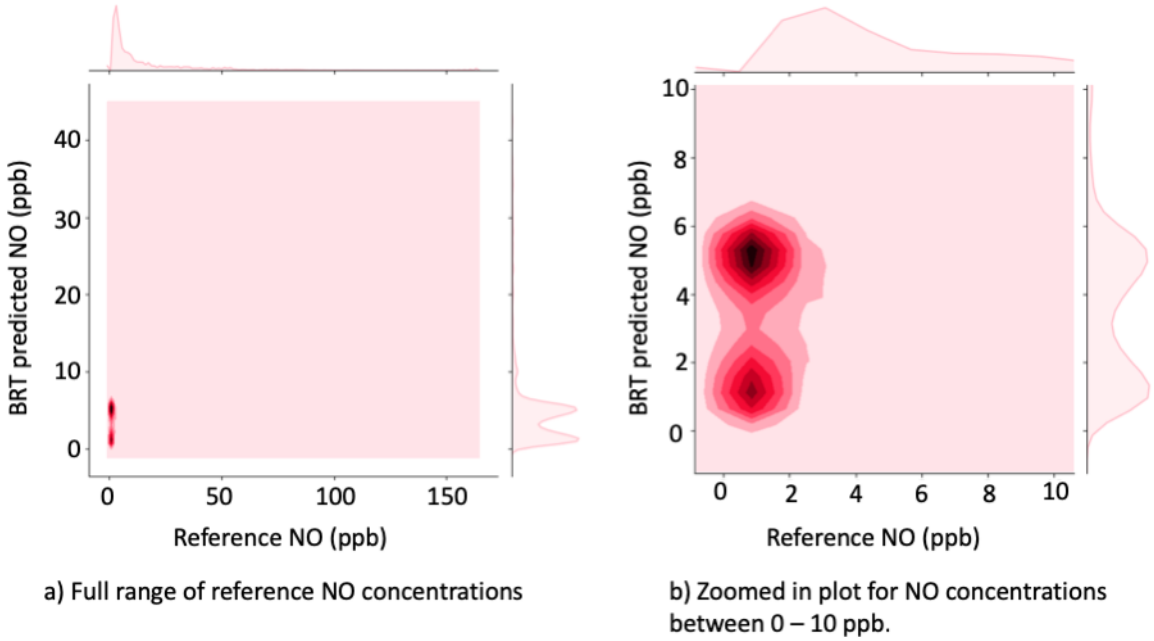

Figure 4.42: The bivariate kernel density function for a) the full range of NO concentrations and b) NO concentrations observed by both the reference and the prediction between 0. and 10 ppb

timeseries in Fig. 4.41. The RMSE between the predicted NO sensor and the NO reference instrument was 9.97 ppb which was reasonable since the reference NO observations ranged from 0 to 164 ppb over the campaign duration, with a mean concentration of 4.7 ppb. BRT failed to capture the full extent of the NO peaks, the maximum reference NO concentration was 164 ppb, yet the maximum NO concentration reported by the BRT predicted NO concentration estimate was 44 ppb. This which was expected as the BRT algorithm is not capable of extrapolation and, between the 10^{th} and 14^{th} June the localised NO/NO_2 emission caused the NO concentration to exceed the maximum NO observed in the training data. The maximum NO concentration observed by the reference instrument in the training data set was 49.5 ppb and this effectively meant that the BRT predicted NO in the testing data set was capped at 44 ppb since there was no extrapolation to produce the BRT NO prediction.

The results from the BRT-NO prediction were examined to identify if the ML algorithm made the NO prediction based upon the corss interferences of the EC sensors inside the instrument or whether the algorithm detected the trends that relate to NO tropospheric chemistry. The NO_2 EC sensors did observe the peaks in NO/NO_2 during the emission of the localised source and therefore if the NO prediction was based upon the scaling up of NO cross interferences the prediction would display larger peaks than observed in Fig. 4.41. This suggests that the prediction was based more on the underlying chemistry between the NO_2 and O_X concentrations as, when the chemistry between the compound changed due to a localised source of NO, the model could not predict the NO peaks. The NO prediction exhibited a NRMSE of 0.23 when compared against the reference NO observations. For reference, the NRMSE for the BRT NO_2 and O_X predictions were 0.0755 and 0.0785 respectively, so, although the NO prediction was reasonable at a first glance, it does contain large amounts of uncertainty. Further investigation was required to deduce if the algorithm was using the underlying chemistry between NO_2 and O_X to predict NO or using the differences in the sensors' sensitivities towards NO as a cross interference. The ML BRT analysis was repeated, this time using the reference measurements for O_3, NO_2 and CO instead of the median NO_2, O_X and CO EC sensors. This produced a reference NO prediction which exhibited similar evaluation criteria compared to when the EC sensors were used to make the NO prediction; linear regression parameters for when the reference NO prediction was compared against the reference NO observations: $R^2 = 0.641$, gradient of slope = 0.371, RMSE = 9.82 ppb, NRMSE = 0.371, Fig. 4.43. The using the reference instruments to produce a BRT NO prediction produced very similar values for the evaluation criteria than when the median EC signals were used instead of the reference instruments to predict the NO concentration with BRT (R_2: 0.637, slope: 0.322, RMSE: 9.97 ppb, NRMSE: 0.228). The reference predicted NO concentration estimate did not observe the higher concentrations of NO that occurred during the NO/NO_2 leak, and there was still quite a large spread of values when the NO concentration was low. Therefore,

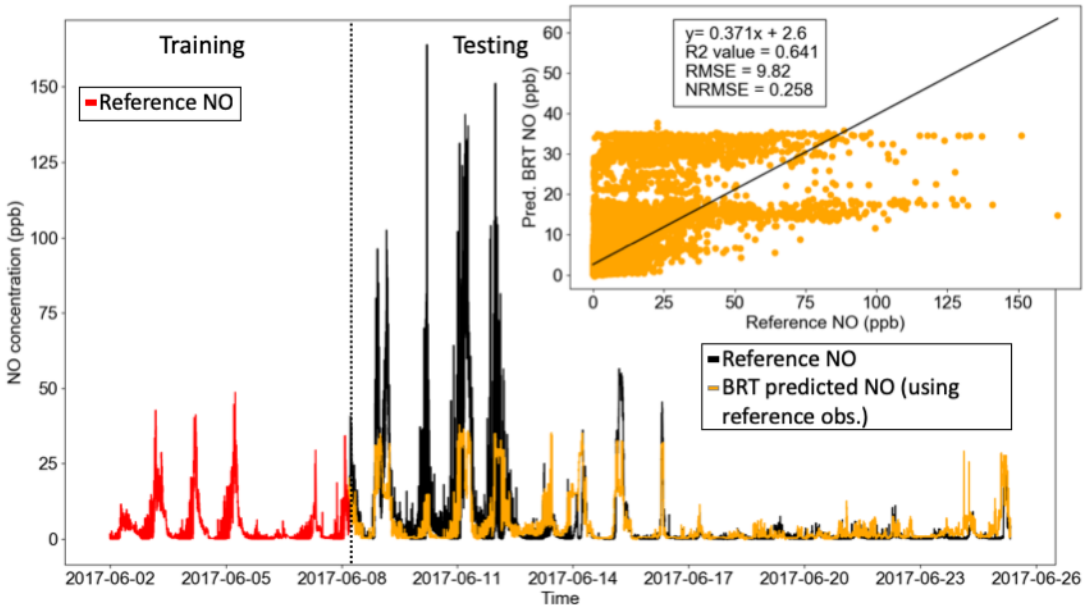

Figure 4.43: Using the NO_2, O_3, O_X (O_3 + NO_2, CO reference instrument data in place of the median NO_2, O_X, O_3 (O_X - NO_2, CO EC data to predict the NO concentration with BRT.

using the reference observations of NO_2, O_3, O_X and CO in place of the median EC signal did not significantly improve the BRT NO prediction. This indicated that the BRT algorithm was using the chemistry relationships between the gaseous species to predict NO, rather than the cross interferences as the reference observations do not experience the same magnitude of cross interferences as the EC sensors - if BRT was using the cross interfering compounds to predict NO the performance of the reference-predicted NO would be expected to differ from the sensor-predicted NO concentration. The the gain feature was used to characterise the decisions made by the trees. The variable contributions for the reference NO prediction (Fig. 4.44, black bars) and the sensors NO prediction (Fig. 4.44 coloured bars) were very similar. The largest contributing variable to both the reference predicted NO and sensor-predicted NO concentrations was the O_3 signal. This was therefore used the most within the decision trees to make the defining decisions when the function was being developed to fit to the data. The NO_{EC} signal was the second largest contributor towards the sensor-predicted NO concentration, which is evidence that the photostationary state was being identified within the BRT algorithm, however, this was only the fifth largest contributor for the reference-predicted NO concentration. This might be explained due to the NO/NO_2 leak which would have caused the relationships between O_3 and NO_2 to be skewed. The overall similar gain contributions for the reference predicted and sensor predicted NO concentration estimates indicated that the relationships that the BRT algorithm detected were more based upon tropospheric and chemical interactions of the gaseous species than the cross interferences upon the EC sensors. To make the NO sensors prediction, the algorithm was detecting the Leighton state relationship between

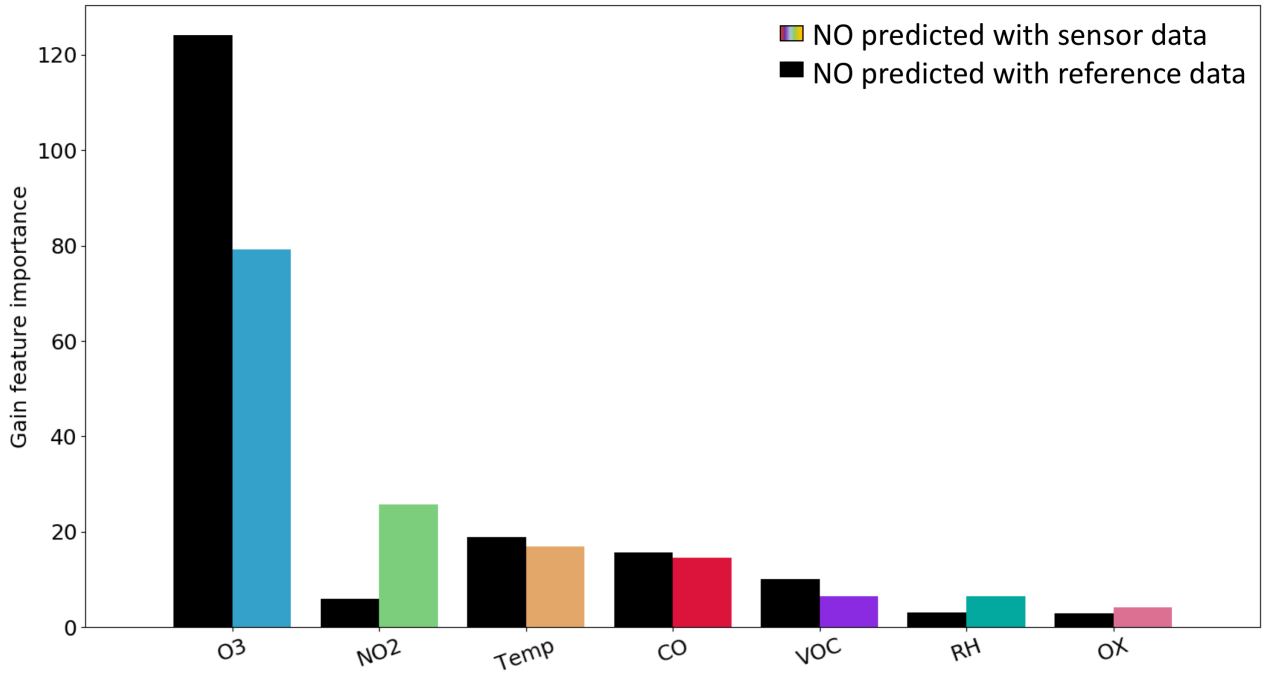

Figure 4.44: The gain contributions for the reference NO BRT concentration estimate made using the NO_2, O_X (O_3+NO_2), CO reference instruments, the median VOC MOS, RH and temperature as training variables (black bars). The gain contribution for the sensor predicted BRT concentration estimate is shown with the coloured bars. The sensor predicted BRT NO concentration estimate used the median NO_2, O_X, O_3 (O_X - NO_2), CO EC sensor signals as well as the median VOC MOS sensor, RH and temperature sensors as training variables.

the compounds, rather than using NO as a cross interference on the NO_2 and O_X EC sensors to predict NO, because the reference observations are selective and do not have cross sensitivities.

Modelling compounds such as NO using ML techniques can only provide an estimate of the compound behaviour and these predictions should be used with care, to suggest a compound concentration but not replace an actual sensor measurement. The NO prediction was not a corrected sensor measurement and co-incidental correlations with completely random variables may produce a similar result. With an in-depth knowledge of the data useful information can be extracted from the trends between the variables, but correlation and causation may lead to misleading predictions. This was shown with a prediction of the Global Active Power (GAP) from a completely unrelated data set. BRT was used over the same number of data points to predict the GAP for a household in France, over the same days of the month, but in 2010. The GAP and the sensor variable are not related, but the algorithm detected a completely co-incidental correlation between the variables. This led to a prediction with a NRMSE of 0.282, comparable to that of the NO BRT prediction (NRMSE NO: 0.23). This prediction worked reasonably well, because the ML detected a correlation between the GAP and the O_3, CO and temperature from the sensor instru-

ment but the causation for this was non-existent. The ML techniques are very powerful at detecting correlations, but these do not necessarily mean that the modelled output is reliable and should not be treated with the same level of confidence as a predicted measurement [72]. In the NO scenario, we have a good understanding of the chemistry behind NO formation and can therefore, using this knowledge with the sensor data to estimate the NO concentration. However, the ML techniques can also detect correlations for variables that are unrelated to the sensor data because a correlation between the variables is coincidental. The ML results must be related to common sense and previous experiments in order to stay relevant to the sensor data.

4.7 Summary

- Warm up time was briefly investigated as part of the Beijing campaign. The warm up period was from 1700H on 30th May until 00:00 2nd June 2017. The MOS sensors showed no signs that they were affected by the power switched on and were more influenced by the changing temperature of the air flow during these three days. The EC sensor did indicate a step change in their signals, which occurred one hour after they received power. This was attributed to the power being switched on as no other environmental changes were observed during this time. Therefore a warm-up time of 4-5 hours is recommended. The warm-up period for the Beijing deployment was longer than this recommendation because the power to the sensor instrument was shut off for 9 hours at 12:00H on the 31st May. The sensor instrument began recording data after the power was restored on 1st June, with no detrimental impacts upon the EC or MOS data that could not be attributed to environmental conditions. Therefore, this was evidence that, after small power cuts, there was no need for a second warm-up period.

- Three out of the 32 MOS sensors failed immediately upon deployment and previous experiments with the MOS sensors have proven that a 5 to 10 % failure rate is common per deployment. If identified earlier these failed sensors could be removed from the cluster and replaced with working sensors. When purchasing LCS sensors it is recommended to expect to need to replace 5 - 50 % almost immediately.

- Two MOS sensors that did not fail immediately began to display substantial amounts of drift after two weeks of deployment monitoring ambient air. Although they were drifting compared to the other MOS, they still reported the same amount of variance within their signals so detecting these as failing sensors would be impossible if they were deployed as individual sensors. The substantial drift indicated that they need to be replaced as they drift further from the median MOS signal.

- The median MOS signal was good for monitoring the general trend of the 31 MOS, without being impacted by those sensors displaying large amounts of drift.

- There was some success in correcting the MOS sensors for rapidly changing temperature and humidity. The baseline appeared less variable after correction and the trace still contained peaks that were potentially due to VOCs.

- The corrected MOS signal contained lots of variation, that, when compared with the GC-FID and SIFT-MS showed some correlations. Certainly, some peaks can be accounted for, proving that the MOS are responding to VOC compounds in the air.

- The SIFT-MS data contained timeseries for 28 compounds, and these were summed to yield a Total VOC timeseries for the SIFT-MS. The corrected median MOS signal correlated well with the SIFT-MS Total VOC signal (R^2: 0.47, 3.82 mV ppb^{-1} gradient). The median MOS signal covaried with the Total VOC SIFT MS concentration, and the covariance was highest for a 10 minute averaging period. This indicated that the corrected median MOS signal was capable of detecting short term VOC pollution peaks.

- The results of the SIFT-MS Total VOC comparison with the corrected median MOS indicated that MOS could be applied to detect steep VOC concentration gradients that occur on short timescales (minutes), which would make them useful for complementing with a GC-FID.

- There were MOS peaks unaccounted for, potentially due to the MOS responding to VOCs not detected by the GC or SIFT.

- The correlation between the four organic acids reported and the corrected median MOS signal was moderate to weak (R^2: -0.22 to -0.48), but also negative (gradients: -16.2 to -118 mV ppb_{-1}). This suggested that organic acids may potentially interact differently to other VOC compounds upon the MOS sensing surface, leading to a decrease in MOS conductance when the organic acid concentrations are increased. Potentially there are other groups of VOC compounds that interact with the MOS sensing surface in this manner and this would lead to the Total VOC concentration not correlating well with methods such as the GC-FID and SIFT-MS which did not detect these species.

- Both the GC-FID and SIFT-MS VOC reference methods provided measurements for a range of compound classes and the MOS sensors appear most sensitive towards the aromatic type compounds.

- Using co-located reference instruments for calibration (SLR) produced EC and (to some extent) MOS sensor data that was closer to the respective reference obser-

vations than just the sensors, however it still had some difficulties calibrating the sensors for lower target compound concentrations.

- Supervised machine learning analysis was able to further refine the calibration models because they can detect and correct for multiple functions between variables leading to the removal of some cross sensitivities.

- Unsupervised ML techniques, which do not use a training label to give the algorithm something to aim for in the training period, were not investigated here as the sensor instrument was co-located with the reference instruments and these gave the algorithms the best chance at making a concentration estimate.

- Over the variable space and sensors used here, the BRT and BLR parametric ML techniques generally exhibited the best performances, but GP does have the advantage that it can determine an error estimate for each data point also.

- Figure 4.29a displayed the BLR predicted NO_2 signal and this was able to extrapolate to reach the high NO_2 concentrations.

- Gaussian process (GP) with a combined linear and Matern32 kernel was optimal for the prediction of NO_2 during the China campaign because it allowed for extrapolation (linear) and also detected smaller, non-linear trends (Matern32) within the data set when the NO_2 was lower.

- BRT and BLR equally improved the concentration estimate for O_X, and since SLR was successful in decreasing the error in the EC data it suggests that the O_X EC are very dependant upon linear relationships over the variable space.

- CO was more difficult to predict owing to the reference measurements sampling from 100 m above the sensor instrument, but ML techniques were useful for improving the CO sensor prediction to be closer to the reference value.

- For any ML technique it is imperative that the sensors are exposed to the full range of conditions during training, that the sensors will experience during deployment. This was especially important for BRT since there is no way for the tree to perform extrapolation of the data.

- GP worked reasonably well with the EC sensors but it is more computationally intensive compared to the gradient boosting techniques used here.

- BRT made a prediction about the concentration of total VOCs, as measured by the SIFT-MS in Beijing. The total VOC prediction only had a moderate correlation with the reference measurements and contained a large proportion of error (NRMSE: 0.25). The BRT predicted Total VOC concentration estimate also used

the EC sensor timeseries, rather than the median MOS signal to make the Total VOC prediction, suggesting that the MOS response is comprised of multiple, complex, linear relationships that make it challenging to extract the Total VOC information out of.

- The error estimate, and correlation value were slightly improved when BRT was used to predict the total aromatic concentration using SIFT-MS data, but overall the BRT-predicted aromatic concentration was not of a high enough quality for use in the field.

- BRT was used to predict the NO concentration at the IAP with a reference NO observation serving as the training label. This was no longer improving the sensor data to fit closer to the reference, rather a modelling approach since there was no NO sensor. The NO prediction was reasonable but did exhibit a high NRMSE: 0.23. The estimate would potentially be useful as the gain feature indicated that the variables NO_2 and O_X make the largest contributions to the prediction, and these are known to be directly linked to the NO concentration in ambient air.

- Using ML techniques is a low-cost method to increase the confidence in sensor data providing that the predictions can be justified by laboratory evidence or knowledge about the behaviour of particular variables. Any correlations can be detected by the ML algorithms, even if they are purely coincidental. Using ML to optimise the EC sensor data could be rationalised based on experimental results and cross interferences, however the MOS sensor predictions were more whimsical and require using with caution.

- The ML was able to correct for the cross interferences exhibited by the EC sensors using the signals form the other co-located EC, within the sensor instrument.

ML analysis approaches, used in combination with the clustering of low-cost sensors were able to optimise the EC sensor data to provide results that were comparable to the reference observations, whilst still maintaining the affordable and low-power budget of the sensor instrument. After co-locating the sensor instrument with reference instruments for a week, the ML algorithms were able to correct for cross interferences and produce a CO, O_X and NO_2 concentration estimate that was accurate, precise and contained low uncertainty when they were compared against the co-located reference observations over the subsequent fortnight.

The application of ML increased the confidence in the EC sensor data, and moves the use of EC sensors closer to an application. The sensor instrument could be used to complement the reference monitoring stations over short time periods (fortnight). The LCS instruments could be co-located with the reference instruments for a week, and then there would be high confidence in the ML-corrected sensor data, if it was moved to a different

location, a short distance away, which still experienced similar environmental conditions. If the concentrations of the gaseous species or environmental conditions changed to be outside of the range experienced by the LSC instrument during the training week this could be flagged as the data will be less uncertain. The LCS may need to be re-calibrated every fortnight by moving it to be co-located with the reference instruments (or by moving a set of reference instruments around to different LSC instruments for calibration every two weeks for a few days) and this re-calibration data could be added to the training data set to extend the range of conditions observed by the reference and LSC instrument in the training data. The application of ML produce increases the applicability of the LCS to be used to increase the spatial density of the air quality network as it improved the quality of EC sensor data.

Chapter 5

Robust quality comparison of a clustered sensor device against reference instruments

5.1 Introduction

The sensor instrument produced results of a high quality, that were close to the reference measurements and displayed a good performance when it was co-located with reference instruments as part of the large Air Quality Campaign in Beijing, China. That initial deployment helped to identify areas to improve the sensor instrument and useful analysis techniques to extract information from the sensor signals. An updated sensor instrument was designed and developed for use in Boulder, Colorado, to investigate the performance of low-cost sensors when deployed in different environmental conditions and also to collect sensor measurements on the move. The general concept of clustering identical sensors within the instrument remained the same but there were a few alterations to improve the operation of the instrument. For example, data collection and storage was still achieved via Arduino and the same micro-computer but the code to do this was changed to automatically run as soon as the instrument received power. This is more beneficial for deploying the sensor instrument as it minimises data loss if the power is lost and does not require a person to be with the instrument to restart the instrument. A few different sensors were introduced to expand the number of pollutants the sensor instrument was able to monitor and potentially enhance the ability to predict the concentration estimate of the compounds using ML.

Three carbon dioxide (CO_2) NDIR sensors (manufacturer : ClairAir, model: Prime2) were housed alongside the EC and MOS sensors inside the sensor instrument. A cluster of four low-cost Optical Particle Counters (OPCs, manufacturer: Alphasense, model: OPC-N2) were also used to monitor Particulate Matter (PM) but these were mounted inside a different enclosure due to their sampling requirements. This OPC manifold was

electronically connected to the sensor instrument to allow the OPC data to be stored on the same micro-computer as the other sensors data.

The sensors were deployed at the NOAA Earth System Research Laboratory in Boulder, Colorado, USA because the laboratories operate reference instruments for all compounds. The sensor instrument was also able to be installed inside the NOAA mobile laboratory, alongside several research-grade instruments and could therefore be used to investigate the performance of the sensor instrument on a mobile platform.

5.2 Static measurements using the sensor instrument

Between the 22nd and 26th February 2018 the low-cost, low-power sensor instrument was deployed inside the NOAA Tropospheric Chemistry laboratories, Boulder, Colorado, USA. The laboratory was temperature controlled and a PTFE sample line ran from a selection of instruments to outside for monitoring ambient air. There were a variety of research-grade instruments, maintained by NOAA's Tropospheric Chemistry division co-located with the sensors inside. Reference measurements for NO_2, O_3, CO and CO_2 were recorded during the static deployment of the sensor instrument. Within the sensor instrument there was CO, O_X and NO_2 measured by a cluster of six EC sensors each, CO_2 via three NDIR sensors and VOCs using a multitude of different MOS. A variety of 8 x TGS2611 methane, 8 x TGS2610 propane/butane, 8 x TGS2602 total VOC and 8 x TGS2620 OVOC MOS were arranged into four clusters inside the sensor instrument. There were internal KNF pumps to control the flow of air to the sensors and RH and humidity probes to monitor the environmental conditions.

During the deployment, the outside temperature was low (-11 to 10 °C) and the humidity of the outdoor air varied from 19 % to 93 % on days where it snowed. These large humidity ranges were likely to impact the EC and MOS sensors signals performance and sensitivities towards target compounds and cross interferences. The sensor instrument was located indoors, however and therefore the temperature and humidity ranges of the air reaching the sensors were reduced to 28.1 - 30.3 °C and 0 to 2.36 g m^{-3} (at the really low humidity's the RH probe measured -5 to 8 % RH).

5.2.1 Reference instruments during the NOAA deployment

Dr. Tom Ryerson managed the Tropospheric Chemistry group at the NOAA Earth System Research Laboratories. The instruments used as reference observations and who was responsible for the maintenance and operation are shown in Table 5.1.

NOAA data was collected and processed by Ken Aiken who posted it on the NOAA data repository for access.

Table 5.1: The people at NOAA who were responsible for each of the different reference instruments used to to evaluate the performance of the sensors.

Target compound	Reference instrument	Description	Who was responsible for operation
Nitrogen dioxide	NOx-CaRD	Nitrogen oxides by Cavity Ring Down Spectroscopy	Zachary Decker
Carbon dioxide (CO_2) and methane (CH_4)	Picarro	Wavelength-scanned cavity ring down spectroscopy	Jeff Peischl
Carbon monoxide (CO)	Modified Los Gatos	Off-axis integrated cavity output spectroscopy	Jeff Peischl
Particulate matter	POPS	Printed Optical Particle Spectrometer	Troy Thornberry
VOCs	PTR-MS	Proton-Transfer-Reaction Mass Spectrometry	Matthew Coggon and Carsten Warneke
VOCs	WAS canisters and GC-MS	Gas Chromatography and Mass Spectrometry	Jessica Gilman

5.2.2 Static EC sensors

The EC sensors have previously been found to have more reproducible and reliable signals than the MOS sensors, but they still benefit from the clustering technique. One NO_2 EC failed upon arrival. Each of the five working NO_2 EC sensors co-varied with each other, and they all reproduced the same variability over time. However, Fig. 5.1 shows that, it is not possible to use EC straight 'out-of the box' as even after the individual factory conversion factors were applied there was still a difference of 103.92 - 121.87 ppb between highest and lowest ranked NO_2 EC sensors. This spread in the sensor signals was relatively consistent throughout the static deployment but this range in signals was larger than a typical ambient concentration of NO_2 and therefore means there can be little confidence within the EC sensor data when the EC are used in a 'plug-and-play' scenario. Deployed as individual sensors in a network without a cluster of co-located, identical EC, it would be difficult to tell which sensors report a high or low systematic error compared to the others. Figure 5.1 depicts one NO_2 EC sensor with an anomalously high signal and one that remained really low (always producing a negative concentration of NO_2) during the deployment. By clustering the EC and using the instantaneous median of the EC cluster the variance of the EC signal is still representative of all the NO_2 sensors, but the impact upon the signal due to sensors with substantial drift is removed. The spreading out of the EC signals was evident with the two other types of EC; the range for the CO EC varied between 84.02 and 150.92 ppb and the O_X EC ranged between 60.13 - 146.25 ppb for the highest and lowest sensors. A comparison between the EC sensors deployed in Beijing

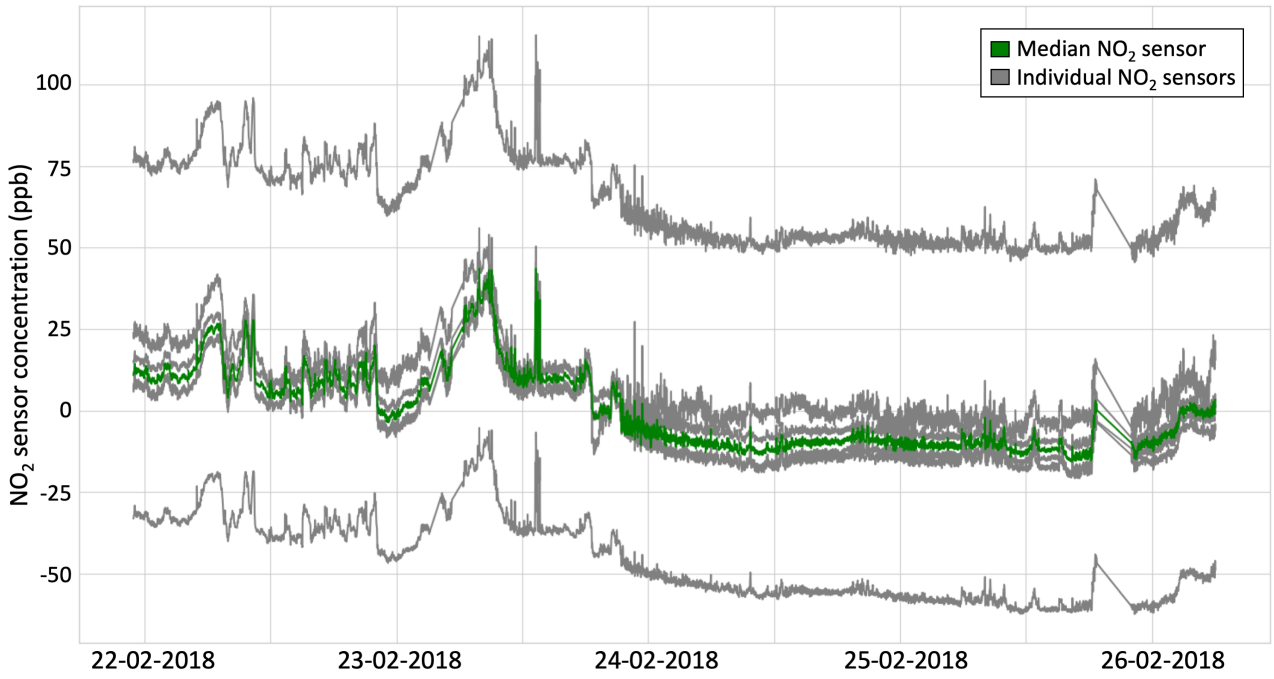

Figure 5.1: The median (green) and the individual (grey) NO_2 EC sensor signals. There are only five NO_2 EC as one failed, therefore there are only five grey lines.

(Chapter 4) and Boulder was made to evaluate if the range between the individual EC signals was equal over the same period (6 days). When the EC sensors were deployed in Beijing, the spread in values reported by each EC sensor cluster was: NO_2 range: 186 - 210 ppb, O_X range: 112 - 130 ppb and CO: 557 - 925 ppb, over the initial 6 day period. Therefore, the EC sensors deployed in Boulder exhibited a smaller range of values from the individual EC within the clusters. This is potentially due to the conditions experienced by the EC sensors. In China the EC experienced air with a higher humidity (RH as measured by RH probe in Beijing: 39 % - 100 %, RH range = 61 %, temp. : 15 - 41 °C) and larger changes in both the dynamic range of the compounds and the humidity than the conditions in Boulder (RH as measured by RH probe in Boulder: -5% - 8 %, RH range = 13 %). These factors will be effective at causing the spreading out of the sensor signals due to the unique sensitivities of each EC towards the temperature, humidity and cross interferences. The larger the range over which these factors vary the more spreading out of the EC sensor signals observed as they each respond to these conditions with small differences in their sensitivities towards these conditions. Although the range in the sensor signals was significant, the covariance between them was high and therefore the median signal (green, Fig. 5.1) reproduces the trend that is representative of all five individual sensors. The instantaneous median was calculated for each of the different types of EC sensor clusters and used to evaluate the EC sensor performance against co-located reference instruments, e.g. Fig. 5.2.

NO_2

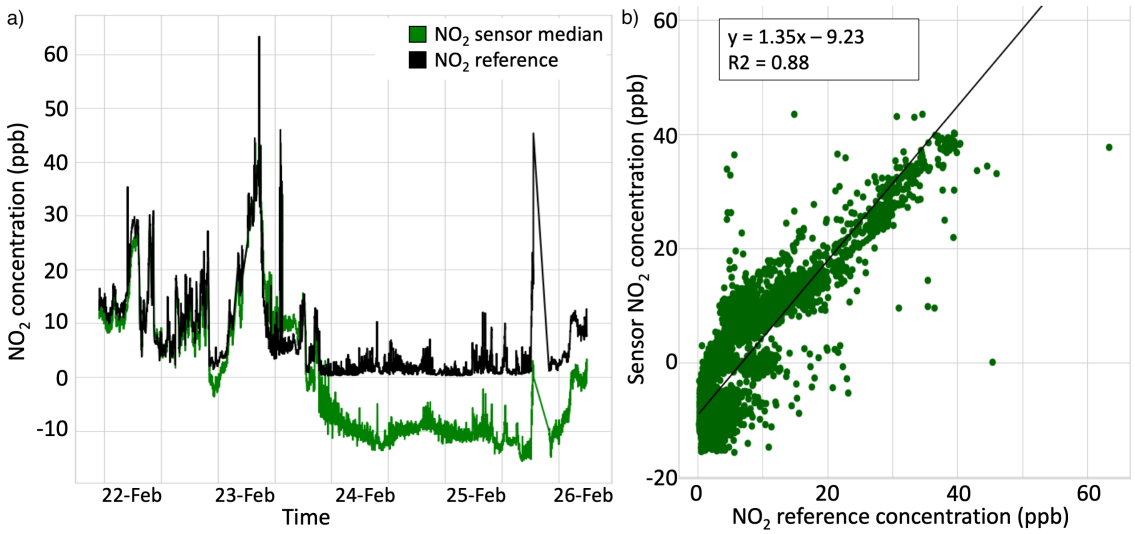

Figure 5.2: a) A comparison of the median NO_2 EC sensor (green) against the reference NO_2 chemiluminescence measurements (black). b) The correlation plot between the two instruments showing how well they correlated.

For the first two days of the static deployment of the sensors, the NO_2 concentration was rather variable. The NO_2 reference instrument observed between 1.5 and 63.3 ppb and the median NO_2 sensor reported a range of between 0 and 43 ppb. There was good agreement between the reference observations and the median NO_2 EC sensor (Fig. 5.2a) during this time. The absolute values from the median NO_2 EC sensor signal generally matched the reference measurements, without any sensor calibration procedures applied. Yet, on the 24th February 2018, the reference NO_2 concentration decreased to between 0 and 10 ppb. The median NO_2 EC signal follows suit, but overestimates the drop in NO_2 concentration, reporting values of around -10 ppb, see Fig. 5.2a. The NO_2 concentration then remained low for the remainder of the static deployment, and the median NO_2 signal maintained that negative offset error of -10 ppb. This sudden deviation of the median NO_2 EC from the reference NO_2 observations supports the theory that the NO_2 EC limit of detection is near 5 ppb. The sensors only began to deviate from the reference observations at lower concentrations whereupon, the median NO_2 sensor displayed a negative error of -10 ppb and the median sensor reported negative values for a concentration. After the 24th February, the variability in the NO_2 mixing ratio was still detected by the median NO_2 EC and was comparable to the reference measurements. However, the absolute concentration values became less accurate and did not recover from the 10 ppb offset for the rest of the static deployment - even when the NO_2 concentration began to rise on the 26th of February. The sudden decrease in NO_2 concentration may indicate a different air parcel, with different environmental conditions that the sensor instrument began sampling. The EC signal may not recover until the environmental conditions of the previous air parcel are restored.

O_X and CO EC

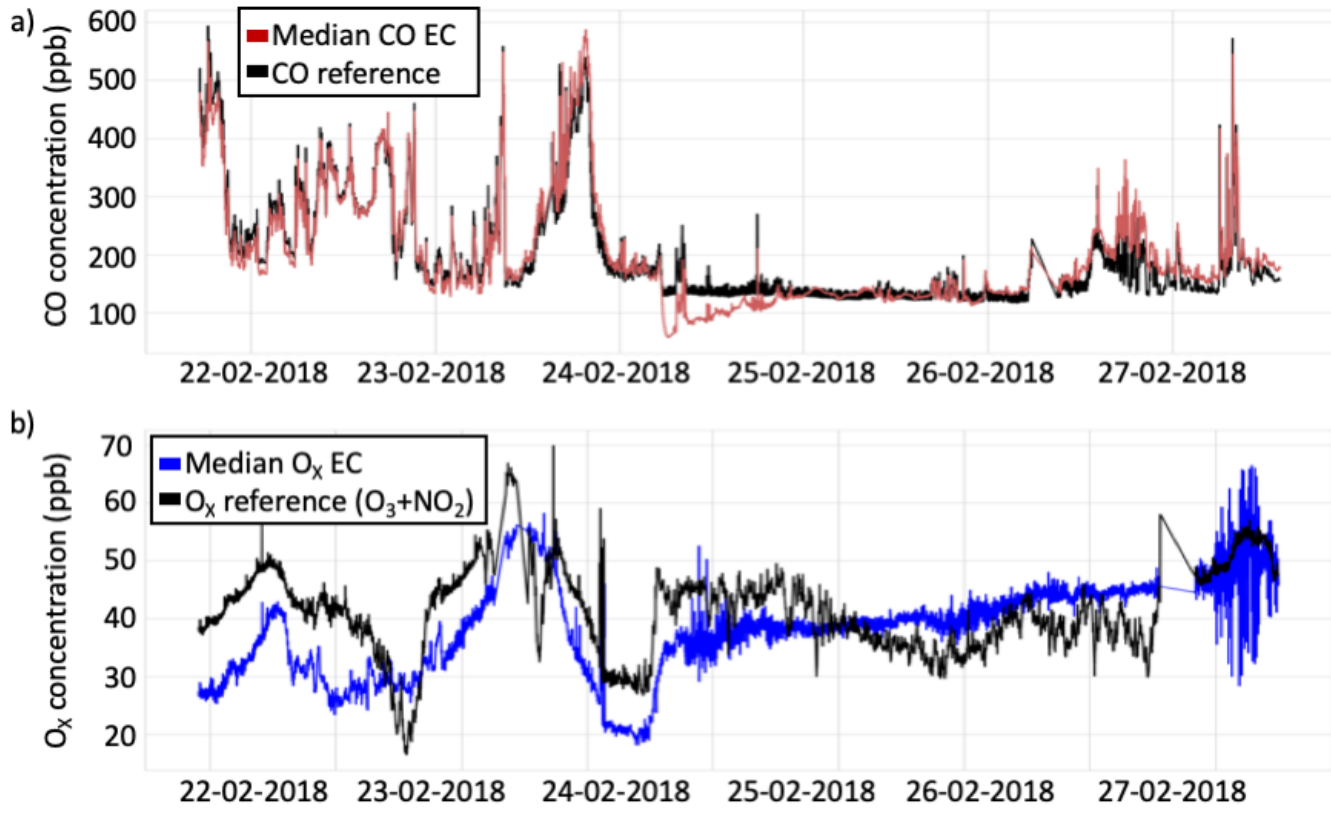

Figure 5.3: Timeseries to compare the variance displayed in the a) O_X reference and median EC sensor signals and in the b) CO reference and median EC signal.

The reference observations of O_X and CO concentrations had similar trends with lots of variability in the reference observations between the 22nd and 24th February 2018, see Fig. 5.3a which shows the reference observations of O_X varying between 16 and 68 ppb (range = 52 ppb) and Fig. 5.3b which shows the CO concentration ranging from between 140 to 515 ppb (range = 375 ppb) over these two days.

Then a decrease and stabilising of the ambient mixing ratio after the 24th February, which lasts for approximately two days, see Fig 5.3a and b. The corresponding median EC sensors agreed better with the reference measurements before the 24th February, when there was more variability in the mixing ratios of the target compounds. The reference CO instrument recorded a range of 153.3 ppb (116.6 to 269.89 ppb) for the CO concentration between the 24th and 26th February. The CO sensors followed the decrease in CO concentrations observed between the 24th to 26th and reported a concentration range of 150.7 ppb (214.3 to 63.6 ppb). Figure 5.3a indicated that the median CO EC sensor closely matched the variability and concentrations observed by the CO reference monitor, with only a few deviations from the reference observations.

The reference O_X concentration range during the same time period was 28.32 ppb (29.64 to 57.96 ppb). The range in O_X concentrations reported by the median O_X EC matched the decrease in O_X variability and concentration between the 24th and 26th February, range was 23.3 ppb (29.2 to 52.5 ppb). The timeseries in Fig. 5.3b shows that the median O_X

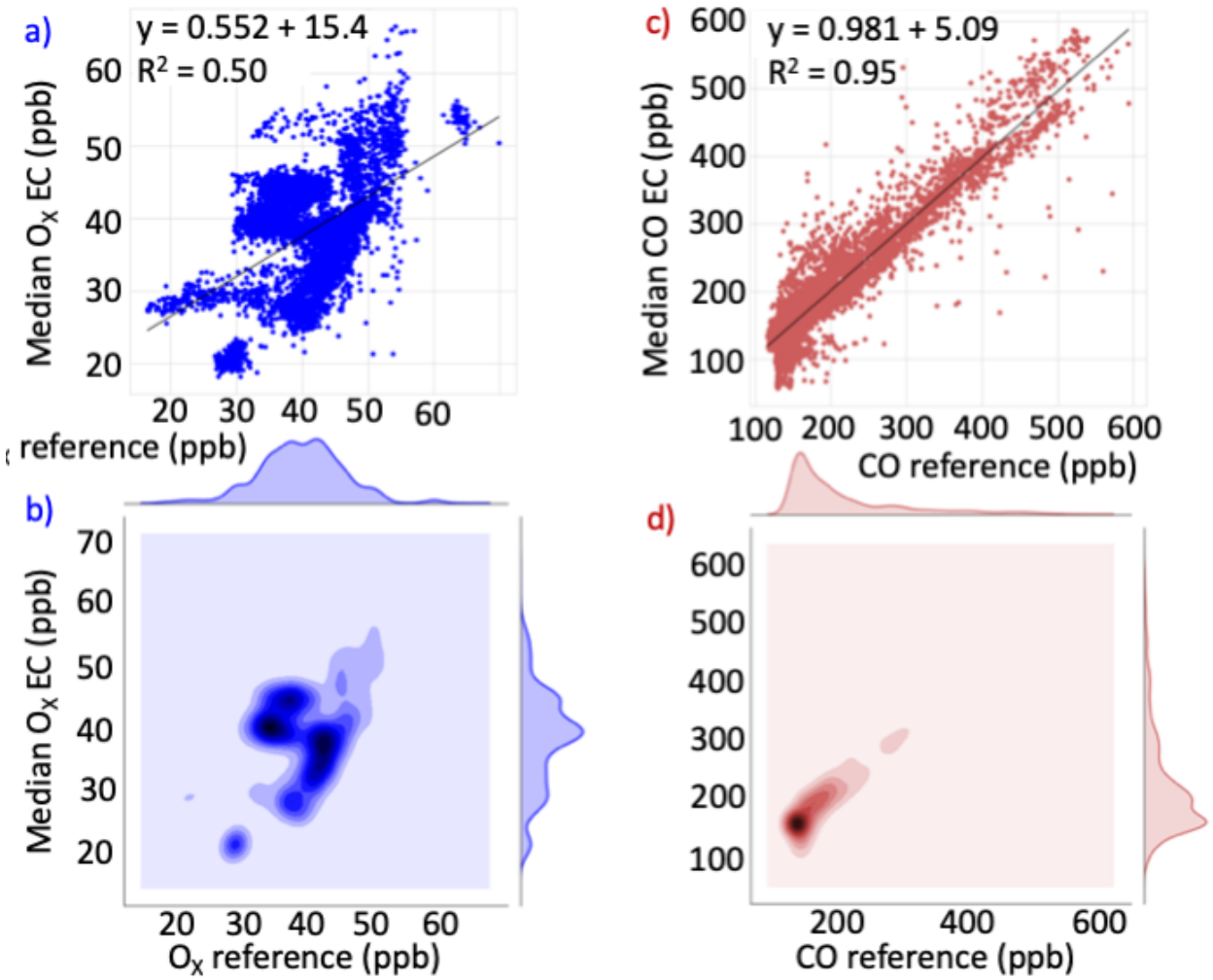

Figure 5.4: The correlation and kernel density distribution plots for the O_X (a and b respectively) and CO (c and d respectively) median EC signals compared against their relevant reference observations for the duration of the static deployment of the sensor instrument.

sensor did not produce a signal that was as close to the O_X reference observations as the median CO EC sensor was to the CO reference measurement.

Linear regression was performed with each of the median EC sensors and their respective reference measurements over the entire duration of their static deployment (22nd - 27th Feb), to investigate the sensitivities of the different sensors when deployed in Boulder.

The median NO_2 EC exhibited a strong, positive correlation with the NO_2 reference instrument (Fig. 5.2b) with an R^2 of 0.88 and a gradient of 1.35. However the median EC sensor did not show a high degree of linearity compared to the NO_2 reference observations, with a large spread of NO_2 concentrations reported for the median EC sensor at low NO_2 concentrations. This deviation from linearity was due to the time period between the 24th and 26th February, where the NO_2 concentrations were low and not variable.

The median O_X EC sensor also displayed a non-linear relationship with the O_X reference observations, Fig. 5.4a. The R^2 value was only moderate (0.5) and the gradient

of the slope was relatively low (0.5) and the data was not close to a 1:1 line. The kernel density plot of the median O_X sensor against the O_X reference data, Fig. 5.4b, showed that there was evidence of some linear behaviour from the median O_X EC, as there was a linear gradient visible within the kernel density plot (between 35 ppb - 50 ppb of reference data, 25 ppb to40 ppb median O_X EC). However, there was a lot of data point concentrated around 40 ppb for the median O_X EC and 35 ppb for the reference O_X concentrations. This is largely composed of the O_X data reported between the 24th and 26th February, when the O_X concentration became less variable.

The CO correlation (Fig. 5.4c) and kernel density distribution (Fig. 5.4d) for the median CO EC and the CO reference measurements both indicated that the median CO EC exhibited a very linear (R^2: 0.95) response to changing CO concentrations (gradient = 0.981). The median CO EC data and CO reference data produced a kernel density distribution that reflected this linearity, with the most concentrated set of data points at 160 ppb for both data sets. After the steep CO concentration decrease that occurred on the 24th February the median CO initially under-predicts the CO concentration by 60 ppb, in an analogous manner to the NO_2 median EC. However, the median CO signal then recovers and increases to be comparable to the reference CO after 8 hours, and from then on correlates well with the reference observations for the remainder of the static deployment.

The individual EC sensor performance was examined using linear regression to identify how well all sensors within a cluster perform against the reference measurement.

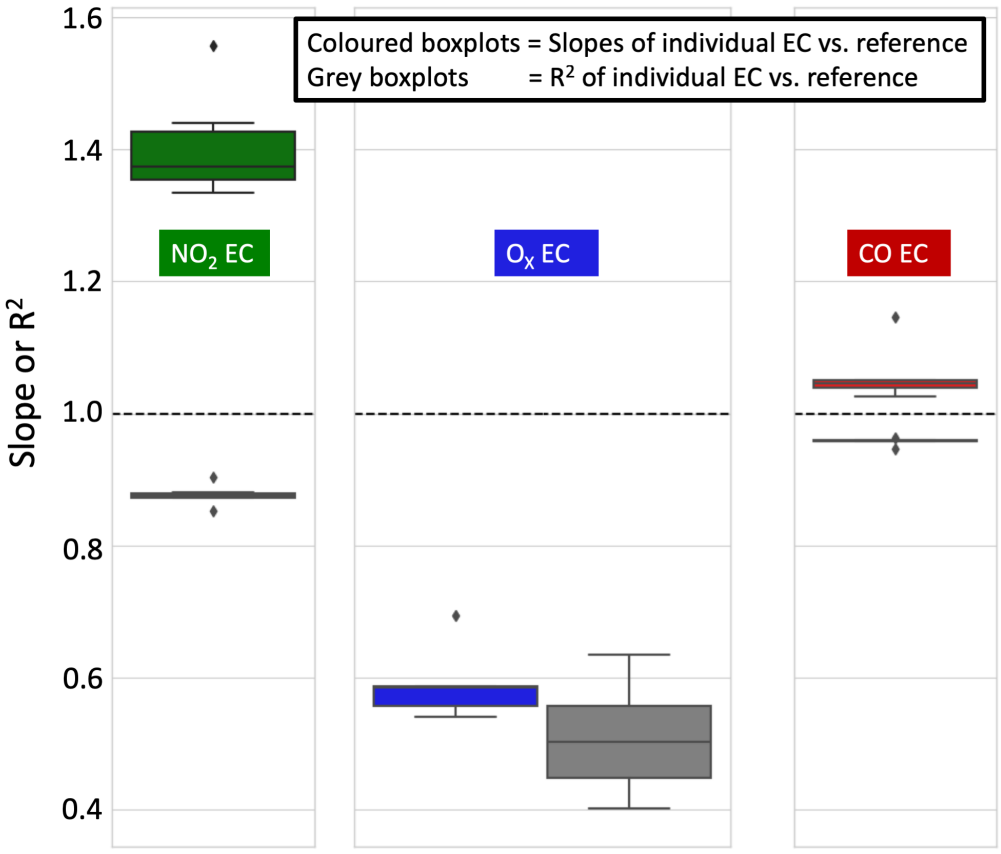

Figure 5.5: The green, blue and red box plots show the slopes of the individual NO_2, O_X and CO EC sensors respectively, when plotted against their corresponding reference instruments. The grey coloured box plots indicate how well correlated the six sensors were to the reference observations as they show the spread of the R^2 values for the linear regression. For all box plots the middle line is the median, the edges of the box represent the interquartile range of the data and the whiskers are for the 5^{th} and 95^{th} percentiles. Any points that lie outside the box are marked as diamonds and indicate anomalous data.

The six CO sensors displayed the most similar performance to their CO reference measurement, exhibiting a narrow range of slopes (1.03 to 1.15) and all with high correlations ($R^2 > 0.94$). There was one CO EC that exhibited a higher sensitivity towards changing CO concentrations. This was the sensor with the gradient of 1.15 and this gradient is an outlier compared to the gradients produced with linear regression of the other 5 CO EC. However this did not cause the correlation of this sensor with the reference to be lower.

The NO_2 sensors were all well correlated with the NO_2 reference instrument (R^2 for all NO_2 EC were >0.85) but the gradients were all higher than 1, as the NO_2 EC all under-predicted the NO_2 concentration between the 24^{th} and 26^{th} February, when the NO_2 ambient concentrations were low and not variable. There was one NO_2 sensor which exhibited an outlying gradient of 1.56; much higher than the other NO_2 EC whose gradients were between 1.34 and 1.43.

The O_X EC appeared to be the poorest performing sensors during the static deployment. One failed upon arrival and the remaining five O_X EC were only moderately cor-

related to the sum of the NO_2 and O_3 reference observations (R^2 between 0.4 and 0.63). Linear regression with each EC against the O_X reference measurements led to low slope values for all O_X EC, indicating they were almost half as sensitive to O_X concentration gradients than the reference instruments.

The dip in the ambient concentrations of all the measured pollutants suggests a change to the air parcel the sensors were monitoring, and the NO_2 and O_X EC sensors performed poorly during the two days over which this change occurred. To investigate this further, the RH of the air flow was plotted up too, as this might explain the median sensors deviations from the reference observations and increase in noise. Figure 5.6 compares the O_X reference observations with the median O_X EC and the relative humidity of the air reaching the sensors. As expected, the median O_X signal matched the profile of the O_X reference instruments, albeit with a linear offset of around 12 ppb for the first three days. Since the median O_X EC exhibited this negative offset, this indicated that at least 3 of the working O_X EC were reporting low values with respect to the reference observations. The dry air (RH = maximum of 8 % as reported by RH probe during this time) may have caused the low offset of the O_X EC sensors as, in very dry conditions, the electrolyte in the EC sensor can begin to dry out which increases the viscosity of the electrolyte [1], causing a decrease in the sensors ability to detect it's target measurand which would potentially lead to a negative offset. On the 24^{th} February, at approximately 0400H, the RH decreased from 6 % to -4 % over a short time period of about an hour. Simultaneously, there was an increase in the noise on the median O_X EC and the sensor began to drift upwards steadily and slowly. The median O_X EC also stopped reproducing the variance which was displayed in the reference O_X measurements and there was more discrepancies between the two signals, see Fig. 5.6. The O_X performance becomes poor compared to the reference O_X observations and this could have been due to a number of reasons. The RH of the air reaching the sensors was already low, as the ambient air was dry in Colorado and the sensor instrument was located inside but sampling outdoor air. This would decrease the RH further. The EC sensors do require some RH to operate properly and an absence of water vapour in the air might cause the sensors to have noisy signals. Or, the five individual O_X EC each experienced larger amounts of inter-sensor variability, driven by the dry or different conditions. This would result in the median O_X EC also becoming extremely noisy and potentially this led to the large amounts of noise observed towards the end of the deployment, on the 26^{th}; again perhaps a side effect of a prolonged exposure to dry air.

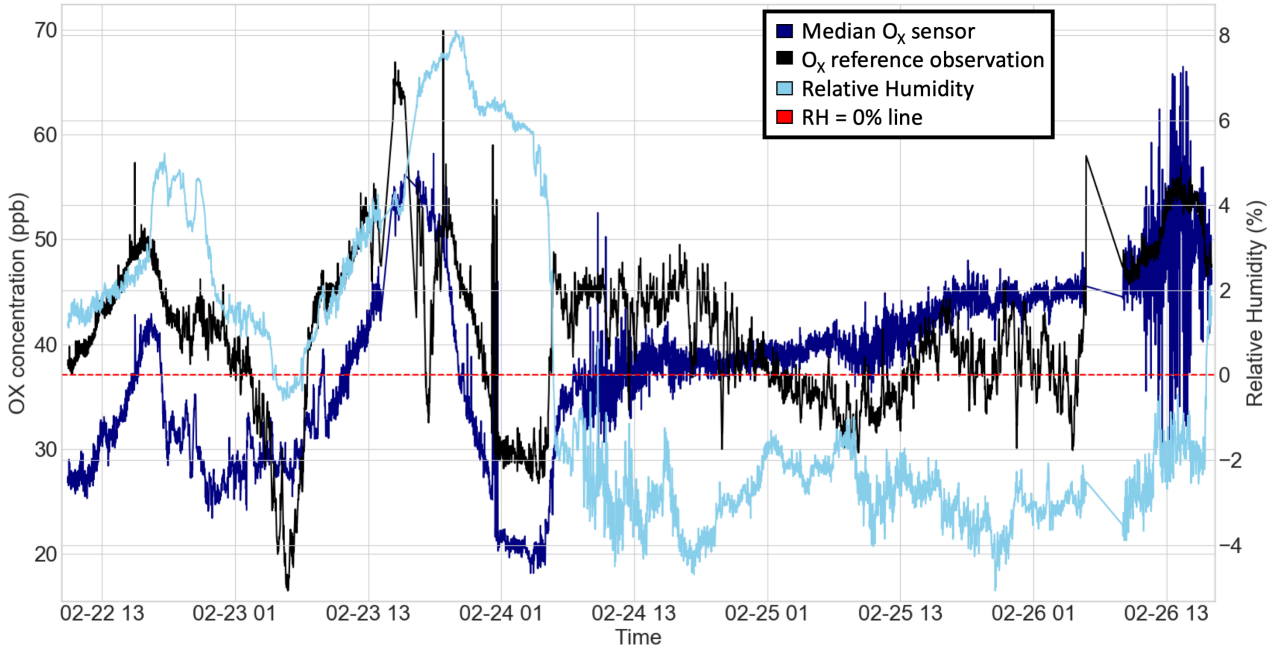

Figure 5.6: The degradation of the O_X EC sensor performance as the relative humidity of the air reaching the EC sensors becomes very low. The probe measured negative values for RH, and this indicated that the air was very dry, around 0 % which is the limit of detection for the RH probe.

The sharp drop in the humidity of the air reaching the sensors is potentially the reason that the NO_2 and CO EC also displayed more deviations from the reference observations around the time of the 24th February. The low humidity affects the sensing surface and hence how the sensors respond towards their target compounds. Under these dry conditions the sensitivity of the sensors is potentially higher than under wetter environments, but also more variable leading to a greater spread of sensors.

5.2.3 CO_2 NDIR devices

In addition to the EC and MOS sensors, there were three CO_2 NDIRs (ClairAir, Prime2) for the detection of CO_2 built into the sensor instrument. The reference CO_2 observations were time averaged to determine a mean data point every nine minutes because the sample line was also used for the NOx-CaRD instrument. The NOx-CaRD provided NO_2 and O_3 reference measurements, but overflowed the sample line with zero air every nine minutes for a short period of time. The CO_2 PICARRO was able to detect this and made the CO_2 reference measurements appear much more noisy than they were. For a fair comparison to the CO_2 reference observations, the NDIR data was also re-sampled to nine minutes.

The time series in Fig.5.7a compare the median of three NDIR sensors (purple) with the CO_2 reference observations (black). There was a large positive offset (40 ppm) between the median NDIR and the reference CO_2 values. The median sensor and the reference CO_2 instrument have a high degree of covariance and the main profile of the reference

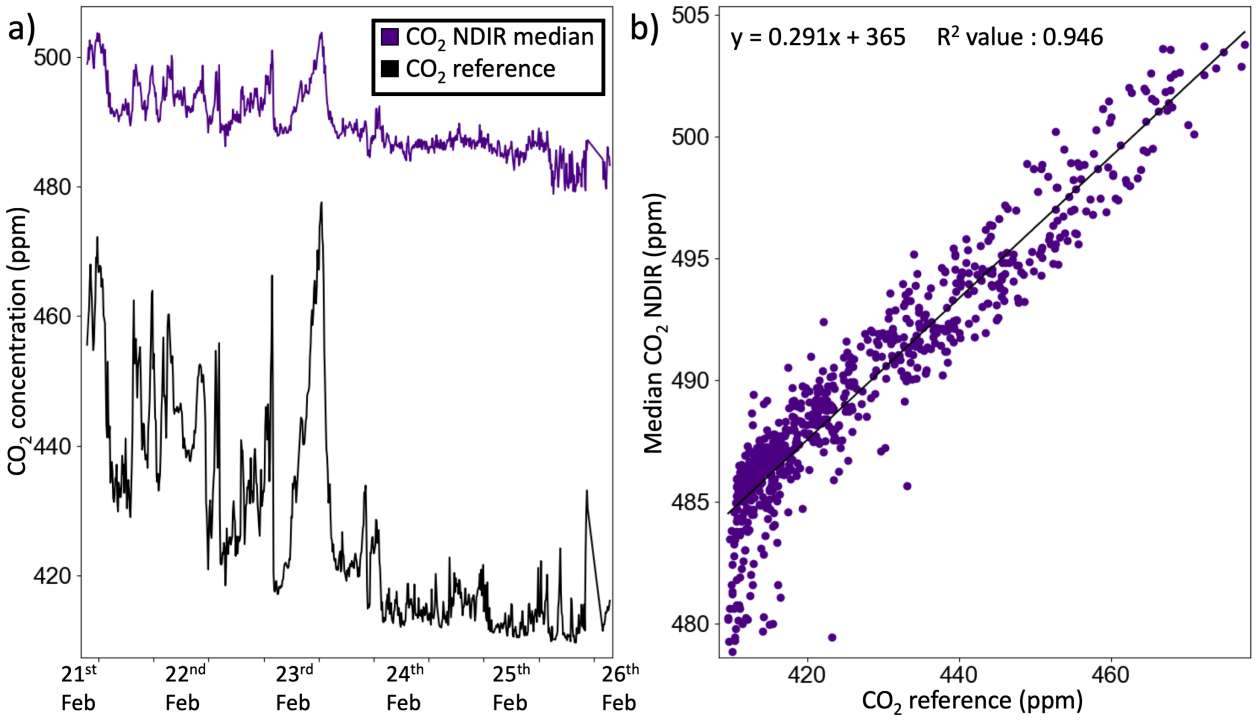

Figure 5.7: The time series, a) of the median of the three CO_2 NDIR (purple) and the CO_2 reference observations (black). The general profile of the reference measurements was detected by the NDIR devices, but the low-cost sensors did not mange to identify the correct absolute CO_2 concentrations. The correlation plot b) of the median NDIR and the reference instrument showed a high degree of linearity in the results, but a lower sensitivity for the NDIRs compared to the reference CO observations.

measurements over the five days of static deployment was detected. The correlation plot between the median CO_2 NDIR and the reference (Fig. 5.7b) showed that there was a high degree of linearity between the two detection techniques and the correlation was good (R^2: 0.91). The sensitivity of the median NDIR was relatively low as the slope between the two devices was 0.285. When the CO_2 reference observations reported the lowest values of CO_2, 400 - 420 ppm during the static deployment, the median NDIR exhibited the largest spread of data; reporting 475 - 490 ppm. In the correlation plot, Fig. 5.7b, this was evident as the slope between the median NDIR and the reference CO_2 was very steep between these values, creating the non-linear curve in the correlation plot. Due to the nature of the NDIR detection technique, the devices were supposed to be less susceptible to cross sensitivities, and the reason for this deviation from linearity might be due to the sensors either exhibiting a downwards drift over the three days or reaching their limits of detection.

After normalisation of each device the covariance-variance matrix showed that all three NDIRs co-varied together and this also matched the profile of the CO_2 reference observations.

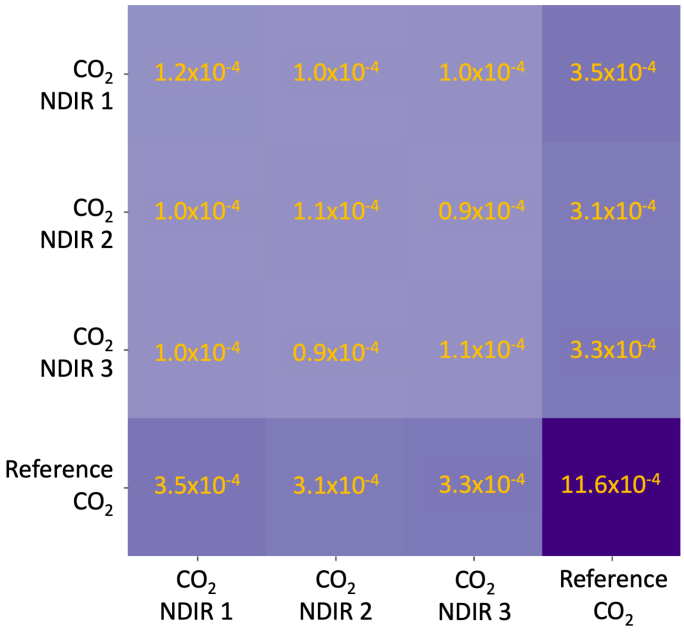

Figure 5.8: A covariance-variance matrix for the three NDIR sensors and the CO_2 reference measurement.

Where each device in Fig. 5.8 meets itself, the variance of the time series is given and all three NDIRs have very similar variance (1.1 x 10^{-4} to 1.2 x 10^{-4}) within their signals therefore all have similar sensitivities and responses towards CO_2. The variance in the reference CO_2 was quite a lot higher than the NDIRs (11.6 x 10^{-4}) due to the reference instrument exhibiting a greater sensitivity towards CO_2 gradients. It was advantageous that the three NDIR devices all displayed a similar amount of variance within their signals as this indicated that the inter-sensor reproducibility was high and the three CO_2

NDIR devices were comparable. However, compared to the CO_2 reference observations, the median CO_2 NDIR signal exhibited a low sensitivity towards changing ambient CO_2 concentrations. The device was designed to be low cost and therefore the expense per NDIR will limit the performance achievable with this technique. The scientific principle for NDIR sensors relies on the Beer-Lambert Law, therefore the sensitivity of the NDIRs could be increased by increasing the path length inside the NDIR; this may be difficult to achieve if the CO_2 NDIR sensors are to remain the same size and cost.

5.2.4 MOS sensors

There was a cluster of eight MOS sensors for each of the four different types (TGS2611 methane, TGS2602 total VOC, TGS2620 OVOC and TGS2630 propane/butane) of MOS sensors in the sensor instrument. The data sheet for the methane MOS (TGS2611) states that they can sense methane between 500 - 10,000 ppm, but it was expected that they will be able to detect at lower, more ambient concentrations, as the other types of MOS sensors have appeared to do in previous experiments. There were 8 methane MOS deployed as one cluster; one failed immediately upon arrival, leaving seven working methane MOS. To examine the amount of inter-sensor variability, the seven sensors had a constant offset applied to the entire time series that ensured that their signals all began at 1 V. The methane MOS spread out gradually over time, reaching a difference of 0.240 V between the highest and lowest reporting sensors over the five days of sampling the ambient air in Colorado, Fig. 5.9.

The spreading out of the methane MOS sensors meant that, as with other low-cost sensors, it is important to improve the reproducibility of the sensor measurements. Therefore the randomised drift was minimised by calculating an instantaneous median of the seven sensors and this was used for further analysis. Previously, the MOS signals have been impacted by changing RH and temperature of the air flow reaching the sensors, and so correlation plots to examine the relationship between the median methane MOS sensor with the RH and temperature were produced, Fig. 5.10a and b. As the relative humidity increased from by 12 %, the median MOS signal decreased, at a rate of -10.6 mV $\%^{-1}$. There was a strong correlation between the median MOS sensor and the RH of the air flow, R^2 : 0.83. This indicated that the median methane MOS sensor exhibited a large dependency on the relative humidity of the air. This was unsurprising given that previously, when the MOS sensors sampled in low humidity's they exhibited high and variable sensitivities towards their target compound, cross sensitivities and other external conditions. The linear parameters (y = -0.0106x + 1.04) deduced from Fig. 5.10a were used to generate an RH correction to account for the impact of RH upon the median MOS signal.

Temperature is another environmental condition that has impacted the MOS signals in previous experiments and so the relationship between the median MOS and the temperature of the air flow was also examined, Fig. 5.10b. There was a positive relationship

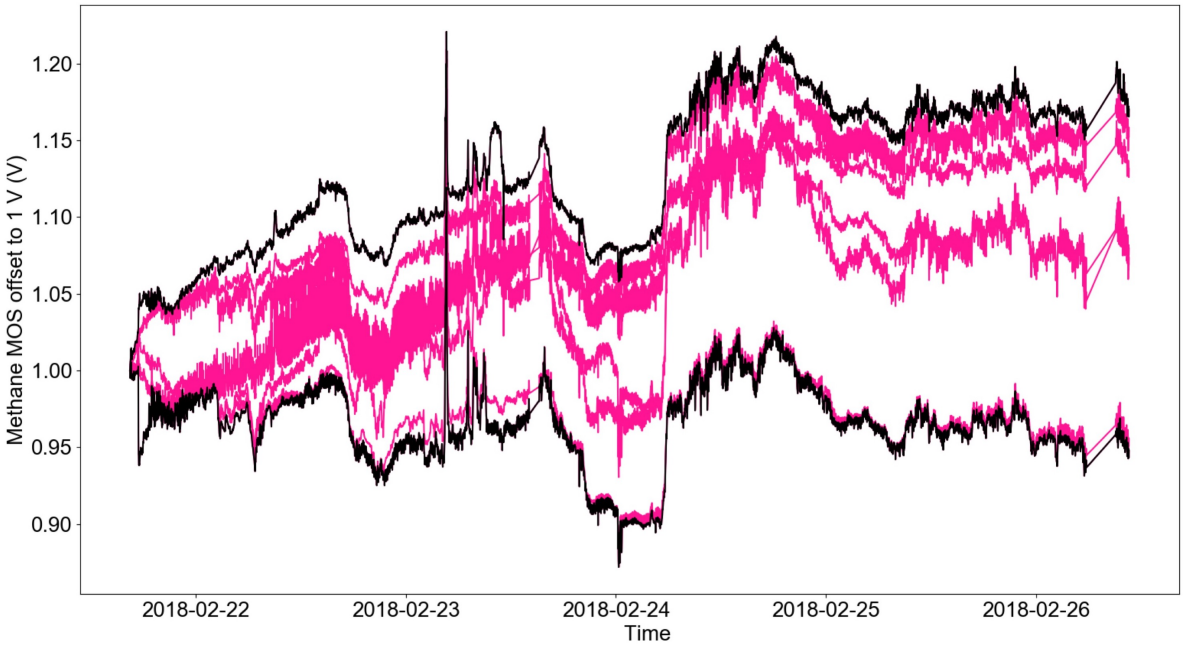

Figure 5.9: The seven methane MOS sensors were constantly offset to all begin at 1 V at the beginning of the deployment to investigate the degree to which they spread apart from each other. The pink lines indicated the individual methane MOS signals, and the black lines represent the highest and lowest reporting sensor.

between increasing temperature and an increasing median MOS signal (gradient: 32.1 mV °C), with a moderate to weak correlation, R^2 : 0.322.

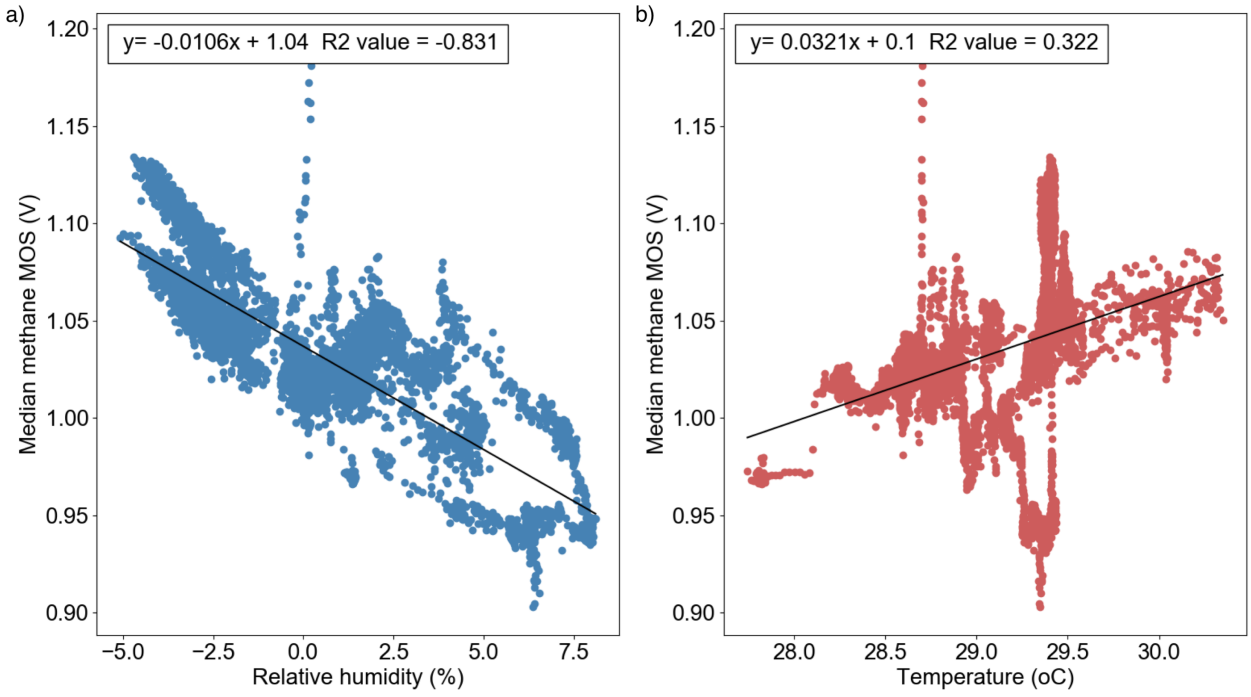

Figure 5.10: The median methane MOS was correlated with a) the relative humidity and b) the temperature of the air flow to allow linear correction factors to be determined in order to correct for changing environmental conditions.

The linear parameters describing the relationship between the humidity (Fig. 5.10a) and the temperature (Fig. 5.10b) were then used to predict a MOS signal based purely upon the humidity and temperature and then this was subtracted from the median methane MOS to leave the temperature and humidity corrected methane MOS signal, see Fig. 5.11. Correcting the median methane MOS signal for RH and temperature decreased the mag-

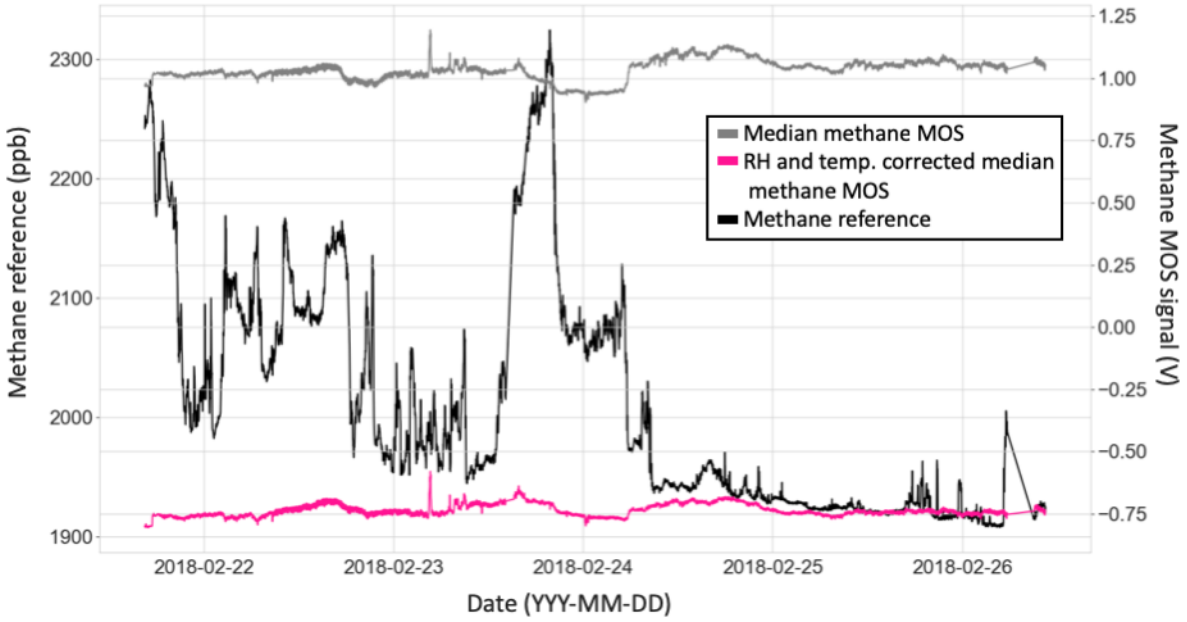

Figure 5.11: The median methane MOS signal before (grey) and after (pink) RH and temperature corrections were applied to the data. The black line is the methane reference measurement.

nitude of the longer term variability of the signal (4 - 6 hours). However, the RH and temperature correction did not impact the short term variability and as such it was hoped that these shorter term peaks were related to changing methane concentrations as the variability that remained in the median methane MOS signal was now more likely due to be from changes in the methane mixing ratio, than environmental changes. The methane reference instrument, a Picarro wavelength scanned cavity ring down spectrometer was averaged to 1 minute data for a fair comparison with the methane MOS, Fig. 5.12.

Even after temperature and humidity corrections the agreement between the reference CH_4 observations and the median methane MOS was still very poor (gradient = -6.02×10^{-6}), with a low correlation (R^2: -0.0235) and high error (NRMSE: 4.83). The reference CH_4 measurements detected more variability in the ambient methane concentration than the methane MOS sensors during the first three days of deployment - before the 24th February. Then the methane concentration decreased and plateaued at approximately 1.95 ppm. The median methane MOS signal displays a different profile, detecting less of the high resolution variability but three major peaks within the entire time series. Two of the peaks co-vary with the variability in the methane concentration from the reference observations and one which occurred after the 24th Feb, when the reference observations

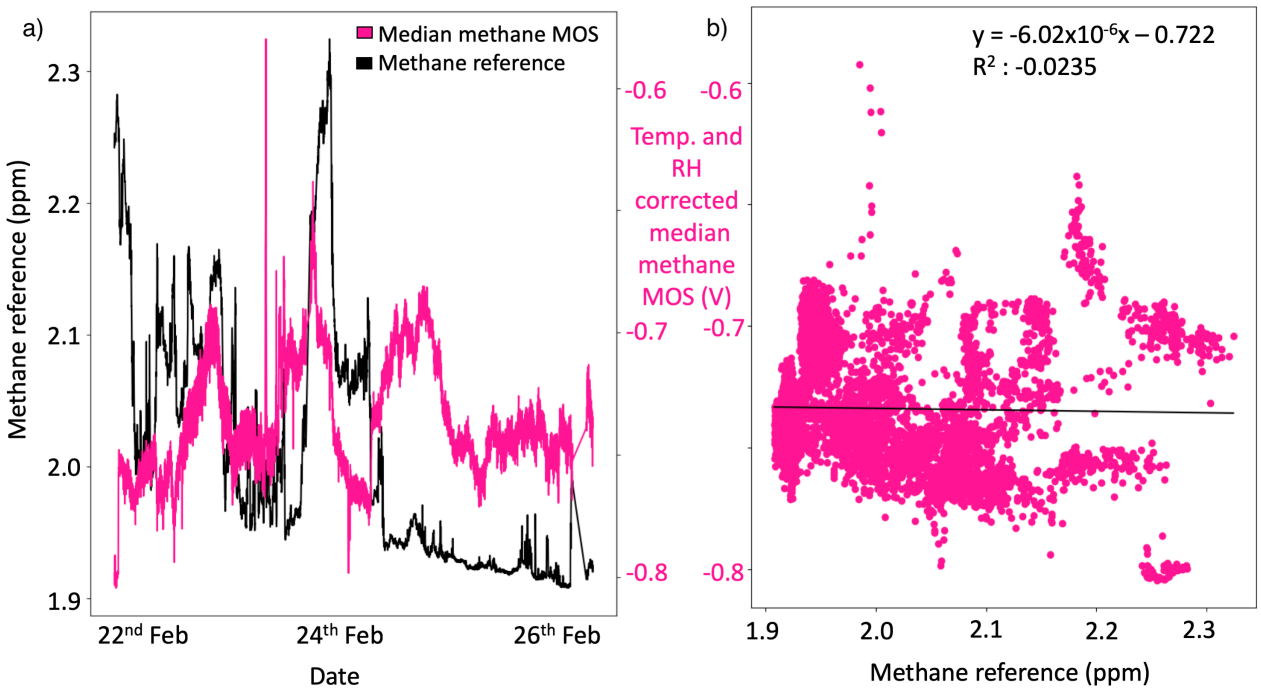

Figure 5.12: a) The ambient methane concentration as measured by the reference instrument (black) and the temperature and humidity corrected median methane MOS (pink), plotted on the secondary y-axis. b) Correlation plot between the two methane measurements.

have decreased. The median methane signal did decrease from -0.7 to -0.75 V and stabilise, but after a time lag of a day compared to the reference instrument. It is not clear from the plots in Fig. 5.12 whether the temperature and humidity corrected median methane MOS sensor was detecting methane. The value of these evaluation parameters (R^2, NRMSE, gradient) to compare the corrected MOS signal with the methane reference indicated that the methane MOS were not responding to changing methane concentrations.

The three other types of MOS sensor also recorded data for the five days over which the sensor instrument was deployed in the laboratory, sampling ambient air from outside. The distribution of the sensors, the median, the interquartile range and the 5^{th} and 95^{th} percentiles are plotted in Fig. 5.13 for the a) total VOC, b) propane/butane and c) OVOC MOS. The y-axis is the same for all three to allow for a better comparison between the three different types of sensor. All three types of MOS displayed similar variability throughout the static deployment when they sampled ambient air - with peaks occurring at the same time, albeit to varying amounts. After the 24^{th} Feb, there was an increase in the noise for the sensors, most likely due to the change in environmental conditions as this was the time whereupon the humidity of the air flowing to the sensors decreased for the next three days. The MOS signals became less variable after this date too, reflecting the behaviour of all the other sensors and reference instruments. This change in variability was evidence that the MOS sensors were responding to the pollution levels as they show the same qualitative trends as the reference instruments. All sensors and reference observations, barring the

methane MOS, observed a decrease in their target measurand concentrations after the 24th February, indicating a new parcel of air. This parcel probably contained a different atmospheric composition and lower amounts of compounds which led to the instrument wide decrease in signal. Both the total VOC and PrBu MOS clusters (dark red and teal respectively in Fig. 5.13) behaved similarly, with one sensor displaying a higher response than the other seven, leading to the 95th percentile (upper grey line in both Fig. 5.13a and b) lying around 0.1 V away from the upper quartile. The remainder of the PrBu MOS sensors were very close in value to each other, and the interquartile range (teal shaded area) was only just distinguishable from the median line (black). The eight OVOC sensors were more evenly spread about the median line.

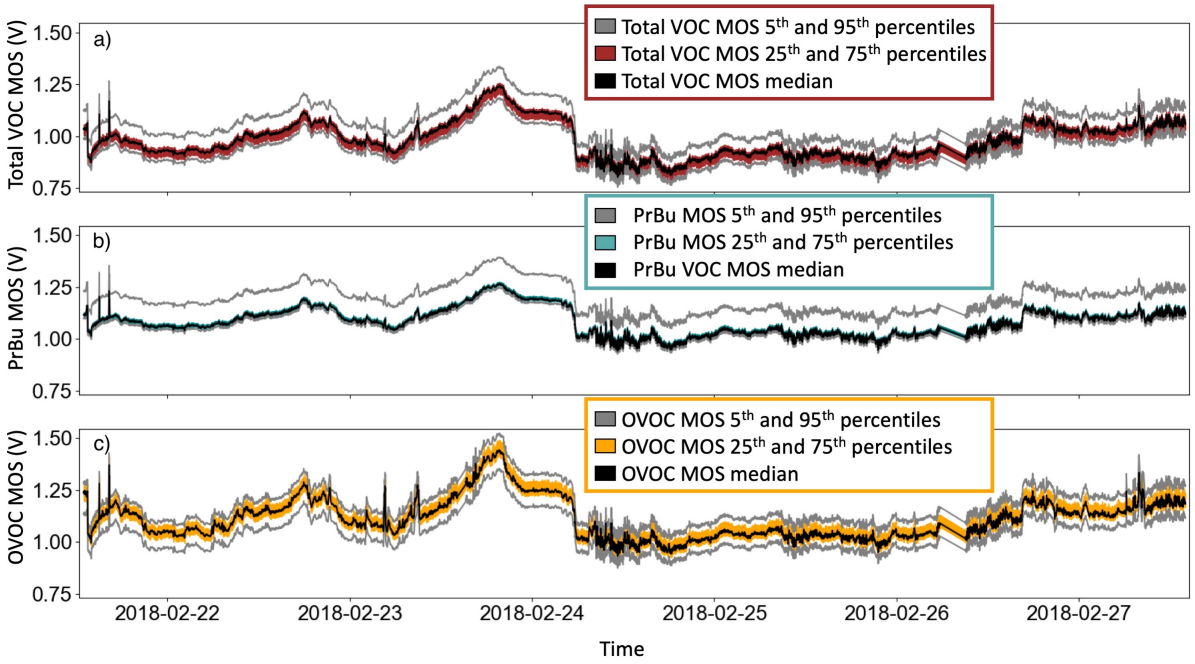

Figure 5.13: The interquartile ranges for the a) total VOC MOS, b) propane/butane and c) OVOC MOS sensors are shown as shaded regions. The grey lines in each plot represent the 5th and 95th percentiles and the black lines are the median of the cluster of MOS sensors.

All types of MOS were impacted by the changing humidity of the air flow and therefore the median VOC, PrBu and OVOC MOS sensor signals were corrected, in an analogous manner to the median methane MOS. Figure 5.14 shows the linear parameters describing the three median MOS relationships with the relative humidity of the air reaching the sensors active surface. The MOS sensors all displayed extremely strong correlations with RH, R^2 >0.91, and had a good agreement with the RH profile for the duration of the static deployment. The linear regression identified relatively high magnitudes for the slopes of the OVOC, VOC and PrBu MOS sensors against RH (30, 21 and 27 mV $\%^{-1}$ respectively) and it was thought that, since there were not many water molecules in the air, the impact per molecule was much greater leading to the MOS response closely following the measured

humidity of the air. The linear regression produced equations that could then be used to determine the MOS response if it was only responding to RH. This was then subtracted from the median MOS signal and the remainder is the RH corrected median MOS depicted by the coloured lines in Fig. 5.14.

a) Linear regression of uncorrected MOS sensors with RH of air flow

	OVOC	PrBu	VOC
Slope (mV %$^{-1}$)	30	21	27
R^2	0.92	0.97	0.92
NRMSE	0.227	0.230	0.229

b) Time series of median MOS sensor after RH correction

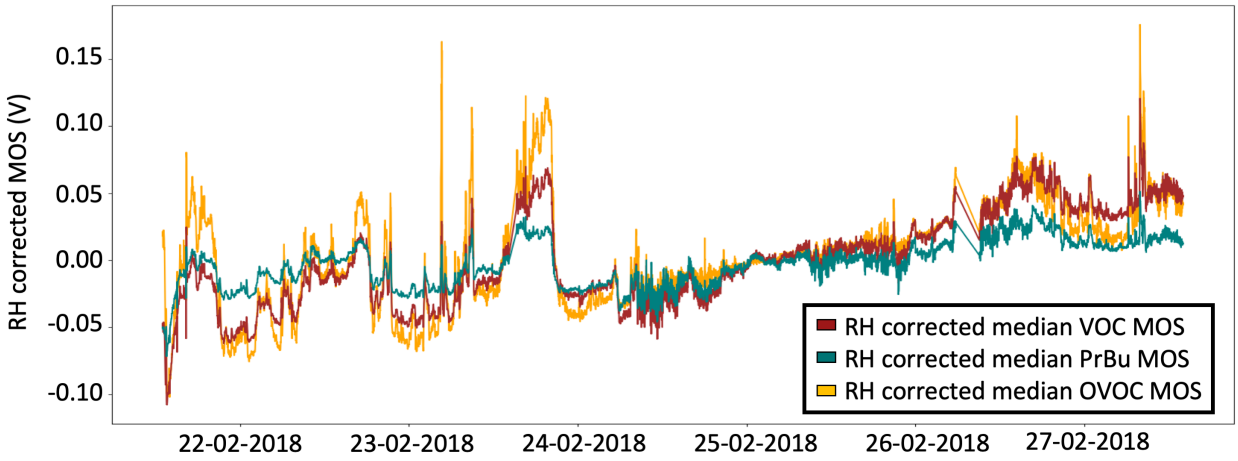

Figure 5.14: a) Each of the median OVOC, PrBu and VOC MOS sensors were correlated separately against the relative humidity of the air flow reaching the sensors. The linear parameters describing their relationships were determined and the slope, R^2 and NRMSE for this regression are in the table. All had strong, positive correlations with the humidity of the air, $R^2 > 0.91$. b) The RH corrected data for the OVOC (orange), VOC (dark red) and PrBu (teal) MOS sensors. A MOS prediction based purely on the RH was determined using the slope and intercept from the linear correlation plots and then this was subtracted away from the median MOS signal to leave the RH corrected signal. After RH correction, the MOS signals all covaried, with each displaying a similar time series.

The humidity corrected data showed a period of high variability for all types of sensor between the 21st and the 24th of Feb, then the signals all became much flatter before they steadily increased for the remainder of the deployment. The three different median MOS sensors detected similar variables in their environment as even after the RH correction their signals were similar.

The temperature was also monitored during the sensors deployment, and the linear regression parameters generated for each type of MOS sensor with temperature.

The correlation of the median of each MOS cluster with temperature was weak, see Table 5.2 and the R^2 between the median MOS and temperature ranged from -0.099 to -0.175. There was also a large amount of error calculated between the relationship with temperature and the median MOS, with the minimal uncertainty (NRMSE) being 467 % for the PrBu and OVOC sensors. The large NRMSE values indicated that there

Table 5.2: Linear regression parameters to describe the linear relationship between the temperature of the air flow and the median MOS signal for the VOC, PrBu and OVOC MOS clusters.

	VOC	PrBu	OVOC
Slope (mV $°C^{-1}$)	-24.4	-20.7	-15.4
R^2	-0.142	-0.175	-0.0993
NRMSE	4.69 (469 %)	4.67 (467 %)	4.67 (467 %)

was only a very weak correlation with temperature and therefore correcting the median MOS with the linear regression parameters was likely to introduce more error within the median MOS signal, rather than improving it by correcting the baseline for temperature. It was thought that the MOS sensor signals were all strongly influenced by the changing humidity conditions and the changes in RH had a larger impact upon the median MOS sensor signal, which overwhelmed the change in MOS signal that was due to changes in the temperature of the air. The range of temperature was also quite narrow (24.4 to 30.3 °C) and subsequently did not effect the total VOC, OVOC or PrBu MOS sensors to any great extent. Therefore, no temperature corrections were made upon the VOC, OVOC and PrBu MOS sensors regarding the temperature of the air for this deployment.

5.3 Machine learning using the static sensors

The machine learning techniques described in Chapter 4 were also used to form part of the analysis of the Boulder sensor instrument.

The linear regression analysis performed upon the EC located in Boulder showed that the sensors had a good agreement with their co-located reference instruments, over the first three days of deployment. Yet there was much more error in the sensor data when the concentrations of the compounds were low, for example when the pollutants ambient concentrations decreased on the 24th February. Machine learning (ML) can potentially optimise the sensor data further, making a concentration estimate that is closer to the reference, especially during those times when the humidity and pollutant concentrations changed rapidly.

The same XGBoost python package was used to run Boosted Regression Trees (BRT) and Boosted Linear Regression (BLR) upon the data collected from the static measurements taken when the sensor instrument was located inside the NOAA laboratories.

There were two approaches used for analysis of the EC sensors:

i The first method uses the algorithms that were previously trained on the first 30 % of the China data set, and apply these to the 5 days of static Boulder sensor data to make concentration estimates of NO_2, O_X and CO. This was interesting to identify how the China ML models performed upon the sensor data where the concentrations

of the target pollutants and the environmental conditions are vastly different.

ii Re-train the ML algorithms to determine new BRT and BLR algorithms. Use the first portion of the Boulder sensor data (20 %) to train the algorithm and apply these new algorithms to the last 80 % to make concentration estimates.

5.3.1 Machine learning with the China BRT and BLR algorithms

Previously, for the analysis of the China sensors data set, BRT and BLR ML models were used to improve the concentration estimates of the target compounds for the EC sensors. Cross validation (5-fold) was used upon the first 30 % of the China data set to tune the hyper-parameters to make a good fit of the algorithm to the data, and the trained model was exposed to 'unseen' data (testing set) to evaluate the performance of the algorithm. It was possible to apply the previously used models, trained on the first 30 % of the China sensor data set and apply these to the five days of data collected in Boulder. The Boulder sensors data set was therefore used as a different testing set for the China-trained ML algorithms. It was interesting to examine how well the China models performed when given a slightly different data set.
Although it was a different data set, the Boulder sensor data set contained the same variables that were collected in the China data set. There were new sensors installed in the sensor instrument but the measurement of NO_2, O_X and CO were still conducted using electrochemical sensors, and total VOCs were monitored using the same brand of metal oxide sensors. Boulder testing set variables were median CO, median NO_2, median O_X, median VOC, RH and temperature. BRT and BLR were used to predict the concentration estimate of NO_2, O_X and CO. The co-located reference instruments were used purely as a comparison for model performance evaluation.

Using the ML algorithms that were trained on the China sensor data will test the robustness of using ML as a calibration procedure and investigate the suitability of training ML in different conditions to the test set. Linear regression was used to evaluate the performance of three different methods: the uncalibrated median EC, the China-trained BRT algorithm and the China-trained BLR algorithms, compared against the respective reference observations, Fig. 5.16.

The BRT-predicted NO_2 prediction was used as an example to show how the comparisons between the different algorithms were made. The example, shown in Fig. 5.15 shows the median NO_2 EC sensor with just the factory conversion factors applied to the sensors (referred to as the uncalibrated sensors, grey), the reference NO_2 observations from Boulder (black) and the NO_2 concentration estimate (green) predicted using the China BRT model upon the Boulder data set.

The uncalibrated NO_2 sensors (grey, Fig. 5.15a) had a better agreement with the

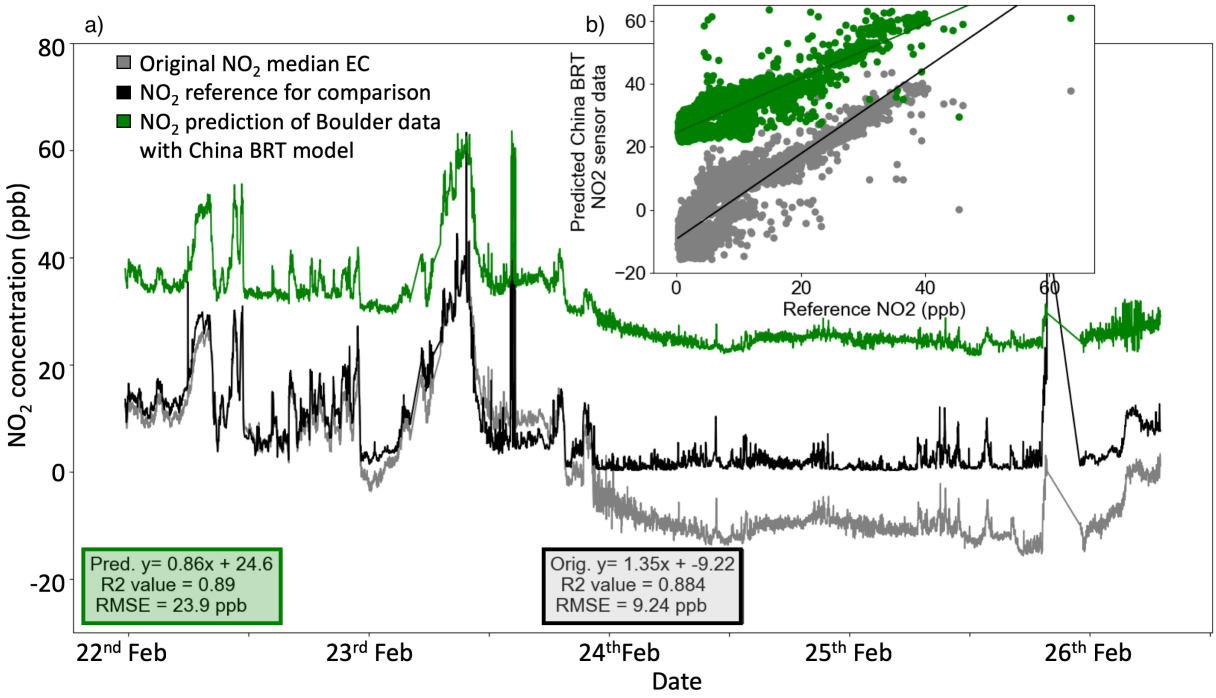

Figure 5.15: The hyper-parameters were unchanged from the China BRT analysis to identify how well the NO_2 BRT algorithm performed when the Boulder static measurements were used as a testing set. The China-trained BRT model predicted the NO_2 concentration (green). The NO_2 reference observations are plotted in black, and the median NO_2 sensor with no calibration model applied is shown in grey.

reference NO_2 observations than the NO_2 predicted using the China-BRT model. The NO_2 prediction was constantly offset by approximately +20 ppb compared to both the reference measurement (black) and the uncalibrated NO_2 median EC. The variability in the NO_2 concentration was detected in the NO_2 China-BRT prediction, but there was no improvement in the covariance of the data compared to just using the median NO_2 EC sensor. Therefore, due to the poorer performance of the China trained NO_2 BRT concentration estimate the calibration model was not robust when the sensor instrument was deployed in a location that has different conditions than the location in which the algorithm was trained in. The BRT ML technique is incapable of extrapolation. Therefore when the chemical and environmental conditions were altered to be beyond the ranges experienced by the algorithm in the training set, the BRT algorithm could not estimate the impact of these changes upon the EC sensors, leading to the +20 ppb offset.

However, the China-BRT algorithm did predict the NO_2 concentration with an essentially equal correlation (R^2: 0.89) with the reference observations than the uncalibrated median NO_2 (R^2: 0.88). The BRT algorithm performed better at not overestimating the NO_2 concentration after the decreased in concentration on the 24th and the NO_2 concentration estimate did not decrease to negative values, or by as much as the EC sensors alone did. Therefore the China-BRT prediction of NO_2 was able to capture the same variance within the data set than the median NO_2 sensor, and hence did not lead to a decrease

	Median EC, no calibration procedure	BRT algorithms trained upon China dataset	BLR algorithms trained upon China dataset
NO_2 EC	y = 1.35x – 9.22 R^2 : 0.884 RMSE : 9.24 ppb NRMSE: 0.1559	y = 0.86x + 24.6 R^2 : 0.890 RMSE : 23.9 ppb NRMSE: 0.5694	y = 0.655x + 32.2 R^2 : 0.882 RMSE : 30.0 ppb NRMSE: 1.0722
O_X EC	y = 0.556x + 15.2 R^2 : 0.505 RMSE : 8.1 ppb NRMSE: 0.1518	y = 0.298x + 39.4 R^2 : 0.539 RMSE : 12.4 ppb NRMSE: 0.2316	y = 0.35x + 26.8 R^2 : 0.481 RMSE : 6.59 ppb NRMSE: 0.1234
CO EC	y = 0.983x + 4.66 R^2 : 0.937 RMSE : 32.4 ppb NRMSE: 0.0616	y = 0.304x + 240 R^2 : 0.571 RMSE : 126 ppb NRMSE: 0.8579	y = 0.461x - 471 R^2 : 0.875 RMSE : 579 ppb NRMSE: 2.1179

Figure 5.16: Summarising the performance of the uncalibrated median EC, the China-trained BRT and China-trained BLR algorithms when they were used to predict the concentration estimate of NO_2 (green), O_X (blue) and CO (red).

in R^2 when compared with the reference, even though the absolute values produced by the China-BRT prediction were further from the reference observations. The uncalibrated NO_2 median EC displayed a RMSE of 9.24 ppb with the reference NO_2 observations, whereas the RMSE for the China-trained BRT NO_2 prediction was 23.9 ppb. There was a lot more error within the China-trained NO_2 BRT signal than the uncalibrated median NO_2 EC.

The results from using first the China-trained CO BRT algorithm and then the China-trained CO BLR algorithm with the CO Boulder data are summarised in Fig. 5.16. The equivalent analysis of the O_X Boulder data, with the China-trained O_X BRT algorithm and the China-trained O_X BLR algorithm is also displayed in Fig. 5.16. The BLR algorithm was investigated because this algorithm does have the ability to extrapolate and therefore if the response of the EC towards the temperature and humidity were linear, these models have a better chance at producing a concentration estimate that is closer to the reference than the uncalibrated EC sensors alone.

The intercept of the linear regression was used to investigate the offset between these different analysis techniques and the reference observations. In all cases, the intercept (offset) of the EC from the reference observations was smallest when the uncalibrated median EC was used, indicating that, out of the three methods used, the uncalibrated EC median was optimum for determining absolute concentration values. Equally, the linear regression slopes were closest to 1 for the comparison of the reference observations with the uncalibrated EC median signals, indicating that the uncalibrated median EC signals exhibited a sensitivity that was more similar to the reference instrument, compared to the China-BRT or China-BLR predicted concentration estimates.

For the NO_2 and CO EC analysis, the RMSE values were the smallest for the uncal-

ibrated sensors. When the China-trained ML techniques were applied the error in the predictions increased and were at least three times higher than the error between the uncalibrated sensors and the reference measurements.

For CO and O_X, applying the respective China-BRT algorithms degraded the sensor performance; the offset increased, the R^2 decreased, and the error within the concentration estimates increased. This was the same for the NO_2 except the R^2 increased slightly due to an improvement of the correlation for the China-trained NO_2 BRT prediction, during times when the concentration of NO_2 was low.

The China-BLR models did not improve the sensor data quality either. The R^2 values between the reference and the China-BLR predictions was always lower than when the uncalibrated EC median was used.

For the NO_2 and CO EC analysis, using China-trained BLR algorithms caused the error estimates (RMSE and NRMSE) to increase; the NRMSE was more than 6 times greater than when it was calculated for the uncalibrated median EC sensors. However, the RMSE was reduced when the China-BLR algorithm was applied to the O_X, from 8.1 ppb (for the uncalibrated median O_X EC against reference) to 6.59 ppb. This reduction in the error estimate was due to a better agreement with the reference observations that occurs at at the beginning of the deployment. Yet after the 24^{th} Feb, during the low humidity period, the O_X prediction was not as good as the uncalibrated O_X median EC.

The China trained BRT ML algorthims were not suitable for improving the quality of the EC sensor data when the sensors were deployed in Boulder, Colorado. This indicated that the relationships and trends that the BRT algorithm learnt during the Beijing training period are different to those that exist between the sensor variables in Boulder. This could be due to a number of reasons. The RH and temperature during the Boulder deployment are very different to that experienced by the EC in China, when the ML algorithm was trained. The temperature and RH are instrumental for determining the sensitivity of the EC towards their target compounds and EC sensor performance. The ML algorithms would not be trained with data to supply them with the information that, at very low RHs, the O_X EC for example, exhibits a linear, low offset. Therefore any of the concentration estimates that use the median O_X EC to make decisions and predictions will be affected and will not be accurate. It would not help to correct the data by applying an offset prior to the application of the ML algorithms because the poorer performance of the ML concentration estimates were due to a combination of the different environmental conditions, and a change in the sensitivity and performance of the EC, not just because the concentration of the compounds were lower than they were in Beijing. It was expected that, because the environmental conditions and concentrations of pollutants were different between the two deployments, it might be challenging for the ML algorithms to make accurate and precise concentration estimates. However, due to the BLR model able to extrapolate to allow predictions over conditions that were not observed within the training

data set, it was thought that this might perform a lot better than the BRT algorithm. BLR did not consistently perform better than BRT therefore it is not possible to use either ML techniques when applying them to data sets with different environmental conditions.

To conclude, it was not appropriate to produce one single ML calibration model, trained on a narrow set of variables and conditions (e.g. China data set), that was appropriate for all environments (e.g. applying to the Boulder data set). ML models must be trained with a data set that encompasses the same environmental conditions as experienced by the sensors during the testing set. It was necessary to re-train the ML algorithms with the training set including humidity's as low as 0 % RH and temperatures to 30 °C with lower concentrations of the target compounds. These environmental conditions would then be more representative of the site of deployment in Boulder.

The sensors were exposed to completely different ranges of outdoor variables when they were deployed in China therefore, because the training data set has only observed the EC sensors behaviour within a temperature range of 15.2 - 42.2 °C, a humidity range of 3.82 - 17.83 g m^{-3} and higher pollutant concentrations there were difficulties when predicting concentration estimates in Boulder. Previous experiments have shown that the sensors can also exhibit non-linear relationships with these variables so, even when the algorithms were capable of extrapolation, e.g. the BLR ML models, these trends were not representative of the EC behaviour in these conditions either.

5.3.2 Retraining the ML algorithms using BRT

New ML based calibration models, which used only data from the Boulder deployment were produced, so that the hyper-parameters were tuned to allow good fitting of the algorithms with data collected at in Boulder. This might improve the performance of the ML analysis and predict concentration estimates of the different pollutants which are closer to the reference observations. The sensor instrument was set-up to monitor ambient air over a week, with a four-hour stabilisation period prior to the start of the training data. Consequently the training and testing data sets were smaller than for the China data. Co-located reference instruments for CO, NO_2, O_X, CO_2 and methane were used as the training labels when a concentration estimate for that specific compound was determined via BRL or BRT. The limited data sets may impact the ML algorithms ability to detect trends between the variables. It was interesting to observe the performance of the BRT ML technique when a 4-day training set was used and identify if it was possible to improve the quality of the sensor data even with a short time scale and a smaller data set.

As with the previous analyses using ML, the sensor variables used were the median CO, NO_2, O_X, O_3 (median O_X - median NO_2) EC , median total VOC MOS, RH and temperature of the air flow to the sensors. The median CO_2 NDIR signal was also included in all the ML algorithms training and testing data sets when the algorithms were re-trained upon the data collected in Boulder. The three other types of MOS sensor - the OVOC,

PrBu and methane MOS were not included because it was difficult to identify if they were responding to their target compounds, or if their signals were overwhelmed by cross sensitivities.

Splitting the data into training and test sets

There were 6565 simultaneous reference and median CO_2 NDIR data points. The training and testing data sets were split into 80 : 20 leaving 5252 data points used in the training period (0900 22nd February 2018 until 20:30 25th February 2018) and 1313 in the testing period (20:30 25th February 2018 until 17:00 26th February 2018).

The NO_2 and O_X concentration estimates were made using 5954 data points in the training set and testing with 1000 data points.

The CO sensors recorded data for the same time period but there was less data available because the data was averaged to every 9 minutes, in order to make a comparison with the reference instrument. The reference instrument was averaged to every 9 minutes to smooth out the response due to the reference instrument responding to the overflow of zero air into the sampling air which occurred every 9 minutes and lasted 10 seconds. Although the EC sensors did not respond on a fast enough time scale to observe this overflowing of air, to make a fair comparison between the CO reference measurement and the CO EC both data sets were averaged to 9 minutes. However, this averaging greatly limited the amount of data points, leading to the CO BRT prediction having 727 data points for training and 182 data points for testing to ensure there was still an 80 : 20 split. Since ML techniques perform better at capturing the relationships between variables when they have access to larger data sets, often more data is advantageous for making predictions over the testing set. It was therefore expected that the ML CO prediction would not be as good as the NO_2 or O_X.

Five-fold cross validation with a randomisation seed of 42 was again used each time the ML algorithms were trained upon the data, to minimise over-fitting. Linear regression was used to compare the BRT-predicted concentration estimates with the relevant reference instrument over the testing period, see Fig. 5.17, coloured data points and coloured trendlines. To identify if applying BRT ML improved the quality of senor data, the uncalibrated median EC or NDIR was also compared to the reference instrument over the same time period as the testing data (20:30 25th February 2018 until 17:00 26th February 2018), see Fig. 5.17 grey data points. The trendlines calculated between the uncalibrated EC and NDIR with the reference are also plotted as grey lines.

The correlation plots between the concentration estimates made by each of the trained BRT algorithms are shown in Fig. 5.17. The NO_2 concentration estimate produced a smaller error estimate than the uncalibrated median NO_2 EC (NRMSE BRT NO_2 prediction: 0.0842, NRMSE uncalibrated NO_2 median: 0.294), see Fig. 5.17a. This indicated that the BRT prediction better predicted the variance within the NO_2 signal, compared to the uncalibrated median EC. Yet, the gradient of the slope between the reference and

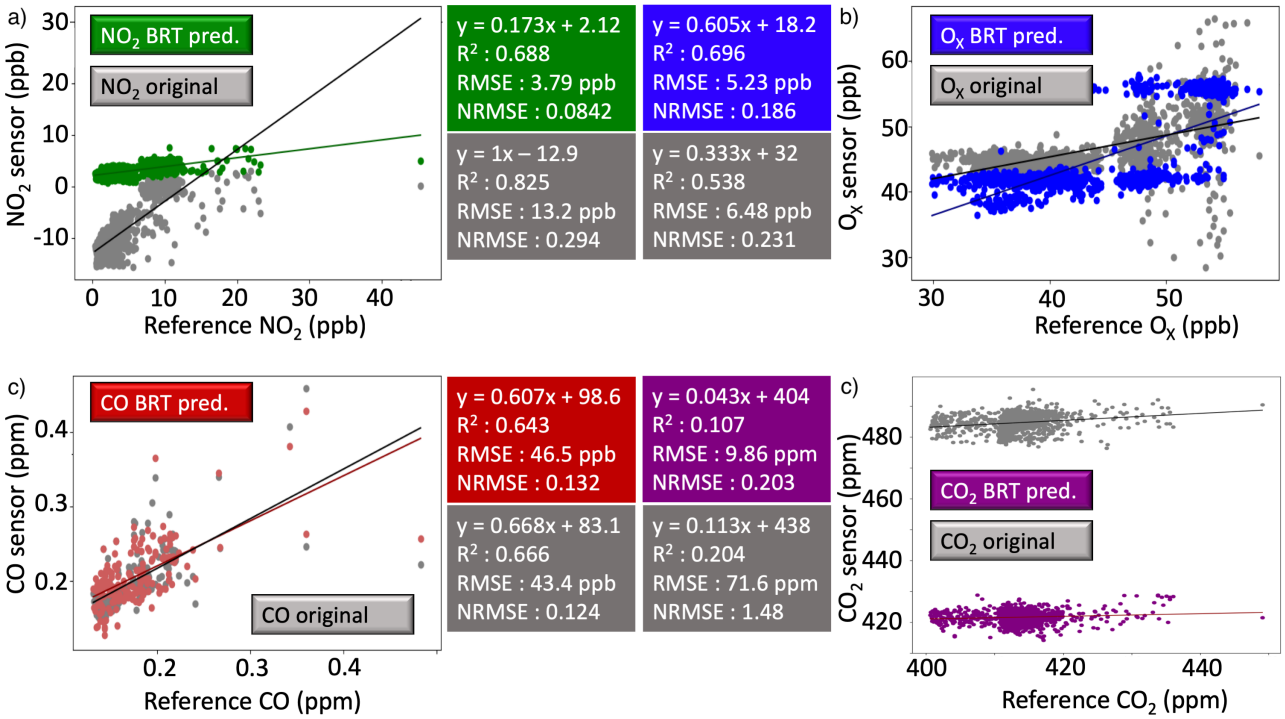

Figure 5.17: The correlation plots between the uncalibrated median sensors (grey) and BRT concentration estimates after the algorithm was trained using only data it had observed in Boulder. a) NO_2 prediction (green), b) O_X prediction (blue), c) CO prediction (red) and d) the CO_2 prediction (purple). The trendlines and parameters calculated via linear regression are also shown for the uncalibrated sensors (grey lines and boxes) and the BRT-predicted concentration estimates (coloured lines and boxes).

the BRT-predicted NO_2 concentration was further away from 1 (gradient 0.173) compared to the uncalibrated median NO_2 EC (gradient (1.0) indicating that the absolute BRT predicted NO_2 concentrations were further from the reference NO_2 observations. The sensitivity of the BRT prediction was reduced compared to the uncalibrated median NO_2 EC. The decrease in the correlation with the reference observations (R^2 value BRT NO_2 prediction: 0.69, uncalibrated NO_2 median: 0.83) was additional evidence that the BRT algorithm did not fully capture the relationships between the sensor variables and the ambient NO_2 concentrations. BRT did not improve the quality of the NO_2 sensor data. This was potentially because the CO EC was the second largest contributor towards the NO_2 BRT prediction in Chapter 4, Fig. 4.31. With limited CO EC data points, the BRT algorithm would be more limited when making decisions in the decision trees.

The BRT prediction of the O_X concentration improved in all the performance criteria shown in Fig. 5.17b. The correlation between the reference observations and the O_X concentration increased (R^2 BRT O_X prediction : 0.70, uncalibrated O_X median: 0.54), the trendline was closer to 1 (BRT predicted O_X:0.61, uncalibrated:0.33) indicating that the BRT predicted concentration estimate was more sensitive towards changing O_X concentrations. The error within the O_X timeseries was also reduced for the BRT-predicted O_X concentration estimate (NRMSE:0.19) compared to the original median O_X EC sensor (NRMSE:0.23). Applying BRT did improve the quality of the O_X sensor observations, although the overall performance of the median O_X EC and the subsequent BRT O_X prediction was poorer compared to the China data analysis.

Due to the limited data points for the CO sensors, the BRT prediction was not expected to improve the CO concentration estimate based upon the median CO signal and this was the case. The correlation was weaker for the BRT-predicted CO (R^2:0.64) than it was for the uncalibrated CO EC median (R^2: 0.67). There was also slightly more error in the BRT-predicted CO estimate (NRMSE:0.29), than there were for the uncalibrated CO median EC (NRMSE:0.12). A longer time series, with higher temporal resolution training data points would allow the BRT algorithm to better detect the relationships between the sensor variables and the CO concentrations and hence allow for an improved BRT-predicted CO concentration estimate.

The BRT-predicted CO_2 concentration estimate, Fig. 5.17d, was also compared with the uncalibrated CO_2 NDIR median. This was the first time the CO_2 NDIR sensors had been deployed as part of the sensor instrument and there were improvements to the quality of NDIR data after applying BRT to the data set. The NRMSE decreased from 1.42 with the uncalibrated median CO_2 to 0.203 for the BRT CO_2 concentration estimate, reducing the uncertainty within the data. The offset of approximately 40 ppm was reduced when using the BRT CO_2 prediction. However, the R^2 value decreased slightly for the BRT predicted CO_2 concentration estimate. The gradient of the line between the BRT-CO_2 concentration (0.043) was lower than for the uncalibrated NDIR median (0.113), which

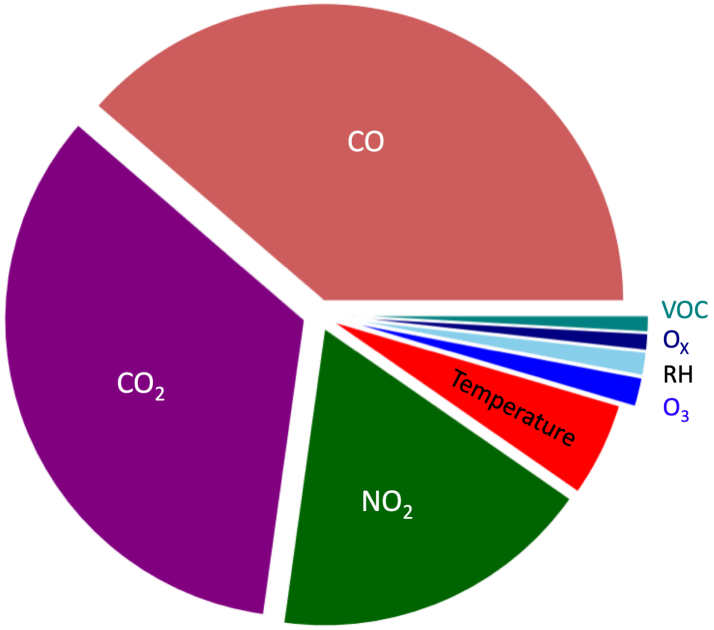

Figure 5.18: The relative contributions of each variable to the CO_2 BRT concentration estimate. CO and CO_2 contributed the most, to very similar degrees.

indicated that the uncalibrated NDIR median was more sensitive at detecting the same changes in ambient CO_2 as the CO_2 reference instrument.

The gain feature showed that each sensor contributed the most to the concentration estimate of its target compound. E.g. the O_X sensors made the largest contribution towards the algorithm trained to predict the O_X concentration. The contribution of each LCS towards the BRT CO_2 prediction are displayed in Fig. 5.18, as this was the first time that the BRT algorithm had been used to make a CO_2 prediction.

Surprisingly, the median CO EC made the largest contribution to the CO_2 concentration estimate, Figure 5.18. The median CO_2 NDIR sensor made the second largest contribution, and together these two variables influenced two thirds of decisions during the training of the BRT algorithm. Ambient CO and CO_2 concentrations are correlated in the troposphere when the emissions are influenced by combustion [57]. Therefore the BRT algorithm may have detected this correlation between the two sensor signals to make the BRT predicted CO_2 concentration estimate hence this was potentially why the median CO EC makes such a large contribution to the BRT prediction for CO_2.

The BRT algorithms applied to the sensor variables improved the quality of the sensor data with limited success. The improvements that BRT made were slight and were not to the same extent of improvement observed with the application of ML techniques to the China data. This was potentially because the smaller data sets meant that the training and testing data had different distributions. ML is less effective when the distributions of the training and testing data are different because the relationships learnt during the training stage are not representative of the behaviour of the sensors in the testing stage.

The distribution functions in Fig. 5.19 shows how the training data was distributed

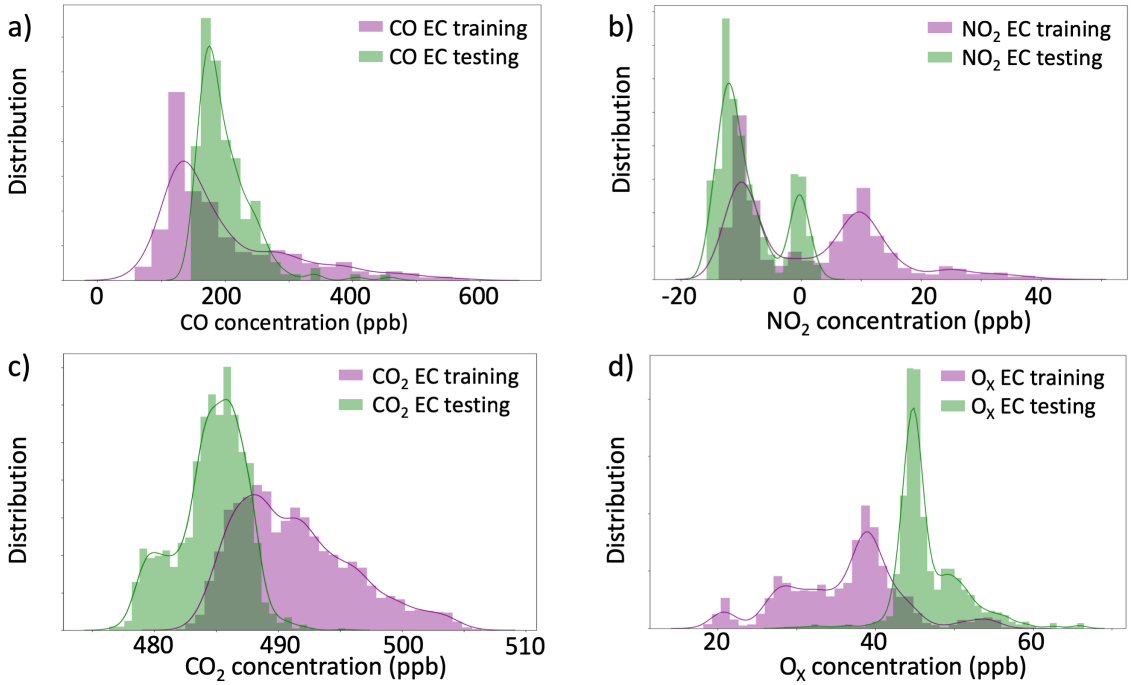

Figure 5.19: The distribution of the training (purple) and testing (green) data for the Boulder data, for a) CO, b), NO_2, c) CO_2 and d) O_X. The more similar the distributions of training and testing data sets, the better the ML prediction. This is because the relationships learnt by the algorithm in the training data will be true of the relationships in the testing data set.

compared to the testing data for a) CO, b) NO_2, c) CO_2 and d) O_X. For the Boulder data, the testing data and the training data had only small domains where the distributions overlapped - and these were the regions where the relationships learnt by the ML during training held true for the testing period. Because the overlap is small, the ML techniques cannot make accurate predictions about the concentration estimates. Where there were large differences between the distributions of training and testing data for one variable, this impacts the quality of the prediction made for any prediction that uses this variable to make a prediction. Therefore, since there were no variables that displayed highly similar distributions between the training and testing data sets, all of the ML predictions would be affected as they all used every variable to some extent.

The training and testing NO_2 distributions were the most similar; they both had the same shape of one large peak at lower concentrations, followed by a smaller peak at 15 - 20 ppb higher concentrations. The similarity of these two distributions led to the BRT predicted NO_2 concentration estimate displaying the most improvement compared to the uncalibrated NO_2 EC median, Fig. 5.20.

The NO_2 EC sensor data contributed in 88 % of the key decisions when identifying the relationship between the sensors and the training label and this sensor had the most similar distribution between the training and testing data set. Therefore the BRT predicted NO_2 prediction was the best out of the concentration estimates produced for the other types

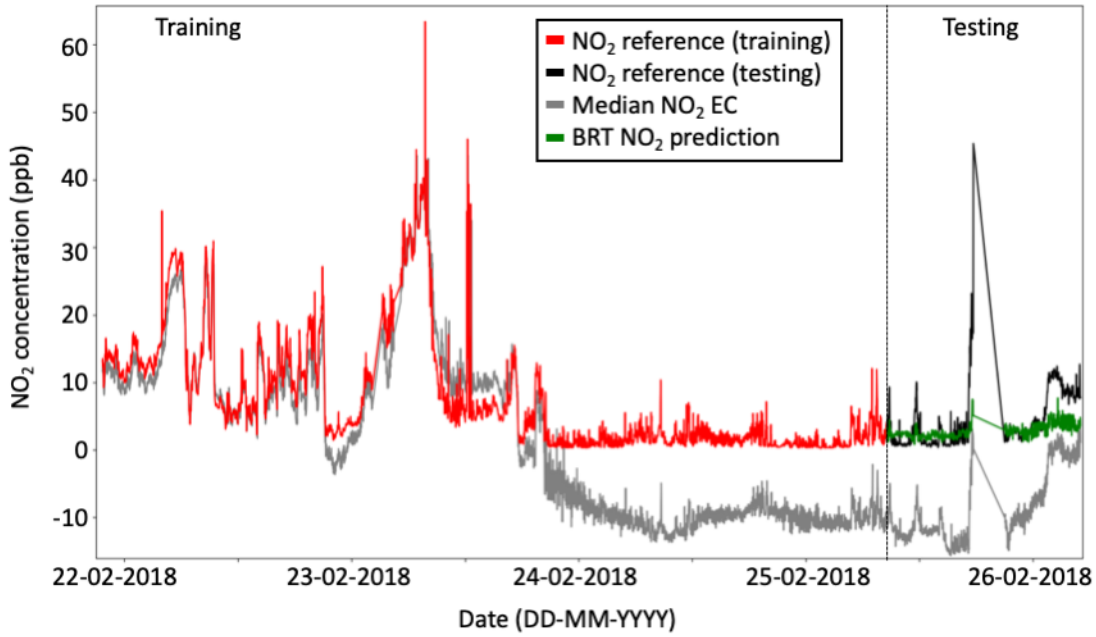

Figure 5.20: The timeseries to investigate the training and testing data for the NO_2 median EC and to compare the NO_2 median EC with the BRT predicted NO_2 concentration estimate.

of sensor.

The sensors experienced much drier air than they have done previously for monitoring ambient air, which may have affected the sensitivities and the amount of random noise in the sensor signals. Over such a short period of time the algorithms found it hard to determine relationships for this degradation of the sensor signals. The O_X EC showed this clearly. In the last two days of sampling air in Boulder, the median O_X signal displayed an exponential increase in noise which overwhelmed the relationships between the O_X sensor, the reference O_X reference observations and the other variables measured by the sensor instrument. This was unexpected and since the training data set did not contain EC sensor data where this was observed, the algorithm found it difficult to respond to. This degradation of the O_X EC signal impacts all the BRT predictions that used the O_X sensor to make a prediction. The O_X EC did not co-vary with the reference O_X observations to the same extent that it did during the China deployment previously. The poorer performance of the median O_X EC hugely impacted the BRT O_X concentration estimate which previously used the median O_X EC to influence the majority of decisions within the tree ensemble that produced the BRT O_X concentration estimate. Instead, the temperature timeseries was the main contributor to the BRT O_X prediction (29 %), whereas the median O_X EC only made the third largest contribution (19 %). impacted the most because this was the prediction which used the median O_X EC for calculating the concentration estimate. A lack of humidity is known to cause a range of unpredictable responses from the EC sensors [206] [104].

To fully optimise the ML models, the training and testing data require their distribution

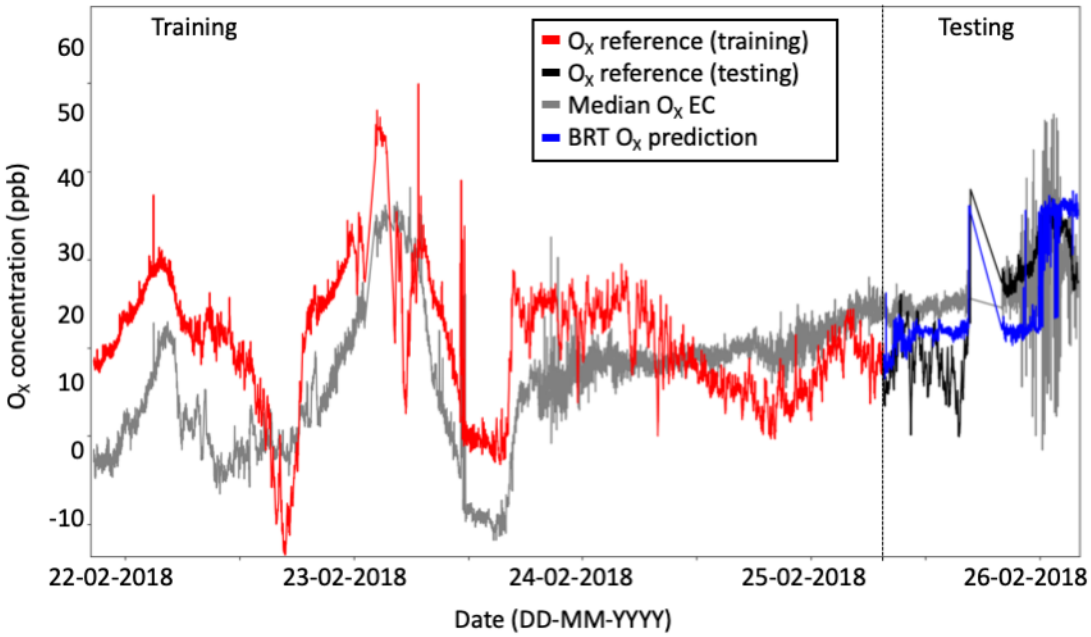

Figure 5.21: The median O_X EC sensor (grey) exhibited a large amount of noise towards the end of the static deployment in Boulder (26th Feb. This influenced the BRT O_X prediction (blue) and other predictions that the median O_X EC was involved with. Reference O_X observations are shown in red and black for the training and testing periods, respectively.

of data to have maximum overlap for the trends learnt by the algorithm to calculate the concentration gradients. More data, with the sensors exposed to a wider range of pollutant concentrations - especially at lower ambient mixing ratios- and environmental conditions was necessary to improve the performance of the BRT ML technique.

There was a noticeable change in the traces for the reference instruments and the EC sensors in the latter half of the data sets. As discussed previously, this was thought to be due to a change in the air parcel the instruments were measuring e.g. from a changing wind direction blowing in air containing pollutants from different sources. The temperature and humidity sensors helped to detect that the air parcel experienced by the sensors on the 24th February exhibited different environmental conditions as the air sampled on the previous day. However, there was nothing as definite as an anemometer measurement to monitor the wind direction and speed, which would be more informative for detecting different air parcels and identifying their back trajectory. Including this information in the sensors data would potentially improve the ML predictions as the algorithm would have data to indicate a different air parcel via the wind direction, temperature, humidity and the concentration of contaminants. Once the algorithm has been trained on such data it would be used to better predict the concentration estimates since the ambient concentration of pollution might always be higher or lower when the wind is blowing from a certain direction especially if the sensors were based downwind of an emission source.

It was hoped that the BRT algorithms trained on the static deployment could be used as a calibration model for the mobile measurements made by the sensors in the following

week. However, there was not consistent evidence that the BRT models were optimal for this, as they did not fully capture the behaviour of the target compounds. BLR and GP did not consistently perform as well as the BRT algorithm for the China data, which was much more suitable for the application of ML techniques as there were more data points and more similar training and testing data sets. Therefore, the other ML techniques were not investigated using the Boulder data set since the BRT was did not perform well when given these variables.

The results from the China and Boulder ML analysis suggested that there are certain caveats required to use ML to it's full potential. For example, the testing and training data must be within the same season, and the distribution of training data and testing data should overlap and be similar. To make a robust prediction over a week to a month, at least a fortnight of training data is required, and the training set should be collected at the same location as the testing set with co-located reference measurements for the training set. During the static sensor instrument deployment, it was suspected that the air parcel that the sensors was measuring had changed. To improve the ML predicted concentration estimates it would be beneficial to additionally monitor wind speed and direction and to extend the training period to add more data during the second air parcel. This would increase the chance that the ML algorithm would learn the different relationships between the sensors and ambient pollutant concentrations during times when the air is similar to that of the second air parcel. Since there were occasions when the ML predicted concentrations were worse than the median EC sensor and there was no consistent improvement of the sensor data using ML techniques on sensor data reported in Boulder, ML techniques were not applied to the mobile sensor measurements. When evaluating the performance of the sensor instrument on a mobile platform, the instantaneous median was used to compare between the LCS and the co-located reference measurements.

5.4 Optical particle counters (OPCs)

There are commercially available low-cost devices called Optical Particle Counters (OPCs) that detect PM_1, $PM_{2.5}$ and PM_{10}. Four of these devices were purchased from Alphasense (OPC-N2)and deployed outside in NOAA's car park to evaluate their performance. Due to the nature of sampling PM, it was a requirement for the OPC box to be located outside, in the environment for which the PM was to be monitored.

The inlet for each OPC was 12 cm of stainless steel 1/4" tubing and flow was driven by an internal fan within each OPC. The inlets were all cut to the same size and were metal to minimise the loss of PM to the walls. Using identical inlets also ensures that the properties of the air flow reaching the sensors (e.g. Reynolds number, turbulence in the inlet) are the same for each OPC device. There were rain shields on the end of the inlets to reduce the effects of turbulent air and to prevent water entering the sensor device. These

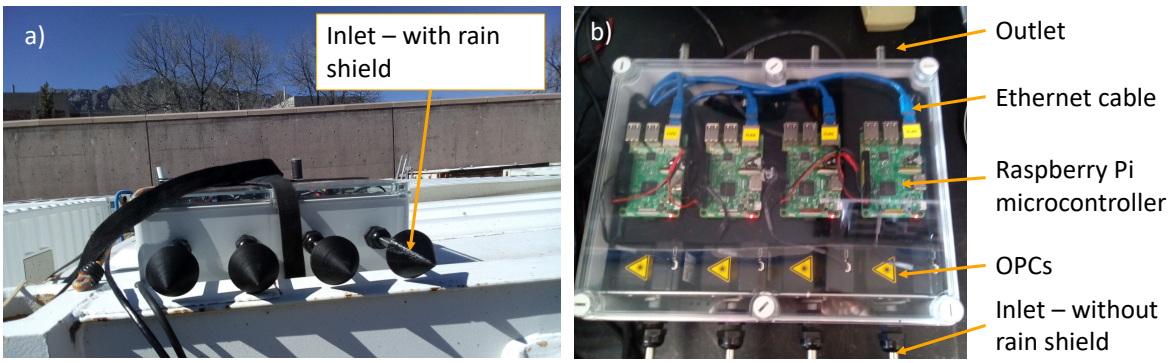

Figure 5.22: Photos of the OPC instrument, containing 4 OPC devices. a) The OPC instrument was located on the roof of a shipping container in the NOAA car park, with the inlets proud of the edge of the container. The inlets had rain shields on the end to minimise water entering the OPC device and to minimise the impact of turbulent air altering the flow of air to the sensor. The black wires which go out the bottom of the photo connect to the front of the main sensor instrument for data storage. The sensor instrument was located inside the shipping container to protect it from the elements. b) A view of the OPC box, which had a transparent lid with labelled parts. Through the lid, the Raspberry Pi's used for data collection and storage, and the OPCs themselves are visible.

were 3D printed using a 'conductive' plastic (1.75mm Conductive PLA by Proto-Pasta) to minimise the loss of PM to the rain shields walls. The four OPCs each required a Raspberry Pi for the collation of data from each device. These were located inside the OPC box and were coded to run when the instrument received power. Data was sent, via an Ethernet cable, to the larger low-cost sensor instrument housed inside the container and the OPC data was stored on the Latte Panda with the other sensors data. The OPC instrument and the POPS were situated upon the roof of a shipping container in the car park, with power supplied from the mains inside the shipping container.

OPC devices use a laser to count the number of particles passing through the inlet. The size of the particles was measured and the OPC returns the count of how many particles were observed for 15 size bins. The OPC software then computes this into three signals; one for the ultra-fine particles: PM_1, one for the medium size particles: $PM_{2.5}$ and then a trace for the large particulate matter: PM_{10}. Figure 5.23 shows the time series for each of the four OPCs at the different size ranges, a) PM_1, b) $PM_{2.5}$ and c) PM_{10}. Out of the four OPC devices only one worked consistently throughout the deployment, but this was an error related to the temperature of the devices, not due to failed sensors. The OPC box was located on the top of the shipping container in the direct sunlight with a transparent lid. With the electronics housed in the same insulated box the temperature inside the instrument exceeded 50 °C. This limit caused three of the OPCs to fail at different times for a short time, until the lid was opened and the box placed in the shade, whereupon they recovered and resumed working. Future use of the OPCs should consider the impacts of the manifold used to house the devices and allow for better ventilation.

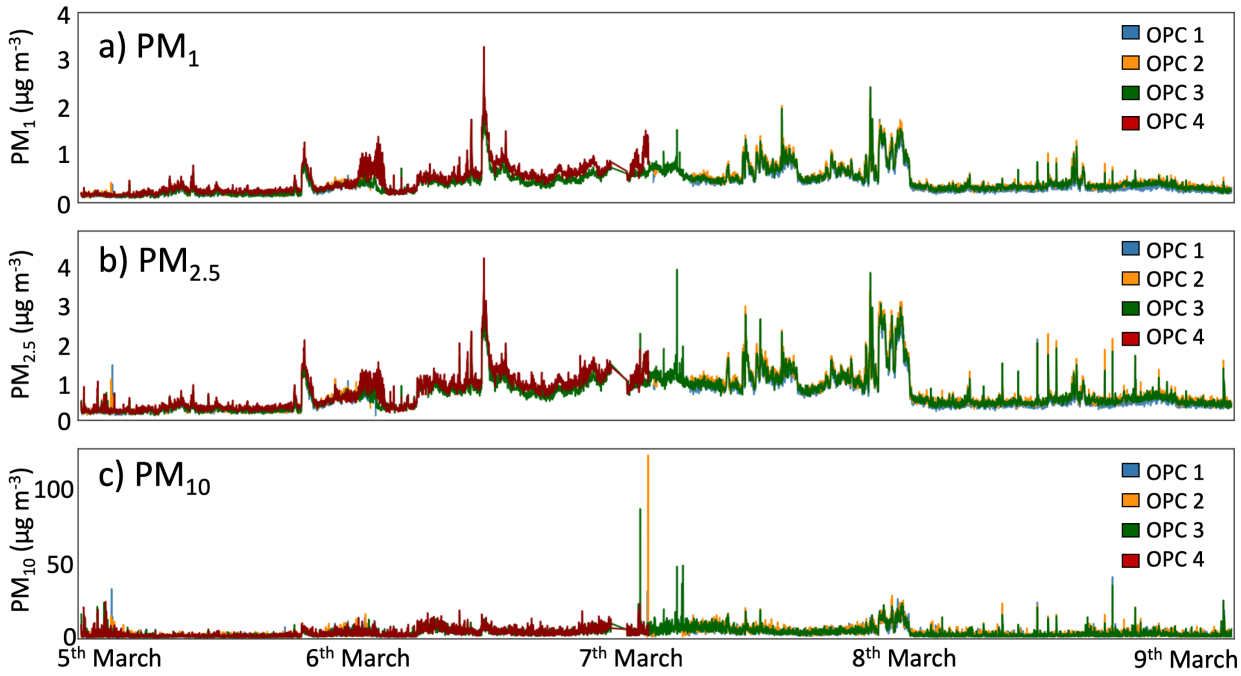

Figure 5.23: Each OPC device recorded the a) PM_1, b) $PM_{2.5}$ and c) PM_{10} levels in the ambient air outside in the NOAA car park. The OPCs PM_1 signal displayed the most variability during the deployment, but the PM_{10} concentrations were much higher than PM_1 or $PM_{2.5}$.

Figure 5.23 a, b and c) shows the timeseries for PM_1, $PM_{2.5}$ and PM_{10}, respectively. Each PM size displays a unique variance during the deployment of the OPC instrument. The variance show that the profiles for the different PM size were different. In general, there was a small amount of all sizes of PM for the first day, then the PM_1 and $PM_{2.5}$ profiles for all OPCs displayed an increase in the amount of peaks between the 6th and the 8th March 2018. After the 8th the variability in the OPC PM signals decreased again. There was less evidence that the PM_{10} variance increased between the 6th and the 8th of March, although the same event on the 8th March could be distinguished from the PM_{10} baseline. There was less day-to-day variability in the PM_{10} signal compared to PM_1 and $PM_{2.5}$. The OPCs recorded that $PM_{2.5}$ was generally slightly higher than the PM_1 signals which was expected.

Typically, the OPCs reported higher concentrations of PM_{10} than $PM_{2.5}$ and PM_1. The maximum concentration of PM_{10} recorded by an OPC was 122.8 μg m^{-3} (by OPC3), whereas the maximum for PM_1 or $PM_{2.5}$ was 3.28 and 4.28 μg m^{-3} (both by OPC4), respectively. These were often very short lived spikes and not all four of the OPCs responded with an increase in signal. The instantaneous median of the four OPC devices for PM_1, $PM_{2.5}$ and PM_{10} was calculated and the maximum values observed by the median trace were much smaller: PM_1 maximum = 2.99 μg m^{-3}, median $PM_{2.5}$ maximum = 3.98 μg m^{-3} and PM_{10} maximum = 47.86 μg m^{-3}.

Figure 5.24 shows three covariance-variance matrices colour-coded by the value of

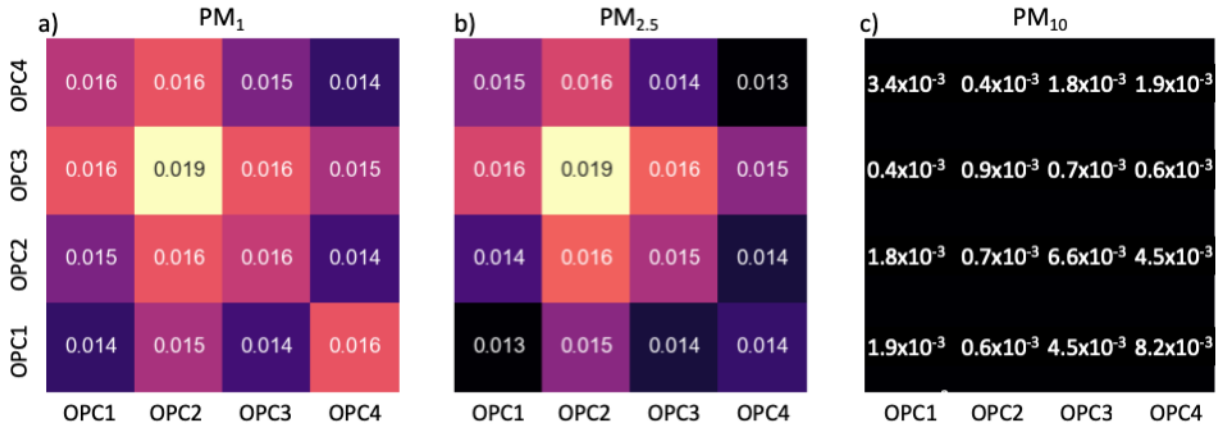

Figure 5.24: The three covariance-variance matrices for the four OPC devices for a) the PM_1 data, b) the $PM_{2.5}$ data and c) the PM_{10} data. These were colour-coded by the value of covariance and variance, with lighter colours depicting higher values. The same colour scale was used between all three matrices so they can be compared easily.

covariance and variance for a) the PM_1 data, b) the $PM_{2.5}$ data and c) the PM_{10} data. Each of the sensors time series was normalised to between 0 and 1 before the covariance-variance matrix was calculated, and the scale of the colour-coding is consistent throughout the three matrices to allow for a comparison between the different PM size ranges. Where the OPCs meet themselves in the matrices, the value for the variance of the data in the time series was produced. For example, OPC2 reported the highest variance in all data sets and was colour-coded with a light yellow square.

It was apparent that the four OPCs had the greatest amount of covariance between them when measuring PM_1 (Fig. 5.24a) as the matrix shows the highest values and lightest colouring. The covariance values between the four OPCs with each other ranged between 0.014 and 0.016 when they detected PM_1. Therefore, there was a small amount of inter-sensor variability in the PM_1 measurements and they displayed the highest reproducibility for the four OPC devices. The values for covariance decreased a small amount (c.a. 0.001) when comparing PM_1 time series to $PM_{2.5}$, but were of similar values. The covariance values between the normalised OPC data were a magnitude lower for the PM_{10} time series, Fig. 5.24c, and hence the covariance-variance matrix was black. Therefore the inter-OPC variability was higher when the OPCs monitored PM_{10}, and so the OPC PM_{10} measurements were less reproducible. There was also less variability in the PM_{10} data, hence the variance squares (where sensors meet themselves in the covariance-variance matrix) were also colour-coded black. The OPCs were all correlated with each other and the R^2 values for the PM_{10} time series ranged between 0.21 - 0.61, suggesting they were only moderately correlated to each other. In contrast, the R^2 between all correlations of OPCs for the PM_1 and $PM_{2.5}$ sensors were all greater than 0.88. The range of R^2 for PM_1 was 0.88 to 0.95 and the $PM_{2.5}$ R^2 values showed a greater correlation with a range of 0.90 to 0.95.

Overall, the PM_1 and $PM_{2.5}$ OPC observations displayed a higher inter-sensor reproducibility compared to the PM_{10} measurements. There would therefore be more confidence in the PM_1 and $PM_{2.5}$ observations if the OPCs were to be used in a network as the data was more robust. Using four separate inlets (even though they were identical) may have also impacted the reproducibility of the OPC sensor observations [30], but this was the most practical option for the deployment of OPCs as each device required it's own air flow to allow the internal pump to draw in ambient air. There was no reference measurement for comparison of the OPC sensors, but it is known that they may exhibit a strong dependence on RH, at high humidities (>85 % RH) [30]. However, this was not thought to have affected the OPC measurements made here as the humidity did not get as high as that during the deployment.

5.5 Mobile measurements of low-cost sensors

There are several benefits to using low-cost sensors for mobile measurements. They are generally more portable and require less power to operate than conventional reference instrumentation and therefore the sensor instrument was suitable for use in a mobile van. For the measurements to be useful for quantifying the pollution during the drive the sensors must exhibit fast response times and the EC and MOS can respond within minutes to changing concentrations of pollutants. Potentially, mobile low-cost sensor measurements would aid identification of hot spots in traffic emissions, allow temporary monitoring of more difficult to reach locations and be useful for more accurate personal exposure estimates to be made. Mobile sensor measurements could provide an easier method for mapping pollution across cities and investigating the cleanest routes for people to commute.

The sensor instrument was deployed inside NOAAs mobile laboratory, a van with the seats stripped out and replaced by instrument racks. There was power at all times in the van supplied either, from the engine when the van moved or from the mains when it was parked back up in the NOAA car park. This ensured that the instruments did not suffer from inaccurate results due to the power being switched on or off suddenly, and then requiring a warm-up period after receiving power again. The sensor instrument was strapped down to an instrument rack base, which had some suspension in the form of spring joints to minimise the impact of bumps in the road. The inlet was connected through a line that went out through the roof of the van, to sample air far away from the vans own exhaust. There will be a temperature and RH difference of the sampled air and the air inside the van, but the sensor instrument had sensors to monitor the environmental conditions of the air reaching the sensors. The sensor instruments internal KF pumps were still switched on to draw air through the sample line and onto the sensors at a steady rate. The OPC manifold was not connected to the van during this experiment.

Figure 5.25: Photos of NOAA's mobile laboratory. a) A side profile, upon which the sample inlets can clearly be seen on the roof of the laboratory, well away from the vans exhaust. b) A photo from the back, with the door open to reveal the GC-MS WAS system loaded into the rack at the back of the van and c) photo of the sensor instrument strapped down to the racks that contain some suspension.

The mobile laboratory drove around Boulder County, Colorado, with the reference instruments and sensors making measurements en route. There were several drives around Boulder County, planned specifically to go through three different areas; the mountains, inner city, and out to the oil and gas fields where hydraulic fracturing (fracking) occurs. Each of these regions has different pollutant emission sources, and it was hoped that the sensors might therefore be exposed to a large dynamic range of atmospheric contaminants.

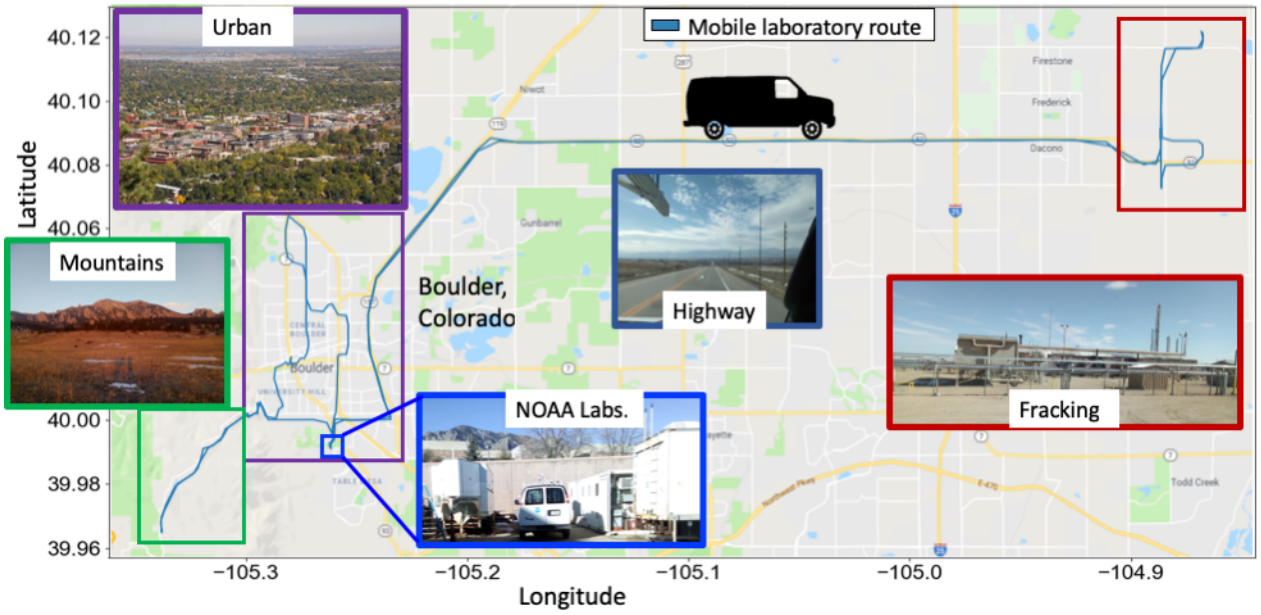

Figure 5.26: The NOAA mobile laboratory moved around Boulder County and the different regions are marked out on the map in the different coloured boxes, with photos showing the region. The blue square depicts the location of the NOAA Laboratories, where each van drive began and ended, and where the sensor instruments were located during the static deployment. Green boxes depict the mountainous region, purple is the urban region of Boulder City and red shows an image of one of the fracking facilities.

The sensor instrument remained on board the mobile laboratory for a period of three

days, and the drives took from thirty minutes to two hours. In between each drive, the van returned to the car park of the NOAA Earth System Research Laboratory (latitude: 39.9925 , longitude: -105.2611). During these times the sensors and reference instruments continued to record data.

The map of where the mobile laboratory was driven is shown in Fig. 5.26. To the North East of Boulder city, there are multiple well sites for the extraction of gas via hydraulic fracturing (fracking). The city can be identified from the map as the region in the purple box - it is composed of many residential streets, busy shopping centres and lots of traffic. To the West, are the foothills of the Rocky Mountains (Fig. 5.26, green box) and this serves as a natural edge to the city so the roads and houses become much more sparse.

5.5.1 Analysis of LCS installed on a mobile platform: mountain road

The initial test drive went West from the NOAA facility (Fig.5.26 blue box) up the road to Flagstaff mountain and back (Fig. 5.26 green box). The drive lasted 30 minutes and the GPS recorded the position of the van every second. The sensor data, the reference observations and the GPS locations were all time averaged to 1 minute and each data set time-aligned for comparison. The reference instruments installed in the van measured CO, CO_2 and CH_4 and these were used to evaluate the performance of the relevant LCS. There are 30 data points in Fig. 5.27 for the comparison of CO, CO_2 and CH_4 reference measurements and sensor data.

The median CO_2 NDIR sensor, Fig. 5.27a, displayed a much less sensitive signal compared to the reference and it appeared as a flat trace when plotted on the same axes to the CO_2 reference observations. The lower sensitivity of the NDIR compared to the CO_2 reference was also observed during the static co-location of the LCS and CO_2 reference. The median CO_2 NDIR timeseries was plotted on the second y-axis in Fig. 5.27 so the variation in the median NDIR signal was more visible. The median NDIR sensor had a steadily increasing signal, which began at 430 ppm and reported CO_2 concentrations of 500 ppm after 30 minutes. The increasing signal of the NDIR also fluctuated by 50 ppm, approximately every 5 minutes. The timeseries of the median NDIR signal was different compared to the variance and shape of the reference CO_2 measurements. The reference CO_2 measurement displayed a more stable signal, with fewer fluctuations and no evidence of a steadily climbing baseline. The reference CO_2 measurements remained relatively low (approximately 430 ppm) until a large peak in CO_2 concentrations, from 428 ppm to 520 ppm, occurred at 17:04 towards the end of the thirty minutes. The spike lasted for three to four minutes but there was no evidence of the CO_2 NDIR signal detecting a peak in CO_2 on the same scale. A second peak in the reference observations may have also occurred at 16:58 as the CO_2 concentration appeared to be decreasing from 470 ppm, however the

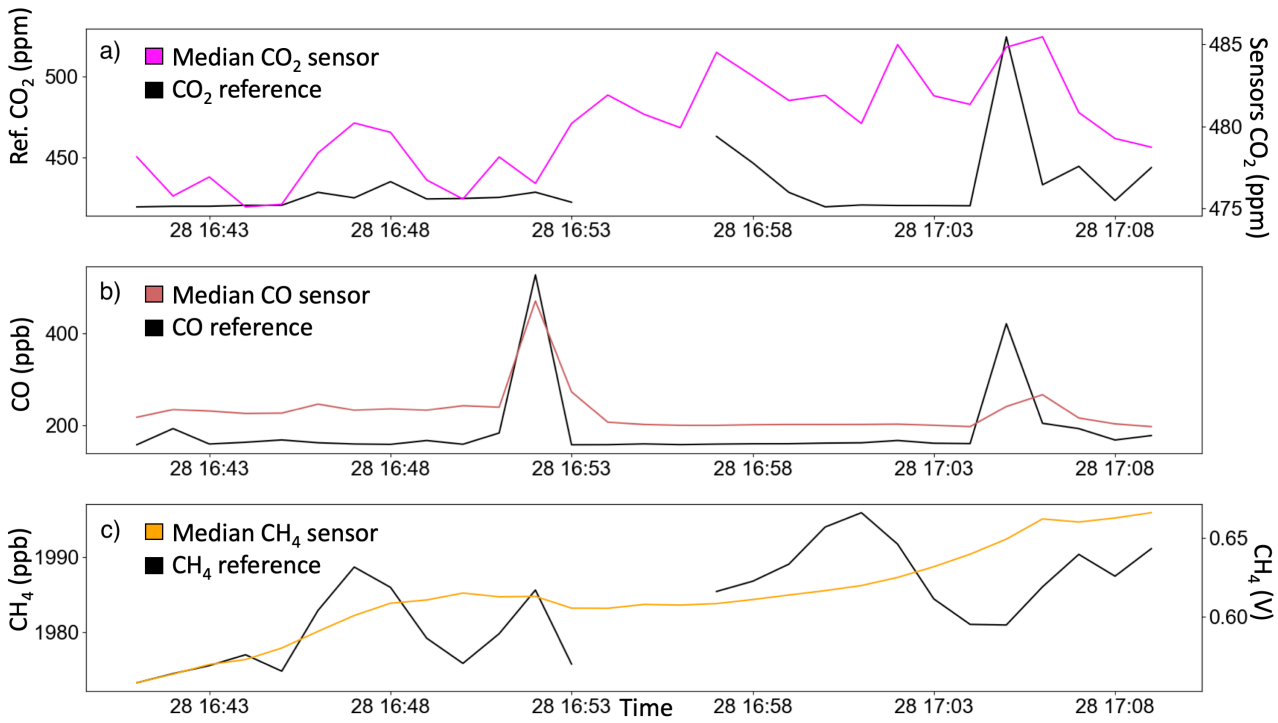

Figure 5.27: The first drive took the mobile laboratory up Flagstaff mountain, where it was expected the emissions of a) CO_2, b) CO and c) CH_4 to be relatively low. The reference observations are shown as black lines, and the instantaneous median of CO_2, CO and CH_4 are pink, red and orange, respectively.

reference instrument reported no data between 16:53 and 16:58 so it was not conclusive. The high offset in the CO_2 NDIR concentrations observed in the static measurements was still present, with the median NDIR signal beginning at 475 ppm, whereas the reference CO observations were 430 ppm.

Figure 5.27b shows that variance in the median CO EC sensor timeseries was comparable to the variance in the reference CO observations. Both instruments detected two major peaks at 16:52 and 17:04 in CO concentration over the same time scales. For the larger peak at 16:52, the median CO EC increased from 216 ppm to 423 ppm, with a peak width of 3 minutes. The CO reference observations increased from 294 ppm to 429 ppm with a peak width of 2 minutes. Both the reference and median CO EC returned to similar baseline values after the peak in CO concentration. During other time, where the CO concentrations were relatively unchanging and the trace was flat the CO EC sensors also displayed the same profile. The median CO EC did however display higher baseline values (approximately 200 - 210 ppm) during periods with no peaks in CO compared to the reference observation which displayed values of 190 - 200 ppm when there were no CO peaks.

The median CH_4 MOS sensor consistently increased from 0.55 V to greater than 0.65 V over the thirty minute drive, Fig. 5.27c. The reference CH_4 observations also increased from 1970 to nearly 2000 ppb of CH_4. However, although both the median CH_4 MOS

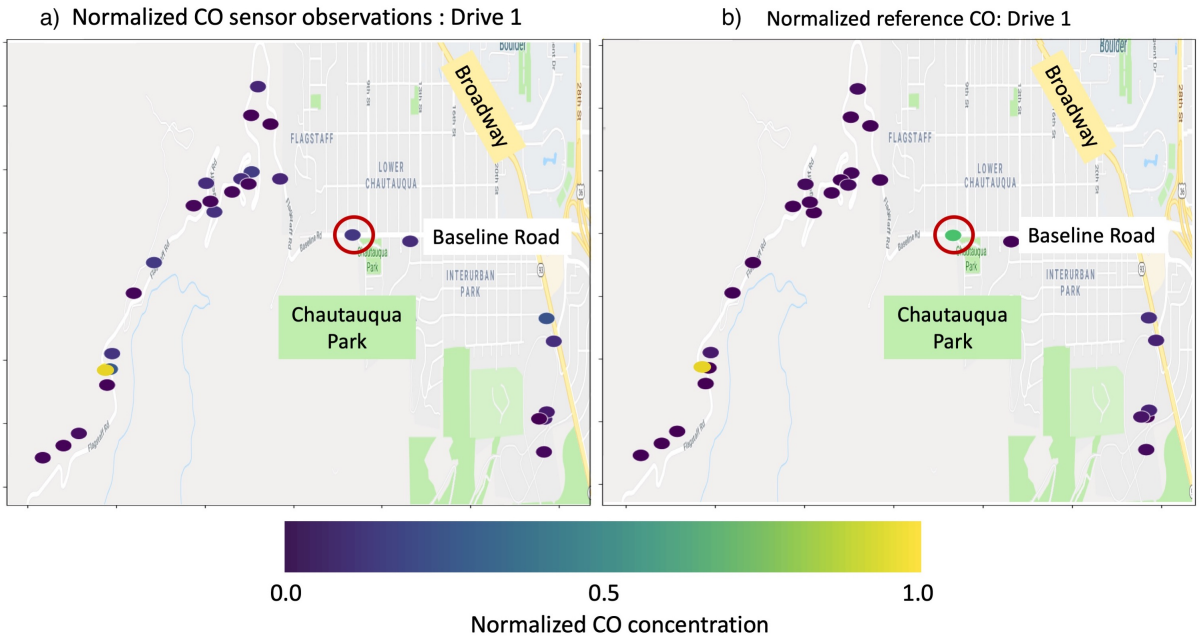

Figure 5.28: The magnitude of the normalised CO concentration at each point of the drive around Boulder for, a) the reference CO instrument and b) the median CO EC sensor. The data points are colour coded so that normalised data points with a value that is close to 0 are purple, and normalised data points close in value to 1 are yellow.

and the reference CH_4 observations both increased, there were differences in the variance of the two timeseries. There was more variation in the reference measurements, which fluctuated by 20 ppb every 5 minutes, whereas the median CH_4 MOS signal displayed a smooth, relatively linear increase in signal.

The reference and median CO EC sensors were each normalised so that their time series lay between 0 and 1. To normalise the data the timeseries was divided by the range in signals for that timeseries. The median CO_2 NDIR was normalised to compare against the normalised reference CO_2 observations also. The 30 measurements from the short drive up the mountain road were projected onto a map of Boulder, for the median CO EC (Fig. 5.28a) and reference CO (Fig. 5.28b) as well as for the median CO_2 NDIR (Fig. 5.29a) and CO_2 reference observations (Fig. 5.29b). The data points on the maps were colour-coded to indicate the value of the normalised data points.

Promisingly, the median CO and CO reference both observed the highest CO concentration (colour-coded with a yellow data point) in the same place and the rest of the trace also appeared very similar. One notable difference was highlighted in the red circle - here the CO EC median recorded a normalised signal of 0.1, whereas the CO reference recorded 0.6. This discrepancy between the two can also be observed in Fig. 5.27b, and was the second peak in the reference CO measurements. The median CO EC displayed evidence of a peak, but it did not quite record the same magnitude of CO as the reference measurement.

There were less similarities between the CO_2 reference observations and the median

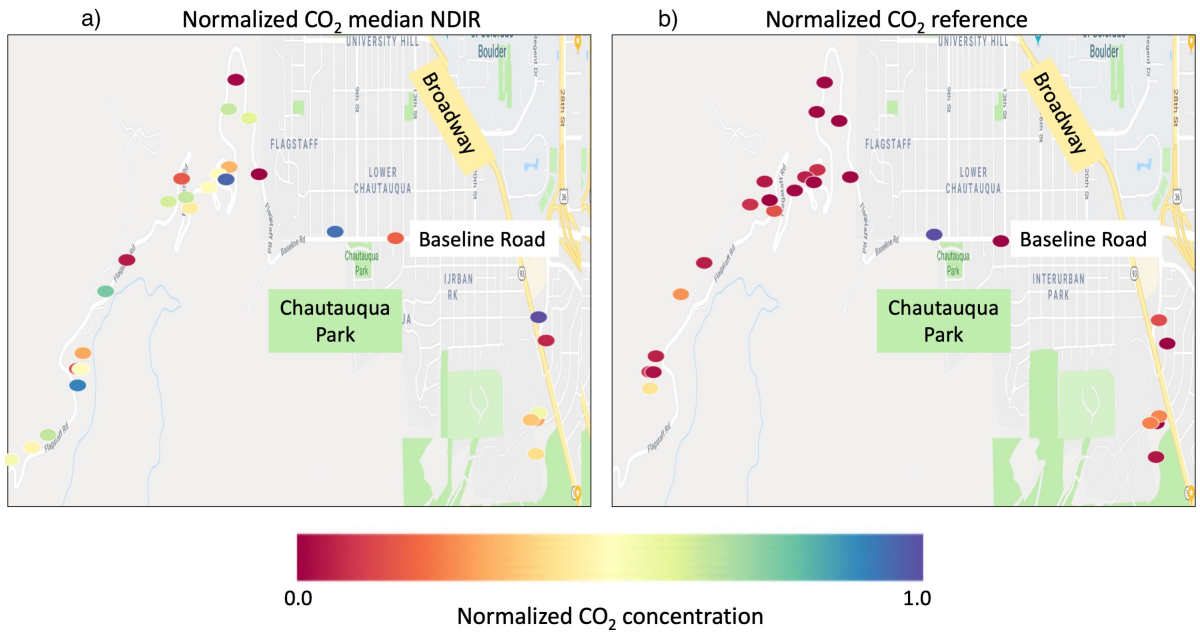

Figure 5.29: The magnitude of the normalised CO_2 concentration at each point of the thirty minute Mountains drive for, a) the reference CO_2 instrument and b) the median CO_2 NDIR sensor. The colour of the data point indicates it's value; normalised data points with a value close to 0 are red, normalised data points with a value close to 1 are blue.

CO_2 NDIR sensor when both normalised timeseries were projected onto a map. Figure 5.29a, shows the CO_2 NDIR median projected onto the Boulder map and there were more different coloured dots in it than Fig. 5.29b. This indicated that the normalised CO_2 NDIR displayed much more variance in the signal than the reference CO_2 observations and therefore there was little covariance between the two. The maximum reference CO_2 data point was observed on Baseline Road and was the only blue data point in Fig. 5.29b, indicating that the normalised value was 1 and there were no other major peaks in the CO reference timeseries. The median CO_2 NDIR signal did display a CO concentration peak at the same location, which was good, but there were three other normalised peaks that indicated a similar values close to one, colour-coded blue and purple. The maximum NDIR concentration was observed in a different location, on Broadway (see Fig. 5.29a, dark blue spot on the yellow line).

5.5.2 Mobile measurements around the inner city and hydraulic fracturing region

A similar analysis procedure was followed for analysing the drives out to the regions where there was a large amount of O&NG activity and into central Boulder to capture urban emissions. The drive to the O&NG region occurred on the evening (19:45) of the 1st March 2018, then the van returned to the NOAA carpark overnight. Whilst the van was parked, the reference instruments and sensor instrument received power from a mains supply and

were still recording data which is included in the timeseries (Fig. 5.30 a, b, and c for CO, CO_2 and CH_4). The next morning, on the 2nd March at 0800, the van was driven around the city of Boulder for three hours, before being parked at the NOAA Laboratories car park again.

A plot of the time series between the CO, CO_2 and CH_4 sensors with their respective reference observations (Fig. 5.30) evaluated the time response of the sensors in the both the moving and stationary vehicle. The timeseries are shaded red and purple when the van was mobile, to indicate when the van was entered the O&NG region and the inner city, respectively. Linear regression between the sensor observations and the reference measurements was also performed to indicate the linearity between these two types of measurement. The corresponding correlation plots are also displayed in Fig. 5.30, to the right of the respective timeseries. The median CO EC signal (red, Fig. 5.30a) and the CO reference measurement (black) showed good agreement with each other (R^2: 0.85) and they recorded similar absolute CO mixing ratios for the duration of the timeseries (intercept for the linear regression of median CO vs. reference CO was 13 ppb). Each reported similar absolute concentrations of CO with a high degree of covariance and the gradient of the slope between the reference CO observations and the median CO EC was close to 1 (gradient: 0.8) indicating that they displayed similar sensitivities towards changing CO concentrations.

The CO_2 NDIR sensors compared relatively well to their reference observations (Fig. 5.30c) albeit with a lower sensitivity (slope : 0.19). The strong, positive correlation between these two type of measurement (R^2 : 0.85) indicated that the CO_2 NDIR devices were capable of detecting short-lived peaks in the CO_2 concentration. There was more variance in both the reference and the NDIR signals during the drives, than there was when the van was stationary. The offset of 80 ppb between the median CO_2 NDIR and the reference CO_2 observations was evident in the timeseries of Fig. 5.30b and in the correlation plot. The correlation plot also indicated that the NDIR response differed depending on the concentration of CO_2 observed by the reference instrument. At reference CO_2 concentrations between 400 to 480 ppm, the median NDIR response was linear (y = 0.24x + 384, R^2: 0.90), although it only displayed a range of 20 ppm (480 to 500 ppm), compared to 100 ppm that the reference instrument covered. At reference CO concentrations greater than 480 ppm, there was very little correlation (R^2:0.27) between the two signals and the median NDIR response was not linear (y = 0.059x + 474).

The median CH_4 MOS sensor displayed a strong, negative correlation with the CH_4 reference measurements, with an R^2 of 0.8. The reference CH_4 concentration began to increase from 1925 ppb at 0500H and peaked at 2400 ppb at 0822H. The CH_4 concentration then decreased to 1920 ppb over 50 minutes and stabilised with a concentration of 1920 ppb at 12:11. This peak in the methane concentration was matched by a dip in the median CH_4 signal, at 0700H the median CH_4 MOS was 0.75 V, and this had decreased to 0.47

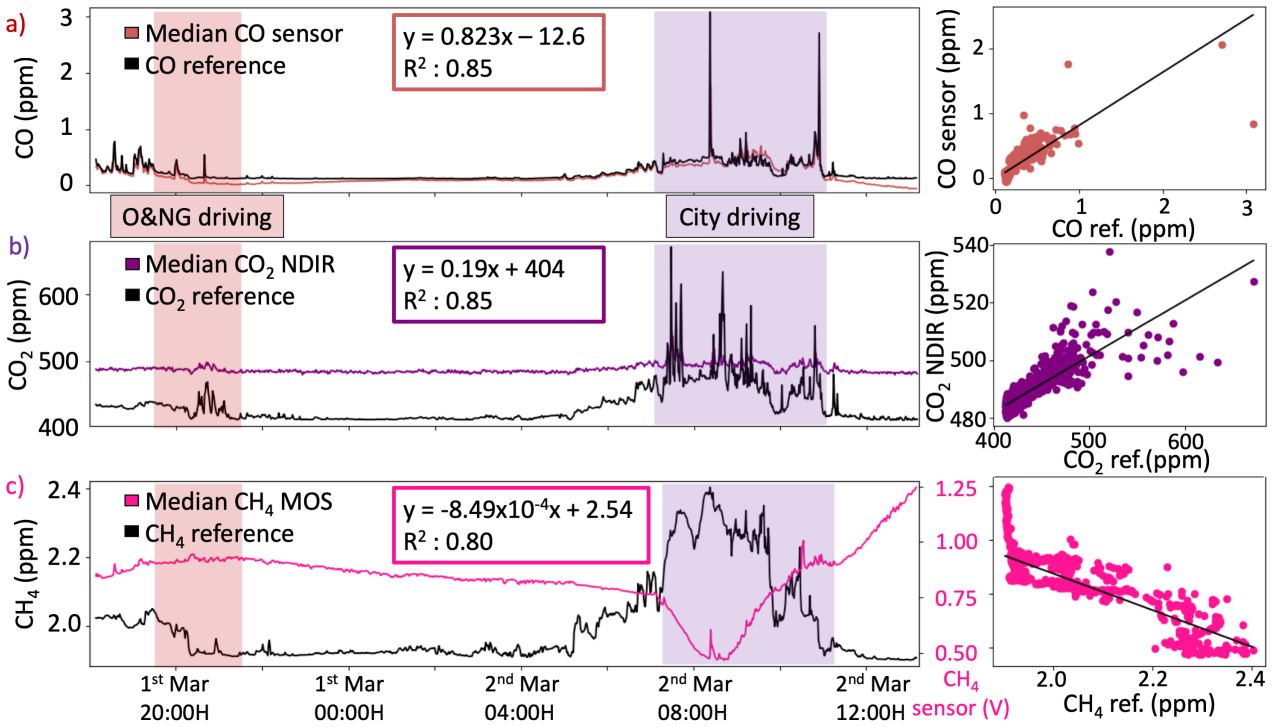

Figure 5.30: Two more drives were completed whilst the sensor instrument and reference instruments for CO, CO_2 and CH_4 were installed inside the van. On the first drive, which occurred at 1930 on the 1_{st} March 2018 and lasted two hours, the van went to a region with a high density of fracking well pads (shaded red). During the second drive the van was driven through the city of Boulder. This drive began on 2^{nd} March (0710H) and lasted for four hours. In between drives the van was stationary and returned to the NOAA car park whereupon the reference and sensor instruments received power via the mains. The reference observations (black) and sensor data (coloured traces) for a) CO (red) , c) CO_2 (purple) and e) CH_4 (pink) are plotted as a timeseries to evaluate the sensor performance. Linear regression, between the reference observation and the sensor measurements was also conducted (see corresponding correlation plots) to provide parameters to describe the linear relationship between the two data sets.

V at 0830H. The median CH_4 MOS signal had then increased to 0.89 V at 1100H, but it did not stabilise like the reference concentration, rather the median MOS signal continued to increase. The shorter term (hourly) variance in the reference CH_4 observations was not detected by the median CH_4 MOS, which displayed fewer fluctuations in the signal. Previous experiments with the MOS sensors have found that they are susceptible to being affected by changing air flow, electrical noise and environmental conditions and it could be that the methane signal was overwhelmed by the MOS response to a cross sensitivity which was more prominent in the mobile laboratory. The lack of covariance detected between the the median CH_4 and CH_4 reference observations led to the conclusion that the median MOS was not detecting changing CH_4 concentrations. Rather the dip in the median CH_4 MOS was more likely due to the effect of the van moving and the subsequent changes to the air flow causing the dip in MOS signal.

The median CO and CO_2 sensor signals were each normalised between 0 and 1 by dividing the signal by the range observed by the sensors. The reference CO and CO_2 observations were also normalised and these normalised data points were projected onto a map of the local area, with colour-coded data to indicated where the peaks occurred. If the normalised data points had a value that was close to 0 (0 - 25) they were colour-coded red, if the value was close to 1 (0.75 - 1.0), they were coloured green to blue. The CO measurements recorded during the drive out to the O&NG region and inner city were projected onto a map of that specific area, to better compare the sensor performance in the different regions. The high degree of covariance between the median CO EC and the CO reference measurements led to their normalised signals yielding very similar map projections. Figures 5.31a and b) depict the normalised reference observations and the normalised sensor measurements made in the O&NG region. Both sets of measurements agreed well, with lower concentrations of CO (normalised CO reference and CO sensor data points displayed a range of 0.01 - 0.1 values, hence were colour coded a dark red) detected on the middle road going North. The reference observations indicated a peak in CO in the top right corner of the plot (a purple dot, within the large blue circle to the top right of the plot), which was matched by a peak in the sensor measurements at the same location (light green dot, circled with a blue outline). The instruments also measured consistently higher CO concentrations when the van was further West, as both the reference and the median CO EC reported normalised sensor values of 0.25 to 0.5 (orange to yellow data points) in the blue rectangular outline. This blue rectangular outline shows the data points that occurred when the van was driving along a busier road and it would be expected that there were higher CO concentrations as the density of traffic increased. In general, there was a good agreement between the CO reference and CO EC sensor observations for the drive to the O&NG region.

This was also the case for the inner city region, Fig. 5.31c) and d) with both instruments recording similar normalised concentrations of CO. The drive in the inner city, Figs.

5.31c and d displayed short-term peaks (on the order of a minute) in CO concentrations that were much larger than the rest of the data set, leading to a plot that contained less variability and hence more of the data points all displayed normalised values close to 0. Therefore the natural log of the CO concentrations for the inner-city drive was used after normalisation of the data set to better compare the reference and sensor observations. There are two purple dots to the bottom of Fig. 5.31c highlighted with the blue horizontal rectangular outline (ii), which were the two locations that displayed the highest CO concentration. These were also identified by the median CO EC sensor (Fig. 5.31d, blue box ii) as there were two purple data points, with normalised values close to 1 in the same two locations. The CO sensors displayed an appropriate time response, as the data points adjacent to the two peaks are red, indicating low CO concentrations. Therefore the recovery time of the sensors was sufficient to observe low CO values one minute after reporting higher CO concentrations. Therefore the sensing surface did not display much of a time lag for responding to the elevated CO concentrations, nor does it become saturated and so report higher values for longer than a minute. There was more variability in the CO reference observations when the van drove North-South on the road to the East (Fig. 5.31c, vertical blue rectangular outline, i), as there were red dots (0.1 of maximum signal) interspersed with green dots (0.7 of maximum reference signal). The median CO sensor again identified this variability and the coloured data points in the corresponding area reflect that in a very similar manner (Fig. 5.31d, i blue box). There was less variability when the van was further East in the plot, as both the reference CO measurements and the median CO sensor reported very consistent values (consistently coloured dots) when the van was in these regions. The CO reference observations were lower (0.01 - 0.1) compared to the maximum observed CO reference data point, and therefore they appear red, whereas the median CO sensor has orange data points showing that these were approximately 0.25 of the maximum reported sensor CO concentration. This was in agreement with the time series plot (Fig. 5.30a) of the reference and median CO; the maximum CO reference observation was 3 ppm, whereas the CO sensors only recorded 2 ppm for the maximum CO concentration.

The CO_2 NDIR sensors and the CO_2 reference observations both displayed lots of variability in the CO concentrations during the drive out to the O&NG region, Fig. 5.32a and b, respectively. The covariance between the two instruments was reasonably high, with both identifying high and low CO_2 concentrations at the same locations. There was a lot of CO_2 variability when the van drove North-South (Fig. 5.32 a and b, inside the blue vertical rectangular outline), and the CO_2 NDIR sensors detected this too. The maximum concentrations of CO_2 were observed here (Fig. 5.32a, purple dots), and the CO_2 NDIR also reported the maximum CO_2 concentration here, although this was on the location adjacent to the reference measurements, so was reported one minute later. The peaks in CO_2 concentration were identified at similar locations for both types of measurement,

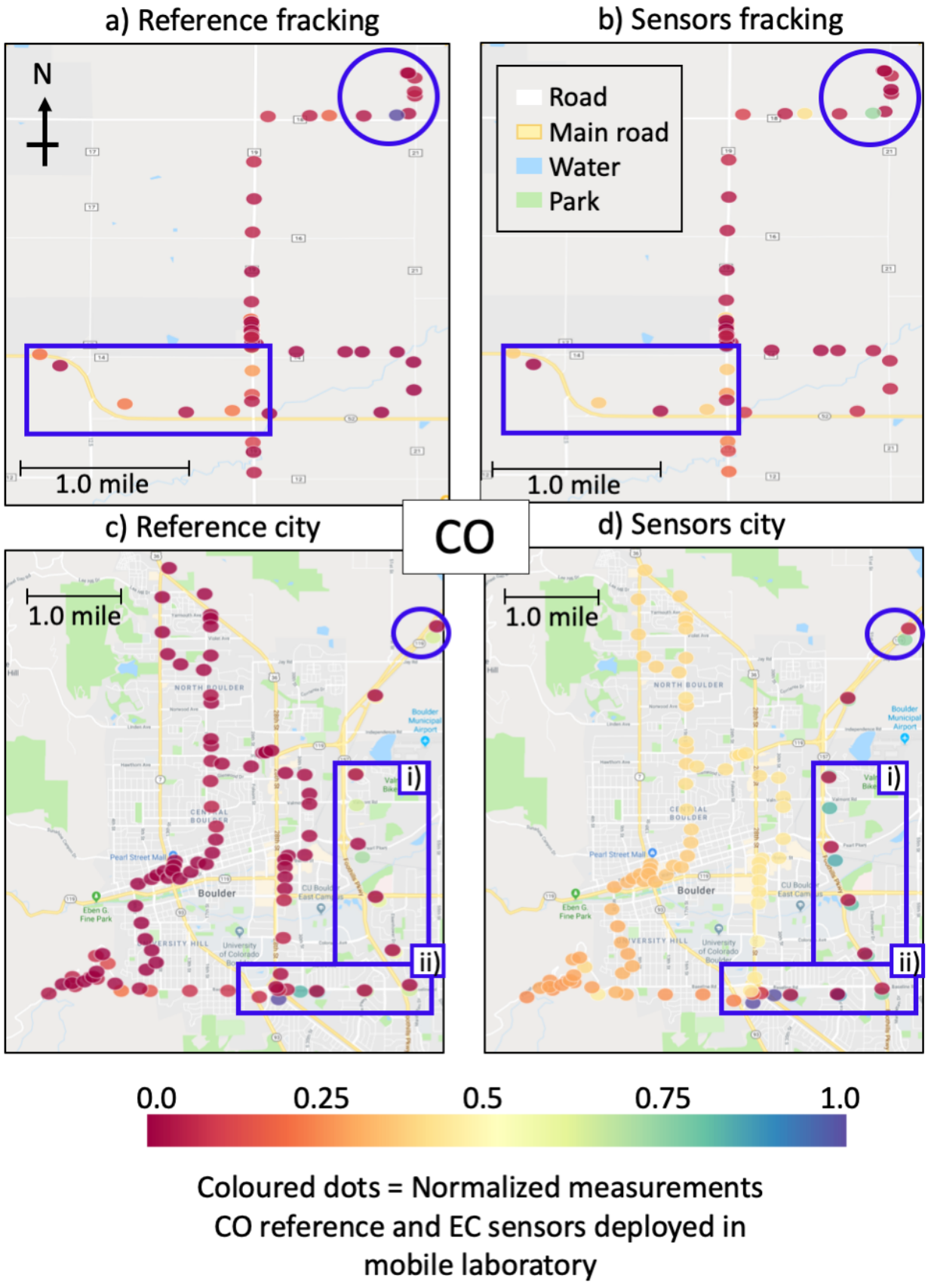

Figure 5.31: The normalised CO reference and sensors data, at the different locations. a) and b) show the reference and sensor measurements at the fracking site. C) and d) are the projections of the measurements when the van was driving through the city centre. For the city drives, the data is on a logarithmic scale to show the changes in variation more.

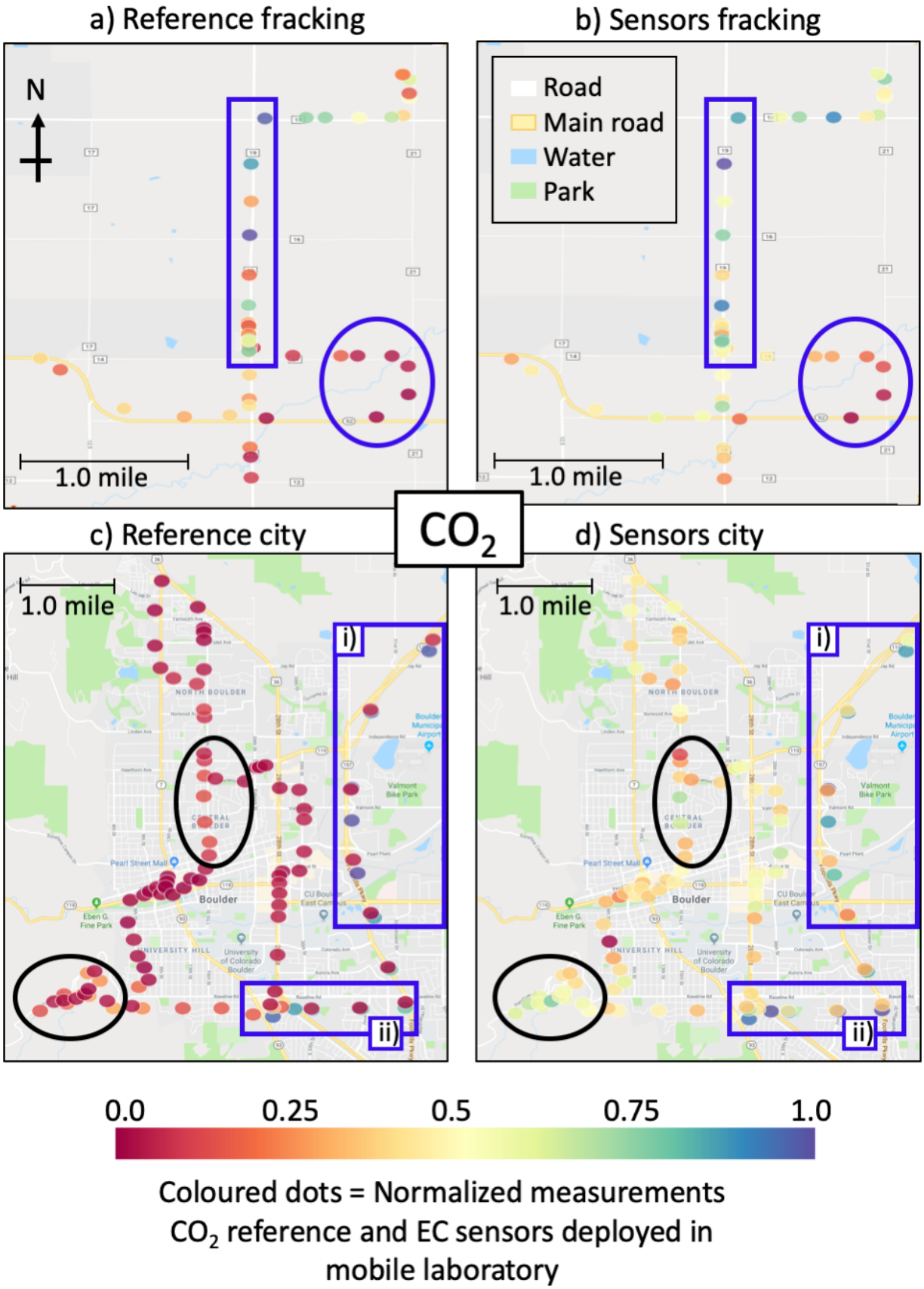

Figure 5.32: The normalised CO_2 reference and median NDIR sensor data, at the different locations. a) and b) show the reference and sensor measurements at the O&NG area. C) and d) are the logarithmic projections of the measurements when the van was driving through the city centre.

which means that the CO_2 NDIR sensors exhibited a similar response time to changing CO_2 concentration levels as the CO_2 reference instrument. The circular outline to the East of the plots in Fig 5.32a and b, shows that both instruments reported the lowest observations detected on the drive to the O&NG region, with similar variability. The normalised CO_2 sensor measurements had a better agreement with the reference instruments in the O&NG regions than they did on the drive up the mountains. This was potentially due to the CO_2 concentration being higher for longer at the urban and O&NG sites than on the mountain drive so the sensors did not require such a fast response time.

The natural log of the normalised CO_2 reference and sensor measurements was used for the drive around the city centre, Fig. 5.32c and d. This was to highlight the changes in the concentration of CO_2, since greater ranges in CO_2 concentration were observed for the inner-city drives. The reference and the sensor measurements co-varied when there was a large amount of variability in the CO_2 concentration towards the East of the plot (i and ii blue rectangular outlines). Both identified the peaks in CO_2 concentration simultaneously, at the same locations, and reported the maximum observed CO_2 in very similar areas. As with the CO concentration, the CO_2 levels were lower towards the West, and both instruments reported lower relative concentrations of CO_2. There were some discrepancies between the two data sets, however, marked on Fig. 5.32c and d with black circular outlines. In both cases, the CO_2 NDIR sensors reported high variability in their measurements (normalised data 0.1 - 0.75), whereas the CO_2 reference observations did not show any appreciable amount of variability at these locations (normalised data approximately 0.1).

The experiments conducted using the mobile laboratory indicate that the EC and NDIR sensors have the potential to perform well on a mobile platform. This has implications for personal exposure monitoring, using sensors to identifying spatial gradients of pollutants and using in a mobile laboratory. Since the CO and CO_2 mobile sensor measurements were capable of identifying regions with higher or lower CO and CO_2 concentrations, they could be applied for source apportionment. However, additional measurements, for wind speed and direction would be required to relate the source to an increase in pollution. The median CO EC was able to detect higher CO concentrations for a busier road intersection proving that it had the time response and resolution to detect changing CO concentrations related to traffic emissions. If the performance of the median CO EC sensors was consistent across the different types of EC sensor then the NO_X and O_X EC can also be used for source apportionment. The methane MOS sensors did not perform as well as the other types of sensor and this might be due to them not being as suited to the monitoring conditions associated with making mobile measurements. To work, they require a fast response time and to be less sensitive towards changing environmental conditions such as the air flow. The mobile sensor measurements might be further improved with additional shock absorption for the sensor instrument. The sensor instrument was

designed to be portable and it's relatively light weight may impact the effectiveness of the shock absorbers it was mounted on, and vibration upon the LCS instrument during measurement may cause detrimental impacts to the sensor data quality [19].

5.6 Deployment of a sensor instrument in a remote location

Another prototype of the sensor instrument was deployed at the Bukit Atur Global Atmospheric Watch (GAW) site in Danum Valley, Borneo, Malaysia. The site is located 4.9814°N and 117.8436°E, in the middle of a pristine, equatorial rainforest, Fig. 5.33.

The emissions of biogenic compounds dominate the local air quality at Danum Valley, and since biogenic emission exhibit a distinctive diurnal pattern [117], it was hoped that the low-cost sensors would also reproduce this pattern. There were two types of MOS sensor included in the sensor instrument; TGS2602 total VOC and TGS2620 OVOC MOS. Both detect the bulk concentration of VOCs and it was thought that the rainforest would provide a relatively unique environment, where there were fewer anthropogenic emissions and hence cross sensitivities to impact the MOS responses. There were difficulties associated with the experiment, such as the environmental conditions. The heat and high humidity's present all year round in a tropical rainforest have meant that it is hard to maintain even research grade instruments for long periods of time. The average daily maximum temperature was 30.7 °C and the average daily minimum temperature was recorded as 22.6 °C between 1986 to 2001 [25]. The annual average temperature at the Bukit Atur research centre at Danum Valley was recorded as 26.8 °C during 1985 - 2006 [175]. The annual mean precipitation for the same time period was 2825 mm [175], with January and October recorded as the months with the most rainfall [25].

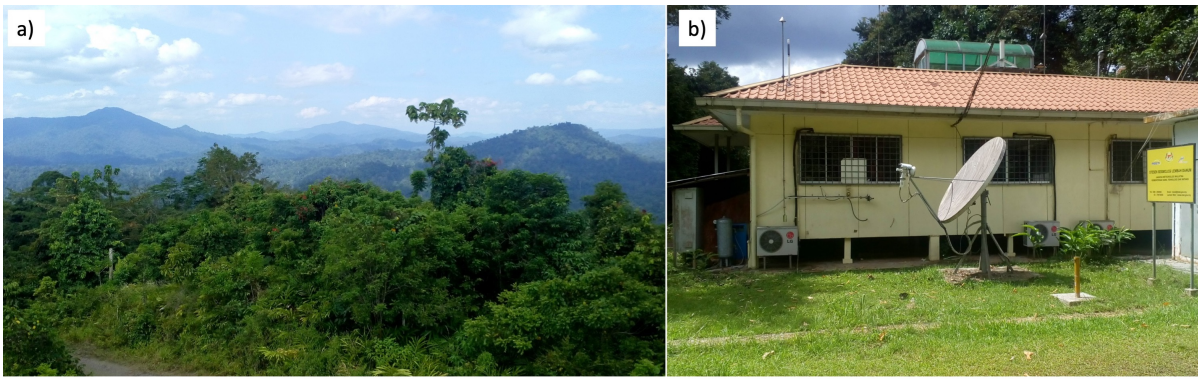

Figure 5.33: Photos to show a) the rainforest surrounding the GAW site where the sensor box was deployed and b) the building that the instruments were housed in.

The sensor instrument was designed and built with a similar scope to that of the sensor instrument deployed in China; there were 50 sensors monitoring gaseous atmospheric

Figure 5.34: The sensor instrument, running at Danum Valley, Borneo. The instrument was located inside a building, with the sampling inlet for all instruments located outside, and a pump to draw in ambient air. The screen displayed the live incoming data going to the Latte Panda for storage and collection.

compounds, six each of the NO_2, O_X and CO EC and the remainder were MOS. Sixteen MOS were TGS2602 to sense total VOC and sixteen were TGS2620 for the detection of more oxygenated species of VOC. An electrical issue caused some of the EC sensors to fail; there were three O_X, three NO_2 and three CO EC sensors that produced sensible readings for the duration of the study.

The sensor instrument was located inside a building so was sheltered from rain and wind, and a large diaphragm pump drew air from the outside into the instruments. Two internal KNF pumps drew air from the main sample line to the sensors to maintain a steady flow of air.

The sensor instrument ran for 68 days in the rainforest, although there were a couple of large power cuts where data was not recorded. An intermittent power supply was anticipated and so the sensor box was connected to a UPS. The micro-computer was also programmed to restart itself and the code for the automatic collection and storage of data after power was restored, to minimise the requirement for a person to be with the instrument at all times. This strategy worked well, as the sensor instrument was able to continue to monitor the atmosphere at the GAW site long after the scientists had left - a useful method for deploying an instrument in a remote location. The deployment was likely to be challenging due to an unstable power source and high humidity's common with the rainforest. All of the low-cost sensors used in the study are known to be affected by changing humidity and the levels expected at Danum Valley remained consistently high; humidity remained greater than 75 % RH throughout the deployment.

5.7 Total VOC TGS2602 MOS in the rainforest

In previous laboratory experiments (described in Chapter 2, Fig. 2.7), the MOS sensors showed a more reproducible sensitivity towards VOCs in more humid air that would be useful for sampling carbon-compounds in the rainforest. There was no working reference VOC instrument located at the site and therefore the MOS output voltage was converted to a $ppb_{[VOC]}$ using a sensitivity of 10 mV pp^{-1}, as this was the sensitivity of the MOS recorded in the laboratory at 90 - 100 % RH. Analysis was performed to investigate how the MOS signals performed in a different environment, relative to the other MOS sensors.

Upon installation of the sensor instrument it was observed that 4 of the total VOC (TGS2602) MOS sensors had failed and they were removed from the subsequent analysis. The median total VOC MOS detected a regular pattern of variability during the deployment (see Fig. 5.35a), with the total VOC concentration ranging between 11.65 and 88.43 $ppb_{[VOC]}$. The standard deviation between all twelve working MOS, shown on the same plot as a yellow shaded area, remained relatively consistent (approximately 15 ppb) throughout sampling. After the sensors were powered back up on the 8th August 2017 there was a period of time where the standard deviation was slightly greater, approximately 30 ppb, but this was reduced back to 15 ppb after a week. The sensitivity of 10 mV ppb^{-1} used was generated using a different set of MOS sensors and in-laboratory calibrations. This value may not be entirely suitable and this was reflected in the absolute concentrations reported by the median MOS sensors. Using this sensitivity, the mean VOC concentration was 33 pp, the maximum 88 ppb and the minimum 11 ppb for the deployment. These values were higher than a realistic VOC concentration. Isoprene is the VOC compound that will have the largest ambient concentration [117] and this was expected to peak to up to 15 ppb in the early afternoon (1300H) [117] but has also been noted to have an average annual peak of 3 to 4 ppb [96]. The sensitivity was used to convert the MOS voltage output into a concentration but the analysis was more concerned with identifying the variance of the median MOS signal and not necessarily concerned with absolute VOC concentrations. The total VOC data was periodic, with peaks in the median MOS signal occurring approximately every 11 to 12 hours, Fig. 5.35a. The magnitude of the peaks was relatively constant, a peak on the 22nd July, 2nnd August and 22nd September had heights of 30, 34 and 27 ppb above the baseline, respectively. There was some evidence of temporal drift in the median MOS signal. When the regular peaks in the median MOS signal were ignored the minimum vales for the median MOS signal indicate the median MOS baseline. During the course of the deployment the minimum values for the median MOS signal (Fig. 5.35a, black line), increased from 20 ppb at the beginning of the deployment, to 30 ppb during the middle portion of the deployment, from 07:45 AM on the 8th August 2017 until 05:20 AM 20th September. The baseline was then restored to its original value of 20 ppb for the remainder of the experiment. The step change of 10 ppb in the baseline occurred immediately after the sensor instrument switched back on

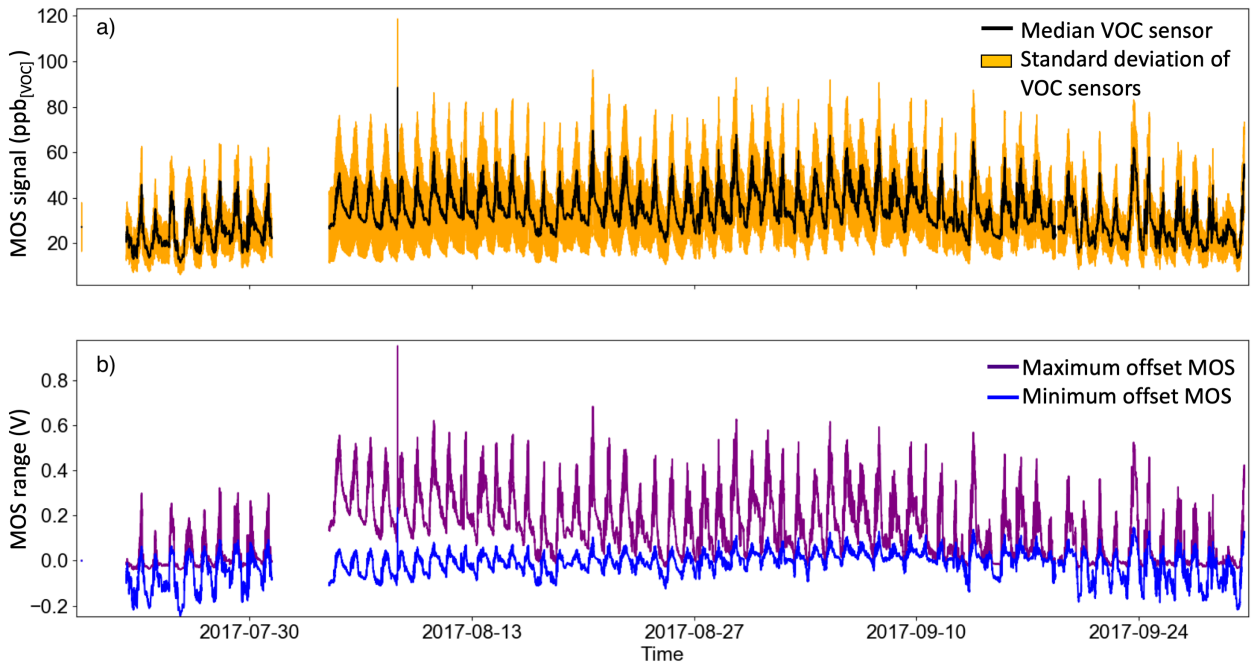

Figure 5.35: The median MOS (a) displayed lots of daily variation during deployment at Danum Valley, and the standard deviation of the 12 working MOS sensors appeared relatively consistent during the 68 days of sampling. The range of the 12 MOS sensors (b) shows that the lowest reporting sensor records much less variation in total VOC than the maximum sensor.

during the power cut. The power cut was therefore the likely cause of the baseline step change.

To investigate the spread of the twelve individual total VOC MOS sensors over the 68 days, the MOS output voltages were all set to 0 V, with the calculated offset applied for the duration of the campaign. Only the maximum (purple) and minimum (blue) reporting sensors are shown in Fig.5.35b for simplification, although these might not always be the same individual sensor. The largest range observed was 0.72 V (71.7 $ppb_{[VOC]}$) at 07:45 AM on the 8th August 2017. This was shortly after the sensors were powered up after the second power cut and therefore might be due to the sensors heaters warming up to optimum temperature and re-stabilising after being switched off. The minimum reporting sensor displays much less variability than the maximum reporting sensor.

5.7.1 TGS2620 OVOC MOS

The other 16 MOS sensors contained inside the sensor instrument were more selective towards oxygenated VOC compounds, OVOC TGS2620 MOS sensors. They are more sensitive towards compounds such as alcohols and were compared to investigate how these sensors performed under the same environmental conditions as the TGS2602 total VOC MOS. The OVOC sensors were all offset to 0V at the beginning of the time series to investigate the spread of the sensors over time.

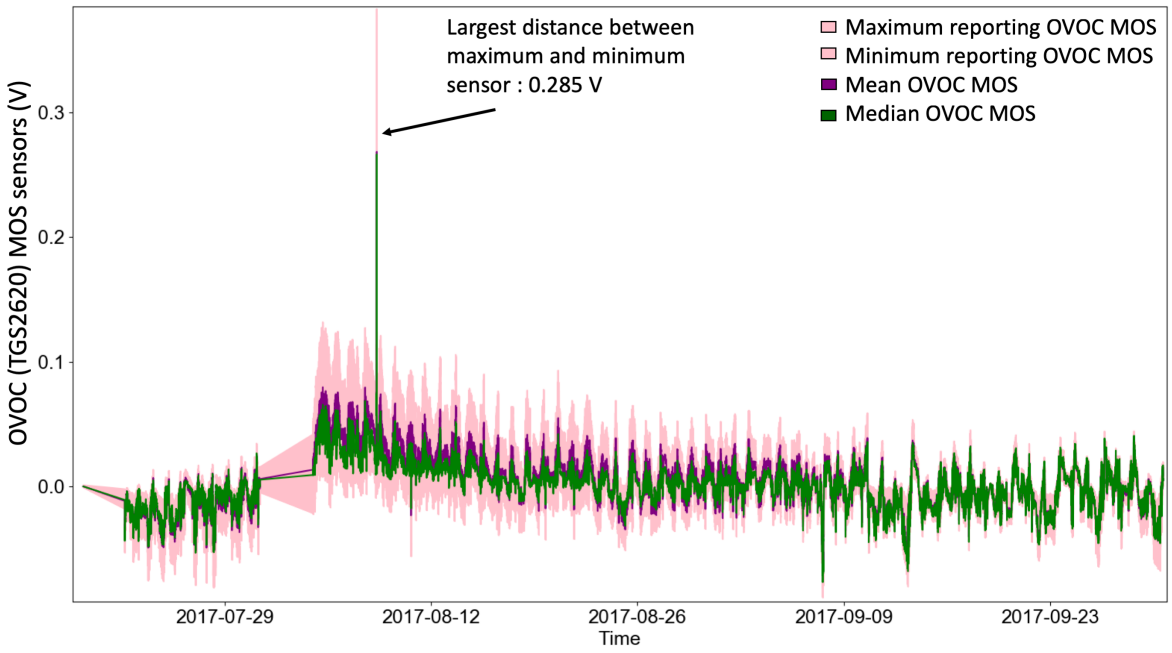

Figure 5.36: The range between the instantaneous highest and lowest reporting OVOC sensors is shown as the pink shaded area, with the largest range between the TGS2620 sensors as 285 mV, on the 8th Aug. The median and mean are also shown here, as green and purple traces respectively.

The median of the 16 TGS2620 sensors did not deviate much from the mean of all the sensors indicating that the sensors exhibited normally distributed data, with no large amounts of data as outliers. The largest difference between the maximum and minimum reporting sensor was 285 mV, which was almost a third of the range observed using the TGS2602 total VC sensors (maximum range: 717 mV). This range occurred at the same time for both sets of sensors, in the early morning of the 8th August 2017. This was in the first third of the data set (see Fig. 5.36), rather than the sensors gradually spreading out over time as seen previously which would result in the largest range found at the end of the data set. If the sensors were just responding the same variables with slightly different sensitivities, it would be expected that they drift apart over time, resulting in the largest range to be near the end of the deployment. Potentially, there was a power surge at this point, as there was a large spike that occurs in both the TGS2620 and TGS2602 MOS data sets, and this caused a large degree of separation between the subsets of 16 MOS. However, this range did decrease again afterwards, returning to what it was before the spike. From the 9th September, in the final portion of the OVOC data, the range is in fact at it's smallest values.

The rainforest conditions were hot (temperature of air flow: 22.1 to 33.8 °C) and humid (absolute humidity of air flow: 486.28 to 1230.53 g m^{-3}), and it was not known how the MOS sensors would respond in these conditions for a prolonged period of time. The two different types of MOS sensor had very different characteristics and displayed different sensitivities towards the temperature and humidity of the air reaching the sensing surface.

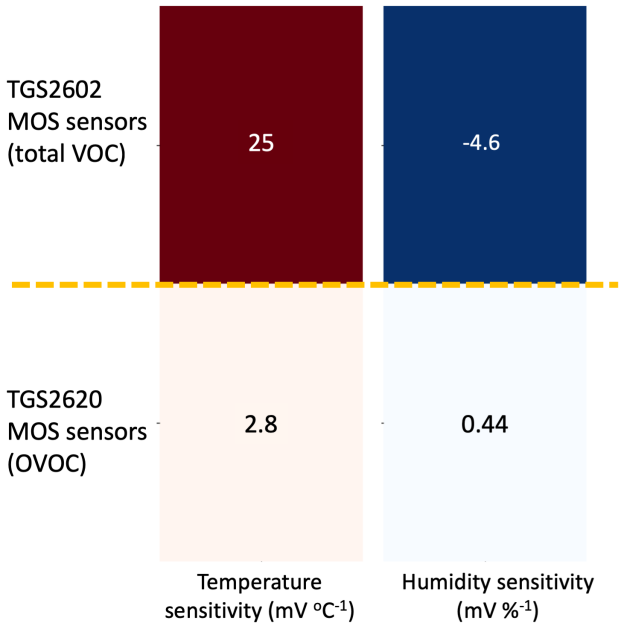

Figure 5.37: The total VOC TGS2602 MOS sensors had a strong negative correlation with humidity and a strong positive correlation with temperature. The OVOC were less sensitive per mV to either condition.

The total VOC TGS2602 MOS exhibited a moderate, positive correlation (R^2: 0.63) with temperature, with a sensitivity of +25 mV $°C^{-1}$, Fig. 5.37. The total VOC MOS sensors exhibited a higher sensitivity to temperature than the OVOC MOS sensors which displayed a gradient of 2.8 mV $°C^{-1}$ when the median OVOC sensor was correlated with temperature. The median OVOC versus temperature correlation was also much weaker (R^2: 0.35) than the equivalent correlation with the median VOC MOS. When the median VOC sensor was correlated with the RH of the air flow, there was a negative gradient with of -4.6 mV $\%^{-1}$, this negative relationship between RH and total VOC MOS response was consistent with the finding from previous experiments (Chapter 2). The correlation was weaker between the RH and median OVOC MOS (R^2 value for this linear regression was -0.36) compared to the correlation between median total VOC MOS and temperature. The OVOC MOS sensors, however, produced a slightly positive correlation with humidity (+0.44 mV $\%^{-1}$), although the correlation was weak (R^2 :0.18). A similar negative magnitude of the response with RH has been observed when the OVOC sensors were calibrated with increasing RH in the laboratory. Overall the OVOC sensors appeared to have been less sensitive towards the environmental conditions experienced by the sensors. Significance bands were determined for the values of the sensitivity of the median OVOC MOS towards changing temperature and humidity of the air reaching the sensors. The median OVOC and temperature data were binned into 1 °C bins over the temperature range recorded by the temperature sensors (22 - 34 °C). The mean and standard deviation (σ) of each bin was calculated. Linear regression was performed upon the median OVOC vs. temperature, median OVOC + 1 σ vs. temperature and median OVOC - 1 σ vs. tem-

perature, and the results are summarised in Fig 5.38a. The same analysis was repeated for the median OVOC MOS over the RH range (65 %), with the RH and median OVOC binned into 5 % RH bins, Fig. 5.38b. The sensitivity values for the median OVOC with temperature and RH were altered from the values calculated previously as the data used to calculate the values in Fig. 5.37 was not binned.

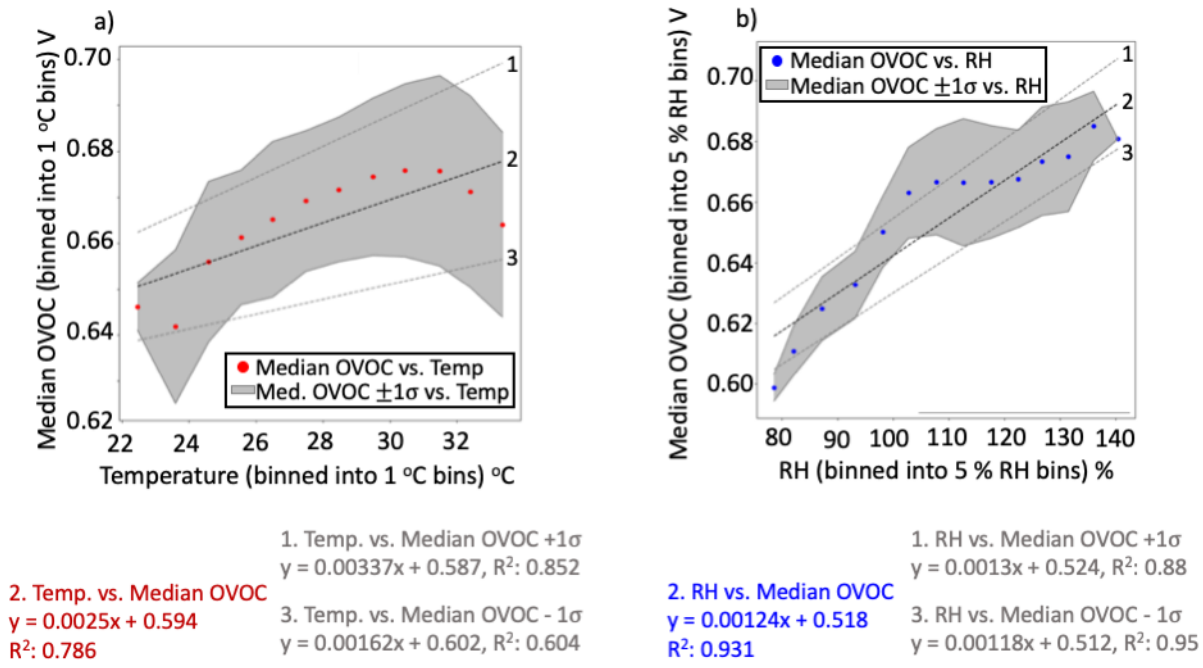

Figure 5.38: Determining the uncertainty in the sensitivity of the median OVOC MOS towards a) temperature and b) RH.

The median OVOC sensitivity towards temperature was therefore 2.5 $\pm^{0.8}_{0.9}$ mV °C^{-1}, hence the uncertainty in the temperate sensitivity is approximately 34 %. The median OVOC sensitivity towards RH was calculated to be 1.24 ± 0.06 mV %$^{-1}$ (uncertainty = 5 %). The median VOC sensitivity towards temperature and RH was also calculated with the same analytical process, using temperature bins of 1 °C and RH bins of 5 %, see Fig. 5.39.

Figure 5.39a indicated that there was indeed a non-linear relationship between increasing temperature and the median MOS signal. In general, as the temperature increased to 30 °C the median MOS signal increased, in a somewhat linear fashion. The sensitivity of the median MOS towards temperature was determined as 23.9 ± 5.7 mV °C^{-1}. The uncertainty in the temperature dependence of the median VOC MOS signal was therefore 24 %. Increasing RH caused a decrease of the median VOC MOS signal (Fig. 5.39b) and when linear regression was performed, the gradient of the slope was 2.0 $\pm^{0.2}_{0.3}$ mV %$^{-1}$, which indicated an uncertainty of 12.5 % for the gradient. As before the linear regression using the binned data for the VOC MOS are slightly different, but still comparable to the linear regression parameters determined using the un-binned data sets.

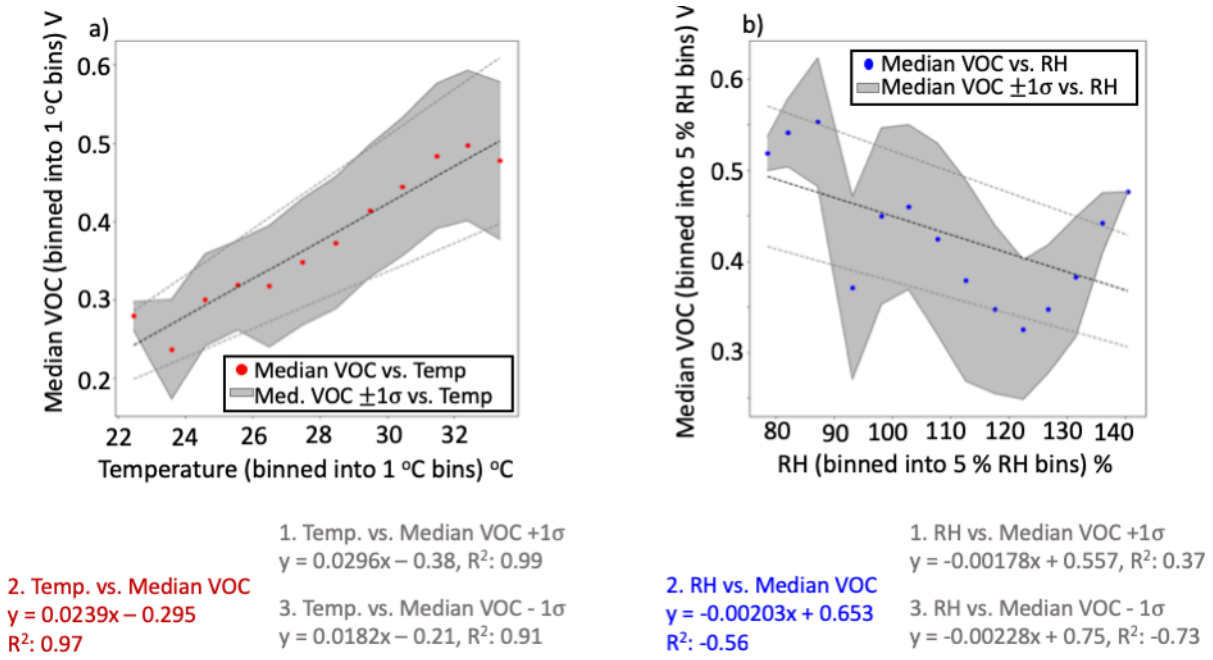

Figure 5.39: The a) temperature and median VOC MOS were binned into 1 °C bins and the mean (red) and standard deviation (1 σ were determined for each bin (grey shaded region). The b) humidity and median VOC MOS were binned into 5 % RH bins and the mean (blue) and standard deviation (1 σ were determined for each bin (grey shaded region). The trendlines between a) temperature and b) RH with the median VOC MOS, the median VOC + 1 σ and the median VOC - 1 σ were calculated to investigate the significance bands of the relationship between the median MOS and environmental conditions.

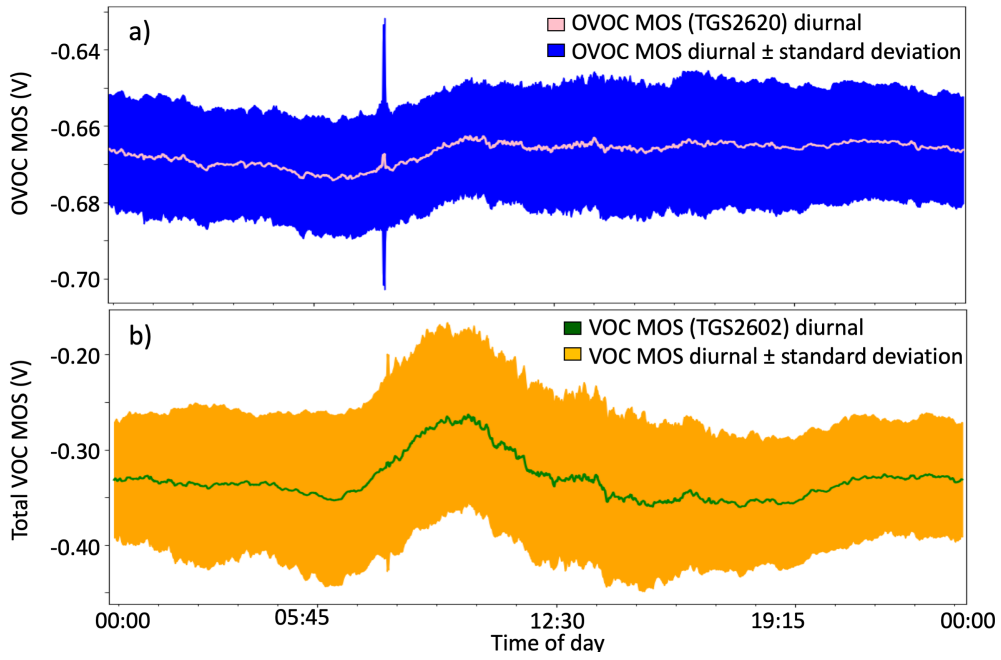

Figure 5.40: Diurnal profiles for a) the median OVOC (TGS2620) MOS sensor and b) the VOC (TGS2602) MOS sensors after temperature and humidity corrections.

Using the linear parameters calculated and summarised in Fig. 5.37 from the correlation of the median MOS with temperature and then humidity using the un-binned data, a simulated MOS signal could be computed for the time series. This was then subtracted away from the median MOS to make a temperature and humidity corrected MOS signal for both the VOC and OVOC MOS sensors, in an analogous manner to the temperature and humidity correction used in the China sensors analysis. The diurnal profiles of temperature and humidity corrected median VOC and OVOC MOS sensors are different, Fig. 5.40.

The OVOC sensors, Fig. 5.40a have a relatively flat diurnal pattern. There was a slight increase of the OVOC sensor signal from 11AM to midday, from -675 to -655 mV, and then the signal was maintained until the late evening where it began to slowly decrease. The standard deviation in the measurements at all hours of the day remained relatively constant too, with the exception of the large spike at 0745H; due to the averaging of the large spike in the data occurring on the 8th August because of the power surge.

The VOC MOS sensors, on the other hand, displayed a much more obvious daily fluctuation in signal, with a steep increase in the signal from -305 mV at 0600H to -205 mV at 1000H, see Fig. 5.40b. Then the signal decreased with the same steepness leading to a symmetrical peak. The signal did rise again, by 50 mV from 1915H until 2200H, whereupon it was constant overnight, until 0600H.

Although there wasn't an instrument capable of detecting VOCs on site during the deployment of the sensor instrument, there had been a GC-FID at the same site in 2008, as part of the Ozone and Particle Photochemical Production above a South-East Asian

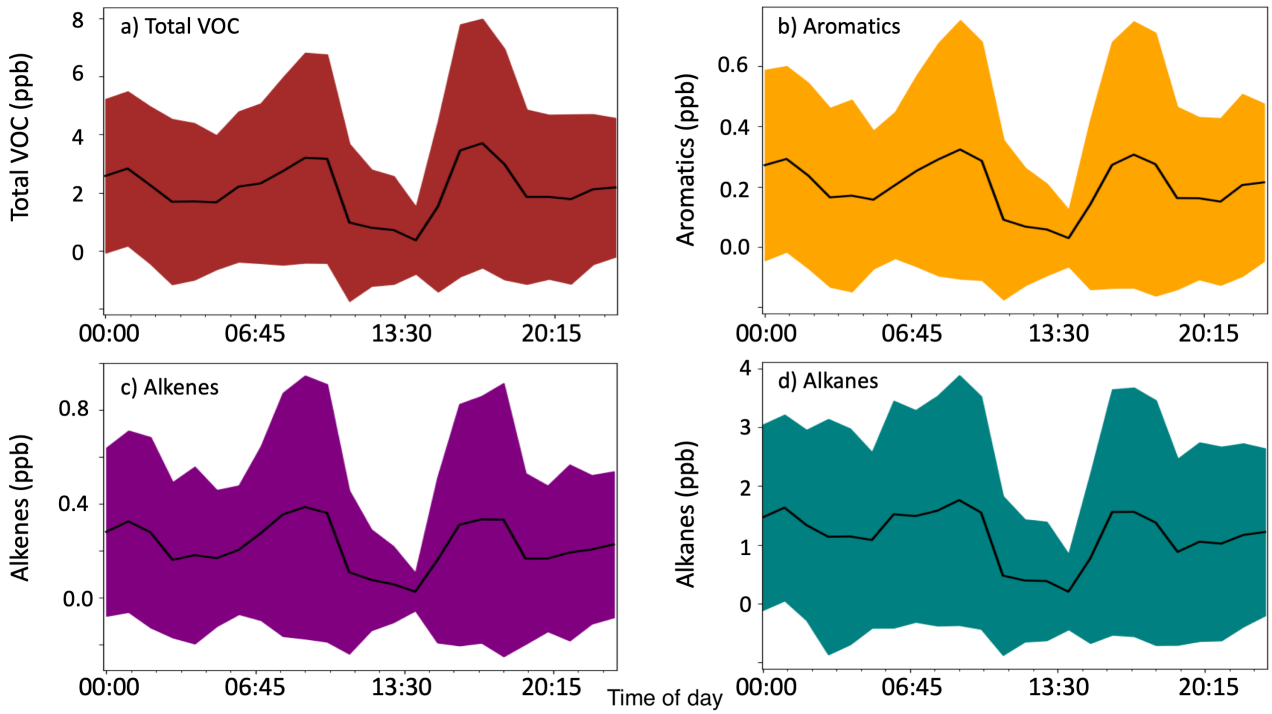

Figure 5.41: Diurnal profiles for a) the total VOC, b) the sum of the aromatic compounds, c) the sum of the alkenes an d) the sum of the alkanes from a reference GC-FID measurement made in 2015.

tropical rainforest (OP3) campaign [139] [96] [117]. GC-FID data was collected over six months as part of the OP3 campaign, yet the sensor instrument was only deployed between July, August and September. The OP3 data for August and September (2008) was used to compare against the sensor data to ensure that they were both monitoring during the same time of year. To investigate the daily variation in VOC compounds, diurnal profiles were plotted for August to September for both campaigns. The GC-FID data was supplied by Dr. James Hopkins from the University of York. The GC data composed of a timeseries of 1-hour averages for thriteen of VOCs: ethane, ethene, propane, propene, iso-butane, n-butane, acetylene, 1-butene, iso-pentane, isoprene, n-heptane, benzene and toluene. The compounds were grouped according to their chemical structure and it was found that the different types of compound; total VOCs, aromatics, alkenes and alkanes, all exhibit a similar profile, Fig. 5.41.

There was a dual peak in all four of the diurnals from the GC data, with one maximum occurring at 0900H and the other at 2100H and a sharp drop off in the mixing ratios of the VOCs at 1330H. One of the main VOCs present in tropical rainforests is isoprene, which exhibits this distinctive pattern, see Fig. 5.42. The concentration of isoprene increases in the morning as more is emitted by plants as the suns strength increases, then it decreases around midday as it reacts with increasing hydroxyl (OH) radical production. As OH concentrations decrease in the afternoons the isoprene concentrations increase again, resulting in the second VOC peak in Fig. 5.41a [117]. The VOC MOS sensors

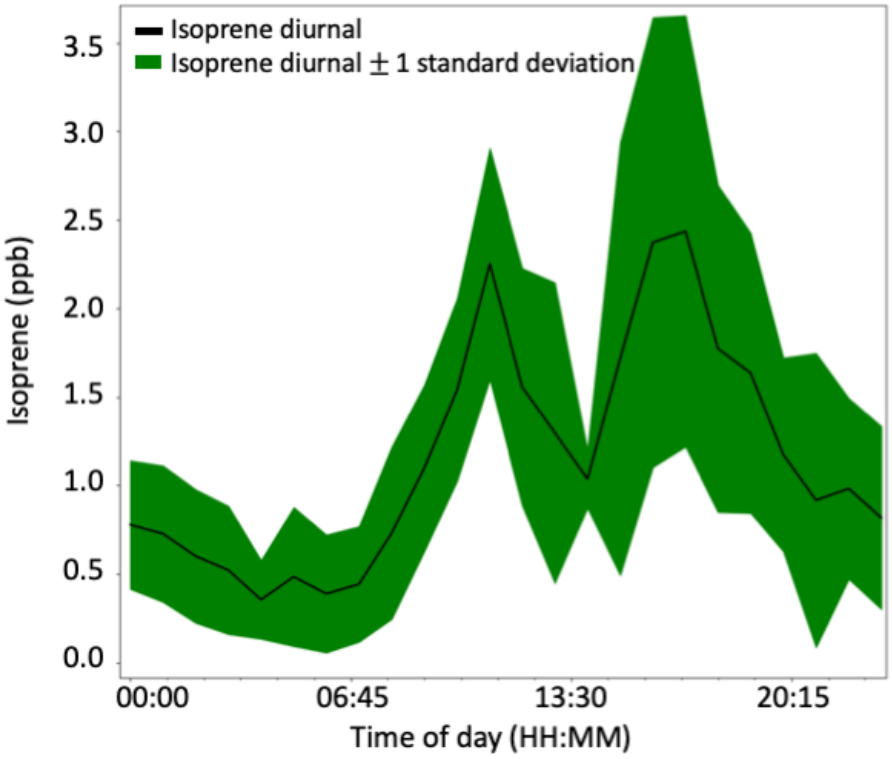

Figure 5.42: Diurnal profile for isoprene concentrations with ± 1 σ, between August and September, measured as part of the OP3 campaign.

certainly observed a peak at around 1000H which decreased to the lowest values at 1330H, which might be indicative of the first isoprene peak 1200H. There was slight evidence of a second VOC peak in the median VOC MOS diurnal profile, just after 1230H. However, unlike the isoprene or other VOC compounds measured using the GC-FID this second peak was subtle and small, a lot smaller than the initial peak in the total VOC MOS sensors profile.

The OVOC sensors did not observe the second peak in VOCs at all. This was indicative that the OVOC sensors were less sensitive towards isoprene and other biogenic VOCs emitted by the rainforest than the total VOC TGS2602 MOS sensors. The OVOC sensors detected a pattern that was more similar to the oxidation products of isoprene. These compounds are typically produced in the morning as isoprene increases, then remain relatively constant for the rest of the day before the concentrations decline slowly throughout the night [117].

5.8 EC in the Rainforest

There were some instruments at the GAW site, but unfortunately none were monitoring NO_2, O_X or CO. The sensor performance could not be calibrated *in situ* but there was some evaluation of the EC sensors after the factory conversion factors were applied.

The sensor instrument contained 4 working CO, 3 NO_2 and 3 O_X EC sensors. These

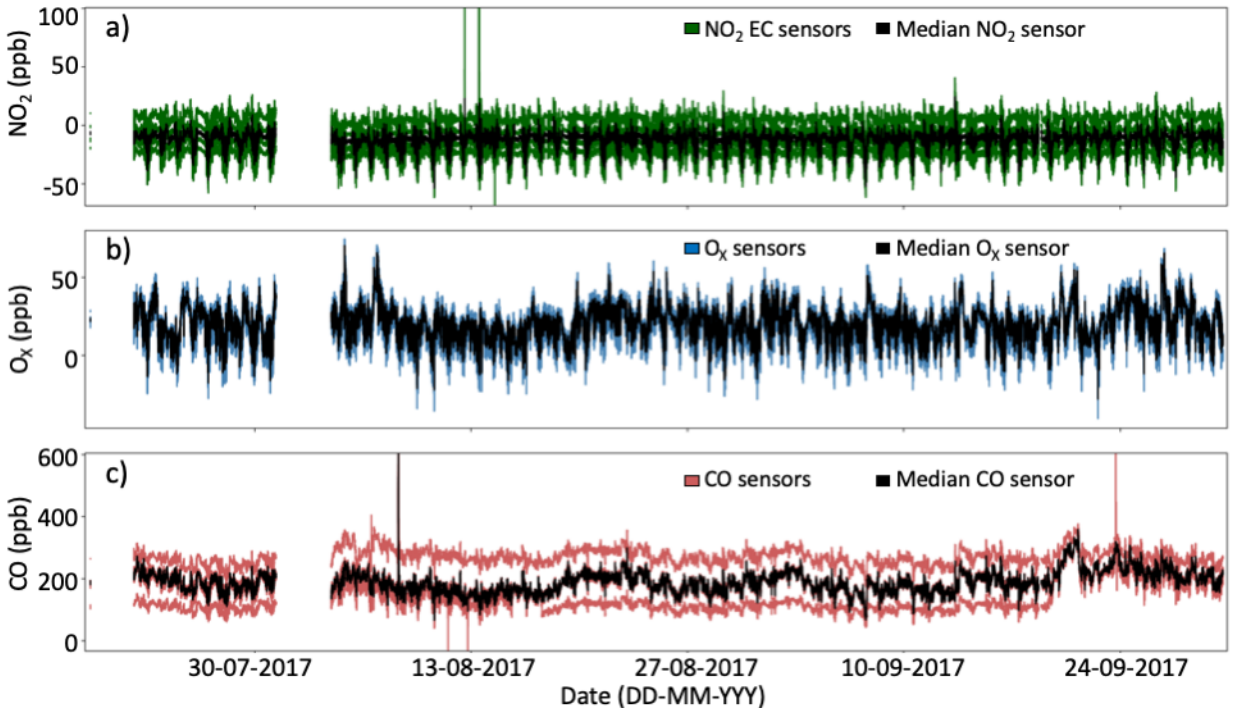

Figure 5.43: The working a) NO_2, b) O_X and c) CO EC sensors monitoring their respective pollutants over the duration of the deployment of the sensor instrument at Danum Valley. The instantaneous median of the cluster is shown in black, and there were two large gaps in the data due to power cuts at the GAW site.

pollutant concentrations were expected to be low in the tropical rainforest as there were few anthropogenic emissions at the Bukit Atar GAW site and the site itself is immediately surrounded by secondary rainforest [117]. There were some anthropogenic emissions from motor vehicles, construction and cooking for example, emitted at the Danum Valley Field Centre, but this was located 10 km away from the GAW site [175] where all the instruments were sampling. The most common wind direction for the Bukit Atar GAW site has been recorded as coming from the southwest. The main source of VOC compounds in the southwest is from the rainforest itself so the composition of compounds within these winds consists of terrestrial, biogenic emissions [117].

The time series in Fig. 5.43 shows the performance of the EC sensors after their individual factory conversion factors were applied. The two large gaps in the data were due to power cuts occurring during the deployment that lasted for a prolonged period of time, meaning that the UPS also shut down. The EC sensors displayed no obvious ill affects from the power cuts which was good, as it was thought that some of the data immediately after the power came back on might need to be removed if the sensors required a warm up time after receiving no electricity. The largest power cut during this deployment lasted 62 hours potentially, the power was returned before the sensors would require a warm up time. This was advantageous when deploying these EC in the field at remote locations that might experience power cuts like the Danum Valley site. There were a few spikes in the NO_2 and CO EC signals (Fig. 5.43a and c) that were suspected to be due to electrical noise,

as they are too short for sensor response to external conditions or compounds. The NO_2 EC displayed very low values during the campaign, suggesting that there was little NO_2 to detect. The median NO_2 signal fluctuated between -54.28 and 24.05 ppb - consistent with the equivalent of 0 ppb - see the evaluation of NO_2 sensors in the China data. The diurnal profile was consistent with a diurnal profile from R.C. Pike et al. 2010, [139], as they also reported a profile which reaches a minimal mid-afternoon, and higher levels at midnight. The OP3 study included ground measurements of O_3 and NO_2 between April and July 2010. The OP3 research mentioned that NO_2 levels were typically less than 0.4 ppbv, and this was potentially why the NO_2 EC struggled to report positive values, as this is near their limits of detection. There was no reference instruments available for *in situ* calibration therefore it is likely the sensors would require calibrating to minimise an offset.

The O_X EC fluctuated a lot more than the NO_2 EC, and the absolute concentrations of ozone (the O_X signal with the NO_2 subtracted - was between 10 and 40 ppb. This was slightly higher than measured by the O_3 reference monitor during the OP3 campaign in 2010 ($[O_3]$ between 0 - 30 ppb, but only > than 20 ppb for a prolonged period on three days), but the positive offset will be in part due to the subtraction of negative values of NO_2. The diurnal profile of O_3, see Fig. 5.44, shows that ozone was typically lowest between 0800H and 0900H then the mixing ratio of ozone increased until 1600H, whereupon it remained high until the evening. The O_3 then decreased overnight to reach it's minima in the morning. This pattern is consistent with the ozone concentration variability seen previously with rainforest experiments (OP3) [139].

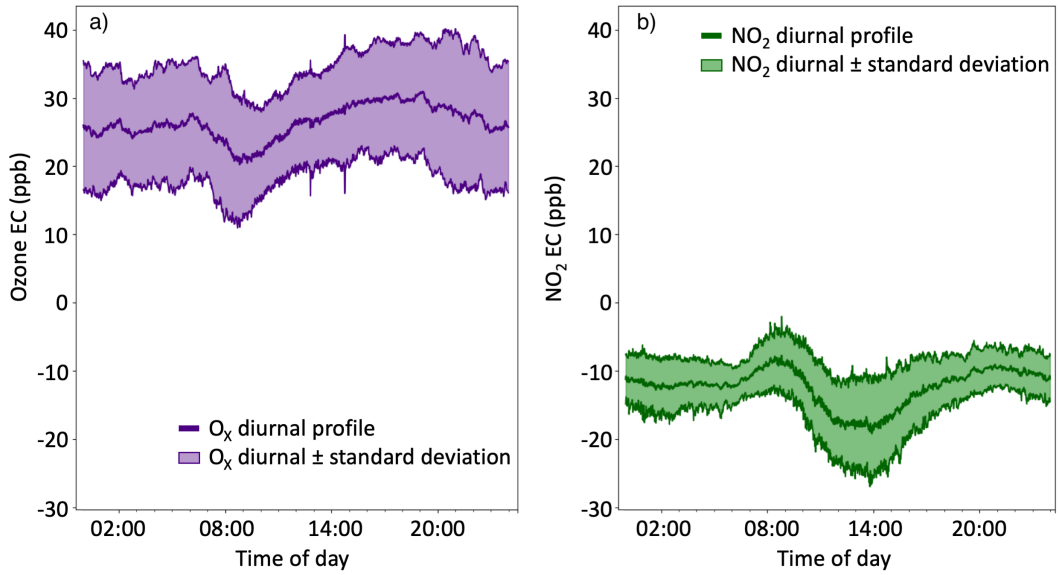

Figure 5.44: Diurnal profiles for a) O_3 and b) NO_2 EC show that, during the deployment of the sensors there was very little NO_2, yet more O_3 observed by the EC - between 10 and 40 ppb- that have a more distinctive daily pattern.

5.9 Summary of Chapter 5

The LCS instrument was deployed in two other locations (Colorado, US and Borneo, Malaysia) to evaluate the EC and MOS sensor performance in different environments. The sensor instrument was co-located with reference instruments in the laboratory, and then on a mobile platform in Colorado. OPC devices were also deployed to monitor PM. In Borneo, the LCS instrument was deployed in a humid environment and largely operated unattended. A summary of the findings from both research campaigns is given below.

5.9.1 NOAA Summary

There were four different models of MOS sensor deployed in Boulder, Colorado.

- The four different types of MOS sensor all performed as well as expected during the static deployment of them; with a high covariance between each individual sensor in the cluster. The instantaneous median MOS signal represented the qualitative signals from the individual signals in the cluster well.

- The CH_4 MOS exhibited strong linear correlations with humidity and temperature. After these corrections were applied the remaining peaks did not have a strong agreement with the reference observations. Although some CH_4 MOS peaks co-varied with peaks in the CH_4 reference observations, this appeared co-incidental as the minimum and maximum CH_4 concentrations observed by the reference instrument were not detected by the CH_4 MOS. The methane MOS was the only model of MOS sensor that had a co-located reference instrument. This was co-located for both the static deployment and for the LCS installation in the van for mobile measurements. The CH_4 MOS signal was compared against the CH_4 reference observations for the mobile measurements. There was a negative correlation between the two timeseries when both were co-located in the van and the median CH_4 MOS displayed a less variable signal that did not co-vary with the CH_4 reference observations.

- The three other types of MOS sensors deployed; the propane/butane, total VOC and OVOC MOS, were all influenced by changing humidity of the air flow. After RH-corrections were applied each median MOS signal displayed very similar profiles. Their target pollutants are likely to co-vary and therefore this was promising for VOC measurements.

Evaluation of the EC, NDIR and OPC devices during their 6-day static deployment and mobile measurements.

- The median NO_2 and CO EC sensors showed a good agreement with their respective reference observations for the first three days of static deployment. The median O_X sensors did not agree as well to the reference observations. This might be due to the

humidity of the air flow being reported as extremely low as the sensor instrument was located indoors but the sample line was drawing in outdoor air with low humidity. Although individual EC sensors displayed different absolute concentrations, the sensors all displayed similar variance in their timeseries, hence inter-sensor reproducibility was high.

- However, all of their performances were degraded during a change in the air that caused the concentration of their target measurands to all decrease steeply. During this period, the ambient concentrations of the pollutants decreased, the humidity decreased and the temperature also changed. Any one of these impacts may have led to the degradation of the EC sensors response. The median EC sensor began to exhibit a consistent low offset, although did continue to reproduce the same profile as the reference observations (low variability response, reporting low pollution concentrations). Only the CO EC appeared to recover from this within the subsequent 8 hours. The results from this deployment indicated that steep pollution and environmental gradients may lead to poorly performing EC sensors.

- ML algorithms that had previously been trained upon the sensor data obtained in Beijing were applied to the sensor data acquired in Boulder, Colorado. Concentration estimates for the EC sensor measurands were determined. Using the China-trained BRT and BLR models did not improve the quality of EC sensor data, as the training conditions (from Beijing) were too different (compared to the conditions experienced by the sensors in Colorado) for the ML algorithms to make an accurate concentration estimate.

- BRT was applied again to the Boulder data, this time training on approximately 80% of the ambient, static data collected in Boulder. This improved the quality of the sensors data in some respects but did not match the improvement observed with the China data. This was due to the training and testing sensors data displaying different distributions of data, related to the event which caused the low concentrations and different environmental conditions mid way through the static sampling deployment.

- The sensor instrument was installed inside a van, with co-located instruments for CO, CO_2 and CH_4. The CO EC and CO_2 NDIR devices worked well on a mobile platform, with good agreement with the co-located reference observations. This identified that the EC and NDIR sensors have a sufficiently fast time response for using on a mobile platform; as the qualitative profiles of the sensor timeseries and reference instruments were similar.

- The EC and NDIR LCS were able to detect low concentrations in the same locations as their respective reference measurements and therefore, with additional data such

as windspeed and direction, it might be possible to used LCS for source apportionment.

- Low-cost OPCs were deployed to examine the performance of a cluster (4) co-located OPCs for monitoring PM. The OPC devices all correlated and co-varied together, indicating that it was possible to obtain reproducible PM measurements from a low-cost PM sensor. It was noted that the OPCs stopped reporting data when the temperature of the OPC manifold exceeded 50 °C. for proper operation of these devices a ventilated manifold is recommended.

5.9.2 Sensors in rainforest summary

- The sensor instrument successfully operated in the tropical rainforest. The high humidity and relatively high temperatures that occur year-round in the rainforest can make this a challenging environmental for instrumentation. The LCS was relatively unattended and collected data for nearly two months. This implies that the LCS instrument could be deployed in remote areas where it is not possible for other instrumentation to operate.

- The temperature and RH corrected median VOC MOS signal exhibited a strong diurnal profile, with one major peak around midday. Reference VOC observations from a campaign in 2008 revealed that isoprene (dominant emission), and other VOC compound groups, exhibit a dual peaked diurnal profile with the peaks occurring around midday. Therefore there was some similarity between the diurnal profile of the VOC MOS and reference VOC measurements. The median OVOC MOS produced a flat looking diurnal pattern and therefore appeared to be less sensitive to the daily biogenic VOC emissions compared to the median VOC signal.

- The EC sensors also collected data for the entire two months, proof that they were able to continuously record data in this high humidity environment. There were a few spikes that were likely to be due to electrical noise than actual changes in the compound concentrations. The inter-sensor variability for the MOS and EC sensors was relatively constant throughout the deployment, indicating that calibrations might have to be conducted on a monthly basis for the EC sensors as there was little sign of temporal drift during the rainforest deployment.

Chapter 6

Recommendations regarding the use of sensors for scientific research

The performance of MOS, EC, NDIR and OPC low-cost sensors (LCS) was characterised in both the laboratory and in the field to evaluate their suitability for use in scientific research. Low cost was defined as being commercially available for less than a tenth of the price of a research-grade instrument. There are a variety of low-cost devices available for the detection of common atmospheric pollutants and the sensors evaluated in this study (EC, MOS, NDIR) were chosen to detect several contaminants that are important for human health and which are monitored for studying air quality. The aim of the project was to characterise sensor behaviour, evaluate their performance and assess their suitability for use in scientific research.

Initially, the laboratory experiments involved using single sensors. Many commercially available multi-sensor arrays are used in research to characterise sensor response and these devices typically contain one sensor per compound [142] [173] [19] [32] [86]. The laboratory work, indoor air study and field work underlined in Chapters 2 and 3 proved that the MOS and EC LCS exhibited low reproducibility that made them unsuitable for use as singly deployed sensors. Over time, a co-located group of identical MOS or EC LCS exhibited a spreading out of their signals as each responded with a unique sensitivity towards physical and chemical conditions. This phenomenon was especially pronounced with the MOS sensors, which were greatly influenced by their surrounding conditions, and the spread of the maximum and minimum reporting sensors was often greater than the signal expected due to the MOS responding to their target compound. The medium-term inter-sensor variability was generally driven by these sensors reacting to these external drivers, as all co-varied together [104] [184]. Due to the non-reproducibility of LCS, single sensors can only be used to qualitatively identify the temporal variability of a specific location and single sensors cannot be used to make comparisons between two different geographic locations. The research shown here has found that even sensors purchased from the same production batch display unique sensitivities towards chemical and physical variables.

During the laboratory experiments in Chapter 2, and the field deployments in Chapters 3,4,5 the MOS and EC displayed relatively poor reproducibility when deployed as they are, with only the factory conversion factors applied. Once a network of sensors has been installed each individual sensor will experience a unique environment and exhibit a unique response depending on that environment. The sensors signals began spreading out after only a few hours, therefore they could not be used to assess the spatial variation of ambient contaminants since, without extremely frequent calibration, there would be no way of knowing which sensor was reporting high values due to the environmental changes and which was detecting larger concentrations of the target compound. The unpredictability with which the MOS sensors began to experience large amounts of drift would also lead to unreliable results.

6.1 Comparison of different types of sensors used

There are different sensor technologies for different pollutants. Typically MOS sensors are commonly used for VOC measurements, EC sensors for gaseous pollutants such as NO_2, O_X, CO, SO_2 etc. [114] and NDIR detects compounds that strongly absorb IR [173]. Low-cost measurements for PM are conducted using OPCs [30]. Sensor arrays, with one sensor per pollutant are commonly used in research to investigate the performance of LCS and their applicability in a network [32] [205] [19] [173] [143].

6.1.1 NO_2 EC

There are multiple studies that have used LCS to monitor ambient concentrations of NO_2 with EC sensors and have reported varying degrees of success. NO_2 EC are often deployed in the field and their performance evaluated by comparing the EC sensor response with other reference instruments such as chemiluminescence detection (CLD) [143] [110] [142] [122] or the NO_2 CAPS [166]. Medium-term (weeks to month) long deployments for EC sensors are common [143] [110] and studies have reported a correlation coefficients that indicate the NO_2 EC correlate positively to the measurements made by reference instruments: R^2 values are typically >0.8 [143] [110] [122]. Popoola et al. reported a comparison of NO_2 EC with a reference CLD instrument at an AQM, which led to an R^2 of 0.95, with the correlation plot producing a linear gradient of 0.938 [142]. A study which deployed two NO_2 EC for a month and compared both with a co-located CLD resulted in a high correlation between the two measurements, R^2: 0.88, 0.85 [143]. However, there are some contrasting studies that indicate that the correlation of NO_2 EC with a co-located reference measurement is poor, unless the NO_2 is corrected for an O_3 interference. With no O_3 correction applied, Lin et al. reported a low correlation co-efficient (R_2 value = 0.02) which indicated no correlation between the NO_2 reference and EC measurement [110]. This was found to be due to the NO_2 EC response towards

changing NO_2 concentrations being overwhelmed by the ECs response to O_3. After linearly correcting for O_3 interference the R^2 value increased to 0.88 and the gradient became close to unity (gradient = 1.07) over the two-month deployment in the field with comparison to the co-located CLD [110]. The NO_2 EC response has been reported as being highly variable towards changing ambient NO_2 concentrations; 7 sensor devices, each containing an NO_2 EC were deployed in the field and co-located with an NO_2 reference. The correlations ranged from poorly correlated (Pearson's coefficient: 0.14) to highly correlated (Pearson's correlation coefficient: 0.76) [86].

In this project the NO_2 EC were deployed with co-located references for just over three weeks in Beijing, China. The comparison of the six individual NO_2 EC with no correction procedures applied, against the NO_2 CAPS measurement (Table 6.1) displayed similar correlations (R^2 from 0.87 to 0.91) to those found in the literature. Although there was some degree of variability between the different NO_2 sensitivities all the correlations of the individual NO_2 EC with the reference instrument were strong and positive, comparable to [143] and [122]. This was evidence that the 6 NO_2 signals were all similar and yet there is a range of EC sensor responses displayed. Use of the instantaneous median of this NO_2 EC cluster would eliminate the effect of one or two of the EC displaying large amounts of drift.

The performance of NO_2 sensors is dependent upon the deployment location, with one study showing a range of R^2 values (0.75 – 0.98) for the inter-sensor comparison of 2 NO_2 EC located at three different sites [19]. This was reflected in the correlation between the NO_2 EC and a co-located reference as there was a range of correlation coefficients (r=0.11 to 0.8) for the same sensors and deployment locations [19]. When the LCS instrument was deployed in Boulder, Colorado (Chapter 4) the median NO_2 sensitivity towards NO_2 was different (gradient = 1.35) to the gradient observed by the median NO_2 EC (gradient = 2.09) observed in Beijing, China. It was also outside of the range of gradients observed by the six individual NO_2 EC (gradients 2.01 to 2.45). This indicated that the location of where the NO_2 were deployed would influence the EC performance due the the NO_2 EC experiencing different conditions, such as environmental factors and the relative concentration of pollutants [104] at different locations. However, the correlation of the median NO_2 EC and the reference observations in Boulder remained high and positive (R^2: 0.88) and the uncertainty was still low (RMSE = 9.24 ppb and NRMSE = 0.16) which was comparable to the NO_2 performance in Beijing (R^2 : 0.8).

When the temperature of the environment surrounding the EC sensors is highly variable (0 – 30 °C), NO_2 may display a weak correlation with temperature (R^2:0.18 [143] [122]), but there is less evidence that the NO_2 response is temperature dependant at smaller temperature ranges (1 – 2 °C) [143]. There is no definite model for how NO_2 EC sensors respond to changing humidity, with one study reporting a decrease in the NO_2 EC signal as RH sharply increased [19], whereas other evidence suggests there is no cor-

Table 6.1: The linear regression parameters obtained when 6 NO_2 EC and the instantaneous median NO_2 EC were correlated with the reference NO_2 instrument during the Beijing deployment (24 days). The linear parameters obtained for the same deployment when different methods (SLR, BLR, BRT and GP) were applied to improve the quality of sensor data. The predicted NO_2 concentration was then evaluated against the reference NO_2 observations using linear regression.

Linear regression parameters	6 individual NO_2 EC	NO_2 median	SLR	BLR	BRT	GP
Gradient	2.01 - 2.45	2.09	1.02	0.95	0.95	0.98
Intercept	-3.15 to -207	-33.4	+7.3	+4.97	+4.97	+2.95
R^2	0.87 to 0.91	0.87	0.86	0.94	0.94	0.94
RMSE (ppb)	23.9 to 181.8	25.3	11.8	6.5	6.5	6.0

relation (R_2: 0.02) between NO_2 EC observations and RH (over 30 – 100 % range) for a two-month in-field deployment and no evidence of long-term drift [110]. During the 24 day deployment of NO_2 EC sensors in Beijing, China (Chapter 4) the median NO_2 EC was found to have a weak, positive correlation (R^2: 0.37) with the humidity of the air reaching the sensors, over the humidity range 35 - 100 % RH. There was a stronger correlation with the temperature of the air (R^2: -0.52) and as the temperature increased from 16 to 41 °C the median NO_2 EC signal decreased.

NO_2 have exhibited variable electronic noise whilst deployed in the field from 5 – 20 ppb [122] [143]. The residual noise of the six NO_2 EC was found to be 3.82 ppb, when the sensors were exposed to zero air in the laboratory for a week during the EC sensor noise characterisation in Chapter 3. The NO_2 sensors have been shown to be highly reproducible, with two co-located in the field displaying a gradient of >0.9 [142]. This was observed with the NO_2 EC sensors deployed in Beijing as the R^2 values for the comparison between all 6 EC were greater than 0.8.

Laboratory calibration, exposing NO_2 EC to 100 ppb of NO_2 displayed that the absolute values reported by the EC were higher than expected (126.4 ppb) [19]. In contrast, the results from this project indicated that the NO_2 EC would under-predict the absolute values of NO_2 when compared to the NO_2 CAPS in the field. The intercept range for the comparison of the 6 NO_2 EC with NO_2 CAPS was found to be from -3.15 to -207 ppb, and the median NO_2 exhibited an intercept of -33.4 ppb, see Table 6.1.

There are some examples in the literature where multi-variate regression techniques, and ML algorithms have been applied to sensor data to correct for cross interferences and make an NO_2 concentration estimate that is closer to the reference observations [205]. Multivariate regression has led to moderate correlations of NO_2 concentrations (Pearson's r value: 0.59 ± 0.17, MAE: 4.6 ±0.7 ppb for 16 NO_2 EC) with the reference, whereas

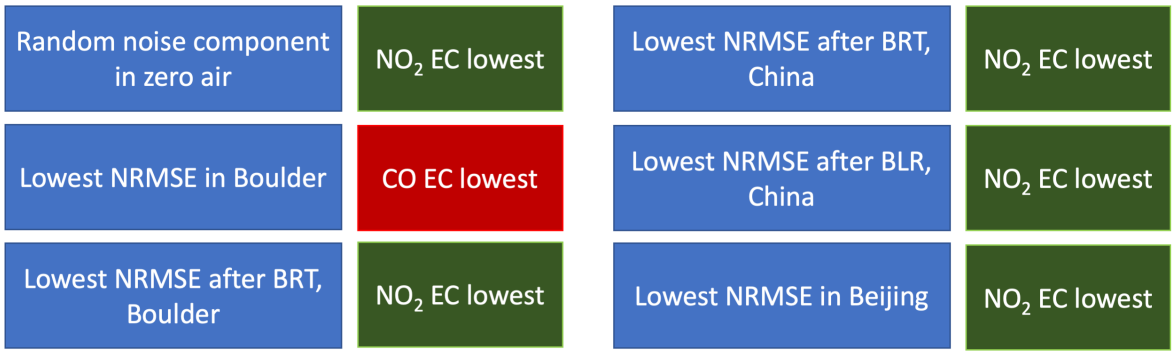

Figure 6.1: Comparing the EC performance over the experiments and field work conducted in the project. The normalised root mean squared error (NRMSE) was used in order to compare between the EC sensor response as the value of NRMSE is not affected by the concentration range over which the evaluation metric was computed (as RMSE is).

Random Forest ML algorithms were able to improve the NO_2 concentration estimate (Pearson's r value: 0.99 $\pm$ 0.01, MAE: 0.5 $\pm$ 0.1 ppb for 16 NO_2 EC) with the same sensor data set [205]. An NO_2 EC with no correction procedures applied, co-located with a reference measurement for 4.5 months displayed a poor correlation (R^2 = 0.12) with NO_2 reference observations and indicated a strong temperature dependence [32]. The NO_2 EC performance was improved with use of a high-dimensional model, to correct for interferences from changing environmental conditions. The modelled NO_2 concentration was correlated with the reference and displayed a gradient of 0.81, a reduced intercept of 3.26 ppb, an increased R^2 value of 0.69 and an RMSE of 4.56 ppb [32]. This RMSE value was comparable to the RMSE achieved when GP, BRT and BLR were applied to the Beijing sensor data set to predict NO_2 concentrations (RMSE: 6.0, 6.5, 6.5, respectively, Table 6.1). A variety of analytical methods were investigated as part of this research project to improve the quality of NO_2 EC sensor data, Table 6.1. Applying SLR, BLR, BRT and GP all improved the NO_2 concentration estimate over the testing data set (16 days) relative to the NO_2 reference as the gradients were all bought closer to one, the offset magnitudes were decreased (and also became positive) the correlation coefficients increased and the measurement of uncertainty (RMSE) decreased, Table 6.1. It was found that, for the Beijing deployment, the GP ML technique was the optimum method for predicting an NO_2 concentration estimate that was closest to the NO_2 CAPS observations. Using GP technique the NO_2 concentration estimate displayed a highly linear (R^2: 0.94, gradient : 0.98) comparison with the NO_2 reference, with the smallest offset (+2.95 ppb) and least amount of uncertainty (RMSE: 6.0 ppb). However, the performance of the BLR and BRT algorithms was comparable and these are more practical for use in the field as they require less computer power to train and apply the ML algorithms to the data set.

Overall, the NO_2 EC sensors performed well compared to the reference measurements and, through use of calibration procedures, were able to accurately determine the ambient concentration of NO_2 over a two-week deployment. This would be useful for the

atmospheric monitoring of NO_2 and, with fortnightly calibration, (which is the frequency of calibrations performed upon all the AURN sites in the UK [37]) the LCS instruments would be appropriate to increase the number of NO_2 measurements in the UK. Out of the different types of EC used in this research, the NO_2 EC consistently produced good performances and often performed the best (see Fig. 6.1). With only the factory conversion factors applied they exhibited the lowest random noise signal in zero air, and the median signal contained the least amount of error compared to the NO_2 reference instrument in Beijing, China, and again performed reasonably in Boulder, Colorado. After the ML algorithms were applied to each median signal from the EC clusters, the NO_2 concentration estimations were closest to the reference measurements.

6.1.2 CO EC

Multi-pollutant sensor devices often include CO EC for monitoring CO concentrations [86] [32] [205]. In-field, month long deployment of CO sensors has proved that the EC responses can be reproducible, displaying only 3 % difference between the mean absolute concentration averages produced by 2 co-located CO [143]. A co-location of a CO EC with a CO reference instrument displayed a strong and positive correlation ($R^2 = 0.78$), although a low sensitivity (gradient = 0.25) [32]. Two CO EC were deployed in the field, as part of an AQMesh sensor unit, and compared to a co-located CO reference monitor. Both sensors displayed a reasonably high correlation with the reference observations (Pearson's r-value: 0.79 and 0.82) [86], and this performance was much better than the three equivalent CO MOS sensors also co-located (r values: -0.40 to -0.14) [86].

The in-field performance of the CO EC, compared to a nearby (CO Aerolaser located 100 m vertically upwards from CO EC) reference monitor was similar to these literature studies for the CO EC sensors deployed in Beijing (Chapter 4). The 6 CO EC displayed correlation coefficients that were moderate to high (R_2: 0.55 to 0.83), Table 6.2 and an increase in CO concentration led to an increase in the CO EC sensor response. However, the performance of the CO EC is expected to be better than it was for the 24-day deployment in Beijing, China as the CO reference monitor was not sampling from the same line as the LCS instrument and O_X and NO_2 reference instruments. When the sensor instrument was stationed at NOAA Colorado, and the CO reference was sampling from the same inlet line during the static measurements a better performance was associated with the median CO EC. The correlation of the CO EC cluster with CO reference instrument, in Colorado for the 6-day static deployment of the CO EC sensors, led to a gradient that was close to 1 (gradient = 0.983), with a high, positive correlation coefficient (R^2: 0.94) and low RMSE (32.4 ppb) and NRMSE (0.06).

In research it has been reported that small environmental temperature changes (1 – 2 °C) cause negligible impacts upon the CO EC sensor signal, but where the temperature range is larger (0 – 30 °C) the CO response has been shown to weakly correlate (R^2:

Table 6.2: The linear regression parameters obtained when 6 CO EC and the instantaneous median CO EC were correlated with the reference NO_2 instrument during the Beijing deployment (24 days). The linear parameters obtained for the same deployment when different methods (SLR, BLR, BRT and GP) were applied to improve the quality of sensor data. The predicted CO concentration was then evaluated against the reference CO observations using linear regression.

Linear regression parameters	6 individual CO EC	CO median	SLR	BLR	BRT	GP
Gradient	1.79 to 2.27	1.97	1.13	1.03	0.73	0.68
Intercept (ppb)	123 to 647	+424	-225	-79.3	+66.4	+110
R^2	0.554 to 0.833	0.64	0.71	0.83	0.74	0.64
RMSE (ppb)	78 to 1370	1011	286	155	163	194

0.06 – 0.15) with temperature [143]. The temperature and humidity of the air reaching the CO EC was monitored during the 24-day deployment in Beijing, China (Chapter 4). The median CO EC displayed only a weak correlation with temperature (R^2: 0.2) and humidity (R^2: 0.3) when the RH ranged from 39 - 100 % and the temperature ranged from 16 to 41 °C.

Broday et al. found that CO EC, integrated into a multi-sensor platform, under-predicted CO concentrations (1292 ppb) when the EC was exposed to a known quantity of CO (1300 ppb) in the laboratory [19]. The performance of CO EC in the laboratory is different to the performance of the same sensor deployed in the field, for example a CO EC displayed a 0.07 ppb offset in a laboratory calibration, and this was increased to 166 ppb when the same calibration was repeated in the field [19]. Evidence from this research project however, suggested that the CO EC exhibited a positive offset. When the CO EC sensors were deployed for 24 days in the field and co-located with the reference CO instrument the intercepts from each of the 6 CO EC ranged from 78 to 1370 ppb, see Table 6.2. During the static 6-day deployment of 6 CO EC in Boulder, Colorado the offset was still positive (+4.66 ppb for median CO EC) but greatly reduced (Chapter 5).

In the literature, CO EC sensors have shown evidence of drift over a two week period when ambient CO concentrations were low [173]. There was no evidence of temporal drift in the CO EC sensor response when they were deployed in the field over at the three different locations (Beijing, Boulder, Borneo). However, the longest of these deployments was 24 days and therefore this deployment time may not be sufficient to identify long-term temporal drift in the CO EC signal. The residual noise of the CO EC in zero air, over a 6-day period was 157 ppb.

There are examples in the literature where statistical regression has been used to ac-

count for environmental interferences upon CO EC sensors [32] [205]. A high-dimensional model was trained to correct for the environmental influences upon the CO signal, and resulted in an improved performance for the CO EC concentration estimate. Gradient became closer to 1 (raw: 0.25, modelled CO: 0.94), with a higher correlation (R^2 raw: 0.78, modelled: 0.88) with the reference observations [32]. The RMSE was used to estimate uncertainty and was reported as 39.2 ppb for the modelled CO estimate [32]. Multivariate linear regression (Pearson's r-values: 0.94 ± 0.06, MAE: 39 ± 13 ppb) and Random Forest ML (Pearson's r-values: 0.99 ± 0.0, MAE: 7.9 ± 1.5 ppb) have also been applied to a 16-week data set containing 19 multi-pollutant sensor nodes to correct for cross interfering compounds that impact the CO EC sensors [205]. The Random Forest ML technique was optimum for correcting cross interferences and provided a better CO concentration estimate than multivariate regression [205].

In Chapter 4, BRT, BLR and GP ML techniques were applied to the 24-day LCS data set to produce a CO concentration estimate, with varying degrees of success. BLR was optimum for improving the CO concentration estimate: the gradient of the linear regression between the reference CO and BLR-CO prediction was 1.03, the intercept was reduced from +424 ppb to -79.3 ppb and the correlation became highly positive (R^2 increased to 0.82), Table 6.2. These ML results were comparable to those in Cross et al., when multivariate regression was used to optimise the CO EC response [32]. The results from this research have shown that the CO EC can provide a robust measurement of ambient CO concentrations after SLR calibration, or the application of ML-techniques, with a co-located reference instrument. These EC would be recommended for use in the field, with a cluster of 6 deployed and integrated into an LCS instrument as the CO EC measurement was useful for allowing corrections to other EC to be made. CO is also an important pollutant to monitor and the EC is an inexpensive method of increasing the number of accurate CO concentration measurements made in a local area.

6.1.3 O_X EC

O_X EC have also been used in research. A laboratory calibration exposing an O_X EC to known concentrations of O_3 the O_X EC compared well (R^2 >0.99) with an equivalent laboratory calibration with the reference instruments [19]. However, the O_X EC sensor was shown to over-predict O_3 (123.4 ppb) in a laboratory experiment where the EC was exposed to 100 ppb span gas [19]. The O_X EC deployed in the field as part of this research project also displayed a positive offset compared to the reference O_X measurements. The O_X EC used in the LCS instrument in Beijing (Chapter 4) displayed a positive offset (intercept for median O_X was +41.9 ppb) compared to co-located O_X reference observations, Table 6.3. The static deployment of the LCS instrument in Boulder, Colorado also displayed a positive intercept (+15.4 ppb) when correlated with the reference O_X observations.

A field deployment of an O_X EC with a co-located O_X reference measurement showed

that there was a poor and negative correlation (R^2 = 0.12, gradient = -0.48) between the two measurements [32]. A negative intercept of -131 ppb indicated that the O_X sensor displayed a large, negative offset in comparison with the reference [32], in contrast to the O_X EC deployed in Beijing and Boulder. Seven O_x ECs, integrated within multi-pollutant sensor nodes (AQMesh, Cairclip, Aeroqual) were deployed in the field and co-located with a reference monitor. After correlation of the 7 timeseries with a reference monitor it was evident that the O_X EC exhibit a highly variable response (Pearson's coefficient ranged from 0.39 – 0.97) to changing O_X concentrations [86]. Another study supported the low reproducibility of O_X EC sensors; three experiments with co-located pairs of O_X EC displayed a range of R^2: 0.38 – 0.62 [19]. In the same experiment, a comparison with a co-located UV photometer revealed a weak to negligible correlation, R^2 values of 0.05 – 0.58 [19]. The O_X EC deployed in the LCS as part of this research project were highly correlated and displayed comparable measurements to a co-located reference measurement (gradient = 1.0, R^2 = 0.84) during the 24-day deployment in Beijing (Chapter 4). There was very little inter-sensor variability between the 6 individual O_X EC in China, over a 24-day deployment. The range of gradients of each O_X EC was 0.935 to 1.1, and the range of R^2 values was between 0.82 and 0.85. However, in Chapter 5, when the LCS instrument was deployed in Boulder for 6-days the comparison with the median O_X EC and the reference O_X observations displayed a lower O_X sensitivity (gradient = 0.56) than for the 24-day deployment in Beijing. The correlation between the reference and median O_X EC for the Boulder deployment was moderate (R^2: 0.5) which indicates that the performance of the O_X EC is impacted by the EC surroundings.

The O_X EC has been shown to be impacted by variable humidity of the air flow to the sensors, with one study observing an increase in the O_X signal with steep increases in RH [19]. Temperature was thought to produce a small interference upon O_X EC signals when they were located in the field [32]. During the LCS deployment in Beijing, the RH varied between 39 - 100 % and the temperature between 16 - 41 °C. The median O_X EC showed a moderate, positive correlation with temperature during the deployment (R^2: 0.5), and a weak, negative correlation with RH (R_2: -0.3).

There are a few examples in the literature where statistical regression models and ML have been applied to LCS data to make an O_X concentration estimate [205] [32]. Multivariate regression was applied to 19 multi-pollutant sensor nodes over a 16 week period, and the O_X concentration estimate was compared with an O_X reference measurement. The Pearson's r-values displayed a strong positive correlation (0.81 ± 0.06), with low MAE values (5.1 ± 0.6 ppb) [205]. The O_X concentration estimate was improved when the same data set was subject to Random Forests ML algorithm to correct for cross interferences (Pearson's r-values:0.99 ± 0.0, MAE: 0.7 ± 0.1 ppb) [205]. A high-dimensional model, trained using environmental variables such as RH and temperature was able to improve the O_X concentration estimate: gradient increased to 0.47, intercept became closer to zero

Table 6.3: The linear regression parameters obtained when 6 O_X EC and the instantaneous median O_X EC were correlated with the reference O_X instrument during the Beijing deployment (24 days). The linear parameters obtained for the same deployment when different methods (SLR, BLR, BRT and GP) were applied to improve the quality of sensor data. The predicted O_X concentration was then evaluated against the reference O_X observations using linear regression.

Linear regression parameters	6 individual O_X EC	O_X median	SLR	BLR	BRT	GP
Gradient	0.935 to 1.1	1.0	0.935	0.904	0.888	0.841
Intercept	-33 to +89.9	+41.9	+9.8	+5.98	+8.23	+9.36
R^2	0.82 to 0.85	0.84	0.95	0.95	0.95	0.91
RMSE (ppb)	26.0 to 89.6	48.7	10.3	9.09	9.18	12.65

(13.1 ppb) and the correlation co-efficient increased from a weak to a moderate correlation (R^2 : 0.39) [32]. The RMSE for the modelled O_X data compared to the reference was 9.71 ppb [32]. This is a similar value, for that observed in Chapter 4, when BRT and BLR ML algorithms were applied to produce an O_X concentration estimate (BLR RMSE: 9.1 ppb, BRT RMSE: 9.2 ppb), Table 6.3. The O_X EC performance during the 24-day deployment in Beijing was found to be very linear and hence the BLR ML technique was optimum for predicting an O_X concentration estimate that was close to reference observations. The O_X EC presented the most linear relationships with the O_3+NO_2 reference observations out of the different types of EC deployed. A high degree of linearity is useful for determining simple and effective calibration models. However, the median O_X signal deviated significantly from the reference measurements when sampling static measurements in Colorado. It was thought that the dry air caused a large amount of random noise to appear in the O_X signals and behave in an unpredictable manner.

The O_X response was reproducible and the median O_X EC reported values that were close to the reference O_X measurements for the Beijing campaign. Therefore, with suitable calibration procedures applied (e.g. SLR, BLR, BRT) this research has shown that these EC would be suitable for use in the field for short-term applications. However, the performance of the O_X was degraded during the Boulder campaign and this was thought to be due to the air that the EC were exposed to being dry [1]. Further experiments, to characterise the performance of O_X EC after pro-longed exposure to air with a RH of less than 10 % are required as this may impact where the O_X EC can be deployed or where additional equipment to increase the humidity of the sampled air might be required. The O_X EC performance was less reliable than the NO_2 and CO EC sensors.

6.1.4 CO_2 NDIR

CO_2 NDIR sensors are used to monitor ambient levels of CO_2 and are also calibrated by co-location with a reference CO_2 instrument in the region where the NDIRs are due to be deployed [119] [205] [131]. A comparison of a CO_2 NDIR with reference measurements (Piccaro) exhibited linear parameters of R^2 : 0.92 and a gradient of 0.955 [142]. Two co-located CO_2 NDIRs correlated well, with gradients of 0.9 – 1.0, indicating high repeatability in their measurements [142]. A one-day comparison between 2 CO_2 NDIR sensors demonstrated reproducibility with a high, positive correlation (R^2: 0.93), and gradient close to 1 (gradient=1.1) [87]. However, one of the NDIR sensors reported an offset of approximately -20 ppm, which was the value of the intercept between the two NDIRs [87]. 6 CO_2 NDIR sensors over a 13-day indoor deployment also reported a high degree of inter-sensor reproducibility, exhibiting Pearson's correlation coefficients between 0.7 and 0.99 [131]. Six CO_2 NDIRs deployed in an indoor environment with ventilation to the outdoor air, were co-located with a reference (cavity-ring down) instrument for 4 weeks [119]. They exhibited a long term drift of 1.2 ppm over the duration of deployment and were highly correlated with the reference observations, RMSE ranged between 5 to 21 ppm, with no NDIR corrections applied [119]. The result of one of the 6 NDIR versus the reference observations yielded the linear regression parameters of gradient = 0.94, intercept = 31.5 and R^2 = 0.97 [119].

During this researchproject, there were 3 CO_2 NDIR sensors deployed for 6-days in Boulder, Colorado with a co-located CO_2 reference instrument. The three NDIRs covaried and were compared against each other using linear regression. The gradients ranged between 0.823 to 0.852 and there were small intercepts (0.069 – 0.081 ppm) which indicated that all displayed similar offsets. All three NDIR devices were all highly and positively correlated (R^2 range: 0.84 – 0.88) with each other, similar to the results reported by [142] [131]. The median CO_2 signal was correlated (R^2 = 0.95) with the reference CO_2 observations in Chapter 5. However, the median CO_2 NDIR displayed a large offset (intercept = 365 ppm) compared to the reference CO_2 observations and a difference in sensitivity (gradient = 0.29) towards changing CO_2 concentrations.

CO_2 NDIR measurements have been improved by the application of multivariate regression [119] and ML techniques [205] in the literature. Multivariate regression, taking into account temperature and atmospheric pressure improved the comparison of the NDIR sensors with the reference observations, and the RMSE decreased from 5 to 21 ppm to 1.7 to 4.3 ppm [119]. A CO_2 concentration estimate was produced by applying Random Forest ML to a data set composed of 19 multi-pollutant sensor nodes. This was found to strongly correlate (Pearson's r-value: 0.99 ± 0.0)to the co-located CO_2 reference observations and was useful for removing the impact of cross interferences (MAE: 1.7 ± 0.3 ppm) upon CO_2 NDIR data [205]. In Chapter 5, ML was applied to the LCS data set to predict a CO_2 concentration during the 6-days when the LCS was making static

measurements. BRT did not predict an improved CO_2 concentration estimate in this case (gradient for uncalibrated = 0.29, for BRT-predicted CO_2 = 0.043, R^2 for uncalibrated = 0.95, for BRT-predicted CO_2 = 0.11). Rather surprisingly, due to the correlation between the NDIRs and reference CO_2 measurements, the CO_2 NDIR timeseries only contributed to a third of the key decisions made by the BRT algorithm. This was thought to be due to a small data set (6-days) and the different distribution of data between training and testing data sets.

The median CO_2 NDIR response was highly correlated with the reference CO_2 observations and each NDIR co-varied with the other co-located NDIRs. Therefore the NDIRs indicated high inter-sensor reproducibility and would be recommended for use in the field to monitor CO_2 concentrations with frequent (fortnightly calibration). However, the NDIRs were only tested over a short period as part of this research so further investigation regarding the stability of their responses and performance in different environments is required.

6.1.5 MOS sensors

MOS are widely investigated for the purposes of air quality monitoring and there are many varieties commercially available for monitoring NH_3, NO_2, O_3, CO_2, CO [59], [8], [172] [136] as well as total VOCs [199]. MOS sensors for the detection of VOCs have been investigated in the laboratory [99] [199]. An array of 14 TGS2602 MOS sensors was tested in the laboratory with one failing immediately from the start of the experiment [199]. Sensor replacement is expected over time [184], and it was not uncommon for MOS sensors to immediately fail during this research project. Throughout all the deployments of MOS sensors in this research project, an average failure rate of 10 % of the MOS sensors was noted for the Total VOC MOS. For the TGS2602 MOS sensors, in China 1 out of 32 failed, in Borneo 4 out of 16 failed, during the indoor air experiment 3 out of 24 failed and in Boulder 0 out of 8 failed. When installing and designing a LCS array it is recommended to purchase an additional 10 % of MOS sensors to replace this failure rate.

During laboratory calibrations with toluene, the sensitivity towards toluene, for 13 TGS2602, in constant conditions (30 – 35% RH, 40 °C) was calculated as 6.00 ± 0.27 (1 σ) mV ppb^{-1} [199]. This magnitude for MOS VOC sensitivity is comparable to the sensitivities identified by calibrating TGS2602 Total VOC MOS in the laboratory in Chapter 2. When a mixture of VOCs was exposed to the TGS2602 MOS sensors they exhibited sensitivities of 2.48 – 13.1 mV ppb^{-1} over a range of humidity's and at laboratory temperature (approximately 21 °C). This spread in the different sensitivity of MOS towards VOCs was more of a concern than the magnitude of the sensitivity observed since this indicated that no single calibration model would be appropriate for multiple MOS that were to be deployed singly.

Out of the array of TGS2602 Total VOC MOS used by Wolfrum et al. 2006 [199],

it was noted that any two MOS sensors exhibited different responses towards the same concentration of VOC calibration gas [199] [99] [60]. This was also observed in this research as in Chapter 2, when 2 or more MOS were exposed to the same VOC gas standard, under the same environmental conditions, individual MOS sensors reported different responses. For example, the mean sensitivity of MOS sensors was 2.55 m V ppb^{-1} when multiple sensors were exposed to the same VOC gas standard at 30 – 40 % RH. There was 6 % variation in the MOS sensors sensitivities for this calibration, which is comparable to the variability in MOS sensitivity calculated by Wolfrum et al. 5 % for the TGS2602 sensitivity [199]. MOS sensors of the same model, co-located in a cluster tend to display high correlation between the sensors, with all responding similarly to their environment [136]. The work using MOS sensors in this research project provides support to this result from Peterson et al. 2017 [136] as for example, 19 MOS sensors deployed in the indoor office environment displayed Pearson's correlation coefficients that were greater than 0.7 for the entire 4-week deployment. However, it was noted that these inter-MOS correlation values changed over time as the MOS sensors exhibited unpredictable and randomly occurring changes to their sensitivity towards VOCs, cross interferences and environmental conditions.

It has been reported in the literature that TGS2602 MOS exhibit different responses towards different VOC compounds and VOC compositions. Wolfrum et al. tested TGS2602 Total VOC MOS with toluene, acetone and isopropanol and found that the MOS were most sensitive towards toluene and least sensitive to isopropanol [199]. This was in agreement with the experiment Chapter 2, where gas standards were separated into individual compounds by GC-MS and the TGS2602 MOS exhibited different responses (peak areas) for each compound. Although in this research project these exact compounds were not exposed to TGS2602 MOS, it was found that the TGS2602 MOS produced larger responses for aromatic compounds (such as toluene) and were less sensitive towards alkanes. The TGS2620 OVOC MOS sensor indicated that it was more sensitive towards different compounds compared to the TGS2602. Therefore, by using a combination of MOS sensor types, and exposing these MOS sensors towards known compositions of VOC mixtures it might be possible to build up a database for different patterns of responses [169] [99]. Pattern recognition analysis upon MOS based data sets then may potentially be useful for source apportionment [169].

Other research studies have shown that the position of the MOS sensor within an airtight manifold did not impact the MOS sensors response to VOCs, but the response time of the MOS was dependent upon the flow rate of the air to the sensor [95]. A flow rate of 1700 mL min^{-1} produced a TGS2620 OVOC MOS sensor response of 12 seconds [95]. During the investigation of how best to position sensors within a Teflon manifold in Chapter 2, it was concluded that the shape of the manifold could influence the MOS response. The chamber manifold led to the poorest results and there was evidence

that MOS in series exhibited increasing smaller responses to VOCs. The flow rate was also found to impact the MOS sensor response, with 1000 LPM or 3000 LPM producing the highest VOC sensitivities with lowest uncertainty.

MOS sensors, TGS2602, TGS2620, TGS2610 and TGS2600 are susceptible to long-term drift over 36 months [184] [60]. This drift is comprised of 'real-drift' where the MOS sensing surface ages or is poisoned over time and 'measurement drift' where changes to the MOS environment lead to the MOS response changing over time [184]. The TGS2602 total VOC sensors used for this research project, in the indoor office experiment displayed a spreading out of MOS signals due to measurement drift. After 4 weeks, the difference between the maximum and minimum reporting sensor was 0.30 V, equivalent to 30 $ppb_{[VOC]}$ if a laboratory-derived conversion factor of 10 mV ppb^{1} was used. This experiment also showed that the sensor drift was unpredictable and random as the order of highest reporting sensor and lowest reporting sensors changed rapidly and randomly over the four weeks. Support vector machine learning has been used in literature to account for measurement drift under laboratory conditions, over three years [184]. Here in Chapter 4, BRT ML techniques were applied to the LCS data set during the 24-day campaign in Beijing to predict the Total VOC concentration, using a co-located SIFT-MS measurement as a training label. In Chapter 4, when the LCS sensors instrument was co-located with and showed a reasonable comparison against a SIFT-MS ML techniques were applied in an attempt to improve the quality of MOS total VOC measurements. Initially, the median VOC MOS was temperature and RH corrected and this resulted in a moderate correlation (R^2: 0.47, gradient: 3.82 mV ppb^{-1}) with the summation of 29 compounds monitored by SIFT-MS. The BRT algorithm was applied to the LCS instrument data set from this deployment to predict a Total VOC concentration estimate by correcting the Total VOC MOS for cross interferences. The Total VOC concentration estimate was compared against the SIFT-MS Total VOC signal. The gradient was 0.46, the intercept was 31.8 ppb, the RMSE = 18.4 ppb and the R^2 was 0.40. Therefore, BRT was not successful at removing the influence of cross inferences upon the MOS signal as the BRT-predicted total VOC concentration was less correlated with the SIFT-MS Total VOC concentration, with a gradient that was far from unity. The median VOC MOS was the fifth out of seven largest contributors towards the Total VOC prediction, so was not even instrumental in producing the prediction. The temperature and humidity corrected median VOC MOS signal was also compared against a co-located GC-FID system. All 29 VOCs monitored by the GC-FID were summed together for each data point and the correlation between the median MOS and total VOCs monitored by GC-FID was weak ($R^2 = 0.21$) and positive (gradient = +0.59). In another co-location with a SIFT-MS measuring ambient air there was no correlation (R^2 <0.03) between the median MOS signal and the compounds detected by the SIFT-MS (Chapter 2).

The median MOS signal performed poorly when compared against two reference VOC

Table 6.4: The Total VOC median, OVOC median, CH_4 median and PrBu median MOS signals were correlated with the humidity of the air reaching the sensors and the temperature to identify if the MOS signals were detecting changes to these environmental conditions.

Linear regression parameters (RH vs. MOS)	TGS2602 Total VOC	TGS2620 OVOC MOS	TGS2611 CH_4 MOS	TGS2610 PrBu MOS
Gradient (mV $\%^{-1}$)	-2.63	+11.0	+9.92	+7.19
R^2	0.81	0.99	0.99	0.99
RMSE	48.21	47.45	47.46	47.63
Linear regression parameters (Temp. vs. MOS)	TGS2602 Total VOC	TGS2620 OVOC MOS	TGS2611 CH_4 MOS	TGS2610 PrBu MOS
Gradient (mV $°C^{-1}$)	+48.3	+0.75	-1.1	+3.6
R^2	0.996	0.11	0.28	0.78
RMSE	28.4	28.7	28.6	28.7

instruments. This was thought to be due to the large influence that temperature [187], humidity [169] [156] and drift [184] have on the MOS sensor signal [8]. A research study using MOS sensors found that, using an exponential decay regression model the TGS2620, TGS2611 and TGS2610 displayed correlations (R^2) of 0.98 – 0.99 with humidity [169]. The TGS2602 had an R^2 of 0.78 with the same exponential decay model [169]. By accounting for temperature and humidity, using a model based upon the n-type semiconductor bands Huerta et al. [81] were able to de-correlate the temperature and humidity response of MOS. The R^2 for their modelled MOS signal with RH and temperature was between 0.90 – 1.0 for the four TGS MOS types shown above [81]. However, over a three month period the sensitivity of the MOS towards temperature and humidity changed and the modelled MOS became less accurate (R^2 <0.7) [81]. The non-linear response of the MOS sensors towards increasing humidity was also recognised in Chapter 2. The sensitivity of the MOS sensors was found to be more impacted by ambient changes of temperature and humidity than it was for cross interferences that were caused by other gaseous compounds. In Chapter 2, the correlation between four different types of MOS sensors with temperature and humidity were tested. Each median MOS signal was strongly correlated to both environmental conditions, Table 6.4.

The influence of changing environmental conditions is so large upon the MOS sensor signal that it was challenging to determine the change in the MOS response that was purely due to the change in the VOC composition and concentration in the atmosphere. The evidence gathered by this research project leads to the conclusion that there are limited applications for MOS sensors. The MOS exhibit low inter-sensor reproducibility so

they should not be deployed as single sensor devices, as the drift in the MOS response can be unpredictable and of varying magnitudes. When using singly deployed MOS sensors it would be difficult to detect which sensors are exhibiting large amounts of temporal drift as the drifting MOS have been shown to continue co-vary with the other MOS sensors. Individual MOS sensors have unique sensitivities towards the target VOC compounds, interfering gases and environmental conditions yet because these sensitivities are not reproducible over time, no single calibration model is appropriate for extracting a useful MOS signal.

6.1.6 Clustering

This project showed that the reproducibility of the MOS and EC LCS response could be improved using a clustering approach. Co-locating identical sensors and using the instantaneous median is recommended for sensor deployment in the field. Typically, groups of LCS display high covariance, but the extent to which the signals go up and down changes, leading to a randomised spreading out of signals. The median sensor signal was able to be representative of all the individual sensors, and removed the effect of any sensors displaying an anomalously high amount of drift. The random short term (hours to day) and medium term (day to weeks) drift due to unpredictable responses towards other variables was minimised when using the median of a cluster. Therefore, the frequency required between calibrations can be reduced when using the average of a cluster of sensors and linear interpolation between calibrations becomes more appropriate. By comparing the individual responses within a cluster, this approach also identifies failing sensors quickly by identifying which sensors began reporting values with large amounts of drift. The sensors used in this study were all inexpensive enough that purchasing multiple devices still maintained the cost benefit. Additionally, each LCS consumes a minute quantity of power and therefore the overall power consumption for a group of LSC devices is still much smaller than it would be for research grade equipment monitoring the same measurands. A small power consumption is hugely advantageous for the deployment of instruments in the field as operational costs are reduced.

6.1.7 Low-cost sensor instrument

For deployment out in the field, the clustering approach was incorporated into a multi-pollutant sensor array. Clusters of different types of sensors, each detecting a different target compound, were built into one instrument. The sensor instrument was designed to make multiple pollutant measurements using different models of LCS; MOS sensors detected total VOC, EC sensors monitored NO_2, O_X and CO. The overall sensor instrument was compact, required low set-up and operational costs and a small power consumption relative to a collection of reference instruments monitoring the same pollutants. This

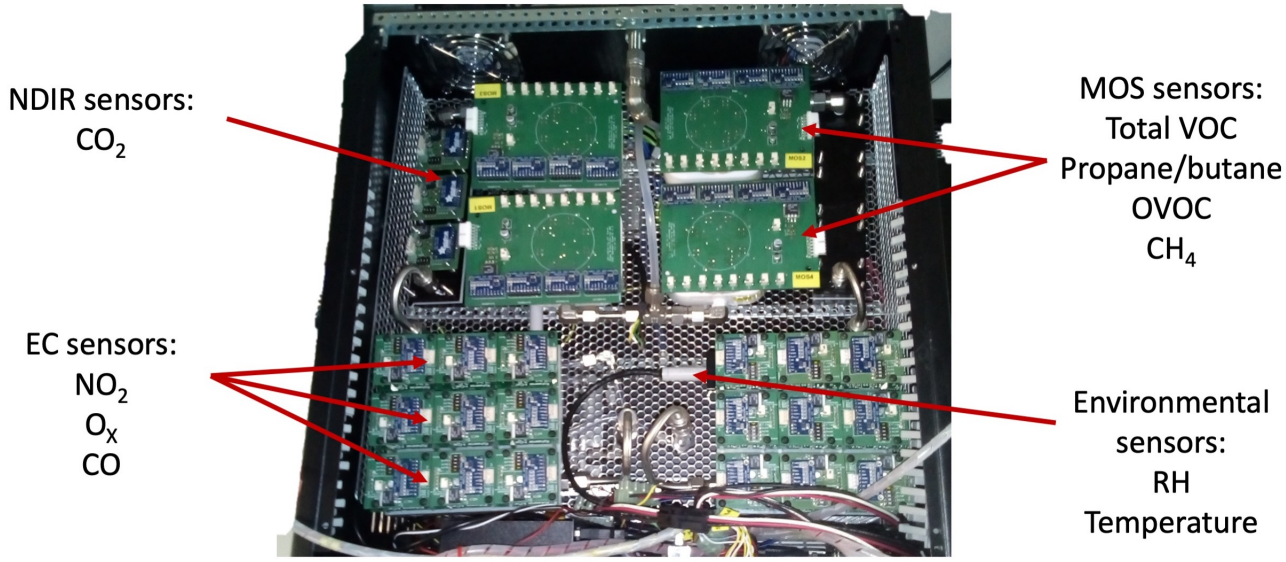

Figure 6.2: Photo showing a version of the sensor instrument which contains different sensors to detect multiple pollutants.

made it more portable and appropriate for use in a high-density network. The use of a multiple pollutant instrument facilitated the correction of cross interferences upon each EC or MOS signal. The ML techniques were applied to the whole LCS data set and used multiple sensors to determine relationships between the sensors and the target compound (training label). The ML then predicted a concentration estimate for any particular compound using all the sensors in the LCS instrument. This meant that cross interferences could be accounted for in the concentration estimate produced by the ML algorithm and the result was often closer to the reference observations than the sensor signal reported by the sensor responsible for detecting the target compound alone.

A sensor instrument, like the one shown in Fig. 6.2, can be used in an analogous manner to an air quality monitoring station. The LCS instrument would require calibration with the reference instruments, then these could be deployed in a localised area.

6.1.8 Calibration

When using MOS, EC and NDIR sensors, none of the sensors were able to report accurate absolute concentrations compared to the equivalent reference observations, when they were used with no calibration procedures applied. Low-cost sensors, like most scientific instruments, require calibration to ensure there is confidence in the results and calibration of the sensor device was required to determine the absolute concentrations of a pollutant. Unlike reference instruments used for gaseous atmospheric measurements, the sensors cannot be calibrated using synthetic gas standards or in a laboratory. Calibration models produced in the laboratory are not representative of the sensor behaviour if the sensors are then removed from the laboratory and placed at a deployment location where the

chemical and environmental conditions are dissimilar [104] [122]. To minimise the set-up and operational costs, there was no pre-detection techniques, such as driers or temperature control, employed to improve LCS sensors detection capacity. Therefore the sensors are exposed to the dynamic ranges of chemical and environmental conditions in which they are placed. The laboratory experiments in Chapter 2 showed that LCS are susceptible to being influenced by changing environmental factors, often with non linear responses, and the presence of compounds that are not the target compound. Calibration procedures must account for these variables and *in situ* calibrations using co-located reference instruments do that. None of the sensors used in this study reported accurate absolute concentrations without calibration, and only in-field calibration provided a calibration environment that was representative of the conditions the sensors experienced during deployment. The sensors within the LCS instrument were calibrated by co-locating the instrument with reference instruments for a period of time. The relationship between the sensor and the reference observations was determined and then pollutants concentrations were calculated by applying this relationship to subsequent sensor data. Week-long co-location of the NO_2, CO and O_X EC sensors with NO_2, CO and O_X reference instruments was suitable for determining the accurately predicting the NO_2 and O_X concentrations for the following two week period using SLR (see Tables 6.1 6.2 and 6.3). There would therefore be high confidence in the EC data if a calibration procedure such as SLR was used, then the LCS was moved to a new location as part of a network and left to monitor for a fortnight. For more accurate concentrations, various ML techniques could be used instead of SLR to calibrate the sensors. To make more accurate prediction and provide the information required for ML to correct for temporal drift the data from each calibration could be added to the training data and the ML algorithm re-trained periodically. Relationships between the sensor variables and environmental conditions that occur over longer timescales are more likely to be detected and used to further optimise the ML-predictions. For the MOS sensors however, when the single sensor is moved away from the reference instrument there is little confidence in the sensor data after only a short time (hours to days) because of the unique sensitivity's to external conditions and drift [184] [60]. Since the comparison of a co-located reference VOC measurement such as GC-FID or SIFT-MS did not indicate a high correlation between the measurements there would be lower confidence in the calibration of VOCs by co-location in the field, although this is the most appropriate method.

Regular calibration is required, to identify if the sensors experience large amounts of drift and to correct for this. The frequency of calibration depends on the sensors temporal drift and may change depending on the environment. It is expected that re-calibration would need to be conducted on at least a bi-weekly basis for the EC but all the deployments of sensors with co-located reference instruments were over a short time scale and therefore this might change over longer time scales. MOS sensors would require more frequent calibration since their responses to the environment and gaseous compounds was variable

over shorter timescales (hours - days).

6.1.9 Machine Learning

During the analysis of the EC sensors, ML techniques were employed to successfully improve the quality of the sensor measurements and make concentration estimates that were more comparable to the reference observations. During the ML training period the algorithms used all available data from the sensor instrument to make concentration estimates for a particular compound. The results were often closer to the reference observations because ML algorithms are exceptional at identifying correlations and trends between variables and could therefore correct for cross sensitivities. The application of multi-variate regression [199] [99] or ML techniques [205] [58] [72] to correct for cross interferences in LCS signals have been applied to LCS in research. However, Random Forests [205] [58] [72] or Artificial Neural Networks [174] [51] have been used, and boosted techniques such as BRT or BLR and GP ML algorithms are less widely applied. These were chosen for the purposes of this research because they can provide additional information as well as producing a concentration estimate corrected for cross interferences. GP calculated an uncertainty estimate for every data point and BRT was capable of producing a measure of how important each variable was to the overall prediction. When applied to the 24-day LCS data set from Beijing, the BRT, BLR and GP ML analysis made concentration estimates that were generally of a higher quality than the values reported from the sensors alone. For use with the sensor data, BRT was optimal because it often performed just as well, or better, than the other algorithms, but also had the capacity to provide information about the algorithms decisions which was important for justifying the ML performance. Although an advantage of using GP was that it could also report the uncertainty in the concentration predictions, it required a substantial amount of processing power for training and testing which is less appropriate for use with an LCS instrument which may need to re-train the ML algorithm after calibration in the field.

The ability of all ML techniques to make accurate predictions depends upon the quality of the training data that the algorithms are given to fit to and train upon. The training period must encompass the full range of conditions that the sensors are likely to be exposed to during deployment. This was made evident in Chapter 5, when the training and testing data for the Boulder sensors displayed a different distribution of data, and the overlap of similarly distributed data was small. The ML did not perform optimally and more training data, of at least a week was required for the ML algorithms to improve the quality of sensor data. The mixing ratio of the pollutants, and the concentration gradients of the species were a lot smaller than in the training set, leading to the ML algorithms making inaccurate predictions. For successful application of ML algorithms the LCS instrument must be exposed to a range of pollution concentrations, with the ranges greater than expected during the testing period. Also temperature and humidity are known

interferents upon the EC and MOS sensors therefore the LCS response to a full range of RH and temperature must be recorded during the training period. During training it may be suitable to co-locate the LCS instrument in the field with reference instruments, then expand the training set conditions with use of gas standards or with laboratory calibrations. It is recommended to use ML such as BRT and BLR to improve the accuracy and precision of sensor based concentration estimates, when sufficient training data sets have been collected. ML analysis was good for improving the quality of EC sensor data and has potential for producing sensor results that are close to reference observations, but only for as long as the relationships learnt during the training period hold true. Although using ML could increase the time required between calibration of the sensors, it would still be necessary to ensure that the predictions are making accurate predictions. For longer term monitoring, since the calibration procedure must include the full range of pollutant concentrations and environmental conditions, the training period may need to be extended. It would also be useful to introduce a flagging system to indicate data at times when a variable has exceeded the range it spanned during the training period. A more thorough inspection of the ML predictions can then be made. Although not tested in this project, iterative ML systems, whereupon the training data is added to by additional co-location with reference monitors and the ML model is then refined upon the extra data would potentially be a powerful tool for LCS pollutant predictions. This would allow for frequent co-location with the reference instruments and up-to-date ML models that account for temporal drift over week to month timescales.

However, caution should be taken when using ML as the measurements take a step away from being sensor observations and become more like modelled data. If the purpose of using LCS to provide an independent measurement of pollution, then using ML for analysis might not be as beneficial. When the NO concentration was predicted using the sensor measurements in China there was no NO sensor measurement and therefore the prediction was based entirely upon the other sensor results and their relationships with each other and the NO reference training label. This modelled NO concentration was generated using the correlations detected by the ML in the training data and should be stated as being a modelled observation of NO.

6.2 Applications of LCS

There are a variety of applications that the LCS data could be used for to improve the assessment of air quality. Each of these is assessed and the findings from this report are summarised to indicate if the LCS used here would be appropriate for a selection of LCS applications.

1 . LCS instruments could be used to supplement existing air quality networks. Currently in the UK, strategically located Air Quality Monitoring (AQMs) stations contain

research grade instruments to evaluate air quality. However, the expense to install and maintain these AQMs means that there are a relatively sparse number of measurements made throughout the UK. LCS have the potential to be deployed in a network to increase the number of air quality measurements made in a localised area, to better represent ambient pollution gradients between AQM sites.

This research project has found that clusters of EC sensors integrated into a multi-pollutant LCS instrument would be suitable to make a high-density network of EC to better characterise gaseous compound concentrations over week+ timescale. After in field calibration, by co-location of the LCS with reference instruments for a week, the EC sensors exhibited a constant sensitivity towards their target compound when compared against the reference measurements for a subsequent two weeks. This was true when simple linear regression or ML techniques were applied to calibrate the median EC sensors. No temporal drift of the EC was observed for the deployments in the field up to three weeks. ML techniques were preferred for optimising the EC sensor data, by correcting for cross interferences and ultimately producing a more accurate concentraiton estimate of EC target measurands. However, the conditions within the training data, in the calibration week, must be similar to the conditions experienced by the EC during the testing data set. Applying ML algorithms retrospectively for the first training period was recommended so a check, to identify if conditions were suitable for ML is recommended. NO_2 and O_X EC sensors had a linear response and maintained a good agreement for two weeks with their respective reference observations in Beijing, China. The research in Chapter 4 therefore indicates that after a week calibration period, the ECs would produce high-quality pollution measurements that would be comparable to reference observations for a fortnight. Multiple LCS instruments, located around an AQM would provide additional measurements to better characterise pollution gradients between AQMs and increase the number of NO_2, O_X and CO measurements in a local region. These pollutants are important to monitor as the spatial gradients of these can be steep and local authorities often report NO_2 exceedances due to a high volume of traffic [37]. The MOS sensors were found to be less suitable for this application as changes to their sensitivity towards their target compounds, environmental conditions and interfering gases are unpredictable and may occur on short timescales (day to week), and these would also impact the instantaneous median of the MOS. Therefore there would be little confidence in the MOS sensor data with no co-located reference. MOS signals are heavily influenced by environmental conditions and large, daily fluctuations in temperature and humidity are expected for deployment outdoors, which were shown to overwhelm the MOS response to ambient VOCs.

2. Personal exposure monitoring; due to their low cost, low power and small size, LCS such as MOS and EC are portable. Therefore they, and a small power supply and data storage system can be carried around, to indicate when and where an individual is exposed to high levels of pollution.

This research has shown that the EC and MOS are capable of producing indicative observations of pollutants. Both these sensors report data at relatively high temporal resolution (seconds) which would be suitable for moving around with the sensors and identifying where a spike in the median signal was produced. For example, an individual could determine where on a walking commute they experienced the highest levels of pollution and look for routes where this pollution hotspot was missed. Whilst, in this application they should not be used to provide absolute concentrations both the MOS and EC have displayed covariance with an equivalent reference monitoring device. However, the data reported from the EC sensors was found to be more reproducible and less impacted by changing environmental conditions than that of MOS data. It is therefore recommended to preferentially use EC for this application. However, for quantitative measurements, even with ML to correct for cross interferences, the absolute concentrations would not be of high quality as moving into different locations, with different environmental conditions would lead to the training and testing data sets exhibiting different distributions. In this scenario the concentration estimate predicted by the ML techniques is likely to be inaccurate. By comparing multiple LCS, for example to monitor NO_2, O_X and CO, additional information regarding the source of these emissions might be extracted from these timeseries.

In Chapter 5, CO EC and CO_2 NDIR sensors were found to be suitable for mobile measurements made by installing the LCS inside a vehicle. Both the median EC and median NDIR signals produced one-minute data that co-varied with co-located reference instruments. The temporal resolution, response time and recovery of the EC and NDIR devices meant that they successfully identified locations where CO and CO_2 concentration variations occurred. CH_4 MOS sensors were tested in the same experiment and the median MOS did not correlation or co-vary with the CH_4 reference observations. This was potentially because the MOS sensor were too susceptible to influence from additional external factors such as vibration of the vehicle, air flow rate and because their response times to changing CH_4 concentrations was not fast enough. MOS sensors were therefore found to be unsuitable for vehicle bound mobile measurements.

3. LCS could be used for source apportionment and characterisation. The low-cost and small size of a LCS instrument means that multiple instruments could be deployed for a short time period to increase the coverage of pollution measurements. Examples of this would be to identify emission sources that were previously unknown or to estimate flux emissions.

The fast response and portability of MOS and EC LCS make them ideal for deploying in a high-density network. By combining the LCS sensor instrument data with additional measurements such as wind speed and direction this may identify localised emission sources that were suspected or previously unknown. After *in situ* co-location with the reference instruments for calibration the LCS could be discretely left unattended to provide data

coverage in a localised area for a fortnight. When the wind was blowing from the emission source to each deployed sensor a peak in the signal would occur. By comparing the results from the spatially spread EC or MOS with wind direction and speed data, the emission source could be identified. The MOS and EC would indicate peaks in their timeseries that could be attributed to a source upwind of the sensors location after the effects of temperature and humidity were ruled out. By monitoring these environmental conditions in the LCS instrument and by comparing the signals of different LCS in the sensor instrument, it is simple to examine if the temperature or humidity had impacted the signal. For example, if the point source emitted CO, the increased response in the CO EC would be compared against the median NO_2 and O_X EC to identify if they were all responding to an environmental condition or if it was a genuine CO peak. The absolute concentrations of the pollutants would not necessarily have to be accurate as this might help to position additional research equipment to quantify the emissions from that source. Since different models of MOS sensors displayed different sensitivities towards VOCs, e.g. the TGS2602 total VOC MOS displayed a higher sensitivity towards aromatic compounds whereas, the TGS2620 OVOC MOS displayed a lower sensitivity towards aromatics, but higher sensitivity towards alkanes, it may be possible to identify sources of VOCs using pattern recognition software. The MOS array would need to be exposed to a comprehensive collection of different VOC compositions in the laboratory or during a training period, and the relative responses of each MOS sensor recorded as a 'fingerprint' for that VOC mixture. Pattern recognition software would then be able to estimate the VOC composition based on the fingerprint of MOS sensor responses that were produced in the field [169].

LCS EC and NDIR would be applicable for estimate the spatial scales impacted by a point source. By deploying multiple LCS instruments at different distances to a point source the magnitude of the peaks in the LCS signal would indicate the distance over which the pollution gradient occurred. The MOS are considered unsuitable for this application as their sensitivity towards VOCs and environmental conditions changed over time, therefore it would be mis-leading to compare the size of MOS signal peaks at different locations.

Indicative estimates of emission fluxes could be determined by deploying multiple sensor instruments at different vertical levels. The EC and NDIR sensors proved that they were capable of fast time resolution data that co-varied with a reference instrument when they were deployed in the van. Therefore, the EC and NDIR sensors could potentially provide information about vertical pollution gradients for multiple pollutants. Each LCS instrument could be calibrate at the ground level with an AQM, then after a suitable calibration week or training data set each could be deployed at different heights for a short term (weeks) experiment. There would be confidence in the data reported by the EC or NDIR sensors for the subsequent few weeks, and the LCS instrument could be further calibrated at each height to ensure that the training conditions were similar to those experienced in the testing period. The low-power, small size, light-weight properties of

a LCS instrument make this a more practical solution than deploying multiple reference instruments on a tall tower.

4. Smart decisions. There are already studies to show how CO_2 NDIR sensors can be used for smart ventilation. By co-locating LCS in and outside of a building the devices can be used to identify if, additional ventilation is required (air quality in <air quality out) or if the outdoor pollution is degrading the indoor air quality and windows should be closed (air quality in >air quality out) [99] [113]. Whilst the EC have been shown to have high inter-sensor reproducibility these sensors may not be suitable for comparing indoor and outdoor air quality. The environmental conditions between the two environments would lead to the air the sample is exposed to being different. Therefore they will be responding to multiple different external conditions and may lead to an inaccurate decisions being made. They could potentially be used for this purpose if separate ML techniques were applied to both locations and it was proven that both sets of EC exhibited the consistent responses over the timescales of the deployment. Both would have to prove they were comparable to a reference a pro-longed period of time (year) as these smart ventilation systems would be used long term. NO_2 EC could provide traffic emissions information to a local authority of council about to be able to make smart decisions about handling traffic flow issues. A LCS instrument could be deployed at a roadside to indicate when the highest pollution episodes were occurring at a junction and to correlate these with traffic light signals. The EC respond on a high enough time resolution to detect peaks in NO_2 due to rush-hour and would be a cost-effective method of identifying the effectiveness of a new mitigation protocol if one was put in place to reduce traffic emissions. The LCS instrument could easily be co-located with a reference monitor by deploying it at a near-by AQM and laboratory experiments could be conducted, to ensure the full range of NO_2, O_3 and CO concentrations were exposed to the LCS instrument during training. The findings from experiments with ML in this research project suggest that, with use of ML and frequent (every two weeks) re-co-location with the reference instruments the concentration estimates of traffic pollution for NO_2, O_3 and CO would be accurate.

VOC LCS displayed a higher temporal resolution than the instrumentation currently used for legislative purposes (GC-FID). On the condition that the VOC MOS sensors could be temperature and humidity corrected, they would be suitable for smart sampling. A cluster of MOS co-located with an automatic WAS sampler could automatically initiate a WAS sample being taken if there was a peak in the median MOS signal (that was not detected in the RH/temp. profile). The real-time total VOC MOS measurements could be used to identify peaks in the bulk atmospheric VOC mixing ratio. This information could be relayed to a micro-computer and be used to automatically initiate a Whole Air Sample, which would be analysed using GC-MS or GC-FID at a later date, see Fig. 6.3. GC-MS or GC-FID analysis would then provide further information about the VOC composition and would quantify the different VOCs that caused the pollution spike. However, the issues of

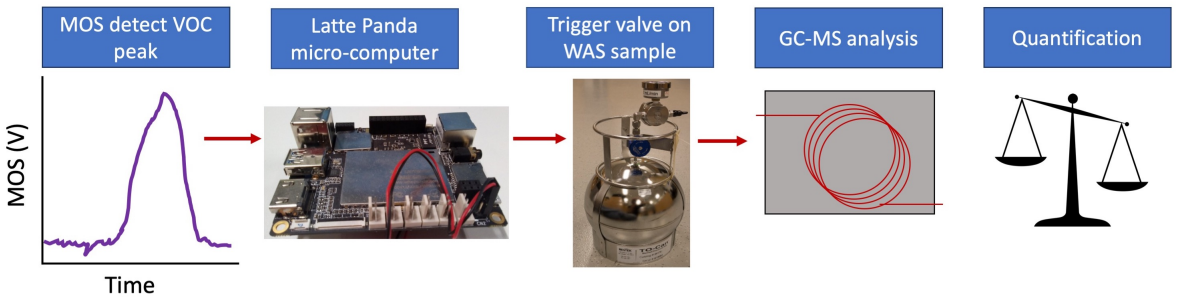

Figure 6.3: Flow chart to show the process by which the real-time spikes in total VOC levels detected by the MOS sensors could be useful for automatically sampling the air for GC-MS analysis. This would decrease the chances of missing peaks in the VOC mixing ratio and help atmospheric research.

the temperature and humidity dependence of the MOS sensor would need to be accounted for. These two environmental conditions could be monitored and a new WAS sample taken only if the peak in MOS signal did not exactly match a peak in the temperature and humidity data. This would not require indicative measurements and be irrespective of drift so long as the sensitivity of the MOS sensors did not drift significantly over the deployment. Chapter 3 found that by using a cluster of MOS the mid-term drift of any individual MOS sensor is reduced making MOS sensors more suitable for this application.

Another use for identifying temporal variability is to determine at what point in the day pollution peaks. This might be useful for identifying diurnal patterns, such as determining when rush hour traffic emissions occur or local sources of pollution that might otherwise be missed. This would be possible by using multiple pollutant LCS instruments and also monitoring the environmental conditions.

5. Citizen science and education The inexpensive nature of LCS make then a viable option for citizen science projects, use by local authorities, schools and the general public. The high time resolution of the measurements is advantageous for as the preliminary results are produced almost immediately after a pollution event. Therefore LCS can be useful for generating awareness of air quality issues. EC cost approximately £50 and MOS are typically around £10. Both of these types of LCS also report data in near real-time and would be useful for educating people about air quality issues. CO, O_X and NO_2 are also criteria pollutants that would be useful for indicating to people where pollution hotspots due to traffic or combustion occur. The LCS instrument produced as part of this thesis was relatively robust and could be supplied to a school for the students to use to gather information about local air quality and learn about pollution. Citizen science projects, to informally identify pollution events and sources could also use MOS and EC sensors. The work conducted in this project would mean that EC sensors would be recommended over MOS as it was found that the EC performance in the field was generally more reliable, closer to a reference and less susceptible to changing environmental conditions than the MOS sensors. OPCs and NDIR sensors are more expensive, on the order of £200, and

therefore might not be as suitable for low-cost use with schools and local authorities. Both these techniques do provide real-time measurements of their target measurands, which is important for education and citizen science.

6.2.1 Future work

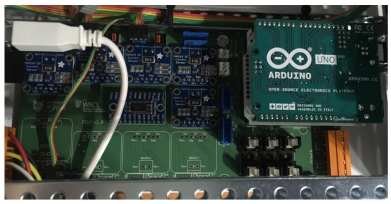

New circuit boards to power electronic components including sensors

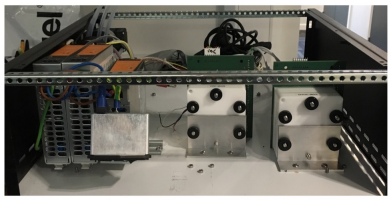

Under side of composite contains MOS sensors, pumps and power supplies.

Figure 6.4: Photos to show some of the changes being made to the next iteration of the sensor instrument. These alterations are occurring to enable the sensor instrument to be easy to use and be able to be assessed remotely.

The work in this research project has shown that the EC sensors can be used to make accurate and precise measurements of ambient levels of pollutants with proper calibration. ML techniques provided a good technique for solving the EC issues around reproducibility and robustness, and therefore there are many applications where EC sensors will be suitable. Further experiments are required to characterise sensor behaviour over longer (month - year) periods of time. The prototype sensor instrument designs used for this research have been used to build a independent sensor instrument, which can be used in 'plug-and-play' format and which are due to be deployed in the near future. The future LCS instrument will continue to use the clustering approach and will monitor multiple pollutants to obtain the optimum sensor data collection. The same type of sensors, MOS, EC and NDIR will be used for the measurement of gaseous atmospheric compounds.

Updates to the sensor instrument include:

Table 6.5: Improvements to the LCS instrument, to optimise the performance of the instrument and to make it simple to use and robust in the field.

Optimisation	Implemented changes to LCS instrument	Expected improvement for LCS
Optimise micro-controller	Replace LattePanda for Raspberry Pi	The prototype LCS used a LattePanda which was analogous to a laptop for data capture and storage. Whilst useful because the LattePanda allowed changes to the code to be made, this was not necessary for future applications now that the code had been refined. Raspberry Pi are less expensive and can be pre-loaded with code so that a new one can be sent out to replace a faulty micro-controller easily and simply.
Optimise LCS instrument interface	Retain USB ports to allow keyboard and mouse to still be added but add a touch screen	This would stream-line the instrument so that it is easy to use and operate by operatives in the field.
Newly designed manifolds for EC	Replace individual EC manifolds for one manifold that is machined out of one piece of Teflon and sandwiched between two sheet of metal	The air flowing through the instrument will only be exposed to the PTFE, to minimise the loss of compounds to the metal joints. The metal will make the manifold airtight and the sensors will remain at the temperature of this thermal sink. The sensors can also be mounted very close together, reducing the space required.
Optimise design of electronic circuit board	The new circuit board incorporates the electronics for more components and reduces the number of wires in the instrument	The design will reduce electrical noise and facilitate the replacement of failing sensors and parts, making the LCS instrument easier to use in the field.
Use of a composite board	All sensors mounted to a composite board	This acts as a Faraday cage, reducing the electrical noise in the sensors. Also thermally isolates the sensors from heat producing components such as power supply and pumps.

Optimising data capture	Add SD clock and SD card to micro-controller (Arduinos)	The SD clock automatically puts a time stamp on the data and the SD card will be used to store a back-up of the data to ensure the data is not lost if the Raspberry Pi fails.
Additional chemical sensors	6 NO EC sensors added	This increases the number of pollutants monitored by the LCS instrument so it is better equipped to correct for cross interferences.
Additional environmental conditions monitored	Pressure, flow rate, box temperature all additionally monitored	Additional environmental parameters that are monitored will help to identify other conditions that may impact the sensors signals. They might also be useful for identifying if the calibration period is significantly different to the conditions experienced by the LCS instrument in the field.
Monitor electrical circuitry	The current drawn from all electrical components is being monitored	This is useful for trouble-shooting and quickly identifying if a component, such as a pump, begins to fail as the drawn current by that component will decrease. A replacement part can then be fitted and quick detection of failing parts maximises data capture. Potentially, the identification of failing sensors can be conducted in this manner too.

Multiple successors to the sensor instrument prototypes are in the process of being built. Two of them will be deployed, co-located with reference instruments to investigate sensor performance over long periods of time. It is not currently known how the sensors behave after prolonged deployments on the time scale of years. The new LCS instruments are due to be deployed to investigate the performance of LCS over longer timescales. The instruments were designed based on the results reported from the LCS instrument prototype used to evaluate LCS in this research project. They have been optimised to improve data capture and increase ease of use to make them more suitable for deployment in the field. One will be deployed in York (England) city centre alongside a NERC super-site for ambient measurements of outdoor air quality. The site is located on top of a building and is a long-term urban monitoring station, so all the relevant reference instruments are present for sensor performance evaluation. Another sensor instrument is to be deployed in South Africa, again at a monitoring site containing reference instruments. The sensors will also be stationed there for over a year and it will be interesting to investigate how the sensors behave in a different climate over longer time scales.

Looking even further into the future there are plans to design an internal calibration unit within the sensor instrument. For a sensor instrument to work as a stand alone unit, there needs to be confidence in the data after it has moved away from reference instruments. A calibration unit, to introduce a gas standard of mixed gases to the sensors, whilst maintaining ambient levels of humidity is required, but would allow a traceable history of sensor responses that can be used to calibrate or identify when the sensors require co-location. This would also be useful for determining the drift of the sensor response to the same calibration gas over time, and would indicate if sensors were failing.

6.2.2 Overall summary

The results from this work have proven that clustered EC LCS can be used to make concentration estimates that are comparable to reference observations. With the application of ML techniques upon a multi-pollutant LCS instrument data set it was possible to calculate accurate NO_2, O_X and CO concentration estimates. Further work and improvements to the MOS sensors are required to produce robust and reproducible total VOC concentration estimates. The LCS instrument would be useful for improving the spatial density of pollution measurements over a short timescale which has many benefits, from better validation of atmospheric models to improved personal exposure estimate. Both indoor and outdoor pollution can be assessed by the LCS measurement, and this work has shown that the EC and NDIR were successful in identifying pollution hotspots whilst installed upon a mobile platform. Using the LCS instrument to monitor multiple criteria pollutants makes it a powerful technique that can be used for source apportionment and characterisation. LCS measurements can be used to establish a network to answer research questions regarding the spatial impact of pollution in a more practical manner than deploying multiple reference instruments. The reliability and robustness of sensor measurements was shown to be sufficient over a short-term period, and can therefore be used to assess the air quality in a localised region or identify the effectiveness of pollution mitigation programmes. With appropriate calibration techniques and LCS can positively contribute to the number of pollution measurements and would be suitable for complementing an existing air quality network.

Abbreviations

AED	Aerodynamic Equivalent Diameter
AQM	Air Quality Monitoring
AURN	Automatic Rural and Urban Network
BAMs	Beta-Attenuation Monitor
BLR	Boosted linear regression
BRT	Boosted regression trees
CAPS	Cavity Attenuated Phase Shift
CE	Counter Electrode
CH_4	Methane
CIMS	Chemical Ionisation Mass Spectrometry
CL	Chemiluminescence
CO	Carbon monoxide
CO_2	Carbon dioxide
CV	Cross validation
DEFRA	Department for Environment, Food and Rural Affair
EA	Environment Agency
EC	Electrochemical sensor
EU	European Union
FFT	Fast Fourier Transform
FID	Flame Ionisation Detection
GC	Gas Chromatography
GC-MS	Gas Chromatography with Mass Spectrometry
GHG	Greenhouse gas
GP	Gaussian Process
IAP	Institute of Atmospheric Physics, Beijing
IR	Infra-Red
ISB	Individual sensor board
LCS	Low cost sensor
LED	Light emitting diode
LoD	Limit of Detection
MAE	Mean Absolute Error

MCERTS	Monitoring emissions to air, land and water
ML	Machine Learning
MOS	Metal oxide sensor
$N2_2$	Nitrogen
NDIR	Non-Dispersive Infra-Red
nm	Nanometer
NMHC	Non-methane hydrocarbons
NO	Nitrogen monoxide
NO_2	Nitrogen dioxide
N_2O_5	Dinitrogen pentoxide
NO_3	Nitrate radical
NO_X	Nitrogen oxides (NO + NO_2)
NPL	National Physics Laboratory
NRMSE	Normalised Root Mean Squared Error
O_3	Ozone
O&NG	Oil and Natural Gas
OVOC	Oxygenated volatile organic compound
PAG	Pure Air Generator
PAH	Polycyclic aromatic hydrocarbons
PAN	Peroxyacyl nitrates
pdf	Probability density function
PFA	Perfluoroalkoxy
PID	Photoionistion detector
POPS	Printed Optical Particle Spectrometer
ppb	Parts per billion
ppm	Parts per million
ppt	Parts per trillion
PM	Particulate matter
PrBu	Propane/butane MOS sensors
RE	Reference Electrode
RH	Relative Humidity
RMSE	Root Mean Squared Error
rtp	Room temperature and pressure
sccm	Standard cubic centimetres per minute
SIFT-MS	Selected Ion Flow Tube with Mass Spectrometry
SLR	Simple Linear Regression
SnO_2	Tin dioxide
SO_2	Sulphur dioxide

SOA	Secondary Organic Aerosol
TEOM	Tapered Element Oscillating Microbalance
TMB	Trimethylbenzene
TSP	Total Suspended Particles
US	United States
UV	Ultra-violet radiation
VOC	Volatile Organic Compound
VUV	Vacuum Ultra-violet
WAS	Whole Air Sample
WE	Working Electrode
WHO	World Health Organisation

Bibliography

[1] Alphasense. AAN 104 How Electrochemical Sensors work, 2016.

[2] Anderson, J. O., Thundiyil, J. G., and Stolbach, A. Clearing the Air: A Review of the Effects of Particulate Matter Air Pollution on Human Health. *Journal of Medical Toxicology 8*, 2 (2012), 166–175.

[3] Aromolo, R., Savi, F., Salvati, L., Ilardi, F., Moretti, V., and Fares, S. Particulate matter and meteorological conditions in Castelporziano forest: a brief commentary. *Rendiconti Lincei 26*, April (2015), 269–273.

[4] Atkinson, R. Atmospheric Chemistry of VOCs and NOx. *Atmospheric Environment 34* (2000), 2063–2101.

[5] Barmpadimos, I., Keller, J., Oderbolz, D., Hueglin, C., and Prévôt, A. S. One decade of parallel fine (PM2.5) and coarse (PM10-PM2.5) particulate matter measurements in Europe: Trends and variability. *Atmospheric Chemistry and Physics 12*, 7 (2012), 3189–3203.

[6] Barsan, N., Koziej, D., and Weimar, U. Metal oxide-based gas sensor research: How to? *Sensors and Actuators, B: Chemical 121*, 1 (2007), 18–35.

[7] Barsan, N., and Weimar, U. Conduction model of metal oxide gas sensors. *Journal of Electroceramics 7* (2001), 143–167.

[8] Barsan, N., and Weimar, U. Understanding the fundamental principles of metal oxide based gas sensors; the example of CO sensing with SnO2 sensors in the presence of humidity. *Journal of Physics : Condensed Matter 15* (2003), 813–839.

[9] Barsan, N., and Weimar, U. Fundamentals of Metal Oxide Gas Sensors. *MCS 2012 – The 14th International Meeting on Chemical Sensors* (2012), 618–621.

[10] Barthelmie, R. J., and Pryor, S. C. Implications of ammonia emissions for fine aerosol formation and visibility impairment - A case study from the Lower Fraser Valley, British Columbia. *Atmospheric Environment 32*, 3 (1998), 345–352.

[11] Batault, F., Thevenet, F., Hequet, V., Rillard, C., Le Coq, L., and Locoge, N. Acetaldehyde and acetic acid adsorption on TiO2 under dry and humid conditions. *Chemical Engineering Journal 264* (2015), 197–210.

[12] Bauwens, M., Stavrakou, T., Müller, J. F., De Smedt, I., Van Roozendael, M., Van Der Werf, G. R., Wiedinmyer, C., Kaiser, J. W., Sindelarova, K., and Guenther, A. Nine years of global hydrocarbon emissions based on source inversion of OMI formaldehyde observations. *Atmospheric Chemistry and Physics 16*, 15 (2016), 10133–10158.

[13] Bell, M., McDermott, A., Zeger, S., Samet, J., and Dominici, F. Ozone and mortality in 95 US urban communities, 1987 to 2000. *JAMA, National Institutes of Health 292*, 19 (2004), 2372–2378.

[14] Blanchard, C. L., and Fairley, D. Spatial mapping of VOC and NOx-limitation of ozone formation in central California. *Atmospheric Environment 35*, 22 (2001), 3861–3873.

[15] Bobbink, R., Hornung, M., and Roelofs, J. M. The Effects of Air-Borne Nitrogen Pollutants on Species Diversity in Natural and Semi- Natural European Vegetation. *Journal of Ecology 86*, 5 (1998), 717–738.

[16] Bohnenstengel, S. I., Belcher, S. E., AIken, A., Allan, J. D., Allen, G., Bacak, A., Bannan, T. J., Barlow, J. F., Beddows, D. C. S., Bloss, W. J., Booth, A. M., Chemel, C., Coceal, O., Marco, C. F. D., Dubey, M. K., Faloon, K. H., Fleming, Z. l., Furger, M., GIetl, J. K., Graves, R. R., Green, D. C., Grimmond, C. S. B., HalIos, C. H., Hamilton, J. F., HarrIson, R. M., Heal, M. R., Heard, D. E., Helfter, C., Herndon, S. C., Holmes, R. E., Hopkins, J. R., Jones, A. M., Kelly, F. J., Kotthaus, S., Langford, B., Lee, J. D., Leigh, R. J., LewiS, A. C., Lidster, R. T., Lopez-HilfIker, F. D., McQuaid, J. B., Mohr, C., Monks, P. S., Nemitz, E., Ng, N. l., Percival, C. J., Prévôt, A. S. H., Ricketts, H. M. A., SokhI, R., Stone, D., Thornton, J. A., Tremper, A. H., Valach, A. C., Visser, S., Whalley, L. K., Williams, L. R., Xu, L., Young, D. E., and Zotter, P. Meteorology, air quality, and health in london, The ClearFlo project. *American Meteorological Society*, May (2015), 779–804.

[17] Booker, F., Muntifering, R., McGrath, M., Burkey, K., Decoteau, D., Fiscus, E., Manning, W., Krupa, S., Chappelka, A., and Grantz, D. The Ozone Component of Global Change: Potential Effects on Agricultural and Horticultural Plant Yield, Product Quality and Interactions with Invasive Species. *Journal of Integrative Plant Biology 51*, 4 (4 2009), 337–351.

[18] Brauer, M., Amann, M., Burnett, R. T., Cohen, A., Dentener, F., Ezzati, M., Henderson, S. B., Krzyzanowski, M., Martin, R. V., Van Dingenen, R., Van Donkelaar, A., and Thurston, G. D. Exposure assessment for estimation of the global burden of disease attributable to outdoor air pollution. *Environmental Science and Technology 46*, 2 (2012), 652–660.

[19] Broday, D. M., Arpaci, A., Bartonova, A., Castell-Balaguer, N., Cole-Hunter, T., Dauge, F. R., Fishbain, B., Jones, R. L., Galea, K., Jovasevic-Stojanovic, M., Kocman, D., Martinez-Iñiguez, T., Nieuwenhuijsen, M., Robinson, J., Svecova, V., and Thai, P. Wireless distributed environmental sensor networks for air pollution measurement-the promise and the current reality. *Sensors (Switzerland) 17*, 10 (2017), 2263.

[20] Broekhuizen, K., Chang, R. Y., Leaitch, W. R., Li, S., and Abbatt, J. P. D. Closure between measured and modeled cloud condensation nuclei (CCN) using size-resolved aerosol compositions in downtown Toronto. *Atmospheric Chemistry and Physics 6* (2006), 2513–2524.

[21] Brown, J. S., Zeman, K. L., and Bennett, W. D. Ultrafine particle deposition and clearance in the healthy and obstructed lung. *American Journal of Respiratory and Critical Care Medicine 166*, 9 (2002), 1240–1247.

[22] Caron, A., Redon, N., Hanoune, B., and Coddeville, P. Performances and limitations of electronic gas sensors to investigate an indoor air quality event. *Building and Environment 107* (2016), 19–28.

[23] Carslaw, D. C., Beevers, S. D., Tate, J. E., Westmoreland, E. J., and Williams, M. L. Recent evidence concerning higher NOx emissions from passenger cars and light duty vehicles. *Atmospheric Environment 45*, 39 (2011), 7053–7063.

[24] Castell, N., Dauge, F. R., Schneider, P., Vogt, M., Lerner, U., Fishbain, B., Broday, D., and Bartonova, A. Can commercial low-cost sensor platforms contribute to air quality monitoring and exposure estimates ? *Environment International 99* (2017), 293–302.

[25] Chappell, N. Danum & Bukit Atur Climatology, 2003.

[26] Chen, T., and Guestrin, C. XGBoost: A Scalable Tree Boosting System. *Knowledge Discovery and Data Mining* (2016).

[27] Chevalier, A., Gheusi, F., Delmas, R., Ordóñez, C., Sarrat, C., Zbinden, R., Thouret, V., Athier, G., and Cousin, J. M. Influence of altitude on ozone levels and variability in the lower troposphere: A ground-based

study for western Europe over the period 2001-2002. *Atmospheric Chemistry and Physics 7*, 16 (2007), 4311–4326.

[28] Clarke, A. G., and Tomlin, A. S. The Atmosphere. In *Understanding our Environment: An Introduction to Environmental Chemistry and Pollution : Edition 3*, R. M. Harrison, Ed., 3 ed. Royal Society of Chemistry, 1992, ch. Chapter 2, pp. 9–70.

[29] Cole, P. V. Comparative effects of atmospheric pollution and cigarette smoking on carboxyhaemoglobin levels in man. *Nature 255*, 5511 (1975), 699–701.

[30] Crilley, L. R., Shaw, M., Pound, R., Kramer, L. J., Price, R., Young, S., Lewis, A. C., and Pope, F. D. Evaluation of a low-cost optical particle counter (Alphasense OPC-N2) for ambient air monitoring. *Atmospheric Measurement Techniques 11*, 2 (2018), 709–720.

[31] Cross, E. S., Hunter, J. F., Carrasquillo, A. J., Franklin, J. P., Herndon, S. C., Jayne, J. T., Worsnop, D. R., Miake-Lye, R. C., and Kroll, J. H. Online measurements of the emissions of intermediate-volatility and semi-volatile organic compounds from aircraft. *Atmospheric Chemistry and Physics 13*, 15 (2013), 7845–7858.

[32] Cross, E. S., Williams, L. R., Lewis, D. K., Magoon, G. R., Onasch, T. B., Kaminsky, M. L., Worsnop, D. R., and Jayne, J. T. Use of electrochemical sensors for measurement of air pollution: Correcting interference response and validating measurements. *Atmospheric Measurement Techniques 10*, 9 (2017), 3575–3588.

[33] Daniel, J. S., and Solomon, S. On the climate forcing of carbon monoxide. *Journal of Geophysical Research Atmospheres 103*, D11 (1998), 13249–13260.

[34] Danielsen, E. F. Stratospheric-Tropospheric Exchange Based on Radioactivity, Ozone and Potential Vorticity. *Journal of the Atmospheric Sciences 25* (1968), 502–518.

[35] De Vito, S., Piga, M., Martinotto, L., and Di Francia, G. CO, NO2 and NOx urban pollution monitoring with on-field calibrated electronic nose by automatic bayesian regularization. *Sensors and Actuators, B: Chemical 143*, 1 (2009), 182–191.

[36] DEFRA. Local Air Quality Management Policy Guidance (PG16). Tech. rep., DEFRA, London, 2016.

[37] DEFRA. Quality Assurance and Quality Control (QA / QC) Procedures for UK Air Quality Monitoring under 2008 / 50 / EC and 2004/107/EC. *Department for Environment, Food and Rural Affairs 2013*, September (2016), 1–106.

[38] DEFRA. UK plan for tackling roadside nitrogen dioxide concentrations. *Department for Environment, Food and Rural Affairs 1* (2017), 1–11.

[39] Dempsey, F. Observations of stratospheric O3intrusions in air quality monitoring data in Ontario, Canada. *Atmospheric Environment 98* (2014), 111–122.

[40] Department for Environment Food & Rural Affairs. Air Pollution in the UK 2016. *Annual Report 2016 Issue 2*, September (2017), 131.

[41] Department for Environment Food & Rural Affairs. DEFRA Monitoring Networks Website, 2019.

[42] Derwent, R. G., Middleton, D. R., Field, R. A., Goldstone, M. E., Lester, J. N., and Perry, R. Analysis and interpretation of air quality data from an urban roadside location in Central London over the period from July 1991 to July 1992. *Atmospheric Environment 29*, 8 (1995), 923–946.

[43] Dinh, T. V., Choi, I. Y., Son, Y. S., and Kim, J. C. A review on non-dispersive infrared gas sensors: Improvement of sensor detection limit and interference correction. *Sensors and Actuators, B: Chemical 231* (2016), 529–538.

[44] Doherty, R. M., Wild, O., Shindell, D. T., Zeng, G., MacKenzie, I. A., Collins, W. J., Fiore, A. M., Stevenson, D. S., Dentener, F. J., Schultz, M. G., Hess, P., Derwent, R. G., and Keating, T. J. Impacts of climate change on surface ozone and intercontinental ozone pollution: A multi-model study. *Journal of Geophysical Research Atmospheres 118*, 9 (2013), 3744–3763.

[45] Dominici, F., Peng, R. D., Bell, M. L., Mcdermott, A., Zeger, S. L., and Samet, J. M. Fine Particulate Air Pollution and Hospital Admission for Cardiovascular. *American Medical Association 295*, 10 (2006), 1127–1134.

[46] Duan, J., Tan, J., Yang, L., Wu, S., and Hao, J. Concentration , sources and ozone formation potential of volatile organic compounds (VOCs) during ozone episode in Beijing. *Atmospheric Research 88* (2008), 25–35.

[47] Dunlea, E. J., Herndon, S. C., Nelson, D. D., Volkamer, R. M., San Martini, F., Sheehy, P. M., Zahniser, M. S., Shorter, J. H., Wormhoudt, J. C., Lamb, B. K., Allwine, E. J., Gaffney, J. S., Marley, N. A., Grutter, M., Marquez, C., Blanco, S., Cardenas, B., Retama, A., Yillegas, C. R., Kolb, C. E., Molina, L. T., and Molina, M. J.

Evaluation of nitrogen dioxide chemiluminescence monitors in a polluted urban environment. *Atmospheric Chemistry and Physics 7*, 10 (2007), 2691–2704.

[48] Edwards, P. M., Brown, S. S., Roberts, J. M., Ahmadov, R., Banta, R. M., deGouw, J. A., Dubé, W. P., Field, R. A., Flynn, J. H., Gilman, J. B., Graus, M., Helmig, D., Koss, A., Langford, A. O., Lefer, B. L., Lerner, B. M., Li, R., Li, S.-M., McKeen, S. A., Murphy, S. M., Parrish, D. D., Senff, C. J., Soltis, J., Stutz, J., Sweeney, C., Thompson, C. R., Trainer, M. K., Tsai, C., Veres, P. R., Washenfelder, R. A., Warneke, C., Wild, R. J., Young, C. J., Yuan, B., and Zamora, R. High winter ozone pollution from carbonyl photolysis in an oil and gas basin. *Nature 514*, 7522 (2014), 351–354.

[49] Environment Agency. Performance Standards for Continuous Ambient Air Quality Monitoring Systems. *MCERTS 8*, June (2012), 1–30.

[50] Environmental Protection Department. Telford and Wrekin Air Quality Annual Status Report (ASR). Tech. rep., Public Protection, Telford and Wrekin Council, Telford, 2018.

[51] Esposito, E., De Vito, S., Salvato, M., Bright, V., Jones, R. L., and Popoola, O. Dynamic neural network architectures for on field stochastic calibration of indicative low cost air quality sensing systems. *Sensors and Actuators, B: Chemical 231* (2016), 701–713.

[52] EU. Directive 2004/107/EC of the European Parliament and the Council of the European Union. *Official Journal of the European Union*, 1882 (2005).

[53] EU. Directive 2008/50/EC of the European Parliament and of the Council of 21 May 2008 on ambient air quality and cleaner air for Europe. *European Union* (2008), 1–62.

[54] European comission. Amendment No 459/2012 as regards emissions from light passenger and commercial vehicles (Euro 6). *Official Journal of the European Union 2012*, 459/2012 (2012), 16–24.

[55] European Commission. Sentinel-5 Precursor: DATA ACCESS AND PRODUCTS. Tech. rep., European Space Agency (ESA), Paris, 2015.

[56] Europen Union. COMMISSION REGULATION (EC) No 692/2008 of 18 July 2008 implementing and amending Regulation (EC) No 715/2007 of the European Parliament and of the Council on type-approval of motor vehicles with respect to emissions from light passenger and commercial veh. *Official Journal of the European Union L199*, 1 (2008), 1 – 136.

[57] Fazlzadeh, M., Rostami, R., Hazrati, S., and Rastgu, A. Concentrations of carbon monoxide in indoor and outdoor air of Ghalyun cafes. *Atmospheric Pollution Research 6*, 4 (2015), 550–555.

[58] Feinberg, S., Williams, R., Hagler, G. S., Rickard, J., Brown, R., Garver, D., Harshfield, G., Stauffer, P., Mattson, E., Judge, R., and Garvey, S. Long-term evaluation of air sensor technology under ambient conditions in Denver, Colorado. *Atmospheric Measurement Techniques 11*, 8 (2018), 4605–4615.

[59] Fine, G. F., Cavanagh, L. M., Afonja, A., and Binions, R. Metal Oxide Semi-Conductor Gas Sensors in Environmental Monitoring. *Sensors 10*, 6 (2010), 5469–5502.

[60] Fonollosa, J., Rodríguez-Luján, I., and Huerta, R. Chemical gas sensor array dataset. *Data in Brief 3* (2015), 85–89.

[61] Fontijn, A., Sabadell, A. J., and Ronco, R. J. Homogeneous Chemiluminescent Measurement of Nitric Oxide with Ozone: Implications for Continuous Selective Monitoring of Gaseous Air Pollutants. *Analytical Chemistry 42*, 6 (1970), 575–579.

[62] Gao, R. S., Telg, H., McLaughlin, R. J., Ciciora, S. J., Watts, L. A., Richardson, M. S., Schwarz, J. P., Perring, A. E., Thornberry, T. D., Rollins, A. W., Markovic, M. Z., Bates, T. S., Johnson, J. E., and Fahey, D. W. A light-weight, high-sensitivity particle spectrometer for PM2.5 aerosol measurements. *Aerosol Science and Technology 50*, 1 (2016), 88–99.

[63] Gerbig, C., Schmitgen, S., Kley, D., Volz-thomas, A., and Dewey, K. An improved fast-response vacuum-UV resonance fluorescence CO instrument. *Journal of Geophysical Research 104* (1999), 1699–1704.

[64] Gibson, N. P., Aigrain, S., Roberts, S., Evans, T. M., Osborne, M., and Pont, F. A Gaussian process framework for modelling instrumental systematics: Application to transmission spectroscopy. *Monthly Notices of the Royal Astronomical Society 419*, 3 (2012), 2683–2694.

[65] Gilman, J. B., Kuster, W. C., Goldan, P. D., Herndon, S. C., Zahniser, M. S., Tucker, S. C., Brewer, W. A., Lerner, B. M., Williams, E. J., Harley, R. A., Fehsenfeld, F. C., Warneke, C., and Gouw, J. A. D. Measurements of volatile organic compounds during the 2006 TexAQS GoMACCS campaign : Industrial influences , regional characteristics , and diurnal dependencies of the OH reactivity. *Journal of Geophysical Research: Atmospheres 114* (2009), 1–17.

[66] Gilman, J. B., Lerner, B. M., Kuster, W. C., and Gouw, J. A. D. Source Signature of Volatile Organic Compounds from Oil and Natural Gas Operations in Northeastern Colorado. *Environmental science & technology 47* (2013), 1297 – 1305.

[67] Google. Area of UK, Google, 2019.

[68] Gulia, S., Nagendra, S. M. S., Barnes, J., and Khare, M. Urban local air quality management framework for non-attainment areas in Indian cities. *Science of the Total Environment 619-620*, 220 (2018), 1308–1318.

[69] Guo, J., Sun, M., Wang, T., and Lu, L. Transportation development and congestion mitigation measures of Beijing, China. *Mitigation and Adaptation Strategies for Global Change 20*, 5 (2015), 651–663.

[70] Gurney, K. R., Razlivanov, I., Song, Y., Zhou, Y., Benes, B., and Abdul-Massih, M. Quantification of fossil fuel CO2 emissions on the building/street scale for a large U.S. City. *Environmental Science and Technology 46*, 21 (2012), 12194–12202.

[71] Hagan, D. H., Isaacman-Vanwertz, G., Franklin, J. P., Wallace, L. M., Kocar, B. D., Heald, C. L., and Kroll, J. H. Calibration and assessment of electrochemical air quality sensors by co-location with regulatory-grade instruments. *Atmospheric Measurement Techniques 11*, 1 (2018), 315–328.

[72] Hagler, G. S., Williams, R., Papapostolou, V., and Polidori, A. Air Quality Sensors and Data Adjustment Algorithms: When Is It No Longer a Measurement? *Environmental Science and Technology 52*, 10 (2018), 5530–5531.

[73] Halasz, I., and Schneider, W. Quantitative Gas Chromatographic Analysis of Hydrocarbons with Capillary Column and Flame Ionization Detector. *Analytical Chemistry 33*, 8 (1961), 978–982.

[74] Helli, O., Siadat, M., and Lumbreras, M. Qualitative and quantitative identification of H 2 S / NO 2 gaseous components in different reference atmospheres using a metal oxide sensor array. *Sensors and Actuators B 103*, 2 (2004), 403–408.

[75] Herndon, S. C., Trimborn, A., Croteau, P. L., Sun, Y. L., Worsnop, D. R., Ng, N. L., Onasch, T. B., Sueper, D., Jayne, J. T., Canagaratna, M. R., and Zhang, Q. An Aerosol Chemical Speciation Monitor (ACSM) for Routine Monitoring of the Composition and Mass Concentrations of Ambient Aerosol. *Aerosol Science and Technology 45*, 7 (2011), 780–794.

[76] Hilboll, A., Richter, A., and Burrows, J. P. Long-term changes of tropospheric NO2 over megacities derived from multiple satellite instruments. *Atmospheric Chemistry and Physics 13*, 8 (2013), 4145–4169.

[77] Holtslag, A. A. M., and Nieuwstadt, F. T. M. Scaling the atmospheric boundary layer. *Boundary-Layer Meteorol 36* (1986), 201–209.

[78] Hong, H.-K., Shin, H. W., Park, H. S., Yun, D. H., Kwon, C. H., Lee, K., Kim, S.-T., and Moriizumi, T. Gas identification using micro gas sensor array and neural-network pattern recognition. *Sensors and Actuators 4005*, 96 (1996), 68–71.

[79] Hopkins, J. R., Jones, C. E., and Lewis, A. C. A dual channel gas chromatograph for atmospheric analysis of volatile organic compounds including oxygenated and monoterpene compounds. *Journal of Environmental Monitoring 13*, 8 (2011), 2268–2276.

[80] Hori, Y., Takahashi, R., Yoshinami, Y., and Murata, A. Electrochemical Reduction of CO at a Copper Electrode. *The Journal of Physical Chemistry B 101*, 36 (1997), 7075–7081.

[81] Huerta, R., Mosqueiro, T., Fonollosa, J., Rulkov, N. F., and Rodriguez-Lujan, I. Online decorrelation of humidity and temperature in chemical sensors for continuous monitoring. *Chemometrics and Intelligent Laboratory Systems 157* (2016), 169–176.

[82] IPCC. Climate Change 2014 Synthesis Report. *IPCC* (2014), 1–31.

[83] Jacob, D. J., Field, B. D., Jin, E. M., Bey, I., Li, Q., Logan, J. A., Yantosca, R. M., and Singh, H. B. Atmospheric budget of acetone. *Journal of Geophysical Research: Atmospheres 107*, D10 (2002), 1–15.

[84] Jerrett, M., Donaire-Gonzalez, D., Popoola, O., Jones, R., Cohen, R. C., Almanza, E., de Nazelle, A., Mead, I., Carrasco-Turigas, G., Cole-Hunter, T., Triguero-Mas, M., Seto, E., and Nieuwenhuijsen, M. Validating novel air pollution sensors to improve exposure estimates for epidemiological analyses and citizen science. *Environmental Research 158* (2017), 286–294.

[85] Ji, D., Cui, Y., Li, L., He, J., Wang, L., Zhang, H., Wang, W., Zhou, L., Maenhaut, W., Wen, T., and Wang, Y. Characterization and source identification of fine particulate matter in urban Beijing during the 2015 Spring Festival. *Science of the Total Environment 628-629* (2018), 430–440.

[86] Jiao, W., Hagler, G., Williams, R., Sharpe, R., Brown, R., Garver, D., Judge, R., Caudill, M., Rickard, J., Davis, M., Weinstock, L., Zimmer-Dauphinee, S., and Buckley, K. Community Air Sensor Network (CAIRSENSE) project: Evaluation of low-cost sensor performance in a suburban

environment in the southeastern United States. *Atmospheric Measurement Techniques Discussions*, June (2016), 1–24.

[87] Jongwon Kwon, Gwanghoon Ahn, Gyusik Kim, Jo Chun Kim, Hiesik Kim, Kwon, J. K. J., Ahn, G. A. G., Kim, G. K. G., Kim, J. C. K. J. C., and Kim, H. K. H. A study on NDIR-based CO2 sensor to apply remote air quality monitoring system. In *ICROS-SICE International Joint Conference 2009* (2009), IEEE, pp. 1683–1687.

[88] Kaly, F., Marticorena, B., Chatenet, B., Rajot, J. L., Janicot, S., Niang, A., Yahi, H., Thiria, S., Maman, A., Zakou, A., Coulibaly, B. S., Coulibaly, M., Koné, I., Traoré, S., Diallo, A., and Ndiaye, T. Variability of mineral dust concentrations over West Africa monitored by the Sahelian Dust Transect. *Atmospheric Research 164-165* (2015), 226–241.

[89] Kamal, M. S., Razzak, S. A., and Hossain, M. M. Catalytic oxidation of volatile organic compounds (VOCs) - A review. *Atmospheric Environment 140* (2016), 117–134.

[90] Karl, T., Graus, M., Striednig, M., Lamprecht, C., Hammerle, A., Wohlfahrt, G., Held, A., Von Der Heyden, L., Deventer, M. J., Krismer, A., Haun, C., Feichter, R., and Lee, J. Urban eddy covariance measurements reveal significant missing NO x emissions in Central Europe. *Scientific Reports 7*, 1 (2017), 1–9.

[91] Karlsson, P. E., Klingberg, J., Engardt, M., Andersson, C., Langner, J., Karlsson, G. P., and Pleijel, H. Past, present and future concentrations of ground-level ozone and potential impacts on ecosystems and human health in northern Europe. *Science of the Total Environment 576* (2017), 22–35.

[92] Kebabian, P. L., Herndon, S. C., and Freedman, A. Detection of nitrogen dioxide by cavity attenuated phase shift spectroscopy. *Analytical Chemistry 77*, 2 (2005), 724–728.

[93] Kebabian, P. L., Wood, E. C., Herndon, S. C., and Freedman, A. A practical alternative to chemiluminescence-based detection of nitrogen dioxide: Cavity attenuated phase shift spectroscopy. *Environmental Science and Technology 42*, 16 (2008), 6040–6045.

[94] Kelly, N. A., and Morgan, C. An evaluation of the tapered element oscillating microbalance method for measuring diesel particulate emissions. *Journal of the Air and Waste Management Association 52*, 12 (2002), 1362–1377.

[95] Konduru, T., Rains, G. C., and Li, C. A customized metal oxide semiconductor-based gas sensor array for onion quality evaluation: system development and characterization. *Sensors (Basel, Switzerland) 15*, 1 (2015), 1252–1273.

[96] Langford, B., Misztal, P. K., Nemitz, E., Davison, B., Helfter, C., Pugh, T. A., MacKenzie, A. R., Lim, S. F., and Hewitt, C. N. Fluxes and concentrations of volatile organic compounds from a South-East Asian tropical rainforest. *Atmospheric Chemistry and Physics 10*, 17 (2010), 8391–8412.

[97] Lee, J. D., Helfter, C., Purvis, R. M., Beevers, S. D., Carslaw, D. C., Lewis, A. C., Møller, S. J., Tremper, A., Vaughan, A., and Nemitz, E. G. Measurement of NOx fluxes from a tall tower in central London, UK and comparison with emissions inventories. *Environmental Science and Technology 49*, 2 (2015), 1025–1034.

[98] Lee Ng, N., Brown, S. S., Archibald, A. T., Atlas, E., Cohen, R. C., Crowley, J. N., Day, D. A., Donahue, N. M., Fry, J. L., Fuchs, H., Griffin, R. J., Guzman, M. I., Herrmann, H., Hodzic, A., Iinuma, Y., Kiendler-Scharr, A., Lee, B. H., Luecken, D. J., Mao, J., McLaren, R., Mutzel, A., Osthoff, H. D., Ouyang, B., Picquet-Varrault, B., Platt, U., Pye, H. O., Rudich, Y., Schwantes, R. H., Shiraiwa, M., Stutz, J., Thornton, J. A., Tilgner, A., Williams, B. J., and Zaveri, R. A. Nitrate radicals and biogenic volatile organic compounds: Oxidation, mechanisms, and organic aerosol. *Atmospheric Chemistry and Physics 17*, 3 (2017), 2103–2162.

[99] Leidinger, M., Sauerwald, T., Conrad, T., Reimringer, W., Ventura, G., and Schütze, A. Selective Detection of Hazardous Indoor VOCs Using Metal Oxide Gas Sensors. *Procedia Engineering 87* (2014), 1449–1452.

[100] Leighton, P. *Photochemistry of Air Pollution*, first ed. Academic Press Inc., New York and London, 1961.

[101] Lelieveld, J., Evans, J. S., Fnais, M., Giannadaki, D., and Pozzer, A. The contribution of outdoor air pollution sources to premature mortality on a global scale. *Nature 525*, 7569 (2015), 367–71.

[102] Lemagnen, K. Hyperparameter tuning in XGBoost, 2018.

[103] Lewis, A., Carslaw, N., Marriott, P., Kinghorn, R., Morrison, P., Lee, A., Bartle, K., and Pilling, M. A larger pool of ozone-forming carbon compounds in urban atmospheres. *Nature 405*, 6788 (2000), 778–81.

[104] Lewis, A., and Edwards, P. Validate personal air-pollution sensors. *Nature* (2016).

[105] Lewis, A. C., Lee, J., Edwards, P. M., Shaw, M. D., Evans, M. J., Moller, S. J., Smith, K., Ellis, M., Gillott, S., White, A., and Buckley, J. W. Evaluating the performance of low cost chemical sensors for air pollution research. *Faraday Discuss. 189* (2016), 85–103.

[106] Lewis, A. C., Zellweger, C., Schultz, M. G., and Tarasova, O. A. Technical advice note on lower cost air pollution sensors. *World Meteorological Organization* (2017), 1–4.

[107] Li, J., Xie, S. D., Zeng, L. M., Li, L. Y., Li, Y. Q., and Wu, R. R. Characterization of ambient volatile organic compounds and their sources in Beijing , before , during , and after Asia-Pacific Economic Cooperation China 2014. *Atmospheric Chemistry and Physics 15*, November 2014 (2015), 7945–7959.

[108] Li, W., Li, L., Chen, C. l., Kacarab, M., Peng, W., Price, D., Xu, J., and Cocker, D. R. Potential of select intermediate-volatility organic compounds and consumer products for secondary organic aerosol and ozone formation under relevant urban conditions. *Atmospheric Environment 178*, February (2018), 109–117.

[109] Li, Y., Juhasz, A. L., Ma, L. Q., and Cui, X. Inhalation bioaccessibility of PAHs in PM 2.5 : Implications for risk assessment and toxicity prediction. *Science of the Total Environment 650* (2019), 56–64.

[110] Lin, C., Gillespie, J., Schuder, M. D., Duberstein, W., Beverland, I. J., and Heal, M. R. Evaluation and calibration of Aeroqual series 500 portable gas sensors for accurate measurement of ambient ozone and nitrogen dioxide. *Atmospheric Environment 100*, 2 (2015), 111–116.

[111] Lippmann, M. Health Effects of Tropospheric Ozone. *Environmental Science and Technology 25*, 12 (1991), 1954.

[112] Liu, F., Beirle, S., Zhang, Q., Dörner, S., He, K., and Wagner, T. NOxlifetimes and emissions of cities and power plants in polluted background estimated by satellite observations. *Atmospheric Chemistry and Physics 16*, 8 (2016), 5283–5298.

[113] Liu, X., Cheng, S., Liu, H., Hu, S., Zhang, D., and Ning, H. A Survey on Gas Sensing Technology. *Sensors 12*, 7 (2012), 9635–9665.

[114] Lung, S. C., Jones, R., Zellweger, C., Karppinen, A., Penza, M., Dye, T., Hüglin, C., Ning, Z., Lewis, A. C., Schneidemesser, E. v., Peltier, R. E., Leigh, R., Hagan, D., Laurent, O., and Carmichael, G. Low-cost sensors for the measurement of atmospheric composition: overview of topic and future applications. Tech. Rep. May, Geneva, Swizterland, 2018.

[115] Luo, M., Shephard, M. W., Cady-Pereira, K. E., Henze, D. K., Zhu, L., Bash, J. O., Pinder, R. W., Capps, S. L., Walker, J. T., and Jones, M. R. Satellite observations of tropospheric ammonia and carbon monoxide: Global distributions, regional correlations and comparisons to model simulations. *Atmospheric Environment 106* (2015), 262–277.

[116] Macias, E. S., and Husar, R. B. Atmospheric Particulate Mass Measurement with Beta Attenuation Mass Monitor. *Environmental Science and Technology 10*, 9 (1976), 904–907.

[117] MacKenzie, a., Langford, B., Pugh, T., Robinson, N., Misztal, P., Heard, D., Lee, J., Lewis, A., Jones, C., Hopkins, J., Phillips, G., Monks, P., Karunaharan, A., Hornsby, K., Nicolas-Perea, V., Coe, H., Gabey, A., Gallagher, M., Whalley, L., Edwards, P., Evans, M., Stone, D., Ingham, T., Commane, R., Furneaux, K., McQuaid, J., Nemitz, E., Seng, Y. K., Fowler, D., Pyle, J., and Hewitt, C. The atmospheric chemistry of trace gases and particulate matter emitted by different land uses in Borneo. *Philosophical Transactions of the Royal Society B 366* (2011), 3177–3195.

[118] Marć, M., Tobiszewski, M., Zabiegała, B., de la Guardia, M., and Namieśnik, J. Current air quality analytics and monitoring: a review. *Analytica chimica acta 853* (2015), 116–26.

[119] Martin, C. R., Zeng, N., Karion, A., Dickerson, R. R., Ren, X., Turpie, B. N., and Weber, K. J. Evaluation and environmental correction of ambient CO2measurements from a low-cost NDIR sensor. *Atmospheric Measurement Techniques 10*, 7 (2017), 2383–2395.

[120] Masson, N., Piedrahita, R., and Hannigan, M. Quantification method for electrolytic sensors in long-term monitoring of ambient air quality. *Sensors (Switzerland) 15*, 10 (2015), 27283–27302.

[121] McKercher, G. R., Salmond, J. A., and Vanos, J. K. Characteristics and applications of small, portable gaseous air pollution monitors. *Environmental Pollution 223* (2017), 102 –110.

[122] Mead, M. I., Popoola, O. A. M., Stewart, G. B., Landshoff, P., Calleja, M., Hayes, M., Baldovi, J. J., Mcleod, M. W., Hodgson, T. F., Dicks, J., Lewis, A., Cohen, J., Baron, R., Saffell, J. R., and Jones, R. L. The use of electrochemical sensors for monitoring urban air quality in low-cost , high-density networks. *Atmospheric Environment 70* (2013), 186–203.

[123] Mellouki, A., Wallington, T. J., and Chen, J. Atmospheric Chemistry of Oxygenated Volatile Organic Compounds: Impacts on Air Quality and Climate. *Chemical Reviews 115*, 10 (2015), 3984–4014.

[124] Mills, G., Pleijel, H., Braun, S., Büker, P., Bermejo, V., Calvo, E., Danielsson, H., Emberson, L., Fernández, I. G., Grünhage, L., Harmens, H., Hayes, F., Karlsson, P. E., and Simpson, D. New stomatal flux-based critical levels for ozone effects on vegetation. *Atmospheric Environment 45*, 28 (2011), 5064–5068.

[125] Moltchanov, S., Levy, I., Etzion, Y., Lerner, U., Broday, D. M., and Fishbain, B. On the feasibility of measuring urban air pollution by wireless distributed sensor networks. *Science of the Total Environment 502* (2015), 537–547.

[126] Monks, P. S., Archibald, A. T., Colette, A., Cooper, O., Coyle, M., Derwent, R., Fowler, D., Granier, C., Law, K. S., Mills, G. E., Stevenson, D. S., Tarasova, O., Thouret, V., Von Schneidemesser, E., Sommariva, R., Wild, O., and Williams, M. L. Tropospheric ozone and its precursors from the urban to the global scale from air quality to short-lived climate forcer. *Atmospheric Chemistry and Physics 15*, 15 (2015), 8889–8973.

[127] NSAI. Ambient air quality — Standard method for the measurement of the concentration of ozone by ultraviolet photometry. 2006.

[128] Ostro, B., Hu, J., Goldberg, D., Reynolds, P., Hertz, A., Bernstein, L., and J., K. M. Associations of Mortality with Long-Term Exposures to Fine and Ultrafine Particles, Species and Sources: Results from the California Teachers Study Cohort. *Environmental Health Perspectives 123*, 6 (2015), 549–556.

[129] Ou Yang, C. F., Lin, Y. C., Lin, N. H., Lee, C. T., Sheu, G. R., Kam, S. H., and Wang, J. L. Inter-comparison of three instruments for measuring regional background carbon monoxide. *Atmospheric Environment 43*, 40 (2009), 6449–6453.

[130] Palmisano, V., Weidner, E., Boon-Brett, L., Bonato, C., Harskamp, F., Moretto, P., Post, M. B., Burgess, R., Rivkin, C., and Buttner, W. J. Selectivity and resistance to poisons of commercial hydrogen sensors. *International Journal of Hydrogen Energy 40*, 35 (2015), 11740–11747.

[131] Pandey, S. K., and Kim, K.-H. The Relative Performance of NDIR-based Sensors in the Near Real-time Analysis of CO2 in Air. *Sensors 7*, 4 (2007), 1683–1696.

[132] Parrish, D. D., Holloway, J. S., and Fehsenfeld, F. C. Routine, Continuous Measurement of Carbon Monoxide with Parts per Billion Precision. *Environmental Science and Technology 28*, 9 (1994), 1615–1618.

[133] Parrish, D. D., Xu, J., Croes, B., and Shao, M. Air quality improvement in Los Angeles—perspectives for developing cities. *Frontiers of Environmental Science and Engineering 10*, 5 (2016).

[134] Pérez, C., Jiménez, P., Jorba, O., Sicard, M., and Baldasano, J. M. Influence of the PBL scheme on high-resolution photochemical simulations in an urban coastal area over the Western Mediterranean. *Atmospheric Environment 40*, 27 (2006), 5274–5297.

[135] Petersen, J., Kristensen, J., Elarga, H., Andersen, R. K., and Midtstraum, A. Accuracy and air temperature dependency of commercial low-cost NDIR CO2 Sensors: An Experimental Investigation. *In Proceedings of COBEE2018 69*, 6 (2018), 203–207.

[136] Peterson, P. J., Aujla, A., Grant, K. H., Brundle, A. G., Thompson, M. R., Hey, J. V., and Leigh, R. J. Practical use of metal oxide semiconductor gas sensors for measuring nitrogen dioxide and ozone in urban environments. *Sensors (Switzerland) 17*, 7 (2017), 1–25.

[137] Petron, G., Guenther, D., Dlugokencky, E., Lang, P., Newberger, T., Wolter, S., White, A., Noone, D., Wolfe, D., and Schnell, R. A new look at methane and Non-methane hydrocarbon emissions from oil and natural gas operations in the Colorado Denver-Julesburg Basin. *Journal of chromatography. A 119*, 11 (2014), 6838–6852.

[138] Piedrahita, R., Xiang, Y., Masson, N., Ortega, J., Collier, A., Jiang, Y., Li, K., Dick, R. P., Lv, Q., Hannigan, M., and Shang, L. The next generation of low-cost personal air quality sensors for quantitative exposure monitoring. *Atmospheric Measurement Techniques 7*, 10 (2014), 3325–3336.

[139] Pike, R. C., Lee, J. D., Young, P. J., Carver, G. D., Yang, X., Warwick, N., Moller, S., Misztal, P., Langford, B., Stewart, D., Reeves, C. E., Hewitt, C. N., and Pyle, J. A. NOx and O3 above a tropical rainforest: An analysis with a global and box model. *Atmospheric Chemistry and Physics 10*, 21 (2010), 10607–10620.

[140] Plass-Dülmer, C., Michl, K., Ruf, R., and Berresheim, H. C2-C8Hydrocarbon measurement and quality control procedures at the Global Atmosphere Watch Observatory Hohenpeissenberg. *Journal of Chromatography A 953*, 1-2 (2002), 175–197.

[141] Pope III, C. A., Burnett, R. T., Thun, M. J., Calle, E. E., Krewski, D., and Thurston, G. D. Lung cancer, cardiopulmonary mortality long-term exposure to Fine Particulate Air Pollution. *The Journal of the American Medical Association 287*, 9 (2002), 1132–1141.

[142] Popoola, O. A., Carruthers, D., Lad, C., Bright, V. B., Mead, M. I., Stettler, M. E., Saffell, J. R., and Jones, R. L. Use of networks of low cost air quality sensors to quantify air quality in urban settings. *Atmospheric Environment 194*, February (2018), 58–70.

[143] Popoola, O. A., Stewart, G. B., Mead, M. I., and Jones, R. L. Development of a baseline-temperature correction methodology for electrochemical sensors and its implications for long-term stability. *Atmospheric Environment 147* (2016), 330–343.

[144] Putman, W. M., Ott, L., Darmenov, A., and daSilva, A. A global perspective of atmospheric carbon dioxide concentrations. *Parallel Computing 55* (2015), 2–8.

[145] Pyle, J. A., Warwick, N. J., Abas, M. R., Archibald, A. T., Ashfold, M. J., Ashworth, K., Carver, G. D., Chance, K., Dorsey, J. R., Fowler, D., Lee, J. D., Gonzi, S., Gostlow, B., Hewitt, C. N., Langford, S. B., Mills, G., Moller, S., Mackenzie, A. R., Nemitz, E., Newton, H. M., Brien, L. M. O., Ong, S., Palmer, I., Peng, L. K., Phang, S. M., Oram, D., Pike, R., Pugh, T. A. M., Rahman, N. A., Robinson, A. D., Sentian, J., Samah, A. A., and Skiba, U. The impact of local surface changes in Borneo on atmospheric composition at wider spatial scales : coastal processes , land-use change and air quality. *Philosophical Transactions of the Royal Society B 366* (2011), 3210–3224.

[146] Rainer, M. Noise power spectral density estimation based on optimal smoothing and minimum statistics. *IEEE Transactions on Speech and Audio Processing 9*, 5 (2001), 504–512.

[147] Rasmussen, C. E., and Williams, C. K. I. *Gaussian Processes for Machine Learning*, 2nd editio ed. The MIT Press, Cambridge, Massachusetts, 2006.

[148] Ravindra, K., Sokhi, R., and Van Grieken, R. Atmospheric polycyclic aromatic hydrocarbons: Source attribution, emission factors and regulation. *Atmospheric Environment 42*, 13 (2008), 2895–2921.

[149] Ravishankara, A. R., Hancock, G., Kawasaki, M., and Matsumi, Y. Photochemistry of Ozone: Surprises and Recent Lessons. *Science 280*, 5360 (1998), 60–61.

[150] Reynolds, S. D., Blanchard, C. L., and Ziman, S. D. Understanding the effectiveness of precursor reductions in lowering 8-Hr ozone concentrations. *Journal of the Air and Waste Management Association 53*, 2 (2003), 195–205.

[151] Ridley, B. A., and Howlett, L. C. An instrument for nitric oxide measurements in the stratosphere. *Review of Scientific Instruments 45*, 6 (1974), 742–746.

[152] Rieder, H. E., Fiore, A. M., Polvani, L. M., Lamarque, J. F., and Fang, Y. Changes in the frequency and return level of high ozone pollution events over the eastern United States following emission controls. *Environmental Research Letters 8*, 1 (2013).

[153] Rinsky, R. A. Leukemia in Benzene Workers. *American Journal of Industrial Medicine 2*, 3 (1981), 217–245.

[154] Rodhe, H., Crutzen, P., and Vanderpol, A. Formation of sulfuric and nitric acid in the atmosphere during long-range transport. *Tellus 33*, 2 (1981), 132–141.

[155] Romain, A. C., and Nicolas, J. Long term stability of metal oxide-based gas sensors for e-nose environmental applications: An overview. *Sensors and Actuators, B: Chemical 146*, 2 (2010), 502–506.

[156] Romain, A.-C., Nicolas, J., and Andre, P. In situ measurement of olfactive pollution with inorganic semiconductors : Limitations due to humidity and temperature influence. *Seminars in Food Analysis 2*, January 1997 (1997), 283–296.

[157] Saide, P. E., Carmichael, G. R., Spak, S. N., Gallardo, L., Osses, A. E., Mena-Carrasco, M. A., and Pagowski, M. Forecasting urban PM10 and PM2.5 pollution episodes in very stable nocturnal conditions and complex terrain using WRF-Chem CO tracer model. *Atmospheric Environment 45*, 16 (2011), 2769–2780.

[158] Sargent, M., Barrera, Y., Nehrkorn, T., Hutyra, L. R., Gately, C. K., Mckain, K., Sweeney, C., Hegarty, J., Wofsy, S. C., Sargent, M., Barrera, Y., Nehrkorn, T., Hutyra, L. R., Gately, C. K., and Jones, T. Anthropogenic and biogenic CO2 fluxes in the Boston urban region. *Proceedings of the National Academy of Sciences 115*, 40 (2018), E9507–E9507.

[159] Schultz, M. G., Akimoto, H., Bottenheim, J., Buchmann, B., Galbally, I. E., Gilge, S., Helmig, D., Koide, H., Lewis, A. C., Novelli, P. C., Plass-Dülmer, C., Ryerson, T. B., Steinbacher, M., Steinbrecher, R., Tarasova, O., Tørseth, K., Thouret, V., and Zellweger, C. The Global Atmosphere Watch reactive gases measurement network. *Elem Sci Anth 3* (2015), 1–23.

[160] Schweizer, D., Cisneros, R., and Shaw, G. A comparative analysis of temporary and permanent beta attenuation monitors: The importance of understanding data and equipment limitations when creating PM2.5air quality health advisories. *Atmospheric Pollution Research 7*, 5 (2016), 865–875.

[161] Seinfield, J. H., and Pandis, S. N. *Atmospheric Chemistry and Physics: From Air Pollution to Climate Change*, third ed. John Wiley and Sons Inc., Hoboken, New Jersey, 2016.

[162] Shapiro, M. Turbulent mixing within Tropopause Folds as a Mechanism for the Exchange of Chemical Constituents between the Stratosphere and Troposphere. *Journal of the Atmospheric Sciences 37* (1979), 994–1004.

[163] Slinn, W. G. N. Estimates for the long-range transport of air pollution. *Water, Air and Soil Pollution 18* (1982), 45–64.

[164] Smith, D., and Španěl, P. Selected ion flow tube mass spectrometry (SIFT-MS) for on-line trace gas analysis. *Mass Spectrometry Reviews 24*, 5 (2005), 661–700.

[165] Smith, K., Edwards, P. M., Evans, M. J. J., Lee, J. D., Shaw, M. D., Squires, F., Wilde, S., and Lewis, A. C. Clustering approaches that improve the reproducibility of low-cost air pollution sensors. *Faraday Discuss. 00*, 0 (2017), 1–17.

[166] Smith, K. R., Edwards, P. M., Ivatt, P. D., Lee, J. D., Squires, F., Dai, C., Peltier, R. E., Evans, M. J., Sun, Y., and Lewis, A. C. An improved low-power measurement of ambient NO2 and O3 combining electrochemical sensor clusters and machine learning. *Atmospheric Measurement Techniques 12*, 2 (2019), 1325–1336.

[167] Snyder, E. G., Watkins, T. H., Solomon, P. A., Thoma, E. D., Williams, R. W., Hagler, G. S., Shelow, D., Hindin, D. A., Kilaru, V. J., and Preuss, P. W. The changing paradigm of air pollution monitoring. *Environmental Science and Technology 47*, 20 (2013), 11369–11377.

[168] Sofen, E. D., Evans, M. J., and Lewis, A. C. Updated ozone absorption cross section will reduce air quality compliance. *Atmospheric Chemistry and Physics Discussions 15*, 14 (2015), 19537–19551.

[169] Sohn, J. H., Atzeni, M., Zeller, L., and Pioggia, G. Characterisation of humidity dependence of a metal oxide semiconductor sensor array using partial least squares. *Sensors and Actuators, B: Chemical 131*, 1 (2008), 230–235.

[170] Sousan, S., Koehler, K., Hallett, L., and Peters, T. M. Evaluation of the Alphasense optical particle counter (OPC-N2) and the Grimm portable aerosol spectrometer (PAS-1.108). *Aerosol Science and Technology 50*, 12 (2016), 1352–1365.

[171] Spinelle, L., Aleixandre, M., and Gerboles, M. *Protocol of evaluation and calibration of low-cost gas sensors for the monitoring of air pollution.* European Commission Joint Research Centre Institute for Environment and Sustainability, 2013.

[172] Spinelle, L., Gerboles, M., Aleixandre, M., and Bonavitacola, F. Evaluation of metal oxides sensors for the monitoring of O3 in ambient air at Ppb level. *Chemical Engineering Transactions 54* (2016), 319–324.

[173] Spinelle, L., Gerboles, M., Villani, M. G., Aleixandre, M., and Bonavitacola, F. Field calibration of a cluster of low-cost commercially available sensors for air quality monitoring. Part B: NO, CO and CO2. *Sensors and Actuators, B: Chemical 238* (2017), 706–715.

[174] Spinelle L, Gerboles M, Kok G, and Sauerwald T. Review of low-cost sensors for the ambient air monitoring of benzene and other volatile organic compounds. Tech. rep., European Commission, Luxembourg, 2015.

[175] Sumari, S. M., Muhamad-Darus, F., Kantasamy, N., and Urban Sinyaw, S. A. Rainwater characterization at Global Atmospheric Watch in Danum Valley, Sabah. *The Malaysian Journal of Analytical Sciences 13*, 1 (2009), 107–119.

[176] Susan C. Anenberg, Horowitz, L. W., Tong, D. Q., and West, J. An Estimate of the Global Burden of Anthropogenic Ozone and Fine Particulate Matter on Premature Human Mortality Using Atmospheric Modeling. *Environmental Health Perspectives 118*, 9 (2010), 1189 – 1195.

[177] Szymanski, W. W., Nagy, A., and Czitrovszky, A. Optical particle spectrometry-Problems and prospects. *Journal of Quantitative Spectroscopy and Radiative Transfer 110*, 11 (2009), 918–929.

[178] Takegawa, N., Kita, K., Kondo, Y., Matsumi, Y., Parrish, D. D., Holloway, J. S., Miyazaki, Y., Toriyama, N., and Kawakami, S. Airborne vacuum ultraviolet resonance fluorescence instrument for in situ measurement of CO. *Journal of Geophysical Research 106*, 20 (2001), 24237 – 24244.

[179] Thelamon, C. Measurement of ozone concentration. *Polymer Testing 3*, 2 (1982), 143–150.

[180] Turner, C. M., Krewski, D., Pope III, C. A., Chen, Y., Gapstur, S. M., and Thun, M. J. Long-term Ambient Fin Particulate Matter Air Pollution and Lung Cancer in a large cohort of never-smokers. *Hellenic Journal of Nuclear Medicine 16*, 2 (2013), 121–124.

[181] Tyndall, G. S., Cox, R. A., Lesclaux, R., Moortgat, G., Pilling, M., Ravishankara, A., and Wallington, T. Atmospheric chemistry of small organic peroxy radicals. *Journal of Geophysical Research 106*, 11 (2001), 12157–12182.

[182] United Nations Economic Commission for Europe. Executive Body for the Convention on Long-range Transboundary Air Pollution: Guidance document on health and environmental improvements using new knowledge, methods and data. *United Nations Economic and Social Council ECE/EB.AIR*, March (2014), 1–14.

[183] Vardoulakis, S., Fisher, B. E., Pericleous, K., and Gonzalez-Flesca, N. Modelling air quality in street canyons: A review. *Atmospheric Environment 37*, 2 (2003), 155–182.

[184] Vergara, A., Vembu, S., Ayhan, T., Ryan, M. A., Homer, M. L., and Huerta, R. Chemical gas sensor drift compensation using classifier ensembles. *Sensors and Actuators, B: Chemical 166-167* (2012), 320–329.

[185] Verma, M., Pervez, S., Majumdar, D., Chakrabarty, R., and Pervez, Y. F. Emission estimation of aromatic and halogenated VOCs from household solid fuel burning practices. *International Journal of Environmental Science and Technology*, 0123456789 (2018).

[186] von Schneidemesser, E., Monks, P. S., and Plass-Duelmer, C. Global comparison of VOC and CO observations in urban areas. *Atmospheric Environment 44*, 39 (2010), 5053–5064.

[187] Wang, C., Yin, L., Zhang, L., Xiang, D., and Gao, R. Metal Oxide Gas Sensors: Sensitivity and Influencing Factors. *Sensors 10*, 3 (2010), 2088–2106.

[188] Wang, S., Davidson, D. F., and Hanson, R. K. Rate constants of long, branched, and unsaturated aldehydes with OH at elevated temperatures. *Proceedings of the Combustion Institute 36*, 1 (2017), 151–160.

[189] Wang, T., Xue, L., Brimblecombe, P., Lam, Y. F., Li, L., and Zhang, L. Ozone pollution in China: A review of concentrations, meteorological influences, chemical precursors, and effects. *Science of the Total Environment 575* (2017), 1582–1596.

[190] Wang, W.-N., Cheng, T.-H., Gu, X.-F., Chen, H., Guo, H., Wang, Y., Bao, F.-W., Shi, S.-Y., Xu, B.-R., Zuo, X., Meng, C., and Zhang, X.-C. Assessing Spatial and Temporal Patterns of Observed Ground-level Ozone in China. *Scientific Reports 7*, 1 (2017), 3651.

[191] Wei, W., Li, Y., Wang, Y., Cheng, S., and Wang, L. Characteristics of VOCs during haze and non-haze days in Beijing, China: Concentration, chemical degradation and regional transport impact. *Atmospheric Environment 194*, September (2018), 134–145.

[192] Whitby, R., Gibbs, R., Johnson, R., Hill, B., Shimpi, S., and R., J. Real-Time Diesel Particulate Measurement Using A Tapered Element Oscillating Microbalance. *SAE Technical Paper 820463* (1982), 17.

[193] WHO. WHO Air quality guidelines for particulate matter, ozone, nitrogen dioxide and sulfur dioxide. *World Health Organization WHO/SDE/PH*, Global update 2005 (2005), 5 – 18.

[194] WHO. *World Health Organization guidelines for indoor air quality: household fuel combustion.*, 1 ed. World Health Organisation, Geneva, 2014.

[195] WHO. Ambient air pollution: A global assessment of exposure and burden of disease. 2016.

[196] WHO. *Evolution of WHO air quality guidelines.* 2017.

[197] Wiegleb, G., and Heitbaum, J. Semiconductor gas sensor for detecting NO and CO traces in ambient air of road traffic. *Sensors and Actuators: B. Chemical 17*, 2 (1994), 93–99.

[198] Williams, H. I. Carbon dioxide poisoning: Report of eight cases, with two deaths. *British Medical Journal 2*, 5103 (1958), 1012–1014.

[199] Wolfrum, E. J., Meglen, R. M., Peterson, D., and Sluiter, J. Metal oxide sensor arrays for the detection, differentiation, and quantification of volatile organic compounds at sub-parts-per-million concentration levels. *Sensors and Actuators B: Chemical 115*, 1 (2006), 322–329.

[200] Working Group on Strategies and Review. Draft guidelines for estimation and measurement of emissions of volatile organic compounds. Tech. Rep. December 2016, United Nations, Geneva, 2016.

[201] Zampolli, S., Elmi, I., Ahmed, F., Passini, M., Cardinali, G. C., Nicoletti, S., and Dori, L. An electronic nose based on solid state sensor arrays

for low-cost indoor air quality monitoring applications. *Sensors and Actuators, B: Chemical 101*, 1-2 (2004), 39–46.

[202] Zhang, H., Wang, S., Hao, J., Wang, X., Wang, S., Chai, F., and Li, M. Air pollution and control action in Beijing. *Journal of Cleaner Production 112* (2016), 1519–1527.

[203] Zhang, Q., Streets, D. G., He, K., and Klimont, Z. Major components of China's anthropogenic primary particulate emissions. *Environmental Research Letters 2*, 4 (2007).

[204] Zhang, X., Xue, Z., Li, H., Yan, L., Yang, Y., Wang, Y., Duan, J., Li, L., Chai, F., Cheng, M., and Zhang, W. Ambient volatile organic compounds pollution in China. *Journal of Environmental Sciences 55* (2017), 69–75.

[205] Zimmerman, N., Presto, A. A., Kumar, S. P. N., Gu, J., Hauryliuk, A., Robinson, E. S., and Robinson, A. L. A machine learning calibration model using random forests to improve sensor performance for lower-cost air quality monitoring. *Atmospheric Measurement Techniques 11*, 1 (2018), 291–313.

[206] Zimmerman, N., Presto, A. A., Kumar, S. P. N., Gu, J., Hauryliuk, A., Robinson, E. S., Robinson, A. L., and Subramanian, R. Closing the gap on lower cost air quality monitoring: machine learning calibration models to improve low-cost sensor performance. *Atmospheric Measurement Techniques Discussions*, 2 (2017), 1–36.